# Transactions of the ASME®

FLUIDS ENGINEERING DIVISION
Technical Editor
DEMETRI P. TELIONIS (1999)
Executive Secretary
PAT WHITE (1999)
Assistants to the Editor
N. W. SCHAEFFLER
J. E. POWELL
Calendar Editor
M. F. ACKERSON

Associate Technical Editors
P. R. BANDYOPADHYAY (1997)
S. BANERJEE (1999)
P. W. BEARMAN (1998)
M. N. DHAUBHADEL (1999)
J. EATON (1999)
F. GIRALT (1997)
J. A. C. HUMPHREY (1997)
F. HUSSAIN (1998)
J. KATZ (1998)
C. MERKLE (2000)
B. SCHIAVELLO (1999)
P. M. SOCKOL (1998)
M. W. SINDIR (1997)
M. SOMMERFELD (1999)
M. S. TRIANTAFYLLOU (1998)

BOARD ON COMMUNICATIONS
Chairman and Vice-President
R. MATES

OFFICERS OF THE ASME
President, KEITH B. THAYER
Exec. Director
D. L. BELDEN
Treasurer
J. A. MASON

PUBLISHING STAFF
Managing Director, Engineering
CHARLES W. BEARDSLEY
Director, Technical Publishing
PHILIP DI VIETRO
Managing Editor, Technical Publishing
CYNTHIA B. CLARK
Managing Editor, Transactions
CORNELIA MONAHAN
Production Assistant
MARISOL ANDINO

**Transactions of the ASME, Journal of Fluids Engineering** (ISSN 0098-2202) is published quarterly (Mar., June, Sept., Dec.) for $195.00 per year by The American Society of Mechanical Engineers, 345 East 47th Street, New York, NY 10017. Periodicals postage paid at New York, NY and additional mailing offices. POSTMASTER: Send address changes to Transactions of the ASME, Journal of Fluids Engineering, c/o THE AMERICAN SOCIETY OF MECHANICAL ENGINEERS, 22 Law Drive, Box 2300, Fairfield, NJ 07007-2300.
**CHANGES OF ADDRESS** must be received at Society headquarters seven weeks before they are to be effective. Please send old label and new address.
**PRICES:** To members, $40.00, annually: to nonmembers, $195.00. Add $40.00 for postage to countries outside the United States and Canada.
**STATEMENT from By-Laws.** The Society shall not be responsible for statements or opinions advanced in papers or . . . printed in its publications (B7.1, Par. 3).



**INDEXED** by Applied Mechanics Reviews and Engineering Information, Inc. Canadian Goods & Services Tax Registration #126148048.

# Journal of Fluids Engineering

**Published Quarterly by The American Society of Mechanical Engineers**

**VOLUME 119 • NUMBER 3 • SEPTEMBER 1997**


## Technical Papers


497 Technical Forum

499 Flow Past Large Obstructions Between Corotating Disks in Fixed Cylindrical Enclosures
Hiroshi Suzuki and Joseph A. C. Humphrey

506 Suppression of Fluid Forces Acting on a Square Prism by Passive Control
H. Sakamoto, K. Tan, N. Takeuchi, and H. Haniu

512 A Numerical Study of Vortex Shedding From a Square Cylinder With Ground Effect
Robert R. Hwang and Chia-Chi Yao

519 Application of Large Eddy Simulation to an Oscillating Flow Past a Circular Cylinder
Xiyun Lu, Charles Dalton, and Jianfeng Zhang

526 Prediction of Transpired Turbulent Boundary Layers With Arbitrary Pressure Gradients
Miodrag Oljaca and James Sucec

533 Effect of a Crossflow at the Entrance to a Film-Cooling Hole
K. A. Thole, M. Gritsch, A. Schulz, and S. Wittig

541 Turbulence Model for Steady and Unsteady Boundary Layers in Strong Pressure Gradients
E. Hytopoulos, J. A. Schetz, and R. L. Simpson

550 Calculation of Fully-Developed Turbulent Flow in Rectangular Ducts With Nonuniform Wall Roughness
M. Naimi and F. B. Gessner

559 Boundary Layer Excitation by Periodic Heating of a Thin Ribbon
B. A. Haven and M. E. Franke

562 Measurements in a Transitional Boundary Layer With Görtler Vortices (Data Bank Contribution)
R. J. Volino and T. W. Simon

569 Numerical Analysis of Turbulent Flow in Fluid Couplings
L. Bai, M. Fiebig, and N. K. Mitra

577 Effects of Efficiency Techniques on Accuracy of Dynamic-Overlapped Grids for Unsteady Flows
Guan-Wei Yen and Oktay Baysal

584 Numerical Experiments on Application of Richardson Extrapolation With Nonuniform Grids
Ismail Celik and Ozgur Karatekin

591 Shape of an Annular Liquid Jet
M. Z. Hasan, Y. Mitsutake, and M. Monde

597 Air Entrainment in the Developing Flow Region of Plunging Jets—Part 1: Theoretical Development
P. D. Cummings and H. Chanson

603 Air Entrainment in the Developing Flow Region of Plunging Jets—Part 2: Experimental (Data Bank Contribution)
P. D. Cummings and H. Chanson

609 The Influence of the Regulator Diameter and Injection Nozzle Geometry on the Flow Structure in Pneumatic Dimensional Control Systems
C. Crnojevic, G. Roy, A. Bettahar, and P. Florent

616 On the Influence of Liquid Elasticity on Mixing in a Vessel Agitated by a Two-Bladed Impeller
A. Youcefi, D. Anne-Archard, H. C. Boisson, and M. Sengelin

623 A Digital Particle Image Velocimetry Investigation of Flow Field Instabilities of Axial-Flow Impellers
K. J. Myers, R. W. Ward, and André Bakker

633 Visualization Measurement and Numerical Analysis of Internal Flow in Cross-Flow Fan
Hiromu Tsurusaki, Yoshinobu Tsujimoto, Yoshiki Yoshida, and Koichi Kitagawa

639 Prediction of Flow Behavior and Performance of Squirrel-Cage Centrifugal Fans Operating at Medium and High Flow Rates
R. J. Kind


(Contents continued on p. 532)

(Contents continued)


647 Theoretical Study of Pressure Fluctuations Downstream of a Diffuser Pump Impeller—Part 1: Fundamental Analysis on Rotor-Stator Interaction
W. Qin and H. Tsukamoto

653 Theoretical Study of Pressure Fluctuations Downstream of a Diffuser Pump Impeller—Part 2: Effects of Volute, Flow Rate, and Radial Gap
W. Qin and H. Tsukamoto

659 Development and Optimization of Screw Machines With a Simulation Model—Part I: Profile Generation
N. Stošić and K. Hanjalić

664 Development and Optimization of Screw Machines With a Simulation Model—Part II: Thermodynamic Performance Simulation and Design Optimization
K. Hanjalić and N. Stošić

671 Riser-Relief Valve Dynamic Interactions
K. K. Botros, G. H. Dunn, and J. A. Hrycyk

680 Tip Clearance and Tip Vortex Cavitation in an Axial Flow Pump
R. Laborde, P. Chantrel, and M. Mory

686 The Erosive Axial Collapse of a Cavitating Vortex: An Experimental Study
M. A. Dominguez-Cortazar, J. P. Franc, and J. M. Michel

692 Experimental Study of Deformation Mechanism of a Water Droplet Impinging on Hot Metallic Surfaces Above the Leidenfrost Temperature (Data Bank Contribution)
Natsuo Hatta, Hitoshi Fujimoto, Kenji Kinoshita, and Hirohiko Takuda

700 Two Types of Nonlinear Pressure-Drop Versus Flow-Rate Relation Observed for Saturated Porous Media (Data Bank Contribution)
J. L. Lage, B. V. Antohe, and D. A. Nield

707 A Two-Phase Cinematic PIV Method for Bubbly Flows
T. R. Oakley, E. Loth, and R. J. Adrian


## Technical Briefs


713 The Production of Shear Flow Profiles in a Wind Tunnel by a Shaped Honeycomb Technique
F. Ahmed and B. E. Lee

716 Analytical Solutions for the Developing Jet From a Fully-Developed Laminar Tube Flow
D. S. Lee, K. D. Kihm, and S. H. Chung

718 The Effect of Negative Spanwise Rotation on Dean Vortices
Liqiu Wang

721 New Parameters Describing Extra Straining Effects in Turbulence Models
Hyon Kook Myong

724 Developing Laminar Flow in Eccentric Annuli
Maged A. I. El-Shaarawi, Habib I. Abualhamayel, and Esmail M. A. Mokheimer

729 Discussion on a Previously Published Paper

730 Fluids Engineering Calendar


## Announcements and Special Notices


518 1999 ASME Mechanics and Materials Conference

525 Transactions Change of Address Form

732 Call for Papers—1998 Fluids Engineering Conference

736 Call for Symposium Papers—1998 Congress

738 Statement of Numerical Accuracy

738 Statement of Experimental Uncertainty

738 Access to the Electronic JFE

738 Submission of Papers

Journal of Fluids Engineering

Technical Forum

# Questions in Fluid Mechanics: Understanding Foams and Foaming

By D. D. Joseph[1]

Foams are common, complex, and not well understood. Most of the common foams are a two-phase medium of gas and liquid with a particular structure consisting of gas pockets trapped in a network of thin liquid films and Plateau borders. Some of the well-known foams are bubble baths, dishwater detergent foams, and the foam head on beer. Technologies impacted by foaming are widespread. Foams can be useful, from shampoos to the placement of sand in cracks in oil fields to increase secondary oil recovery. But foams can be undesirable in many chemical applications such as the high-temperature cracking of hydrocarbon oils, and unsightly downstream of paper mills. Foams are very hard to control. All foams are unstable, but some are more unstable than others, a subject in which our understanding is far from complete.

**What are the conditions required to create and maintain foams?** A foam cannot form in a pure liquid; surfactants are required. Foams are thermodynamically unstable; when left to rest they collapse. To create a foam it is necessary to introduce gas at a rate faster than the collapse rate of bubbles. The rates required to create foams depend on the foaming mixture and the means by which the gas is introduced. In dishwater the gas is stirred in by a water jet, in soda water an abrupt drop in pressure causes rising gas bubbles to foam, and foaming bubble reactors, in which gas and surfactant in water are continuously injected, will foam only when the gas velocity crosses a critical threshold for a fixed liquid velocity [1]. A general theory giving critical conditions for foam formation observed in practice has yet to be given.

**Where is the foam?** Foaming systems segregate under gravity, foam above and bubbly liquid below. The foam in foaming bubble reactors is created at a mysterious phase change interface between the foam and bubbly mixture across which the topology, gas fraction and velocities are sharply discontinuous. Foam fractions can be reduced to zero by increasing the liquid or decreasing the gas velocity to values below the foam threshold. The factors controlling the formation and position of such an interface are unknown. Even the interface below a head of beer drops when the beer foams strongly; beer drinkers know that there is a lot of liquid in the head stabilized by the alcohols and other surfactant in the beer. The so called "foamy" oils which produce anomously high rates of primary oil recovery are something like a very viscous beer in which the gas bubbles rise very slowly; when the bubbles rise fast enough, foam appears at the well head [2]. Since foams have ever so much gas, they are much lighter and rise to the top or are centrifuged to the center.

**What is the difference between foaminess and stability?** Creation and maintenance of foams are different; the former relates to foaminess and the latter to stability. Bad champagne foams even more strongly than beer under mild depressurization; but the champagne foams don't last long. We can get the same head on beer and champagne initially on depressurization, but champagne foam is much less stable. Devices for measuring foaminess have been described but theories for these devices are not known [3, 4]. Though there is a huge literature on the stability of foams, many questions remain unanswered.

**Surface Tension vs. Gibbs Elasticity** It is thought that small surface tension is required for good foaming systems but good foamers appear to correlate more strongly with the rate at which surface tension changes than how much it changes. People who study the stability of foams have come to realize that "Gibbs elasticity," which is related to surface tension gradients and Maragnoni effects, is even more important than the value of the tension [1, 4]. Gibbs elasticity measures the change of surface tension with area; a change in area induces a change of concentration, so that the measure combines deformation with material properties. The lowest tension in a surfactant mixture is realized when it saturates the surface. In the highly turbulent surfactant mixture the stretched portions of bubble surfaces desaturate and can absorb more; the saturation condition (CMC) seems not to enter into the dynamics. Many material properties enter into the creation and stability of foams; viscosity, density, diffusion and film thickness of the bulk liquid as well as a number of interfacial properties other than tension are relevant. It can be said that the collective action of all these factors is not understood.

**How are foams controlled with solid particles?** Defoaming literature [5] focuses on the action of hydrophobic liquids and solids in breaking aqueous foams. Silicon oils are effective but they degrade at the high temperatures found in commercial reactors. Hydrophobic particles break foam in laboratory tests, but even hydrophilic particles will suppress foam by fluidized bed mechanisms recently discovered [1]. The solid particles fluidize in the bubbly mixture below the foam, but not in the foam, they increase liquid holdup by bed expansion and greater wetted area. Suppression of foam with a fluidized bed is a new and practical idea which needs further study. The beneficial effects of fluidized particles are even greater when hydrophobic particles are used [6].

[1] Aerospace Engineering and Mechanics, University of Minnesota, 107 Akerman Hall, 110 Union St. SE, Minneapolis, MN 55455.

**Foams are non-Newtonian. What are their rheological properties?** Foam rheology is another important subject for applications which is not well understood. Foams can trap and immobilize small and light particles, showing that foams have an effective yield stress. This property makes foam a good drilling fluid for carrying away cuttings in oil-field drilling. When foam flows there is some kind of viscosity after yield, but particles won't circulate in the foam, and the foam itself does not circulate as an ordinary fluid. Foams have viscoelastic properties like polymer solutions; heavy particles driven into the foam by turbulence in the bubbly mixture fall back out of the foam lined up in a vertical chain of linked particles, characteristic of particle solutions. This kind of particle migration has not been discussed before. Complex and exotic, the true nature of foams has yet to be revealed.

**Acknowledgment** This work was supported by NSF (CTS), ARO (Math) and Intevep S. A. Lloyd Trefethen helped me to distill this short version of an earlier essay which is available on request.

## References

1 Guitian, J., and Joseph, D. D., "How Bubbly Mixtures Foam and Foam Control Using a Fluidized Bed," to be published, *J. Multiphase Flow,* 1997.

2 Maini, B., "Foamy Oil in Heavy Oil Production," *J. Canadian Petroleum Technology,* Vol. 35 (6), pp. 2–4, 1996.

3 Prud'homme, R. K., and Saad, S. A., (Eds.), "Foams: Theory Measurements, and Applications," *Surfactant Science Series,* Vol. 57, 1996.

4 Edwards, D. A., Brenner, H., and Wasan, D. T., *Interfacial Transport Processes and Rheology,* Butterworth-Heinemann, 1991.

5 Garrett, P. R., (Ed.), "Defoaming: Theory and Applications," *Surfactant Science Series,* Vol. 45, Marcel Dekker, Inc. 1993.

6 Mata, C., and Joseph, D. D., "Foam Control Using a Fluidized Bed of Hydrophobic Particles," to be published, *Int. J. Multiphase Flow,* 1997.

# Technological Competitiveness: A Fluids Engineers' Viewpoint

## Column 8—An Update by Jules L. Dussourd[1]

This is an update to earlier editorials on a topic that is just as timely today as it was some years ago when a visible surfacing of shortcomings in our technological competitiveness in fluid handling machines became apparent. At that time, our industry suffered a major loss in market share for these products to competitors overseas. Today, while we may feel good about our current booming economy, the rebound has not brought about a recapture of this market. Instead, it has drawn its strength from the blossoming out of the electronic industry, producing a proliferation of service jobs, albeit at the expense of manufacturing and fluids engineering jobs. Competitiveness in our fluids engineering based industry is still in need of a boost, just as much now as it did then.

A few years ago, to confront this issue, a broad based initiative was launched by the Fluids Engineering Division. Eventually, after much soul searching, the initiative led to the recognition that there was a need to direct more attention to the procedures going into the design of certain fluid based products.

This conclusion was reached through panel sessions and forums at ASME conferences and it was stated and publicized as white papers and editorials in this Journal. One proposed solution was a plan for more direct cooperation between universities' and industry's engineers with the ASME as a facilitator, thereby infusing into the design process an enhanced adeptness with analytical design tools. Another idea was based on the vision of enormous time savings, potentially possible if our basic technologies were made available to users through instantaneously exercisable software, through the good offices of the technical societies, in addition to the printed word in the Transactions.

Both recommendations dealt with design software in one form or another through the intermediary of the ASME and this in turn evoked issues of liability. This was pointed out early by the Board Committee on Technical Development. To address this issue, the ASME Committee on Legal Affairs was called upon and formally commissioned to deliver an opinion in '96.

At the '96 Congress and Exhibition in Atlanta this committee, on the strength of searches it had executed, not only rendered a favorable opinion but made the further recommendation that the ASME Council on Engineering look into the overall feasibility of a software based, as well as a Transactions based ASME as the way to the future. This is a revolutionary undertaking. Obviously, in addition to liability, there are other issues such as availability, standardization, quality, cost/benefit, and practicality.

If a positive recommendation to this proposal were to be made by the Council on Engineering, the users of the technologies thus disseminated by the ASME, could have instantaneous access, say through an ASME web site, to software giving direct numerical solutions to the theories developed by authors of papers at conferences, or to many of the often laborious solutions of basic engineering problems addressed in textbooks or in original papers. The ones to benefit from this service are the users, such as the product engineer developing his design or the applied researcher working on an advanced product for industry.

Now that the Council on Engineering has become involved, the original FED initiative is in the hands of the relevant ASME governing bodies for a decision about the need for an overall study. While this was one of the key elements of the original FED proposal to come under study, it is the more fundamental one and the one most likely to have a profound effect in enhancing the effectiveness of the design procedures going into industrial fluid machines.

With this development, the role of FED has been formally ended, at least for the time being. But continued individual support is hereby solicited to help ASME be a leader in reaching out into this future, taking advantage of the advances now revolutionizing all forms of communications. To sum up this initiative, it may be useful to recall that the fundamental charter of societies like the ASME calls for the dissemination of technological know-how by all effective means, not just through the publication of technical literature.

[1] Jules L. Dussourd & Associates, Fluids Engineering Consultants, Princeton, NJ 08540

**Foams are non-Newtonian. What are their rheological properties?** Foam rheology is another important subject for applications which is not well understood. Foams can trap and immobilize small and light particles, showing that foams have an effective yield stress. This property makes foam a good drilling fluid for carrying away cuttings in oil-field drilling. When foam flows there is some kind of viscosity after yield, but particles won't circulate in the foam, and the foam itself does not circulate as an ordinary fluid. Foams have viscoelastic properties like polymer solutions; heavy particles driven into the foam by turbulence in the bubbly mixture fall back out of the foam lined up in a vertical chain of linked particles, characteristic of particle solutions. This kind of particle migration has not been discussed before. Complex and exotic, the true nature of foams has yet to be revealed.

**Acknowledgment** This work was supported by NSF (CTS), ARO (Math) and Intevep S. A. Lloyd Trefethen helped me to distill this short version of an earlier essay which is available on request.

## References

1 Guitian, J., and Joseph, D. D., "How Bubbly Mixtures Foam and Foam Control Using a Fluidized Bed," to be published, *J. Multiphase Flow,* 1997.

2 Maini, B., "Foamy Oil in Heavy Oil Production," *J. Canadian Petroleum Technology,* Vol. 35 (6), pp. 2–4, 1996.

3 Prud'homme, R. K., and Saad, S. A., (Eds.), "Foams: Theory Measurements, and Applications," *Surfactant Science Series,* Vol. 57, 1996.

4 Edwards, D. A., Brenner, H., and Wasan, D. T., *Interfacial Transport Processes and Rheology,* Butterworth-Heinemann, 1991.

5 Garrett, P. R., (Ed.), "Defoaming: Theory and Applications," *Surfactant Science Series,* Vol. 45, Marcel Dekker, Inc. 1993.

6 Mata, C., and Joseph, D. D., "Foam Control Using a Fluidized Bed of Hydrophobic Particles," to be published, *Int. J. Multiphase Flow,* 1997.

# Technological Competitiveness: A Fluids Engineers' Viewpoint

## Column 8—An Update by Jules L. Dussourd[1]

This is an update to earlier editorials on a topic that is just as timely today as it was some years ago when a visible surfacing of shortcomings in our technological competitiveness in fluid handling machines became apparent. At that time, our industry suffered a major loss in market share for these products to competitors overseas. Today, while we may feel good about our current booming economy, the rebound has not brought about a recapture of this market. Instead, it has drawn its strength from the blossoming out of the electronic industry, producing a proliferation of service jobs, albeit at the expense of manufacturing and fluids engineering jobs. Competitiveness in our fluids engineering based industry is still in need of a boost, just as much now as it did then.

A few years ago, to confront this issue, a broad based initiative was launched by the Fluids Engineering Division. Eventually, after much soul searching, the initiative led to the recognition that there was a need to direct more attention to the procedures going into the design of certain fluid based products.

This conclusion was reached through panel sessions and forums at ASME conferences and it was stated and publicized as white papers and editorials in this Journal. One proposed solution was a plan for more direct cooperation between universities' and industry's engineers with the ASME as a facilitator, thereby infusing into the design process an enhanced adeptness with analytical design tools. Another idea was based on the vision of enormous time savings, potentially possible if our basic technologies were made available to users through instantaneously exercisable software, through the good offices of the technical societies, in addition to the printed word in the Transactions.

Both recommendations dealt with design software in one form or another through the intermediary of the ASME and this in turn evoked issues of liability. This was pointed out early by the Board Committee on Technical Development. To address this issue, the ASME Committee on Legal Affairs was called upon and formally commissioned to deliver an opinion in '96.

At the '96 Congress and Exhibition in Atlanta this committee, on the strength of searches it had executed, not only rendered a favorable opinion but made the further recommendation that the ASME Council on Engineering look into the overall feasibility of a software based, as well as a Transactions based ASME as the way to the future. This is a revolutionary undertaking. Obviously, in addition to liability, there are other issues such as availability, standardization, quality, cost/benefit, and practicality.

If a positive recommendation to this proposal were to be made by the Council on Engineering, the users of the technologies thus disseminated by the ASME, could have instantaneous access, say through an ASME web site, to software giving direct numerical solutions to the theories developed by authors of papers at conferences, or to many of the often laborious solutions of basic engineering problems addressed in textbooks or in original papers. The ones to benefit from this service are the users, such as the product engineer developing his design or the applied researcher working on an advanced product for industry.

Now that the Council on Engineering has become involved, the original FED initiative is in the hands of the relevant ASME governing bodies for a decision about the need for an overall study. While this was one of the key elements of the original FED proposal to come under study, it is the more fundamental one and the one most likely to have a profound effect in enhancing the effectiveness of the design procedures going into industrial fluid machines.

With this development, the role of FED has been formally ended, at least for the time being. But continued individual support is hereby solicited to help ASME be a leader in reaching out into this future, taking advantage of the advances now revolutionizing all forms of communications. To sum up this initiative, it may be useful to recall that the fundamental charter of societies like the ASME calls for the dissemination of technological know-how by all effective means, not just through the publication of technical literature.

[1] Jules L. Dussourd & Associates, Fluids Engineering Consultants, Princeton, NJ 08540

# Flow Past Large Obstructions Between Corotating Disks in Fixed Cylindrical Enclosures

**Hiroshi Suzuki**
Associate Professor,
Department of Mechanical Engineering,
Hiroshima University,
Japan

**Joseph A. C. Humphrey**
Professor and Dean,
Department of Mechanical Engineering,
College of Engineering,
Bucknell University,
Lewisburg, PA 17837

*Numerical calculations have been performed for isothermal, laminar, three-dimensional flow past one or two fixed obstructions radially aligned and symmetrically located between a pair of disks corotating in a fixed cylindrical enclosure. The single-obstruction cases respectively model the influence on the flow of (a) a magnetic head arm support and (b) an air lock. The dual-obstruction cases model the simultaneous presence of these two objects. The air lock produces an interdisk cross-stream plane blockage of 62 percent while the two head arm supports produce blockages of 31 percent and 62 percent, respectively. For the cases with the air lock and arm support simultaneously present, the circumferential angle between them is fixed to 40 or 80 deg. Velocity, pressure, shear stress and the disk torque coefficient are predicted mostly for a Reynolds number ($Re = \Omega R_2^2/\nu$) corresponding to 10,000, approximately, where $R_2$, $\Omega$, and $\nu$ are the disk radius, the disk angular velocity in rad/s, and the kinematic viscosity of air at 300 K, respectively. The calculations show that a large blockage significantly alters the interdisk flow characteristics by markedly raising the pressure ahead of an obstruction and accelerating the flow through the empty space around it. This induces a detached region of reversed flow ahead of the obstruction, quite distinct from that in its wake. The disk surface pressure distributions point to a potential source of dynamical instability in rotating disk flows with obstructions. By redefining the torque coefficient and Reynolds number to account for dual blockage effects the relationship between these two quantities generally follows the theoretical expression of Humphrey et al. (1992). It is shown that the bulk of the drag on an obstruction is form drag as opposed to friction drag.*

## Introduction

**Background to the Problem of Interest.** Rotating disk flows are relevant to a variety of industrial equipment including turbomachinery components, heat and mass exchangers and magnetic disk storage devices (MDSD). This investigation is concerned with the motion of air between corotating disks in a configuration approximating current miniaturized MDSD typical of the hard drives in some current workstations and desktop computers. However, because of the geometrical simplifications invoked, the study is of more general value.

Earlier work on the fluid mechanics of corotating disks in fixed enclosures typical of MDSD has been reviewed by Abrahamson et al. (1991) and Humphrey et al. (1991). The latter reference provides a taxonomy of possible flow fields according to, for example: geometry, whether the interdisk flow is obstructed or not, ventilated or not, and laminar or turbulent. The present investigation is concerned with the case of unventilated, obstructed, isothermal, laminar flow between a pair of disks corotating in a fixed, axisymmetric enclosure. The configuration of interest is shown in Fig. 1. It allows for the presence of one or two relatively large obstructions radially aligned along the midplane of the interdisk space. Although simplified by the assumption of a cylindrical enclosure to facilitate numerical analysis, the approximation is realistic in that it preserves the basic physics. The dimensions shown in the figure are typical of some current computer disk drives.

For a comprehensive analysis and more recent summary of the current state of understanding of unventilated, unobstructed, enclosed corotating disk flows, see Humphrey et al. (1995). The corresponding analysis for obstructed flows, the subject of this work, has not yet been performed. Notwithstanding, we note the experimental investigations by Abrahamson et al. (1989), Tzeng and Humphrey (1991), Hudson and Eibeck (1991), Usry et al. (1993), Gor et al. (1994), and Girard et al. (1995) using obstructions of rectangular cross-section. With reference to Fig. 1, obstruction blockage is defined here as $\beta = [tL]/[H(a + R_2 - R_1)]$ where $L$ ($=L_A$ or $L_t$) is the length of the obstruction in question. In particular, the measurements obtained by Tzeng and Humphrey and Usry et al. are for relatively thin (fin-shaped) obstructions with $7 \leq \beta \leq 16$ percent, while those obtained by Gor et al. are for thicker (block-shaped) obstructions with $\beta = 23$ percent and 46 percent. Tzeng and Humphrey show that the form drag on a thin obstruction increases non-monotonically with increasing obstruction length, and that for a fixed obstruction length it tends to an asymptotic limit with increasing Re. A comparison between the studies by Usry et al. and Gor et al. shows that for Re = 22,000 the rms of the streamwise velocity component 90 deg downstream of a thick obstruction, and at a radial location corresponding to the space between the obstruction tip and the hub, is two to three times larger than for a thin obstruction. Potential sources of unsteadiness in these flows include a rotationally driven shear instability originating near the enclosure wall (Humphrey et al.) and the presence of the obstruction. However, for flows with high Reynolds number and obstructions with $t/H > 0.75$, approximately, the primary source of unsteadiness will be shearing of fluid accelerating past the obstruction tip; see Abrahamson et al., Gor et al., and Girard et al.

Detailed analytical and/or numerical studies of the unobstructed flow between enclosed corotating disks typical of MDSD have been performed by Chang et al. (1989, 1990), Schuler et al. (1990) and Humphrey et al. (1992, 1995). However, we have been unable to uncover comparable numerical

Contributed by the Fluids Engineering Division for publication in the JOURNAL OF FLUIDS ENGINEERING. Manuscript received by the Fluids Engineering Division May 3, 1996; revised manuscript received December 12, 1996. Associate Technical Editor: O. Baysal.

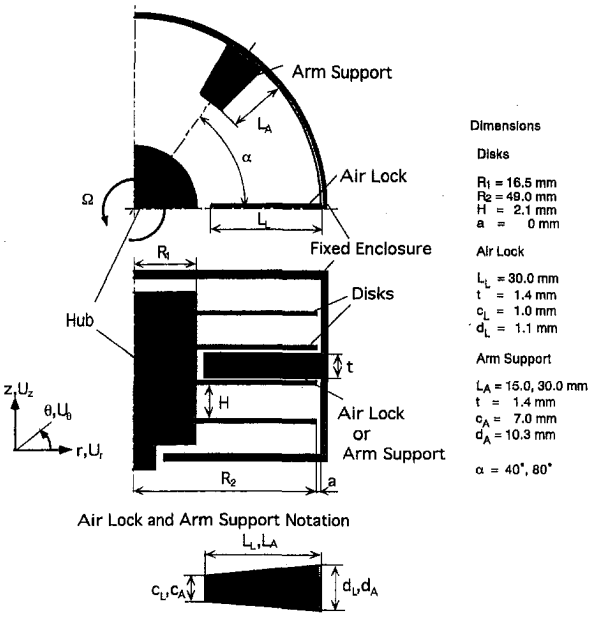


**Fig. 1 Flow configuration consisting of a stack of disks corotating in a fixed cylindrical enclosure. The figure shows two typical interdisk space obstructions (an air lock and an arm support), here drawn only between the center pair of disks. All relevant dimensions and the cylindrical coordinate system are defined.**

investigations for highly obstructed flow ($\beta > 50$ percent). Chang and Li (1990) present numerical results in qualitative agreement with the mean and rms circumferential velocity components measured by Tzeng and Humphrey (1995) in a mildly obstructed turbulent flow with $\beta \leq 16$ percent. Predictions of the cross-stream secondary flow reveal a complex recirculating motion immediately downstream of the obstruction. However, with increasing $\theta$ the fluid motion rapidly recovers the mean characteristics of an unobstructed flow. Because these results are for obstructions with $\beta$ much smaller than in current MDSD they are of limited interest or value to this study.

Time-averaged measurements of the disk torque coefficient, obtained by Daily and Nece (1960) in a single-disk geometry without obstructions, and by Hudson and Eibeck (1991) in disk stacks with single interdisk obstructions ranging in blockage from $\beta = 0$ to 60 percent, approximately, are the target of the theoretical analysis by Humphrey et al. (1992) spanning the laminar and turbulent flow regimes. They derive a general correlation with two adjustable coefficients capable of predicting energy dissipation to within ±11 to ±20 percent, depending on the number of disks in the stack. Critical to the universality of the correlation is the scaling of the characteristic velocity ($\Omega R_2$) by the quantity $(1 - [tL]/[HR_2])$ in their definition of a modified Reynolds number, $\mathrm{Re}_M$. The scaling accounts for the increase in dissipation due to flow acceleration in the space between the rotating hub and the obstruction tip. Thus, in that work $\mathrm{Re}_M = \mathrm{Re}/(1 - [tL]/[HR_2])$, a relation of special relevance to the interpretation of present predictions of the disk torque coefficient in the presence of obstructions.

**Objective of This Study.** We are concerned here with the numerical calculation of the three-dimensional flow in the space between the center pair of disks for the configuration shown in Fig. 1, with one or two obstructions present in the interdisk space. (Although not shown in the figure, equivalent obstructions are presumed to exist in the interdisk spaces above and below the center one, thus preserving reflection symmetry with respect to any disk not adjacent to the top or bottom of the enclosure.) One obstruction type corresponds to the magnetic head arm support typical of MDSD, the other to an air lock whose function is to release the magnetic head arm support when the disks start rotating.

The significance of this study lies in the fact that the obstructions investigated represent much larger blockages, especially in the axial direction, than investigated previously. As will be shown, in the case when the obstructions are simultaneously present the resulting flow is significantly altered relative to the single obstruction case. To our knowledge there is no experimental or numerical study corresponding to the highly obstructed flows of interest here, particularly for geometries with two obstructions simultaneously present.

It was stated above that the dimensions in Fig. 1 are typical of some current computer disk drives. Yet the aim of the industry is to produce even smaller devices with larger speeds of rotation. For a drive with dimensions equal to half those shown in the figure and rotating at 10,000 rpm the characteristic Reynolds number would be $\mathrm{Re} = 4 \times 10^4$, approximately. Using for guidance the experimental results of Daily and Nece (1960) for single disks rotating in fixed unobstructed enclosures, this value of Re is well below that required for transition to turbulence (which is $\mathrm{Re} > 1.5 \times 10^5$ when $H/R_2 > 0.05$). While the flow-shearing effects of an obstruction in the interdisk space might, in principle, lower the value of Re for transition, the small values of $H/R_2$ in current and, especially, future disk drives disallow major oscillations in the axial direction of the air flow in the wake of the obstruction. This, combined with large levels of damping through viscous dissipation, should work to stabilize the flow in the interdisk space. For these reasons we have focused on calculating the present configuration in the laminar flow regime, setting the highest value of Re accurately resolvable with the grid refinements available.

## Numerical Methodology

**Summary.** The CUTEFLOWS algorithm has been used to perform the numerical calculations of this study. Details of the code and of its testing are extensively documented in Humphrey et al. (1995) and the references therein. A summary of the finite differencing approach, the solution methodology and the code testing is provided here. Additional grid refinement tests conducted for the present investigation are discussed in the section on "Results and Discussion."

The numerical algorithm uses finite difference approximations of the exact conservation equations for mass, momentum and energy expressed in Cartesian or cylindrical coordinates and assuming incompressible, constant property flow. The difference equations are derived on a staggered grid using a control volume approach. The algorithm explicitly calculates the time evolution of primitive variables (velocity, pressure and temperature). The conservation equations are discretized in space employing a second-order accurate central differencing scheme for the diffusion and pressure terms, and a third-order accurate upstream weighted differencing scheme for the convection terms.

The set of time-dependent ordinary differential equations resulting for the velocity components at their respective grid locations is solved employing a second-order accurate Runge-Kutta algorithm. For this, the velocity field at each new time step is decomposed into two contributions, involving and not involving the pressure field, respectively. The pressure-less contribution to velocity is computed directly using an RK2 algorithm. The pressure contribution is calculated using the discrete Poisson equation for pressure that results from the imposition of the divergence-free condition for the velocity field at the end of each half-time step. In this calculation, the numerical advantages afforded by the conjugate gradient procedure makes it the solution method of choice.

The convergence of the numerical solution is assessed by monitoring the value of the total mass residual. The iteration sequence within a time step is terminated when this residual

falls below a preset value. Monitoring the time variation of the dependent variables at selected points in the flow establishes the rate of convergence of the algorithm towards a steady or steady-periodic solution.

The CUTEFLOWS algorithm has been subjected to numerous rigorous tests including the calculation of: (1) two-dimensional unsteady bluff body flows (Treidler, 1991; Tatsutani et al., 1993; and Li and Humphrey, 1995); (2) steady and unsteady rotating disk flows (Humphrey et al., 1992, 1995); (3) two backward-facing step benchmark problems corresponding to isothermal (Tatsutani et al., 1992) and nonisothermal (Iglesias et al., 1993) flow conditions, respectively; (4) two-dimensional wall-driven enclosure flows (Phinney and Humphrey, 1996). These tests have definitively established the goodness of the algorithm and provide guidance concerning the anticipated level of grid refinement necessary for the calculations of the present study.

**Calculation Conditions and Grid Testing.** Calculations were performed for the geometrical configuration and dimensions corresponding to the center pair of disks shown in Fig. 1, with the dimension of the gap between the disk rim and the enclosure wall, $a$, set equal to zero. This approximation greatly simplifies the implementation of boundary conditions and is justified by the findings of Humphrey et al. (1992) who show that integral quantities especially, such as the disk torque coefficient, are essentially independent of the quantity $a$ for values $a/R_2 < 0.08$. The majority of the calculations were performed with the disk speed of rotation fixed to 600 rpm, corresponding to Re = 9615. For the obstruction representing a magnetic head arm support two lengths were explored, $L_A/(R_2 - R_1) = 0.462$ and 0.923, corresponding to interdisk blockages of $\beta = 31$ and 62 percent, respectively. For the obstruction representing an air lock the length was $L_L/(R_2 - R_1) = 0.923$, corresponding to $\beta = 62$ percent. In the cases with both obstruction types simultaneously present in the interdisk space, the circumferential angle between them was fixed to $\alpha = 40$ or 80 deg. As shown in Fig. 1, the obstructions were tapered in the radial direction to conform with the cylindrical coordinate system used.

No-slip and impermeable wall boundary conditions were imposed for the three velocity components at all solid surfaces. Thus: $U_z = U_\theta = U_r = 0$ on all five surfaces of an obstruction and along the enclosure wall; $U_z = U_r = 0$ and $U_\theta = \Omega R_1$ at $R_1$, the rotating hub surface; and $U_z = U_r = 0$ and $U_\theta = \Omega r$ along both of the disk surfaces. Anticipating the possibility of time-dependent non-axisymmetric wavy solutions, of the type predicted by Humphrey et al. (1995) for unobstructed disk flows, calculations were performed for the whole interdisk space. However, both the test cases explored on the three grids tested, discussed below, and all of the cases calculated subsequently, converged to steady flows which were symmetric about the interdisk symmetry plane. Notwithstanding, initial calculation transients involving asymmetric meanderings of the flow across the symmetry plane precluded applying the grids used to a half interdisk space in order to increase numerical accuracy. (In fact, attempts to do this yielded unconverged results.) Therefore, all of the grid tests and subsequent calculation cases are for the entire interdisk space.

Nonuniform grids were employed to increase node densities in regions of steep velocity gradients in each of the coordinate directions (especially near surfaces and downstream of the obstructions) using grid expansion factors smaller than 1.2. The $(r, z, \theta)$ grids explored were (28, 28, 40), (28, 28, 57) and (34, 34, 50). The calculation time step used was $\Delta t = 10^{-5}$ s, yielding a maximum value of $\Delta z^2/\nu\Delta t \leq 36$ on the (28, 28, 57) grid. The calculations at Re = 9615 were always started from rest, with converged calculation times typically taking about 300 hours on a dedicated IBM RISC/6000. The calculations at higher Re were initiated using the converged results for the nearest lower value of Re.

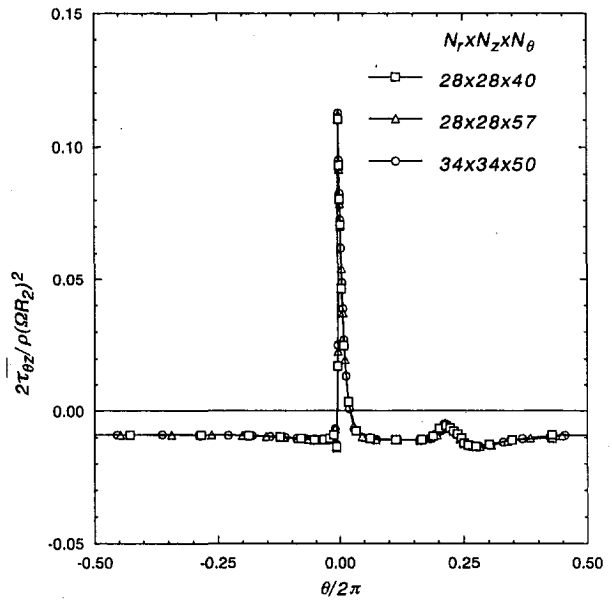


**Fig. 2 Circumferential variation of the radially averaged wall shear stress (circumferential component) plotted as a function of grid refinement. Calculations are for the case of two obstructions simultaneously present in the interdisk space: an air lock with $\beta = 62$ percent and a magnetic head arm support with $\beta = 31$ percent, separated by an angle $\alpha = 80$ deg.**

Of the additional grid refinement tests performed for this study, we present in Fig. 2 the results obtained for the circumferential variation of the radially averaged wall shear stress component, $\overline{\tau}_{\theta z}|_w = (R_2 - R_1)^{-1} \int_{R_1}^{R_2} \tau_{\theta z}|_w dr$. These calculations are for the case of two obstructions simultaneously present in the interdisk space: an air lock with $\beta = 62$ percent and a magnetic head arm support with $\beta = 31$ percent separated by an angle $\alpha = 80$ deg. These and other results for the average wall shear stress are discussed for their physical content further below, in the section on "Results and Discussion." Here we simply note the very small differences in $\overline{\tau}_{\theta z}|_w$ among the three grids explored. The same is true for detailed profiles of $U_z$, $U_\theta$, and $U_r$ provided in Humphrey and Suzuki (1996), henceforth referred to as H&S, for the same flow configuration and conditions, and calculated on the same grids, from which the distributions of $\overline{\tau}_{\theta z}|_w$ shown in Fig. 2 were derived. For example, for the $U_\theta$ component the profiles display differences ranging from 2 to 4 percent between the (28, 28, 40) and the (28, 28, 57) grids, and from 1 to 2 percent between the (28, 28, 57) and the (34, 34, 50) grids. Accordingly, all subsequent calculations upon which the data in Figs. 3 to 6 are based were performed using the (28, 28, 57) grid. This degree of grid refinement guaranteed between 4 and 8 nodes for resolving the rotating disk and fixed wall boundary layers of the flow. Although present calculations are not free of numerical diffusion, we estimate that the average inaccuracy of the field variables predicted on the (28, 28, 57) grid is less than 5 percent.

## Results and Discussion

This section presents primarily the results for two obstructions simultaneously present in the interdisk space. The complete set of results for single and dual obstructions is available in H&S. All of the cases calculated converged to steady flow solutions which were symmetric about the interdisk midplane and devoid of the circumferentially periodic foci of axial vorticity characteristic of unobstructed flows.

**Velocity.** Isocontours of the circumferential velocity component, $U_\theta$, calculated on the interdisk midplane are shown in Fig. 3 for the case of the air lock and an arm support simultane-

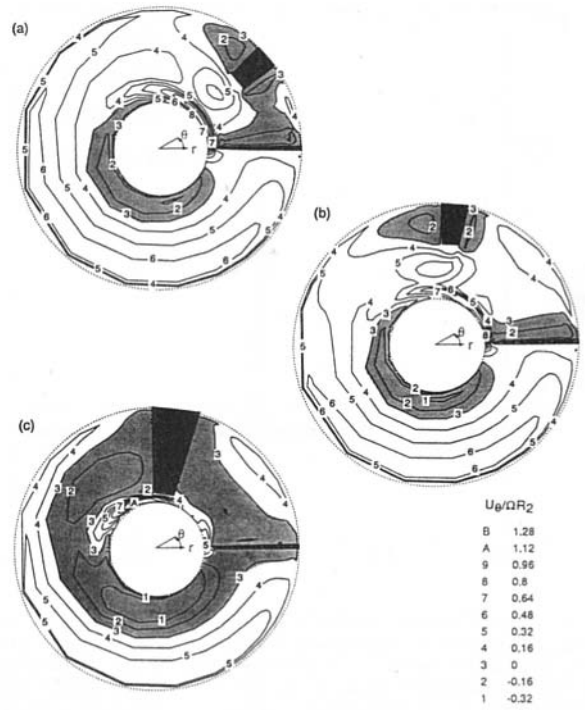


**Fig. 3 Isocontours of the circumferential velocity component in the interdisk midplane for the dual obstruction cases with: (*a*) $\alpha$ = 40 deg and $L_A/(R_2 - R_1)$ = 0.462 ($\beta$ = 31 percent); (*b*) $\alpha$ = 80 deg and $L_A/(R_2 - R_1)$ = 0.462 ($\beta$ = 31 percent); (*c*) $\alpha$ = 80 deg and $L_A/(R_2 - R_1)$ = 0.923 ($\beta$ = 62 percent). In all cases $L_L/(R_2 - R_1)$ = 0.923 ($\beta$ = 62 percent). Reversed flow regions are shown in gray.**

ously present in the flow. Both the effects of obstruction separation angle (Figs. 3(*a*) and 3(*b*)) and of arm support blockage (Figs. 3(*b*) and 3(*c*)) are illustrated. Not surprisingly, the contours reveal reversed flow regions ($U_\theta < 0$) immediately behind both obstructions. Unusual, however, is the new finding of a reversed flow region over a large fraction of the interdisk midplane (near the hub between $\theta$ = 180 and 350 deg, approximately, relative to the angular location of the air lock). This flow reversal was observed for all configurations involving the air lock, and for the case of the larger arm support when solely present. It was not observed for the case of the smaller arm support when solely present. The phenomenon is due to the combination of two effects. First, the presence of a large obstruction in the interdisk space induces a large pressure rise in the fluid approaching the obstruction relative to the fluid in its wake. Second, in passing through the gap between the hub and the tip of a large obstruction, the accelerating flow causes a large pressure reduction immediately downstream of the obstruction. These two effects combine to induce the flow reversal observed near the hub. Note, however, that because the disks and the hub rotate with positive $U_\theta$, there cannot be a true "separation" of the flow along any of these surfaces in the classical sense; that is, with the wall stress equal to zero somewhere along these surfaces.

Midplane contours of $U_\theta$ for the case of a single arm or lock obstruction (not shown here) reveal velocity flow patterns qualitatively similar to those shown in Fig. 3. The only configuration not displaying the region of flow reversal between $\theta$ = 180 and 350 deg was that corresponding to the smaller arm support. Consequently, we conclude that the generation of this type of flow reversal requires a minimum blockage of the interdisk space. While no attempt was made to determine this minimum blockage, its value lies between $L_A/(R_2 - R_1)$ = 0.462 ($\beta$ = 31 percent) and $L_A/(R_2 - R_1)$ = 0.923 ($\beta$ = 62 percent) for the geometrical and dynamical flow conditions investigated.

**Pressure.** Midplane pressure contours corresponding to the velocity results in Fig. 3, provided in H&S, illustrate the large pressure drops that arise in the flows past one and two obstructions, especially when their cross-sections are large. The effect is shown even more clearly by plotting the circumferential variation of the radially averaged pressure acting on a disk surface, $\bar{P}|_w = (R_2 - R_1)^{-1} \int_{R_1}^{R_2} P(\theta, r)|_w dr$, as a function of $\theta/2\pi$. The results are given in Figs. 4(*a*) and 4(*b*) where the reference pressure, $P_0$, is the value of $P$ at $\theta$ = 180°, $r = R_1$ and $z$ = 0. The circumferential variations of $\bar{P}|_w$, especially for single obstructions, are fairly self-explanatory. Except for the following remarks, they require no special elaboration. For the case of two obstructions simultaneously present, we note the marked difference between the shape of the $\bar{P}|_w$ profile when both obstructions are large relative to the other cases plotted. It is clear that the fluid trapped between two large obstructions remains

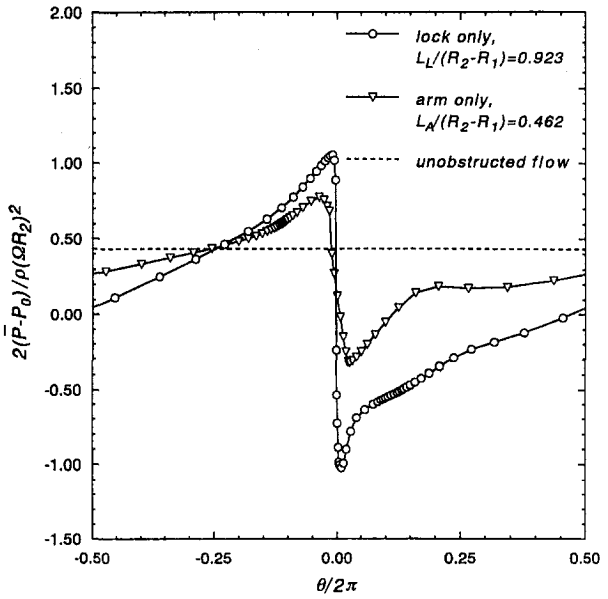


Fig. 4(*a*)

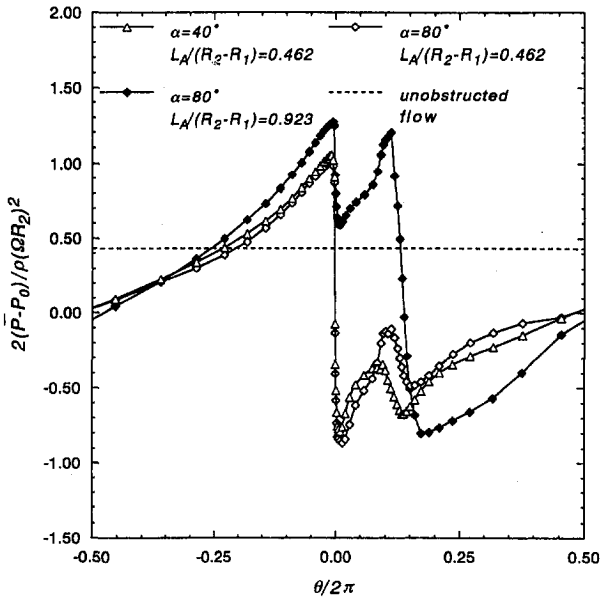


Fig. 4(*b*)

**Fig. 4 Circumferential variation of the radially averaged pressure on the surface of a disk with: (*a*) one obstruction and (*b*) two obstructions. Dashed line corresponds to unobstructed flow case.**

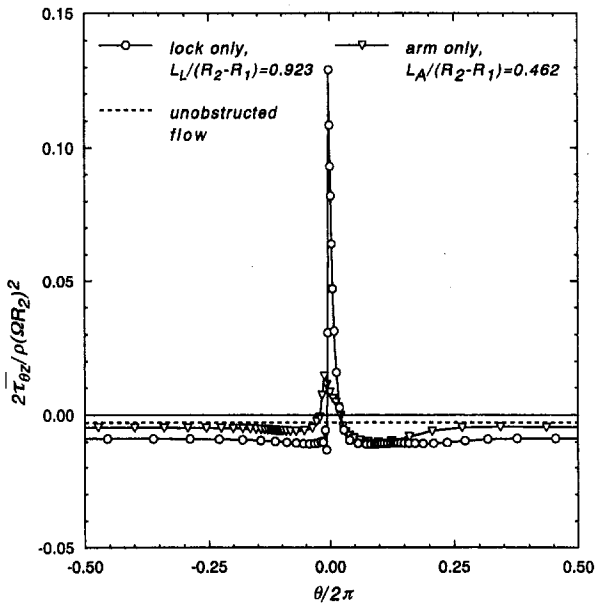


Fig. 5(*a*)

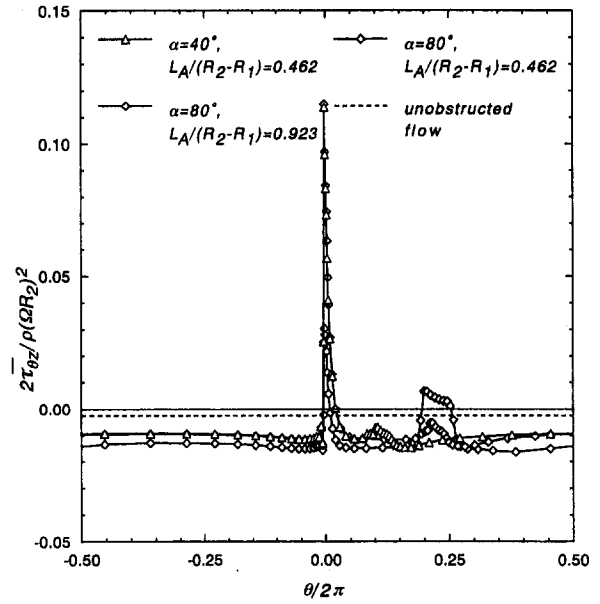


Fig. 5(*b*)

**Fig. 5 Circumferential variation of the radially averaged wall shear stress (circumferential component) on the surface of a disk with: (*a*) one obstruction and (*b*) two obstructions. Dashed line corresponds to unobstructed flow case.**

at relatively low velocity and maintains a corresponding high pressure. Of the two effects, blockage and separation angle, the former has the stronger influence on the distribution of $\bar{P}|_w$.

While the above are steady-state results, the circumferential variation of the radially averaged pressure points to a potential source of flow-driven dynamical instability in current MDSD. In all cases, some fraction of a disk surface experiences a larger pressure-induced force acting normal to it than the complementary fraction and, failing the existence of the exact (symmetrical) pressure distribution on the other surface of the same disk, a net torque will arise about an axis normal to the disk axis of rotation. In current MDSD, particularly at high Reynolds number, the flow in the obstructed interdisk space is expected to be unsteady, and phase differences between the instantaneous circumferential distributions of pressure acting on either side of a disk have the potential for inducing complex dynamical instabilities.

**Shear Stress.** Contour plots of the $\tau_{\theta z}$ component of stress acting on a disk surface are provided in H&S for one and two obstructions present in the interdisk space. Corresponding profiles of the radially averaged wall stress, $\bar{\tau}_{\theta z}|_w$, defined above, are plotted in Figs. 5(*a*) and 5(*b*) as a function of $\theta/2\pi$. In all cases the profiles show the disk dragging on the air that approaches an obstruction ($\bar{\tau}_{\theta z}|_w < 0$ for $\theta/2\pi < 0$). However, to get past an obstruction the bulk of the air must accelerate through the gap between the tip of the obstruction and the rotating hub. This causes the local speed of the air to exceed that of the disk with the consequence that $\bar{\tau}_{\theta z}|_w$ is positive in and downstream of this gap, the magnitude of $\bar{\tau}_{\theta z}|_w$ increasing with increasing blockage.

When two obstructions are present, the first is always the air lock and the initial increase in $\bar{\tau}_{\theta z}|_w$ is quite marked. Past the lock the flow decelerates and $\bar{\tau}_{\theta z}|_w$ reverts to a negative value. If the second obstruction is the large arm support with the same blockage as the lock, the flow is reaccelerated to the point that $\bar{\tau}_{\theta z}|_w$ becomes positive again. Otherwise, the value of $\bar{\tau}_{\theta z}|_w$ remains negative. These complicated variations in $\bar{\tau}_{\theta z}|_w$ are reflected in the distributions of the disk torque coefficient discussed next.

**Disk Torque Coefficient.** Calculations of the disk total torque coefficient, $C_M = 2T/\rho\Omega^2 R_2^5$, where $T = \int_0^{2\pi}\int_{R_1}^{R_2} \tau_{\theta z}|_w r^2 dr d\theta$ is the torque for one of the two disk surfaces, were performed for the various dual obstruction configurations with Re = 9615, and for the air lock on its own for three higher values of the Reynolds number. (Note that the hub surface contribution to $C_M$ amounted to less than 1 percent of that due to the disk surfaces for all the cases investigated.) The values for $C_M$ at Re = 9615 revealed large geometrically dependent differences; see H&S. However, it was found that these could be reduced by scaling velocity in the definitions of $C_M$ and Re as recommended in Humphrey et al. (1992) to account for the effect of flow acceleration due to the obstructions. Thus, redefining the Reynolds number as $\mathrm{Re}_M^* = \mathrm{Re}/[(1 - tL/HR_2)|_A(1 - tL/HR_2)|_L]^{1/2}$ and the torque coefficient as $C_M^* = C_M[(1 - tL/HR_2)|_A(1 - tL/HR_2)|_L]$ in order to conform to the theory in the limit of a very large and

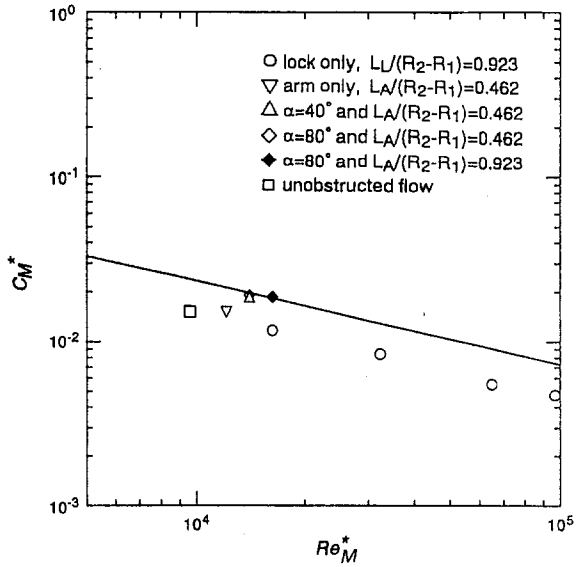


**Fig. 6 Variation of the modified disk torque coefficient, $C_M^*$, with the modified Reynolds number, $\mathrm{Re}_M^*$, for unobstructed and obstructed flow configurations. The solid line shows the variation predicted by theory, $C_M^* \propto \mathrm{Re}_M^{*-1/2}$.**

**Table 1 Form ($C_p = D_p/[1/2\rho(\Omega R_2)^2 tL_i]$) and skin friction ($C_f = D_f/[1/2\rho(\Omega R_2)^2 1/2(c_i + d_i)L_i]$) coefficients for the single and dual interdisk obstruction cases ($i = L$ or $A$) with Re = 9615. $D_p$ and $D_f$ are the sum total of the $\theta$-aligned pressure and the shear forces, respectively, acting on the surfaces of the obstructions.**

| Case | Lock | | Arm | |
|---|---|---|---|---|
| | $C_p$ | $C_f$ | $C_p$ | $C_f$ |
| Lock only with $L_L/(R_2 - R_1) = 0.923$ | 1.99 | 0.27 | — | — |
| Arm only with $L_A/(R_2 - R_1) = 0.462$ | — | — | 1.52 | 0.11 |
| Both with $\alpha = 40°$ and $L_A/(R_2 - R_1) = 0.462$ | 1.78 | 0.25 | 0.65 | 0.12 |
| Both with $\alpha = 80°$ and $L_A/(R_2 - R_1) = 0.462$ | 1.80 | 0.26 | 0.63 | 0.08 |
| Both with $\alpha = 80°$ and $L_A/(R_2 - R_1) = 0.923$ | 0.66 | 0.15 | 1.98 | 0.10 |

a very small obstruction simultaneously present, the results in Fig. 6 were obtained. The continuous line in the figure shows the expected theoretical variation which, according to the analysis of Humphrey et al. (1992), is of the form $C_M^* \propto \mathrm{Re}_M^{*-1/2}$ in the laminar flow regime. The air lock calculations display the $-\frac{1}{2}$ exponent dependence and, whereas the rescaling has significantly diminished geometrical dependent differences, these remain for the dual-obstruction cases pointing to the need for a more generally applicable correlation.

Values of the obstruction form drag ($C_p = D_p/[\frac{1}{2}\rho(\Omega R_2)^2 tL_i]$) and skin friction ($C_f = D_f/[\frac{1}{2}\rho(\Omega R_2)^2 \frac{1}{2}(c_i + d_i)L_i]$) coefficients ($i = L$ or $A$) are provided in Table 1 for each of the flow configurations explored with Re = 9615. In every case the bulk of the drag on either obstruction is form drag, but skin friction is not negligible. Inspection of the values in the table shows that placing an arm downstream of the lock works to lower both the form and friction drag on the lock, the total drag force reduction being as much as 64 percent (relative to the lock on its own) if the arm and lock are of the same (large) cross-section. It is also clear from these results that the form drag on the arm downstream of the lock is significantly reduced (relative to the arm on its own) if the arm is smaller than the lock. In contrast, when the arm and lock are of equal (large) cross-section, the form drag on the arm exceeds that of the lock by a factor of 3, approximately. These findings, including the unintuitive three-fold increase in form drag just mentioned, are readily explained by reference to the circumferential distributions of pressure plotted in Fig. 4*b*.

## Summary and Conclusions

The isothermal flow in the space between a pair of disks corotating in a cylindrical enclosure, with one or two obstructions present, has been investigated. Time-dependent, fully-elliptic, three-dimensional forms of the momentum and continuity equations were solved numerically with a procedure that is second-order accurate in both space and time. Careful grid refinement tests were performed, and in all cases the results converged to steady flow solutions which were symmetric about the interdisk midplane and devoid of the circumferentially periodic foci of axial vorticity characteristic of unobstructed flows.

The numerical study has been restricted to the laminar flow regime for three reasons: (1) because the trend in the disk drive industry is towards larger speeds of rotation ($\mathrm{Re} \propto \Omega$) but smaller geometries ($\mathrm{Re} \propto R_2^2$) with deliberately induced/controlled streamlined flow to minimize track misregistration; (2) to allow the necessary grid refinement to calculate the flow accurately and reveal correct physical trends; (3) to avoid the introduction of state-of-the-art turbulence models which have yet to be proven for this highly complex class of flows involving the coexistence of laminar and turbulent regions when $\mathrm{Re} > 10^5$, approximately.

The calculations reveal a strong geometrical dependence of the velocity field and its associated integral (derived) quantities. A striking finding is the presence of a detached region of reversed flow near the hub in the interdisk space upstream of an obstruction when its blockage is large. The geometrical dependence of the flow is also reflected in the form and friction drag coefficients of the obstructions, and the disk torque coefficient. Attempts to correlate the latter quantity via an extension of the correlation derived by Humphrey et al. (1992) were successful but point to the need to improve the estimate for the characteristic velocity in the correlation when two obstructions are simultaneously present in the interdisk space. The disk surface pressure distributions obtained suggest a potential source of dynamical instability in rotating disk flows with obstructions. This bears upon the major problem of track misregistration in MDSD and is the subject of continuing research.

## Acknowledgments

This investigation was initiated at the University of California at Berkeley. Partial support for the study was provided by Quantum Corporation, Milpitas, California. The bulk of the calculations were performed on a RISC6000 machine provided to JACH by the IBM Almaden Research Center in San Jose, California. HS gratefully acknowledges funding received from the Japanese Ministry of Education, Science and Culture, to support a sabbatical stay at the University of California at Berkeley. Thanks go to Dr. G. Li for his assistance in initiating the calculations.

## References

Abrahamson, S. D., Eaton, J. K., and Koga, D. J., 1989, "The Flow Between Shrouded Corotating Disks," *Physics of Fluids A*, Vol. 1, No. 2, pp. 241–251.

Abrahamson, S. D., Chiang, C., and Eaton, J. K., 1991, "Flow Structure in Head-Disk Assemblies and Implications for Design," *Advances in Information Storage Systems*, Vol. 1, pp. 111–132.

Chang, C. J. and Li, H., 1990, "Three-Dimensional Numerical Simulation of Flows for Corotating Disks," *Proceedings of the 1990 ASME International Computers in Engineering Conference and Exhibition*, ASME, New York, Vol. 2, pp. 387–392.

Chang, C. J., Schuler, C. A., Humphrey, J. A. C., and Greif, R., 1989, "Flow and Heat Transfer in the Space Between Two Corotating Disks in an Axisymmetric Enclosure," ASME *Journal of Heat Transfer*, Vol. 111, pp. 625–632.

Chang, C. J., Humphrey, J. A. C., and Greif, R., 1990, "Calculation of Turbulent Convection Between Corotating Disks in Axisymmetric Enclosures," *International Journal of Heat and Mass Transfer*, Vol. 33, pp. 2701–2720.

Daily, J. W., and Nece, R. E., 1960, "Chamber Dimension Effects on Induced Flow and Frictional Resistance of Enclosed Rotating Disks," ASME *Journal of Basic Engineering*, Vol. 82, p. 217.

Girard, J., Abrahamson, S., and Uznanski, K., 1995, "The Effect of Rotary Arms on Corotating Disk Flow," ASME JOURNAL OF FLUIDS ENGINEERING, Vol. 117, pp. 259–262.

Gor, D., Humphrey, J. A. C., and Greif, R., 1994, "Ventilated Flow Between Corotating Disks with Large Obstructions in a Fixed Cylindrical Enclosure," ASME JOURNAL OF FLUIDS ENGINEERING, Vol. 116, pp. 828–834.

Hudson, A., and Eibeck, P., 1991, "Torque Measurements of Co-Rotating Disks in an Axisymmetric Enclosure," ASME JOURNAL OF FLUIDS ENGINEERING, Vol. 113, pp. 648–653.

Humphrey, J. A. C., Chang, C. J., Li, H. W., and Schuler, C. A., 1991, "Unobstructed and Obstructed Rotating Disk Flows: A Summary Review Relevant to Information Storage Systems," *Advances in Information Storage Systems*, Vol. 1, pp. 79–110.

Humphrey, J. A. C., Schuler, C. A., and Iglesias, I., 1992, "Analysis of Viscous Dissipation in Disk Storage Systems and Related Flow Configurations," *Physics of Fluids A*, Vol. 4, pp. 1415–1427.

Humphrey, J. A. C., Schuler, C. A., and Webster, D. R., 1995, "Unsteady Laminar Flow Between a Pair of Disks Corotating in a Fixed Cylindrical Enclosure," *Physics of Fluids*, Vol. 7, pp. 1225–1240.

Humphrey, J. A. C., and Suzuki, H., 1996, "Numerical Calculation of Laminar Flow Past Large Obstructions Between Corotating Disks in Fixed Cylindrical Enclosures," Thermofluids Laboratory Report TF-96-02-01, Thermofluids Laboratory, Department of Aerospace and Mechanical Engineering, University of Arizona, Tucson.

Iglesias, I., Humphrey, J. A. C., and Giralt, F., 1993, "Numerical Calculation of Two-Dimensional Buoyancy-Assisted Flow Past a Backward-Facing Step in a Vertical Channel," *Computational Aspects of Heat Transfer, Benchmark Prob-*

*lems,* B. F. Blackwell and B. F. Armaly, eds., ASME, New York, HTD-Vol. 258, pp. 63–72.

Li, G., and Humphrey, J. A. C., 1995, "Numerical Modeling of Confined Flow Past a Cylinder of Square Cross-Section at Various Orientations," *International Journal of Numerical Methods in Fluids,* Vol. 20, pp. 1215–1236.

Phinney, L., and Humphrey, J. A. C., 1996, "Extension of the Wall-Driven Enclosure Flow Problem to Toroidally Shaped Geometries of Square Cross-Section," ASME JOURNAL OF FLUIDS ENGINEERING, Vol. 118, pp. 779–786.

Schuler, C. A., Usry, W., Weber, B., Humphrey, J. A. C., and Greif, R, 1990, "On the Flow in the Unobstructed Space Between Shrouded Corotating Disks," *Physics of Fluids A,* Vol. 2, 1760–1770.

Tatsutani, K., Devarakonda, R., and Humphrey, J. A. C., 1993, "Unsteady Flow and Heat Transfer for Cylinder Pairs in a Channel," *International Journal of Heat and Mass Transfer,* Vol. 36, pp. 3311–3328.

Tatsutani, K., Usry, W. R., and Humphrey, J. A. C., 1992, "Numerical Calculation of Two-Dimensional Laminar Flow and Heat Transfer for a Backward-Facing Step Using CUTEFLOWS," *Benchmark Problems for Heat Transfer Codes,* B. F. Blackwell and D. W. Pepper, eds., ASME, New York, HTD-Vol. 222, pp. 1–6.

Treidler, E. B., 1991, "An Experimental and Numerical Investigation of Flow Past Ribs in a Channel," Ph.D. thesis, University of California, Berkeley.

Tzeng, H., and Humphrey, J. A. C., 1991, "Corotating Disk Flow in an Axisymmetric Enclosure With and Without a Bluff Body," *International Journal of Heat and Fluid Flow,* Vol. 12, pp. 194–201.

Usry, W., Humphrey, J. A. C., and Greif, R., 1993, "Unsteady Flow in the Obstructed Space Between Disks Corotating in a Cylindrical Enclosure," ASME JOURNAL OF FLUIDS ENGINEERING, Vol. 115, pp. 620–626.

**H. Sakamoto**
Professor,
Department of Mechanical Engineering,
Kitami Institute of Technology,
Kitami, 090, Japan

**K. Tan**
Associate Professor,
Department of Mechanical Engineering,
Kushiro National College of Technology,
Kushiro, 084, Japan

**N. Takeuchi**
Graduate Student.

**H. Haniu**
Associate Professor.

Department of Mechanical Engineering,
Kitami Institute of Technology,
Kitami, 090, Japan

# Suppression of Fluid Forces Acting on a Square Prism by Passive Control

*Suppression of fluid forces acting on a square prism by passive control of the approaching flow was investigated in the present study. Flow was controlled using a small flat plate upstream of the prism. The position of the flat plate was varied within the range of $S/W = 0 \sim 3.0$ (S: distance between the flat plate and square prism, W: width of square prism) and the width h of the flat plate ranged from 2 mm to 8 mm ($h/W = 0.05 \sim 0.19$). Steady and unsteady fluid forces, vortex shedding frequency, and flow pattern were systematically investigated. The maximum reduction of time-averaged drag was 75 percent, and the maximum reduction in fluctuating lift and drag was 95 and 80 percent, respectively, using a flat plate $\frac{1}{10}$ of the size of the square prism.*

## 1 Introduction

The suppression of fluid forces and vortex shedding over a bluff body has received much attention, because practical applications are foreseen in various areas of engineering. Many methods for such suppression have been developed, and several have been successful (Zdravkovich, 1981). All previous methods have been designed to reduce fluid forces by controlling the separated shear layer and then suppressing the formation of the vortex. Many researchers have investigated the suppression of fluid forces acting on a circular cylinder, which is a fundamental bluff body configuration. However, little research has been conducted on the rectangular cylinder, which is an equally valid bluff body configuration. Bearman (1965) attempted to reduce time-averaged drag by fitting a splitter plate onto the rear of the rectangular cylinder. Both Lesage and Gartshore (1987) and Igarashi and Itoh (1993) reduced time-averaged drag by setting a small rod upstream of a square prism, and Sakamoto et al. (1991) reduced both the time-averaged and fluctuating fluid forces by inserting a small cylinder into the separated shear layer. However, most of this research has only investigated time-averaged drag, whereas research concerning the fluctuating fluid forces that act on rectangular cylinders is very rare. However, because fluctuating fluid forces can generate aerodynamic oscillation of bluff bodies, the suppression of fluctuating fluid forces is very important in engineering applications.

The aim of the present work was to reduce the fluid forces acting on a square prism by exerting passive control on an approaching flow using a small flat plate (hearafter referred to as the control plate) upstream of the square prism. The position and width of the control plate were varied systematically, and the magnitude of reduction of the steady and unsteady fluid forces was determined in order to identify the optimum position and width of the control plate. In addition, the mechanism of the flow control, the structure of the controlled wake, and the behavior of the controlled approaching flow are discussed in detail based on the vortex shedding pattern and visualized flow pattern around the square prism. The applicability of the present method for reducing fluid forces and suppressing vortex shedding is also evaluated.

## 2 Experimental Arrangement and Procedure

The experiments were performed in a low-speed, closed-circuit wind tunnel. The test section of the tunnel was rectangular, with a height of 0.6 m, a width of 0.4 m, and a length of 5.4 m. Two types of square prisms were used for the experiment: one with two load cells inside for the measurement of fluid forces, and another with a semiconductor pressure transducer inside for the measurement of static and fluctuating pressure. Both prisms had a width of 42 mm and a length of 400 mm, spanning the width of the test section of the wind tunnel. The prism used for the measurement of fluid forces consisted of an active section and a dummy section, as shown in Fig. 1. The load cells, attached with four semiconductor strain gauges, were installed inside the prism. The load cell installed in the active section measured the combination of fluid forces and other forces caused by vibration transmitted through the prism support. The load cell installed in the dummy section only measured the forces caused by the vibrations. The fluid forces alone were determined by subtracting the output of the load cell installed in the dummy section from that of the load cell installed in the active section. The width $h$ of the control plate was 2, 3, 4, 5, 6, and 8 mm ($h/W = 0.05 \sim 0.19$). The control plate was set in tension on the centerline upstream of the square prism, as shown in Fig. 2. No vibration of the control flat plate was generated during measurement.

Experiments were performed at a constant free-stream velocity of $U_o = 20$ m/s. The position of the control plate was varied within the range of $S/W = 0 \sim 3.0$ along the centerline ($y = 0$) upstream of the prism. The corresponding Reynolds number, Re ($=U_oW/\nu$), was $5.6 \times 10^4$. The turbulence intensity of the freestream was below 0.2 percent. The flow on the axial plane through the mid-section of the prism was visualized using smoke. Important symbols and the definition of the coordinate system used in the present study are shown in Fig. 2. The blockage effect of the test prism was 7 percent, and was not corrected.

Contributed by the Fluids Engineering Division for publication in the JOURNAL OF FLUIDS ENGINEERING. Manuscript received by the Fluids Engineering Division February 13, 1996; revised manuscript received February 11, 1997. Associate Technical Editor: M. S. Triantafyllou.

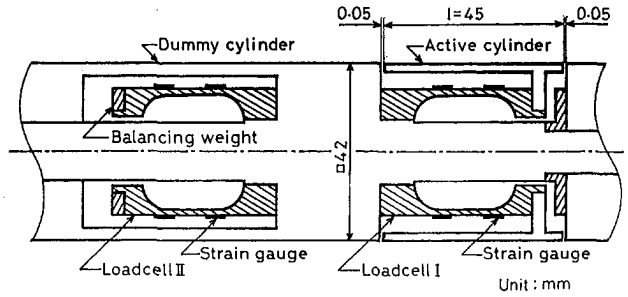


Fig. 1 Arrangement of load cell installed in square prism

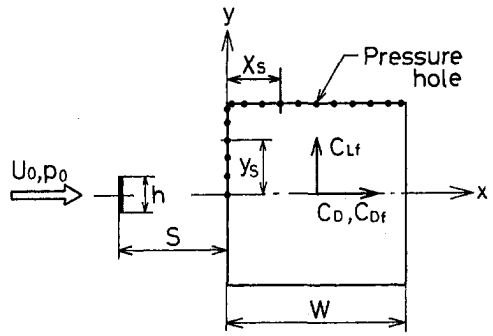


Fig. 2 Definition sketch and coordinate system

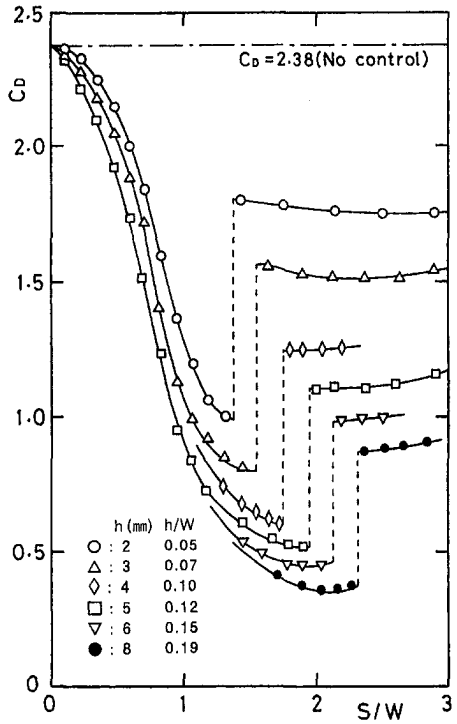


Fig. 3 Time-averaged drag coefficient for different spacings $S/W$ and widths $h$ of control plate. (Uncertainty in $C_D$: within ±3 percent.)

## 3 Results and Discussion

**3.1 Control of Time-Averaged Drag.** Figure 3 shows the relationship between the time-averaged drag coefficient $C_D$ and the position of the control plate $S/W$ on the centerline ($y = 0$) upstream of the square prism in relation to the varying width of the control plate within the range of 2 mm to 8 mm ($h/W = 0.05 \sim 0.19$). The value of $C_D$ decreases as both the distance between the control plate and the square prism $S/W$ and the width of the control plate increase. Thus, the optimum position of the control plate that minimizes the value of $C_D$ could be determined for each control plate width. Furthermore the matter to which notice should be paid with respect to the distribution of $C_D$ is that the value of these is drastically changed, i.e., a so-called jump phenomenon is observed in the value of $C_D$ within a specific range of $S/W$ for every width of the control plate. The jump phenomenon is also observed when two square prisms or circular cylinders with the same dimensions are arranged in tandem (Sakamoto and Haniu, 1988; Arie et al., 1983). The observation of this phenomenon with two bodies in tandem having a size ratio of less than 1/10 and different configurations is interesting.

The maximu drag reduction values $(C_{D0} - C_D)/C_{D0}$ ($C_{D0}$: time-averaged drag coefficient without control plate) are shown in Table 1. The maximum reduction of time-averaged drag is approximately 80 percent when the size of the control plate is approximately $\frac{1}{10}$ that of the square prism. Previously, the authors (1994) reduced the time-averaged drag of a square prism to approximately 30 percent by directly controlling the separated shear layer with the use of small flat plates $\frac{1}{10}$ of the size of the prism, suggesting that indirect control of the separated shear layers by changing the characteristics of the approaching flow is more effective than direct control of these separated shear layers.

Table 1 Maximum reduction in $C_D$ for different widths of control plate

| Width of control flat plate h | 2 mm | 3 mm | 4 mm | 5 mm | 6 mm | 8 mm |
|---|---|---|---|---|---|---|
| Size ratio of control plate and square prism h/w | 0.048 | 0.071 | 0.095 | 0.119 | 0.143 | 0.191 |
| Maximum values of drag reduction | 58 % | 66 % | 75 % | 79 % | 82 % | 85 % |

## Nomenclature

$A$ = projected area of active section of prism
$C_D$ = time-averaged drag coefficient of prism = $D/(0.5\ \rho U_o^2 A)$
$C_{Df}$, $C_{Lf}$ = r.m.s drag and lift coefficient = $\sqrt{D_f^2}$, $\sqrt{L_f^2}/(0.5\rho U_o^2 A)$
$C_{DT}$ = time-averaged total drag coefficient = $C_D + (h/W)C_{Dh}$
$C_{Dh}$ = time-averaged drag coefficient of control plate = $D_h/(0.5\rho U_o^2 h)$
$C_p$ = time-averaged pressure coefficient = $(p - p_o)/(0.5\rho U_o^2)$
$C_{pb}$ = time-averaged base pressure coefficient = $(p_b - p_o)/(0.5U_o^2)$
$C_{pf}$ = r.m.s pressure coefficient = $\sqrt{p_f^2}/(0.5\rho U_o^2)$
$D$, $D_h$ = time-averaged drag acting on prism and control plate
$D_o$ = time-averaged drag acting on prism without control plate
$D_T$ = time-averaged total drag including control plate
$D_f$, $L_f$ = fluctuating drag and lift acting on prism
$h$ = width of control plate
$p_b$ = base pressure acting on prism
$p_f$ = fluctuating pressure acting on prism
$p_o$, $U_o$ = static pressure and velocity of free-stream
$S$ = spacing between prism and control plate
$W$ = width of prism
$x_s$, $y_s$ = position of piezometric holes of surface of prism
$\gamma_1$, $\gamma_2$ = average time interval of modes 1 and 2

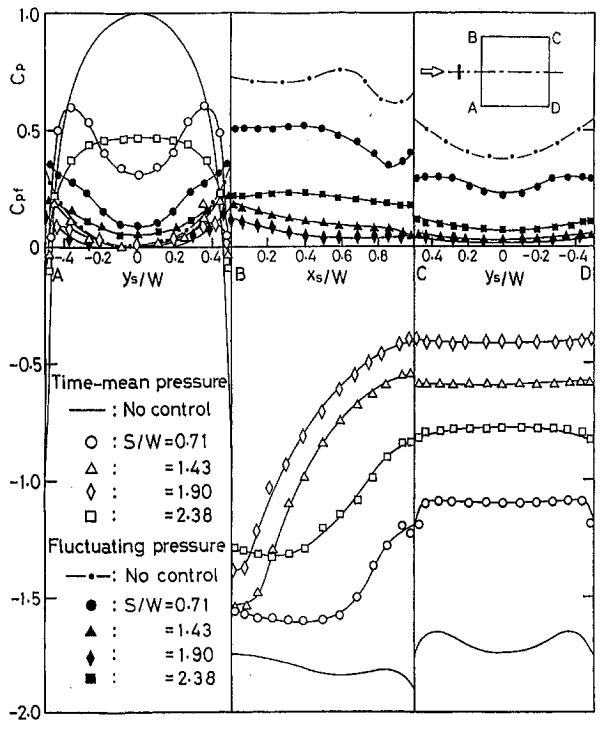


**Fig. 4 Distribution of time-averaged pressure coefficient and r.m.s. pressure coefficient. (Uncertainty in $C_p$ and $C_{pf}$: within ±3 percent.)**

Koenig and Roshko (1985) studied the time-averaged drag of the forward portion of a circular cylinder, the axis of which was parallel to a wind-tunnel freestream and which was shielded by a disk placed coaxially upstream of the flat face of the cylinder. They reported that the drag of the forward portion of a circular cylinder decreases from 0.72 to 0.01 under optimum conditions of the disk diameter and gap, and for such optimum shielding the stream surface which separates from the disk reattaches smoothly onto the front edge of the cylinder, in what is formed a cavity flow. In the present method, although the control plate upstream of the prism produces a shielding effect, the drag reduction of the drag is caused by a decrease in the base pressure value on the rear surface of the square prism rather than the shielding effect of the control plate because the rolling-up of the shear layer from the trailing edge is very weak. Therefore the present method is essentially different from that of Koenig and Roshko.

Figure 4 shows the distribution of the time-averaged pressure coefficient $C_p$ and that of the fluctuating pressure coefficient $C_{pf}$ on the square prism when a control plate with a width of $h$ = 5 mm was positioned at $S/W$ = 0.71, 1.43, 1.90, and 2.38. When the control plate was positioned at a distance smaller than $S/W$ = 1.95, where the jump phenomenon occurs, the flow that separated from the control plate reattached to the front surface of the square prism, and a quasi-stationary vortex region formed between the two bodies. As a result, the front surface of the square prism was exposed to the vortex region, and the pressure value on the front surface decreased. Specifically, $C_p$ and $C_{pf}$ on the front surface of the square prism reached a minimum at approximately $S/W$ = 1.90, immediately before the jump phenomenon occurs. In the range exceeding the jump phenomenon range, the value of $C_p$ on the front surface is considerably smaller than that without the control plate due to the influence of the wake of the control plate. In addition, the base pressure coefficient on the rear surface of the square prism is very small at any $S/W$ value because the rolling-up of the shear layer from the trailing edge is weak. The base pressure value also reaches its minimum immediately before the jump phenomenon range, and begins to recover at distances that exceed the jump phenomenon range. Furthermore, because the time-averaged pressure acting on the front surface is reduced from 0.7 to 0.1 by the shielding effect of the control plate, the contribution of the shielding effect of the control plate to the reduction of the time-averaged drag is about 30 percent. On the other hand, since the base pressure acting on the rear surface is reduced from 1.7 to 0.4, the contribution to the reduction of the time-averaged drag is about 70 percent. Therefore the reduction of the time-averaged drag is caused by the decrease of the base pressure value rather than the sheilding effect of the control plate.

**3.2 Control of Fluctuating Fluid Forces and Vortex Shedding.** Figures 5 and 6 show the r.m.s. values of the fluctuating lift coefficient $C_{Lf}$ and the drag coefficient $C_{Df}$ when the position $S/W$ and the width $h$ of the control cylinder are varied within the ranges of $S/W = 0 \sim 3.0$ and $h = 2 \sim 8$ mm, respectively. The maximum reductions of $C_{Lf}$ and $C_{Df}$ for each width of the control plate are shown in Table 2. $C_{Lf}$ and $C_{Df}$ are lowest immediately before the jump phenomenon range. The maximum reductions of $C_{Lf}$ and $C_{Df}$ are approximately 95 and 80 percent, respectively, with a control plate as large as $\frac{1}{10}$ of the size of the square prism. Thus, fluctuating fluid forces can be almost entirely suppressed using a control plate that is considerably smaller than the square prism. $C_{Lf}$ and $C_{Df}$ begin to recover in the range of $S/W$ beyond the jump phenomenon range, but remain considerably smaller than without the control plate. For example, with a control plate of $h$ = 8 mm ($h/W$ = 0.19), the reduction of $C_{Lf}$ is 90 percent. Thus, $C_{Lf}$ is almost entirely suppressed even if the control plate is located in the $S/W$ range beyond the jump phenomenon range.

Figure 7 shows the waveforms and the power spectrum distribution of the fluctuating lift using a control plate with width $h$ = 3 mm ($h/W$ = 0.07). As shown in Fig. 7($c$) and ($d$), in the vicinity of the jump phenomenon range, no distinct spectrum peak value was observed. Fluctuating lift is caused by the Karman vortex formed downstream of the square prism. Therefore, it can be concluded that alternate vortex shedding is perfectly restricted immediately before the jump phenomenon range. Another notable feature is that when a control plate was positioned

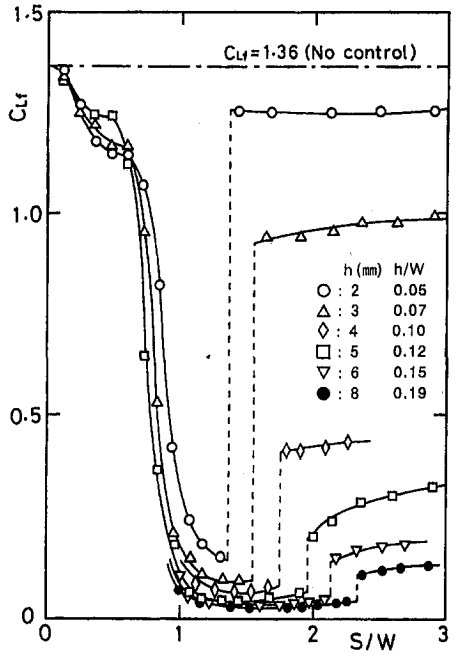


**Fig. 5 R.m.s. lift coefficient for different spacings $S/W$ and widths $h$ of control plate. (Uncertainty in $C_{Lf}$: within ±3 percent.)**

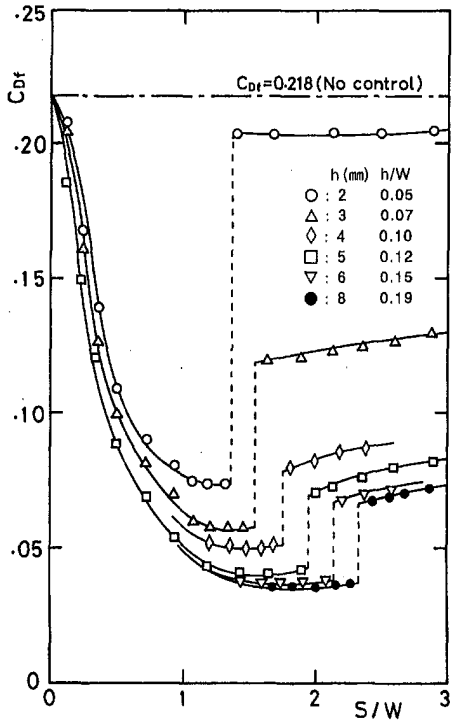


**Fig. 6 R.m.s. drag coefficient for different spacings $S/W$ and widths $h$ of control plate. (Uncertainty in $C_{Df}$: within ±3 percent.)**

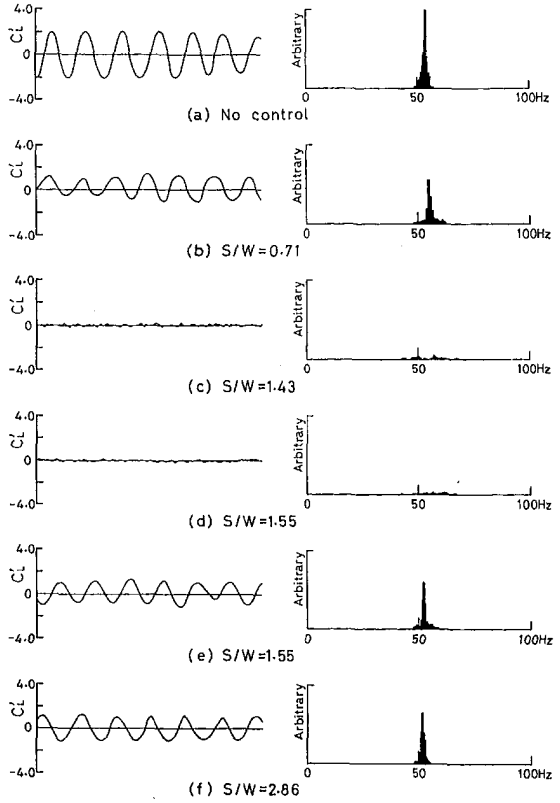


**Fig. 7 Waveform and power spectrum of fluctuating lift**

at $S/W = 1.55$ both a large and a small amplitude signal of fluctuating lift were observed as shown in Fig. 7($d$) and ($e$). Thus, a bistable phenomenon occurs when the control plate is located within the jump phenomenon range. This phenomenon is also observed with two square prisms or circular cylinders in a tandem arrangement, and is interesting in relation to flow instability.

**3.3 Classification of Controlled Flow Patterns.** Figure 8 shows schematic sketches of the three different flow patterns observed at different positions of the control plate. Pattern A is generated in the range from $S/W = 0$ to the distance $S/W$ at which the formation of the Karman vortex street begins to be perfectly suppressed. In this pattern, one of the separated shear layers of the control plate attached to the front surface of the square prism rolls in between the bodies to form a quasi-stationary vortex region, and the others flow out along the side surface of the square prism. The rolling-up of the shear layer separated from the square prism is weak, whereby the formed Karman vortex becomes fairly obscure. Pattern B is generated at the $S/W$ distance immediately before the jump phenomenon range. In this pattern, the suppression of fluctuating fluid forces is caused by the formation of a flow pattern in which the shear layer that separated from the control plate attaches to both sides of the front surface of the square prism. One flows into the quasi-stationary region formed between the two bodies, and the other again separates from the leading edge of the square prism. The small-scale vortices conveyed by the shear layer separated from the leading edge are diffused in the course of transportation due to interference with the wake of the control plate, and dissipate instead of becoming a large-scale Karman-type vortex. This suppression of Karman vortex formation reduces the fluctuating fluid forces acting on the square prism. Pattern C is generated at $S/W$ distances beyond the jump phenomenon range. In this pattern, Karman vortex streets are formed behind both the control plate and the square prism. However, since the position of the rolling-up of the shear layer of the square prism recedes downward due to turbulent diffusion, the fluid forces become smaller than without the control plate.

Figure 9 shows observed smoke patterns at different positions of a control plate with a width of 4 mm. The Reynolds number $Re = 6.5 \times 10^3$ employed in this observation is smaller than the $5.6 \times 10^4$ adopted for the measurement of fluid forces, but this difference does not influence qualitative evaluation. In the flow visualization shown in Fig. 9($a$), without a control plate, the formation of a Karman vortex street is clearly observed. The flow visualization shown in Fig. 9($b$) is pattern A. The shear layers of the control plate are attached to the front surface

**Table 2 Maximum reductions in $C_{Lf}$ and $C_{Df}$ for different widths of control plate**

| Width of control flat plate h | 2 mm | 3 mm | 4 mm | 5 mm | 6 mm | 8 mm |
|---|---|---|---|---|---|---|
| Size ratio of control plate and square prism h/w | 0.048 | 0.071 | 0.095 | 0.119 | 0.143 | 0.191 |
| Maximum values of fluctuating lift reduction | 90 % | 93 % | 95 % | 97 % | 98 % | 98 % |
| Maximum values of fluctuating drag reduction | 68 % | 76 % | 78 % | 82 % | 83 % | 83 % |

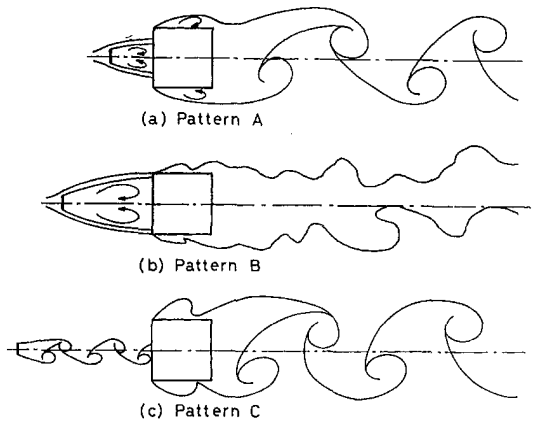


**Fig. 8 Classification of controlled wake flow patterns**

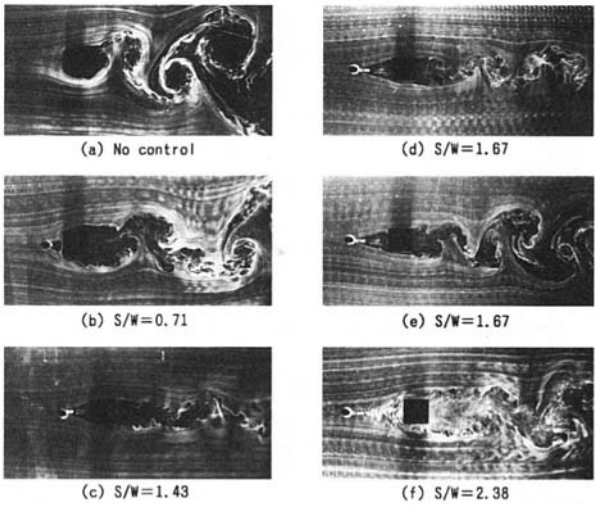


**Fig. 9 Smoke patterns of wake flow for different positions of control plate**

of the square prism, and the front surface of the prism is exposed to the wake of the control plate within a considerable range. The position of the rolling-up of the shear layers separated from the square prism recedes downward, and the width of the wake becomes narrower than without the control plate. The flow visualization shown in Fig. 9($c$) is pattern B, in which alternate vortex shedding from the square prism is perfectly suppressed. The flow visualization shown in Fig. 9($f$) is pattern C, generated with the control plate in the region beyond the jump phenomenon range. Alternate vortex shedding is observed behind either the square prism or the control plate. The flow patterns shown in Fig. 9($d$) and ($e$) are generated with the control plate in the jump phenomenon range. This pattern is slightly different from that observed during the measurement of fluid forces, due to a different Reynolds number. Both pattern B and pattern C are clearly observed.

**3.4 Characteristics of the Flow in the Jump Phenonenon Range.** Figure 10($a$) shows a sample time history of the pressure fluctuation on the side surface of the square prism

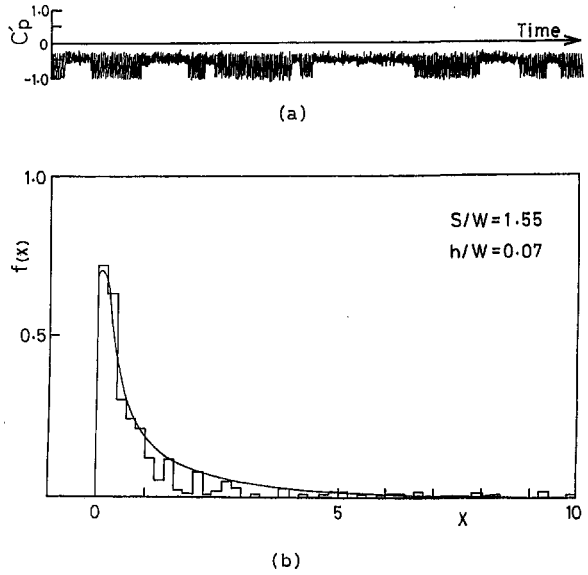


**Fig. 10 Switching of flow occured in jump phenomenon range. (*a*) Sample record of pressure fluctuation on side surface of prism. (*b*) Probability density distributions of intervals during which mode 1 prevails.**

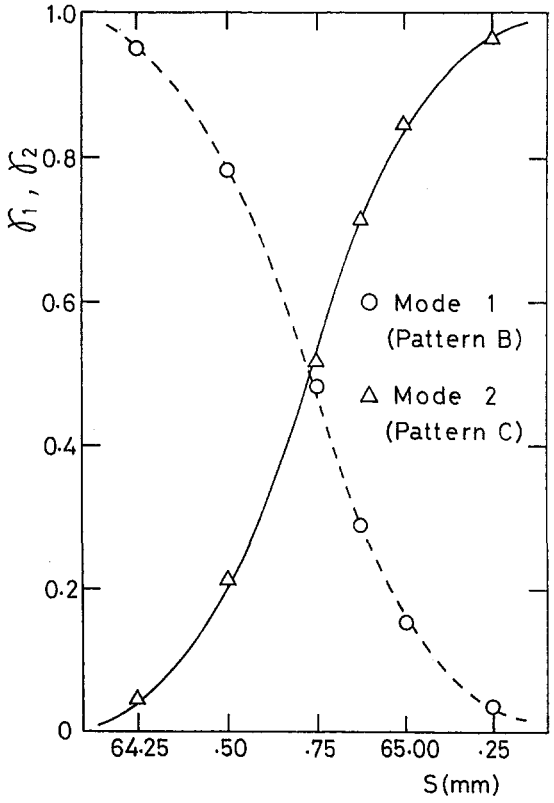


**Fig. 11 Average time intervals of modes 1 and 2**

when a control plate with a width of $h = 3$ mm is located within the jump phenomenon range, at $S/W = 1.55$. A switching phenomenon is observed in the flow mode of this region. Little pressure fluctuation is observed in pattern B (mode 1), in which no vortex shedding is created, whereas large pressure fluctuation is observed in Pattern C (mode 2), in which vortex shedding is created. Kim and Durbin (1988) investigated the statistical properties of the mode-switching phenomenon of flow around a pair of circular cylinders arranged side-by-side in a uniform flow, and reported that the probability density distributions of the time intervals of the individual modes are approximately represented by a Gamma distribution. Figure 10($b$) shows likewise the probability density distributions of the time intervals for pattern B generated with the control plate in the jump phenomenon range. The distributions are approximately represented by the Gamma distribution

$$f(x) = \frac{\lambda}{\Gamma(r)}(\lambda x)^{r-1}e^{-\lambda x} \tag{1}$$

where $x = t/T$ ($T$: the average time duration of pattern B), and $r$ and $\lambda$ are constants related to the mean value $x_m$ ($=1$) and the variance $x_{var}$ of $x$ by $x_m = r/\lambda$ and $x_{var} = r/\lambda^2$. Figure 11 shows the fractions of time during which mode 1 or mode 2 prevailed, denoted as $\gamma_1$ and $\gamma_2$ ($\gamma_1$: mode 1, $\gamma_2$: mode 2), respectively. In the middle of the jump phenomenon range, at $S = 64.75$ mm, modes 1 and 2 occured at the same probability.

Figure 12 shows the interval $S_c/h$ between the two bodies where the switching phenomenon began to appear for varying widths of the control plate. The interval $S_c/h$ is expressed by the following equation:

$$Sc/h = W/h + 8.0 \tag{2}$$

**3.5 Optimum Width of the Control Plate.** As described in Sections 3.1 and 3.2, fluid forces, and especially of time-averaged drag decrease as the width of the control plate in-

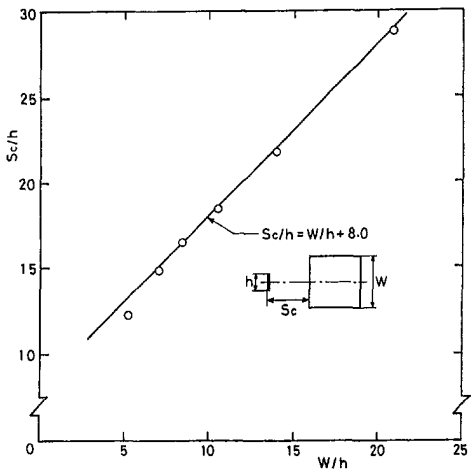


**Fig. 12 Spacing occured jump phenomenon**

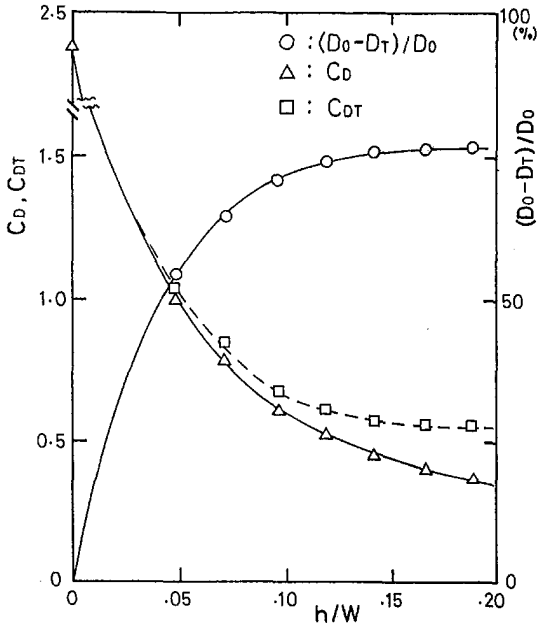


**Fig. 13 Minimum values of time-averaged drag of prism and total drag including control plate**

creases. However, provided that the drag produced by the control plate increases at a greater rate than that of the reduction of the drag of the square prism, the total drag $D_T$, which is the sum of the drag $D_h$ of the control plate and that of the square prism, does not decrease. The drag $D_h$ of the control plate is estimated on the basis of the free-streamline theory developed by Parkinson and Jandali (1970), which states that the drag can be predicted using the base pressure measured for each control plate. Figure 13 shows the minimum values of $C_D$ and $C_{DT}$ at different widths of the control plate. The total drag coefficient $C_{DT}$ is expressed by the following equation:

$$C_{DT} = (D + D_h)/(0.5\rho U^2 W) = C_D + C_{Dh}(h/W), \quad (3)$$

where $D_0$ is the drag of the square prism without the control plate, $D_T$ is the minimum total drag value, and $(D_0 - D_T)/D_0$ is the reduction of total drag. As shown in Fig. 13, the reduction of total drag remains almost constant at approximately 75 percent when the ratio between the control plate and the square prism exceeds $h/W = 0.12$ ($h = 5$ mm). In addition, because the fluctuating fluid forces are almost entirely suppressed beyond $h/W = 0.1$, it can be concluded that the optimum width of the control plate is up to $\frac{1}{10}$ of the size of the square prism.

## 4 Conclusions

The objective of this paper was to investigate the suppression of fluid forces acting on a square prism by introducing a small flat plate upstream of the prism. The main results of the present study are summarized as follows:

(1) Because the maximum reduction of the time-averaged total drag, which is the sum of the drag acting on the control plate and that acting on the square prism, remains almost constant at approximately 75 percent beyond $h/W = 0.12$, the optimum width of the control plate is determined to be as large as $\frac{1}{10}$ of the size of the square prism.

(2) The maximum reductions in the fluctuating lift and drag are approximately 95 and 85 percent, respectively, using a control plate with a width of 4 mm. Thus, fluctuating fluid forces can be almost entirely suppressed using a control plate $\frac{1}{10}$ of the size that of the square prism.

(3) Three wake flow patterns resulted from varying the position of the control plate. The greatest reduction of fluid forces acting on the square prism occurs in the flow pattern in which alternate vortex shedding is perfectly suppressed.

(4) Two patterns (or modes) that switch randomly over time appear if the spacing between the square prism and the control plate is within an appropriate range. The statistical properties of the mode switching are the same as those observed in the case of flow around two circular cylinders with the same dimensions arranged in tandem or side-by-side.

## References


Bearman, P. W., 1965, "Investigation of the Flow Behind a Two-Dimensional Model with a Blunt Trailing Edge and Fitted with Splitter Plates," *Journal of Fluid Mechanics,* Vol. 21, Part 2, pp. 241–255.

Arie, M., Kiya, M., Moriya, M., and Mori, H., 1983, "Pressure Fluctuations on the Surface of Two Circular Cylinders In Tandem Arrangement," ASME JOURNAL OF FLUIDS ENGINEERING, Vol. 105, No. 2, pp. 161–167.

Igarashi, T., and Itoh, S., 1993, "Drag Reduction of a Square Prism (1st Report, Flow Control Around a Square Prism Using a Small Vortex Shedder)," *Transaction of JSME,* Vol. 59, No. 568, pp. 3701–3707.

Kim, H. J., and Durbin, P. A., 1988, "Investigation of the Flow between a Pair of Circular Cylinders in the Flopping Regime," *Journal of Fluid Mechanics,* Vol. 196, pp. 431–448.

Koenig, K., and Roshko, A., 1985, "An Experimental Study of Geometrical Effects on the Drag and Flow Field of Two Bluff Bodies Separated by a Gap," *Journal of Fluid Mechanics,* Vol. 156, pp. 167–204.

Lesage, F., and Gartshore, I. S., 1987, "A Method of Reducing Drag and Fluctuating Side Force on Bluff Bodies," *Journal of Wind Engineering and Industrial Aerodynamics,* Vol. 25, No. 2, pp. 229–245.

Parkinson, G. V., and Jandali, T., 1970, "A Wake Source Model for Bluff Body Potential Flow," *Journal of Fluid Mechanics,* Vol. 40, Part 3, pp. 577–594.

Sakamoto, H., Tan, K., and Haniu, H., 1991, "An Optimum Suppression of Fluid Forces by Controlling a Shear Layer Separated from a Square Prism," ASME JOURNAL OF FLUIDS ENGINEERING, Vol. 113, No. 2, pp. 183–189.

Sakamoto, H., and Haniu, H., 1994, "Suppression of Fluid Forces of Square Prism by Controlling Separated Shear Layer (Controlled by a Fine Flat Plate)," *Transaction of JSME,* Vol. 60, No. 573, pp. 1575–1582.

Sakamoto, H., and Haniu, H., 1988, "Effect of Free-Stream Turbulence on Characteristics of Fluctuating Forces Acting on Two Square Prisms in Tandem Arrangement," ASME JOURNAL OF FLUIDS ENGINEERING, Vol. 110, No. 2, pp. 140–146.

Zdravkovich, M. M., 1981, "Review and Classification of Various Aerodynamic and Hydrodynamic Means for Suppressing Vortex Shedding," *Journal of Wind Engineering and Industrial Aerodynamics,* Vol. 7, No. 2, pp. 145–189.

**Robert R. Hwang**
Professor.

**Chia-Chi Yao**
Research Scientist.

Institute of Physics, Academia Sinica, Taipei, Taiwan

# A Numerical Study of Vortex Shedding From a Square Cylinder With Ground Effect

*A numerical study has been conducted to investigate the behavior of the vortical wake created by a square cylinder placed in a laminar boundary-layer flow. The calculations are performed by solving the unsteady 2D Navier-Stokes equations with a finite-volume method. The Reynolds-number regime investigated is from 500 to 1500. Another parameter that is varied is the distance of the cylinder from the wall. The initial and subsequent development of the vortex shedding phenomenon are investigated. The presence of the wall is found to have strong effects on the properties of these vortices, as well as lift, drag, and Strouhal number.*

## 1 Introduction

Flow over a bluff body is an active research topic of various disciplines in many engineering problems. It produces wake flow which is frequently associated with unsteady and periodic vortex shedding that is causing dynamic forces on the structure. When a wall or ground is present in the flow, the shear effect makes the velocity of the approaching stream vary in the direction normal to the bluff body. Then the behavior of vortex shedding behind an obstacle parallel to the ground will be affected significantly. Typical examples are the vibrations of pipelines laying on the sea-bottom under the effect of the sea-currents; pipelines and bridges under the effect of the wind, etc. Vortex shedding will cause a noticeable erosion of the supports of these structures.

The problems of vortex shedding from bluff bodies have been extensively studied since the pioneering work of Strouhal (1878) and Von Karman (1912). Excellent surveys of vortex-induced oscillations of bluff bodies have been given by Bearman (1984) and Williamson (1996). Studies on the problems of wake development and vortex shedding behind a rectangular cylinder in free-stream flows have recently been investigated both numerically and experimentally by Davis et al. (1982), Franke and Rodi (1990), Okajima (1982, 1990), Okajima et al. (1992), and Kelkar et al. (1992). There are only a few investigations on the subjects of wake development and vortex shedding behind an obstacle under shear due to the presence of a wall. Kiya et al. (1980) and Kwon et al. (1992) investigated experimentally vortex shedding from a circular cylinder in moderate Reynolds-number shear flows. Ayukawa et al. (1993) conducted an experimental study on the effect of the shear rate on the Strouhal number for a uniform shear flow over a square cylinder. It can be noticed that the shear rate influences not only the vortex shedding frequency and the drag coefficient but also the flow development in the wake of a bluff body. No walls are present in these shear flows considered. Davis et al. (1984) and Mukhopadhyay et al. (1992) investigated the vortex structure behind a rectangular cylinder in a confined channel. The presence of this confined wall leads to numerous changes in the characteristics of the flow about cylinder, including the increase of drag coefficient and Strouhal number, and moving recirculation zones between the wake and walls. Beside these studies for laminar flow, Franke and Rodi (1991) have calculated the vortex shedding past a square cylinder with various turbulence models. Durao et al. (1991) have measured the velocity characteristics of the flow around a square cylinder placed near a channel wall with laser-Doppler velocimetry at Re = $1.36 \times 10^4$ to get detailed results of time averaged mean flow properties, turbulence intensities and Reynold stresses. These data revealed the structural difference of near wakes with and without vortex shedding from the wall effects.

The presence of a wall modifies in a certain number of ways the behavior of the vortical shedding behind a cylinder. When a two-dimensional square cylinder is attached to a plane wall, regular vortex shedding is absent (e.g., Good and Joubert, 1968). When there is a gap between the cylinder and the wall the onset of vortex formation appears at a critical gap height. Tanigushi et al. (1983) found that this value is 0.5 times the side of a square cylinder. It would be interesting to understand the influence of a nearby wall on vortex shedding. Experiments on the flow around a square cylinder placed at various heights above a wall at high Reynolds numbers were carried out by Durao et al. (1991) and Bosch and Rodi (1995). Durao et al. found the critical value for the gap beyond which vortex shedding occurs to be in the range $s/B = 0.25, \ldots, 0.5$ at Re = 13600. In the experiments of Bosch and Rodi, steady flow was observed for $s/B = 0.25$ while vortex shedding was observed for $s/B = 0.5$ at Re = 22000. Although some studies on this configuration at high Reynolds number [$O(10^4)$] have been conducted, the study on vortex-shedding flow past square cylinders near walls in laminar Reynolds-number range on the other hand, has not yet been investigated. A study on the laminar Reynolds-number range may be considered to complement the previous works for the influence of a nearby wall on the vortex-shedding flow.

The present work performs a numerical investigation of a square cylinder which is placed parallel to the wall and perpendicular to a boundary-layer flow at different distances from the wall. In order to consider the extreme cases between the cylinder placed in and outside of the boundary layer, a thick boundary layer of five cylinder lengths is considered in this study. A much thinner boundary layer in which the boundary-layer thickness is only 0.8 cylinder lengths is also included to delineate the effects of the shear flow and of the wall itself in the laminar boundary layer. In the present study, we assume that the boundary layer flow is free from turbulence, therefore only a two-dimensional laminar flow field at different Reynolds numbers is investigated. We find that velocity field induced by the vortices is distorted by the velocity gradient and by the presence of the wall. There are two parameters to describe the wall effect for a given boundary-layer flow, one is the gap height of the cylinder to the wall and the other is the Reynolds number of the boundary-layer

Contributed by the Fluids Engineering Division for publication in the JOURNAL OF FLUIDS ENGINEERING. Manuscript received by the Fluids Engineering Division April 1, 1996; revised manuscript received April 1, 1997. Associate Technical Editor: P. W. Bearman.

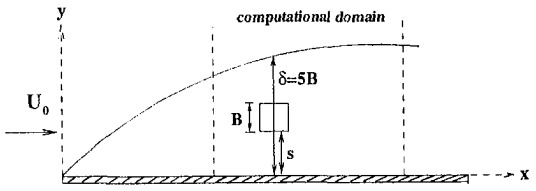


Fig. 1 The considered flow problem

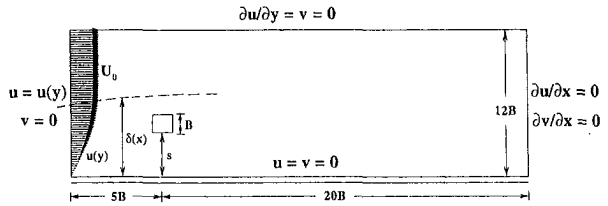


Fig. 2 Calculation domain and boundary conditions for the flow problem

flow. Varying these parameters, the wall effects on the wake development and vortical shedding behind a square cylinder and on the aerodynamic forces acting on the cylinder are investigated.

In practice, flows past bluff bodies at high Reynolds numbers are usually influenced by stochastic turbulent fluctuations, and they are often three-dimensional in the boundary layer flows. Extensions to including the effect of turbulent fluctuations through a turbulence model and to three-dimensional flows should be addressed in the future study. The work presented here is only a first step toward the development of a more general calculation method.

## 2 Formulation of Flow Problems

The physical problem considered in this study is a two-dimensional boundary layer flow of an incompressible fluid around a square cylinder. Figure 1 shows the geometry and coordinates of the flow problems. Square cylinder of side B is placed in a boundary layer of thickness $\delta$ at a gap distance $s$ from the wall. The two-dimensional boundary-layer flow is generated from a uniform stream over a flat plate. $U_0$ is the uniform velocity of the fluid outside the boundary layer thickness. The two-dimensional Navier-Stokes and continuity equations for unsteady incompressible viscous flow can be written in dimensionless form as

$$\frac{\partial u}{\partial x} + \frac{\partial v}{\partial y} = 0 \tag{1}$$

$$\frac{\partial u}{\partial t} + u\frac{\partial u}{\partial x} + v\frac{\partial u}{\partial y} = -\frac{\partial P}{\partial x} + \frac{1}{\mathrm{Re}}\left(\frac{\partial^2 u}{\partial x^2} + \frac{\partial^2 u}{\partial y^2}\right) \tag{2}$$

$$\frac{\partial v}{\partial t} + u\frac{\partial v}{\partial x} + v\frac{\partial v}{\partial y} = -\frac{\partial P}{\partial y} + \frac{1}{\mathrm{Re}}\left(\frac{\partial^2 v}{\partial x^2} + \frac{\partial^2 v}{\partial y^2}\right) \tag{3}$$

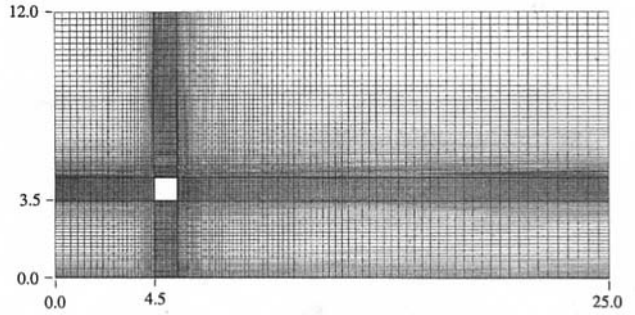


Fig. 3 The arrangement of the computational grid in the computational domain for $s/B = 3.5$

Table 1 Grid independence test ($\mathrm{Re} = 10^3$, $\delta/B = 5.0$)

| $s/B$ | Grid number | St | $C_{Dav}$ |
|---|---|---|---|
| 3.5 | 130 × 100 | 0.111 | 1.66 |
| | 260 × 200 | 0.110 | 1.69 |
| | (difference) | 0.9% | 1.8% |
| 5.5 | 130 × 110 | 0.121 | 1.93 |
| | 260 × 220 | 0.119 | 1.97 |
| | (difference) | 1.7% | 2.0% |

with the following dimensionless variables:

$$x = \frac{x^*}{B}, \quad y = \frac{y^*}{B}, \quad t = \frac{t^* U_0}{B}, \quad P = \frac{P^*}{\rho U_0^2},$$

$$u = \frac{u^*}{U_0}, \quad v = \frac{v^*}{U_0}, \quad \mathrm{Re} = \frac{U_0 B}{\nu}$$

where $u$, $v$ are the dimensionless velocity components in the $x$ and $y$ directions, respectively, in a Cartesian reference frame. $P$ is the dimensionless pressure; $\nu$ is the kinematic viscosity; $\rho$ is the density of the fluid and Re is the Reynolds number.

In order to make the problem computationally feasible, artificial confining boundaries are sufficiently far from the cylinder so that their presence has little effect on the characteristics of the flow near the square cylinder. For the case of $s/B = 7.5$, the distance between the artificial boundary and the upper surface of cylinder is set to 5.5 $B$. Figure 2 shows the computation domain in which the equations are solved and the outer boundary conditions are specified. The initial and boundary conditions for solving Eqs. (1), (2), and (3) are as follows:

at $t = 0$; $u = u(y)$ everywhere outside the cylinder

for $t > 0$

$$\text{top boundary} \quad \frac{\partial u}{\partial y} = 0, \quad v = 0$$

$$\text{right boundary} \quad \frac{\partial u}{\partial x} = 0, \quad \frac{\partial v}{\partial x} = 0$$

## Nomenclature

$A$ = frontal area of the cylinder
$B$ = length of the square cylinder
$C_{Dav}$ = time-averaged drag coefficient
$C_{Lrms}$ = rms value of fluctuating lift coefficient
$f$ = frequency of vortex shedding
$P$ = dimensionless pressure
$P^*$ = dimensional pressure
Re = Reynolds number ($=U_0 B/\nu$)
$s$ = gap height of cylinder from the wall
$S_D$ = spectrum of the drag force variation
$S_L$ = spectrum of the lift force variation
St = Strouhal number ($=fB/U_0$)
$t$ = dimensionless time
$t^*$ = dimensional time
$u$, $v$ = dimensionless velocity components in the ($x$, $y$) direction
$u^*$, $v^*$ = velocity components in the ($x^*$, $y^*$) direction
$U_0$ = velocity outside the boundary layer
$\rho$ = density of fluid
$\nu$ = kinematic viscosity of fluid
$\delta$ = the boundary layer thickness

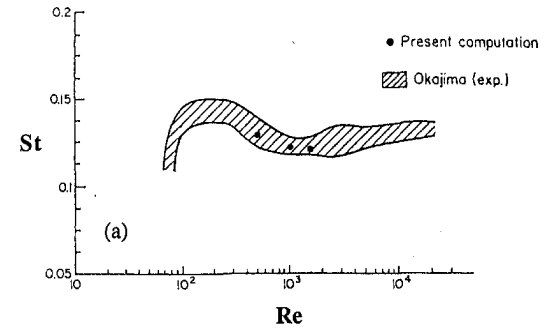


Fig. 4(*a*)

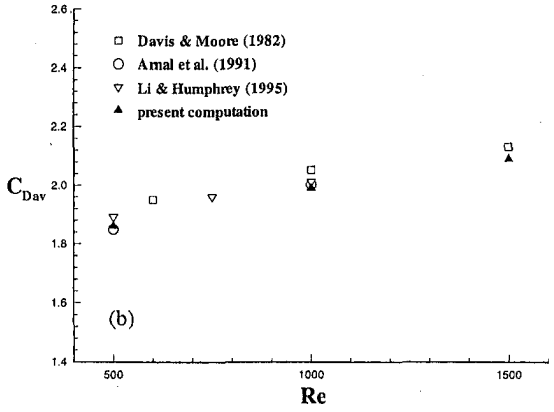


Fig. 4(*b*)

**Fig. 4 Comparison among (*a*) Strouhal number, St, and (*b*) drag coefficient, $C_{Dav}$, results for the flow past a square cylinder in a free stream**

At the entrance of the domain, the velocity profile $u(y)$ is obtained from the laminar boundary layer of Blasius solution (Schlichting, 1979). At the cylinder and the bottom wall, the no-slip condition is applied.

## 3 Method of Solution

In this study, the governing equations are solved numerically for those boundary conditions specified previously. We employ a finite-volume method to solve the equations in primitive variables on a nonuniform and staggered MAC (marker and cell) grid system. The computation domain is divided into Cartesian cells. Mesh cells are concentrated around the square cylinder and along the bottom wall. One of the nonuniform grids is illustrated as Fig. 3. The position of the cylinder can be placed in various gap heights to the wall. In the staggered grid system, pressures are defined at cell centers and normal velocities are defined at cell faces.

To solve the partial differential equations, Eqs. (1), (2), and (3), the convection terms of the transport equation are discretized by the power-law scheme (Patankar et al., 1972) while the diffusion and source terms are treated by the second-order central difference. The hybrid scheme of the power-law descretization which switches between UDS (upwind interpolation) and CDS (central difference) may have a second order approximation when the nonuniform grid is refined (Ferziger and Peric, 1996). For time discretization the fully implicit first-order Euler scheme is chosen. It provides high stability but requires small time step in order to obtain accurate solutions (more than 100 time steps per period of vortex shedding are used). The coupling between the continuity and momentum equations is achieved with the SIMPLE-C predictor-corrector algorithm of Van-Doormaal and Raithby (1984). The system of linear algebraic equations is solved by the alternating direction line by the line iteration method. The convergence criterion is specified as the average of mass source over all flow field being smaller than $10^{-7}$.

The nonuniform computational meshes employed in this study ranges in size from $130 \times 100$ to $130 \times 155$ for various values of $s/B$, with the first and second number being the number of mesh points in the $x$-direction and in the $y$-direction respectively. The grid is finer near both the surfaces of the square cylinder and the bottom wall to better resolve the gradients near the wall. The first point at a distance from each wall is $0.01B$. Small time steps ($\Delta t = 0.025$) are utilized in the initial phase to resolve the fluid motion of the impulsive start. Time steps are then increased to a value of $\Delta t = 0.05$ without significant increase in the number of iterations required to converge at each step. Numerical experiments have also been conducted to determine an adequate grid distribution for the present study. Refinement of the numerical grid by a factor of 2.0 is performed in the computations for two cases of $s/B = 3.5$ and 5.5 at $\mathrm{Re} = 10^3$. Table 1 indicates the comparison of the Strouhal number and the amplitude of the average drag coefficients from the two grid distributions in each case. It shows that the differences for those cases are all less than 2 percent. Therefore, results that are presented in this study are considered to be grid independent.

## 4 Results and Discussion

The presence of the ground affects a certain number of ways the behavior of the vortical row shedding behind a square cylinder. Using the previously described numerical method, series of numerical computations have been carried out for a boundary layer flow around the cylinder at various gap heights from the wall. It is made of the pictures which present the phenomenon of vortex shedding either in an undisturbed stream or in presence of a wall. In the present study the cylinder is placed in the section such that the boundary layer thickness is $\delta = 5B$ at different gap heights from the wall. A case in which the boundary-layer thickness is thinner (only 0.8 cylinder lengths) is also conducted for comparison.

In order to assess the accuracy of the numerical computation of the present study, the case of a uniform flow past a square cylinder was computed for Re = 500, 1000 and 1500 and compared with previous studies. In Fig. 4($a$) we compare the variation of Strouhal number with Reynolds number with experimental data of Okajima (1982). Figure 4($b$) is the computed averaged-drag coefficient $C_{Dav}$ compared with some predicted results of Davis and Moore (1982), Arnal et al. (1991), and Li and Humphrey (1995). The computed Strouhal numbers of this study fall in the experimental results of Okajima. The computed averaged-drag coefficients are also in close agreement with numerical results of previous studies.

The behavior of the vortical wake behind a cylinder placed at various gap distances from the ground is determined from

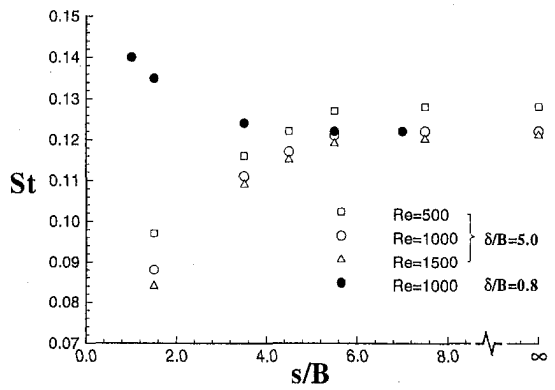


**Fig. 5 Variation of Strouhal number with gap height ratio at different Reynolds number**

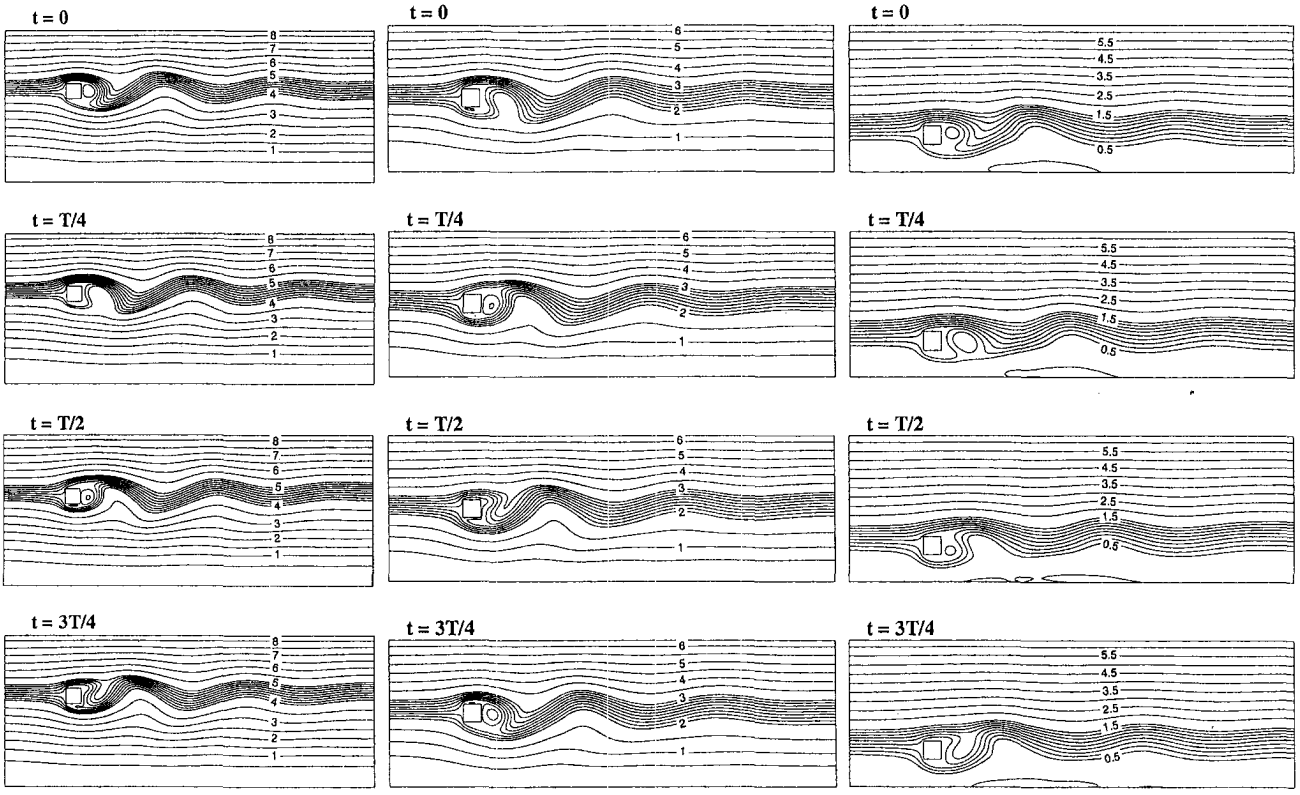


Fig. 6(*a*) Fig. 6(*b*) Fig. 6(*c*)

**Fig. 6 Streamlines during one periods of vortex shedding for Re = $10^3$, $\delta/B$ = 5.0 and (*a*) $s/B$ = 5.5; (*b*) $s/B$ = 3.5; (*c*) $s/B$ = 1.5**

the analysis of the evolution of the flow development. The ground effect on the flow development behind a square cylinder is investigated by varying the gap height ratio $s/B$. All of the results in the computations are obtained in the range of the stationary periodic flow pattern (over seven shedding cycles were run). The dynamic forces acting on the cylinder come from the influence of vortex shedding on the distribution of pressure and shear stress. The vortex-shedding frequency ($f = 1/T$) can be determined from the time period of the oscillation of the lift coefficient, and then the Strouhal number ($St = fB/U_0$) is obtained.

Some results are presented in the following. Figure 5 shows the calculated Strouhal number in relation to the gap height ratio, $s/B$ at different Reynolds numbers for the thickness ratio of the boundary layer, $\delta/B = 5$. When the cylinder is immersed in the boundary layer ($s/B < 5$), the velocity field induced by the vortices is distorted both by the velocity gradient and by the presence of the wall. It results in inhibiting the flow development of wake and decreasing the shedding frequency. The frequency of vortex shedding decreases with the decrease of gap height ratio of the cylinder to the wall. The decrease becomes more significant in the higher values of Reynolds number flows. When the cylinder is placed outside the laminar boundary layer (i.e., $s/B > 5$), the Strouhal number differs insignificantly from that of the uniform flows.

A typical history of the streamlines of flow pattern during one Strouhal shedding period for $s/B$ = 5.5, 3.5, 1.5 of Re = $10^3$ with $\delta/B = 5$ is shown in Figs. 6(*a*), 6(*b*), and 6(*c*). It can be noticed from the stream function contours that the velocity gradient of the boundary layer flow makes the stagnation streamline on the upstream side of the cylinder biased upward toward the fast side of the flow. For the case of $s/B$ = 1.5 a recirculation zone is formed behind the cylinder on the ground and the formation of the reattachment influences the vortex shedding of the wake flow. When the cylinder is closer to the ground, the recirculation zone becomes larger and further influences the development of the vortex shedding. It is found that when $s/B = 0.5$, the wake behind the cylinder becomes stationary and vortex shedding is prohibited. Figure 7 shows the streamlines of the flow pattern for $s/B = 0.5$ at Re = $10^3$.

In order to delineate the effects of the shear flow and of the wall itself, a much thinner boundary layer of $\delta/B = 0.8$ is considered and the calculated Strouhal number with respect to the gap height ratio at Re = $10^3$ for $\delta/B = 0.8$ is also illustrated in Fig. 5 for comparison. The Strouhal number increases with decreasing the gap height ratio. This is different from that of the thick boundary layer, $\delta/B = 5$ aforementioned. In the thick boundary layer, when the cylinder is immersed in the boundary layer, the shear effect decreases the velocity of the stream which collides with the cylinder. While in the thin boundary layer the wall effect increases the velocity at the gap similar to the blockage effect of the confinement. With increasing blockage ratio the value of Strouhal number increases as studied by Davis et al. (1984) and Mukhopadhyay et al. (1992). The decrease of the gap height ratio in the thin boundary layer will correspond to the increase of the blockage ratio in confined flow. It is then evident that the value of Strouhal number increases with de-

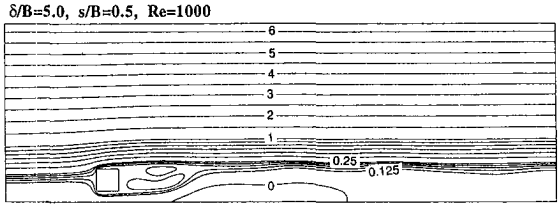


**Fig. 7 Streamlines for Re = $10^3$, $\delta/B$ = 5.0 and $s/B$ = 0.5**

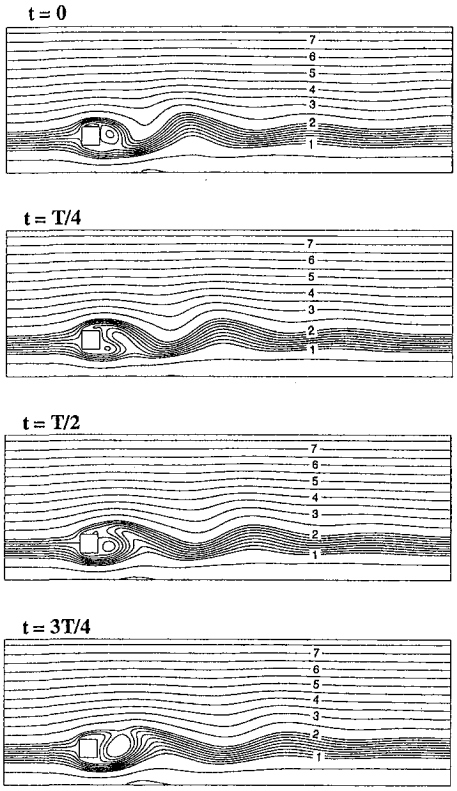


Fig. 8(*a*)

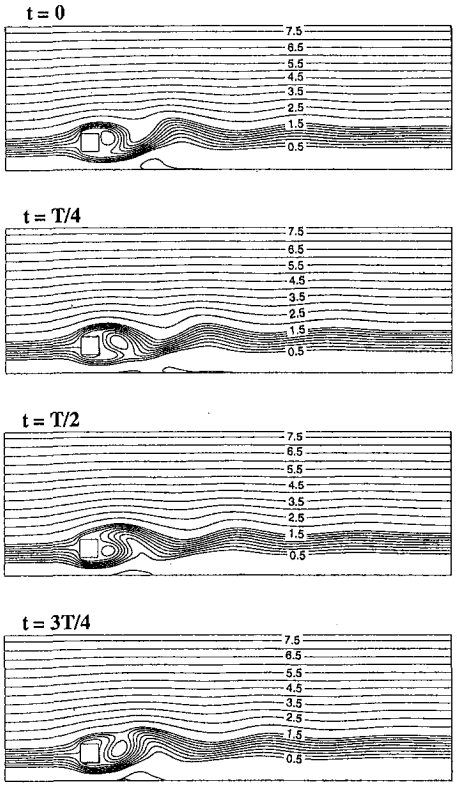


Fig. 8(*b*)

**Fig. 8 Streamlines during one periods of vortex shedding for Re = $10^3$, $\delta/B$ = 0.8 and (*a*) $s/B$ = 1.5; (*b*) $s/B$ = 1.0**

creasing the gap height ratio in the thin boundary layer. Figure 8 presents the flow patterns during one Strouhal shedding period at $s/B$ = 1.5 and 1.0 with $\delta/B$ = 0.8 and Re = $10^3$.

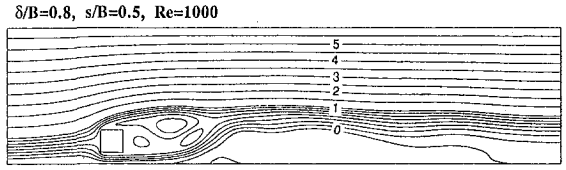


**Fig. 9 Streamlines for Re = $10^3$, $\delta/B$ = 0.8 and $s/B$ = 0.5**

It is clearly seen that the gap flow between the cylinder and the wall is apparently accelerated by the presence of a wall. As the gap height ratio becomes small (e.g., $s/B$ = 0.5), the wake behind the cylinder as shown in Fig. 9 becomes stationary.

The behavior of the average drag coefficient, $C_{Dav}$, as a function of the gap height ratio, $s/B$ at different Reynolds number for the thick boundary layer, $\delta/B$ = 5 is illustrated in Fig. 10. The term $C_{Dav}$ is defined as $C_{Dav} = F_{Dav}/(\frac{1}{2}\rho U_0^2 A)$ in which $F_{Dav}$ is the average drag force, $U_0$ is the velocity of the free stream, and $A$ is the frontal area of cylinder normal to the approaching stream. To obtain $C_{Dav}$, the instantaneous drag coefficient is first computed at each time step by integrating the surface pressure and friction around the square. As the stationary vortex shedding is achieved, the instantaneous drag coefficient is averaged over several shedding cycles to obtain $C_{Dav}$. The figure shows that $C_{Dav}$ decreases significantly with the decrease of $s/B$ for cylinder immersed in the boundary layer. When the cylinder is placed outside the boundary layer (i.e., $s/B > 5$), $C_{Dav}$ differs insignificantly from that of uniform flow.

For the thin boundary layer, $\delta/B$ = 0.8, the variation of $C_{Dav}$ with respect to $s/B$ is also plotted in Fig. 10. It shows that the time-averaged drag coefficient is increased dramatically as the gap height becomes small. The wall that leads to an increase of the average drag coefficient and the Strouhal number is just the same as that in the confined flow. The average lift coefficient for all cases considered in this study is $O(10^{-2})$ or less. Table 2 is a summary chart of computational results which presents the effect of wall on Strouhal number, drag, and lift coefficients at Re = $10^3$ for two thickness ratios of boundary layer.

Figures 11 and 12 present the power spectra of the time histories of drag and lift coefficients for various gap height ratios at two thickness ratios of the boundary layer with Re = $10^3$. It is seen that a subharmonic has entered into the fluctuation of $C_D$ due to the distortion of the vortices behind the cylinder caused by the velocity gradient in the presence of the wall. The relative strength of the subharmonic to the first harmonic increases at smaller $s/B$. The induced subharmonics become more significant in the thin boundary layer at the presence of a wall. The fluctuating lift coefficient still contains the first

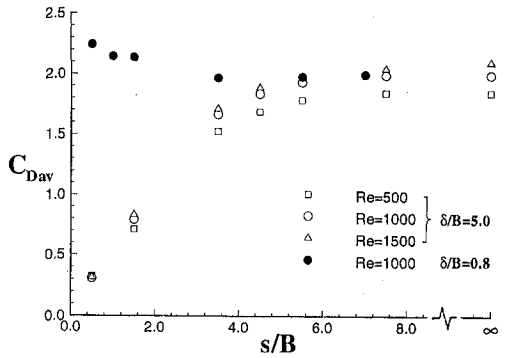


**Fig. 10 Variation of the average drag coefficient with gap height ratio at different Reynolds number**

Table 2 Summary chart of computational results for two thickness ratios of boundary layer (Re = $10^3$)

| Configurations | $s/B$ | St | $C_{Dav}$ | $C_{Drms}$ | $C_{Lav}$ | $C_{Lrms}$ |
|---|---|---|---|---|---|---|
| $\delta/B = 0.8$ | 5.5 | 0.122 | 1.98 | 0.10 | 0.00 | 1.12 |
| | 3.5 | 0.124 | 1.97 | 0.09 | −0.02 | 1.13 |
| | 1.5 | 0.135 | 2.14 | 0.11 | −0.05 | 1.14 |
| | 1.0 | 0.140 | 2.15 | 0.07 | −0.06 | 1.00 |
| | 0.5 | No shedding | 2.24 | 0.00 | −0.40 | 0.00 |
| $\delta/B = 5.0$ | ∞ | 0.122 | 1.99 | 0.10 | 0.00 | 1.18 |
| | 7.5 | 0.122 | 1.99 | 0.10 | 0.02 | 1.14 |
| | 5.5 | 0.121 | 1.94 | 0.09 | 0.03 | 1.09 |
| | 4.5 | 0.117 | 1.83 | 0.09 | 0.04 | 1.03 |
| | 3.5 | 0.111 | 1.66 | 0.09 | 0.06 | 0.90 |
| | 1.5 | 0.088 | 0.79 | 0.04 | 0.03 | 0.36 |
| | 1.0 | 0.080 | 0.50 | 0.00 | 0.03 | 0.00 |
| | 0.5 | No shedding | 0.31 | 0.00 | 0.02 | 0.00 |

harmonic in all cases considered in this study and its strength (spectrum amplitude) decreases with decreasing gap height ratio. The thick boundary layer has faster decay of the spectrum strength than that of the thin boundary layer. It means that the vortical intensity of the wake has faster decay in the ground effect for the thick boundary layer than that for the thin boundary layer.

## 5 Conclusion

With the numerical simulation of a finite-volume method, the presence of a wall in a flow past a square cylinder is successfully performed. The formation of vortex shedding in the wake of the cylinder is influenced when a wall is present. In the thick boundary layer (e.g., $\delta/B = 5$), the presence of a wall will distort the vortices (flattening) and lead to a decrease of the Strouhal number and the average drag coefficient. For the thin boundary layer (e.g., $\delta/B = 0.8$), the wall leads to an increase of the Strouhal number and the average drag coefficient. At a critical gap height (e.g., $s/B = 0.5$), the vortex shedding is suppressed by the flow reattachment on the wall to form a recirculation zone and the wake behind the cylinder becomes stationary. With the presence of a wall, a subharmonic in the fluctuating drag is induced and its strength (spectrum amplitude) compared with the first harmonic increases as the gap height ratio decreases.

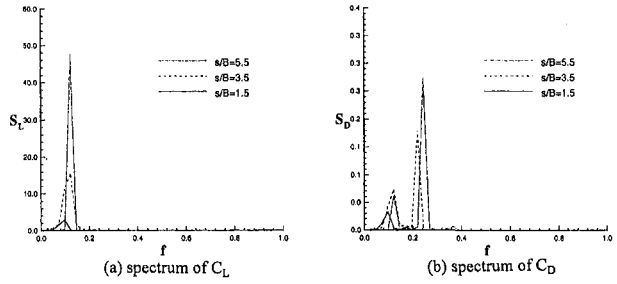


**Fig. 11 The fluctuating spectra of lift and drag coefficients for various $s/B$ at Re = $10^3$ and $\delta/B = 5.0$**

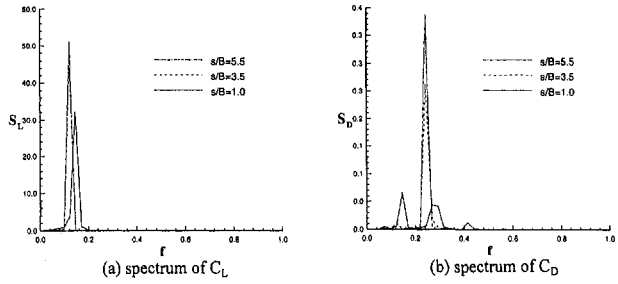


**Fig. 12 The fluctuating spectra of lift and drag coefficients for various $s/B$ at Re = $10^3$ and $\delta/B = 0.8$**

## Acknowledgment

This work was supported both by the National Science Council under grant No. NSC84-2211-E-001-001 and by the Institute of Physics, Academia Sinica.

## References

Arnal, M. P., Goering, D. J., and Humphrey, J. A. C., 1991, "Vortex shedding from a Bluff Body on a Sliding Walls," ASME JOURNAL OF FLUIDS ENGINEERING, Vol. 113, pp. 384–398.

Ayukawa, K., Ochi, J., Kawahawa G., and Hirao T., 1993, "Effects of Shear Rate on the Flow around a Square Cylinder in a Uniform Shear Flow," *Journal of Wind Engineering and Industrial Aerodynamics,* Vol. 50, pp. 97–106.

Bearman, P. W., 1984, "Vortex Shedding from Oscillating Bluff Bodies," *Annual Review of Fluid Mechanics,* Vol. 16, pp. 195–222.

Bosch, G., and Rodi, W., 1995, "Simulation of Vortex Shedding past a Square Cylinder near a Wall," *Proceedings 10th Symposium on Turbulent Shear Flows,* Pennsylvania State University, pp. 4.13–4.18.

Davis, R. W., and Moore, E. F., 1982, "A Numerical Study of Vortex Shedding from Rectangles," *Journal of Fluid Mechanics,* Vol. 116, pp. 475–506.

Davis, R. W., Moore, E. F., and Purtell, L. P., 1984, "A Numerical—Experimental Study of Confined Flow around Rectangular Cylinders," *Physics of Fluids,* Vol. 27, No. 1, pp. 46–59.

Durao, D. F. G., Gouveia, P. S. T., and Pereira, J. C. F., 1991, "Velocity Characteristic of the Flow Around a Square Cross Section Cylinder Placed Near a Channel Wall," *Experiments in Fluids,* Vol. 11, pp. 341–350.

Ferziger, J. H., and Peric, M., *Computational Methods for Fluid Dynamics,* Springer, 1996.

Franke, R., and Rodi, W., 1990, "Numerical Calculation of Laminar Vortex Shedding Flow past Cylinders," *Journal of Wind Engineering and Industrial Aerodynamics,* Vol. 35, pp. 237–257.

Franke, R., and Rodi, W., 1991, "Calculation of Vortex Shedding Past a Square Cylinder with Various Turbulence Models," *Proceedings of 8th Symposium on Turbulent Shear Flow,* Munich, pp. 20.1.1–20.1.6.

Good, M. C., and Joubert, P. N., 1968, "The Form Drag of Two-Dimensional Bluff Plates Immersed in the Turbulent Boundary Layers," *Journal of Fluid Mechanics,* Vol. 31, pp. 547–582.

Kelkar, K. M., and Patankar, S., 1992, "Numerical Prediction of Vortex Shedding behind a Square Cylinder," *International Journal for Numerical Methods in Fluids,* Vol. 14, pp. 327–341.

Kiya, M., Tamura, H., and Arie, M., 1980, "Vortex Shedding from a Circular Cylinder in Moderate-Reynolds-Number Shear Flow," *Journal of Fluid Mechanics,* Vol. 141, pp. 721–735.

Kwon, T. K., Sung, H. J., and Hyun, J. M., 1992, "Experimental Investigation of Uniform-Shear Flow past a Circular Cylinder," ASME JOURNAL OF FLUIDS ENGINEERING, Vol. 114, pp. 457–460.

Li, G., and Humphrey, J. A. C., 1995, "Numerical Modelling of Confined Flow past a Cylinder of Square Cross-Section at Various Orientations," *International Journal for Numerical Methods in Fluids,* Vol. 20, pp. 1215–1236.

Mukhopadhyay, A., Biswas, G., and Sindararajan, T., 1992, "Numerical Investigation of Confined Wakes behind a Square Cylinder in a Channel," *International Journal for Numerical Methods in Fluids,* Vol. 14, pp. 1473–1484.

Okajima, A., 1982, "Strouhal Numbers of Rectangular Cylinders," *Journal of Fluid Mechanics,* Vol. 123, pp. 379–398.

Okajima, A., 1990, "Numerical Simulation of Flow around Rectangular Cylinders," *Journal of Wind Engineering and Industrial Aerodynamics,* Vol. 33, pp. 171–180.

Okajima, A., and Sakai, H., 1992, "Numerical Simulation of Laminar and Turbulent Flows around Rectangular Cylinders." *International Journal for Numerical Methods in Fluids,* Vol. 15, pp. 999–1012.

Patankar, S. V., and Splading, D. B., 1972, "A Calculation Procedure for Heat, Mass and Momentum Transfer in Three-Dimensional Parabolic Flows," *International Journal of Heat and Mass Transfer,* Vol. 5, pp. 1878–1886.

Schlichting, H., 1979, *Boundary Layer Theory,* 7th ed., McGraw-Hill, New York.

Strouhal, V., 1878, "Ueber Eine Besondere Art Der Tonerregung," *Ann. Phys. und Chemie,* Neue Folge, Bd. 5, Heft 10, pp. 216–251.

Taniguchi, S., Miyakoshi, K., and Dohda, S., 1983, "Interference between Plane Wall and Two-dimensional Rectangular Cylinder," *Transaction of Japanese Society of Mechanical Engineering,* 49–447, pp. 2522–2529.

Van-Doormaal, J. P., and Raithby, G. D., 1984, "Enhancements of the SIMPLE Method for Predicting Incompressible Fluid Flows," *Numerical Heat Transfer,* Vol. 7, pp. 147–163.

Von Karman, Th., and Rubach, H., 1912, "Ueber Den Mechanismus Des Flussigkeits und Luftwiderstandes," *Phys. Zeitschr.,* Bd. 13, Heft 2, pp. 49–59.

Williamson, C. H. K., 1996, "Vortex Dynamics in the Cylinder Wake," *Annual Review of Fluid Mechanics,* Vol. 28, pp. 477–539.

# Application of Large Eddy Simulation to an Oscillating Flow Past a Circular Cylinder

**Xiyun Lu**[1]
Postdoctoral Fellow.

**Charles Dalton**
Associate Dean of Engineering.

**Jianfeng Zhang**[2]
Doctoral Student.

Department of Mechanical Engineering,
University of Houston,
Houston, TX 77204

*Three-dimensional sinusoidally oscillating flows around a circular cylinder are investigated by using a viscous flow method (VFM) and a large eddy simulation (LES). A second-order accurate in time fractional step method and a combined finite-difference/spectral approximation are employed to solve the filtered incompressible Navier-Stokes equations. To demonstrate the viability and accuracy of the method, we calculate two cases of steady approach flows at Reynolds numbers Re = 100 using VFM and Re = $10^4$ using LES. For sinusoidally oscillating flows at $\beta$ = 1035, the flow is 2D for KC < 0.5, 3D for 0.5 < KC < 2, and turbulent for KC > 2. For KC = 0.5, 0.8 and 1, the flow is calculated using VFM. For KC = 2, 3, 4, 5, 8 and 10, we have simulated the flow using LES with the Smagorinsky subgrid scale model. The drag and inertia coefficients are calculated from the in-line force acting on the cylinder and are in very good agreement with experimental data.*

## 1 Introduction

In the present study, 3D incompressible sinusoidally oscillating flows around a circular cylinder are investigated using the large eddy simulation (LES) method. The physical problem being modeled is a simplification of wave forces acting on an offshore platform. Here, we model the wave action on a platform leg to be a sinusoidal oscillation of the fluid in the horizontal plane past a fixed circular cylinder. The three-dimensionality present in the flow is due to the natural instability of the 2D flow at sufficiently large Reynolds numbers, leading to the development of wake turbulence. This wake turbulence is carried with the wake vortices as they oscillate back and forth due to the flow reversal in the sinusoidal oscillation.

The numerical procedure is verified by the case of a steady approach flow past a cylinder which depends only on the Reynolds number while the flow generated by the oscillation of the cylinder, or oscillating flows around the cylinder, can be characterized by two parameters. One is the Keulegan-Carpenter number, defined as $KC = U_m T/D$. The other is the Reynolds number $Re = U_m D/\nu$, or $\beta = D^2/\nu T$ which is the ratio of Reynolds number to Keulegan-Carpenter number. Here $U_m$ is the maximum velocity of the ambient flow, $T$ is the period of oscillation, $D$ is the diameter of the cylinder, and $\nu$ is the kinematic viscosity.

Even though LES has been used by many investigators, most applications have been limited to internal flows. In recent years, some researchers have applied LES to steady approach flows around a cylinder. But, very little work has been done for oscillating flows past a cylinder using LES. Most numerical studies for oscillating flows around a cylinder were only based on laminar flow and a 2D simulation, e.g., see Wang and Dalton (1991) and Justesen (1991). Some experiments, e.g., Sarpkaya (1986), have shown that flows should become 3D and then turbulent as the governing parameters increase in value. A brief synopsis is that, at a given value of $\beta$, the flow goes through a series of different flow regimes as KC changes, For a given value of $\beta$, the flow is 2D and laminar at low KC. As KC increases, a viscous transition to a 3D wake occurs. The next regime, occurring with increase in KC value, is that wake turbulence is generated. The final regime is identified as one in which separation has occurred after further increase in KC. In particular at $\beta$ = 1035, we note, from Sarpkaya's (1986) Fig. 7, that the transition to a 3D wake (the Honji instability) occurs at KC $\simeq$ 1.1, transition to turbulence occurs at KC $\simeq$ 1.5 and separation at KC $\simeq$ 1.9. We recognize that there could be some experimental scatter in these values, especially at larger values of $\beta$, even leading to uncertainty about the order in which the regimes appear.

The Honji instability is a 3D vortical instability first discovered by Honji (1981). Honji's experiments showed that, when $\beta$ is between 50 and 800, the flow becomes 3D when KC is between 1.2 and 2.4. The critical KC for the flow to become unstable to 3D disturbances, $KC_{cr}$, shows a steeper decrease with increasing $\beta$ when $\beta$ is smaller than 200. When $\beta$ exceeds 200, $KC_{cr}$ decreases much more slowly. When KC is greater than $KC_{cr}$, the streak sheets form steady mushroom-like structures on the sides of the cylinder which are perpendicular to the direction of oscillation. These structures have equal spacing along the axial direction, and lie alternatively on the two sides. Honji also observed that, when KC is further increased to be greater than a transitional KC number, $KC_t$, the flow becomes turbulent due to long-standing separation of the Stokes layer (the layer of high vorticity and gradients close to the wall of the cylinder). For the range of $\beta$ considered, the difference between $KC_t$ and $KC_{cr}$ is relatively invariant (between 0.9 and 1.2). Apparently separation occurs after the Honji instability, at a KC value between $KC_{cr}$ and $KC_t$.

Here, we perform a 3D LES calculation of an oscillating flow past a circular cylinder with verification demonstrated by a steady approach flow calculation.

## 2 Governing Equations

The governing equations are the filtered incompressible Navier-Stokes equations. To nondimensionalize the governing equations, we use two sets of scales. For the oscillating flows, we use the radius of the cylinder, $R$, for the length scale; the maximum freestream velocity, $U_m$, for the velocity scale; the period of oscillation, $T$, for the time scale. For the steady approach flows, we use the radius of the cylinder, $R$, for the length scale; the freestream approach velocity, $U$, for the velocity

[1] Permanent address: Dept. of Modern Mech., Univ. of Sci. & Tech. of China, Hefei, Anhui 230026, China.

[2] Present address: Halliburton, Houston, Texas.

Contributed by the Fluids Engineering Division for publication in the JOURNAL OF FLUIDS ENGINEERING. Manuscript received by the Fluids Engineering Division June 5, 1996; revised manuscript received March 11, 1997. Associate Technical Editor: P. W. Bearman.

scale; $R/U$ for the time scale. These scalings for oscillating flow resulted in two nondimensional numbers, the Reynolds number, $\mathrm{Re} = 2RU_m/\nu$, and the Keulegan-Carpenter number, $\mathrm{KC} = U_mT/2R$. The nondimensional filtered governing equations are given as

$$\nabla \cdot \mathbf{V} = 0, \tag{1}$$

$$\frac{1}{\alpha}\frac{\partial \mathbf{V}}{\partial t} + (\nabla \times \mathbf{V}) \times \mathbf{V} = -\nabla\phi + \frac{2}{\mathrm{Re}}\nabla^2\mathbf{V} - \nabla \cdot \mathbf{T}, \tag{2}$$

where $\mathbf{V}$ is the resolved velocity vector, $\mathbf{T}$ is the turbulent stress tensor, $\phi$ is the nondimensional pressure head, defined as $\phi = p + \mathbf{V}\cdot\mathbf{V}/2$, $t$ is the nondimensional time, and $p$ is the nondimensional pressure; $\alpha = 2\mathrm{KC}$ for oscillating flows and $\alpha = 1$ for steady approach flows. The governing equations were in polar-cylindrical coordinate form for solution.

In the present computation, we use the eddy viscosity model of Smagorinsky to model the turbulent stress. As indicated by Speziale (1985), this model is Galilean invariant. The Smagorinsky eddy viscosity model is given as

$$\tau_{ij} = -2\nu_T S_{ij} = -2C_s^2\tilde{\Delta}^2 S_{ij}\sqrt{2S_{ij}S_{ij}}, \tag{3}$$

where $S_{ij}$ is the strain rate tensor and $C_s$ and $\tilde{\Delta}$ are the model constant and characteristic length respectively. A value of $C_s = 0.1$ was used for all of the calculations and $\tilde{\Delta}$ is the cube root of the product of the mesh sizes.

In the present calculation, for sinusoidally oscillating flows starting from rest, the velocity is zero everywhere at the beginning of the calculation and is given by $U(t) = U_m \sin(2\pi t/T)$. For steady approach flows, the initial velocity is taken as the 2D potential flow velocity. On the wall of the cylinder, we use the no-slip and no-penetration boundary conditions for velocity. Far from the cylinder, we use the condition that the wake vorticity crosses the boundary undisturbed. In the circumferential and axial directions, we use periodic boundary conditions. No wall damping was used.

## 3 Numerical Method

We use a second-order fractional step method to discretize the governing equations in time. In this approach, we first obtain an intermediate velocity, $\hat{\mathbf{V}}$, by omitting pressure and using an Euler scheme on the convective terms and the Crank-Nicolson scheme on the viscous terms. This intermediate velocity is corrected by pressure, which is obtained through a Poisson equation, to satisfy the continuity equation. Finally, the boundary conditions on velocity are applied to get the velocity at the next time step. In this section, we present this procedure in semi-discrete formulation in vector form.

The intermediate velocity, $\hat{\mathbf{V}}$, is obtained from

$$\frac{1}{\alpha}\frac{\hat{\mathbf{V}} - \mathbf{V}^n}{\Delta t} = -\mathbf{N}^n + \mathbf{T}^n + \frac{1}{2}\mathbf{L}^n, \tag{4}$$

where the superscripts refer to time step, $\mathbf{N}$, $\mathbf{T}$, and $\mathbf{L}$ represent the convective terms, turbulent stress term and viscous terms respectively. The velocity $\hat{\mathbf{V}}$ is corrected by pressure to obtain a second intermediate velocity, $\tilde{\mathbf{V}}$, from

$$\frac{1}{\alpha}\frac{\tilde{\mathbf{V}} - \hat{\mathbf{V}}}{\Delta t} = -\nabla\phi^{n+1/2}. \tag{5}$$

Finally, the velocity at time step $n+1$ is obtained from

$$\frac{1}{\alpha}\frac{\mathbf{V}^{n+1} - \tilde{\mathbf{V}}}{\Delta t} = \frac{1}{2}\mathbf{L}^{n+1}. \tag{6}$$

In this equation, the pressure head, $\phi$, is unknown; to determine it, we apply the continuity equation. Since we intend to satisfy the continuity equation for every time step, $n$ or $n+1$, we first take the divergence of Eq. (6) and set

$$Q^{n+1} = \nabla \cdot \mathbf{V}^{n+1} = 0, \tag{7}$$

and we obtain

$$\tilde{Q} = \nabla \cdot \tilde{\mathbf{V}} = 0. \tag{8}$$

Then we take the divergence of Eq. (5) and apply Eq. (8) to get

$$\nabla^2\phi^{n+1/2} = \frac{\nabla \cdot \hat{\mathbf{V}}}{\alpha\Delta t}. \tag{9}$$

After $\phi^{n+1/2}$ is found from by Eq. (9) with appropriate boundary conditions, $\tilde{\mathbf{V}}$ and $\mathbf{V}^{n+1}$ can be calculated from Eqs. (5) and (6), respectively. No boundary conditions are necessary for either of the two intermediate velocities. This fractional-step method is a combination of the ideas of Kim and Moin (1985) and Karniadakis et al. (1991).

To control this time-splitting error, we use the consistent scheme developed by Karniadakis et al. (1991) on boundary conditions for pressure on solid boundaries where the velocity vanishes, i.e.,

$$\frac{\partial\phi}{\partial n} = -\frac{2}{\mathrm{Re}}\mathbf{n}\cdot\nabla \times (\nabla \times \mathbf{V}), \tag{10}$$

where $n$ refers to the direction normal to the wall and $\mathbf{n}$ is the unit normal vector. Because we only have one direction (i.e., radial direction) which does not have a periodic boundary condition, we use a combined Fourier spectral approximation, in the circumferential and axial directions, and a finite-difference approximation, in the radial direction, to discretize the governing equations. In the radial direction, the coordinate transformation, $r = e^{\xi}$, is used to generate a finer mesh near the wall of the cylinder than further away from it. Thus we can specify a uniform mesh size $\Delta\xi$ in the computational domain because we expect the variations of flow variables to be greater near the wall.

## 4 Force Description

Determination of the velocity field allows the instantaneous force to be calculated from an integration of the circumferential pressure and vorticity distributions on the cylinder surface.

Nondimensionalizing the in-line force and the transverse force by $\rho U^2 d/2$ to obtain the drag and lift coefficients, we have

$$C_F = -\frac{1}{2}\int_0^{2\pi}\frac{\partial\hat{\omega}_s}{\partial\xi}\cos\theta d\theta - \frac{2}{\mathrm{Re}}\int_0^{2\pi}\hat{\omega}_s\sin\theta d\theta, \tag{11}$$

$$C_L = -\frac{1}{2}\int_0^{2\pi}\frac{\partial\hat{\omega}_s}{\partial\xi}\sin\theta d\theta - \frac{2}{\mathrm{Re}}\int_0^{2\pi}\hat{\omega}_s\cos\theta d\theta, \tag{12}$$

where $p_s$, the surface pressure, has been replaced using the azimuthal component of the Navier-Stokes equations and $\hat{\omega}_s$ is the nondimensional vorticity on the cylinder surface.

The force in a wavy flow situation is traditionally decomposed into two parts: a drag part, proportional to the fluid velocity squared, and an inertial part, proportional to the fluid acceleration. This force description is referred to as the Morison equation (see Sarpkaya and Isaacson, 1981) and its dimensionless form is

$$C_F = C_D\sin\theta|\sin\theta| + C_M\frac{\pi^2}{\mathrm{KC}}\cos\theta, \tag{13}$$

where $C_F$ is the dimensionless force coefficient, $C_M$ is the inertia coefficient and $C_D$ is the drag coefficient.

Equation (13) is multiplied by $\cos\theta$ and integrated to give

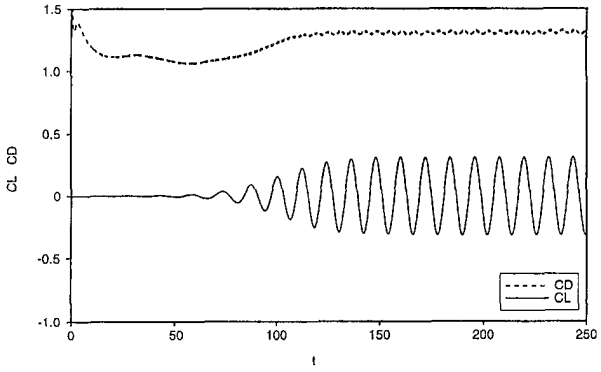


Fig. 1 Drag and lift coefficients versus time for Re = 100

$$C_M = \frac{\mathrm{KC}}{\pi^3}\int_0^{2\pi} \cos\theta\, C_F d\theta. \tag{14}$$

Then (13) is multiplied by sin $\theta$ and integrated to give

$$C_D = \frac{3}{8}\int_0^{2\pi} \sin\theta C_F d\theta. \tag{15}$$

## 5 Discussion of Results

To illustrate the computational procedure, we choose $\beta$ = 1035, and let KC values range from 0.5, where the flow is 2D and laminar, to 10.0, where the flow is 3D and turbulent. This range of KC values takes us through the complete range of flow behaviors that are expected in an oscillating flow past a fixed circular cylinder. Each calculation will be carried through 50 cycles, except for KC = 8, 10 where the calculation was reduced to 30 cycles because of the increased computational effort. The force coefficients are determined by averaging the calculated

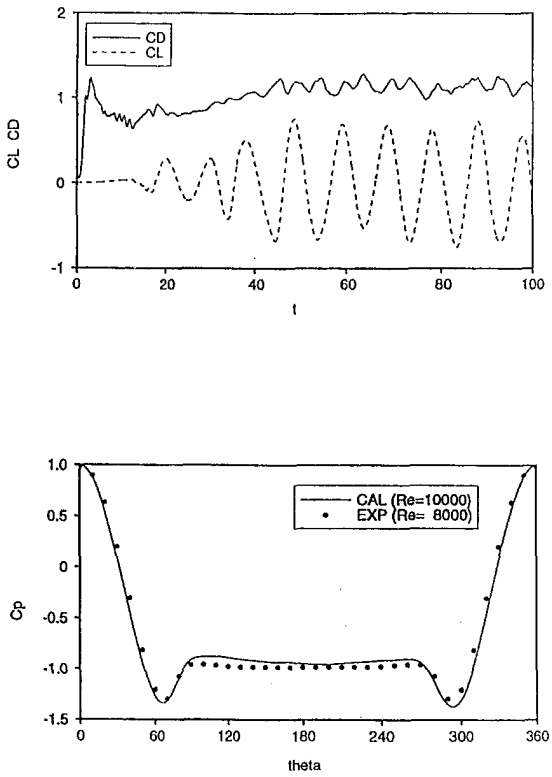


Fig. 2 Steady approach flow past a cylinder at Re = $10^4$ (3D LES). (*a*) Drag and lift coefficients versus time; (*b*) time-averaged pressure coefficient versus circumferential angle (data from Norberg, 1992).

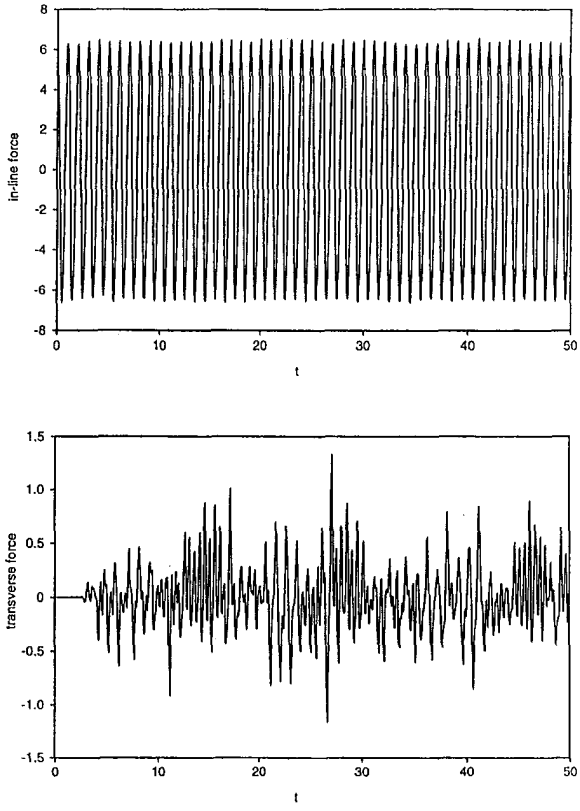


Fig. 3 In-line and transverse force coefficients versus time for KC = 3.0 and $\beta$ = 1035

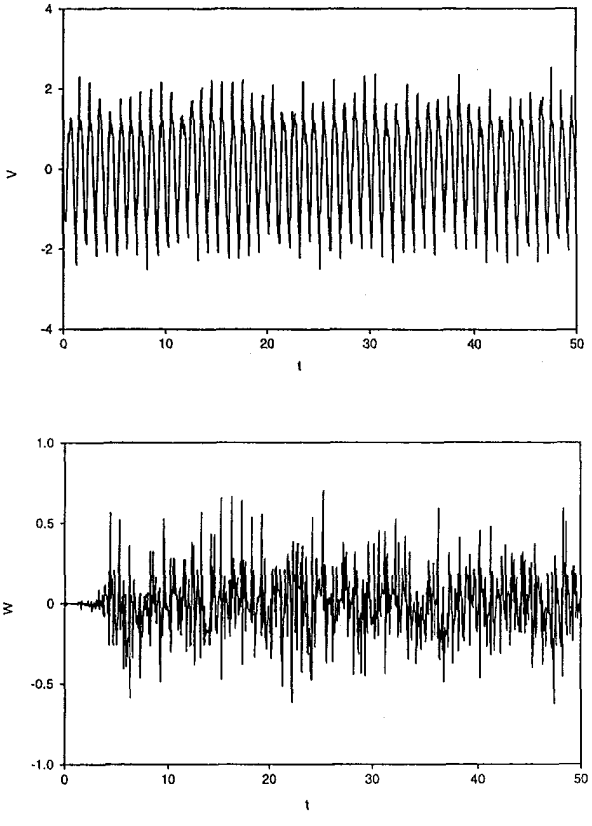


Fig. 4 Velocity components at ($r$, $\theta$, $z$) = (1.15, $\pi$/4, 0) for KC = 3.0 and $\beta$ = 1035. (*a*) $v$, the $\theta$ component; (*b*) $w$, the $z$ component.

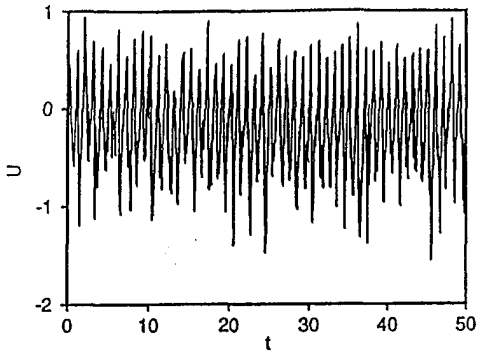


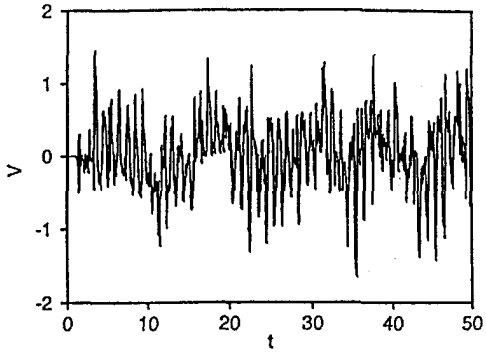


Figs. 5(*a* and *b*)

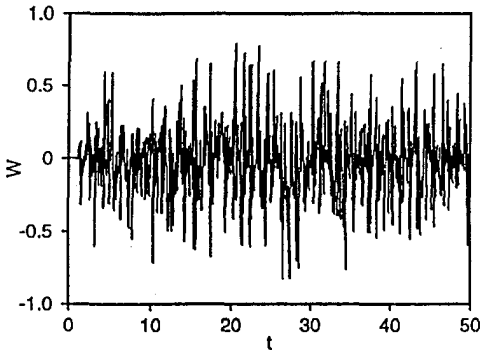


Fig. 5(*c*)

**Fig. 5 Velocity components at ($r$, $\theta$, $z$) = (1.5, 0, 0) for KC = 4.0 and $\beta$ = 1035. (*a*) $u$, the $r$ component; (*b*) $v$, the $\theta$ component; (*c*) $w$, $z$ component.**

results from the twentieth to the fiftieth cycles, except for KC = 8, 10 where the averaging was done between the sixteenth and thirtieth cycles.

The number of mesh points for the calculations was 160 × 128 × 16 in the $r$, $\theta$, $z$ directions respectively. The effect of grid size was examined extensively by Zhang (1995) and the mesh system and time step used in these LES calculations were found to be satisfactory for a stable, converged solution. The convergence study compared results for several different meshes ranging from 128 × 64 × 8 (radial, circumferential, axial) to 160 × 128 × 16 to 240 × 192 × 32 with at least two axial values used at each set of radial and circumferential values. The complete details of the convergence study are not presented here for the sake of brevity. The computational domain is $25R$ in the radial direction, and $4R$ in the axial direction. The $z$ dependence was suppressed for KC = 0.5, 0.8, 1.0 since the physical flow was expected to be 2D. An earlier study by Zhang and Dalton (1995) demonstrated that $z$-direction disturbances

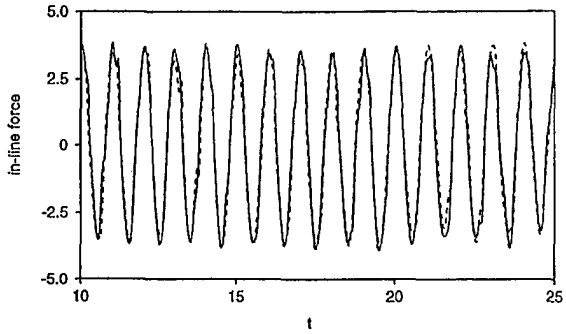


**Fig. 6 Validation for different grid resolutions and time steps at KC = 5.0, $\beta$ = 1035. —— : 160 × 128 × 16, $\Delta t$ = 0.001; - - - - : 240 × 192 × 16, $\Delta t$ = 0.0005.**

are damped for these cases. The time step was 0.002 for the laminar cases and 0.001 for the turbulent flow cases, except at KC = 8, 10 where the time step was 0.0002.

To validate the code, we ran two steady approach-flow cases, Re = 100 and $10^4$. The mesh sizes and time step are as given above. For Re = 100, the 2D drag and lift coefficients, $C_D$ and $C_L$, are shown in Fig. 1. Extremely good agreement is found with the experimental values of $C_{D,\text{avg}} \simeq 1.3$, $C_{L,\text{max}} \simeq 0.3$, and Strouhal number, $S \simeq 0.16$. Our calculated values are $C_{D,\text{avg}} = 1.29$, $C_{L,\text{max}} = 0.3$, and $S = 0.168$. At Re = $10^4$, the 3D results are shown in Fig. 2. Again, very good agreement with the experimental values is found. The average $C_D$ values are $C_{D,\text{cal}} = 1.15$ and $C_{D,\text{exp}} \simeq 1.2$; the r.m.s. $C_L$ values are $C_{L,\text{cal}} = 0.46$ and $C_{L,\text{exp}} \simeq 0.4$ to 0.5; the values of $S$ are $S_{\text{cal}} = 0.206$ and $S_{\text{exp}} \simeq 0.21$. The time-averaged pressure coefficient is also shown in Fig. 2; good agreement is shown with data at a slightly

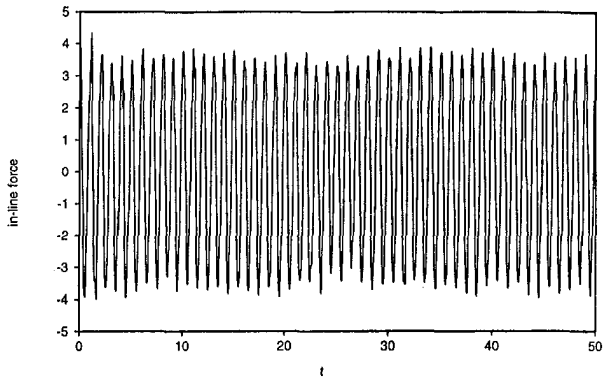


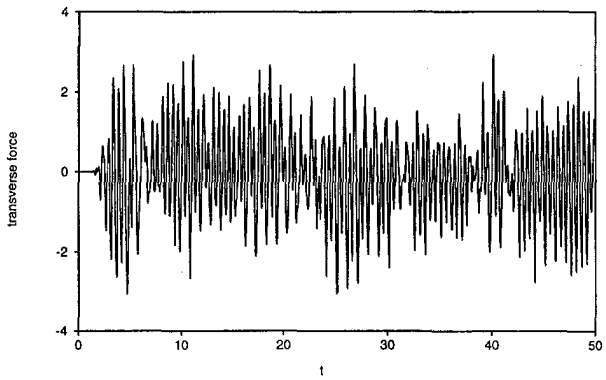


**Fig. 7 In-line and transverse force coefficients versus time for KC = 5.0 and $\beta$ = 1035**

different value of Re. Further documentation of the code is found in Zhang (1995).

For the oscillating flow, the lowest KC values, KC = 0.5, represents a straightforward 2D laminar flow calculation, requiring no turbulence modeling. The physical wake remains symmetric, so the force acts only in the direction of the oscillating flow; no transverse force is present. The numerical wake also remained symmetric with the calculated transverse force as zero. The comparison between the calculated and experimental force coefficients is shown in Table 1, where the experimental values are from Sarpkaya (1986). The $C_M$ comparison is quite good while the $C_{D,\text{cal}}$ value is about 6 percent higher than the experimental value of Sarpkaya. Wang (1968) obtained a solution to this 2D problem, via the method of inner and outer expansions, which has become known as the Stokes-Wang solution. Since the physical flow is still 2D at KC = 0.5, we can compare our calculated values to the theoretical results of Wang, which are $C_D = 1.66$ and $C_m = 2.07$. We note an extremely good comparison with our values of 1.65 and 2.05, respectively.

For $0.8 \leq \text{KC} \leq 2$, the flow has become 3D but still remains viscosity dominated, i.e., no turbulence is established yet, according to Sarpkaya (1986). As seen in Table 1, the calculated $C_D$ values agree quite well with the experimental values through KC = 1.0 with the calculated values being about 10 percent low at KC = 1.5 and 2. The agreement between calculated and experimental values of $C_M$ remains quite good through this 3D viscous regime.

At KC = 3.0, the flow is well established in the 3D turbulent range as documented by Sarpkaya (1981). The in-line and transverse forces are shown in Fig. 3 and the regularity of the force is obvious. The transverse force is no longer zero, although it is relatively small compared to the in-line force. The transverse force coefficient $C_L$ is not sinusoidal in its behavior, as is the in-line coefficient $C_F$. The presence of a nonsinusoidal $C_L$ implies that the wake has become asymmetric and the periodic reversal of the oscillating flow, along with the induced velocity effects of the wake vortices, produces an irregularity in the transverse force. Figure 3 shows very little variation in peak $C_F$ which implies a relatively weak wake asymmetry; this observation is substantiated by the magnitude of $C_L$. The $\theta$ and $z$ components of the dimensionless velocity are shown in Fig. 4 at $(r, \theta, z) = (1.15, \pi/4, 0)$. The $\theta$-component at KC = 3, which corresponds to a fluid oscillation amplitude of only $0.96R$, still has a strong oscillatory character. The motion, with small oscillation amplitude, doesn't generate large wake vortices (although they have become slightly asymmetric) and the $\theta$ velocity still bears a potential flow identity but with obvious induced-velocity effects. The axial velocity, in Fig. 4(*b*), has developed after about the fourth cycle of oscillation and shows the random character expected of the wake turbulence.

All three velocity components at KC = 4 are shown in Fig. 5 at $(r, \theta, z) = (1.5, 0, 0)$ which is behind the rear stagnation point on the cylinder. The radial component is shown in Fig. 5(*a*). For a symmetric wake, the radial velocity would be negative at (1.5, 0, 0). However for this asymmetric wake, we note that the radial velocity varies between positive and negative. The power spectrum of the radial velocity (not shown here) shows the energy is focused at the oscillatory period and the first subharmonic. The asymmetry of the wake is shown quite clearly in the $\theta$-component of velocity in Fig. 5(*b*). It is also noted from comparing Figs. 4(*b*) and 5(*c*) that the maximum values of the $z$-component have also increased as KC increased from 3 to 4.

The next case to discuss is KC = 5. As KC increases, it is reasonable to expect that a mesh size effect could influence the results. So, we offer another convergence test. Figure 6 shows the in-line force coefficient for two different mesh sizes: $160 \times 128 \times 16$, $\Delta t = 0.001$; $240 \times 192 \times 10$, $\Delta t = 0.0005$. The force coefficients are virtually identical. They are in phase with very little difference in peak values over the entire 25 cycles

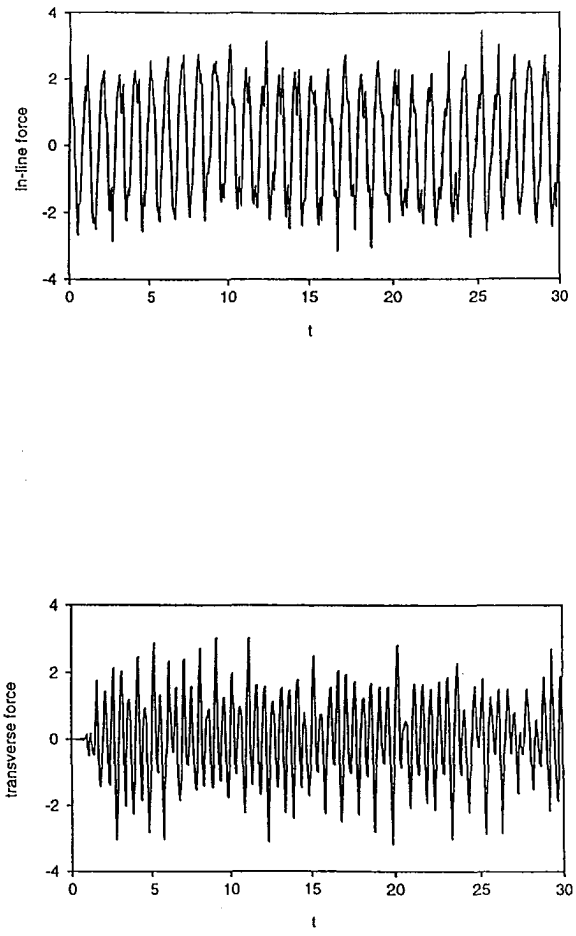


**Fig. 8 In-line and transverse force coefficients versus time for KC = 8.0 and $\beta$ = 1035**

shown in Fig. 6. Thus, we continue with the $160 \times 128 \times 16$ mesh system with a time step of 0.001.

The physical flow for KC = 5 is one with an increased asymmetry in the 3D turbulent wake. The calculations of $C_F$ and $C_L$ are shown in Fig. 7. A comparison of Figs. 3 and 7 shows that $C_{F,\max}$ has decreased, as expected, as KC increased. The $C_F$ plot at KC = 5 shows more irregularity due to the increased asymmetry of the wake vortices. The transverse force at KC = 5 has increased by a factor of about two over that at KC = 3.

The results for the force coefficients at KC = 8 and $\beta$ = 1035 are shown in Fig. 8. The influence of a higher harmonic is seen in the in-line force coefficient while the transverse force coefficient shows the randomness expected due to the sweep of an unsymmetric vortex wake back and forth over the cylinder. The cases for KC = 3 and KC = 8, shown in Figs. 3 and 8, respectively, show the effect of increasing KC when the wake is turbulent (for both cases). The larger KC means that the fluid oscillation has increased by a factor of 8/3 (the ratio of KC numbers). The increase in fluid oscillation distance means that the wake vortices have formed a greater asymmetry and the wake turbulence has become more established. The velocity components at $(r, \theta, z) = (1.5, \pi/4, 0)$ are shown in Figs. 9(*a–c*). The 3D nature of the flow, the $Z$-component of velocity, is shown in Fig. 9(*c*). The magnitude of $\omega$ at KC = 8 in Fig. 9(*c*) is no greater than the $\omega$-magnitude at KC = 4 (shown in Fig. 5(*c*)).

The last case to present is at KC = 10. The in-line force coefficient, shown in Fig. 10, is similar to the KC = 8 result with essentially the same magnitude and higher harmonic influence. A spectral analysis of the KC = 10 result yielded a peak

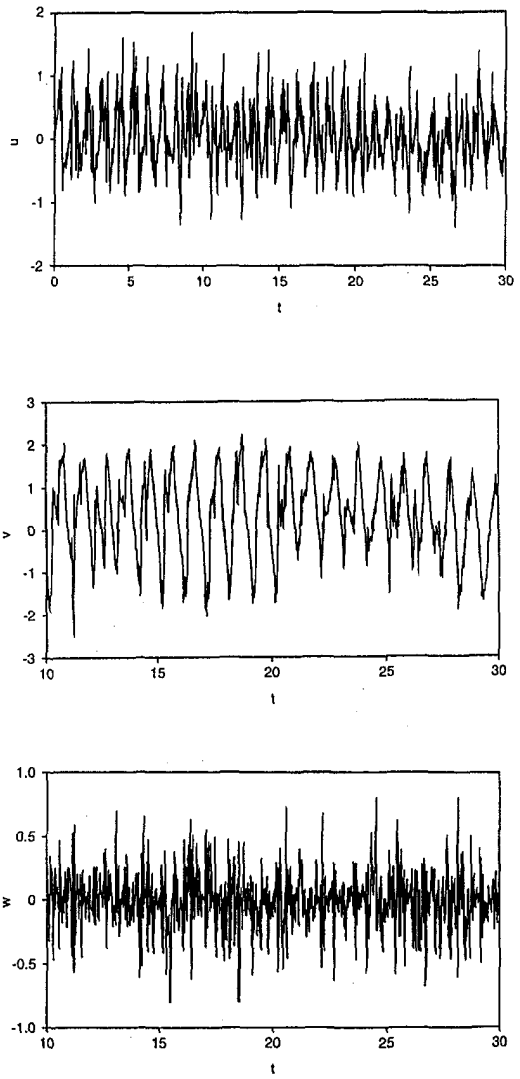


Fig. 9 Velocity versus time at $(r, \theta, z) = (1.5, \pi/4, 0)$ for KC = 8.0 and $\beta$ = 1035. (*a*) Radial velocity versus time; (*b*) circumferential velocity versus time; (*c*) axial velocity versus time.

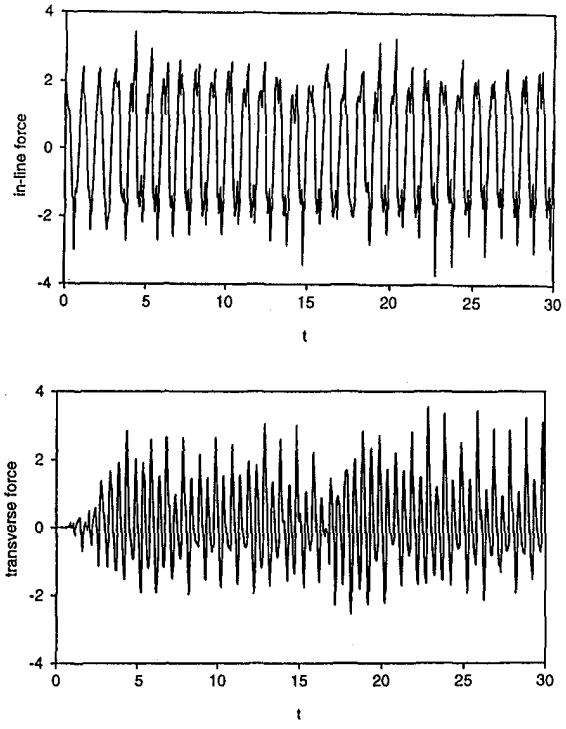


Fig. 10 In-line and transverse force coefficients versus time for KC = 10.0 and $\beta$ = 1035

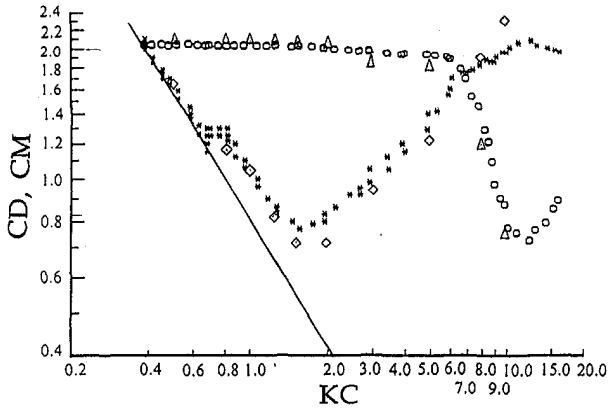


Fig. 11 Comparison of calculated $C_D$, $C_M$ values to Sarpkaya's data (1986) for $\beta$ = 1035. ◇ calculated $C_D$, * experimental $C_D$, △ calculated $C_M$, ○ experimental $C_M$, —— Stokes-Wang theory.

at a frequency of one with a lesser peak at a frequency of 3 and an even lesser peak at a frequency of 2. The transverse force coefficient at KC = 10, shows an irregular behavior when plotted against time, similar to that shown for all of the turbulent wake cases, i.e., from 3 ≤ KC ≤ 10. This randomness in the transverse force coefficient is due to the asymmetric nature of the wake vortices which increases as KC increases.

Figure 11 shows a plot of $C_D$ and $C_M$ versus KC for $\beta$ = 1035. The calculated values are noted to agree extremely well with the experimental values.

The Cray C90 computer at the Pittsburgh supercomputer center was used for these calculations. A typical run time was approximately 10 Service Units of Cray C90 time for 50 cycles of fluid oscillation. An electronic version containing spectral results of this paper is available on www.me.uh.edu/faculty_and_staff/faculty/Dalton.html.

## 6 Conclusions

We have performed an LES primitive-variables solution of the time-dependent Navier-Stokes equations using a fractional step method to advance time for the case of an oscillating incompressible fluid past a fixed circular cylinder. The Smagorinsky model was used to represent the eddy viscosity. Our goal is to represent wave forces on a circular cylinder. To this end, we have calculated values of $C_D$ and $C_M$ from the Morison equation which agree quite well with experimental data representing the same flow. The axial wake structure has been calculated within the limits of the finite length of cylinder considered herein. A longer cylinder length would be necessary to determine to what extent the axial structure would be affected by the particular finite computational length of this study.

## Acknowledgments

We are grateful to NSF for Grant ID INT924844 and to the Pittsburgh Supercomputing Center for Grant CBT910047P used in support of this project. We acknowledge the Journal of Fluid Mechanics for the use of Figure 13. An earlier version of this paper was given at the Third International Symposium on Engineering Turbulence Modelling and Measurements on Crete in May 1996.

## References


Honji, H., 1981, "Streaked Flow Around an Oscillating Circular Cylinder," *Journal of Fluid Mechanics,* Vol. 107, pp. 509–520.

Justesen, P., 1991, "A Numerical Study of Oscillating Flow Around a Circular Cylinder," *Journal of Fluid Mechanics,* Vol. 222, pp. 157–196.

Karniadakis, G. E., Israeli, M., and Orszag, S. A., 1991, "High-Order Splitting Methods for Incompressible Navier-Stokes Equations," *Journal of Computational Physics,* Vol. 97, pp. 414–443.

Kim, J., and Moin, P., 1985, "Application of a Fractional-Step Method to the Incompressible Navier-Stokes Equations," *Journal of Computational Physics,* Vol. 59, pp. 308–323.

Norberg, C., 1992, "Pressure Forces on a Circular Cylinder in Cross Flow," *IUTAM Symposium on Bluff Body Wakes, Dynamics and Instabilities,* Gottingen, Sept. 7–11.

Sarpkaya, T., and Isaacson, M., 1981, *Mechanics of Wave Forces on Offshore Structures,* Van Nostrand Reinhold, New York.

Sarpkaya, T., 1986, "Force on a Circular Cylinder in Viscous Oscillatory Flow at low Keulegan-Carpenter Numbers," *Journal of Fluid Mechanics,* Vol. 165, pp. 61–71.

Speziale, C. G., 1985, "Galilean Invariance of Subgrid-Scale Stress Models in the Large Eddy Simulation of Turbulence," *Journal of Fluid Mechanics,* Vol. 156, pp. 55–62.

Wang, C. Y., 1968, "On High Frequency Oscillating Viscous Flows," *Journal of Fluid Mechanics,* Vol. 32, pp. 55–68.

Wang, X., and Dalton, D., 1991, "Oscillating Flow Past a Rigid Circular Cylinder: A Finite-Difference Study," ASME JOURNAL OF FLUIDS ENGINEERING, Vol. 113, pp. 377–383.

Zhang, J., 1995, "A Numerical Study of Three-Dimensional Unsteady Flows Past a Circular Cylinder," PhD dissertation, University of Houston.

Zhang, J., and Dalton, C., 1995, "The Onset of Three-Dimensional Wake in Two-Dimensional Oscillatory Flow Past a Circular Cylinder," *Proceedings of the 6th Asian Congress of Fluid Mechanics,* Singapore, pp. 1508–1511.

# Prediction of Transpired Turbulent Boundary Layers With Arbitrary Pressure Gradients

**Miodrag Oljaca**
Graduate Student,
Woodruff School of Mechanical Engineering,
Georgia Institute of Technology,
Atlanta, GA 30332

**James Sucec**
Professor,
Department of Mechanical Engineering,
University of Maine,
Orono, ME 04469

*An integral method, using Coles combined inner and outer law as the velocity profile, is developed for calculation of turbulent boundary layers with blowing or suction and pressure gradients. The resulting ordinary differential equations are solved numerically for the distribution of skin friction coefficient and integral thickness along the surface. Comparisons of predicted skin friction coefficients with experimental data are made for a wide range of blowing and suction rates and for various pressure gradients, including adverse, zero and a strong favorable gradient. In addition to good agreement with experimental data for constant blowing fractions F, the method is also successfully tested on cases where the blowing fraction is variable with position. Predictions, in general, exhibit satisfactory agreement with the data. The integral method predictions are comparable to, or better than, a number of finite difference procedures in a limited number of cases where comparisons were made.*

## Introduction

The problem of calculating the skin friction coefficient distribution along a surface covered by a turbulent boundary layer, with the combined effects of transpiration and pressure gradient, is important both in its own right and because the solution is needed to solve for the convective heat flux distribution. Possible applications here include blades and vanes of gas turbine engines, combustor liner cooling, and rocket nozzles.

Viability and feasibility of integral prediction methods, as compared to finite difference solutions of the partial differential form of the conservation laws, were supported by the results of the second Stanford conference, Kline et al. (1981), for turbulent boundary layer flows without transpiration. At that time, there were no integral methods for transpired flows presented for evaluation at the conference.

Das and White, (1986) and Das (1988) present a relatively simple integral method for turbulent boundary layers with pressure gradient, but with no transpiration. They used Coles combined law of wall and wake along with an empirical correlation for the wake strength, $\pi$. Numerical solution of a single ordinary differential equation resulted in the skin friction coefficient distribution. Comparisons with experimental results were favorable. Das (1992) reformulated the integral method of Das and White (1986) to an inverse mode in which the displacement thickness distribution in $x$ is prescribed as the input. This resulted in good predictions for separated turbulent boundary layers. Integral methods which addressed the calculation of the transpired turbulent boundary layer include those of Torii et al. (1966) and of Thomas and Kadry (1990). The early results of Torii et al. (1966) were for zero pressure gradient. The model employed assumptions that some functions in transpired flow had the same form as the known ones in untranspired flow and also used an approximation to relate the momentum thickness Reynolds number to the $x$ Reynolds number. The more recent work by Thomas and Kadry (1990), uses a polynomial approximating sequence for the shear stress variation across the boundary layer, in conjunction with mixing length relations, to solve numerically for a velocity profile. This numerical velocity profile information is used to perform integrations, numerically, which are needed in the finite difference solution of the $x$ momentum equation. Comparisons are made, for a range of constant blowing fractions, $F$, to experimental data for zero pressure gradient and for an adverse pressure gradient. Some of these results compare favorably with finite difference solutions for two test cases at the second Stanford conference (Kline et al., 1981). However, they didn't start their calculations until after the third data point, beyond the region of the largest gradients in $C_f$. Their integral method also requires some fairly complicated numerical work in order to be used.

The work being presented here represents a generalization and extension of the previous work of Das and White (1986) and Das (1988) to the more complex problem posed by transpiration at the surface. The use of the combined law of wall and wake in the form valid for transpired turbulent boundary layers (Coles, 1971) along with the aid of inner variables and a variable transformation, allows the exact analytic evaluation of all needed integrals to become a practical task. Solution of the resulting ordinary differential equations leads to the distribution of skin friction coefficient, momentum thickness, and other integral parameters along the surface.

## Analysis

The present development is for a constant property two-dimensional turbulent boundary layer, which is steady on the average and subject to surface transpiration and streamwise pressure gradient. The governing conservation laws are those for mass and $x$ momentum. Their partial differential forms are integrated across the boundary layer and the following inner variables are introduced.

$$u^* = \sqrt{\tau_w/\rho}, \quad u^+ = u/u^*, \quad u_s^+ = u_s/u^*,$$

$$y^+ = u^* y/\nu, \quad \text{and} \quad \delta^+ = u^* \delta/\nu.$$

This gives the following form of integral $x$ momentum equation.

$$u_s \frac{d}{dx}\int_o^{\delta^+} u^+ dy^+ - \frac{d}{dx}\int_o^{\delta^+} u^* u^{+2} dy^+ + u_s^+ \frac{du_s}{dx}\delta^+ = \frac{u^{*2} + u_s^2 F}{\nu} \quad (1)$$

Contributed by the Fluids Engineering Division for publication in the JOURNAL OF FLUIDS ENGINEERING. Manuscript received by the Fluids Engineering Division August 14, 1996; revised manuscript received January 12, 1997. Associate Technical Editor: P. M. Sockol.

The blowing fraction $F = v_w/u_s$. Next, the momentum thickness, $\theta$, and the displacement thickness, $\delta^*$, are written in terms of inner variables, namely,

$$\theta = \frac{\nu}{u_s}\int_o^{\delta^+} u^+ dy^+ - \frac{\nu}{u_s u_s^+}\int_o^{\delta^+} u^{+2} dy^+ \quad (2)$$

$$\delta^* = \frac{\nu\delta^+ u_s^+}{u_s} - \frac{\nu}{u_s}\int_o^{\delta^+} u^+ dy^+ \quad (3)$$

Using Eqs. (2) and (3) in Eq. (1) gives the more compact form shown next. The shape factor $H = \delta^*/\theta$.

$$\frac{d\theta}{dx} + \left(\frac{H+2}{u_s}\right)\frac{du_s}{dx}\theta = \frac{1}{u_s^{+2}} + F \quad (4)$$

The velocity profile needed for evaluation of the integrals in Eqs. (2) and (3) is taken to be Coles (1971) combined inner and outer law for transpired turbulent boundary layers. Coles (1971) provided extensive evidence that this velocity profile fits experimental data remarkably well. To achieve some conciseness of form the new variable $\sigma$ is defined as follows,

$$\sigma = \frac{1}{K}\ln y^+ + A(x) \quad (5)$$

Using Eq. (5), the Coles (1971) combined inner and outer law for transpired turbulent boundary layers can be written as shown next.

$$u^+ = \sigma + \frac{\pi}{K}W + \frac{v_w^+}{4}\left[\sigma^2 + \frac{2\pi}{K}\sigma W + \frac{\pi^2}{K^2}W^2\right] \quad (6)$$

In Eq. (6), $\pi(x)$ is the wake strength parameter and $W$, the wake function, is given by the following commonly used polynomial representation due to Moses (Das and White, 1986).

$$W(y/\delta) = 2[3(y/\delta)^2 - 2(y/\delta)^3] \quad (7)$$

Next, the velocity profile, Eq. (6), must be used to evaluate the integrals which appear in Eqs. (2) and (3). If $\sigma$ and $W$ from Eqs. (5) and (7) are inserted into Eq. (6), $u^+$ will contain twelve terms, and this must be squared for use in Eq. (2). It was noticed that much of this work could be reduced if the new variable $\sigma$, defined in Eq. (5) was used as the integration variable instead of $y^+$. Thus, it follows from Eq. (5) that

$$dy^+ = K\exp(\sigma - A)d\sigma \quad (8)$$

Here, $A$ is an additive function in the velocity profile that is, in general, a function of $x$ for a transpired turbulent boundary layer, and is discussed in a separate section immediately following Eq. (12). Using this, it turns out to be practical to perform the needed integrations analytically. Thus, after defining,

$$\phi = \ln\delta^+ + KA - 1, \quad (9)$$

one finds that,

$$\int_o^{\delta^+} u^+ dy^+ = \frac{\delta^+\phi}{K} + \frac{\delta^+\pi}{K} + \frac{v_w^+\delta^+}{4K^2} \times\left[\phi^2 + 1 + 2\pi\left(\ln\delta^+ - \frac{5}{12}\right) + 2AK\pi + \frac{52\pi^2}{35}\right] \quad (10)$$

The result for $\int_o^{\delta^+} u^{+2} dy^+$ is prohibitively long to be included here and is available in Oljaca (1993). The integrity of these integrations was checked several times, both analytically and also by numerical calculation of the original integrals for a number of representative cases. The numerical integrations agreed with the analytic expressions to within 0.05 percent for most of the test cases. Details are available in Oljaca (1993).

With the integrals evaluated which are needed in Eqs. (2) and (3) for $\theta$ and $\delta^*$, the derivative of $\theta$ required in Eq. (4) is performed analytically and Eq. (4) takes the following form.

$$B_1\frac{d\delta^+}{dx} + B_2\frac{dA}{dx} + B_3\frac{d\pi}{dx} + B_4\frac{dv_w^+}{dx} + B_6\frac{du_s^+}{dx} = B_7 \quad (11)$$

In order to solve for variables defined in Eq. (11), it is necessary to find expressions for $\delta^+$, $A$, $\pi$, $v_w^+$ and $u_s^+$ along with their derivatives, and solve simultaneously with Eq. (11). The coefficients, $B_1 \rightarrow B_7$, are algebraic functions of $\delta^+$, $A$, $\pi$, $v_w^+$ and $u_s^+$ and are available in Oljaca (1993). Since $v_w^+$ can be written as $v_w^+ = Fu_s^+$, it follows that

$$\frac{dv_w^+}{dx} = F\frac{du_s^+}{dx} + u_s^+\frac{dF}{dx} \quad (12)$$

**Relations for *A*.** A number of proposals have been suggested in the literature for the form of $A(x)$, the function which appears in the velocity profile, Eqs. (6) and (5). Stevenson (1963) finds that his data are represented well when $A$ is chosen to be constant, as it is for no transpiration. However, the weight of the evidence seems to indicate that $A$ depends on $v_w^+$ or $F$. Bradshaw (1967) recommends for suction, $F < 0$, a relation that can be written as follows.

$$A = 5 + 1375v_w^{+2} \quad F < 0 \quad (13)$$

Simpson (1970), on the basis of his data, suggests the use of the following expression.

## Nomenclature

$A$ = additive function in velocity profile
$C_f = 2\tau_w/\rho u_s^2$ skin friction coefficient
$F = v_w/u_s$ blowing fraction
$H = \delta^*/\theta$ shape factor
$K$ = 0.41 von Karman's constant
$K_a = (\nu/u_s^2)du_s/dx$ acceleration parameter
$L$ = reference lengths
$P$ = static pressure
$\mathrm{Re}_x$, $\mathrm{Re}_\theta = u_s x/\nu$, $u_s\theta/\nu$ Reynolds numbers
$u$, $u_s$ = local $x$ component and freestream velocity
$u^* = \sqrt{\tau_w/\rho}$ friction velocity
$u^+$, $u_s^+ = u/u^*$, $u_s/u^*$
$v_w$ = local $y$ component of velocity at the surface
$v_w^+ = v_w/u^*$
$x$ = space coordinate along the surface
$y$ = space coordinate perpendicular to the surface
$y^+ = yu^*/\nu$
$W$ = wake function, Eq. (7)
$\beta$ = defined in Eq. (17). Clauser's equilibrium parameter
$\delta$ = local hydrodynamic boundary layer thickness
$\delta^+ = \delta u^*/\nu$
$\delta^*$ = local displacement thickness
$\Delta = \sigma$ at $y^+ = \delta^+$
$\Delta x$ = lattice spacing in $x$ direction
$\theta$ = local momentum thickness
$\nu$ = kinematic viscosity
$\pi$ = Coles wake strength
$\rho$ = mass density
$\sigma$ = defined by Eq. (5)
$\tau_W$ = local wall shear stress
$\phi$ = defined by Eq. (9)

$$A = 5 + \left(\frac{2}{v_w^+}\right)[\sqrt{1 + 10.81 v_w^+} - 1] - 10.81 \quad (14)$$

By analysis of blowing data from Kline et al. (1981), Silva-Freire (1988) develops the following relation for blowing, $F > 0$, and implies its validity for suction, as well.

$$A = 5 - 512F \quad F > 0 \quad (15)$$

It was decided to use Eqs. (13) and (15) for $A$ in the present work. With this, the derivatives of $A$ can be written as

$$\frac{dA}{dx} = 2750\, u_s^+ F\left[u_s^+ \frac{dF}{dx} + F\frac{du_s^+}{dx}\right], \quad F < 0$$
$$\frac{dA}{dx} = -512\frac{dF}{dx}, \quad F > 0 \quad (16)$$

Equation (16) for the derivative of $A$ can now be used simultaneously with Eq. (11).

**Wake Strength Relation.** For an equilibrium boundary layer, the wake strength, $\pi$, in the velocity profile, Eq. (6), depends only upon the Clauser pressure gradient parameter, $\beta$, (Mellor and Gibson, 1966).

$$\beta = \frac{\delta^*}{\tau_w}\frac{dP}{dx} \quad (17)$$

The present work uses a slightly modified form of the $\beta$-$\pi$ relation recommended by White (1991), a relation based on the correlation of a large number of data points.

$$\beta = -0.5 + 0.76\pi + 0.42\pi^2 \quad (18)$$

In Eq. (18), 0.5 has replaced the 0.4 used in the original relation in White (1991). There were two reasons for the modification. First, the wake strength, $\pi$, goes to zero as $\beta \to -0.5$, not $-0.4$, (Mellor and Gibson, 1966). For $\beta = 0$, the original expression gives $\pi = 0.426$ which is somewhat lower than the values usually recommended and observed. $\pi$ values greater than 0.5 are indicated for $\beta = 0$ by the data given in Coles (1971). In fact, a $\beta - \pi$ relation specifically for favorable pressure gradients, in Das and White (1986), gives $\pi = 0.55$ at $\beta = 0$. The change which gave Eq. (18) gives a value of $\pi = 0.513$ at $\beta = 0$.

With the aid of Euler's equation of motion and some of the inner variable expressions, Eq. (17) can be rewritten as follows.

$$\beta = -\delta^* \frac{u_s^{+2}}{u_s}\frac{du_s}{dx} \quad (19)$$

Substituting this into Eq. (18), differentiating (18) with respect to $x$ and using Eq. (3) for $\delta^*$ gives the $\pi$ derivative shown next.

$$\frac{d\pi}{dx} = S_1\frac{du_s^+}{dx} + S_2\frac{d^2u_s}{dx^2} + S_3\frac{du_s}{dx} + S_4\frac{d\delta^+}{dx} + S_5\frac{dA}{dx} + S_7\frac{dv_w^+}{dx} \quad (20)$$

$S_1$, $S_2$, etc. are functions of $\delta^+$, $u_s^+$, $A$, $\pi$, $v_w^+$, $u_s$ and $du_s/dx$, (Oljaca, 1993). Equation (20) provides an additional relation for the wake strength that can be used simultaneously with Eq. (11).

The last equation needed for closure is given by the velocity profile, Eq. (6), evaluated at $y^+ = \delta^+$, where $u^+ = u_s^+$, and then differentiating. This leads to the next equation,

$$\frac{d\delta^+}{dx} = C_o\left[C_2\frac{dF}{dx} + C_3\frac{du_s^+}{dx} - K\frac{dA}{dx} - 2\frac{d\pi}{dx}\right] \quad (21)$$

**Solution Procedure for the Equations.** Equation (12) was used to eliminate $dv_w^+/dx$ from Eqs. (11) and (20). That done, the remaining Eqs. (11), (16), (20), and (21) were put in a form suitable for solution by a fourth-order Runge-Kutta-Gill method, given in White (1991), for simultaneous ordinary differential equations. The step size, $\Delta x$, was continually cut in half until two successive solutions gave results sensibly independent of the step size used. Typical of the step size refinement was a case of Andersen et al. (1972) in which $F \sim 0.002\, x^{-0.17}$ and $u_s \sim x^{-0.15}$. Here the step size was reduced until the maximum change in $C_f/2$ was of magnitude 0.1 percent leading to a nondimensional step size of $\Delta(x/L) = 0.0032$.

Initial values of $u_s^+$, $\delta^+$, $\pi$, and $A$ are needed to start the solution of the set of differential equations. Generally what is known is the value of $C_f/2$ at the starting position $x_o$. This gives the initial value of $u_s^+$ since $u_s^+ = \sqrt{C_f/2}$. With this and the specified blowing fraction function, $F$, one has $v_w^+ = Fu_s^+$ and, therefore, from the appropriate equation, (13) or (15), the value of $A$ is found. Eliminating $\beta$ between Eqs. (18) and (19) gives,

$$-\frac{u_s^{+2}}{u_s}\frac{du_s}{dx}\delta^* = -0.5 + 0.76\pi + 0.42\pi^2 \quad (22)$$

Next Eqs. (3) and (10) are combined to eliminate the integral and give $\delta^*$ with functional form:

$$\delta^* = f[\delta^+, \pi, u_s^+, A, u_s(x)] \quad (23)$$

The function $f$, in Eq. (23), is quadratic in $\pi$ so that when $\delta^*$ is eliminated between (22) and (23), the result is a quadratic equation for $\pi$ in terms of $\delta^+$ which we write as follows.

$$\pi^2(x_o) + D_1\pi(x_o) + D_2 = 0 \quad (24)$$

$D_1$ and $D_2$ are known functions of $\delta^+$ and of the known values of $u_s^+$ and $A$. The last equation needed is the velocity profile, Eq. (6), evaluated at $y^+ = \delta^+$ where the wake function, Eq. (7), has the value 2. Defining $\Delta$ as the value of $\sigma$ at $y^+ = \delta^+$, Eq. (6) becomes,

$$u_s^+ = \Delta + \frac{2\pi}{K} + \frac{v_w^+}{4}\left[\Delta^2 + \frac{4\pi}{K}\Delta + \frac{4\pi^2}{K^2}\right] \quad (25)$$

Finally, Eqs. (24) and (25) are solved iteratively as follows. A low value of $\delta^+$ is chosen as a first estimate. Equation (24) is then solved for the value of $\pi(x_o)$. These values for $\pi$ and $\delta^+$ are used in Eq. (25) to calculate $u_s^+$. This procedure is repeated until the value of $u_s^+$ calculated from Eq. (25) agrees with the known value at $x_o$.

A similar procedure is used to calculate starting values if the momentum thickness Reynolds number is known at $x_o$ rather than the skin friction coefficient.

## Results and Discussion

The comparisons between predicted skin friction coefficients $C_f$, and experimental data are shown in the various figures. These results include cases of blowing ($F > 0$) and suction ($F < 0$) where $F$, in general, is variable with distance, $x$, along the surface. Included are cases of constant freestream velocity, $u_s$, adverse pressure gradients (decelerating flows) and, for a couple of cases, favorable pressure gradients (accelerating flows). A few cases in which there is a step change in transpiration rate are also shown. Finally, some representative predictions of momentum thickness Reynolds number $\mathrm{Re}_\theta$, as a function of $x$ are also given. The predictions of $C_f/2$ were begun with the measured value at the first data point unless otherwise indicated. The same is true for $\mathrm{Re}_\theta$ predictions. The results predicted with the wake model of the present work are shown as either a function of $\mathrm{Re}_x$ or $x/L$ depending on the way the experimental data was presented by the different sources in the references.

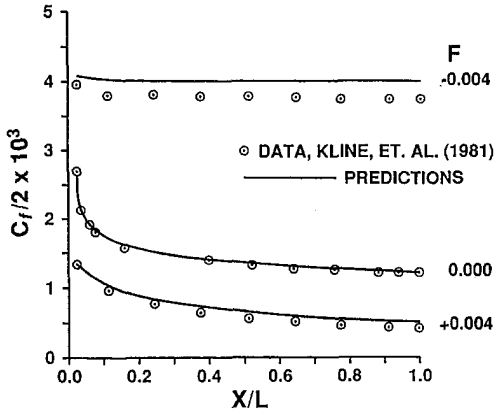


**Fig. 1 Predictions and data. $F = 0.0$, $u_s$ = constant, $L$ = 5m.; $F = +0.004$, $u_s$ = constant and $F = -0.004$, $u_s \sim x^{-0.15}$, $L$ = 2.286 m (7.5 ft) Test cases from second Stanford Conference.**

Figure 1 shows predictions and data for three test cases used at the second Stanford Conference (Kline et al., 1981). For the case of zero pressure gradient and $F = 0$, the agreement between predictions and data is very good as would be expected for this simplest case. Agreement also seems very reasonable for the other two cases shown, suction and deceleration ($F = -0.004$ and $u_s(x) \sim x^{-0.15}$) and strong blowing ($F = +0.004$) and zero pressure gradient. In fact, predictions of the present method compare favorably to predictions by the various finite difference methods presented at the second Stanford conference, (Kline et al., 1981). It is noteworthy that the magnitude of the skin friction coefficient for $F = +0.004$ is significantly lower than for $F = 0$. Blowing reduces the value of the skin friction coefficient due to the fact that the boundary layer becomes thicker and the velocity gradient at the wall becomes smaller. In the limit of very strong blowing the entire boundary layer would be blown off, and the $C_f$ would be reduced to zero. On the other side, the magnitude of the $C_f$ increases with increasing suction as it approaches the asymptotic suction limit of $C_f = -2F$.

The data in Figs. 2 and 3 are from Simpson et al. (1969) and is for zero pressure gradient. Figure 2 shows data for a range of constant blowing fraction, $F$, from very strong suction, $F = -0.00757$ to very strong blowing, $F = +0.0078$. Predicted curves of $C_f/2$ versus $\mathrm{Re}_x$, the solid lines, exhibit, for the most part, good agreement with the data for these zero pressure gradient cases. Figure 3 shows results for suction and blowing which is inversely dependent upon $x^{0.20}$, where the exact functional form of $F$ is shown to the right of the plot. Agreement of predictions and data is similar to that for the constant $F$ results of the previous figure.

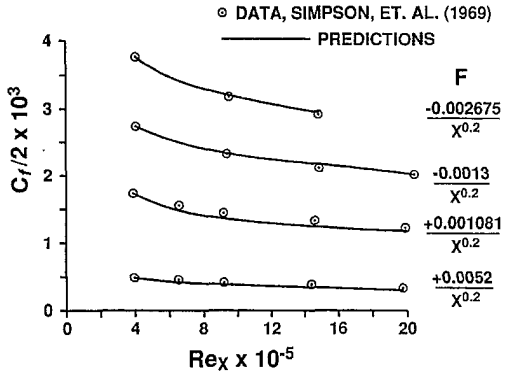


**Fig. 3 Predictions and data. $u_s$ = constant. $F \sim \pm x^{0.2}$**

In Fig. 4 are shown experimental results of Andersen et al. (1972) for constant $F$ from 0.00 to 0.008 and zero pressure gradient. It is important to note that the difference between predictions for $F = 0.00$ in Fig. 1 and Fig. 4 is due to the fact that experimental initial conditions for $C_f/2$ at the same $x/L$ position are different due to different starting conditions near $x = 0$. Overall, predictions seem to be adequate though they are somewhat high for $F = +0.00375$ and 0.008. The integrity of much of the data of Andersen et al. (1972) has survived the scrutiny of the evaluators at the second Stanford conference (Kline et al., 1981). However, they did conclude that the data for $F$ greater than 0.004 may have three dimensional effects associated with it and this was particularly true for $F = +0.008$. Figure. 5 shows data, also from Andersen et al. (1972), for the most complicated cases, namely, simultaneous deceleration with $u_s(x) \sim x^{-0.15}$, and variable blowing with $F \sim x^{-0.17}$. The meaning of the expressions for variable $F$ shown in Fig. 5 and also in Fig. 3 is slightly different. In Fig. 3, $F$ is exactly represented with the given functional form, while in Fig. 5 the number which appears first, for example, the $-0.004$ in $F = -0.004/x^{0.17}$ in the top curve of Fig. 5, refers to the value of $F$ at the first data point while the power on $x$, the 0.17, gives the general

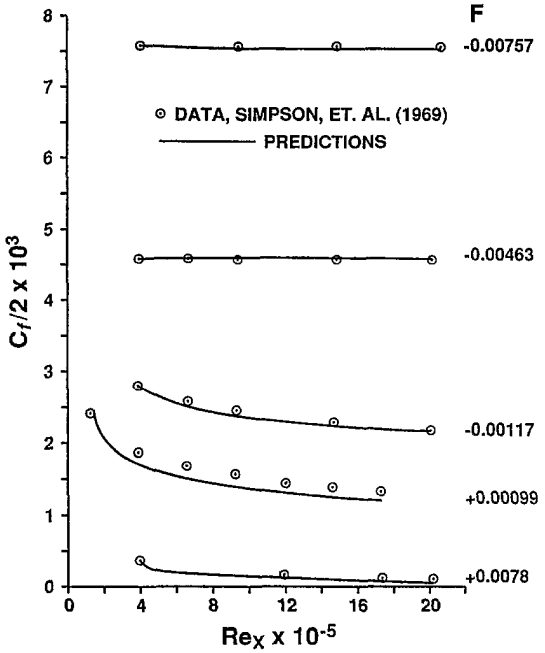


**Fig. 2 Predictions and data. $u_s$ = constant**

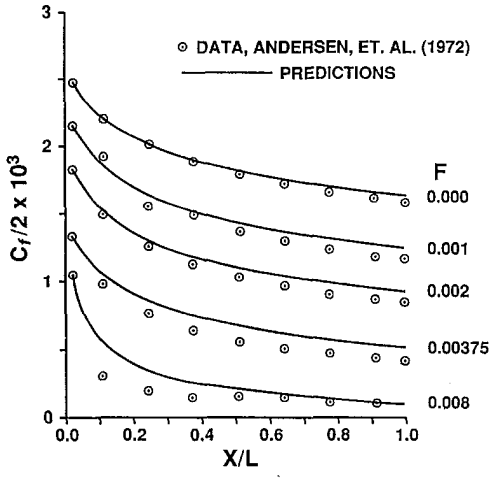


**Fig. 4 Predictions and data. $u_s$ = constant. $L$ = 2.286 m (7.5 ft)**

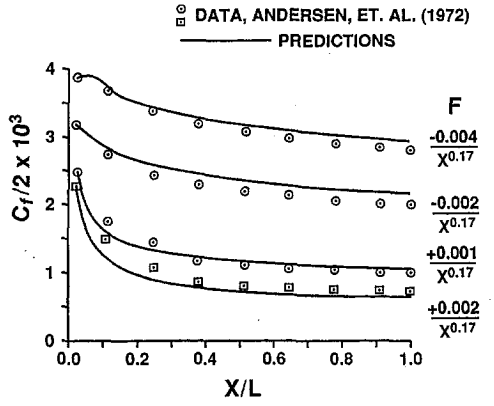


Fig. 5 Predictions and data. $u_s \sim x^{-0.15}$, $F \sim \pm x^{-0.17}$, freestream velocity $u_s$, and blowing fraction, $F$, both varying with $x$. $L$ = 2.286 m (7.5 ft)

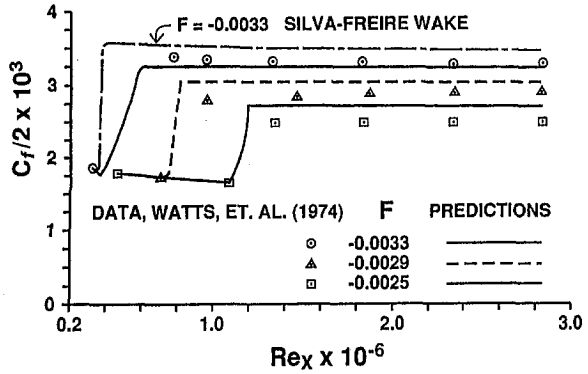


Fig. 7 Predictions and data. $u_s$ = constant. Step change in $F$ from $F$ = 0.00 to: $F = -0.0033$, $x > 0.308$ m: $F = -0.0029$, $x > 0.6096$ m: $F = -0.0025$, $x > 0.9144$ m

functional dependence of $F$ on $x$. The actual expression for $F$, in this case, is $F = -0.004\,[c/(a + bx)]^{0.17}$. Shown are cases for both variable suction and variable blowing. There is reasonable agreement between predictions and the data.

Shown next in Fig. 6 are results for accelerating flows. The solid curves represent predictions obtained using the wake model of the present work, while the dashed curves represent predictions of the simpler Silva-Freire model developed in Sucec and Oljaca (1995). Results of the Silve-Freire method are included both to be comprehensive and to show a case where the Silve-Freire method fails to predict experimental data satisfactorily. The top solid curve is for $F = +0.00395$ and a strong acceleration with nominal value of the acceleration factor, $\bar{K}_a$, being $2.0 \times 10^{-6}$ and constant over most of the surface. The experimental data is from Lloyd et al. (1970). Predictions are high for the last three data points. For the lower solid curve, the data are from Thielbahr et al. (1972). $F$ is constant at +0.0058 while the acceleration factor $\bar{K}_a$ is sensibly constant at $1.45 \times 10^{-6}$ over the first half of the surface and then drops abruptly to zero for the last 40 percent of the surface. The predicted results follow the data remarkably well even in the "relaxing" boundary layer on the last 40 percent of the surface.

Results for a step change of $F$ from 0 to a constant negative value, when there is no pressure gradient, are shown in Fig. 7. The data are due to Watts et al. (1974). For the top solid curve $F = 0.00$ for $0 < x < 0.308$ m and $F = -0.0033$ for $x > 0.308$ m. For the middle dashed curve, $F$ remains at 0.00 for $x <$ 0.6096 m and then changes to −0.0029 while for the lowest curve $F = 0.00$ for $x < 0.9144$ m before changing to $F =$ −0.0025. The predictive method used a linear ramp for $F$ to approximate the step change in $F$. This was needed because the present formulation could not accommodate the large change in $F$ and in $C_f/2$ that occurs in the step without getting a negative quantity under a square root. Agreement with the data range from good to fair.

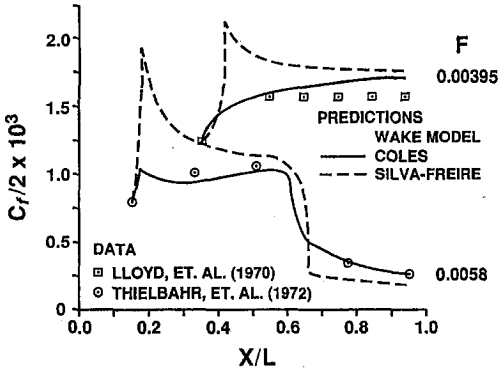


Fig. 6 Predictions and data. Accelerating flows. $F = +0.0058$, $\bar{K}_a = 1.45 \times 10^{-6}$, $L$ = 2.286 m (7.5 ft); $F = +0.00395$, $\bar{K}_a = 2 \times 10^{-6}$, $L$ = 1.016 m (3.33 ft)

In Sucec and Oljaca (1995), some of these same transpiration cases were computed using a simpler wake model due to Silva-Freire (1988). The last two terms of Eq. (6) in the Coles wake model are replaced by a single simpler term, $v_w^+ \tilde{\pi} W/K$, in the Silva-Freire model. $\tilde{\pi}$, a second wake strength parameter, is given by the following expression.

$$\tilde{\pi} = -1.95 \ln |F| - 3.1 \qquad (26)$$

Predicted results using the Coles wake model of the present work were compared to those of the simpler wake model employed in Sucec and Oljaca (1995). It was found that in three of the five cases of Andersen et al. (1972), in which both $F$ and $u_s$ are constant, the Silva-Freire wake model gave better results. It is felt that this is due to the fact that the wake strength relation, equation (26), was determined from the data of these five cases. For cases in which either $u_s$, or $F$, or both vary with $x$, the results were mixed. In some of these cases, both models gave essentially the same results, while in others, Coles wake model gave better results and in still others, the Silva-Freire model was better. However, in the accelerating flows of Thielbahr et al. (1972) and of Lloyd et al. (1970), as well as the cases of Watts et al. (1974) which had step changes in $F$, the Coles wake model clearly yielded better predictions. This is evident in Fig. 6 where the Silva-Freire wake results are shown as the dashed curves while the solid curves are for the wake model of Coles used in the present work. In Fig. 7, the predictions of the Silva-Freire wake model are shown for the single case of a step change in $F$ from 0 to a value of $F = 0.0033$. Once again, the results, though not as pathological as in Fig. 6, are not as good as the results of the present paper. Though not shown, this is also true for the other two cases shown in Fig. 7.

The breakdown of the Silva-Freire wake model for the two cases of severe acceleration in Fig. 6 is caused by the fact that the wake strength parameter, given by Eq. (26), is independent of the Clauser parameter, $\beta$, defined in Eq. (17). Unlike the Coles wake strength $\pi$ which, as given in Eq. (18), depends upon $\beta$ and gradually goes to zero during an acceleration as $\beta$ approaches −0.5, $\tilde{\pi}$ retains its value, dependent on $F$, until $\pi$ reaches zero. At this point, (no wake) $\tilde{\pi}$ must be set equal to zero and this causes the abrupt, and large, increases in $C_f/2$, which are seen as the vertical spikes in Fig. 6. It is this deficiency of the Silva-Freire wake strength, $\tilde{\pi}$, namely, no dependence upon the pressure gradient parameter $\beta$, along with the fact that $\tilde{\pi}$ doesn't approach zero as $F \to 0$ and hence must be set to zero at a low value of $F$ (see Eq. (26)) which causes us

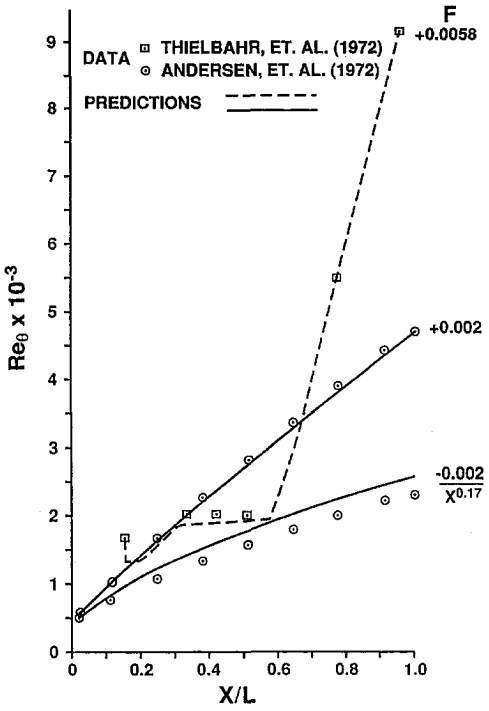


Fig. 8 Momentum thickness predictions and data. $F = +0.0058$, accelerating flow, $\bar{K}_a = 1.45 \times 10^{-6}$; $F = +0.002$, $u_s$ = constant; $F \sim -0.002/x^{0.17}$, $u_s \sim x^{-0.15}$. $L = 2.286$ m (7.5 ft)

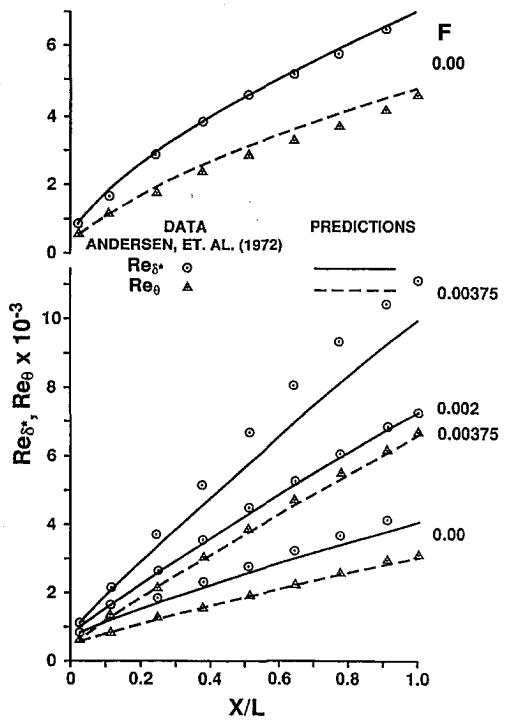


Fig. 9 Momentum and displacement thickness Reynolds number predictions and data

to recommend the use of the Coles wake model, embodied in Eq. (6), for the general case where $u_s$ is a function of $x$.

Besides prediction of the skin friction coefficient it is also possible to compute other important hydrodynamic parameters, although there is limited amount of experimental data for these parameters. Some calculations of momentum thickness Reynolds number, $Re_\theta$, are shown in Fig. 8 for some representative cases of $F$ values and pressure gradients. The dashed curve represents the predictions for the case of strong blowing, $F = +0.0058$ and an acceleration over the first 60 percent of the surface, the case from Thielbahr et al. (1972) discussed in connection with Fig. 6. Predicted $Re_\theta$ values follow the data well. The middle curve is for $F = +.002$ and $u_s$ a constant and is from Andersen et al. (1972). The data points are also from Andersen et al. (1972) for the lowest curve, variable suction, $F \sim -0.002x^{-0.17}$ and deceleration, $u_s(x) \sim x^{-0.15}$. Predictions are somewhat high for this case.

Figure 9 shows some additional momentum thickness Reynolds number predictions, the dashed curves, and some representative displacement thickness Reynolds number results as the solid curves. The $F = 0.00$ results at the top of the figure are for $u_s \sim x^{-0.20}$ while those at the bottom of the figure are for constant $u_s$. Predictions compare pretty well with the data for all cases except for the displacement thickness when $F = 0.00375$.

## Conclusion

Cole's form of the law of the wake for a turbulent boundary layer with transpiration is used as the velocity profile for the integral $x$ momentum equation written in terms of inner variables. The numerical solution of this equation gives predictions, of skin friction coefficient and momentum thickness, that exhibit reasonable agreement with experimental data. These predictions included cases of blowing and suction, for both constant and variable with $x$ transpiration and for cases of zero, adverse and favorable pressure gradients. Particularly encouraging is the fact that present method predicts well the experimental data for complex cases of "relaxing" boundary layer and step change in blowing function. Present predictions also compared well with some of the finite difference techniques used at the second Stanford Conference. Continuation of the basic approach presented to the associated heat transfer problem is being worked on now.

## References


Andersen, P. S., Kays, W. M., and Moffat, R. J., 1972, "The Turbulent Boundary Layer on a Porous Plate: An Experimental study of the Fluid Mechanics for Adverse Free Stream Pressure Gradients," Report No. HMT-15 Dept. of Mechanical Engrg., Stanford University, Stanford, CA.

Bradshaw, P., 1967, "Mixing Length Velocity Profile in Boundary Layers with Transpiration," *AIAA Journal,* Vol. 5, No. 9, pp. 1674–75.

Coles, D., 1971, "A Survey of Data for Turbulent Boundary Layers with Mass Transfer," *Rand Corporation Report,* No. P-4697, pp. 25–1 to 25–15.

Das, D. K., and White, F. M., 1986, "Integral Skin Friction Prediction for Turbulent Separated Flows," ASME JOURNAL OF FLUIDS ENGINEERING, Vol. 108, pp. 476–482.

Das, D. K., 1988, "A Simple Theory for Calculating Turbulent Boundary Layers Under Arbitrary Pressure Gradients," *International Journal of Engineering Fluid Mechanics,* Vol. 1, pp. 83–99.

Das, D. K., 1992, "An Inverse Inner Variable Theory for Separated Turbulent Boundary Layers," ASME JOURNAL OF FLUIDS ENGINEERING, Vol. 114, pp. 543–553.

Kline, S. J., Cantwell, B. J., and Lilley, G. M., eds., 1981, "The 1980–81 AFOSR-HTMM Stanford Conference on Complex Turbulent Flows," Stanford University, Stanford, CA.

Lloyd, R. J., Moffat, R. J., and Kays, W. M., 1970, "The Turbulent Boundary Layer on a Porous Plate: An Experimental Study of the Fluid Dynamics with Strong Favorable Pressure Gradients and Blowing" Report No. HMT-13, Department of Mechanical Engrg., Stanford University, Stanford, CA.

Mellor, G. L. and Gibson, D. M., 1966, "Equilibrium Turbulent Boundary Layers," *Journal of Fluid Mechanics,* Vol. 24, Part 2, pp 225–253.

Oljaca, Miodrag, 1993, "Prediction of Shear Friction Coefficients in Transpired Turbulent Boundary Layers with Arbitrary Pressure Gradient," M.S. thesis, University of Maine, Orono, ME.

Silva-Freire, A. P., 1988, "An Asymptotic Solution for Transpired Incompressible Turbulent Boundary Layers," *International Journal Heat Mass Transfer,* Vol. 31, pp. 1011–1021

Simpson, R. L., Moffat, R. J., and Kays, W. M., 1969, "The Turbulent Boundary Layer on a Porous Plate: Experimental Skin Friction with Variable Injection and Suction," *International Journal of Heat Mass Transfer,* Vol. 12, pp. 771–789.

Stevenson, T. N., 1963, "A Law of the Wall for Turbulent Boundary Layers with Suction or Injection," Report Aero No. 166, College of Aeronautics, Cranfield, 18 pages, also available from NTIS as N64-19323.

Sucec, J., and Oljaca, M., 1995, "Calculation of Turbulent Boundary Layers with Transpiration and Pressure Gradient Effects," *International Journal of Heat Mass Transfer,* Vol. 38, pp. 2855–2862.

Thielbahr, W. H., Kays, W. M., and Moffat, R. J., 1972, "The Turbulent Boundary Layer on a Porous Plate: Experimental Heat Transfer with Uniform Blowing and Suction, with Moderately Strong Acceleration," ASME *Journal of Heat Transfer,* Vol. 94, pp. 111–118.

Thomas L. C., and Kadry, H. M., 1990, "A One Parameter Integral Method for Turbulent Boundary Layer Flow," ASME JOURNAL OF FLUIDS ENGINEERING, Vol. 112, pp. 433–436.

Torii, K., Nishiwaki, N., and Hirata, M., 1966, "Heat Transfer and Skin Friction in Turbulent Boundary Layer with Mass Injection," *Proceedings of the Third International Heat Transfer Conference,* Vol. 3, Chicago, pp. 34–48.

Watts, K. C., Brundrett, E., Nicoll, W. B., and Strong, A. B., 1974, "Design and Construction of a Wind Tunnel for Mass Transfer Studies in Incompressible Boundary Layers" ASME JOURNAL OF FLUIDS ENGINEERING, Vol. 96, pp. 311–316.

White, F. M., 1991, *Viscous Fluid Flow,* Second Edition, McGraw-Hill, New York, pp. 451–452, 459–464.

# Effect of a Crossflow at the Entrance to a Film-Cooling Hole

**K. A. Thole**[1]
Assistant Professor.

**M. Gritsch**
Dipl.-Ing.

**A. Schulz**
DR.-Ing.

**S. Wittig**
Professor.

Institut für Thermische Strömungsmaschinen, Universität Karlsruhe, Karlsruhe, Germany

*Understanding the complex flow of jets issuing into a crossflow from an inclined hole that has a short length-to-diameter ratio is relevant for film-cooling applications on gas turbine blades. In particular, this experimental study focused on the effect of different velocities in a coflowing channel at the cooling hole entrance. Flows on both sides of the cooling hole (entrance and exit) were parallel and in the same direction. With the blowing ratio and the mainstream velocity at the hole exit remaining fixed, only the flow velocity in the channel at the hole entrance was varied. The Mach number at the hole entrance was varied between $0 < Ma_c < 0.5$, while the Mach number at the hole exit remained constant at $Ma_\infty = 0.25$. The velocity ratio and density ratio of the jet were unity giving a blowing ratio and momentum flux ratio also of unity. The single, scaled-up film-cooling hole was inclined at 30 deg with respect to the mainstream and had a hole length-to-diameter ratio of $L/D = 6$. Flowfield measurements were made inside the hole, at the hole inlet and exit, and in the near-hole region where the jet interacted with the crossflow at the hole exit. The results show that for entrance crossflow Mach numbers of $Ma_c = 0$ and 0.5, a separation region occurs on the leeward and windward side of the cooling hole entrances, respectively. As a result of this separation region, the cooling jet exits in a skewed manner with very high turbulence levels.*

## Introduction

Understanding the complex interaction of a jet injected into a crossflow is a phenomena of particular interest to the gas turbine industry. The primary motivation is such that by providing better blade cooling, higher turbine efficiencies can be attained by increasing turbine inlet temperatures. One such blade cooling technique is film-cooling whereby compressor bleed air is exhausted through the turbine blade surface through cooling holes. These holes typically have relatively short length-to-diameter ratios and are inclined relative to the crossflow at the jet exit. Although there are a large number of possible flow conditions at the cooling hole entrance, there have been no past film-cooling flowfield studies that have investigated the link between what is happening on the inside of the turbine blade to what is happening on the outside of the turbine blade as the film-cooling jet exits. Instead, past film-cooling studies have not considered a crossflow at the hole entrance but rather a stagnant plenum supply or very long supply tubes giving unrealistically long hole length-to-diameter ratios. The emphasis of this paper is understanding how a crossflow at the entrance of a film-cooling hole can affect the jet as it issues into a crossflow at the exit.

Understanding the effects of a crossflow at the entrance to a short hole in which the exiting flow is not yet fully developed can have implications for both numerical and experimental simulations of film-cooling. Depending upon where the film-cooling hole is located in an actual turbine blade, there are a number of different hole inlet conditions that can occur. In this study, the flow at the cooling hole entrance was considered to be parallel and in the same direction (co-flowing) to the flow at the exit of the cooling hole as would occur, for example, in the midportion of a nozzle guide vane (see Fig. 1).

The study reported in this paper is aimed at film-cooling holes for gas turbine blades where typical hole length-to-diameter ratios are short and inclined relative to the crossflow at the hole exit. Specifically, the hole length-to-diameter ratio in this investigation was an $L/D = 6$ and the inclination angle was 30 deg relative to the entrance and exit crossflows. A single, scaled-up round cooling hole with parallel crossflows at the entrance and exit of the hole was investigated. In this study, only the crossflow Mach number at the hole entrance was varied between $0 < Ma_c < 0.5$ while the Mach number at the hole exit was held constant at $Ma_\infty = 0.25$. The jet-to-mainstream velocity ratio (VR) and density ratio (DR) remained constant for all conditions at VR = 1 and DR = 1.

The following sections briefly review relevant jet-in-crossflow studies, give a description of the flow facility used for these experiments, and describe the discharge coefficient and flowfield results. After the flowfield results are discussed, there is an additional section discussing a physical description of the flow which is then followed by some conclusions.

## Previous Studies

Previous studies have documented the flowfield of jet injection into a crossflow with both long (typically not used in gas turbine applications) and short jet hole lengths. These studies have encompassed a range of injection angles, and jet-to-mainstream velocity (VR) and density (DR) ratios. With the exception of the discharge coefficient study reported by Hay et al. (1983), there are no film-cooling studies in the open literature that have investigated the effect of a crossflow at the hole entrance.

Normal jet injection studies with unit density ratio (DR = 1), such as Crabb et al. (1981) and Andreopoulos and Rodi (1984), showed two obvious effects on the mean flowfield; the degree of which depended on the jet-to-mainstream velocity ratio. First, the jet was bent over by the crossflow at the exit and second the crossflow was deflected upward by the jet blockage. Both of these studies had relatively long supply holes for the jet at $L/D = 30$ for the Crabb et al. study and $L/D = 12$ for the Andreopoulos and Rodi study. Andreopoulos and Rodi found at a low velocity ratio (VR = 0.5) that the effect of the crossflow at the jet exit was to skew the exiting jet profile and force the jet to exit primarily from the downstream half of

[1] Present address: Mechanical Engineering Department, University of Wisconsin, 1513 University Avenue, Madison, WI 53706-1572.

Contributed by the Fluids Engineering Division for publication in the JOURNAL OF FLUIDS ENGINEERING. Manuscript received by the Fluids Engineering Division July 11, 1996; revised manuscript received January 29, 1997. Associate Technical Editor: L. Nelik.

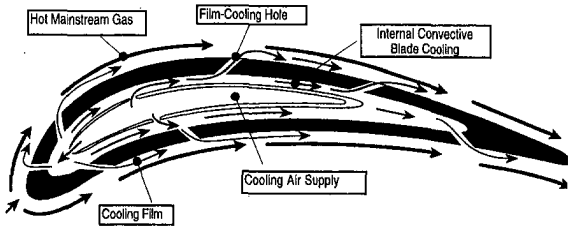


**Fig. 1 Illustration of a flow configuration inside a nozzle guidevane**

the hole exit plane. In fact, Andreopoulos and Rodi found at this low velocity ratio that the jet started to bend while still inside the hole passage. In contrast, at a high velocity ratio (VR = 2) they found that the jet bending occurred after the jet exited the hole passage.

Andreopoulos and Rodi also discussed that the resulting turbulence characteristics are a combination of several mechanisms. These mechanisms include the turbulence being transported to the jet hole exit from the upstream boundary layer and from inside the hole itself, turbulence being produced due to various mean velocity gradients, and turbulence being subjected to the strong streamline curvature as result of the bending jet. Andreopoulos and Rodi found at the jet centerline the location of the maximum turbulence kinetic energy and turbulent shear stress coincided with the maximum streamwise velocity gradient and concluded that the mean velocity gradient, $dU/dy$, was the dominant turbulent production mechanism.

Flowfield studies of inclined jet injection, with relatively short hole length-to-diameter ratios, include the experimental studies by Pietrzyk (1989), Pietrzyk et al. (1989), Subramanian et al. (1992), and numerical studies by Leylek and Zerkle (1994), Benz et al. (1993), and Garg and Gaugler (1995). Pietrzyk (1989) made flowfield measurements for an inclined jet (35 deg) subjected to a strong crossflow for jet-to-mainstream velocity ratios of VR = 0.25, 0.5, and 1 at a density ratio of DR = 1 and velocity ratios of VR = 0.25 and 0.5 at a density ratio of DR = 2. The hole length-to-diameter ratio was typical of what would be found in gas turbine applications at $L/D$ = 3.5. The cooling hole for their configuration was supplied by a stagnant plenum. One of the dominating mechanisms hypothesized by Pietrzyk et al. (1989) was the formation of a separation region on the leeward side of the cooling hole entrance at high velocity ratios. As the jet-to-mainstream velocity ratio increased and the separation region began to form on the leeward side of the cooling hole, the jet fluid was pushed into the windward portion of the cooling hole. Hence, the primary jet exit location was shifted from the leeward side of the cooling hole at low blowing ratios, similar to Andreopoulos and Rodi (1984), to the windward side of the cooling hole. This separation region was a result of the large turning angle encountered by the coolant on the leeward side of the hole.

In addition to skewing the exiting jet profile, Pietrzyk et al. (1989) found a change in the location of the peak turbulence levels for different velocity ratio jets. At a low velocity ratio of VR = 0.25, a turbulence level of nominally Tu = 4 percent or less exited the cooling hole. As the jet interacted with the mainstream, the peak turbulence level was Tu = 12 percent which occurred at 2.5 hole diameters downstream of the jet hole center. The primary mechanism for this turbulence level was the large streamwise velocity gradient, $dU/dy$. At a high velocity ratio, where the formation of the separation region at the hole entrance was hypothesized, the turbulence levels exiting the cooling hole was Tu = 20 percent. This high turbulence level was equal to the peak turbulence level occurring downstream of the cooling hole due to the streamwise velocity gradient.

Leylek and Zerkle (1994) documented a full three-dimensional computational study to complement the experimental results of Pietrzyk et al. (1989). Included in their model was the supply plenum, cooling hole, and the mainstream crossflow. In the study of Leylek and Zerkle, the separation inside the jet hole was evident. Leylek and Zerkle also found that at large length-to-diameter ratios ($L/D > 3$) and high blowing ratios ($M > 1$) or small length-to-diameter ratios ($L/D < 3$) and low blowing ratios ($M < 1$), the flow inside the cooling hole became more similar to a fully developed turbulent pipe flow. Benz et al. (1993) also realized the importance of simulating the flow inside the jet hole as they prescribed a uniform velocity profile at the cooling hole entrance that resulted in a skewed jet exit profile for a film-cooling hole in the leading edge region of a turbine blade.

As mentioned earlier, Hay et al. (1983) studied the effects of jet entrance and exit crossflows on the discharge coefficients of film-cooling holes. Being able to predict the discharge coefficients is critical in the sizing of film-cooling holes since an excess of unnecessary coolant fluid represents a loss in the turbine working fluid. Hay, et al. investigated a range of Mach number crossflows at the inlet and exit of their cooling hole, hole inclination angles, and hole length-to-diameter ratios. They found that the crossflow at the jet entrance had a stronger effect on the discharge coefficient relative to the effect of the crossflow at the hole exit. For example, in the case where the crossflow at the hole entrance, which was parallel and in the same direction as the flow at the hole exit, increased from $Ma_c = 0$ to $Ma_c = 0.4$, the discharge coefficient increased by 30 percent. In contrast, as the exit Mach flow increased from $Ma_\infty = 0$ to $Ma_\infty = 0.5$, the discharge coefficient decreased by only 10 percent

## Nomenclature

$C_D$ = discharge coefficient = actual mass flowrate/ideal mass flowrate
$D$ = cooling hole diameter
DR = jet-to-mainstream density ratio
$L$ = cooling hole length measured along the centerline axis
$M$ = jet-to-mainstream blowing or mass flux ratio, $M = \rho_j V_j / \rho_\infty V_\infty$
$Ma_c$ = Mach number of the crossflow at the jet hole entrance
$Ma_\infty$ = Mach number of the crossflow at the jet hole exit
$P_{t,c}$ = stagnation pressure at hole entrance
$p_\infty$ = static pressure at the hole exit
$Re_D$ = Reynolds number based on hole diameter
$Re_\theta$ = Reynolds number based on momentum thickness
Tu = turbulence intensity (percent)
$u', v'$ = streamwise and vertical rms velocities
$U, V$ = streamwise and vertical mean velocity components
$V_j$ = total jet velocity based on inlet hole diameter and mass flux
VR = jet-to-mainstream velocity ratio
$x$ = streamwise distance measured from the cooling hole centerline
$y$ = vertical distance measured from the top of the cooling hole
$y_c$ = vertical distance measured from the bottom of the coolant channel
$z$ = spanwise distance measured from the cooling hole centerline
$\delta_{99}$ = boundary layer thickness, 99 percent point
$\theta$ = momentum thickness
$\rho$ = density

### Subscripts and Superscripts

$c$ = crossflow conditions at the hole entrance
$\infty$ = crossflow conditions at the hole exit

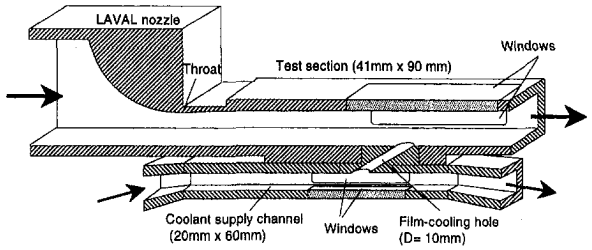


**Fig. 2 Schematic of the test rig showing the primary channel at the cooling hole exit and the supply channel at the cooling hole entrance**

for pressure ratios of $1.05 < P_{t,c}/p_\infty < 1.4$ and remained constant when the pressure ratios were $P_{t,c}/p_\infty > 1.4$.

The exiting velocity profile can, in fact, have a significant impact on the heat transfer occurring downstream of the film-cooling hole. The importance of the exiting jet profile on surface heat transfer is critical and best described by Garg and Gaugler's (1995) study. The numerical results presented by Garg and Gaugler (1995) showed large differences in surface heat transfer depending upon the exiting jet velocity and temperature profiles for several film-cooled turbine blades. Garg and Gaugler presented heat transfer predictions that had differences by as much as 50–60 percent depending upon whether a parabolic or one-seventh jet profile was assumed to exit the cooling hole. In addition, Schmidt et al. (1996) presented a discussion on the hole length-to-diameter effects which, in fact, causes differing exiting jet profiles. In comparing their data, which had an $L/D = 4$, to the data of Sinha et al. (1991), which had an $L/D = 1.75$, a clear detachment and reattachment of the jet from the downstream surface occurred for the shorter $L/D = 1.75$, but not for the longer $L/D = 4$.

These experimental and numerical results illustrate the importance of understanding the formation of the jet inside the cooling hole before the jet exits into the mainstream crossflow. A skewed exiting jet profile increases the penetration of the jet since there is a higher effective velocity in some locations at the jet exit. An increased penetration of the jet can cause a detachment of the jet from the downstream blade surface. This jet detachment has a large penalty in turbine blade cooling. In addition to a skewed jet profile, the separation region occurring at the hole inlet produces relatively high turbulence levels for the exiting jet. These high turbulence levels will increase the coolant fluid diffusion and reduce the thermal protection of the blade.

To evaluate how the entrance condition ultimately affects the film-cooling flowfield, the facility used for these experiments included a channel at the film-cooling hole entrance and exit, which could provide either a plenum condition or crossflow condition. The channel at the hole entrance represents the internal core of a nozzle guide vane while the channel at the hole exit represents the external flow around the nozzle guide vane. In the study presented here, the hole geometry as well as the supply channel geometry was based on a consensus of European gas turbine companies. The following section describes the experimental facility used for these experiments.

## Experimental Facility

The experiments discussed in this paper were conducted in a test facility at the Institut für Thermische Strömungsmaschinen (ITS), Universität Karlsruhe. This facility is described in detail by Wittig et al. (1996) with previous shaped film-cooling hole studies, also conducted in this facility, reported by Thole et al. (1996). A sketch of the test section, which contained the single, scaled-up film-cooling hole is shown in Fig. 2. The jet hole entrance and exit crossflow channels were controlled independently, which allowed the effect of the entrance Mach number crossflows to be studied.

**Table 1 Flow conditions for exit and entrance crossflow conditions**

| | Exit crossflow conditions | Entrance crossflow conditions |
|---|---|---|
| Mach number | 0.25 | 0, 0.30, and 0.5 |
| Mean freestream velocity (m/s) | 85.0 | 0, 102.7, and 168.0 |
| Freestream turbulence intensity (%) | 2 | 1 |
| Total temperature at injection (K) | 300 | 300 |
| Re$D$ | $5.2 \times 10^4$ | $6.6 \times 10^4$ |
| $\delta_{99}/D$ at $x/D = -5$ | 0.8 | |
| Re$\theta$ at $x/D = -5$ | 3000 | |
| $\delta_{99}/D$ at $x/D = -7$ | | 0.2 |

The primary channel at the jet exit was 90 mm in width and 41 mm in height while the supply channel at the jet entrance was 60 mm in width and 20 mm in height. The hole diameter for these experiments was 10 mm and was machined into a flat aluminum test plate that was 30 mm thick. For these studies, the holes were machined to have sharp corners which, in fact, may not be representative of an actual turbine blade depending on the manufacturing procedure used. The round hole was inclined at 30 deg giving a hole length-to-diameter ratio of $L/D = 6$. The flow conditions in the primary and supply channels are given in Table 1. The jet-to-mainstream velocity ratio and density ratio were constant at VR = 1 and DR = 1 for all of the flowfield results presented in this paper.

The air for both flow channels was supplied by a large compressor that has a capacity of producing 1 kg/s at 11 Bars. Flow for the coolant channel was also provided by the compressor, but driven by a sealed external blower in the supply flow loop. The turbulence levels at both the entrance and exit to the cooling hole were a result of those naturally occurring in both of the flow loops.

The flowrate in the supply channel was varied to give the different Mach numbers at the hole entrance. For the $Ma_c = 0.3$ case, the mass flowrate in the supply channel was 0.12 kg/s. In contrast, for each of the three channel conditions studied the flowrate through the cooling hole was fixed at 7.5e−03 kg/s giving a velocity ratio of VR = 1. Fixing this mass flowrate was achieved by adding the 7.5e−03 kg/s to the supply channel which was then ejected from the hole. To reduce the uncertainty, the mass flowrate through jet hole was determined by measuring this mass flowrate entering the secondary supply channel. Leak tests were conducted on the secondary supply channel to insure that all of the mass flowrate entering the supply channel was exhausted only through the cooling hole. The discharge coefficients, pressure ratios, and stagnation and static pressure ratios for all three flow entrance crossflow conditions are shown in Table 2. Note that the high velocity condition in the channel ($Ma_c = 0.5$) may be undesirably high for internal flows in an actual turbine vane, but was studied to better understand the hole entrance effects. In addition, the crossflow velocity that is present at the hole entrance depends on a number of design considerations.

The inlet flow conditions for both the jet entrance and exit channel flows are shown in Fig. 3. The boundary layer profile

**Table 2 Flow conditions for the three entrance crossflow conditions**

| | Stagnation pressure, $P_{t,c}$ (mbars) | Hole exit static pressure $p_\infty$ (mbars) | Pressure ratio, $P_{t,c}/p_\infty$ | Discharge coefficient, $C_d$ |
|---|---|---|---|---|
| $Ma_c = 0.0$ | 1097.5 | 996.6 | 1.10 | 0.72 |
| $Ma_c = 0.3$ | 1086.4 | 996.9 | 1.09 | 0.72 |
| $Ma_c = 0.5$ | 1176.0 | 996.2 | 1.18 | 0.47 |

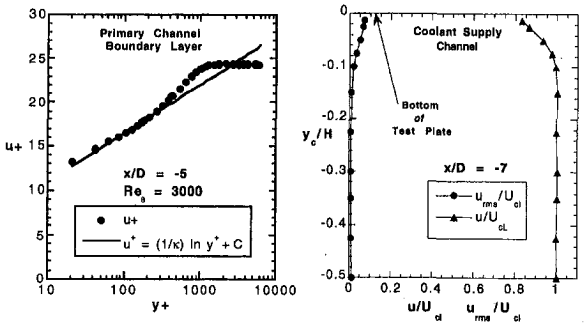


**Fig. 3 Inlet flow conditions for the primary channel and for the supply channel**

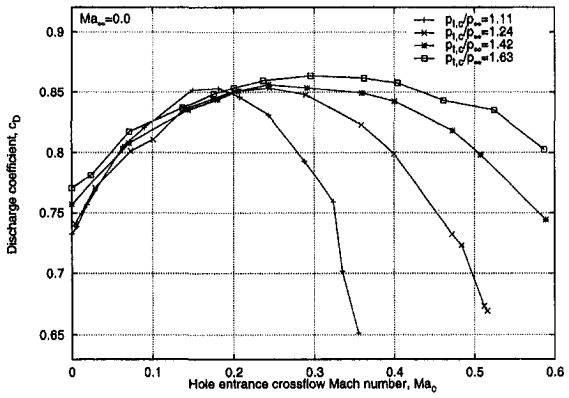


**Fig. 4 Discharge coefficient measurements for a range of entrance crossflow Mach numbers ($Ma_c$) and no exit crossflow ($Ma_\infty$ = 0)**

measured in the primary channel (at the jet exit) was measured five hole diameters upstream of the hole centerline. The coolant supply channel (at the jet hole entrance) was measured seven hole diameters upstream of the hole centerline. As illustrated in Fig. 3, the bottom of the test plate refers to the inlet to the coolant hole. The supply channel flow was considered to be a boundary layer flow with a thickness of $\delta_{99} \approx 2$ mm ($y_c/H = -0.1$) as compared to a channel half-height of 10 mm at a location of seven hole diameters upstream of the hole inlet.

A two-component, coincident, fiber optic laser Doppler velocimeter (LDV) was used to measure velocity fields for the three flow cases. The commercial Dantec LDV system had an 85 mm fiber optic probe and Enhanced Burst Spectrum Analyzers. A beam expander reduced the probe volume size to a diameter of 74 $\mu$m and a length of 0.6 mm. The data was bias corrected using residence time weighting. Both the primary and supply channel flows were seeded with oil (DES) particles having a mean diameter of 0.5 $\mu$m. Because the supply channel and primary flow were at different pressures, valves were used downstream of the seeder such that the seeding injection was independently controlled to avoid velocity biases.

The test section in the mainstream channel had glass on both side walls and top walls which allowed for optical access. The LDV was positioned on the side of the test section to measure the streamwise and vertical velocity components and was positioned on the top of the test section to measure the streamwise velocity components inside the jet hole. When positioned on the side of the test section, the LDV was rotated at 45 deg and tilted at nominally 4.5 deg to allow near-wall measurements. As a result of the tilt, the vertical velocity, $v$, reported in this paper contains a small lateral velocity component. Similarly when the LDV was positioned on the top of the test section, a 7 deg tilt was needed to avoid severe surface reflections. In both measurement configurations, however, the tilt has no affect on the streamwise velocity component.

## Uncertainty Estimates

Based on a 95 percent confidence interval, both bias and precision uncertainties were quantified. The data presented in this paper were typically averaged over 10,000 points or more depending on the data rate. The bias uncertainty for the mean velocities were 0.4 percent whereas the precision uncertainties were one percent in the freestream and 3.4 percent near the wall. The precision uncertainty for the rms velocity measurements were 1.4 percent in the freestream and 5.8 percent near the wall. The precision uncertainty in the turbulent shear stress was 5.6 percent. Positioning the LDV probe volume with respect to the hole was $\Delta x = \pm 0.05$ mm, $\Delta y = \pm 0.05$ mm, and $\Delta z = \pm 0.05$ mm. The uncertainty in setting the coolant mass flowrate was two percent and the overall uncertainty in the discharge coefficient was four percent.

## Discharge Coefficient Measurements

Discharge coefficients were measured for a number of conditions. Figure 4 shows the variation of the discharge coefficients as a function of the crossflow at the hole entrance alone. Note that for the data presented in Fig. 4, there is no crossflow at the hole exit.

The four curves represent different ratios of total coolant (at jet hole entrance) to static (at jet hole exit) pressure ($P_{t,c}/p_\infty$) ratios between $1.11 < P_{t,c}/p_\infty < 1.63$. Similar to the results presented by Hay et al. (1983) who investigated a $P_{t,c}/p_\infty$ ratio greater than 1.6, as the entrance crossflow Mach number increases to $Ma_c = 0.4$, so does the discharge coefficient. However, at $P_{t,c}/p_\infty = 1.63$ there is a decrease in the discharge coefficient as the crossflow Mach number at the inlet increases beyond $Ma_c = 0.4$. This increase in the discharge coefficient followed by a decrease occurs for all pressure ratios. Although the maximum discharge coefficient for all the pressure ratios investigated is between $C_d = 0.85$ and 0.86, the $Ma_c$ at which this maximum occurs decreases as the $P_{t,c}/p_\infty$ ratio decreases. For the lowest pressure ratio, $P_{t,c}/p_\infty = 1.11$, the maximum occurs at a $Ma_c = 0.18$ while at the highest pressure ratio, $P_{t,c}/p_\infty = 1.63$, the maximum occurs at $Ma_c = 0.3$. The data also indicate that as the pressure ratio across the hole increases, the $Ma_c$ range over which the discharge coefficient is a maximum increases. Gritsch et al. (1997) show that the same trends occur even when there is a crossflow up to a $Ma_\infty = 0.6$ at the exit of the hole.

Hay et al. (1983) attributed the increased discharge coefficient to the additional dynamic head. Figure 4 clearly indicates that there is an additional effect occurring as the inlet crossflow Mach number is increased beyond the condition of the maximum discharge coefficient. This effect will be clarified in the following sections of this paper which describe the flowfield measurements. It is clear, however, that the crossflow at the hole entrance plays a key role in the discharge coefficient for that jet hole at all pressure ratios.

## Flowfield Results

Although flowfield measurements have previously been reported for round film-cooling holes with a crossflow at the jet exit, as mentioned in the introduction, there have not been any studies which have investigated the effect of a crossflow at the jet entrance. The following sections present the mean flowfield results and turbulent flowfield characteristics for single, scaled-up round jet hole all at a velocity ratio of VR = 1. The three cases presented are for jet entrance crossflow Mach numbers at $Ma_c = 0$, 0.3, and 0.5. The jet exit crossflow Mach number remained constant for all of the flowfield tests at $Ma_\infty = 0.25$.

The turbulent flowfield measurements are presented in terms of turbulence levels which use the measured rms velocities

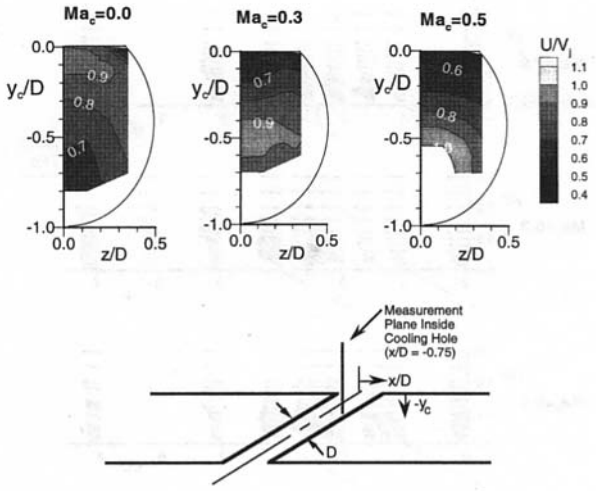


Fig. 5 Mean streamwise velocity contours inside the jet hole at $x/D = -0.75$ for entrance crossflows of $Ma_c = 0$, 0.3, and 0.5

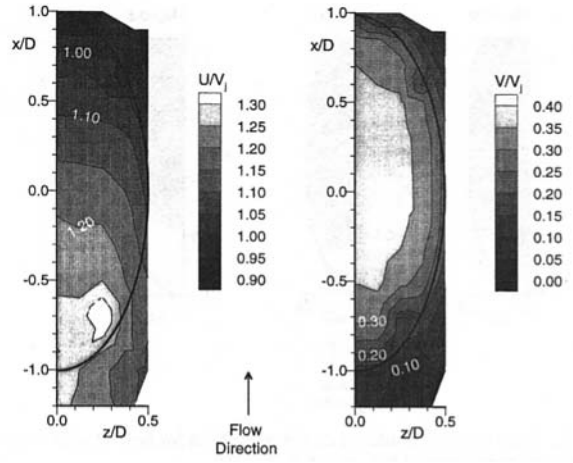


Fig. 6 Mean streamwise and vertical velocity contours at the entrance to the jet hole at $y_c/D = -0.15$ with a crossflow at the hole entrance of $Ma_c = 0.3$

referenced with the relevant mean velocity rather than the local mean velocity. For the turbulence levels presented inside and just at the jet hole exit plane, the streamwise rms velocities are used and normalized by the average jet velocity, $Tu_j$ (percent) $= 100 \times \sqrt{u'^2}/V_j$, whereas the turbulence levels presented after the jet has exited into the crossflow, the streamwise and vertical rms velocities are normalized by the mean mainstream velocity, Tu (percent) $= 100 \times \sqrt{0.5(u'^2 + v'^2)}/U_\infty$. Since these tests were conducted at a VR = 1, both the mean mainstream and average jet velocities are the same.

**Flowfield Inside Jet Hole.** To fully understand the jet profile at the hole exit, measurements were made inside the jet hole passage as shown by the measurement plane in Fig. 5. The mean streamwise velocity component inside the jet hole were measured by placing the LDV above the jet hole. Reflection effects were minimized by putting a slight tilt on the LDV and by painting the inside surface of the hole with a velvet black paint. The measurements were taken in a vertical-spanwise plane at a streamwise distance of $x/D = -0.75$ upstream of the hole centerline or just 0.25 hole diameters downstream of the windward edge of the cooling hole. This location was chosen because it was the farthest upstream position that still allowed the LDV beams to cross as they entered into the cooling hole.

The streamwise mean velocity contours inside the cooling hole for the three different entrance crossflow Mach numbers ($Ma_c = 0$, 0.3, and 0.5) are shown in Figure 5. The streamwise velocity contours are normalized by the total jet velocity. As indicated by the figures, the position at which the highest contour level occurs depends strongly upon the entrance crossflow Mach number. For the plenum-type supply ($Ma_c = 0$), a large portion of the jet (highest streamwise velocity contour) is at the top portion of the cooling hole. This placement of the jet is consistent with previous studies (Leylek and Zerkle, 1994). The previous computational study by Leylek and Zerkle has shown that when there is no crossflow at the hole entrance, i.e., a stagnant plenum, the jet inside the hole is pushed towards the windward edge of the hole because of the separation region on the leeward entrance to the hole. These experiments confirm that in fact the jet has been pushed toward the windward side which would appear at the top of the vertical-spanwise plane at $x/D = -0.75$.

As the cross-flow Mach number is increased at the hole entrance, the position of the maximum streamwise velocity contour shifts toward the leeward side of the cooling hole. Where the entrance crossflow Mach number is $Ma_c = 0.3$, the maximum streamwise velocity is located primarily in the center of the hole ($y/D = -0.5$). There is only a slight shift toward the leeward side (bottom) of the cooling hole for the higher crossflow entrance Mach number, $Ma_c = 0.5$. Figure 6 shows the total velocity contours (based on the streamwise and vertical velocity components) at the hole entrance of the jet for the $Ma_c = 0.3$ crossflow condition. These measurements were taken at $y_c/D = -0.15$ which is downward into the supply channel measured at the entrance of the cooling hole. Figure 6 indicates that a large portion of the jet is entering in the center of the cooling hole.

The turbulence levels inside the jet holes (based on the rms of the streamwise velocity fluctuations and the mean freestream velocity) are quite different for the three different entry Mach number crossflows. Figure 7 shows a comparison of those turbulence level contours. Very high turbulence levels occur for both the low and high entry crossflow conditions ($Ma_c = 0$ and 0.5). The peak turbulence levels for these two cases are nominally Tu = 17 percent. The turbulence levels for the condition in which the entry and exit crossflow Mach numbers are matched $Ma_c = 0.3$ is much lower with a peak at Tu = 10.5 percent. It is clear that for the portion of the hole that was mapped, most of the hole has overall lower turbulence levels for the $Ma_c = 0.3$ case. High turbulence levels exiting the hole for film-cooling applications can have a detrimental effect in that the jet fluid will tend to mix with the "hot" mainstream fluid more rapidly and not be as effective in cooling the blade surface.

**Flowfield at the Jet Exit.** The total velocity contours (based on the mean streamwise and vertical velocity components), measured in a streamwise-spanwise plane just at the exit of the hole ($y/D = 0.1$), are shown in Figs. 8. Depending upon the development of the jet inside of the cooling hole, there are countervening effects between the crossflow at the jet exit, which tends to bend the jet, and the jet velocity profile itself,

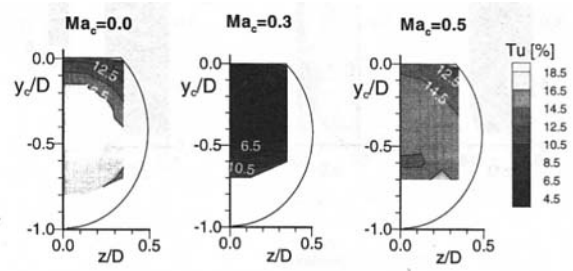


Fig. 7 Turbulence level contours inside the jet hole at $x/D = -0.75$ for entrance crossflows of $Ma_c = 0$, 0.3, and 0.5

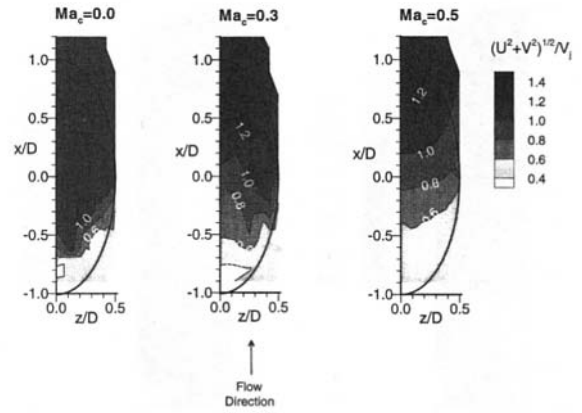


**Fig. 8 Total velocity contours at the exit of the jet hole at $y/D$ = 0.1 for entrance crossflows of Ma$_c$ = 0, 0.3, and 0.5**

which may have a higher momentum in particular regions due to the skewed velocity profile.

As shown in the previous section for the low Mach number crossflow at the hole entrance, Ma$_c$ = 0, a large portion of the jet is located in the windward side of the cooling hole. The skewing of jet profile for the Ma$_c$ = 0 case would be such that the jet flow is able to counteract the mainstream crossflow at the jet exit. In fact, the jet exit location begins near the windward side of the cooling hole. At a Ma$_c$ = 0.3, the jet exit moves more towards the leeward side of the cooling hole and at a Ma$_c$ = 0.5, the jet exit is even more near the leeward side of the cooling hole at relatively high velocities. The skewing of the jet as it exits the cooling hole causes a higher penetration into the crossflow at the exit of the hole (as will be shown in the next section).

The turbulence levels (based on the streamwise and vertical velocity components and the mean freestream velocity) at the jet exit, shown in Fig. 9, are similar to those seen inside the jet hole. Note that there is a change in the scale used for the turbulence level contours as compared to the scale that was used in Fig. 7. Very high turbulence levels occur for the Ma$_c$ = 0 and 0.5 cases whereas for the Ma$_c$ = 0.3 case the turbulence levels are much lower. The peak turbulence level exiting those cooling holes is Tu = 16 percent and Tu = 21 percent for the Ma$_c$ = 0 and Ma$_c$ = 0.5 cases, respectively. The peak turbulence level exiting the hole for the Ma$_c$ = 0.3 case is lower at Tu = 11 percent.

**Flowfield in the Mainstream Crossflow.** The mean streamwise-vertical velocity vectors, measured at the jet centerline in the streamwise-vertical plane, are shown in Fig. 10. As

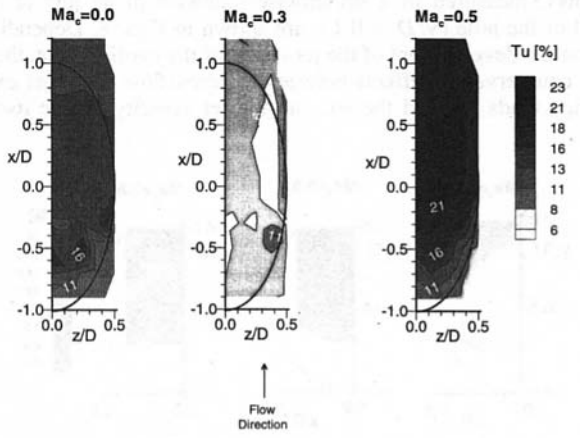


**Fig. 9 Turbulence level contours at the exit of the jet hole at $y/D$ = 0.1 for entrance crossflows of Ma$_c$ = 0, 0.3, and 0.5**

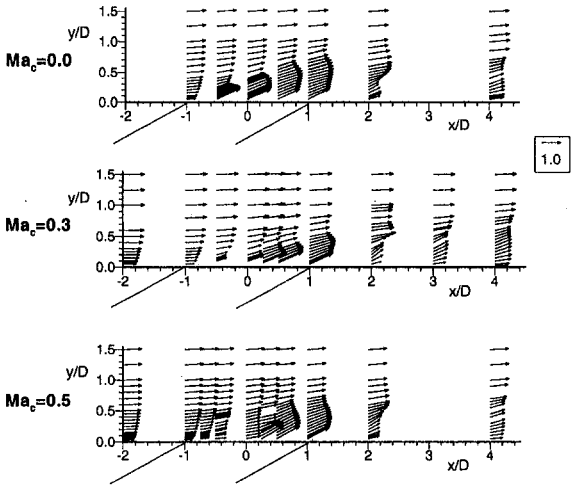


**Fig. 10 Mean velocity vectors in the exit crossflow at the hole centerline ($z/D$ = 0) for entrance crossflows of Ma$_c$ = 0, 0.3, and 0.5**

expected from the previous discussion, the Ma$_c$ = 0 case shows a strong vertical jet penetration which begins near the upstream edge of the cooling hole. In comparison, the Ma$_c$ = 0.5 crossflow at the entrance causes the jet to exit from the leeward side of the cooling hole.

Figure 11 shows the streamwise and vertical velocity profiles in the near-hole region at the jet centerline at $x/D$ = 0 and 1. These figures clearly show that for no crossflow at the hole entrance (Ma$_c$ = 0) the jet has exited the cooling hole $x/D$ = 0. At the downstream edge of the jet hole, $x/D$ = 1, the Ma$_c$ = 0.5 case shows higher streamwise and vertical velocity components indicating the exit location near the leeward side of the hole.

The turbulence level contours, measured at the jet centerline in a streamwise-vertical plane, are shown in Fig. 12. As discussed in the previous section the turbulence levels exiting the hole are significantly higher for the Ma$_c$ = 0 and Ma$_c$ = 0.5 entrance conditions. In addition, large mean streamwise velocity gradients for the Ma$_c$ = 0 and Ma$_c$ = 0.5 entrance conditions are causing higher peak turbulence levels after the jet has exited the cooling hole in comparison to the Ma$_c$ = 0.3 case. The peak turbulence levels, which occur at $x/D$ = 2, are Tu = 28 percent for the Ma$_c$ = 0 case and Tu = 36 percent for the Ma$_c$ = 0.5 case. In contrast, at $x/D$ = 2 the peak turbulence level for the Ma$_c$ = 0.3 case was Tu = 16 percent.

## Physical Description of Entrance Crossflow Effects

The previous sections describe the flowfield differences occurring when a crossflow is present at the entrance to a represen-

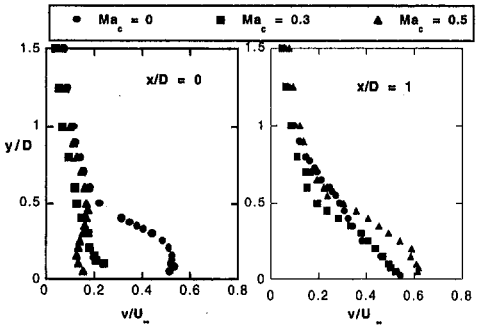


**Fig. 11 Comparison of the streamwise and vertical velocity components in the near-hole region at the hole centerline ($z/D$ = 0) for entrance crossflows of Ma$_c$ = 0, 0.3, and 0.5**

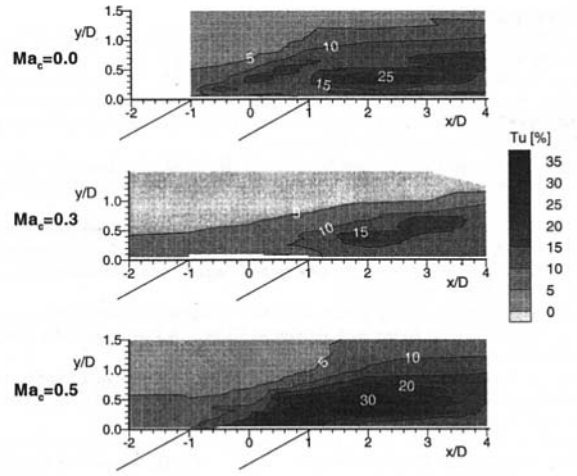


**Fig. 12 Turbulence level contours in the exit crossflow at the hole centerline ($z/D = 0$) for entrance crossflows of $Ma_c = 0$, 0.3, and 0.5**

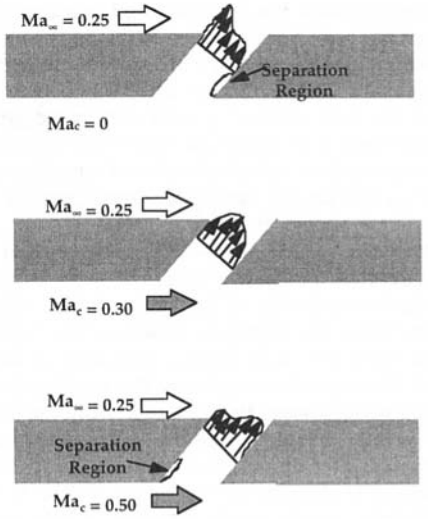


**Fig. 13 Physical interpretation of the effects that a crossflow at the jet hole entrance has on the jet flowfield**

tative film cooling hole as it exits into a crossflow. This section gives a physical description of this jet flow.

At a velocity ratio of VR = 1 with no crossflow at the hole entrance, previous studies have shown that a separation region occurs on the leeward side of the hole entrance (Pietrzyk et al., 1989 and Leylek and Zerkle, 1994). These previous studies have shown that there are a number of effects that result from this separation region. First, the exiting profile is skewed causing more jet fluid to exit from the windward side of the jet hole. This skewed profile causes a higher penetration distance of the jet into the mainstream. As was discussed in the introduction, when the separation region occurs on the leeward side of a short $L/D$ hole in which the skewness of the profile would be more prominent than for a long $L/D$ hole where the velocity profile had more time to readjust from the separation, adiabatic effectiveness measurements indicated the cooling jet detaches and then reattaches to the downstream surface (Schmidt, et al., 1996). Second, the exiting jet has very high turbulence levels which promotes a more rapid mixing with the hot mainstream. The data presented in this paper concurs that when there is no crossflow at the entrance to the jet hole ($Ma_c = 0$) a large portion of the jet exits from the windward side of the hole having turbulence levels higher than would occur say, for example, a pipe flow.

Pietrzyk (1989) presents a good description of the shear layers occurring due to the cooling jet/mainstream interaction at low and high velocity ratios. The shear gradients are particularly relevant since the $dU/dy$ gradients at the jet centerline are responsible for the turbulence production. At velocity ratios greater than VR > 0.5, he shows a windward shear layer that occurs at the interface between the mainstream and the cooling jet as the jet exits the hole; a wake region behind the jet which is formed due to the jet blockage; and a wall-jet layer formed downstream of the wake region near the wall. Pietrzyk (1989) pointed out that the highest turbulence production occurs in the windward shear layer, or rather the interface between the jet and the mainstream, and is primarily a result of the large $dU/dy$ velocity gradients. Similarly in this paper for the case with no crossflow entrance to the jet hole ($Ma_c = 0$), the peak turbulence levels occurred at an $x/D = 2$ where the most intense $dU/dy$ velocity gradients occurred.

For the cases presented in this paper in which a strong crossflow existed, the $Ma_c = 0.5$ crossflow also showed elevated turbulence levels exiting from the cooling hole, similar to the case with no crossflow at the hole entrance. However, the jet profile exiting from the cooling hole is much different in that a large portion of the jet is skewed towards the leeward side of the cooling hole. In the highest entrance crossflow case, there are even higher $dU/dy$ velocity gradients because the higher jet velocities are interacting with the low-speed fluid near the wall. As a result, turbulence levels even higher than those for the no crossflow case ($Ma_c = 0$) occur. For the case where the entrance crossflow is $Ma_c = 0.3$, the turbulence levels are significantly lower exiting the hole and the velocity profile indicates that the jet exits more towards the middle portion of the hole. This more uniform jet profile then reduces the velocity gradient and, subsequently, the turbulence production.

As the Mach number increases at the entrance to the jet hole from $Ma_c = 0$ to $Ma_c = 0.5$, the separation region which forms changes from the leeward side of the jet to the windward side of the jet hole. This effect is shown schematically in Figure 13. Since the turbulence levels are fairly low and the jet profile inside the hole appears to be more symmetric for the $Ma_c = 0.3$ entrance crossflow, the effect of the separation region, if there is a separation region, is not very large. In the $Ma_c = 0$ case, the downstream fluid has a large turning angle to overcome which causes the separation on the leeward side of the hole entrance. In the $Ma_c = 0.5$ case, the upstream fluid has an effectively large turning angle to overcome which causes a separation on the windward side of the hole entrance. Consistent with those separation regions are that both the $Ma_c = 0$ and $Ma_c = 0.5$ cases have high turbulence levels occurring inside the hole.

The discharge coefficients which were presented showed the entrance crossflow effect alone. Those results indicated that there was an entrance crossflow condition in which the discharge coefficient was a maximum. Below a $Ma_c < 0.15$, all of the pressure ratio cases indicated increases in discharge coefficients as the $Ma_c$ increased. The increase in the discharge coefficient with increasing $Ma_c$ occurs because the separation region on the leeward side of the hole passage begins to become minimal. For the low pressure ratio case of $P_{t,c}/p_\infty = 1.11$, the discharge coefficient begins to rapidly decrease at a $Ma_c = 0.2$ indicating that the total pressure is not high enough to overcome the frictional and separation losses. For the high pressure ratio case $P_{t,c}/p_\infty = 1.63$, the additional total pressure is enough to overcome the losses for a larger $Ma_c$ range.

## Conclusions

The results presented in this paper indicate the importance of understanding not only the effects of the crossflow at the jet exit, but also flowfield effects at the jet hole entrance. The flowfields for a round, inclined hole having a short length-to-

diameter ratio in which the jet is exposed to a crossflow at the hole entrance have not been reported in the open literature prior to this investigation. These types of flows commonly occur as film-cooling holes on gas turbine blades and, in particular, a crossflow at the hole entrance occurs for nozzle guide vanes. With improvements and changes to inner blade convective cooling schemes, an understanding as to how a crossflow at the hole entrance can influence the exiting jet profile and the discharge coefficients (hole sizing) is needed.

The mean velocity field measurements show that when the jet has no crossflow at the hole entrance, there is a separation region on the leeward side of the hole entrance which causes the jet to exit from the upstream portion of the hole. Alternatively, when there is a high velocity crossflow at the hole entrance, there is a separation region on the windward side of the hole entrance which causes the jet to exit from the downstream portion of the hole. These skewed profiles lead to higher turbulence production after the jet interacts with the mainstream.

In addition to a skewing of the jet as it exits the hole, increased turbulence levels inside the cooling hole and reduced discharge coefficients occur because of this separation region. As turbulence levels increase, the jet fluid would have a tendency to mix quickly with the mainstream at the jet exit. From a gas turbine film-cooling standpoint, this effect is detrimental because of the decreased cooling capability.

## Acknowledgments

This study was partly funded by the European Union through grant by the Brite Euram program "Investigation of the Aerodynamics and Cooling of Advanced Engine Turbine Components" under Contract AER2-CT92-0044. The authors wish to express their gratitude to the partners involved in the program for the permission to publish this paper and to R. Clifford from Rolls-Royce, who played an active role in initiating and coordinating the work program.

## References

Andreopoulos, J. and Rodi, W., 1984, "Experimental Investigation of Jets in a Crossflow," *Journal of Fluid Mechanics,* Vol. 138, pp. 93–127.

Benz, E. Wittig, S., Beeck, A., and Fottner, L., 1993, "Analysis of Cooling Jets near the Leading Edge of Turbine Blades," 72nd Fluid Dynamics Panel Meeting and Symposium on *Computational and Experimental Assessment of Jets in Cross Flow,* Winchester, UK, Paper no. 37.

Crabb, D., Durao, D. F. G., and Whitelaw, J. H., 1981, "A Round Jet Normal to a Crossflow," ASME JOURNAL OF FLUIDS ENGINEERING, Vol. 103, pp. 143–153.

Garg, V. K. and Gaugler, R. E., 1995, "Effect of Velocity and Temperature Distribution at the Hole Exit on Film Cooling of Turbine Blades," presented at the International Gas Turbine and Aeroengine Congress and Exposition, Houston Texas, ASME Paper No. 95-GT-2.

Gritsch, M. Schulz, A. and Wittig, S., 1997, "Discharge Coefficient Measurements of Film-Cooling Holes with Expanded Exits," ASME Paper No. 97-GT-165, Orlando, Florida.

Hay, N., Lampard, D., and Benmansour, S., 1983, "Effect of Crossflows on the Discharge Coefficient of Film Cooling Holes," ASME *Journal of Engineering for Power,* Vol. 105, pp. 243–248.

Leylek, J. H. and Zerkle, R. D., 1994, "Discrete-Jet Film Cooling: A Comparison of Computational Results with Experiments," ASME *Journal of Turbomachinery,* Vol. 116, pp. 358–368.

Pietrzyk, J. R., Bogard, D. G., and Crawford, M. E., 1989, "Hydrodynamic Measurements of Jets in Crossflow for Gas Turbine Film Cooling Application," ASME *Journal of Turbomachinery,* Vol. 111, pp. 1139–145.

Pietrzyk, J. R., 1989, "Experimental Study of the Interaction of Dense Jets with a Crossflow for Gas Turbine Applications," Ph.D. dissertation, University of Texas at Austin.

Schmidt, D. L., Sen, B., and Bogard, D. G. 1996, "Film Cooling with Compound Angle Holes: Heat Transfer," ASME *Journal of Turbomachinery,* Vol. 118, pp. 800–806.

Sinha, A. K., Bogard, D. G., Crawford, M. E., 1991, "Film Cooling Effectiveness Downstream of a Single Row of Holes with Variable Density Ratio," ASME *Journal of Turbomachinery,* Vol. 113, pp. 442–449.

Subramanian, C. S., Ligrani, P. M., Green, J. G., Doner, W. D., and Kaisuwan, P., 1992, "Development and Structure of a Film-Cooling Jet in a Turbulent Boundary Layer with Heat Transfer," *Rotating Machinery Transport Phenomena, Proceedings of the Third International Symposium on Transport Phenomena and Dynamics of Rotating Machinery* (ISROMAC-3), pp. 53–68.

Thole, K. A., Gritsch, M., Schulz, A., and Wittig, S., 1996, "Flowfield Measurements for Cooling Holes with Expanded Exits," ASME Paper No. 96-GT-174, Birmingham England.

Wittig, S., Schulz, A., Gritsch, M., and Thole, K. A., 1996, "Transonic Film Cooling Investigations: Effects of Hole Shapes and Orientations," ASME Paper No. 96-GT-222, Birmingham England.

# Turbulence Model for Steady and Unsteady Boundary Layers in Strong Pressure Gradients

**E. Hytopoulos**
Graduate Research Assistant; now at SGI/Cray Research. Mem. ASME

**J. A. Schetz**
J. Byron Maupin Professor, Department of Aerospace and Ocean Engineering Department. Fellow ASME

**R. L. Simpson**
Jack E. Cowling Professor, Department of Aerospace and Ocean Engr. Dept. Fellow ASME

Virginia Polytechnic Institute and State University, Blacksburg, VA 24061

*A new turbulence model for two-dimensional, steady and unsteady boundary layers in strong adverse pressure gradients is described. The model is developed in a rational way based on understanding of the flow physics obtained from experiments. The turbulent shear stress is given by a mixing length model, but the mixing length in the outer region is not a constant times the boundary layer thickness; it varies according to an integral form of the turbulence kinetic energy equation. This approach accounts for the history effects of the turbulence. The form of the near-wall mixing length model is derived based on the distribution of the shear stress near the wall, and it takes into account the pressure and convection terms which become important in strong adverse pressure gradients. Since the significance of the normal stresses in turbulent kinetic energy production increases as separation is approached, a model accounting for this contribution is incorporated. Experimental data indicate a change in turbulence structure near and through separation. Such a change can be significant and is accounted for here using an empirical function. The complete model was tested against steady and unsteady, two-dimensional experimental cases with adverse pressure gradients up to separation. Improved predictions compared to those obtained with other turbulence models were demonstrated.*

## Introduction

Interest in calculating two-dimensional, steady and unsteady, boundary-layer flows in strong pressure gradients is old, but it remains very important due to the large number of fluid flow devices that work under these conditions. A number of formulations have been used to predict those flows (Schetz, 1993). The simplest methods employ the mixing length or eddy viscosity concepts, which have been proven very useful in equilibrium boundary layers. Although reasonable agreement has been obtained for some cases, the validity of such an approach is questionable in view of the experimental findings which indicate that, in the case of strong adverse pressure gradient and/or separation, the shear stress profile depends not only on the local velocity profile and distance from the wall but also on the upstream development of the turbulence (i.e., the "history" of the turbulence). This observation has led some to develop models that attempt to account for the lag of the large eddy structure to the local conditions of the shear flow. Bradshaw et al. (1967) were among the first to employ the turbulence kinetic energy (T.K.E) equation for the development of the Reynolds shear stress. Assuming that the ratio of the Reynolds shear stress and the turbulence kinetic energy is constant along a streamline and introducing empirical functions for the dissipation and diffusion terms, they were able to transform the T.K.E. equation to an equation for the development of the shear stress. Despite the ability to account for "history" effects, this approach has disadvantages (McDonald and Camarata, 1968). The most important, is that the method requires the knowledge of the distribution of certain empirical functions across the boundary layer, with the diffusion function being the most uncertain one. They used flat plate boundary layer data to obtain their functions.

Johnson and King (1984) proposed a hybrid Reynolds stress/eddy viscosity model. Starting from the experimental observation that the maximum shearing stress is the proper scaling parameter for strong adverse pressure gradient and separating flows, they proposed an ordinary differential equation for the maximum turbulent shear stress that was heuristically deduced from the differential turbulence kinetic energy equation. The proportionality factor in the eddy viscosity model for the outer region is adjusted so that the maximum shear stress predicted from the model coincides with the value calculated from the ordinary differential equation. This approach predicts lower values of the outer eddy viscosity in the near-separation and separated zone, compared to simpler models, giving velocity profiles, surface pressure and skin friction coefficients that are in better agreement with experiments. The model still requires empirical functions for the diffusion and the dissipation of T.K.E. Simpson (1987) and Menter (1991) compared this model to others and concluded that it gave superior results for strong adverse pressure gradients for steady two-dimensional flow.

Dindar and Kaynak (1992) compared the unsteady Johnson-King model calculations with those of the Baldwin-Lomax and Cebeci-Smith models for the flow over an oscillating airfoil at a reduced frequency of 0.1. The comparison indicates that the Johnson-King model gives results in better agreement with the data. Srinivasan et al. (1993) compared the performance of an algebraic eddy viscosity model based on the Renormalization Group theory (Yakhot and Orzag, 1986) the Johnson-King model, the Baldwin-Barth model (Baldwin and Barth, 1991) and the Spalart-Allmaras model (Spalart and Allmaras, 1992) for the flow over an oscillating airfoil at a reduced frequency of 0.1. They found that for unsteady attached flow the first two and the last model give good agreement with experiments. For the light-stall case, the same models give only qualitatively correct results for airload hysteresis. For the deep stall cases on the downstroke the results were not even qualitatively correct.

Higher order methods, which involve extra equations for the T.K.E., dissipation rate $\epsilon$ and/or the Reynolds stresses have also been used. A review can be found in the papers by Simpson (1987) and Hytopoulos and Simpson (1993).

The present paper, introduces a new approach to the prediction of boundary layer flows in the presence of strong pressure

Contributed by the Fluids Engineering Division for publication in the JOURNAL OF FLUIDS ENGINEERING. Manuscript received by the Fluids Engineering Division October 18, 1995; revised manuscript received March 10, 1997. Associate Technical Editor: R. W. Metcalfe.

gradients. The assumptions built into the basic model have been chosen to be consistent with experimental and theoretical findings, so that the model can be rationally extended to the prediction of unsteady and three-dimensional flows. The basic features of the turbulence model include: ($a$) the use of the integrated T.K.E. equation as a way of taking into account "history" effects, ($b$) the use of $\tau_{max}$ as the scaling factor, ($c$) a model for the shear stress profile in the near wall region, where the assumption $\tau = \tau_w$, is not valid for strong adverse pressure gradients, ($d$) the contribution of normal stresses, and ($e$) an empirical function that attempts to take into account the change of the turbulence structure near separation. All of this results in an auxiliary differential equation for the factor in the outer region mixing length model. This is coupled to a numerical treatment of the differential equations of motion.

## Development of the Model

**The Role of the T.K.E. Equation.** One of the key pieces of experimental information is the observation that for boundary layers in strong adverse pressure gradients and separated flows the most important scaling parameter is not the wall stress, but the maximum shear stress. Also, for flows varying rapidly in the streamwise direction, the convection and diffusion of the Reynolds shear stresses cannot be neglected, so models based on an equilibrium assumption are not appropriate. This has led many researchers to transform the T.K.E. equation into an equation for the Reynolds shear stress based on the finding that the ratio of the Reynolds stress to the T.K.E. is almost constant across the boundary layer (at least for $.15\delta < y < .75\delta$). This constant is approximately 0.15 for a zero pressure gradient, and it becomes lower for adverse pressure gradients. Further, empirical correlations have been introduced for the diffusion and dissipation terms of the equation and the T.K.E. equation has been applied along the path of maximum turbulent kinetic energy ($s$) leading to an ordinary differential equation governing the streamwise development of $\tau_{max}$ (Johnson and King, 1984). The direction ($s$) has subsequently been taken as simply the streamwise direction. The rational extension of this assumption to unsteady and/or three-dimensional cases is not obvious.

Because of the above and the well-known uncertainty in the specification of the diffusion term, it was decided that an integral approach for the T.K.E. equation was advantageous here, since use of the boundary-layer theory assumptions along with integration across the boundary layer from the wall to the far-field, eliminates the diffusion term. The partial differential T.K.E. equation is reduced to an ordinary differential equation (O.D.E) for the steady flow case and to a partial differential equation in ($x$, $t$) for the unsteady case. The new equation governs the development of the maximum stress $\tau_{max}$ in time ($t$) and space ($x$) and is the mechanism through which the "history" effects are taken into account. After integrating and keeping the normal stress term, the T.K.E. equation reads (Schetz et al., 1993):

$$\int_0^\infty \left( \frac{\partial K}{\partial t} + \frac{\partial UK}{\partial x} + \overline{uv}\frac{\partial U}{\partial y} + (\overline{u^2} - \overline{v^2})\frac{\partial U}{\partial x} + \overline{\epsilon} \right) dy + \mathrm{VK}]_0^\infty = 0 \quad (1)$$

The ratio of the Reynolds shear stress to the T.K.E. is expressed in the following way:

$$\frac{\tau}{\rho K} = A_1 F^{-p} = \alpha_1 \quad (2)$$

It was observed experimentally that the ratio of the shear stress to the T.K.E. is reduced in the presence of an adverse pressure gradient (Bradshaw, 1967), this is taken into account here through an empirical relationship (Shiloh et al., 1981). The ratio is taken to be equal to $A_1 F^{-p}$, where $A_1$ is a constant chosen here as 0.25, and $p = 1.25$.

The factor $F$ expresses the ratio of the total turbulence energy production to that from the shear stress (Shiloh et al., 1981), and it is defined as:

$$F = 1 + \left( (\overline{u^2} - \overline{v^2})\frac{\partial U}{\partial x} \right) \left( \overline{uv}\frac{\partial U}{\partial y} \right)^{-1} \quad (3)$$

As separation is approached, both the normal stresses and the velocity gradient in the $x$ direction increase, resulting in increased production of T.K.E. due to the normal stresses. At the same time, the production due to shear stresses is decreasing, resulting in a ratio between the two terms of up to 0.5 (Simpson et al., 1977). The normal stress effects in the turbulence energy equation can be modeled using the approximation that $F$ is constant across the boundary layer, which is true for the mid-region of the boundary layer (Simpson et al, 1981). The model proposed by Collins and Simpson (1978) and Shiloh, Shivaprasad and Simpson (1981) is used here. This model is based on the assumption that the stresses can be related to the T.K.E., at the location where the shear stress becomes maximum, in the following way:

$$\overline{u^2} - \overline{v^2} = 2C_1 K / F^{1/4} \quad (4)$$

Combining this with the definition of $F$ and the ratio of the shear stress to the T.K.E ($= A_1 F^{-1.25} = a_1$), $F$ can be expressed in terms of the mean flow variables as follows:

$$F = \left( 1 + \frac{C_1}{A_1} \frac{\left(\frac{\partial U}{\partial x}\right)_{max}}{\left(\frac{\partial U}{\partial y}\right)_{max}} \right)^{-1} \quad (5)$$

Shiloh et al. (1981) report a value of 2.79 for the ratio of the two constants. The subscript (max) indicates that the derivatives are evaluated at the location where the Reynolds shear stress profile has a maximum, where one also has a finite non-zero value for $(\partial U/\partial x)/(\partial U/\partial y)$. Thus the modeled term of $F$ is well-behaved even in cases where $\partial U/\partial y \to 0$ somewhere within the boundary layer, such as in a wall-jet flow.

A model, based on dimensional considerations, was introduced for the calculation of the dissipation term:

$$\overline{\epsilon} = \frac{\tau^{3/2}}{L_d} \quad (6)$$

The dissipation length ($L_d$) is taken to be equal to the mixing length in the Law of the Wall region. This is consistent with the observation that the production and the dissipation are the two dominant terms in this region of the flow and they almost cancel each other, being closely equal and opposite in magnitude. A problem with Eq. (6) is that it predicts zero dissipation on the wall. Theoretical results (So et al., 1992) show the asymptotic value on the wall is:

$$\epsilon^+ = 2\frac{K^+}{(y^+)^2} \quad (7)$$

Despite this deficiency, the model equation predicts a maximum at about the same location where DNS solutions predict the existence of a plateau. The simplest approach and the one followed here is to assume that the dissipation between the wall and the location where the model predicts a maximum value is constant and equal to the maximum value.

The dissipation length in the near wall region has to be modified using the van Driest damping function, but a different damping constant is required for the results to be consistent with the values predicted from DNS. Wolfstein (1967) has also

adopted different values for the mixing and dissipation lengths in his near-wall damping functions. A value of $A^+$ between 12 and 14 seems to give good agreement, and the value of 14 has been used here. The dissipation length for the outer region is assumed proportional to the boundary layer thickness just as for the mixing length. The constant of proportionality has been chosen equal to 0.082, a value which is lower than the usually used value of 0.09 for the mixing length, but in good agreement with the experimentally observed values of Simpson et al. (1977). In equilibrium regions, we take the mixing length in the outer region to be $l_m = C\delta$ with $C = 0.09$ and the dissipation length to be $L_d = C_d\delta$ with $C_d = 0.082$. As $C$ is reduced by the auxiliary equation in strong adverse pressure gradients, it is assumed that $C_d = (0.082/0.09)C$.

Introducing Eqs. (2), (5), and (6) into Eq. (1), one obtains:

$$\frac{\partial}{\partial t}(\tau_{\max} I_t) + \frac{\partial}{\partial x}(\tau_{\max} I_c) - (\tau_{\max} I_p) + (\tau_{\max}^{3/2} I_d) = 0 \quad (8)$$

where

$$I_t = \int_0^\infty \frac{fF^p}{A_1}\,dy, \quad I_c = \int_0^\infty U\frac{fF^p}{A_1}\,dy,$$

$$I_p = \int_0^\infty \frac{\partial U}{\partial y} fF\,dy, \quad I_d = \int_0^\infty \frac{f^{3/2}}{L_d}\,dy,$$

and $f$ is the non-dimensionalized Reynolds stress profile with respect to the maximum value at the $x$ location and time $t$. The four integrals are functions of the time ($t$) and space ($x$) variables only. In the case of a steady flow, the time derivative is zero, and Eq. (8) becomes an O.D.E. The integration of the equation requires the specification of the maximum shear stress as an initial condition at the beginning of the computational domain. The model also requires an initial distribution for the velocity and stress fields. This information can be supplied by initially solving for the flow variables using a simple algebraic model.

In unsteady flow, Eq. (8) becomes a P.D.E., and both initial and boundary conditions are required. An initial distribution of the maximum shear stress as a function of the spatial coordinate ($x$) at time $t = 0$, as well as the value of $\tau_{\max}$ at $x = x_0$ as a function of time, are required. The first condition can be obtained by a steady solution at $t = 0$. The second condition can be given either by experimental results or by a simple algebraic model.

**Mixing Length Distribution.** The governing equation for the maximum shear stress does not predict the shear stress across the boundary layer. It only provides a scaling factor for the shear stress profile at each $x$ location. To complete the calculation of the shear stress, a formula that relates the shear stress to the other mean flow variables and its maximum value must be proposed. A mixing length formula based on an expression for the stress profile has been chosen to accomplish this task.

The mixing length is usually assumed proportional to the distance from the wall for the near wall region and proportional to the boundary layer thickness in the outer region (Schetz, 1993). The near wall formulation assumes a constant distribution of shear stress given as the product of the mixing length, $\kappa y$, the velocity scale, ($\kappa y \partial U/\partial y$) and the velocity gradient ($\partial U/\partial y$). In an attempt to improve this deficiency, Johnson and King (1984) proposed an approximate near-wall model that uses the same length scale but introduces the square root of the maximum shear stress as the characteristic velocity scale in their eddy viscosity formulation. Johnson and Coakley (1990) have proposed another algebraic velocity scale which is derived based on the assumption of a linear stress distribution between the wall and the maximum values of the shear stress. Here, a new mixing length formulation is proposed based on an expression for the distribution of the near wall shear stress profile. The derivation is based on the observation that the Law of the Wall remains valid even in the presence of strong adverse pressure gradients (Ludwieg and Tillman, 1950, McDonald, 1969). Extending the expression that Coles (1955) presented for the momentum equation for steady, two-dimensional flow to the case of unsteady flow and neglecting the normal stress term, one can write:

$$\frac{\tau}{\tau_w} = 1 + y^+p^+ + \frac{\nu}{u_\tau^2}\frac{\partial u_\tau}{\partial x}\int_0^{y^+} h^2(y^+)dy^+ + \frac{\nu}{u_\tau^3}\frac{\partial u_\tau}{\partial t} y^+h(y^+) \quad (9)$$

The function $h(y^+) = U/u_\tau$ depends on $y^+$ only, and it can be calculated from the universal Law of the Wall. An extended mixing length formula for the inner region can now be derived, if we require that:

$$l_m^2\left(\frac{\partial U}{\partial y}\right)^2 = \tau \quad (10)$$

where $\tau$ is given by Eq. (9), rather than the usual assumption $\tau = \tau_w$ or some ad hoc assumed variation. The expression for the mixing length becomes:

$$l_{m,\text{in}} = \kappa y D\left(1 + y^+p^+ + \frac{\nu}{u_\tau^2}\frac{\partial u_\tau}{\partial x}\int_0^{y^+} h^2(y^+)dy^+ + \frac{\nu}{u_\tau^3}\frac{\partial u_\tau}{\partial t} y^+h(y^+)\right)^{1/2} \quad (11a)$$

where $D$ ($=1 - \exp(-y^+/A^+)$) is the van Driest damping function. The mixing length in the outer region is:

$$l_{m,\text{out}} = C\delta \quad (11b)$$

A hyperbolic tangent function is used for blending the inner and outer mixing length region expressions,

$$l_m = l_{m,\text{out}}\left(\tanh\left(\frac{l_{m,\text{in}}}{l_{m,\text{out}}}\right)\right) \quad (12)$$

The mixing length approach (Eqs. 10–12) is used to calculate the shear stress distribution across the boundary layer, while Eq. (8) determines the maximum shear stress level. This is accomplished by adjusting the value of $C$, at each ($x$, $t$), so that the maximum value of the shear stress predicted from Eq. (10) is equal to the one predicted from the auxiliary equation (Eq. 8), at the same location.

**Numerical Implementation.** The closure model (Eqs. (8), (10), (11$a$–$b$), and (12)) coupled with the incompressible, steady and unsteady, boundary layer equations provide a closed system of equations that is solved numerically. The momentum and continuity equations have been discretized using the Finite-Element Method (F.E.M) (Schetz et al., 1993). The details of the method and extensive investigation of the numerical accuracy have been presented in the same reference. Based on the results of that investigation, the bilinear element (with a global error behaving as $h^2$) was chosen for all the runs presented in this work.

For steady cases, Eq. (8), is an ordinary differential equation, and is integrated using a Runge-Kutta method. For unsteady cases, Eq. (8) is a partial differential equation, and using the transformation $Q = I_t\tau_{\max}$, it can be written as follows:

$$\frac{\partial Q}{\partial t} + \frac{\partial (WQ)}{\partial x} - AQ + BQ^{3/2} = 0 \qquad (13)$$

where:

$$A = \frac{I_p}{I_t}, \quad B = \frac{I_d}{I_t^{3/2}}, \quad W = \frac{I_c}{I_t} \qquad (14)$$

Equation (14) has the form of a wave equation; the coefficient $W$ represents the speed of propagation of the wave. It is solved with a Crank-Nicolson time differencing scheme.

## Test Cases and Performance of the Model

The predictive ability of the model has been evaluated using four well-documented incompressible, turbulent flow test cases: (*a*) flow over a flat plate, (*b*) Samuel and Joubert steady, strong adverse pressure gradient flow (Samuel and Joubert, 1974), (*c*) Simpson, Chew and Shivaprasad (1981) steady, strong adverse pressure gradient flow with separation, and (*d*) Simpson et al. (1983) unsteady, strong adverse pressure gradient flow with separation.

The first case is the simplest turbulent flow, and all proposed models must be able to predict it correctly. The next two steady flow cases have been used as test cases for the 1980–1981 AFOSR-HTTM-Stanford conference on complex turbulent flows (Kline et al., 1981). This allows the comparison of the performance of the new model with the performance of a number of models used at the conference. Finally, the unsteady flow of Simpson et al (1983) was chosen for two main reasons: (*i*) it is a logical extension to the steady experiment (case *c*) and (*ii*) the reduced frequency of the experiment is an excellent representation of flows of engineering interest. The predictions with the new model are compared to the predictions of other models that are available in the literature for these cases.

**Turbulent Flow over a Flat Plate.** The inlet profile at $Re_\theta = 5000$ was created by using the log law for the inner region and the Coles Law of the Wake (Schetz, 1993) for the outer region. The skin friction coefficient calculated using both the new model and the simple algebraic model show a very small difference. Both results are also in excellent agreement with the usual skin friction laws, and all other variables are predicted accurately.

**Samuel and Joubert Steady Adverse Pressure Gradient Flow.** The case involves a flow with an increasingly adverse pressure gradient. The calculation starts at $x = 0.855$ meters.

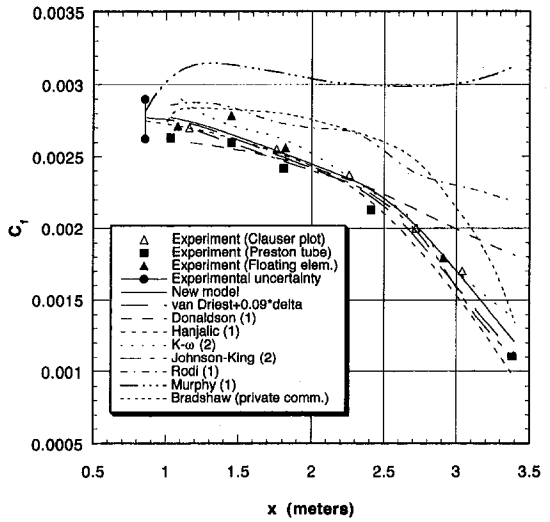


**Fig. 1 Skin friction coefficient for the Samuel and Joubert (1974) experiment. Comparison with the data and the results from other models. $c_f = \tau_w/(1/2\rho U_e^2)$. (1): from Kline et al. (1981), (2): from Menter (1993).**

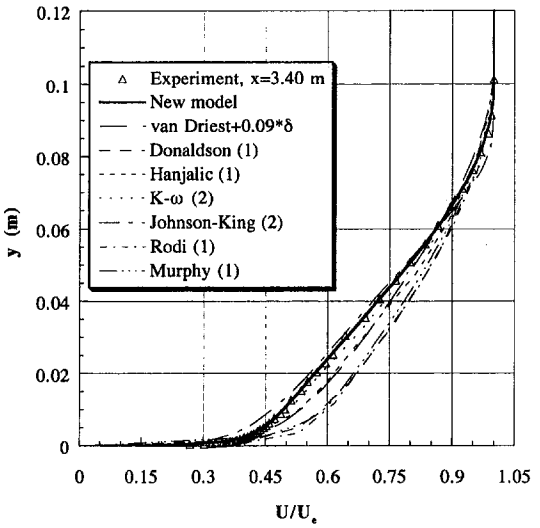


**Fig. 2 Velocity profile for the Samuel and Joubert (1974) experiment at $x = 3.40$ m. Comparison with the data and results from other models. (1): from Kline et al. (1981), (2): from Menter (1993).**

The $U$-component of the velocity at the starting location was taken from the experimental results, and $V$ was set equal to zero. The free-stream velocity is obtained from experimental data and it is applied as a boundary condition on the upper boundary of the numerical domain. The pressure gradient is then calculated using the Bernoulli equation.

The results presented here were obtained on a 200 × 74 grid, equally-spaced in the $x$-direction, and with a geometric progression in the $y$-direction. The node nearest to the wall was chosen so that $y^+ = 1 \div 3$. These values were chosen after numerical experimentation indicating no further changes in the solution.

Figure 1 presents the results of calculations with the new model and other models (Kline et al., 1981 and Menter, 1993) and the data. The comparison shows that the new model performs equally well or better than the other models.

Figure 2 gives velocity profiles. This clearly shows that the calculations of the new model are again equal to or better than the other models. Figure 3 shows that as the pressure gradient is increasing, the simple algebraic model fails to reproduce the Law of the Wall, which the experimental results obey (Samuel and Joubert, 1974).

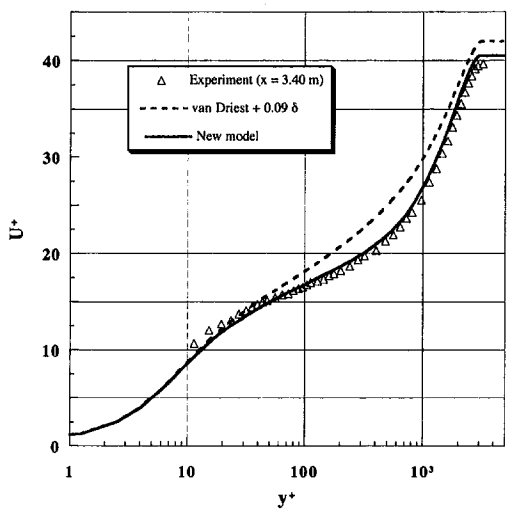


**Fig. 3 Samuel and Joubert (1974). Velocity profile at $x = 3.40$ m. Wall law plot.**

Comparisons for the shear stress profile for the last station are presented in Fig. 4, which indicates that even for this sensitive variable, the new model performs equally well or better than any other model.

**Simpson, Chew and Shivaprasad Steady Flow With Separation.** This flow has a much stronger adverse pressure gradient. The location $x = 0.8051$ meters was chosen as the starting point. There was some concern regarding the low Reynolds number based on the momentum thickness at this station, $Re_\theta = 1677$. Below $Re_\theta = 5000$, some suggest a variation of the constants describing the Law of the Wall with the Reynolds number (Simpson, 1970). The numerical domain is extended up to the point that the method predicts separation. This is done for two reasons: *a*) a boundary layer code, cannot solve for reverse flow, and *b*) the mixing length expression for the inner region is not compatible with the experimental observations for separated flows. The U-velocity profile at the starting location is obtained from the experimental results, while $V$ is set equal to zero. The free-stream velocity was applied as a boundary condition on the upper boundary and the pressure gradient was obtained from the Bernoulli equation.

The results presented here have been obtained on a 200 × 75 grid, equally spaced in the $x$-direction and with geometric progression in the $y$-direction. The node nearest to the wall was chosen so that $y^+ = 1 \div 3$. No changes were observed in the solution on a finer grid.

Figure 5 shows the calculations for skin friction compared with the data. The comparison indicates that the performance of the new model is very good. Velocity profiles are presented in Figs. 6 and 7. The comparison indicates that as separation is approached, a log region still exists, but the $U^+$ intercept of the Law of the Wall seems to be lower which implies a change in the constant in the Law of the Wall. Intermittent backflow might be playing an important role. The comparison also indicates that the new model tends to give a fuller profile for this location.

The stress profiles are presented in Fig. 8. Compared to the results of Pletcher and Mellor, the calculations of the new model are again equal or superior.

**Simpson, Chew and Shivaprasad Unsteady Flow With Separation.** The amplitude of the unsteady motion is approximately 0.3, and the reduced frequency, $\omega L/2\bar{U}_{ei} = 0.61$. The initial station was again not easy to choose due to low Reynolds number effects; it was decided that the same $x$ location could be used for the unsteady flow. To avoid any region of separation

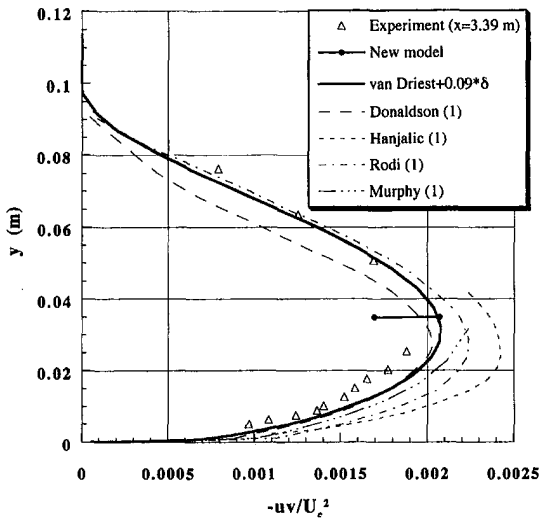


**Fig. 4 Samuel and Joubert (1974) experiment. Stress profile at $x = 3.39$ m. Comparison with the data and results from other models. (1): from Kline et al. (1981).**

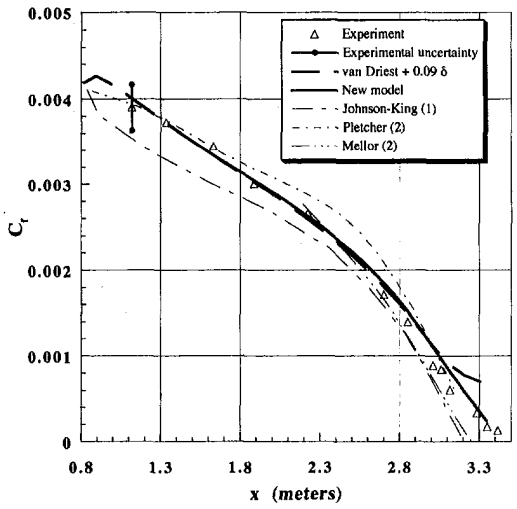


**Fig. 5 Simpson, Chew and Shivaprasad (1981) steady experiment. Skin friction coefficient. Comparison with the data and results from other models. (1): from Johnson and King (1984), (2): from Kline et al. (1981).**

during the unsteady simulation, the domain extends up to the location $x = 2.75$ m.

The free-stream velocity could be written in terms of a Fourier series as follows:

$$U_e = \bar{U}_e\left(1 + \sum_{i=1}^{n} \frac{\tilde{U}_{ie}}{\bar{U}_e} \cos(\omega t - \phi_{ie})\right) \tag{15}$$

where $\tilde{U}_{ie}$ is the amplitude of each harmonic and $\phi_{ie}$ is the phase lag. The ratio of the first harmonic to the mean velocity and $\phi_{ie} = 200°$ was experimentally found to be approximately constant up to $x = 3.0$ meters. The higher harmonics have amplitudes of less than three percent, so the numerical representation used here includes only the first harmonic. In this case, a phase lag of 196 degrees gives better agreement with the experiment. The results presented here were obtained on a 130 × 50 grid.

An Euler implicit integration scheme was used for the momentum equations. The Crank-Nicolson scheme was used for the integration of the auxiliary P.D.E. After experimentation with the value of the time step, the division of the cycle into 1350 steps was used for obtaining the results presented here. The repeatability of the solution was checked using the maximum shear stress, displacement and momentum thickness as criteria. All of those parameters indicated that by the third cycle a periodic solution was obtained.

The results start with the average skin friction coefficient equal to the average wall shear over a cycle divided by one half the average free-stream velocity value squared. Figure 9 shows the results of the calculations, the unsteady data and the steady data. The new model and the simple algebraic model both give results in very good agreement with the unsteady experiment up to $x = 2.3$ m.

The velocity profile, at $x = 2.74$ m, is presented in Fig. 10. This location is close to the point where intermittent backflow appears, and it has stronger pressure gradients during part of the cycle. The new model proves that it has a superior performance in strong pressure gradients.

Turning attention from the time-averaged results to instantaneous variations, we first present the phase lag of the wall shear stress with respect to the free-stream velocity. Both the new model and the simple algebraic model give almost identical results which are in good agreement with the experiment in Fig. 11.

Figure 12 presents the ratio of the 1st harmonic of the wall shear stress to the mean value. Both models predict the same

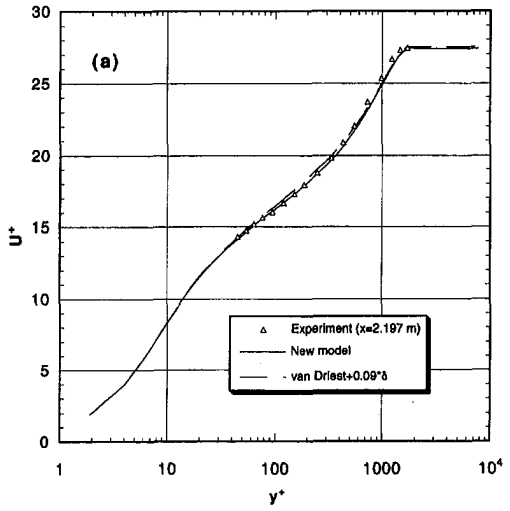


Fig. 6(*a*)

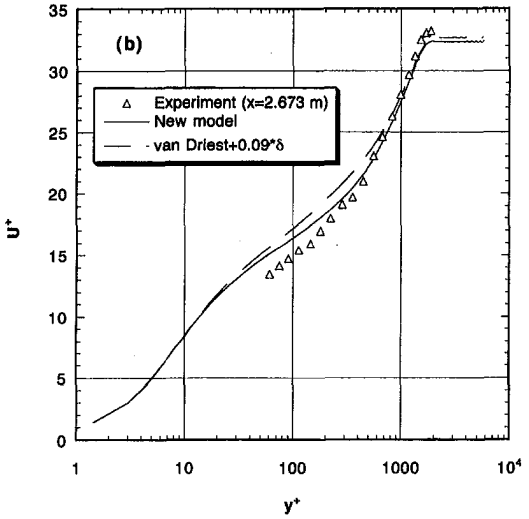


Fig. 6(*b*)

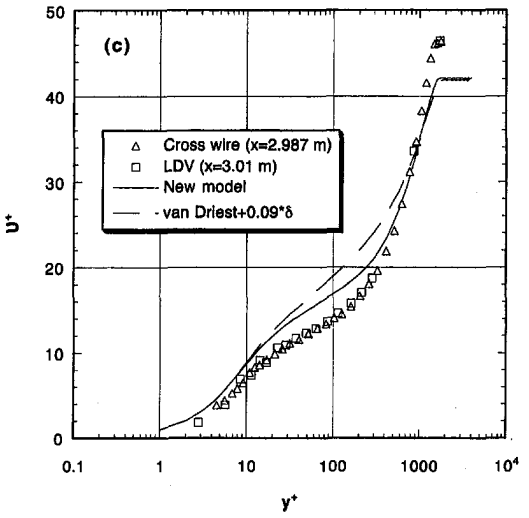


Fig. 6(*c*)

**Fig. 6 Simpson, Chew and Shivaprasad (1981) steady experiment. Velocity profiles in Wall Law coordinates.**

ratio, which is lower than the 0.667 from experiment. The two models indicate an increasing amplitude as the pressure gradient becomes stronger and backflow appears, in contrast with experiment. The same behavior but with a sharper increase is exhibited by the quasi-steady model of Houdeville and Cousteix (Cousteix et al., 1979).

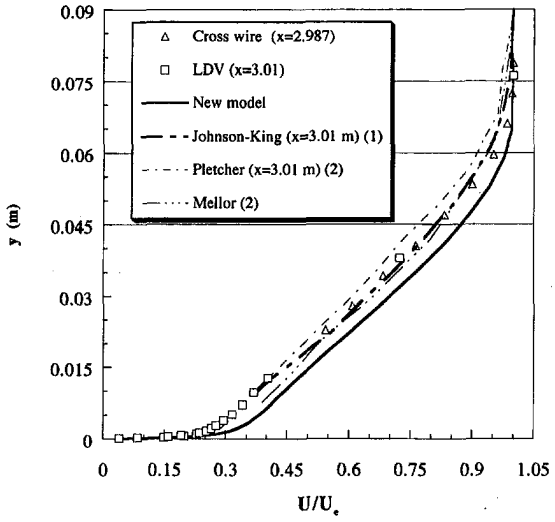


**Fig. 7 Simpson, Chew and Shivaprasad (1981) steady experiment. Velocity profile at $x$ = 3.01 m. Comparison with the data and results from other models. (1): from Johnson and King (1984), (2) from Kline et al. (1981).**

The ratio of the first harmonic of the velocity to the mean value as a function of $y$ for the location $x$ = 2.74 meters is presented in Fig. 13. The comparison indicates that both the new model and the simple algebraic model predict the correct trends, but the new model gives values that are in better agreement with the experiment. The phase lag of the first harmonic as predicted from the two models for $x$ = 2.74 meters is shown in Fig. 14. The comparison indicates that both models are in agreement with the experimental results.

Figure 15 compares the velocity profiles at $x$ = 2.74 meters. These are the phase-averaged profiles that correspond to: (*a*) free-stream velocity minimum, (*b*) free-stream velocity equal to the average velocity and increasing, (*c*) free-stream velocity maximum, and (*d*) free-stream velocity equal to the average value and decreasing. All four figures indicate that the new model gives profiles that are in better agreement with the experimental profiles compared to the simple algebraic model.

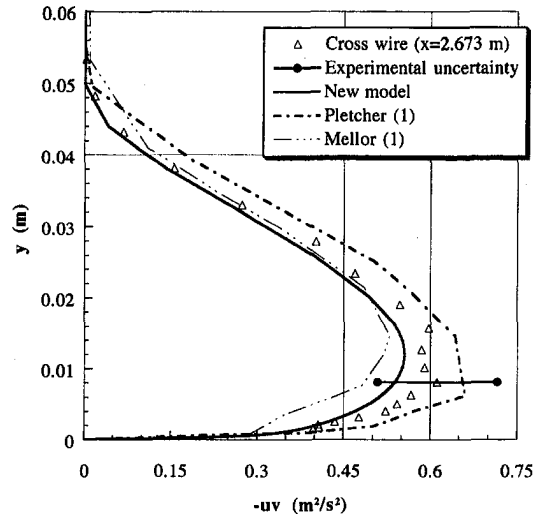


**Fig. 8 Simpson, Chew and Shivaprasad (1981) steady experiment. Stress profiles at $x$ = 2.673 m. Comparison with the data and results from other models. (1): from Kline et al. (1981).**

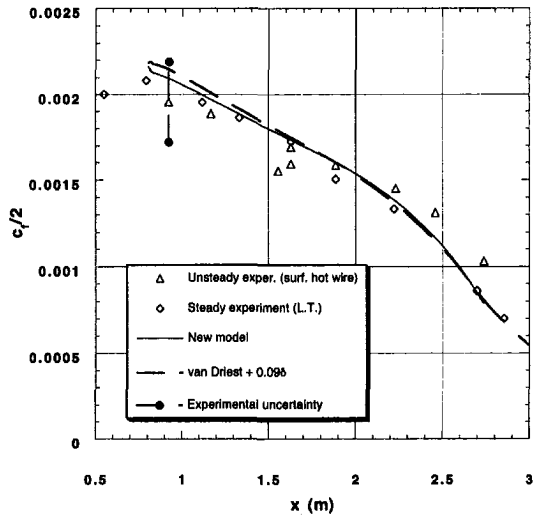


Fig. 9 Simpson et al. (1983) unsteady experiment. Time-averaged skin friction coefficient.

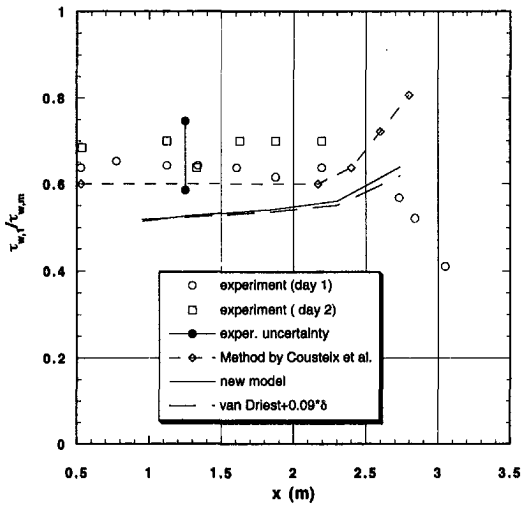


Fig. 12 Simpson et al. (1983) unsteady experiment. Wall shear stress. Ratio of the amplitude of the first harmonic to the time-averaged value.

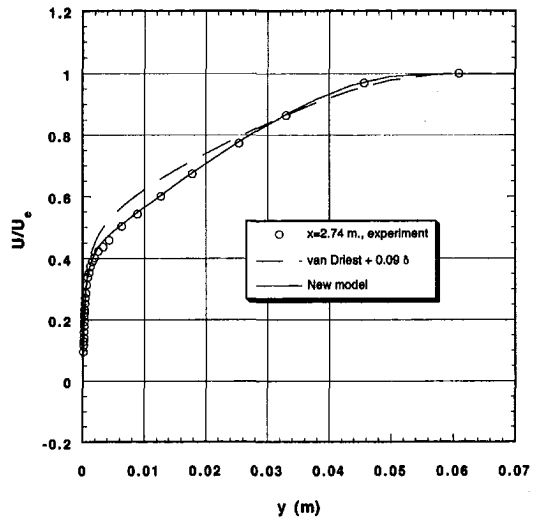


Fig. 10 Simpson et al. (1983) unsteady experiment. Time-averaged velocity profile at $x = 2.74$ m.

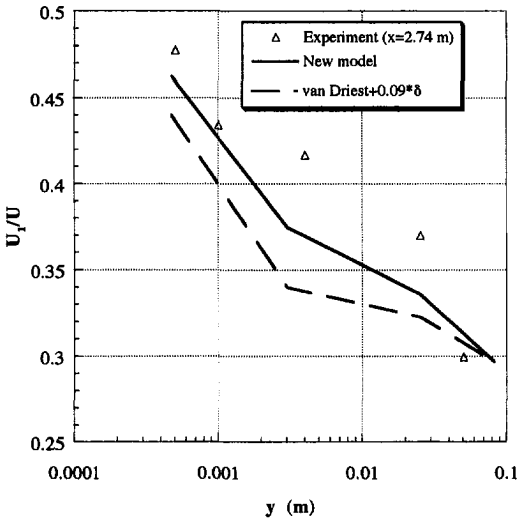


Fig. 13 Simpson et al. (1983) unsteady experiment. Ratio of the amplitude of the first harmonic of velocity to the time-averaged value as a function of $y$.

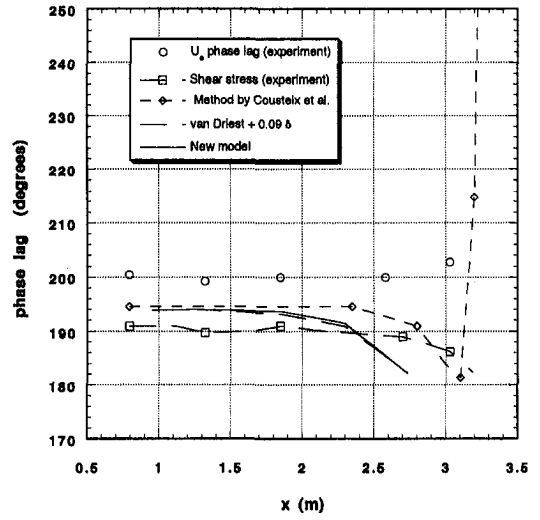


Fig. 11 Simpson et al. (1983) unsteady experiment. Phase lag of the wall shear with respect to the freestream.

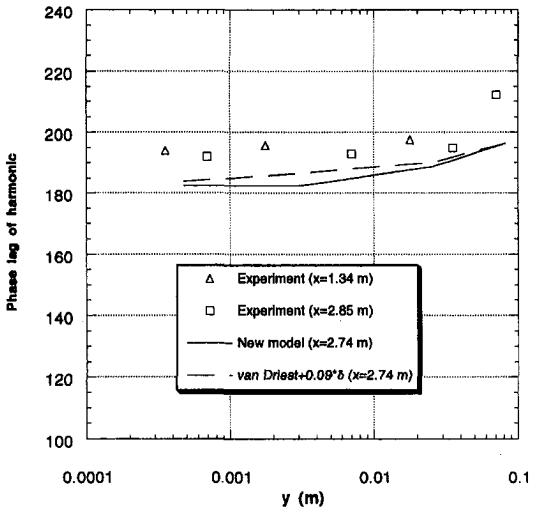


Fig. 14 Simpson et al. (1983) unsteady experiment. Phase angle of first harmonic of velocity as a function of distance from the wall.

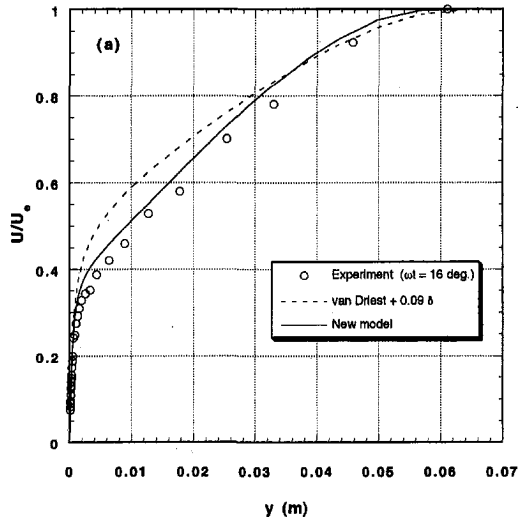


Fig. 15(*a*)

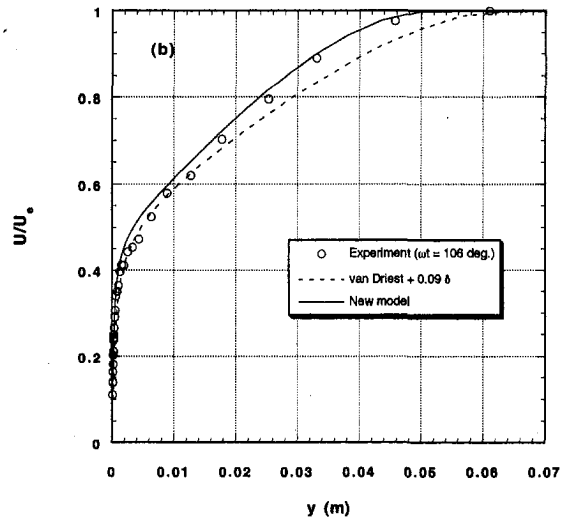


Fig. 15(*b*)

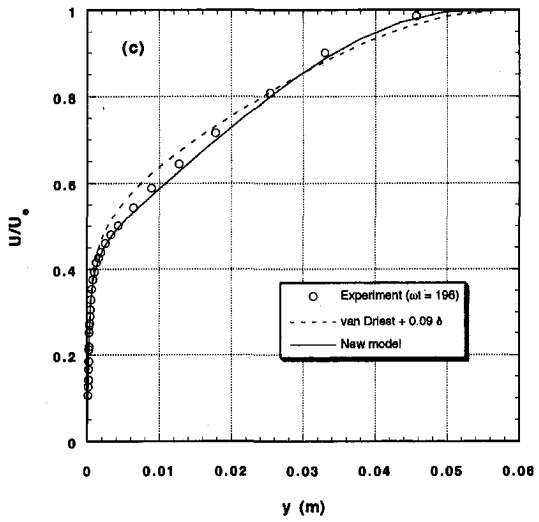


Fig. 15(*c*)

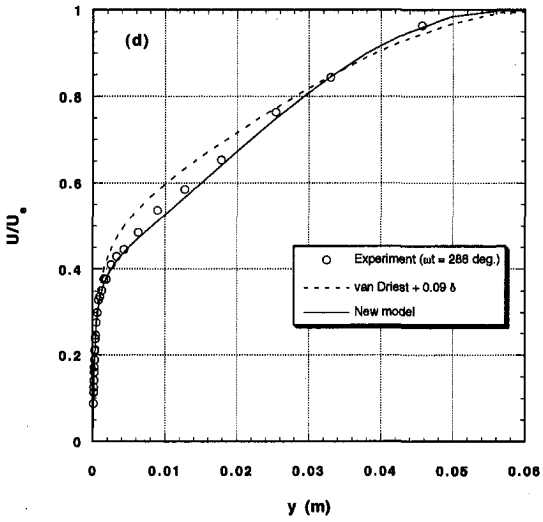


Fig. 15(*d*)

**Fig. 15 Simpson, Shivaprasad and Chew unsteady experiment. Phase average velocity at $x$ = 2.74 m. (*a*) $U_e$ = minimum, (*b*) $U_e = U_{mean}$ and increasing, (*c*) $U_e$ = maximum, and (*d*) $U_e = U_{mean}$ and decreasing.**

## Discussion

A new, general and rational approach has been developed for the prediction of steady and unsteady, turbulent boundary layer flows under the presence of strong adverse pressure gradients up to separation. The foundations of the new method are based on experimental observations. The model uses the integrated T.K.E equation in an attempt to take into account the "history" effects of turbulence, which eliminates the need for any assumptions concerning the path of the maximum shear stress. This becomes important in the case of unsteady flows where the assumption that the path is parallel to the $x$-axis is questionable. The extension of the Johnson-King concept to unsteady, free-stream flow is not straightforward, since the $J$-$K$ $\tau_{max}$ transport equation cannot be associated with a particular position or path in an unsteady flow. Hysteresis of the shearing stress profiles precludes the use of the simple, smoothed $J$-$K$ stress profile. We believe we have made a fundamental contribution in providing a rational basis for a $\tau_{max}$ transport equation for unsteady flows. The integrated formulation, coupled with the boundary layer theory assumptions, eliminates the diffusion term of the equation, the modeling of which is uncertain. The resulting auxiliary differential equation governs the development of the maximum shear stress which is used as a scaling parameter.

A mixing length approach is used for describing the stress profile across the boundary layer, and a model based on the distribution of the near wall shear stress has been developed. The mixing length for the outer region is assumed proportional to the boundary layer thickness, but the proportionality factor can vary with the streamwise distance. The variation of this factor is governed by the requirement that the maximum value of the stress profile must be equal to the value that the auxiliary equation predicts. The model in its present form requires determination of the boundary layer thickness as a part of the calculation in order to find the mixing length in the outer region. This might be viewed by some as a limitation in extending the model for use in Navier-Stokes equation codes, because difficulties in finding the outer edge of an embedded boundary layer have been reported as a result of numerical "noise" in the predicted velocity profiles when crude grids are used. That is more properly to be viewed as a numerical problem than a turbulence modeling issue. Nonetheless, one could modify the present model using, as but one example, the approach in the Baldwin-Lomax algebraic model for finding the equivalent of the boundary layer thickness.

The new model also incorporates the important contribution of the normal stresses in T.K.E production. This term has been

modeled in an approximate, but rational way. In order to account for the change of the turbulence structure as separation is approached, a model has been incorporated for the variation of the Bradshaw constant $a_1$. It was also found that allowing the outer layer dissipation factor to vary proportionally with the mixing length factor improved the results.

The complete model was implemented into a Finite Element Method code solving the boundary layer equations. The implementation of the model into any other numerical method is straightforward. The model is designed in such a way, that the momentum equations solver sees it only as a means of providing mixing length values.

The model was tested against four flow cases. For the turbulent flat plate case, the model gave identical results with the simple algebraic model, as it should. The next two cases tested the ability of the model for steady flows in the presence of strong pressure gradients up to, but not including, separation.

The new model gave improved results compared to the simple algebraic model for all flow variables. Specifically, the new model gave excellent results for all flow variables when compared with the experimental results of Samuel and Joubert. The model performs, for this case, equally well or better when compared to other turbulence models available in the literature. For the steady Simpson experiment, which has a much stronger pressure gradient, the results were improved over the algebraic model. Some differences with the experimental results may be the result of some of the modeling assumptions breaking down very close to separation and/or the presence of intermittent backflow. In general though, the new model exhibited the correct trends for this test case. The real strength of the model becomes obvious when the velocity profiles are plotted on a semilogarithmic scale. Unlike the algebraic model, the new model reproduces the Law of the Wall in the presence of strong adverse pressure gradients, as the experimental results indicate.

For the unsteady strong adverse pressure gradient test case, the new model showed improved performance in predicting the time-averaged values of the flow variables. The velocity profiles near separation are in excellent agreement with the data. The good agreement between the predicted and the experimental phase-averaged velocity profiles indicates the ability of the model to give superior results not only in the time-averaged sense but also for each phase of the cycle.

## Acknowledgments

This work was partially supported by the Office of Naval Research Grant N00014-92-J-1129 (James A. Fein, Program Manager) and by U.S. Army Research Office Grant DAAL03-92-G-0098 (Thomas Doligaski, Program Manager).

## References

Baldwin, B., and Barth, T. J., 1991, "A one-equation Turbulence Transport Model for High Reynolds Number Wall-Bounded Flows," AIAA 91-0610.

Bradshaw, P., 1967, "The Turbulence Structure of Equilibrium Boundary Layers," *Journal of Fluid Mechanics,* Vol. 29, pp. 625–645.

Bradshaw, P., Ferris D. H., and Atwell N. P., 1967, "Calculation of Boundary-Layer Development Using the Turbulent Energy Equation," *Journal of Fluid Mechanics,* Vol. 28, Part 3, pp. 593–616.

Coles, D., 1955, "The Law of the Wall in Turbulent Shear Flow," *50 Jahre Grenzsschichtforshung,* F. Vieweg & Sohn, Braunschweig.

Collins, M. A., and Simpson, R. L., 1978, "Flow-Field Prediction of Separating Turbulent Shear Layers," *AIAA Journal,* Vol. 16, pp. 291–292.

Cousteix, J., Houdeville, R., and Raynaud, M., 1979, *Proceedings of 2nd Symposium on Turbulent Shear Flow,* Imperial College, London, pp. 6.12–6.17.

Dindar, M., and Kaynak, U., 1992, "Effect of Turbulence Modeling on Dynamic Stall of a NACA0012 Airfoil," AIAA 92-0027.

Goldberg, P., 1966, "Upstream History and Apparent Stress in Turbulent Boundary Layers," Gas Turbine Laboratory, Report No. 85, M.I.T..

Hytopoulos, E., and Simpson, R. L., 1993, "Critical Evaluation of Recent Second-Order Closure Models," AIAA 93-0081.

Johnson, D. A. and Coakley, T. J., 1990, "Improvements to a Nonequilibrium Algebraic Turbulence Model," *AIAA Journal,* Vol. 28, No. 11.

Johnson, D. A., and King, L. S., 1984, "A new Turbulence Closure Model for Boundary Layer Flows with Strong Adverse Pressure Gradients and Separation," AIAA paper 84-0175.

Kline, S. J., Cantwell, B. J., and Lilley, G. M., 1981, 1980-81 AFOSR-HTTM-Stanford Conference on Complex Turbulent Flows, Stanford University, California.

Ludwieg, H., and Tillman, W., 1950, "Investigation of the Wall Shearing Stress in Turbulent Boundary Layers," NACA TM 1285.

McDonald, H., 1969, "The effect of Pressure Gradient on the Law of the Wall in Turbulent Flow," *Journal of Fluid Mechanics,* Vol. 35, pp. 311–336.

McDonald, H., and Camarata, F. J., 1968, "An extended mixing length approach for computing the turbulent boundary layer development," *Computation of Turbulent Boundary Layers,* Proceedings of the AFOSR-IFP-Stanford conference, Stanford University, pp. 83–98.

Menter, F. R., 1991, "Performance of Popular Turbulence Models for Attached and Separated Adverse Pressure Gradient Flows," AIAA-91-1784.

Menter, F. R., 1993, "Zonal Two Equation $K$-$\omega$ Turbulence Models for Aerodynamic Flows," AIAA 93-2906.

Samuel, A. E., and Joubert, P. N., 1974, "A Boundary Layer Developing in a Increasingly Adverse Pressure Gradient," *Journal of Fluid Mechanics,* Vol. 66, Part 3, pp. 481–505.

Schetz, J. A., Hytopoulos, E., Gunzburger, M., 1993, "Numerical Solution of the Boundary Layer Equations Using the Finite Element Method," ASME JOURNAL OF FLUIDS ENGINEERING, Vol. 114, No. 4, p. 504.

Schetz, J. A., 1993, *Boundary Layer Analysis,* Prentice-Hall, Englewood Cliffs, NJ.

Shiloh, K., Shivaprasad, B. G., and Simpson, R. L., 1981, "The Structure of a Separating Turbulent Boundary Layer. Part 3. Transverse Velocity Measurements," *Journal of Fluid Mechanics,* Vol. 113, pp. 75–90.

Simpson, R. L., 1987, "A Review of Two-Dimensional Turbulent Separated Flow Calculation Methods," *Boundary Layer Separation,* F. T. Smith, ed., Springer-Verlag, Heidelberg.

Simpson, R. L., 1970, "Characteristics of Turbulent Boundary Layers at Low Reynolds Numbers With and Without Transpiration," *Journal of Fluid Mechanics,* Vol. 42, part 4, pp. 769–802.

Simpson, R., Chew, Y.-T., and Shivaprasad, B. G., 1981, "The Structure of a Separating Turbulent Boundary Layer. Part 1. Mean Flow and Reynolds Stresses," *Journal of Fluid Mechanics,* Vol. 113, pp. 23–51.

Simpson, R. L., Shivaprasad, B. G., and Chew, Y.-T., 1983, "The Structure of a Separating Turbulent Boundary Layer. Part 4. Effects of Periodic Free-Stream Unsteadiness," *Journal of Fluid Mechanics,* Vol. 127, pp. 219–261.

Simpson, R. L., Strickland, J. H., and Barr, P. W., 1977, "Features of a Separating Turbulent Boundary Layer in the Vicinity of Separation," *Journal of Fluid Mechanics,* Vol. 79, Part 3, pp. 553–594.

So, R. M. C., Zhang, H. S., and Speziale C. G., 1992, "Near-wall Modeling of the Dissipation-Rate Equation," AIAA 92-0441.

Spalart, P. R., and Allmaras, S. R., 1992, "A One-Equation Turbulence Model for Aerodynamic Flows," AIAA 92-0439.

Srinivasan, G. R., Ekaterinaris, J. A., and McCroskey, W. J., 1993, "Dynamic Stall of an Oscillating Wing. Part 1: Evaluation of Turbulence Models," AIAA 93-3403.

Wolfstein, M., 1967, "Convection Processes in Turbulent Impinging Jets," Imperial College, Heat Transfer Section Rep SF/R/2.

Yakhot, V. and Orzag, S. A., 1986, "Renormalization Group Analysis of Turbulence. 1-Basic Theory," *Journal of Scientific Computing,* Vol. 1, No. 1, pp. 3–51.

# Calculation of Fully-Developed Turbulent Flow in Rectangular Ducts With Nonuniform Wall Roughness

**M. Naimi**
Principal Engineer,
Boeing Commercial Airplane Group,
The Boeing Company,
Seattle, WA 98124

**F. B. Gessner**
Professor,
Department of Mechanical Engineering,
University of Washington,
Seattle, WA 98195

*The predictive capabilities of four transport-type turbulence models are analyzed by comparing predictions with experimental data for fully-developed flow in (1) a rectangular duct with a step change in roughness on one wall (Case 1), and (2) a square duct with one rib-roughened wall (Case 2). The models include the Demuren-Rodi (DR) k-ϵ model, the Sugiyama et al. (S) k-ϵ model, the Launder-Li (LL) Reynolds stress transport equation model, and the differential stress (DS) model proposed recently by the authors. For the first flow situation (Case 1), the results show that the DS model yields improved agreement between predicted and measured primary and secondary mean velocity distributions in comparison to the DR and LL models. For the second flow situation (Case 2), the DS model is superior to the DR and S models for predicting experimentally observed mean velocity, turbulence kinetic energy, and Reynolds stress anisotropy behavior, especially in the vicinity of a corner formed by the juncture of adjacent smooth and rough walls. The results are analyzed in order to explain why the DR model leads to the formation of a spurious secondary flow cell near this corner that is not present in the experimental flow.*

## Introduction

The nature of turbulence-driven secondary flow in straight, rectangular ducts is sensitive to local wall roughness conditions. More specifically, secondary flow can arise by virtue of a peripheral step change in wall roughness in addition to corner generated secondary flows that exist in this type of duct configuration. If periodically spaced ribs are located normal to the primary flow on one or more walls of the duct, then these walls have an effective roughness different from that of adjacent smooth walls. This combination of mixed wall roughness conditions also alters secondary flow patterns in the cross plane from those which exist in a wholly smooth-walled duct. The use of artificially roughened duct walls is of practical interest in heat transfer applications where rib-roughening of a gas turbine blade passage has been proposed as a means of augmenting heat transfer between the passage coolant and exposed blade surfaces (Han, 1988; Hsieh and Hong, 1989; and Zhang et al., 1993), and as a means of facilitating active cryogenic cooling of aerodynamically heated surfaces on hypersonic aircraft (Youn et al., 1994).

Previous research on flow in rectangular ducts with periodically spaced ribs has focused primarily on two aspects of the overall problem, namely: (1) understanding the nature of local flow and heat transfer in the entire duct cross section midway between, and directly above, adjacent ribs, and (2) understanding the nature of local flow and heat transfer in the duct midplane region, with specific emphasis on Nusselt number behavior along the rib-roughened surface and the sensitivity of this behavior to rib geometry, spacing, permeability, offset distance from the wall, etc. Experimental and numerical investigations in these two areas have generally been for a rectangular duct flow that is both hydrodynamically and thermally fully developed, as interpreted for a duct with periodically spaced ribs. Experimental studies in the first area include studies of flow in a square duct with one rib-roughened wall (Fujita et al., 1989, 1990a) and with two opposite rib-roughened walls (Fujita et al., 1988; Yokosawa et al., 1989). Additional data are also available for flow in a 2:1 aspect ratio rectangular duct with one rib-roughened long or short wall (Fujita et al., 1989, 1990b), with two opposite rib-roughened long walls (Hirota et al., 1996) and with two opposite rib-roughened short walls (Hirota et al., 1993, 1994a, 1995). In all of these studies one specific square rib configuration and a fixed rib spacing were employed. The data from these studies generally provide detailed information on local flow behavior directly above, and midway between, adjacent ribs, including axial mean velocity profiles, secondary flow vectors, distributions of five of the six Reynolds stress components, and peripheral wall shear stress distributions along the smooth-walled portions of the duct. This type of information and details of local flow behavior in the duct midplane region for ribs positioned on opposite long walls of a 2:1 aspect ratio rectangular duct are provided by Liou et al. (1993a), who applied LDV techniques to measure the flowfield in contrast to the above-mentioned studies, which employed hot-wire techniques. A few related experimental studies have also been conducted that provide information on local temperature distributions in the cross plane and peripheral Nusselt number distributions along the smooth-walls of a square duct with one rib-roughened wall (Hirota et al., 1994b) and with two opposite rib-roughened walls (Fujita et al., 1988). The numerical predictions of Sugiyama et al. are generally in good agreement with experimental results from the above-mentioned studies for flow in a square duct with one or two opposite rib-roughened walls (1993a, 1993b, 1993c), and for flow in a 2:1 aspect ratio rectangular duct with one rib-roughened long wall (1993d). More recent predictions by Sugiyama et al. (1995) underestimate, however, experimentally observed peripheral Nusselt number variations in a square duct with one rib-roughened wall when the duct walls are maintained at a constant elevated temperature by external heating.

The afore-mentioned studies show that different secondary flow patterns can be generated in a rib-roughened square or

Contributed by the Fluids Engineering Division for publication in the JOURNAL OF FLUIDS ENGINEERING. Manuscript received by the Fluids Engineering Division August 1, 1996; revised manuscript received May 5, 1997. Associate Technical Editor: P. M. Sockol.

rectangular duct depending on the number and orientation of walls with periodically-spaced ribs. In order to clarify one aspect of the overall problem, namely the sensitivity of secondary flow predictions to wall roughness conditions, this paper will focus on predicting local flow behavior in a square or rectangular duct that has only one roughened wall. Before doing so, however, it is expedient to summarize briefly studies related to the second area mentioned earlier, namely data and predictions that focus on local flow and heat transfer behavior in the duct midplane region, so that complexities present in the flow can be fully appreciated. Only studies related to flow and heat transfer over periodically spaced ribs positioned on one wall of the duct will be discussed. The nature of the results is qualitatively similar to that which has been observed in square and rectangular ducts with two opposite rib-roughened walls, where recent studies have examined the sensitivity of local heat transfer and friction factor behavior to rib shape (Liou and Hwang, 1993), rib pitch and rib height (Liou and Hwang, 1992, 1993), rib stagger (Hong and Hsieh, 1993), rib permeability (Hwang and Liou, 1995), combined rib-groove effects (Zhang et al., 1994), duct aspect ratio, (Hong and Hsieh, 1993) and orthogonal duct rotation in order to simulate more adequately actual flow conditions in a gas turbine blade passage (Zhang et al., 1993, Hsieh and Hong, 1995, Iacovides et al., 1996).

Flow in rectangular ducts with periodically spaced ribs is characterized by local flow separation and reattachment processes that occur between adjacent ribs for rib spacings that have typically been employed in previous studies. These processes affect local wall temperature and Nusselt number distributions, as measured, in recent years by means of laser holographic interferometry techniques applied to flow in rectangular ducts having a constant heat flux boundary condition on the rib-roughened wall. The results of Lockett and Collins (1990), for example, show that maximum heat transfer occurs at the forward top corner of a square-sectioned rib, whereas minimum heat transfer (maximum wall temperature) occurs near the base corner of the rearward facing rib wall. In a subsequent study, Liou et al. (1993b) investigated the influence of rib height and rib spacing on local wall temperature and Nusselt number distributions on a rib-roughened surface and found that a rib pitch-to-rib height ratio of 10 maximized the average heat transfer between the duct and its surroundings for their particular operating conditions. Their results also indicated the presence of a local temperature hot spot at the rear base rib corner for all rib configurations. In order to alleviate these hot spots, Hwang and Liou (1994) have proposed the use of square ribs with staggered rows of in-line holes in the axial flow direction (perforated ribs). For their particular operating conditions, they found that a maximum increase in the average Nusselt number occurs when the net hole open area is about 44 percent of the rib face area, and that hot spots behind the ribs can be eliminated if the rib hole open area is sufficient to allow through flow into the rib base region. In subsequent work, Liou et al. (1995) proposed an alternate method for eliminating hot spots behind ribs, namely to position the ribs at a fixed offset distance from the wall. Their results demonstrate the effectiveness of this concept and show that improvements in thermal performance based on a constant pumping power constraint can be as high as 100 percent, provided that the ratio of gap height-to-rib thickness is at or below 0.58, with 0.38 being the optimum value over the range of Reynolds numbers considered in their work.

On the basis of the previous discussion, it should be evident that the present state-of-the-art for predicting local flow and heat transfer in a rib-roughened rectangular duct has not yet addressed the issue of how flow along the juncture of a rib-roughened wall with a bounding smooth wall should be modeled. Heat transfer studies have generally been confined to the duct midplane region, including a recent large-eddy simulation study which examines the time-dependent nature of flow next to a rib-roughened wall (Braun and Neumann, 1996), and the flow studies mentioned earlier focus primarily on the nature of flow in the cross plane directly above, and midway between, adjacent ribs. There is a need, therefore, to investigate how well previously proposed turbulence models apply over the entire flow field, not just in the midplane region or at specific streamwise locations in the duct. In order to advance our knowledge in this area, the present paper addresses the issue of which of four transport equation models performs best in terms of predicting secondary flow behavior in a rectangular duct with mixed wall roughness conditions. Proper simulation is important because secondary flow effects alter local wall temperature distributions, so that improper simulation can lead to inaccurate prediction of peripheral variations in the local Nusselt number. From the standpoint of computational convenience (and practicality), predictions in this paper are restricted to streamwise-averaged flow behavior and do not account for local flow behavior in the immediate vicinity of a corner formed by a rib end face in contact with a smooth endwall. The specific question addressed in this paper is whether or not any of the four selected turbulence models can predict the relative size and strength of experimentally observed secondary flow cells in the flow and their distorting effect on the primary flow and local turbulence structure. If the comparisons made produce positive results, then future work can focus on the applicability of the best performing model to predict the full complexity of the actual flow, including flow over individual ribs and local corner effects generated by rib-endwall junctures.

## Prescribed Turbulence Models

The present study was motivated by the level of performance exhibited by the Reynolds stress transport equation (DS) model proposed recently by the authors for predicting developing turbulent flow in a smooth-walled rectangular duct (Naimi and Gessner, 1995). In that study it was shown that the DS model is computationally efficient and leads to better agreement between predictions and experiment than alternate turbulence models proposed by Demuren and Rodi (1984) and by Myong and Kobayashi (1991). In the present study results based on the DS model are compared with those based on the Demuren and Rodi (DR) $k$-$\epsilon$ model, the (S) $k$-$\epsilon$ model formulated by Sugiyama et al. (1991), and the (LL) Reynolds stress transport equation model proposed recently by Launder and Li (1993, 1994). All four models employ modeled forms of the Reynolds stress transport equations, which can be written in compact form as:

$$C_{ij} - D_{ij} = P_{ij} + \Phi_{ij} - \epsilon_{ij} \tag{1}$$

where $C_{ij} - D_{ij}$ is the convection-minus-diffusion effect, $P_{ij}$ corresponds to mean-strain rate generation, $\Phi_{ij}$ is the pressure-strain effect, and $\epsilon_{ij}$ represents viscous dissipation. In the DR and S models a transport equation for the turbulence kinetic energy, $k$, is generated by letting $j = i$ in Eq. (1) and specifying a gradient diffusion model for $D_{ij}$. In order to develop algebraic expressions for the individual Reynolds stresses, $C_{ij} - D_{ij}$ is set equal to zero in the DR model, which is equivalent to assuming that each Reynolds stress component is in local equilibrium. As an alternative, Sugiyama et al. (1991) adopt the relatively simple model proposed by Rodi (1976) to model the convection-minus-diffusion effect on the individual Reynolds stresses, namely:

$$C_{ij} - D_{ij} = \frac{\overline{u_i u_j}}{k}(P - \epsilon) \tag{2}$$

In the Reynolds stress transport equation model proposed by Launder and Li (1993, 1994), $D_{ij}$ is modeled in terms of an eddy diffusivity tensor and $C_{ij} - D_{ij}$ is represented as:

$$C_{ij} - D_{ij} = U_l \frac{\partial \overline{u_i u_j}}{\partial x_l} - \frac{\partial}{\partial x_l}\left(\upsilon + c_s \overline{u_k u_l}\frac{k}{\epsilon}\right)\frac{\partial \overline{u_i u_j}}{\partial x_k} \quad (3)$$

with $c_s = 0.22$. An alternative expression adopted by Naimi and Gessner (1995) utilizes a "weighted" version of the convection-minus-diffusion effect of the form:

$$C_{ij} - D_{ij} = \alpha_{CD}\left[U_l \frac{\partial \overline{u_i u_j}}{\partial x_l} - \frac{\partial}{\partial x_l}\left(\upsilon + \frac{\upsilon_t}{\sigma_k}\right)\frac{\partial \overline{u_i u_j}}{\partial x_l}\right] + (1 - \alpha_{CD})\frac{2}{3}\delta_{ij}(P - \epsilon) \quad (4)$$

where $\alpha_{CD} = 0.75$, $\sigma_k = 1.0$, $P$ is the production rate of turbulence kinetic energy, and $\epsilon$ is its dissipation rate.

In order to model pressure-strain behavior, the DR, DS, and S models all assume that the total effect is the combined result of turbulent interactions $\phi_{ij,1}$, mean-strain rate effects, $\phi_{ij,2}$, and wall proximity effects, $\phi_{ij,w}$, so that

$$\Phi_{ij} = (\phi_{ij} + \phi_{ji})_1 + (\phi_{ij} + \phi_{ji})_2 + (\phi_{ij} + \phi_{ji})_w \quad (5)$$

with

$$(\phi_{ij} + \phi_{ji})_1 = -c_1 \frac{\epsilon}{k}\left(\overline{u_i u_j} - \frac{2}{3}\delta_{ij}k\right) \quad (6)$$

and

$$(\phi_{ij} + \phi_{ji})_2 = (a_{ij}^{mi} + a_{li}^{mj})\frac{\partial U_l}{\partial x_m} \quad (7)$$

where Eq. (6) corresponds to the model proposed by Rotta (1962) and Eq. (7) is the model proposed by Launder et al. (1975) in which $a_{ij}^{mi}$ is represented as a linear combination of the Reynolds stresses, namely:

$$a_{ij}^{mi} = \alpha\delta_{ij}\overline{u_m u_i} + \beta(\delta_{ml}\overline{u_i u_j} + \delta_{mj}\overline{u_i u_l} + \delta_{il}\overline{u_m u_j} + \delta_{ij}\overline{u_m u_l}) + c_2\delta_{mi}\overline{u_l u_j} + [\eta\delta_{mi}\delta_{lj} + \nu(\delta_{ml}\delta_{ij} + \delta_{mj}\delta_{il})]k \quad (8)$$

Following Launder et al. wall proximity effects in Eq. (5) are modeled as:

$$(\phi_{ij} + \phi_{ji})_w = c_1'\frac{\epsilon}{k}\left(\overline{u_i u_j} - \frac{2}{3}\delta_{ij}k\right) + + (b_{ij}^{mi} + b_{li}^{mj})\frac{\partial U_l}{\partial x_m} f_d \quad (9)$$

In Eq. (9) the wall damping function, $f_d$, is modeled in terms of von Karman's constant, $\kappa$, Prandtl's length scale, $l_p$, and the effective distance from the wall $\langle S \rangle$ by the relationship:

$$f_d = \left(\frac{l_p}{\kappa\langle S \rangle}\right)^n \quad (10)$$

where $n = 1$ (linear wall damping) in the DS and S models, and $n = 2$ (quadratic wall damping) in the DR model. Naimi and Gessner (1995) applied both the DR and DS models to predict developing turbulent flow in a smooth-walled square duct. Their results clearly show that a linear wall damping function is more appropriate and that quadratic wall damping is required in the DR model only because the wall correction coefficients in their pressure-strain model yield Reynolds stress anisotropy levels that are too high in the near-wall region.

In reference to Eq. (10), Prandtl's length scale, $l_p$, can be written in alternate form as:

$$l_p = \frac{(c_\mu^* \xi_p)^{3/4} k^{3/2}}{\epsilon} \quad (11)$$

where $c_\mu^* = c_\mu = 0.09$ and $\xi_p = 1$ in the DR and S models. In the DS model, $c_\mu^*$ is not specified a priori, but is a calculated coefficient whose numerical value depends on $\xi_p$, the ratio of the production rate of turbulence kinetic energy from the primary flow to its dissipation rate. The DR, DS, and S models all utilize Buleev's (1963) length scale to model the behavior of the effective distance $\langle S \rangle$ in Eq. (10). The tensor $b_{ij}^{mi}$ in Eq. (9) has the same functional form as $a_{ij}^{mi}$, except that the primary coefficients in the expression for $a_{ij}^{mi}$ ($\alpha$, $\beta$, $\eta$, $\upsilon$, and $c_2$) are replaced by primed (wall correction) coefficients (cf. Launder, Reece, and Rodi, 1975, Eqs. (18)–(20)). In the DR model, $\alpha$, $\beta$, $\eta$, and $\upsilon$ are expressed in terms of $c_2$ after constraints dictated by symmetry, continuity, and the application of Green's third identity are applied to $a_{ij}^{mi}$. This procedure reduces the number of primary coefficients in Eqs. (6)–(8) from six to two, namely $c_1$ and $c_2$. If a similar procedure is applied to $b_{ij}^{mi}$, then the net result is two independent wall correction coefficients in Eq. (9), namely $c_1'$ and $c_2'$. By applying the continuity constraint to $a_{ij}^{mi}$ and $b_{ij}^{mi}$ in a different manner, Gessner and Eppich (1981) show that three independent coefficients can be generated for the primary ($c_1$, $c_2$, $\gamma$) and wall correction ($c_1'$, $c_2'$, $\gamma'$) coefficients, which are the coefficients employed in the DS model. A similar procedure was followed by Sugiyama et al. (1991) in order to specify three independent primary ($c_1$, $c_2$, $\zeta$) and wall correction ($c_1'$, $c_2'$, $\zeta'$) coefficients in their pressure-strain model. This approach, as noted by Sugiyama et al., allows greater flexibility in matching pressure-strain coefficients to experimental data.

In contrast to the aforementioned studies which model near-wall pressure-strain effects as a separate entity, Launder and Li (1993, 1994) have proposed an alternate pressure strain model which eliminates the need for simulating wall effects separately, namely:

$$\Phi_{ij} = \phi_{ij,1} + \phi_{ij,2} \quad (12)$$

where $\phi_{ij,1}$ is an extended version of the turbulence interaction model originally proposed by Rotta (1962) and $\phi_{ij,2}$ represents the effects of mean-strain rate interactions and is cubic in form relative to highest-order products of the Reynolds stress tensor. Explicit (and lengthy) expressions for $\phi_{ij,1}$ and $\phi_{ij,2}$ are given by Launder and Li (1993, 1994) and will not be repeated here.

The behavior of the dissipation rate tensor $\epsilon_{ij}$ in Eq. (1) is simulated in all four models by means of the isotropic relationship:

$$\epsilon_{ij} = \tfrac{2}{3}\delta_{ij}\epsilon \quad (13)$$

The transport equation for the isotropic dissipation rate $\epsilon$ is essentially the same in the DR, DS, and S models, except for minor variations in the specified coefficients. The transport equation for $\epsilon$ in the LL model is qualitatively similar, except that the diffusion term is modeled in terms of components of the Reynolds stress tensor, not the turbulence kinetic energy, and the coefficient of the "destruction of dissipation" term ($c_{\epsilon 2}$) is not constant, but is sensitive to Reynolds stress anisotropy. Both of these differences can be considered minor relative to the differences that exist among the pressure-strain component of the four models under study. Accordingly, any observed differences among results predicted by these models can be attributed primarily to the manner in which pressure-strain effects have been simulated.

This conclusion can be justified further by referring to the expressions for the convection-minus-diffusion effect in the Reynolds stress transport equations given by Eqs. (3) and (4). In his developing square duct flow predictions, Naimi (1993) coded Eqs. (3) and (4) as alternate representations for the same

effect and found that predicted mean velocity ($U$) and turbulence ($k$ and $\overline{uv}$) distributions based on Eq. (3) were essentially the same as those based in Eq. (4). Some numerical instabilities were encountered, however, when Eq. (3) was applied in rough wall duct flow calculations, as described by Naimi (1993), and therefore Eq. (4) was adopted in generating the DS model results presented in this paper. These results are expected to be the same as those which would have been generated if Eq. (3) had been used in place of Eq. (4).

## Test Cases

In order to investigate the predictive capabilities of the four selected turbulence models, two test cases were examined: (1) Hinze's (1973) fully-developed flow in a partially roughened, rectangular duct having a 4.9:1 aspect ratio and Fujita et al.'s (1989) periodic fully-developed flow in a square duct with one roughened wall. The walls of Hinze's 450 mm × 90 mm duct were smooth, except for two roughened portions on one long wall, each 175 mm in length and symmetrically positioned about the duct midplane, with an open (smooth) area between these two portions. The roughness elements in his duct consisted of uniformly distributed plastic grains glued to the wall along the length of the duct, with an average roughness height of 4 mm. The 50 mm × 50 mm square duct of Fujita et al. was roughened by means of a square (1 mm × 1 mm) ribs mounted on one wall normal to the axial flow direction at 10 mm intervals along the length of the duct. Data were taken at $x/D_h = 126$ (Hinze) and $x/D_h = 90$ (Fujita et al.), where $D_h$ is the duct hydraulic diameter, starting with uniform flow at the duct inlet ($x = 0$). The operating Reynolds number based on hydraulic diameter and maximum/bulk velocity was fixed in each study, namely $\mathrm{Re} = 1.5 \times 10^5$ (Hinze) and $\mathrm{Re} = 6.5 \times 10^4$ (Fujita et al.).

Hinze's test case represents the "purer" rough wall flow study, inasmuch as his roughness elements were uniformly distributed over a portion of one duct wall. Fujita et al.'s test case with periodically spaced ribs is also acceptable, however, inasmuch as data taken by the authors show that flow distributions measured in the entire duct cross section directly above a rib are very similar to those measured midway between ribs, except in the near-wall region adjacent to the rib-roughened wall. Accordingly, the data of Fujita et al. can still serve as a basis for comparison with numerical predictions based on assumed streamwise homogeneity of the flow, i.e., predictions which do not account for local flow behavior over individual ribs or at the juncture of these ribs with a bounding wall. The data presented in this paper correspond to that which Fujita et al. measured between adjacent ribs.

## Numerical Method of Solution

For Hinze's test case, comparisons are made with DR and LL model results generated, respectively, by Demuren and Rodi (1984) and Launder and Li (1994). The S model results for Fujita et al.'s test case are taken directly from computed results presented by Sugiyama et al. (1993, 1995). Inasmuch as DR model predictions for this test case are not available in Demuren and Rodi's paper, the DR model was coded in the present study in order to make more comprehensive comparisons with Fujita et al.'s results. The full system of equations which describe the DS model is given by Naimi and Gessner (1995). In order to solve the system of equations corresponding to either the DR or DS model, a revised version of the staggered cell, three-dimensional, streamwise-marching (parabolized in the primary flow direction) SIMPLER algorithm of Patankar (1980) was employed. Second-order backward differencing was utilized in the primary flow ($x$) direction to model the convection terms. In the transverse flow ($y$ and $z$) directions the convection and diffusion terms were modelled by means of Patankar's power law formulation, which is considered to be a nominally first-order accurate scheme. For the present calculations, however, the local cell Peclet number was sufficiently small, so that convection and diffusion gradients in the cross plane could be determined by means of second-order accurate central differencing. This was possible because of the relatively low magnitude of the transverse mean velocity components, $V$ and $W$, which were typically less than 6 percent of the axial bulk mean velocity, $U_b$.

At the duct inlet ($x/D_h = 0$), a low turbulence level, uniform mean flow was prescribed, and $k$ and $\epsilon$ were assigned nominally small values, so that the turbulent eddy viscosity was several times larger than the kinematic viscosity. At this location, the Reynolds shear stress components were set equal to zero and each Reynolds normal stress component was set equal to $(\frac{2}{3})\,k$. For both the DR and DS model simulations described in this paper, the first meshline near a bounding wall was positioned at a $y^+$ location within the interval $30 \le y^+ \le 100$, so that the law-of-the-wall could be applied as a wall function on that line. The velocity component normal to the wall was set equal to zero on the wall and the binormal velocity component on the first meshline was determined by means of the procedure outlined by Tatchell (1975). For the DS model, a zero gradient condition was applied to each Reynolds stress component at the wall, and the dissipation rate on the first meshline was set equal to the turbulence kinetic energy production rate on that line. In applying the DR model, the wall functions for $U$, $k$, and $\epsilon$ prescribed by Demuren and Rodi (1984) for smooth and roughened walls were utilized.

Starting with the above initial conditions, the system of equations was solved for each test case over the whole development length of the duct. The initial forward step size was typically $0.0025\,D_h$, but was progressively increased to $0.0125\,D_h$. The convergence criteria included a residual check on all of the flow properties and global (duct cross section) mass flow conservation. The local and global mass flow criteria were $1 \times 10^{-10}$ and $1 \times 10^{-15}$, respectively, when normalized by the bulk mass flow rate. For Hinze's duct, a 40 × 100 clustered grid in the cross plane (duct half section) was specified, whereas a 20 × 40 clustered grid in the duct half section was used to predict the flow investigated by Fujita et al. Computations performed with finer grids in the cross plane indicated that essentially grid independent solutions had been reached for the two test cases using the above-specified grids. DR and DS model computations were performed on an HP715 workstation. Approximately 3.5 hours were required to complete the DS model computations for Fujita et al.'s test case, whereas roughly 25 hours of CPU time were required to compute Hinze's test case. Similar computational times were observed when the DR model was employed.

In applying the DS model to predict Hinze's flow, the B constant in the log-law wall function for the roughened wall was prescribed as −8.0, rather than −4.6, as specified by Demuren and Rodi, in order to obtain improved agreement between predicted and measured secondary flow levels. When the DR and DS models were applied to predict Fujita et al.'s flow, B was specified as −7.3 for the rib-roughened wall on the basis of experimental results obtained by Hirota et al. (1994). This value ($B = -7.3$) differs slightly from the rough wall value prescribed by Sugiyama et al. (1993a, 1995) in their predictions for this test case ($B = -8.4$), which is based on the earlier measurements of Fujita et al. (1988). In order to examine the effect of this difference on the results, DS model computations were also performed for Fujita et al.'s flow with $B$ specified as −8.4. This change in $B$ from −7.3 to −8.4 caused a slight increase in the secondary flow (less than 5 percent), and a shift in axial mean velocity and turbulence kinetic energy contour positions near the rough wall by an amount less than 1.0% of the half duct width.

## Results and Discussion

**Hinze's Flow.** The evolution of the secondary flow field in Hinze's duct predicted by the DS model is shown in Fig. 1 as a function of dimensionless streamwise distance along the duct ($x/D_h$). In the inlet region at $x/D_h = 15$ (Fig. 1$a$), it can be seen that five secondary flow cells have been generated in the half duct cross section with two cells of unequal strength roughly centered about each corner bisector and an additional cell centered near the step change in wall roughness that exists at $z/b = 0.78$. Downstream of $x/D_h = 15$, the clockwise vortex near the lower left corner (at $y = z = 0$) and the clockwise vortex near the upper left corner (at $y/(2a) = 1$, $z = 0$) grow in lateral extent until they combine to form a single clockwise vortex near the left duct wall which maintains its integrity between $x/D_h = 30$ and $x/D_h = 126$. Beyond $x/D_h = 15$, the relatively weak counter-clockwise vortex near the lower left corner and the counter-clockwise vortex above the step change in roughness also grow in lateral extent until they combine to form a single counter-clockwise vortex that exists at the fully-developed state ($x/D_h = 126$). The counter-clockwise "pocket" vortex originally formed near the upper left corner of the duct continues to exist over the entire flow development length, so that three discrete secondary flow cells exist in the final, fully-developed state. These results are in complete accord with the three cell structure predicted by the LL model, as demonstrated by Launder and Li (1994).

The distorting influence of the secondary flow on the primary flow at the fully-developed state is shown in Fig. 2, where comparisons are made between Hinze's measured (dashed-line) velocity distributions and predicted (solid-line) distributions based on the DR, LL, and DS models. In reference to DR model predictions, it can be seen that the distortion of isovelocity contours near the lower wall between $z/b = 0.8$ and $z/b = 1.0$ is underestimated by this model (Fig. 2($a$)), which implies that secondary flow levels predicted by the DR model are too low. In contrast, Fig. 2($b$) shows that distortion of isovelocity contours in this region is overpredicted by the LL model, which implies that secondary flow levels predicted by this model are too high. A comparison of Figs. 2($a$), 2($b$), and 2($c$) shows that the DS model yields predicted contours that agree best with Hinze's data throughout the duct cross section. These results are compatible with predicted and measured secondary flow distributions on the duct midplane ($z/b = 1.0$), as shown in Fig. 3, which indicates that the DS model, in comparison to the DR and LL models, yields best overall agreement between predicted and measured distributions. In this context it should be noted that the negative secondary flow velocities measured by Hinze near the upper wall ($y/(2a) = 1.0$) are questionable, inasmuch as these negative velocities correspond to an outwardly directed secondary flow away from the upper wall which should distort isovelocity ($U$) contours in this region. Inasmuch as no such distortion is evident in Fig. 2, the negative values in Fig. 3 are probably incorrect, so that lack of agreement between model predictions and data near the upper wall in Fig. 3 is not indicative of deficiencies in model performance. This same conclusion was reached by Launder and Li (1994), who attributed the negative secondary flow values measured by Hinze (1973) near the upper wall to possible probe interference effects. Inasmuch as Hinze does not provide details of his measurement technique, other than mentioning that hot wires were used, this statement may well be true, noting that Gessner (1964) had to correct secondary flow velocities measured by means of a single wire rotation technique for wall interference effects.

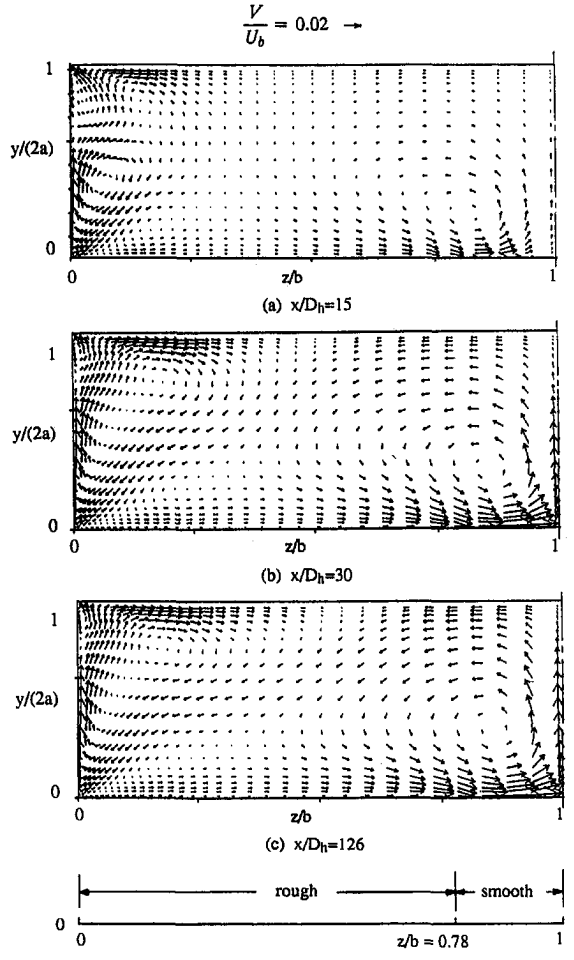


**Fig. 1 DS model predictions of secondary flow evolution in Hinze's duct**

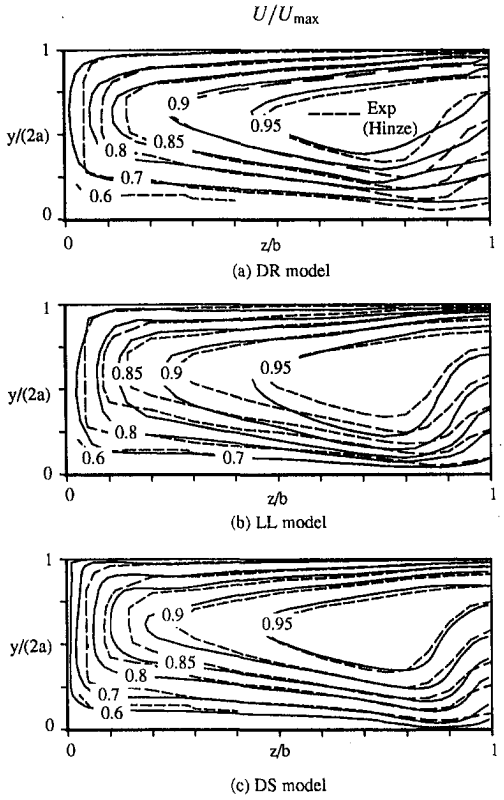


**Fig. 2 Primary isovelocity contours for Hinze's flow**

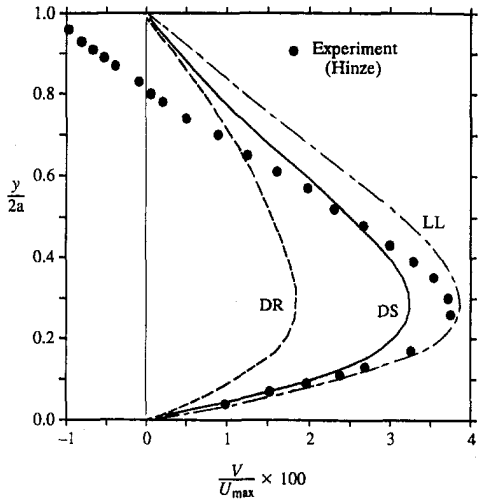


Fig. 3 Secondary flow velocity profiles on the duct midplane $z/b = 1$ for Hinze's flow

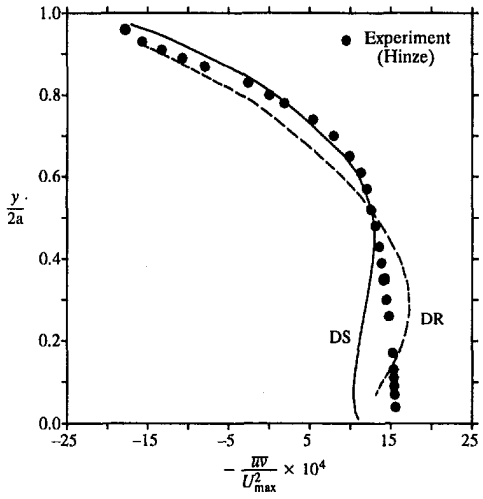


Fig. 4 Turbulence shear stress profiles on the duct midplane $z/b = 1$ for Hinze's flow

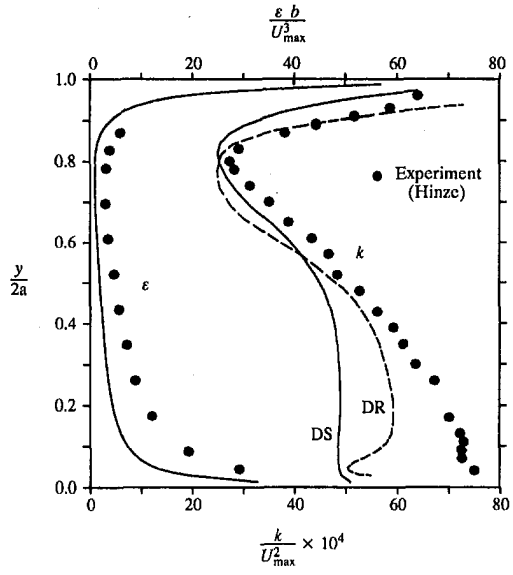


Fig. 5 Turbulence kinetic energy and dissipation rate profiles on the duct midplane $z/b = 1$ for Hinze's flow

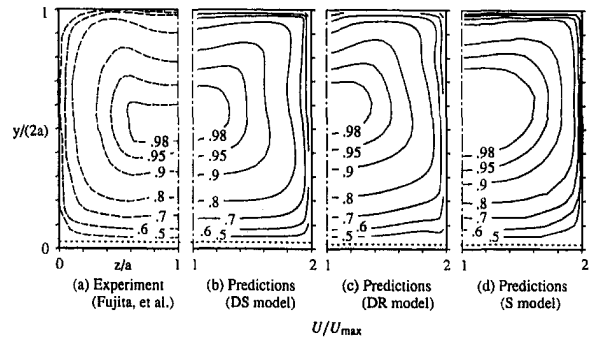


Fig. 6 Primary isovelocity contours for Fujita et al.'s flow

Figures 4 and 5 compare DR and DS model predictions of turbulence-related variables on the duct midplane ($z/b = 1.0$) with Hinze's data. Both models exhibit some relative strengths, with the DS model predicting $\overline{uv}$ profile behavior that is generally in better agreement with its experimental counterpart (Fig. 4), whereas the DR model yields better agreement between predicted and measured $k$ profiles (Fig. 5). This figure also shows that DS model predictions of $\epsilon$ are in qualitative agreement with Hinze's data. Predicted $\epsilon$ levels are approximately half of that measured by Hinze and probably lie within the uncertainty level of this difficult-to-measure variable.

**Fujita et al.'s Flow.** Isovelocity (dashed-line) contours measured by Fujita et al. (1989) in the half cross section of a square duct with periodically spaced ribs on one (lower) wall are shown in Fig. 6($a$). Predictions based on the DS, DR, and S models are shown as mirror-image contours in Figs. 6($b$), 6($c$), and 6($d$), respectively. From this figure it can be seen that $S$ model predictions in the central region of the duct yield primary flow velocity values that are too high compared to the experimental results, and that the level of outward distortion of experimental contours away from the upper wall in the duct midplane region is underestimated by this model. In contrast, both the DR and DS model predictions are in relatively good agreement with the experimental contours, except in a small region near the lower corner, where contours predicted by the DR model have inflection points indicative of a possible secondary flow cell in this region (refer to the region near $z/a = 2.0$ in Fig. 6($c$). This supposition is confirmed by the secondary flow patterns in Fig. 7, which shows that the DR model predicts a secondary flow cell near the corner formed by the juncture of the smooth and rough walls (at $y = 0$, $z/a = 2.0$) that is not present in the experimental flow (compare Figs. 7$a$ and 7$c$). Indeed, the data in Fig. 7($a$) show that only one dominant secondary flow cell is present in the experimental flow, although the pattern in the upper left corner appears to indicate that

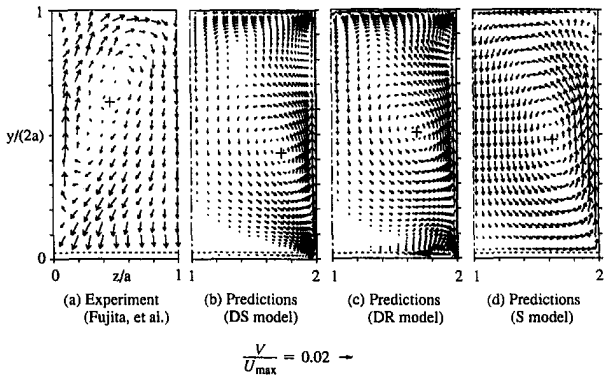


Fig. 7 Secondary flow velocity vectors for Fujita et al.'s flow

another, much smaller, secondary flow cell may also exist. Predictions by the DR, S, and DS models in that order predict the presence of a moderate, weak, and very weak secondary flow cell in the upper right (mirror image) corner which may be a real effect. The direction of experimental secondary flow near the lower corner at $y = z = 0$ in Fig. 7(*a*) is predominantly inward toward the corner, an effect simulated only by the DS model. All three models predict the dominant secondary flow cell observed in the experimental flow, but not the position of its center, with the DS model providing the best overall simulation.

Predicted wall shear stress distributions are compared with distributions measured in the duct cross section midway between adjacent ribs in Fig. 8. The upper set of distributions apply along the smooth wall normal to the rib-roughened wall, whereas the lower set applies to the smooth wall opposite to this wall. In reference to the upper figure, it can be seen that the DR and DS models both initially overpredict and then underpredict wall shear stress levels measured by Fujita et al. (1989). Predicted distributions based on these models also exhibit uncharacteristic "dips" that are not present in the experimental distribution. In contrast, predictions based on the S model are in relatively good agreement with experiment along the entire wall, except for slightly lower predicted values beyond $y/(2a) = 0.4$. In reference to the lower figure, S model predictions now show the poorest agreement with experiment of the three models tested. The S model distribution has a noncharacteristic peak near $z/a = 0.1$ and underestimates wall shear stress levels in the mid-region of the wall. The DS model also underestimates wall shear stress levels in this region, whereas the DR model yields the best overall agreement between predictions and experiment. None of the models performs consistently

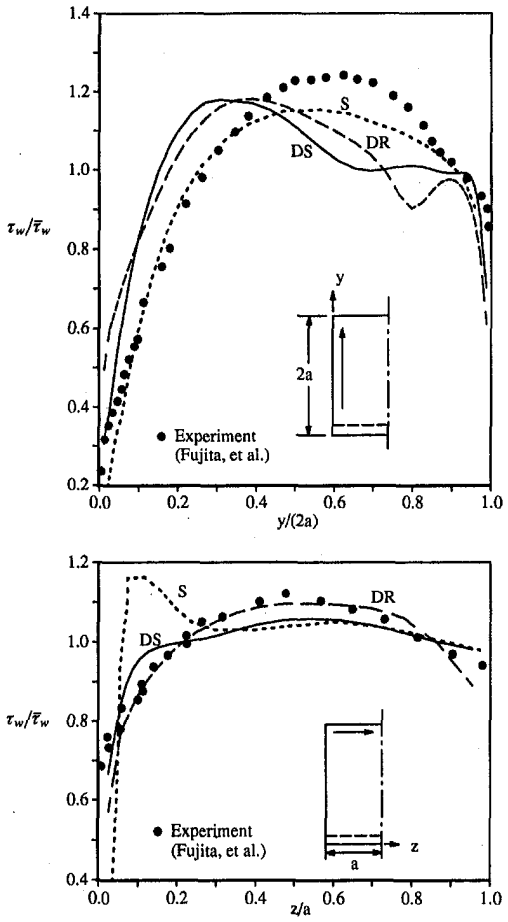


Fig. 8 Peripheral wall shear stress distributions for Fujita et al.'s flow

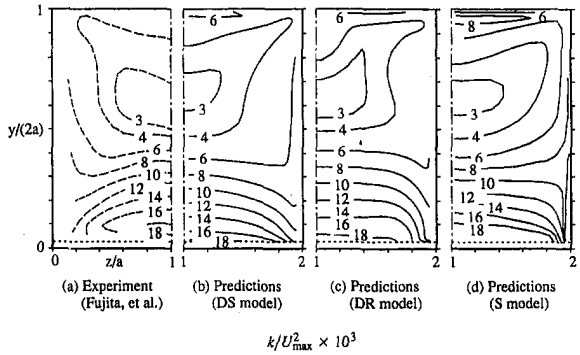


Fig. 9 Turbulence kinetic energy contours for Fujita et al.'s flow

well along both walls, however, so no definitive conclusions can be drawn regarding which model is the best performer relative to local wall shear stress predictions. Both the DR and DS models lead to peripherally averaged (global) wall shear stress values normalized by the bulk dynamic pressure, 0.030 and 0.029, respectively, which underpredict the resistance coefficient measured by Fujita et al. (0.035) at the same operating Reynolds number ($6.5 \times 10^4$) by approximately 15 percent. This discrepancy is due primarily to an underprediction of the actual total pressure loss that occurs along a rib-roughened wall, inasmuch as total pressure losses incurred by rib-induced flow separation are not simulated by either model.

Experimental contours of the turbulence kinetic energy are compared with contours predicted by the DR, DS, and S models in Fig. 9. The distortion of experimental contours near the upper wall is simulated relatively well by the DR and DS models; the S model does not capture the observed variations as effectively. It can also be seen that the DR and S models lead to relatively high gradients (as demonstrated by contour convergence) near the lower corner formed by the juncture of the smooth and rough walls at $y = 0$, $z/a = 2$. This effect is even more evident if one compares experimentally measured Reynolds stress anisotropy contours with predicted contours based on the three models. Figure 10 shows that relatively high gradients of $\overline{w^2} - \overline{v^2}$ exist near the lower corner at $y = 0$, $z/a = 2$ in contours predicted by the DR and S models that are not present in the experimental flow or in contours based on the DS model. The high concentration of gradients of $\overline{w^2} - \overline{v^2}$ predicted by the DR model near the lower corner correlates well with the position of the fictitious vortex predicted by this model (compare Figs. 7*c* and 10*c*). Inasmuch as cross-planar gradients of $\overline{w^2} - \overline{v^2}$ and $\overline{vw}$ act as a source or sink effect relative to the generation or destruction of axial vorticity in the flow, it would appear that inaccurate prediction of $\overline{w^2} - \overline{v^2}$ and $\overline{vw}$ by the DR model is responsible for the fictitious corner vortex predicted by this

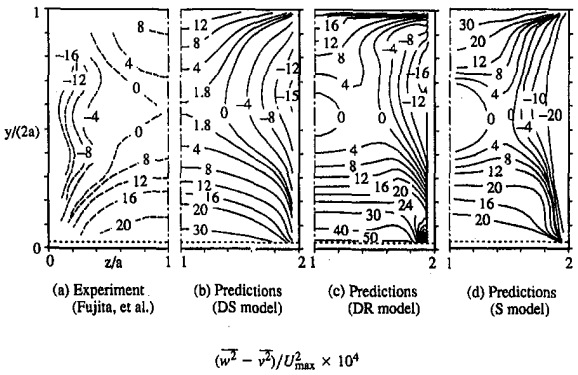


Fig. 10 Reynolds stress anisotropy contours for Fujita et al.'s flow

model. In order to explore this point further, consider the DR model expressions for $\overline{w^2} - \overline{v^2}$ and $\overline{vw}$, which, if secondary flow effects are neglected as a first approximation, can be written, respectively, as:

$$\overline{w^2} - \overline{v^2} = \frac{2\beta c_\mu}{c_1}\frac{k^3}{\epsilon^2}\left[\left(\frac{\partial U}{\partial y}\right)^2 - \left(\frac{\partial U}{\partial z}\right)^2\right] \tag{14}$$

$$\overline{vw} = -\frac{2\beta c_\mu}{c_1}\frac{k^3}{\epsilon^2}\left(\frac{\partial U}{\partial y}\right)\left(\frac{\partial U}{\partial z}\right) \tag{15}$$

where $c_1$ and $\beta$ are the same coefficients as those which appear in Eqs. (6) and (8), respectively. In the DR model $c_\mu$ is specified as 0.09 throughout the flowfield, but as Cazalbou and Bradshaw (1993) have demonstrated, $c_\mu$ actually varies continuously across the width of typical two-dimensional channel and flat plate boundary layer flows. Their high Reynolds number estimates of $c_\mu$ for the near-wall (equilibrium) region vary between 0.055 and 0.065. If this range of values is also applicable to the near-wall region of streamwise corner flows, then specifying $c_\mu$ as 0.09 in Eqs. (14) and (15) can lead to an axial vorticity source effect that is too high in the corner region and, in turn, the generation of a spurious secondary flow cell. This possibility was examined by calculating the field variation of $c_\mu$ from DS model results for Fujita et al.'s test case from the following expression:

$$c_\mu = \frac{\epsilon}{k^2}\frac{(\overline{uv}^2 + \overline{uw}^2)^{1/2}}{[(\partial U/\partial y)^2 + (\partial U/\partial z)^2]^{1/2}} \tag{16}$$

which is an extended version of the two-dimensional expression for $c_\mu$ analyzed by Cazalbou and Bradshaw (1993). The behavior of the ratio of the production rate of turbulence kinetic energy from the total mean flow to its dissipation rate, $\xi$, was also evaluated from DS model results, inasmuch as the expressions for $\overline{w^2} - \overline{v^2}$ and $\overline{vw}$ given by Eqs. (14) and (15) are also based on the assumption that $\xi = 1$ everywhere in the flow. The calculated field variations of $\xi$ and $c_\mu$ are shown in Fig. 11. From the figure it can be seen that $\xi = 1$ is a reasonable approximation throughout the flow, except in the central region of the duct and near the corner bisector of the upper right corner, which is formed by the juncture of two adjacent smooth walls. It can also be seen, however, that $c_\mu$ is much less than 0.09 in the near-wall and near-corner regions of the duct, noting that $c_\mu \cong 0.05$ in these regions. In reference to Eq. (14), this behavior implies that specifying $c_\mu$ as 0.09 should lead to elevated $\overline{w^2} - \overline{v^2}$ contour levels, behavior that is clearly evident in Fig. 10, where DR model contour values for $\overline{w^2} - \overline{v^2}$ near the smooth wall at $y/(2a) = 1$ and near the rough wall at $y = 0$ exceed DS model contour values, which are in relatively good agreement with experimentally observed behavior.

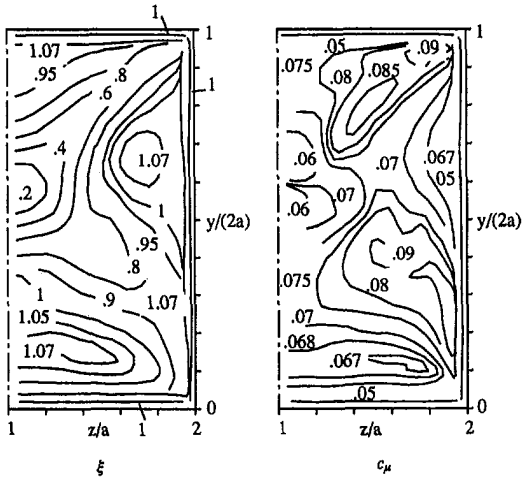


**Fig. 11 DS model predictions of the behavior of $\xi$ and $c_\mu$ for Fujita et al.'s flow**

On the basis of these observations, it appears that the high concentration of gradients of $\overline{w^2} - \overline{v^2}$ predicted by the DR model in the vicinity of the smooth-rough wall juncture at $y = 0$, $z/a = 2$ (Fig. 10(*c*)) and the corresponding spurious secondary flow cell (Fig. 7(*c*)) are a direct result of specifying an elevated value for $c_\mu$ (0.09) in this region. More representative behavior is predicted by the DS model, which does not require a priori specification of $c_\mu$, noting that in the vicinity of the smooth-rough wall juncture, experimentally measured primary flow velocity, secondary flow velocity, turbulence kinetic energy, and Reynolds stress anisotropy distributions are all predicted with relatively good accuracy (compare Fujita et al.'s results with DS model predictions in Figs. 6, 7, 9, and 10, respectively.)

## Concluding Remarks

The predictive capabilities of four transport-type turbulence models have been examined as they apply to the prediction of fully-developed turbulent flow in a rectangular duct with mixed wall roughness conditions. The test cases included one case for which a step change in uniform wall roughness existed on one wall (Hinze's flow) and another case for which equally spaced ribs were positioned on one wall normal to the axial flow direction (Fujita et al.'s flow). The primary criterion for evaluating model performance was accurate prediction of the secondary flow field and its distorting influence on other flow variables. For both test cases, the comparisons made in this paper show that the DS model yields the best performance with respect to predicting primary and secondary flow velocity distributions on, and near, the duct midplane for Hinze's flow and with respect to predicting local flow behavior in the entire duct cross section for Fujita et al.'s flow, including the corner region near a smooth-rough wall juncture. Extension of this model to predict local flow behavior in the immediate vicinity of individual ribs in a rib-roughened duct and in the immediate vicinity of a rib-endwall juncture obviates the use of the law-of-the-wall as a valid near-wall boundary condition, which is the only wall function employed in the DS model, and the use of Buleev's length scale model to simulate wall damping effects on pressure-strain behavior. Replacement of these model components in order to simulate local flow behavior over individual ribs and near a rib-endwall juncture more accurately is a formidable task, even if wall topography parameters are eliminated from the pressure-strain model, as proposed by Launder and Li (1993, 1994). From a modeling point of view, large-eddy simulation (LES) techniques may offer the only viable alternative for modeling the flow accurately over these geometric configurations, recognizing that the actual flow over rib-roughened walls is characterized by time-dependent phenomena that can only be captured by the application of direct numerical simulation or LES techniques.

## References


Braun, H., and Neumann, H., 1996, "Experimental and Numerical Investigation of Turbulent Heat Transfer in a Channel with Periodically Arranged Rib Roughness Elements," *Engineering Turbulence Modelling and Experiments 3*, W. Rodi and G. Bergeles, eds., Elsevier, Amsterdam, pp. 643–654.

Buleev, N. I., 1963, "Theoretical Model of the Mechanism of Turbulent Exchange in Fluid Flows," *AERE Translation 957*, Atomic Energy Research Establishment, Harwell, England.

Cazalbou, J. B., and Bradshaw, P., 1993, "Turbulent Transport in Wall-Bounded Flows. Evaluation of Model Coefficients Using Direct Numerical Simulation," *Physics of Fluids*, Vol. 5, No. 12, pp. 3233–3239.

Demuren, A. O., and Rodi, W., 1984, "Calculation of Turbulence-Driven Secondary Motion in Non-Circular Ducts," *Journal of Fluid Mechanics*, Vol. 140, pp. 189–222.

Fujita, H., Yokosawa, H., Hirota, M., and Nagata, C., 1988, "Fully Developed Turbulent Flow and Heat Transfer in a Square Duct with Two Roughened Facing Walls," *Chemical Engineering Communications,* Vol. 74, pp. 95–110.

Fujita, H., Yokosawa, H., and Hirota, M., 1989, "Secondary Flow of the Second Kind in Rectangular Ducts with One Rough Wall," *Experimental Thermal and Fluid Science,* Vol. 2, pp. 72–80.

Fujita, H., Hirota, M., and Yokosawa, H., 1990a, "Experiments on Turbulent Flow in a Square Duct with a Rough Wall," *Memoirs of the Faculty of Engineering,* Nagoya University, Vol. 41, No. 2, pp. 280–294.

Fujita, H., Hirota, M., and Yokosawa, H., Hasegawa, M., and Gotoh, I., 1990b, "Fully Developed Turbulent Flows through Rectangular Ducts with One Roughened Wall," *JSME International Journal,* Vol. 33, No. 4, pp. 692–701.

Gessner, F. B., 1964, "Turbulence and Mean Flow Characteristics of Fully-Developed Flow in Rectangular Channels," PhD thesis, School of Mechanical Engineering, Purdue University.

Gessner, F. B., and Eppich, H. M., 1981, "A Near-Wall Pressure-Strain Model for Turbulent Corner Flows," *Proceedings of the Third Symposium on Turbulent Shear Flows,* University of California-Davis, Sept. 9–11, 1981, pp. 2.25–2.32.

Han, J. C., 1988, "Heat Transfer and Friction Characteristics in Rectangular Channels with Rib Turbulators," ASME *Journal of Heat Transfer,* Vol. 110, No. 2, pp. 321–328.

Hinze, J. O., 1973, "Experimental Investigation on Secondary Currents in the Turbulent Flow Through a Straight Conduit," *Applied Scientific Research,* Vol. 28, pp. 453–465.

Hirota, M., Fujita, H., Yokosawa, H., and Tanaka, Y., 1993, "Experimental Study of Fully Developed Turbulent Flow in a Rectangular Duct with Two Roughened Facing Walls," *Proceedings of the Ninth Symposium on Turbulent Shear Flows,* pp. 307.1–307.4.

Hirota, M., Fujita, H., Yokosawa, H., and Tanaka, Y., 1994a, "Turbulent Flow in a Rectangular Duct with Roughened Short-Side Walls," *Proceedings of the International Symposium on Turbulence, Heat and Mass Transfer,* Lisbon, pp. II.1.1–II.1.4.

Hirota, M., Fujita, H., and Yokosawa, H., 1994b, "Experimental Study on Convective Heat Transfer for Turbulent Flow in a Square Duct with a Ribbed Rough Wall (Characteristics of Mean Temperature Field)," ASME *Journal of Heat Transfer,* Vol. 116, No. 2, pp. 332–340.

Hirota, M., Fujita, H., Yokosawa, H., and Tanaka, Y., 1995, "Measurement of Fully Developed Turbulent Flow through Rectangular Duct with Roughened Short-Side Walls," *Transactions of JSME,* Vol. 61, No. 582, pp. 420–427 (in Japanese).

Hirota, M., Fujita, H., Yokosawa, H., and Tanaka, Y., 1996, "Characteristics of Turbulent Flow in a Rectangular Duct with Rib-Roughened Long-Side Walls," accepted for presentation at the *Ninth International Symposium on Transport Phenomena (ISTP-9) in Thermal Engineering,* Singapore, June 25–28, 1996.

Hong, Y.-J., and Hsieh, S.-S., 1993, "Heat Transfer and Friction Factor Measurements in Ducts With Staggered and In-Line Ribs," ASME *Journal of Heat Transfer,* Vol. 115, No. 1, pp. 58–65.

Hsieh, S.-S., and Hong, Y.-J., 1989, "Separating Flow Over Repeated Surface-Mounted Ribs in a Square Duct," *AIAA Journal,* Vol. 27, No. 6, pp. 770–776.

Hsieh, S.-S., and Hong, S.-S., 1995, "Heat Transfer Coefficients in an Orthogonally Rotating Duct with Turbulators," ASME *Journal of Heat Transfer,* Vol. 117, No. 1, pp. 69–78.

Hwang, J.-J., and Liou, T.-M., 1994, "Augmented Heat Transfer in a Rectangular Channel with Permeable Ribs Mounted on the Wall," ASME *Journal of Heat Transfer,* Vol. 116, No. 4, pp. 912–920.

Hwang, J.-J., and Liou, T.-M., 1995, "Heat Transfer and Friction in a Low-Aspect-Ratio Rectangular Channel with Staggered Perforated Ribs on Two Opposite Walls," ASME *Journal of Heat Transfer,* Vol. 117, No. 4, pp. 843–850.

Iacovides, H., Jackson, D. C., Kelemenis, G., Launder, B. E., and Yuan, Y.-M., 1996, "LDA Study of the Flow Development Through an Orthogonally Rotating U-Bend of Strong Curvature and Rib-Roughened Walls," *Engineering Turbulence Modelling and Experiments 3,* W. Rodi and G. Bergeles, eds., Elsevier, Amsterdam, pp. 561–570.

Launder, B. E., Reece, G. J., and Rodi, W., 1975, "Progress in the Development of a Reynolds-Stress Turbulence Closure," *Journal of Fluid Mechanics,* Vol. 68, Part 3, pp. 537–566.

Launder, B. E., and Li, S.-P., 1993, "On the Prediction of Flow Over Riblets via 2nd-Moment Closure," *Near-Wall Turbulent Flows,* (R. M. C. So, C. G. Speziale, and B. E. Launder eds.,), Elsevier Science Publishers, New York, pp. 739–748.

Launder, B. E., and Li, S.-P., 1994, "On the Elimination of Wall-Topography Parameters from Second-Moment Closure," *Physics of Fluids,* Vol. 6, No. 2, pp. 999–1006.

Liou, T.-M., and Hwang, J.-J., 1992, "Turbulent Heat Transfer Augmentation and Friction in Periodic Fully Developed Channel Flows," ASME *Journal of Heat Transfer,* Vol. 114, No. 1, pp. 56–64.

Liou, T.-M., and Hwang, J.-J., 1993, "Effect of Ridge Shapes on Turbulent Heat Transfer and Friction in a Rectangular Channel," *International Journal of Heat and Mass Transfer,* Vol. 36, No. 4, pp. 931–940.

Liou, T.-M., Wu, Y.-Y., and Chang, Y., 1993a, "LDV Measurements of Periodic Fully Developed Main and Secondary Flows in a Channel with Rib-Disturbed Walls," ASME JOURNAL OF FLUIDS ENGINEERING, Vol. 115, No. 1, pp. 109–114.

Liou, T.-M., Hwang, J.-J., and Chen, S.-H., 1993b, "Simulation and Measurement of Enhanced Turbulent Heat Transfer in a Channel with Periodic Ribs on One Principal Wall," *International Journal of Heat and Mass Transfer,* Vol. 36, No. 2, pp. 507–517.

Liou, T.-M., Wang, W.-B., and Chang, Y.-J., 1995, "Holographic Interferometry Study of Spatially Periodic Heat Transfer in a Channel with Ribs Detached From One Wall," ASME *Journal of Heat Transfer,* Vol. 117, No. 1, pp. 32–39.

Lockett, J. F., and Collins, M. W., 1990, "Holographic Interferometry Applied to Rib-Roughness Heat Transfer in Turbulent Flow," *International Journal of Heat and Mass Transfer,* Vol. 33, No. 11, pp. 2439–2449.

Myong, H. K., and Kobayashi, T., 1991, "Prediction of Three-Dimensional Turbulent Flow in a Square Duct With an Anisotropic Low-Reynolds-Number $k$-$\epsilon$ Model," ASME JOURNAL OF FLUIDS ENGINEERING, Vol. 113, No. 4, pp. 608–615.

Naimi, M., 1993, "Numerical Simulation of Turbulence-Induced Secondary Flow in Rectangular Ducts," PhD Thesis, Department of Mechanical Engineering, University of Washington.

Naimi, M., and Gessner, F. B., 1995, "A Calculation Method for Developing Turbulent Flow in Rectangular Ducts of Arbitrary Aspect Ratio," ASME JOURNAL OF FLUIDS ENGINEERING, Vol. 117, No. 6, pp. 249–258.

Rodi, W., 1976, "A New Algebraic Relation for Calculating the Reynolds Stresses," *Zeitschrift für Angewandte Mathematik und Mechanik,* Vol. 56, pp. T219–T221.

Rotta, J. C., 1962, "Statistische Theorie Nichthomogener Turbulenz," *Zeitschrift für Physik,* Vol. 129, pp. 547–572.

Sugiyama, H., Akiyama, M., and Serizawa, T., 1991, "Numerical Analysis of Developing Flow in a Square Duct Using Reynolds Stress Model," *Proceedings of the ASME/JSME Thermal Engineering Joint Conference,* Vol. 3, pp. 159–165.

Sugiyama, H., Akiyama, M., Matsumoto, M., Hirata, M., and Ninomiya, N., 1993a, "Numerical Analysis on Fully Developed Turbulent Flow in a Square Duct with a Rough Wall," *Transactions of JSME,* Vol. 59, No. 561, pp. 1510–1517 (in Japanese).

Sugiyama, H., Akiyama, M., Matsumoto, M., Hirata, M., and Ninomiya, N., 1993b, "Numerical Analysis of Fully Developed Turbulent Flow in a Square Duct with Two Roughened Facing Walls," *Transactions of JSME,* Vol. 59, No. 561, pp. 1502–1509 (in Japanese).

Sugiyama, H., Akiyama, M., Matsumoto, M., Hirata, M., and Ninomiya, N., 1993c, "Numerical Analysis of Fully Developed Turbulent Flow in a Square Duct with Two Facing Roughened Walls," *Journal of Computational Fluid Dynamics,* Vol. 2, No. 3, pp. 319–338.

Sugiyama, H., Akiyama, M., Matsumoto, M., Furusawa, S., and Hirata, M., 1993d, "Numerical Analysis of Fully Developed Turbulent Flow in a Rectangular Duct with One Roughened Long-Side Wall," *Transactions of JSME,* Vol. 59, No. 568, pp. 3781–3788 (in Japanese).

Sugiyama, H., Akiyama, M., and Matsumoto, M., 1995, "Numerical Analysis of Turbulent Structure and Heat Transfer in a Square Duct With One Rough Wall," *Proceedings of the ASME/JSME Thermal Engineering Joint Conference,* L. S. Fletcher and T. Aihara, eds., Book No. HO933A, ASME Publications, New York.

Tatchell, D. E., 1975, "Convection Processes in Confined, Three-Dimensional Boundary Layers," Ph.D. dissertation, Mechanical Engineering Department, Imperial College, London.

Yokosawa, H., Fujita, H., Hirota, M., and Iwata, S., 1989, "Measurement of Turbulent Flow in a Square Duct with Roughened Walls on Two Opposite Sides," *International Journal of Heat and Fluid Flow,* Vol. 10, No. 2, pp. 125–130.

Youn, B., Yuen, C., and Mills, A. F., 1994, "Friction Factor for Flow in Rectangular Ducts with One-Side Rib Roughened," ASME JOURNAL OF FLUIDS ENGINEERING, Vol. 116, No. 9, pp. 488–493.

Zhang, N., Chiou, J., Fann, S., and Yang, W.-J., 1993, "Local Heat Transfer Distribution in a Rotating Serpentine Rib-Roughened Flow Passage," ASME *Journal of Heat Transfer,* Vol. 115, No. 3, pp. 560–567.

Zhang, Y. M., Gu, W. Z., and Han, J. C., 1994, "Heat Transfer and Friction in Rectangular Channels With Ribbed or Ribbed-Grooved Walls," ASME *Journal of Heat Transfer,* Vol. 116, No. 1, pp. 58–65.

**B. A. Haven**
Major USAF; Assistant Professor,
Department of Aeronautics,
United States Air Force Academy, CO
80840

**M. E. Franke**
Professor,
Air Force Institute of Technology,
Wright-Patterson AFB, OH 45433.
Fellow ASME

# Boundary Layer Excitation by Periodic Heating of a Thin Ribbon[1]

## Introduction

Active boundary layer control has generated much interest due to benefits associated with controlling laminar-to-turbulent transition. Moving the transition region downstream often reduces the overall drag and heat transfer at the surface, whereas moving the transition region forward may be useful in preventing boundary layer separation. A potential means of active boundary layer control is to create selective disturbances to either cancel or reinforce those natural disturbances preceding transition.

The role of two-dimensional periodic disturbances, or Tollmien-Schlichting (T-S) waves, in boundary transition was demonstrated by Schubauer and Skramstad (1947) and Klebanoff et al. (1962). These T-S waves mark the first stage in the progression from laminar to turbulent flow. Many experiments have explored two-dimensional wave superposition techniques as a means of delaying transition by prolonging the time between the initial formation of the T-S waves and the further developments leading to turbulent flow. Wave superposition techniques, such as electromagnetically excited ribbons, surface vibration, periodic heating, and sound, were tried by Thomas (1983), Gilev (1985), Liepmann et al. (1982), Maestrello (1985), and Gedney (1983). More recently, control of random disturbances was studied by Pupator and Saric (1989). Active boundary layer control using a disturbances superposition technique is contingent upon the ability to introduce disturbances of a prescribed nature. To delay transition, the created disturbances must exhibit amplitude and phase characteristics capable of reducing or canceling the boundary layer disturbances, whereas to enhance transition, the disturbances need to excite or increase the instability.

This paper describes a technique for introducing controlled periodic disturbances into a boundary layer with a pulsed-voltage input to a thin nichrome ribbon. The input results in periodic heating and cooling of the ribbon, which causes it to vibrate as a result of thermal expansion and contraction. This is similar to the technique described by Kudelka and Franke (1989). The excited ribbon, when positioned within a boundary layer, introduces periodic disturbances in the boundary layer. This paper further describes the physical parameters governing the ribbon vibration, illustrates the boundary layer response on a flat plate to the ribbon vibration and shows that selective disturbances reinforce boundary layer transition.

## Experimental Apparatus and Procedure

The experiments were structured to determine the physical response of the ribbon to a given input and the subsequent response of the boundary layer to the vibration of the ribbon. The experiments were performed on a flat plate in two wind tunnel facilities. Both wind tunnels are open-circuit, suction-type wind tunnels and provide low-speed, low-turbulence flow throughout the test section. The wind tunnel at the Air Force Institute of Technology (AFIT) has a 0.23 by 0.23 by 0.9 m test section. The maximum flow velocity through the empty test section is 16.5 m/s with a turbulence level $u/U$ of approximately 0.25 percent over the entire velocity range. The L-2A wind tunnel at the von Karman Institute for Fluid Dynamics (VKI), Belgium has an octagonal test section 0.28 m wide and 1.3 m long. The maximum flow velocity through the empty test section is 36 m/s with a turbulence level $u/U$ of 0.5 percent for flow velocities between 6 and 25 m/s.

The two flat plate models used in this study were fabricated from 11-mm-thick, fiber-reinforced phenolic and differed from each other only in the width required to completely span the test section of the respective tunnel in which they were used. Both models were equipped with a 0.07-m-long flap at the trailing edge to adjust the oncoming streamlines to improve the flow at the leading edge.

The ribbons were placed on or near the surface of the model and perpendicular to the flow direction. The ribbon width was either 0.8 or 1.6 mm, the ribbon thickness was 0.13 mm, and the ribbon length varied from 0.2 to 0.3 m. The ribbon resistances varied from 1.2 to 4.4 ohms. Two methods were used to mount the ribbons to the models. The first method was to rest the ribbon on the model surface and wrap the ends around the edges of the model as shown in Fig. 1($a$). Spring tension was applied from beneath the model to take up slack as the ribbon expanded during heating. With this design, the ribbon could be located at any streamwise position along the model surface. The second method is shown in Fig. 1($b$). The streamwise placement of the ribbon was either at 0.1 or 0.13 m from the leading edge, and the distance above the surface was varied from 0 to 8.4 mm. Tension was applied in-line with the ribbon using a spring attached to one end. The spring force was monitored with a strain gage balance attached to the other end of the ribbon.

The general equipment arrangement consisted of two basic systems. The first used a function generator and a power amplifier to supply an electrical square wave pulse input to the ribbon. The input characteristics were measured with a digital voltmeter, frequency counter, and/or oscilloscope. The second monitored the physical motion of the ribbon due to the square wave pulse with a Fotonic (light) sensor and the effects on the boundary layer with a hot wire anemometer. A spectrum analyzer and an oscilloscope were used with the Fotonic sensor and anemometer. Ribbon temperatures were measured with thermocouples welded to the ribbons and temperature indicating paints and labels.

## Results and Discussion

**Ribbon Temperature and Vibration.** The behavior of the nichrome ribbon depended on the pulsed voltage input and the

[1] This paper is declared a work of the U.S. Government and is not subject to copyright protection in the United States. The views expressed herein are those of the authors and do not reflect the official policy or position of the U.S. Air Force, Department of Defense, or the U.S. Government.

Contributed by the Fluids Engineering Division for publication in the JOURNAL OF FLUIDS ENGINEERING. Manuscript received by the Fluids Engineering Division April 22, 1997; revised manuscript received May 14, 1997. Associate Technical Editor: D. P. Telionis.

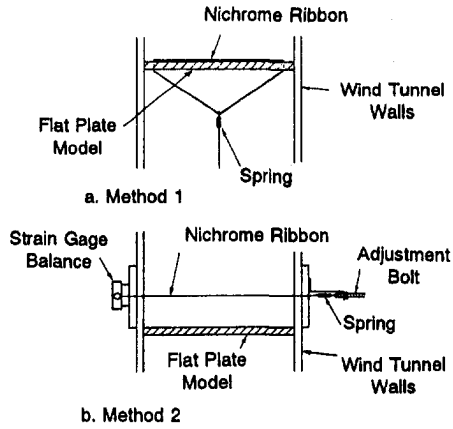


Fig. 1 Ribbon tension system

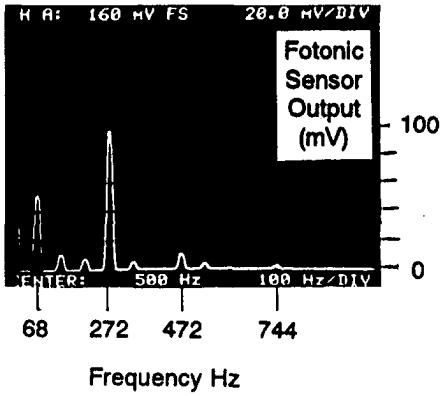


Fig. 3 Frequency spectrum of ribbon vibration. Input: 68 Hz at 5.3 Vrms, No flow.

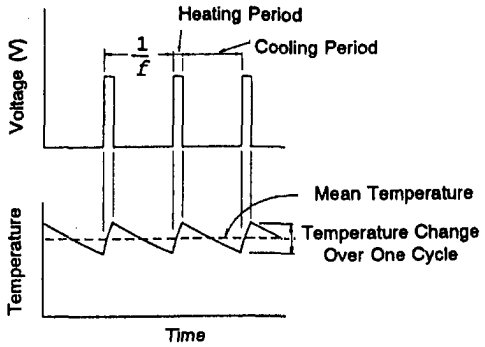


Fig. 2 Voltage input and ribbon response

physical properties of the ribbon material. The ribbon temperature variation resulting from the pulsed voltage input is shown schematically in Fig. 2. Periodic heating and cooling caused the ribbon to expand and contract and to vibrate. Neglecting gravity effects and assuming the vibration takes place in a single plane, the vibration resulting from this input can be qualitatively described as one-dimensional. For a ribbon with fixed ends, the natural frequencies are similar to those for a stretched wire fixed at two ends, which is described by Thompson (1965) as integral multiples of $(n/2l)(T/m)^{1/2}$. Modeling the ribbon as a thermally thin wall with only convective heat transfer at the surface leads to a time constant $\tau$ for the ribbon expressed as $mlc/hA$.

The average ribbon temperature varied from 35–66°C above ambient depending on input voltage, flow conditions, and ribbon location. From calculations based on the time constant, the temperature change of the ribbon over one cycle (heating over $\frac{1}{8}$ of the period and cooling over $\frac{7}{8}$ of the period) was found to be approximately 1°C. Based on a coefficient of thermal expansion of $13.7 \times 10^6$ mm/mm°C and a length of 0.3 m, the change in ribbon length was only about 0.004 mm over one cycle. These results are for a frequency input of approximately 100 Hz. A lower input frequency would give more time for heating and cooling over a cycle, resulting in larger changes in temperature and length.

In the experiments, ribbon vibration frequencies and amplitudes varied depending on the input frequency for fixed input voltage, tension, and freestream conditions. When the ribbon vibrated, the frequencies observed were integral multiples to the input frequency. For a ribbon with a density, width, thickness, and length of 8246 kg/m$^3$, 0.8 mm, 0.13 mm, and 0.3 m, respectively, the calculated fundamental natural frequency of a stretched wire would vary from approximately 40 to 60 Hz for a ribbon tension range from 0.5 to 1.0 N.

The ribbon vibration response to a pulsed voltage at 68 Hz with no flow is shown in Fig. 3. As indicated by the Fotonic sensor output, the ribbon vibration consisted of many harmonics of this input frequency. The input frequency was apparently close to the natural frequency or a multiple thereof. The frequency peaks, with their corresponding signal amplitude in parentheses, were 68 Hz (52 mV), 136 (10.4), 204 (7.3), 272 (96.1), 340 (4.88), 472 (10.7), 540 (3.66), and 744 Hz (2.14 mV).

Changes in the input frequency, input voltage, ribbon tension, and/or freestream velocity resulted in changes to the ribbon vibration characteristics. The highest ribbon amplitudes generally occurred at the higher frequencies, such as 272 Hz and above, even when excited by lower frequency inputs. In all cases, frequency inputs falling between those that produced the higher amplitude responses yielded significantly reduced amplitudes at the higher frequencies.

**Boundary Layer.** The boundary layer response to the vibrating ribbon with a 100 Hz input is shown in Fig. 4. Immediately downstream of the ribbon, the boundary layer oscillations were dominated by a 300 Hz component, trace $(a)$. At a distance 166 mm from the ribbon, the amplitude of the 300 Hz frequency component had diminished and the dominant frequency became 200 Hz, trace $(b)$. Trace $(c)$ shows the predominance of the 100 Hz component 216 mm from the ribbon. The amplitude of this 100 Hz disturbance was much larger than either of the previous disturbances.

## Nomenclature

$A$ = surface area
$c$ = specific heat
$f$ = frequency
$h$ = convective heat transfer coefficient
$l$ = length of ribbon
$m$ = mass per unit length
$\mathrm{Re}_\delta$ = Reynolds number, $U\delta/\nu$
$T$ = tension
$U$ = mean velocity at boundary layer edge
$u$ = velocity fluctuation in $x$-direction
$V$ = voltage
$x$ = distance from plate leading edge
$y$ = distance above plate surface
$\delta$ = displacement thickness
$\nu$ = kinematic viscosity
$\tau$ = time constant, $mlc/hA$

**Subscript**

$r$ = ribbon

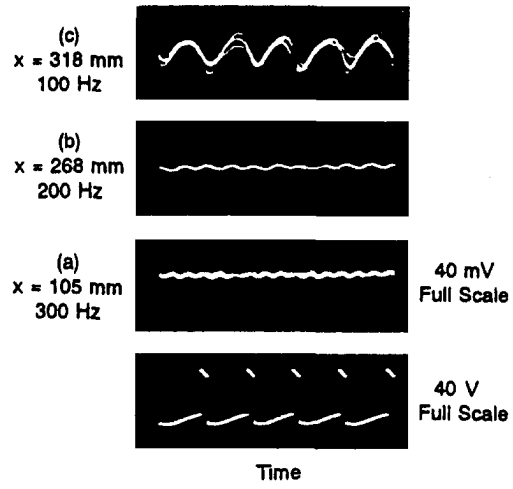


**Fig. 4 Boundary layer response at three locations downstream of vibrating ribbon. Input: 100 Hz at 5.97 Vrms, $x_r$ = 102 mm, $U$ = 10 m/s.**

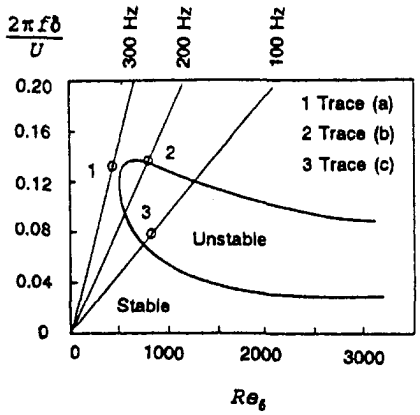


**Fig. 5 Curve of neutral stability for Fig. 4**

The evolution of the propagating disturbances in Fig. 4 is shown on the stability diagram in Fig. 5 (Schlichting, 1979). The three lines emerging from the origin represent lines of constant $2\pi f\nu/U^2$, which correspond to constant frequency lines for the 100, 200, and 300 Hz components. The 300 Hz line lies entirely in the stable region. This explains the damping of this component. The 200 Hz line passes through the instability region and reaches maximum amplification near $Re_\delta = 730$. Beyond this point, the 200 Hz disturbance is damped and the 100 Hz disturbance enters the instability region, which explains the growth in the 100 Hz component.

Similar stability results occurred with an 87 Hz input signal for which the amplitude of the 87 Hz signal and five higher harmonic frequencies all initially decreased with distance along the plate boundary layer. Only the 87 Hz signal, after decreasing significantly in amplitude, started to increase again beyond 200 mm from the ribbon. This behavior again is consistent with the damping and amplification of the disturbances predicted by Fig. 5.

In similar experiments, it was found that a vibrating ribbon placed entirely outside the boundary layer induced periodic velocity disturbances directly behind the ribbon but not within the boundary layer. Also, when the ribbon was glued to the surface, no effects on turbulence intensity were detected within the boundary layer as a result of strictly periodic heating and cooling.

The influence of the vibration amplitude on boundary layer transition is illustrated in Fig. 6. Trace ($a$) shows a small amplitude disturbance created by the 926 Hz, 3.7 Vrms input to the ribbon. At the downstream location, $x$ = 457 mm, the boundary layer remained laminar, having a turbulence intensity of 1.6 percent, trace ($b$). Trace ($c$) shows that a much larger disturbance is created as the result of an 819 Hz, 3.7 Vrms input to the ribbon. The influence of this larger disturbances is seen downstream. At $x$ = 457 mm, trace ($d$), the boundary layer shows more than an 8-fold increase in the turbulence intensity over that of trace ($b$) to 13.8 percent.

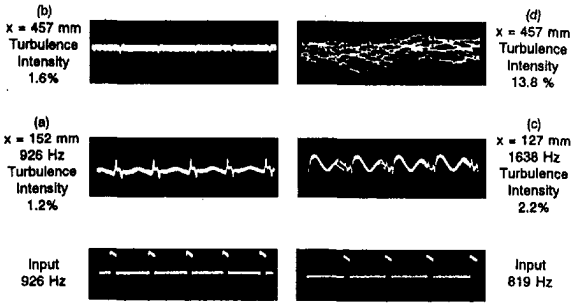


**Fig. 6 Influence of ribbon disturbance on turbulence intensity at $x$ = 457 mm. Input: 3.7 Vrms, $x_r$ = 127 mm, $y_r$ = 2.0 mm, $U$ = 6.3 m/s.**

## Conclusions

A thin nichrome ribbon can be made to vibrate with significant amplitudes by pulsing it with a periodic voltage at particular frequencies. The frequency components of the ribbon vibration are harmonics of the input forcing frequency. The disturbances created by the vibrating ribbon due to periodic heating and cooling are transmitted to the boundary layer of the air flowing over the ribbon. The boundary layer oscillations created by the vibrating ribbon have the same frequency composition as the ribbon vibration. The amplitudes of the individual frequency components change as the boundary layer develops. The observed downstream amplification and damping of selected frequency components agree with the predictions of linear stability theory. Boundary layer transition can be enhanced for particular amplitude and frequency voltage input to the ribbon. Further studies should be considered for the use of this means of boundary layer control.

## References

Gedney, C. J., 1983, "The Cancellation of a Sound-Excited Tollmien-Schlichting Wave with Plate Vibration," *Physics of Fluids*, Vol. 26, pp. 1158–1160.

Giliv, V. M., 1985, "Tollmien-Schlichting Wave Excitation on the Vibrator and Laminar-Turbulent Transition Control," 1984 IUTAM Symposium on Laminar-Turbulent Transition, Novosibirsk, Springer-Verlag.

Klebanoff, P. S., Tidstrom, K. D. and Sargent, L. M., 1962, "The Three-Dimensional Nature of Boundary Layer Instability," *Journal of Fluid Mechanics*, Vol. 12, 1, pp. 1–32.

Kudelka, L. and Franke, M. E., 1989, "Boundary Layer Disturbances By Periodic Heating of a Thin Ribbon," Paper AIAA-89-0651, AIAA 27th Aerospace Sciences Meeting, Reno, NV, American Institute of Aeronautics and Astronautics.

Liepmann, H. W., Brown, G. L. and Nosenchuck, D. M., 1982, "Control of Laminar Instability Waves Using a New Technique," *Journal of Fluid Mechanics*, Vol. 118, pp. 187–200.

Maestrello, Lucio, 1985, "Active Transition Fixing and Control of the Boundary Layer in Air," Paper No. AIAA-85-0564, AIAA Shear Flow Conference, Boulder, CO, American Institute of Aeronautics and Astronautics.

Pupator, P. T. and Saric, W. S., 1989, "Control of Random Disturbances in a Boundary Layer," AIAA-89-1007, American Institute of Aeronautics and Astronautics.

Schlichting, Herman W., 1979, *Boundary Layer Theory*, Seventh Edition, McGraw-Hill, New York.

Schubauer, G. B. and Skramstad, H. K., 1947, "Laminar Boundary-Layer Oscillations and Stability of Laminar Flow," *Journal of the Aeronautical Sciences*, Vol. 14, pp. 69–78.

Thomas, Andrew S. W, 1983, "The Control of Boundary-Layer Transition Using a Wave Superposition Principle," *Journal of Fluid Mechanics*, Vol. 137, pp. 233–250

Thompson, W. T., 1965, *Vibration Theory and Applications*, Prentice Hall, Englewood Cliffs, NJ.

# Measurements in a Transitional Boundary Layer With Görtler Vortices

## (Data Bank Contribution)*

**R. J. Volino**
Assistant Professor,
Department of Mechanical Engineering,
United States Naval Academy,
Annapolis, MD 21402

**T. W. Simon**
Professor,
Heat Transfer Laboratory,
Department of Mechanical Engineering,
University of Minnesota,
Minneapolis, MN 55455

*The laminar-turbulent transition process has been documented in a concave-wall boundary layer subject to low (0.6 percent) free-stream turbulence intensity. Transition began at a Reynolds number, $Re_x$ (based on distance from the leading edge of the test wall), of $3.5 \times 10^5$ and was completed by $4.7 \times 10^5$. The transition was strongly influenced by the presence of stationary, streamwise, Görtler vortices. Transition under similar conditions has been documented in previous studies, but because concave-wall transition tends to be rapid, measurements within the transition zone were sparse. In this study, emphasis is on measurements within the zone of intermittent flow. Twenty-five profiles of mean streamwise velocity, fluctuating streamwise velocity, and intermittency have been acquired at five values of $Re_x$, and five spanwise locations relative to a Görtler vortex. The mean velocity profiles acquired near the vortex downwash sites exhibit inflection points and local minima. These minima, located in the outer part of the boundary layer, provide evidence of a "tilting" of the vortices in the spanwise direction. Profiles of fluctuating velocity and intermittency exhibit peaks near the locations of the minima in the mean velocity profiles. These peaks indicate that turbulence is generated in regions of high shear, which are relatively far from the wall. The transition mechanism in this flow is different from that on flat walls, where turbulence is produced in the near-wall region. The peak intermittency values in the profiles increase with $Re_x$, but do not follow the "universal" distribution observed in most flat-wall, transitional boundary layers. The results have applications whenever strong concave curvature may result in the formation of Görtler vortices in otherwise 2-D flows.*

## Introduction

Streamwise concave curvature is inherently destabilizing, and can lead to early transition from laminar to turbulent flow. Under some conditions, concave curvature will cause the formation of stationary, streamwise vortices, known as Görtler vortices, as first described by Görtler (1940). The first direct experimental evidence of Görtler vortices was provided by Gregory and Walker (1956) through flow visualization, and by Tani (1962) through flow measurements. A schematic of Görtler vortices on a concave wall is shown in Fig. 1. Several investigators have considered Görtler vortices and their effect on transition. Liepmann (1943) noted that transition occurs at lower momentum thickness Reynolds numbers ($Re_\theta$) on concave walls than on flat walls. He found that transition occurred when the Görtler number, G, was between 6 and 9, decreasing with the free-stream turbulence intensity (FSTI). He stated that the transition mechanism on convex walls was similar to that on flat walls, but different than that on concave walls, due to the vortices. Wortmann (1969) observed instabilities in Görtler vortices which caused spanwise shifting or "tilting" of the vortex pairs. The shifting occurred in a "completely steady manner," and caused inflection points in the mean streamwise velocity profiles. Bippes (1978) did not observe the inflection point profiles described by Wortmann, but reported spanwise meandering of the vortices. Swearingen and Blackwelder (1982) observed steady vortices which appeared at repeatable locations. The locations were believed to be determined by the geometry of the upstream screens in the wind tunnel. Transition to turbulence occurred at G values between 6.7 and 9. Mean streamwise velocity profiles normal to the wall and in the spanwise direction showed strong inflection points. Aihara and Koyama (1981) and Aihara et al. (1984) reported that horseshoe vortices were generated by Görtler vortices, and that the horseshoe and Görtler vortices then interacted, causing transition to turbulence. Riley et al. (1989) observed transition on concave surfaces under various free-stream turbulence conditions. They reported that on strongly curved surfaces, the Görtler vortices meander, and that when G exceeds 15 to 20, spanwise variations in boundary layer parameters cannot be detected. Crane et al. (1987) and Leoutsakos and Crane (1990) provided intermittency measurements at a few stations in transitional boundary layer flows in which Görtler vortices were present. They found very short transition lengths, typically about four boundary layer thicknesses, at the upwash locations of the vortices. Their flows were complicated by nonzero streamwise pressure gradients. Winoto and Low (1991) used spectral analysis to detect transition in a flow with Görtler vortices. Finnis and Brown (1996) considered laminar boundary layers with Görtler vortices subject to favorable pressure gradients. They noted that favorable pressure gradients raise the critical Görtler number for transition. Recently, Baughn et al. (1995) and Eckert et al. (1995) reported preliminary evidence of Görtler vortices on the pressure sides of turbine airfoils under low FSTI conditions. The evidence of the vortices appeared downstream of the separation zone near the leading edge of the airfoils, in a region of concave-curvature and favorable pressure gradient. Several other investigators have considered boundary layers with Görtler vortices. Floryan (1991) and Saric (1994) provided reviews.

* Data have been deposited to the JFE Data Bank. To access the file for this paper, see instructions on p. 738 of this issue.

Contributed by the Fluids Engineering Division for publication in the JOURNAL OF FLUIDS ENGINEERING. Manuscript received by the Fluids Engineering Division July 22, 1996; revised manuscript received March 31, 1997. Associate Technical Editor: J. A. C. Humphrey.

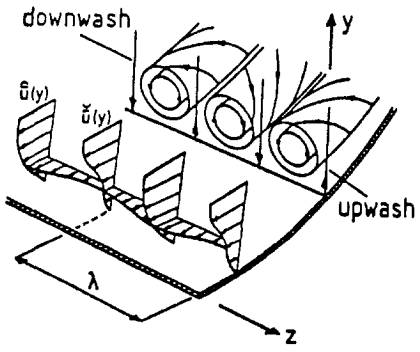


**Fig. 1 Schematic of Görtler vortices (from Crane and Sabzvari, 1984)**

Kim and Simon (1991) and Kim et al. (1992) considered cases on a concave wall with a constant radius of curvature of 1 m. Included in the study was a case taken under low (0.6 percent) FSTI conditions. The free-stream velocity was held constant at 17.2 m/s throughout the test section. The concave curvature led to the formation of stable Görtler vortices, which were first observed downstream of the first measurement station. The test wall was heated, and the vortices were observed with liquid crystal thermometry as warm and cold streaks. The vortices originated in the laminar flow region and persisted through transition into and throughout the fully-turbulent boundary layer, downstream. The vortices increased in size as the boundary layer grew and remained visible to the end of the test section. Kim and Simon (1991) took measurements at five streamwise stations in this flow. The flow was laminar at the first station, transitional at the second, and fully-turbulent by the third. Transition occurred farther upstream in this flow (where $Re_{x_s} = 3.5 \times 10^5$ and $Re_{x_e} = 4.7 \times 10^5$) than in a similar low-FSTI case done on a flat wall (where $Re_{x_s} = 8.8 \times 10^5$ and $Re_{x_e} = 13.8 \times 10^5$). Velocity and temperature profiles at $Re_x = 9.7 \times 10^5$, $Re_\theta = 665$ followed the turbulent velocity and temperature laws of the wall in the inner part of the boundary layer ($y^+ < 200$), but the wake was strongly affected by the curvature and vortices. Data were acquired at the upwash and downwash locations of the vortices at each station. These locations appear to be stable in that they always appeared at the same spanwise positions.

In this study, more detailed documentation of this Kim and Simon (1991) case is provided. Kim and Simon (1991) acquired mean and fluctuating velocity profiles at two spanwise positions at a single streamwise position in the transition region. In the present study, streamwise velocity profiles were acquired at five spanwise positions at each of five values of $Re_x$ in the transition region to better document the effect of the Görtler vortices on transition. Detailed measurements of mean velocity, turbulence intensity, and intermittency are provided. In contrast to many of the earlier studies, which focused on the initiation of transition in boundary layers with Görtler vortices, attention in the present study is on the path from the beginning to the end of transition and the role of the Görtler vortices in the transition process.

## Facility

All experiments were conducted in an open-return, blown-type wind tunnel. Details are available in Kim and Simon (1991). Air is drawn in through a filter, a heat exchanger, a screen pack, and a nozzle. Görtler vortex locations are believed to be determined by the most downstream screen in the screen pack. The nozzle has a 10.6:1 contraction ratio and a 68.6 cm $\times$ 11.4 cm exit area. The 6:1 aspect ratio at the exit was chosen to minimize secondary flows at the centerline of the curved test section. Downstream of the nozzle, the flow enters the test section, a curved channel. The test wall, 68.6 cm wide $\times$ 138 cm long, has a constant radius of curvature of 97 cm. At the leading edge of the test wall is a suction slot, used to bleed off the boundary layer which grows in the nozzle. The flow rate at the suction slot was adjusted to provide flow parallel to the test wall approaching the leading edge, as indicated by a wool tuft. The outer wall of the test section is a flexible polycarbonate sheet which was positioned to give a zero streamwise pressure gradient.

**Instrumentation.** Velocity measurements were made using a boundary layer type hot-wire probe (TSI model 1218-T1.5) and a constant-temperature, hot-wire bridge (TSI model IFA-100). The hot-wire sensor diameter and active length are 3.8 $\mu$m and 1.27 mm, respectively. The active length is about 50 wall units. The uncertainty in mean velocity is 3–5 percent, except in the very near wall region ($y^+ < 5$) where conduction effects between the hot-wire and the test wall are significant and near-wall corrections (Wills, 1962) are applied. The uncertainty in the fluctuating velocity, $\overline{u}'$, is 5 percent, except very near the wall where attenuation due to spatial resolution effects is possible. Ligrani and Bradshaw (1987) warn of reductions in measured turbulence quantities very near the wall due to the finite spatial resolution of hot-wire probes, and present a correlation showing a 25 percent reduction in $\overline{u}'$ at $y^+ = 17$ when the active length is 50 wall units. An analog circuit (described by Kim and Simon, 1991) was used with the hot-wire signals to distinguish between turbulent and non-turbulent regions of the transitional flow. The circuit determines the first

## Nomenclature

$C_f = \tau_w/(\rho U_\infty^2/2)$, skin friction coefficient
FSTI = free-stream turbulence intensity
$f(\gamma)$ = function of intermittency
$G = Re_\theta\sqrt{\theta/R}$, Görtler number
$n$ = turbulent spot production rate
$\hat{n} = n\nu^2/U_s^3$, dimensionless turbulent spot production rate
$Re_x$ = Reynolds number based on distance from leading edge
$Re_\theta$ = momentum thickness Reynolds number
$U$ = local streamwise velocity
$U_s$ = free-stream velocity at start of transition
$U_{cw}$ = core velocity extrapolated to the wall
$U_\infty$ = free-stream velocity
$u^+ = \overline{U}/u_\tau$ local velocity in wall coordinates
$\overline{u}'$ = rms of fluctuating component of streamwise velocity
$u_\tau = \sqrt{\tau_w/\rho}$, friction velocity
$x$ = streamwise coordinate
$y$ = coordinate normal to the wall
$y^+ = yu_\tau/\nu$, distance from wall in wall coordinates
$z$ = coordinate in spanwise direction
$\delta_{99.5}$ = 99.5 percent boundary layer thickness
$\gamma$ = intermittency (fraction of time flow is turbulent)
$\nu$ = kinematic viscosity
$\rho$ = density
$\theta$ = momentum thickness
$\theta_a$ = spanwise averaged momentum thickness
$\sigma$ = turbulent spot propagation parameter
$\tau_w$ = wall shear stress

### Subscripts

$s$ = transition start
$e$ = transition end

### Superscripts

overbar = time-averaged

Table 1 Measurement of locations

| Streamwise Station | $Re_x$ | Spanwise Station |
|---|---|---|
| 1 | $3.73\times10^5$ | a - downwash centered |
| 2 | $3.98\times10^5$ | b - midway between a and c |
| 3 | $4.03\times10^5$ | c - midway between a and e |
| 4 | $4.25\times10^5$ | d - midway between c and e |
| 5 | $4.44\times10^5$ | e - upwash centered |

and second time derivatives of the instantaneous hot-wire voltage. When either of these derivatives is above a threshold value, the flow is declared turbulent. The uncertainty in the intermittency (fraction of the time the flow is turbulent), $\gamma$, is 5 percent. At each point in the velocity profiles, data were acquired for 40 seconds at a 100 Hz sampling rate but with sampling time of less than $1 \times 10^{-5}$ seconds. The hot wire signal was low-pass filtered at 5 kHz. The hot-wire was moved for profile measurements with a motorized traversing assembly capable of a minimum step size of 5 $\mu$m. All data acquisition and probe traversing were controlled with a desktop computer through an IEEE interface bus.

## Results

**Mean Velocity Profiles.** Twenty-five velocity profiles were measured at different effective streamwise positions and different cross-stream positions within the transition region as shown in Table 1. Instead of moving the probe to different streamwise positions within the transition zone, all measurements were taken at $x = 0.36$ m (designated station 2 by Kim and Simon, 1991) and the free-stream velocity was varied from 16.5 m/s to 20 m/s. Although increasing the Reynolds number by increasing the free-stream velocity is not exactly equivalent to increasing Re by moving downstream (due to strength of curvature effects associated with boundary layer growth), the two methods of varying Re are approximately equivalent if the transition zone is short, as in the present case. The free-stream turbulence level remained nearly constant at 0.6 percent as the velocity was varied. Free-stream spectra are available in Volino and Simon (1994). The location and size of the vortices remained constant over the free-stream velocity range considered. Vortex locations were determined by traversing the hot-wire probe in the spanwise direction at a constant $y$ position of 0.4 mm from the test wall. The position of maximum velocity was taken as the downwash, and the position of minimum velocity was taken as the upwash. The vortices were approximately 2.2 mm wide (upwash to downwash). This compares to a boundary layer thickness, $\delta_{99.5}$, of approximately 3 mm.

Figure 2($a$) shows mean velocity profiles[1] at $Re_x = 3.7 \times 10^5$. Distance from the wall is normalized using the spanwise averaged momentum thickness. Momentum thickness varied by approximately 25 percent in the spanwise direction. The variation in the profiles with spanwise position is obvious. The near-wall velocities are highest at the downwash positions. Since the boundary layer tends to be thinner at the downwash location, the velocity gradients tend to be higher there. Some of the profiles, particularly the downwash profile, have strange shapes with inflection points. These are believed to be caused by spanwise "tilting" of the Görtler vortices, as depicted in Fig. 3. Similar behavior was noted by Wortmann (1969). A profile taken normal to the test wall will cut through a tilted vortex. As the probe is moved away from the wall, its position relative

[1] The velocity in the core of the channel varies in the $y$-direction due to the curvature of the test section. $U_{cw}$ is a velocity extrapolated from the core to the test wall, as described by Kestoras and Simon (1993). It is used in place of the free-stream velocity, $U_\infty$.

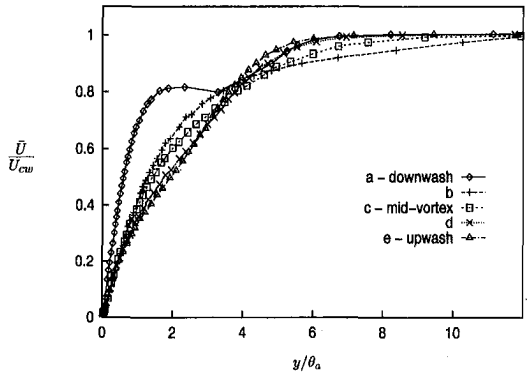


Fig. 2($a$)

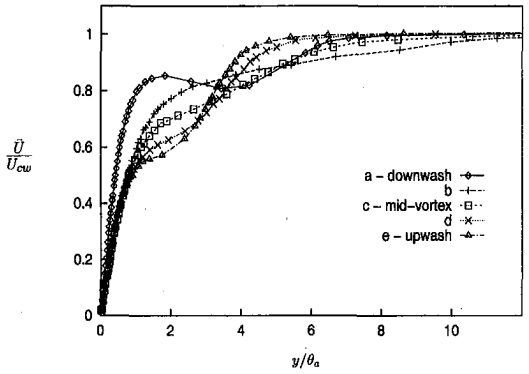


Fig. 2($b$)

**Fig. 2 Mean streamwise velocity profiles at ($a$) Lowest $Re_x$ ($=3.7 \times 10^5$) and ($b$) highest $Re_x$ ($=4.4 \times 10^5$). Uncertainties: abscissa 10, ~0, 10; ordinate 3, 2, 3.6. Uncertainty for each axis given in percent as 1) bias, 2) precision, and 3) overall uncertainty.**

to the upwash and downwash locations will change. The upwash and downwash positions, therefore, are only accurate at the test wall. This makes the definition of the various boundary layer thicknesses somewhat ambiguous. Momentum thickness, for example, was thickest at locations "$a$" and "$e$" corresponding to the upwash and downwash locations, and thinnest at location "$b$." If the vortices were not tilted, one would expect the largest momentum thickness at the upwash and the smallest at the downwash. Because of the ambiguity, spanwise averaged values are used in this paper.

Figure 2($b$) shows the mean velocity profiles at $Re_x = 4.4 \times 10^5$. The near wall gradients are higher than in the lower Reynolds number profiles. This is expected, since the skin friction should increase as the boundary layer proceeds through transition. The profiles also appear more inflectional than at the lower Reynolds numbers.

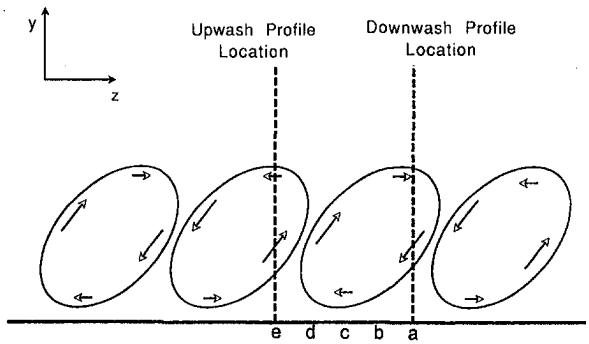


**Fig. 3 Upwash and downwash profiles cutting through "tilted" vortices**

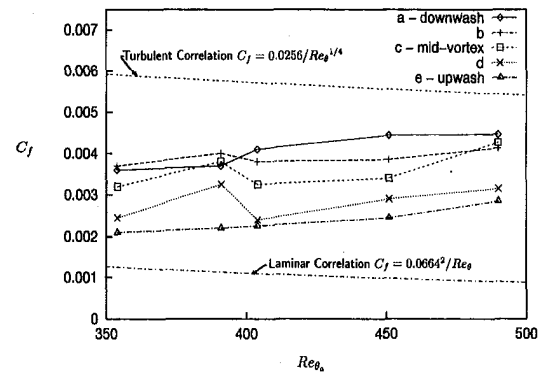


**Fig. 4 Skin friction coefficient versus $Re_{\theta_a}$. Uncertainties: abscissa 6, 10, 12; ordinate 5, 10, 11. Uncertainty for each axis given in percent as 1) bias, 2) precision, and 3) overall uncertainty.**

When plotted in wall coordinates (see Volino and Simon, 1995a), the low $Re_x$ profiles of Fig. 2($a$) appear somewhat laminar-like. The high-$Re_x$ profiles of Fig. 2($b$) appear more turbulent-like, and are closer to the turbulent law of the wall shape. This is particularly true near the upwash location. Because the boundary layer is thickest at the upwash, the boundary layer there should tend to be more mature (higher $Re_\theta$), and should therefore tend to be farther along in the transition process.

**Skin Friction.** Skin friction coefficients were determined from the velocity profiles by fitting the very near-wall data to the line $u^+ = y^+$. Skin friction coefficient values are plotted versus $Re_{\theta_a}$ in Fig. 4. In general, $C_f$ is highest at the downwash locations, where the boundary layer is thinnest. Skin friction coefficients generally increase at each spanwise position as $Re_\theta$ increases and the boundary layer proceeds through transition. Standard correlations for laminar and fully-turbulent boundary layers on flat plates are shown for reference. The laminar correlation follows from the Blasius solution and the turbulent correlation is from Schlichting (1979). The data lie between the laminar and turbulent correlations, as expected for a transitional boundary layer.

**Fluctuating Velocities.** Profiles of fluctuating streamwise velocity, $\bar{u}'$, are plotted in Fig. 5. The fluctuations are normalized on $U_{cw}$. The downwash profiles are shown in Fig. 5($a$) and the upwash in Fig. 5($b$). The fluctuation level rises as $Re_x$ is increased. There is a near-wall peak in all of the profiles at $y/\theta \approx 1$ ($y^+ = 22$) and a second peak in the downwash profiles at $y/\theta \approx 5$ ($y^+ \approx 100$). The near-wall peak is typical of all boundary layers. The second peak is attributed to the Görtler vortices. A peak in the outer part of a boundary layer with Görtler vortices was reported also by Swearingen and Blackwelder (1987). This peak occurs at the location of the local minimum in the mean velocity profiles (Fig. 2). The fluctuation levels at the upwash (Fig. 5($b$)) are higher than those in the corresponding downwash profiles and a typical flat-wall turbulent boundary layer ($\bar{u}'/u\tau$ approaches 5 at the upwash, compared to a peak value of 2 to 2.5 in most turbulent boundary layers). This indicates that the fluctuation level in the outer part of the boundary layer is high relative to the local wall shear stress, suggesting significant turbulence production in the outer part of the boundary layer. The near-wall peak is broader at the upwash than at the downwash. At the higher $Re_x$, at the upwash location, the near-wall peak shows some signs of dividing into two peaks, one at $y/\theta \approx 1$ and the second at $y/\theta \approx 2.5$. This second peak location corresponds to the emergence of an inflection point in the mean velocity profiles at the upwash location (Fig. 2($b$)).

**Intermittency.** Profiles of the intermittency, $\gamma$, were measured along with the velocity profiles. These are shown for the downwash (Fig. 6($a$)) and the upwash (Fig. 6($b$)) locations. In the downwash profiles the near-wall intermittency rises from near zero at the lowest $Re_x$ to about 85 percent at the highest $Re_x$. There is a peak in $\gamma$ near $y/\theta = 5$. This peak corresponds to the local minimum in the mean velocity seen in the downwash profiles (Fig. 2), and the second peak in $\bar{u}'$ (Fig. 5($a$)). The inflection point in the mean velocity profile, caused by a tilting of the vortices, appears to be a source of turbulence production. This causes a local rise in the intermittency above the near-wall values. This suggests that the instability which causes the tilting of the Görtler vortices, by producing a region of high mean velocity gradient near the inflection point, may be driving the transition process in this flow. Swearingen and Blackwelder (1987) state that the Görtler vortices do not break down to turbulence themselves, but set up a flow field which is unstable to other instabilities. These secondary instabilities cause the breakdown to turbulence. Figure 6($b$) shows the intermittency profiles at the upwash locations. As at the downwash locations, there is a regular progression through transition. The intermittency drops very near the wall in the upwash profiles. The intermittency should go to zero at the wall, where the velocity goes to zero and viscous effects dominate. This near-wall drop was not resolved in the downwash profiles, possibly because the boundary layer is thinner at the downwash locations. A comparison of Figs. 6($a$) and 6($b$) shows that in the near wall region ($y/\theta < 2$) the intermittency tends to be slightly higher at the upwash locations than at the corresponding downwashes. As stated above, the boundary layer is thicker at the upwash locations, so it is reasonable to expect that transition would occur there first, resulting in higher intermittencies. Several

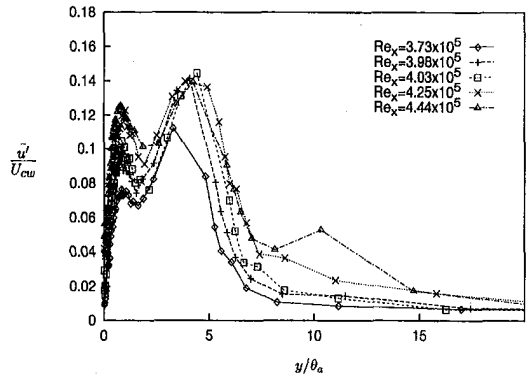


**Fig. 5($a$)**

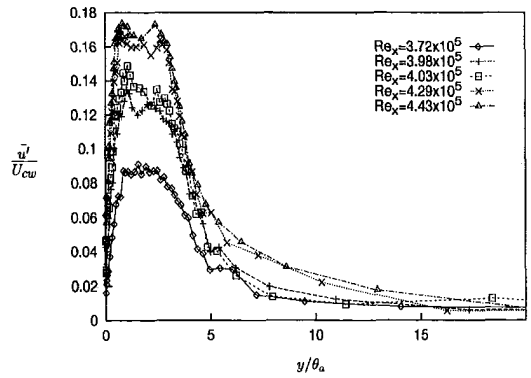


**Fig. 5($b$)**

**Fig. 5 Fluctuating streamwise velocity profiles at ($a$) downwash locations and ($b$) upwash locations. Uncertainties: abscissa 10, ~0, 10; ordinate 3, 4, 5. Uncertainty for each axis given in percent as 1) bias, 2) precision, and 3) overall uncertainty.**

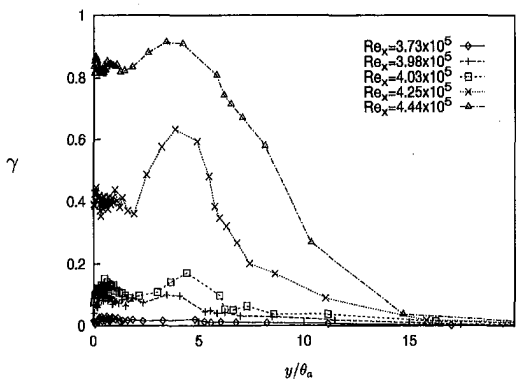


Fig. 6(*a*)

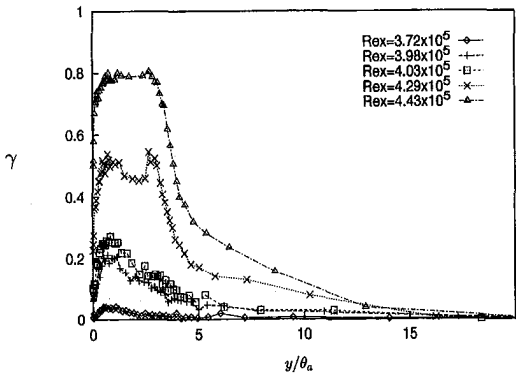


Fig. 6(*b*)

**Fig. 6 Intermittency profiles at (*a*) downwash locations and (*b*) upwash locations. Uncertainties: abscissa 10, ~0, 10; ordinate 4, 3, 5. Uncertainty for each axis given in percent as 1) bias, 2) precision, and 3) overall uncertainty.**

investigators provide additional evidence that transition begins at the locations of inflection points in the upwash velocity profiles, where a shear layer instability develops. Finnis and Brown (1996) discuss "meandering" or "sinuous" flow at these locations, or alternatively the formation of horseshoe or crossflow vortices which lead to rapid breakdown to turbulence at the inflection point locations. Finnis and Brown (1996) cite evidence from several studies including Bippes (1978) and Swearingen and Blackwelder (1987). In agreement with the above results, Leoutsakos and Crane (1990) noted that transition begins at upwash locations, near a region of high shear, and proceeds rapidly, by lateral spreading. Lateral spreading would tend to equalize the upwash and downwash intermittencies, and at $\mathrm{Re}_x = 4.44 \times 10^5$, the upwash and downwash have nearly equal near wall intermittencies of 0.8.

*Transition Location.* The transition start and end locations can be determined from the transitional flow intermittency data by using Narasimha's (1984) theory, which, in turn, was derived from Emmons' (1951) theory of turbulent spots. The highest $\gamma$ value in the $\gamma$ vs $y$ profile at each streamwise measuring station in a test are selected and used to calculate the function

$$f(\gamma) = (-\ln(1-\gamma))^{-1/2}, \qquad (1)$$

which is then plotted versus $x$ or $\mathrm{Re}_x$ (plotting versus $\mathrm{Re}_x$ is equivalent to plotting versus $x$ in cases with unaccelerated flow and constant fluid properties, such as the present case). For most flows along flat-walls, the data lie along a straight line in these coordinates. A least-squares fit to the data is extrapolated to $f(\gamma) = 0$ and $f(\gamma) = 2.146$, which correspond to $\gamma = 0$ and $\gamma = 0.99$, respectively. The corresponding $\mathrm{Re}_x$ values at the two extrapolated points are taken as the locations of the start and end of transition, $\mathrm{Re}_{x_s}$ and $\mathrm{Re}_{x_e}$, respectively. Volino and Simon (1995b) applied this technique to find the transition start and end locations in several flows along flat plates. The extrapolation technique could not be applied in a straightforward manner in the present case along the concave wall, however. The present data, when plotted as $f(\gamma)$ versus $\mathrm{Re}_x$, do not lie along a straight line. The trajectory of $f(\gamma)$ versus $\mathrm{Re}_x$ changes slope within the transition region. Thus, $\mathrm{Re}_{x_s}$ and $\mathrm{Re}_{x_e}$ were determined in this case using two extrapolations. The data near the start of transition were extrapolated to $f(\gamma) = 0$ to determine $\mathrm{Re}_{x_s}$, and the high-$\gamma$ data were extrapolated to $f(\gamma) = 2.146$ to find $\mathrm{Re}_{x_e}$. This was done at three of the spanwise locations for this case, corresponding to the downwash (a), upwash (e) and mid-vortex (c) locations of the Görtler vortices. Transition start and end locations are given in terms of $\mathrm{Re}_x$ and $\mathrm{Re}_\theta$ in Table 2. At the three spanwise positions, $\mathrm{Re}_\theta$ was between 361 and 403 at the start of transition, and between 500 and 686 at the end of transition. At the 0.6 percent FSTI of the present case, correlations such as those given by Abu-Ghannam and Shaw (1980) or Mayle (1991) predict transition start at $\mathrm{Re}_\theta \approx 600$ and transition end at $\mathrm{Re}_\theta \approx 1600$. In terms of $\mathrm{Re}_x$, these flat wall correlations predict transition start at about $1 \times 10^6$, compared to the measured value of $0.35 \times 10^6$ in the present case. Hachem and Johnson (1990) present a transition correlation for concave walls. When applied to the present case, their correlation predicts $\mathrm{Re}_x = 0.25 \times 10^6$, an improvement over the flat wall correlation. Concave curvature is causing early transition in the present case.

**Table 2 Transition start and end and turbulent spot propagation rates based on intermittency measurements**

| Position | $\mathrm{Re}_{x_s}$ $\times 10^{-6}$ | $\mathrm{Re}_{x_e}$ $\times 10^{-6}$ | $\mathrm{Re}_{\theta_s}$ | $\mathrm{Re}_{\theta_e}$ | effective $\hat{n}\sigma \times 10^{11}$ at trans. start | effective $\hat{n}\sigma \times 10^{11}$ at trans. end | effective overall $\hat{n}\sigma \times 10^{11}$ |
|---|---|---|---|---|---|---|---|
| Up-wash | 0.356 | 0.472 | 403 | 686 | 14.2 | 93.4 | 34.2 |
| Mid-Vortex | 0.353 | 0.467 | 363 | 500 | 11.7 | 105.2 | 35.4 |
| Down-wash | 0.350 | 0.468 | 361 | 586 | 5.9 | 91.7 | 33.0 |

*Intermittency Distribution.* The intermittency within the transition zone is plotted as a function of the dimensionless streamwise coordinate $(\mathrm{Re}_x - \mathrm{Re}_{x_s})/(\mathrm{Re}_{x_e} - \mathrm{Re}_{x_s})$ in Fig. 7. The abscissa is a modified version of a coordinate used by Dhawan and Narasimha (1958). Dhawan and Narasimha used $(x - x_s)/(x_e - x_s)$, with $x_s$ taken at $\gamma = 0.25$ and $x_e$ taken at

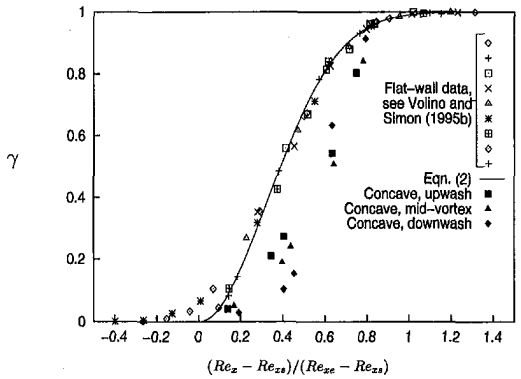


**Fig. 7 Intermittency distributions through transition. Uncertainties: abscissa 4, 10, 11; ordinate 4, 3, 5. Uncertainty for each axis given in percent as 1) bias, 2) precision, and 3) overall uncertainty.**

$\gamma = 0.75$. Here, $\mathrm{Re}_{x_s}$ is taken at the extrapolated $\gamma = 0$ location and $\mathrm{Re}_{x_e}$ at the extrapolated $\gamma = 0.99$ location. The modification was done to give $\mathrm{Re}_x$ estimates which are closer to the actual start and end of transition. The change was purely algebraic; the theory remains exactly as Dhawan and Narasimha presented it. Dhawan and Narasimha presented a formula which, when modified to take the changed abscissa into account is

$$\gamma = 1 - \exp\left(-4.6\left(\frac{\mathrm{Re}_x - \mathrm{Re}_{x_s}}{\mathrm{Re}_{x_e} - \mathrm{Re}_{x_s}}\right)^2\right) \tag{2}$$

This curve is plotted along with the experimental data in Fig. 7. Volino and Simon (1995b) found good agreement between the theoretical curve and data from several studies done in unaccelerated and accelerated flow along flat plates. Gostelow and Walker (1991) showed that the agreement is also good for adverse pressure gradient cases on flat plates. The present data indicate that the theory does not always hold when curvature effects are introduced. Although it is possible to force any two data points from an experimental case to fit the theoretical curve (through appropriate choice of $\mathrm{Re}_{x_s}$ and $\mathrm{Re}_{x_e}$), it is impossible to fit all of the concave-wall data to the theoretical curve. This behavior is believed to be due to a change in the transition mechanism associated with the Görtler vortices in the low-FSTI concave-wall flow. On the concave wall, transition tends to progress more slowly, in a relative sense, during early transition and more quickly during later stages of transition, compared to flat-wall behavior. The Dhawan and Narasimha (1958) model is based on the growth of turbulent spots in the near-wall region. Since the Görtler vortex flow includes an additional mechanism for turbulence production in the outer part of the boundary layer, it might be expected that the transition path should deviate from that given by Eq. (2).

*Turbulent Spot Propagation Rate.* The production and growth of turbulent spots in the transition region can be calculated using the information provided above and Dhawan and Narasimha's (1958) theory. As given by Mayle (1991),

$$\gamma = 1 - \exp\left(-\frac{n\sigma}{U_\infty}(x - x_s)^2\right) \tag{3}$$

where $n$ is the turbulent spot production rate and $\sigma$ is the turbulent spot propagation parameter. A dimensionless spot production rate, $\hat{n}$, is defined as $n\nu^2/U_s^3$. The velocity, $U_s$, is the free-stream velocity at the start of transition. The product $\hat{n}\sigma$ is directly related to the length of the transition zone. Given the location of the transition start and $\hat{n}\sigma$, it should be possible to calculate the location of the end of transition and the intermittency within the transition region. From the above discussion, one can show that

$$\hat{n}\sigma = \frac{4.6}{(\mathrm{Re}_{x_e} - \mathrm{Re}_{x_s})^2} \tag{4}$$

in unaccelerated flow, where $\mathrm{Re}_{x_s}$ and $\mathrm{Re}_{x_e}$ are taken at $\gamma = 0$ and $\gamma = 0.99$. A single value of $\hat{n}\sigma$ is applied through transition.

Spot propagation rates were calculated for the present case and several flat wall cases, and are plotted in Fig. 8. Also shown is a correlation given by Mayle (1991). Mayle (1991) and Volino and Simon (1995b) showed that data from several flat-wall studies agreed well with this correlation. In flat-wall cases, where the intermittency data agree with Narasimha's (1984) theory, the choice of a single $\hat{n}\sigma$ for the entire transition region is appropriate. For the concave-wall case, however, the local effective $\hat{n}\sigma$ values increase as one moves downstream through transition. The first three $\gamma$ values in each of the three concave-wall curves in Fig. 7 were used to determine an effective local $\hat{n}\sigma$ at the start of transition. Similarly, the last two $\gamma$ values in each curve were used to determine an effective local $\hat{n}\sigma$ for the end of transition. These are presented in Table 2 for the upwash, downwash and mid-vortex locations of this case. In Fig. 8, all the concave wall $\hat{n}\sigma$ lie significantly above Mayle's correlation. The effective $\hat{n}\sigma$ increases by an order of magnitude between the beginning and the end of transition. An effective overall $\hat{n}\sigma$, based on the extrapolated $\mathrm{Re}_{x_s}$ and $\mathrm{Re}_{x_e}$ values given in Table 2, is also presented.

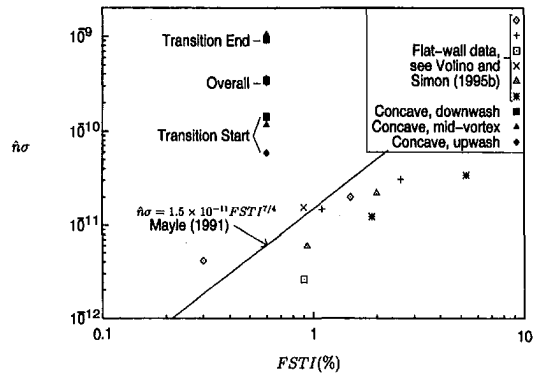


**Fig. 8 Turbulent spot production rate based on $\gamma$. Uncertainties: abscissa 3, 4, 5; ordinate 3, 20, 20. Uncertainty for each axis given in percent as 1) bias, 2) precision, and 3) overall uncertainty.**

## Conclusions

The flow in this case is interesting and complex due to the presence of the stable Görtler vortices. These vortices appear to dominate the transition process. The vortices cause inflection points in the mean velocity profiles, which lead to a breakdown to turbulence at a location which is far from the wall relative to the equivalent location in a flat-wall boundary layer. Transition occurs farther upstream than in flat-wall cases of comparable FSTI. The transition zone is shortened and the path through transition, in terms of the intermittency, is altered by the presence of the vortices.

## JFE Data Bank Contribution

The data bank contribution includes 25 files containing data from the 25 velocity profiles considered in this paper. Each file contains a table with columns of $y$, $U$, $y^+$, $u^+$, $u'$ and intermittency. Also included is a header containing information such as the local skin friction coefficient, boundary layer thicknesses, and Reynolds numbers. An explanation file contains a nomenclature for the data files.

## Acknowledgments

This work was sponsored by the NASA Lewis Research Center under grant NASA/NAG-1249. The grant monitor is Fred Simon.

## References

Abu-Ghannam, B. J., and Shaw, R., 1980, "Natural Transition of Boundary Layers—The Effects of Turbulence, Pressure Gradient and Flow History," *Journal of Mechanical Engineering Science,* Vol. 22, No. 5, pp. 213–228.

Aihara, Y., and Koyama, H., 1981, "Secondary Instability of Görtler Vortices: Formation of Periodic Three-Dimensional Coherent Structure," *Transactions of the Japan Society for Aeronautical and Space Sciences,* Vol. 24, No. 64, pp. 78–94.

Aihara, Y., Tomita, Y., and Ito, A., 1984, "Generation, Development and Distortion of Longitudinal Vortices in Boundary Layers along Concave and Flat Plates," *IUTAM Symposium on Laminar-Turbulent Transition,* Novosibirsk, pp. 447–454, ed. Kozlov, V. V., ed., Springer, Berlin.

Baughn, J. W., Butler, R. J., Byerley, A. R., and Rivir, R. B., 1995, "An Experimental Investigation of Heat Transfer, Transition and Separation on Turbine Blades at Low-Reynolds Number and High Turbulence Intensity," ASME Paper No. 95-WA/HT-25.

Bippes, H., 1978, "Experimental Study of the Laminar-Turbulent Transition of a Concave Wall in a Parallel Flow," NASA TM-75232.

Crane, R. I., and Sabzvari, J., 1984, "Laser-Doppler Measurements of Görtler Vortices in Laminar and Low-Reynolds-Number Turbulent Boundary Layers," *Laser Anemometry in Fluid Mechanics,* Adrian, R. J. et al., eds., LADOAN-Instituto Superior Technico, Lisbon, pp. 19–35.

Crane, R. I., Leoutsakos, G. and Sabzvari, J., 1987, "Transition in Pressure-Surface Boundary Layers," ASME *Journal of Turbomachinery,* Vol. 109, pp. 296–302.

Dhawan, S., and Narasimha, R., 1958, "Some Properties of Boundary Layer Flow During the Transition from Laminar to Turbulent Motion," *Journal of Fluid Mechanics,* Vol. 3, pp. 418–436.

Eckert, E. R. G., Goldstein, R. J., Olson, S. J., and Wang, H. P., 1995, Personal communication, University of Minnesota.

Emmons, H. W., 1951, "The Laminar-Turbulent Transition in a Boundary Layer—Part I," *Journal of Aeronautical Science,* Vol. 18, pp. 490–498.

Finnis, M. V., and Brown, A., 1996, "The Streamwise Development of Görtler Vortices in a Favorable Pressure Gradient," ASME *Journal of Turbomachinery,* Vol. 118, pp. 162–171.

Floryan, J. M., 1991, "On the Görtler Instability of Boundary Layers," *Progress in Aerospace Sciences,* Vol. 28, pp. 235–271.

Gregory, N., and Walker, W. S., 1956, "The Effect on Transition of Isolated Surface Excrescences in the Boundary Layer," ARC Repl., R&M, No. 2779, pp. 1–10.

Görtler, H., 1940, "Uber eine Dreidimensionale Instabilität Laminarer Grenzschichten an Konkaven Wänden," Ges. d. Wiss. Göttingen, Nachr. a. d. Math. Phys. Kl. 2:1 (also NACA TM 1375, 1954).

Gostelow, J. P., and Walker, G. J., 1991, "Similarity Behavior in Transitional Boundary Layers Over a Range of Adverse Pressure Gradients and Turbulence Levels," ASME *Journal of Turbomachinery,* Vol. 113, pp. 617–625.

Hachem, F., and Johnson, M. W., 1990, "A Boundary Layer Transition Correlation for Concave Surfaces," ASME Paper No. 96-GT-222.

Kestoras, M. D., and Simon, T. W., 1993, "Combined Effects of Concave Curvature and High Free-Stream Turbulence Intensity on Boundary Layer Heat and Momentum Transport," ASME Paper No. 93-WA/HT-56.

Kim, J., and Simon, T. W., 1991, "Free-Stream Turbulence and Concave Curvature Effects on Heated Transitional Boundary Layers, Vol. I—Final Report," NASA CR 187150.

Kim, J., Simon, T. W., and Russ, S. G., 1992, "Free-Stream Turbulence and Concave Curvature Effects on Heated Transitional Boundary Layers," ASME *Journal of Heat Transfer,* Vol. 114, No. 2, pp. 338–347.

Leoutsakos, G., and Crane, R. I., 1990, "Three-Dimensional Boundary Layer Transition on a Concave Surface," *International Journal of Heat and Fluid Flow,* Vol. 11, No. 1, pp. 2–9.

Liepmann, H. W., 1943, "Investigation on Laminar Boundary Layer Stability and Transition on Curved Boundaries," NACA Advanced Confidential Report 3H30 (also Wartime Report W-107).

Ligrani, P. M., and Bradshaw, P., 1987, "Spatial Resolution and Measurements of Small-Scale Turbulence in the Viscous Sublayer Using Subminiature Hot-Wire Probes," *Experiments in Fluids,* Vol. 5, pp. 407–417.

Mayle, R. E., 1991, "The Role of Laminar-Turbulent Transition in Gas Turbine Engines," ASME *Journal of Turbomachinery,* Vol. 113, pp. 509–537.

Narasimha, R., 1984, "Subtransitions in the Transition Zone," *IUTAM Symposium on Laminar-Turbulent Transition,* Novosibirsk, Kozlov, V. V., ed., Springer, Berlin, pp. 141–151.

Riley, S., Johnson, M. W., and Gibbings, J. C., 1989, "Boundary Layer Transition of Strongly Concave Surfaces," ASME Paper No. 89-GT-321.

Saric, W. S., 1994, "Görtler Vortices," *Annual Review of Fluid Mechanics,* Vol. 26, pp. 379–409.

Schlichting, H., 1979, *Boundary Layer Theory,* 7th ed., McGraw-Hill, New York.

Swearingen, J. D., and Blackwelder, R. F., 1982, "Breakdown of Streamwise Vortices near a Wall," *IUTAM Symposium on Structure of Complex Turbulent Shear Flow,* Marseille, pp. 10–19, Dumas, R. and Fulachier, L., eds., Springer, Berlin, pp. 10–19.

Swearingen, J. D., and Blackwelder, R. F., 1987, "The Growth and Breakdown of Streamwise Vortices in the Presence of a Wall," *Journal of Fluid Mechanics,* Vol. 182, pp. 255–290.

Tani, I., 1962, "Production of Longitudinal Vortices in a Boundary Layer along a Curved Wall," *Journal of Geophysical Research,* Vol. 67, pp. 3075–3080.

Volino, R. J., and Simon, T. W., 1994, "Transfer Functions for Turbulence Spectra," *Unsteady Flows in Aeropropulsion,* ASME AD-Vol. 40, pp. 147–155.

Volino, R. J., and Simon, T. W., 1995a, "Measurements in Transitional Boundary Layers under High Free-Stream Turbulence and Strong Acceleration Conditions," NASA CR 198413.

Volino, R. J., and Simon, T. W., 1995b, "Bypass Transition in Boundary Layers Including Curvature and Favorable Pressure Gradient Effects," ASME *Journal of Turbomachinery,* Vol. 117, pp. 166–174.

Wills, J. A. B., 1962, "The Correction of Hot-Wire Readings for Proximity to a Solid Boundary," *Journal of Fluid Mechanics,* Vol. 12, pp. 388–396.

Winoto, S. H., and Low, H. T., 1991, "Transition of Boundary Layer Flows in the Presence of Görtler Vortices," *Experiments in Fluids,* Vol. 10, pp. 281–284.

Wortmann, F. X., 1969, "Visualization of Transition," *Journal of Fluid Mechanics,* Vol. 38, pp. 473–480.

**L. Bai**
Doctoral Candidate.

**M. Fiebig**
Professor and Head,
Heat and Mass Transfer.
Mem. ASME

**N. K. Mitra**
Professor.
Mem. ASME

Institut für Thermo- und Fluiddynamik,
Ruhr-Universität Bochum, 44780 Bochum,
Germany

# Numerical Analysis of Turbulent Flow in Fluid Couplings

*Numerical simulation of three-dimensional unsteady turbulent flows in fluid couplings was carried out by numerically solving Navier-Stokes equations in a rotating coordinate system. The standard k-ϵ model was used to take turbulence into account. A finite volume scheme with colocated body-fitted grids was used to solve the basic equations. Computed flow structures show the vortex generation and its effect on the torque transmission. Computed local velocity and torque flow compare well with measurements.*

## 1 Introduction

A fluid coupling is used for torque transport from a prime mover to a machine without mechanical contact. A coupling consists of an input rotor (pump impeller) with radial vanes and a similar matching output rotor (turbine runner), facing each other with a small gap without mechanical contact. These two disks are enclosed in a casing which is mounted on the shaft of the pump and rotates with the pump, see Fig. 1(*a*). The casing is filled with a liquid (generally an oil of low viscosity), and the pump is driven by a prime mover, e.g., an electric motor or an internal engine. A circulatory motion of the fluid relative to the rotation of the coupling in the passage between the vanes of the pump and turbine sets up, Fig. 1(*b*). The turbine is dragged by the circulatory fluid and rotates with a lower speed than the pump. The difference in the pump and turbine speeds is called the slip. Without the slip a solid body rotation will set in and a relative motion between the fluid and the rotors will be absent. The circulatory motion appears as a large vortex, see Fig. 1(*b*), and the circulatory fluid transmits the torque. The center of the vortex where the circumferential velocity vanishes is denoted as the neutral point and its distance from the axis as the nutral radius $r_N$. For efficient torque transport the neutral point should lie in the gap between the pump and the turbine and the full circulatory fluid should move from to one to the other. If the circulation remains confined mainly in one half of the torque converter (pump or turbine), the transmitted torque will be substantially reduced. Secondary vortices may appear in the corners, see Fig. 1(*b*). These vortices do not contribute to the torque transport since the associated circulation is confined either in the pump or in the turbine. Any flow structure which causes secondary motion confined in one half of the coupling causes a loss in transported torque.

The main difference between torque converters which are used in automatic transmission of automobiles and fluid couplings is that in the former the fluid does not flow directly from the pump to the turbine as in couplings but through a stator. This gives a dominant direction of the circulating fluid in a torque converter (e.g., from rotor to stator to rotor) and also causes a loss in the transmitted torque. In contrast to the torque converter a fluid coupling transmits the same torque from the pump to the turbine.

Fluid couplings are commonly used to drive air compressors and pumps in power plants and chemical industries. Further uses are found in mechanical handling equipments, conveyors, elevators, hoists, mining, earth moving machineries, power plants of ships and some transmission system of large trucks and rail road trains, see Langlois (1979).

The couplings can be classified depending on the amount of oilfilling as fixed-fill and adjustable fill. Even for the fixed-fill coupling, it is not generally completely filled in order to allow thermal expansion of the oil. The dissipative heating can raise the oil temperature substantially (80°C or more, see Höller, 1989) since only free convection on finned outside surface of the casing is used in practice for cooling.

The adjustable-fill is used for starting, braking and in general for controlling the amount of the transmitted torque. In both operational conditions then the circulating fluid is in general a two-phase mixture of oil and air. Only in ideal experimental situation an adjustable filling system can maintain a fully filled coupling in operation, see Middelmann (1992).

In order to avoid resonant vibration the input and output rotors have different number of blades. Because of the absence of a dominant direction of the fluid flow these blades are simply radial and not profiled.

During operation the fluid in the high pressure side (i.e., the pump) moves radially between the vanes of the pump from the axis toward the rim and then axially toward the turbine and flows between vanes of the turbine toward the turbine hub and thereafter from the turbine to the pump. Because of the rotational speed difference or slip and because of the difference in number of blades in pump and turbine, the circulating fluid suffers continuous impact of the blades since they are not aligned with the incoming fluid. Consequently, the flow is expected to be turbulent particularly at large slip even with low rotational speed or at small slip with large rotational speed. As already mentioned, because of the absence of a stator vane there is no main flow direction through the blades. This makes it difficult to measure the flow properties in fluid couplings. In the case of torque converters the mean velocity and the Reynolds stresses have been measured, see a summery of Lakshminarayana (1991). In contrast, the investigations in the case of fluid couplings have been limited to measure the transmitted torques, see Langlois (1979). Recently Middelmann (1992) used a one component Laser-Doppler-Anemometer to measure the mean velocity in the axial direction at one selected point.

In contrast to several numerical studies of torque converters, see e.g., Rai (1989), calculations of the three dimensional unsteady flow in fluid couplings have been reported only by the authors' group, Kost et al. (1994), Bai Li (1994), and Bai Li et al. (1994).

Contributed by the Fluids Engineering Division for publication in the JOURNAL OF FLUIDS ENGINEERING. Manuscript received by the Fluids Engineering Division June 22, 1994; revised manuscript received April 21, 1997. Associate Technical Editor: L. Nelik.

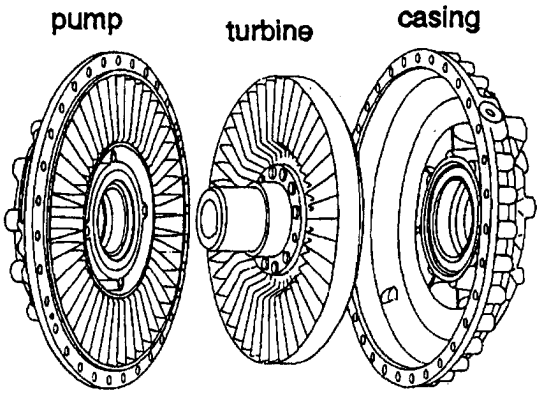


Fig. 1(*a*) Schematic of a fluid coupling

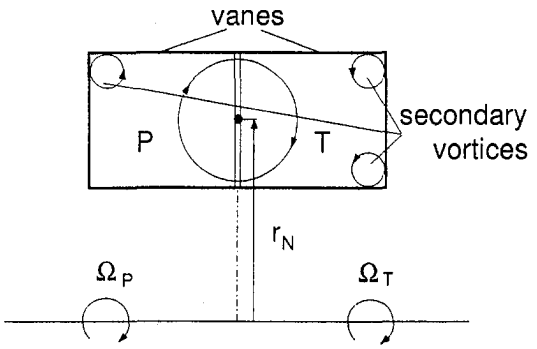


Fig. 1(*b*) Schematic of the circulatory motion of the fluid in the vane channel i.e., in the passage between the vanes of the pump and the turbine; $r_N$: neutral radius where circumferential speed is zero

Kost et al. (1994) developed a computational scheme based on finite volume technique to solve nonsteady three dimensional Navier-Stokes equations in body-fitted coordinates on a rotating reference frame. Kost et al. (1994) computed only laminar flows for a fully filled coupling and observed the dependence of the transmitted torque on the flow structure, particularly the vortices and circulating zones. The numerical results compared reasonably well with experiments at small slip, but deviated substantially at large slip. Clearly turbulent flow computations at large slip are needed. The problem there is the implementation of proper turbulence model.

For no slip, i.e., for the same rotational speeds for the pump and the turbine, a solid body rotation will be obtained. Slip will introduce disturbance in the flow. The two parameters, the rotational speeds of the pump and the turbine (or the rotational speed of the pump and the slip) will determine whether the circulatory flow betwen the vane channels of the turbine and the pump will be laminar or turbulent. The vanes will naturally introduce further disturbance. Analysis of stability and transition of such flows has never been reported. However, Laser velocimetric measurements of Middelmann (1992) show the turbulent nature of flow in a fluid coupling. The circulatory flow in the coupling is expected to show strong streamline curvature and nonisotropy in turbulence structure. A proper description of turbulence requires possibly Reynolds stress model. Such models need higher order correlations which are for complex geometries unknown. Besides computations with such model can be quite expensive. It should be mentioned that the computation of flow field in a fluid coupling with a standard k-$\epsilon$ model has not been reported. A standard k-$\epsilon$ model may not be too far from reality for the case of large rotational speed, large slip and large number of blades.

The main purpose of the present work is to test the validity of the standard k-$\epsilon$-turbulence model for the flow simulation in a fluid coupling. Flow field and the resulting torque have been computed with this turbulence model and wall law in couplings for different speeds, slips and geometry. Computational results are compared with available experiments.

## 2 Mathematical Model

**2.1 Basic Equations.** The coupling is assumed to be completely filled with an incompressible viscous fluid. The flow in the coupling is described by the three dimensional unsteady Reynolds averaged Navier-Stokes equations in conjunction with

## Nomenclature

$a$ = coefficients of discretized equations
$A$ = surface area of vane channel
$B$ = breadth
$\mathbf{c}$ = velocity vector in absolute system
$c_1$, $c_2$, $c_\mu$ = constants in turbulence model
$c_m$ = absolute velocity component in $x$-direction
$\mathbf{f}$ = Coriolis vector
$d$ = hubdiameter
$D$ = diameter
$E$ = wall function constants in Eq. (2.14)
J = Jacobian
$k$ = turbulent kinetic energy
$\mathbf{j}$ = unit vector in axial direction
$G$ = production rate of turbulent kinetic energy $k$
$M$ = rotational moment
$p_s$ = hydrostatic pressure
$p$ = reduced pressure: $p = p_s - \frac{1}{2}\cdot\rho\cdot(\Omega\times\mathbf{r})(\Omega\times\mathbf{r})$
$r$ = radius
$\mathbf{r}$ = position vector
Re = Reynolds number, with $\Omega_P D$ as reference velocity
$s$ = slip
$S_\phi$ = source term
$S_c$, $S_p$ = linearized component of source terms $S_\phi = S_c + S_p\phi$
$\mathbf{u}$ = velocity vector in relative system
$t$ = time
$U_i$ = covariant velocity components
$U_o$ = reference velocity
$V$ = control volume
$\dot{V}$ = volume flow rate
$x_i$ = generalized coordinates, $i$ = 1, 2, 3
$y_i$ = Cartesian coordinates, $i$ = 1, 2, 3
$Z$ = number of vanes
$\alpha$ = underrelaxation factor
$\beta_j^i$ = cofactor of J
$\lambda$ = nondimensional moment
$\lambda_m$ = time-averaged $\lambda$
$\delta$ = axial distance between pump and turbine
$\delta n$ = distance from wall
$\epsilon$ = dissipation rate
$\zeta_d$ = d/$D$
$\zeta_B$ = B/$D$
$\zeta_\delta$ = $\delta/D$
$\mu$, $\nu$ = dynamic and kinematic viscosity respectively
$\mu_t$, $\nu_t$ = turbulente dynamic and kinematic viscosity, respectively
$\rho$ = density
$\sigma_k$, $\sigma_\epsilon$ = constants in k-$\epsilon$-turbulence model
$\omega_j^i$ = difference operator in momentum equations defined in Eq. (2)
$\Omega$ = angular velocity

**Indices**

$nb$ = neighbor, $nb$ = $E$, $W$, $N$, $S$, $T$, $B$
$N$ = neutral point or line
$P$ = center point of a control volume; pump
$r$ = radial
$T$ = turbine
$W$ = wall

the eddy viscosity concept. The equations in body-fitted coordinates using Cartesian velocity components are written in a nondimensional form for a coordinate system rotating with a constant angular velocity $\Omega_P$:

Continuity equation:

$$\frac{\partial U_i}{\partial x_i} = 0 \tag{1}$$

Momentum:

$$\mathrm{J}\frac{\partial u_k}{\partial t} + \frac{\partial}{\partial x_i}\left[s \cdot U_i u_k - \frac{\nu_{\text{eff}}}{\mathrm{J}\cdot\mathrm{Re}}\left(B_j^i \frac{\partial u_k}{\partial x_j} + \beta_j^i \omega_k^j\right) + p\beta_k^j\right] = \mathrm{J}\cdot f_k \tag{2}$$

with

$$U_i = u_j\beta_j^i; \quad B_j^i = \beta_k^i\beta_k^j; \quad \omega_j^i = \frac{\partial u_i}{\partial x_k}\beta_j^k \tag{3}$$

Here, the Einstein summation convention is assumed. The curvilinear coordinates $x_1$, $x_2$, $x_3$ and the Cartesian coordinates $y_1$, $y_2$, $y_3$ are shown in Fig. 2. The Cartesian velocity components $u_k$, k = 1, 2, 3 are nondimensionalized by $U_o = (\Omega_P - \Omega_T)\cdot D$, $\Omega_P$ and $\Omega_T$ denote, respectively, the angular velocity of the pump and turbine. $\beta_j^i$ is the cofactor in the Jacobian J of the coordinate transformation $y_i = y_i(x_j)$. $f_k$ is the Cartesian component of the Coriolis force $\mathbf{f} = 2\mathbf{u} \times \mathbf{j}$. $p$ stands for the reduced pressure, which includes the static pressure, the influence of the centrifugal acceleration and the turbulent fluctuation pressure.

The dimensionless parameter in Eq. (2) is the Reynolds number Re, which is defined with a reference velocity $\Omega_P D$:

$$\mathrm{Re} = \frac{\rho(\Omega_P \cdot D)D}{\mu} = \frac{\rho\Omega_P D^2}{\mu} \tag{4}$$

$s$ is the nondimensional slip between the pump impeller and the turbine, which is defined as:

$$s = 1 - \frac{\Omega_T}{\Omega_P} \tag{5}$$

$\nu_{\text{eff}}$ is the nondimensional effective dynamic viscosity:

$$\nu_{\text{eff}} = \nu_t + 1 \tag{6}$$

The nondimensional turbulent viscosity $\nu_t$ is given by:

$$\nu_t = s^2 \cdot \mathrm{Re}\, c_\mu \frac{k^2}{\epsilon} \tag{7}$$

Instead of the Reynolds number and the nondimensional slip one can define as dimensionless parameters the Ekman number

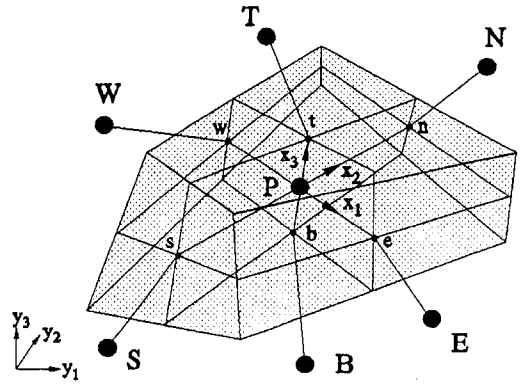


Fig. 2 Three-dimensional control volume and nomenclature

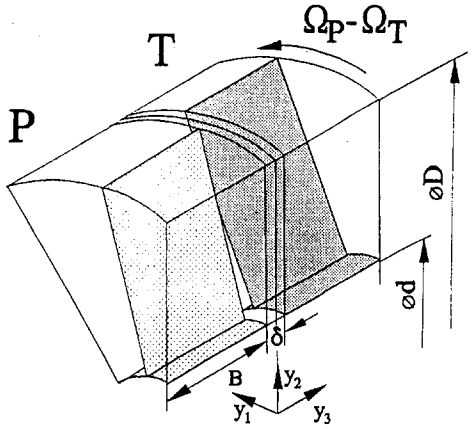


Fig. 3 Computational domain: *P*—pump, *T*—turbine, Ω—angular velocity; $\zeta_d = d/D$, $\zeta_B = B/D$, $\zeta_\delta = \delta/D$

$= \nu/\Omega_P D^2$ and the Rossby number which for the present case will be the same as the slip, see Kost et al. (1994).

The turbulence kinetic energy $k$ is nondimensionalized by $U_o^2$ and its dissipation $\epsilon$ by $U_o^2\Omega_P$. They are computed by using the standard k-$\epsilon$ model of Launder and Spalding (1979) in body-fitted coordinates:

$$\mathrm{J}\frac{\partial k}{\partial t} + \frac{\partial}{\partial x_i}\left[sU_i k - \frac{\nu_t}{\mathrm{J}\cdot\mathrm{Re}}\left(B_j^i \frac{\partial k}{\partial x_j}\right)\right] = \mathrm{J}(G - \epsilon) \tag{8}$$

$$\mathrm{J}\frac{\partial \epsilon}{\partial t} + \frac{\partial}{\partial x_i}\left[sU_i \epsilon - \frac{\nu_t}{\mathrm{J}\cdot\mathrm{Re}}\left(B_j^i \frac{\partial \epsilon}{\partial x_j}\right)\right] = \mathrm{J}\left(c_1 \frac{\epsilon}{k} G - c_2 \epsilon^2/k\right) \tag{9}$$

$G$ denotes the production rate of $k$, which is given by:

$$G = \frac{\nu_t}{\mathrm{Re}\cdot\mathrm{J}^2}\left(\frac{\partial u_i}{\partial x_j}\beta_j^n + \frac{\partial u_j}{\partial x^m}\beta_i^m\right)\left(\frac{\partial u_i}{\partial x^n}\beta_j^n\right) \tag{10}$$

The standard constants are employed:

$$c_\mu = 0.09,\ c_1 = 1.44,\ c_2 = 1.92,$$

$$\sigma_k = 1.0,\ \sigma_\epsilon = 1.3$$

**2.2 Boundary Condition.** The analysis of the flow field in fluid couplings with rectangular meridional shape is limited to one pitch by assuming equal number of blades in the pump impeller and in the turbine and by prescribing periodic boundary conditions at the boundary surfaces in the circumferential direction of the computational domain (cf. Fig. 3). Since the geometric form of the blades is simple, it is possible to use one grid block for the calculation.

The blades of the turbine runner are treated as internal obstacles moving relative to the computational domain. Figure 4 shows a sketch of this procedure. The timestep is determined by the grid resolution in the circumferential direction. This procedure is suitable to avoid the problems arising from matching the flow quantities due to patched or overlaid grids, which move relative to each other, see Rai (1989). But it is not suitable for complex geometric form, e.g. torque converters.

Except the boundary surfaces in the circumferential direction the other boundaries are walls. The wall functions given by Launder and Spalding (1979) are employed to describe the boundary condition along the walls of the pump impeller and

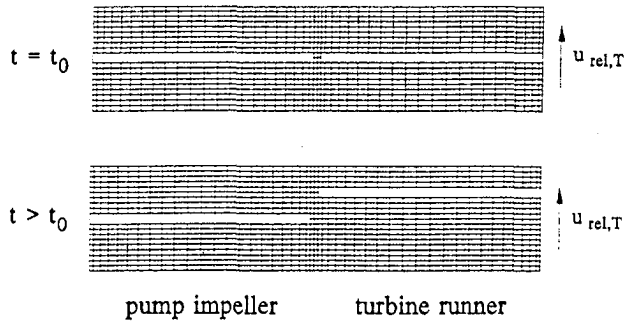


**Fig. 4 Sketch of the relative movement of the turbine blade through computational domain in the circumferential cross-section ($r$ = constant); arrow: direction of the relative velocity of the turbine $u_{rel,T}$**

the turbine. The velocity vectors at the walls are described by the no slip condition:

$$\mathbf{u}_w = \begin{cases} \mathbf{0}, & \text{pump impeller} \\ -(\mathbf{j} \times \mathbf{r}), & \text{turbine runner} \end{cases} \tag{11}$$

## 3 Method of Solution

Using Cartesian velocity components the basic equations are discretized by employing a finite-volume scheme. The flow domain is subdivided into a finite number of control volumes (CV). All dependent variables are defined in the centerpoint $P$ of the CV (cf. Fig. 2 for grid arrangement and nomenclature). Integration of the momentum Eqs. (2) for each CV leads to a balance equation of momentum fluxes through the CV faces and volumetric sources. The diffusive part of the momentum fluxes can be obtained by assuming linear variation of the variables between adjacent grid points. Evaluation of the convection fluxes requires discretization schemes for interpolating the variable values at the CV faces from their nodal values.

In the present code, the convective fluxes are split into an implicit part which is obtained by first-order upwind differencing, and an explicit part containing the difference between the second-order accurate central differencing scheme and the upwind approximation. This technique originally suggested by Khosla and Rubin (1979) is known to enhance the stability of the iterative solution algorithm. The resulting finite volume equation for variable $\phi$ can then be written in general form:

$$\frac{a_P \phi_P}{\alpha_\phi} = \sum a_{nb}\phi_{nb} + b_\phi^* + \frac{1-\alpha_\phi}{\alpha_\phi} a_P \phi_P^* \tag{12}$$

where the coefficients $a_{nb}$ represent the combined convection and diffusion effects and $b_\phi^*$ contains the discretized source terms (i.e., transient term, pressure gradient, and Coriolis term) and explicitly treated parts of the convection and diffusion fluxes.

Since the equations are nonlinear and strongly coupled by the convective and Coriolis term, for the convergence of the iterative solution procedure under-relaxation of variable changes ($\phi_P - \phi_P^*$) with a factor $0 < \alpha_\phi \leq 1$ is necessary in order to enhance the diagonal dominance of the coefficient matrix.

At each timestep, the velocity, the pressure, the k and $\epsilon$ fields are interactively calculated with the SIMPLEC algorithm of Van Doormal and Raithby (1984). In order to avoid an oscillatory pressure field due to the nonstaggered variable arrangement a special interpolation has been used to determine the mass fluxes through CV faces from the adjacent CV-centered quantities, see Rhie and Chow (1983). The pressure and velocities are coupled through a pressure correction equation, which is of the form of Eq. (12).

The strongly implicit procedure (SIP) of Stone (1968) is used here to solve the discretized equations. Within each SIMPLEC procedure only one iteration is performed for the momentum, k and $\epsilon$ equations, and the pressure-correction equation is iterated (inner iteration) until the residual norm is reduced by a factor of $\frac{1}{5}$ or the maximum 25 iterations (inner iteration) are reached.

After the inner iterations next iteration for the momentum, k and $\epsilon$ equations are performed. The iterative convergence was achieved when the sums of residue of each equation became less than $10^{-3}$. Now the new pressure, velocity and k and $\epsilon$ fields are obtained for the new time step. The computations for the next time step can be started. For this time step the relative position of the pump and turbine is changed by a grid. A periodic solution is obtained when the flow field in every relative position of the pump and turbine corresponds to the flow field of the previous period. This generally needs computations in five successive geometric periods. With the present code the convergence for steady laminar flows in a 90 deg bend and in a diffusor history has been investigated and compared with multigrid convergence, see Bai Li et al. (1993). Multigrid convergence acceleration for the present computation has been planned for future. The present computations needed 200 outer iterations for each time step.

## 4 Results and Discussion

With the simulated velocity feld the torque can be calculated. Using moment of the momentum theorem, the torque can be written as:

$$M = \frac{d\mathbf{L}}{dt} = \frac{\partial \hat{L}}{\partial t} + \int_A \rho(\mathbf{r} \times \mathbf{c}) d\dot{V} \tag{13}$$

with

$$\hat{L}(t) = \int_V \rho(\mathbf{r} \times \mathbf{c}) dV$$

The substantive derivative of Eq. (13) has been divided into an unsteady part of the transmitted torque which is the result of local unsteadiness of the velocity field and a convective part caused by the change of the moment of momentum experienced by the fluid between the entrance and exit of the impeller. The torque transmission coefficient $\lambda$ of a fluid coupling is defined as:

$$\lambda = \frac{M(t)}{\rho \Omega_P D^5} \tag{14}$$

and the mean value of the torque transmission coefficient $\lambda_m$ can be obtained by an integration of $\lambda$ over the time period.

Computations have been performed for different dynamical parameters Re and $s$ with the following geometrical parameters (cf. Fig. 3):

$$\zeta_d = d/D = 0.326, \quad \zeta_B = B/D = 0.281, \quad \zeta_\delta = \delta/D = 0.01;$$

number of the blades $Z = 24, 48$;

or

$$\zeta_d = d/D = 0.337, \quad \zeta_B = B/D = 0.267, \quad \zeta_\delta = \delta/D = 0.01;$$

number of the blades $Z = 12$;

The typical number of grids used is $35 \times 28 \times 56$. The typical computation time for one calculation on an IBM RISC System/6000 530H computer is about 72 CPU hours.

In order to estimate the numerical error the grid dependance of the results we computed the flow with 24288 cells (grid 1), 54880 cells (grid 2), and 76440 cells (grid 3) for the same flow condition. The time averaged nondimensional moments $\lambda_m$

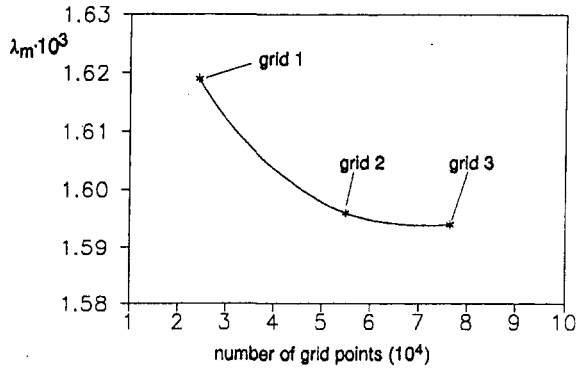


**Fig. 5 Nondimensional time-averaged moment $\lambda_m$ versus grid points; geometry: $\zeta_d = 0.326$, $\zeta_B = 0.281$, $\zeta_\delta = 0.01$, $Z = 24$, Re $= 6.7 \cdot 10^6$, $s = 0.05$**

computed from there three grids are plotted in Fig. 5. The difference in $\lambda_m$ between grid (2) and grid (3) is 0.13 percent and difference in $\lambda_m$ between grid (1) and grid (2) is 1.44 percent. An extrapolation of the curve in Fig. 5 to grid-independent results shows that the results of grid (2) will differ from grid independent value by 2.7 percent. In the present work, we have used for the systematic study the grid (2).

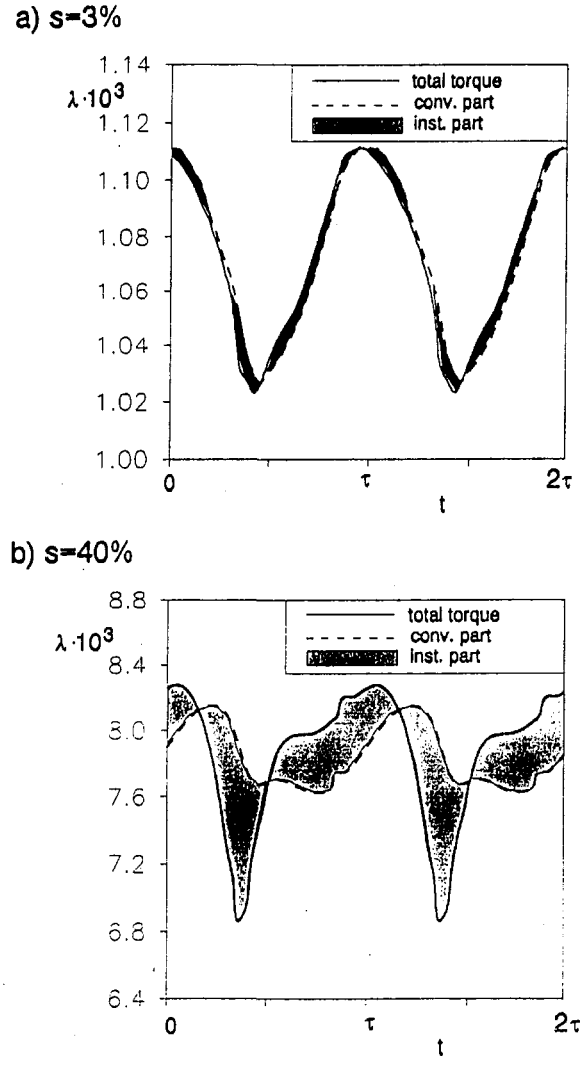


**Fig. 6 Nondimensional moment $\lambda$ as function of nondimensional time; geometry: $\zeta_d = 0.326$, $\zeta_B = 0.281$, $\zeta_\delta = 0.01$, $Z = 24$, Re $= 6.7 \cdot 10^6$**

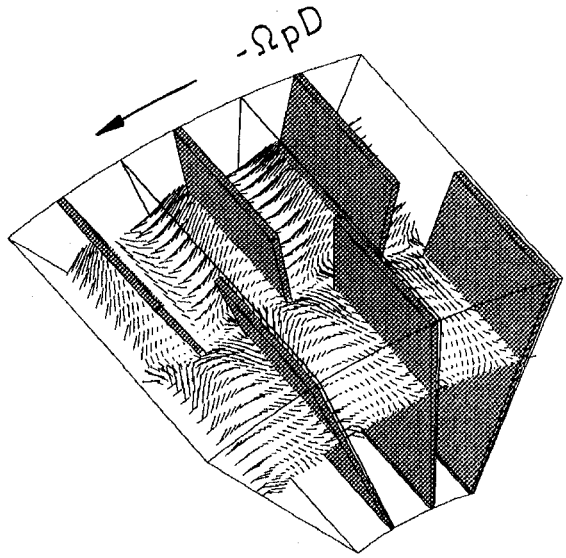


**Fig. 7(*a*) Instantaneous velocity (relative to pump system) in circumferential cross-section at neutral point $r_N/D = 0.370$ for Re $= 6.7 \cdot 10^6$, $s = 1 - \Omega_T/\Omega_P = 0.40$; arrow: direction of the absolute rotation of the coupling; left: pump; right: turbine; geometry: $\zeta_d = 0.337$, $\zeta_B = 0.267$, $\zeta_\delta = 0.01$, $Z = 12$**

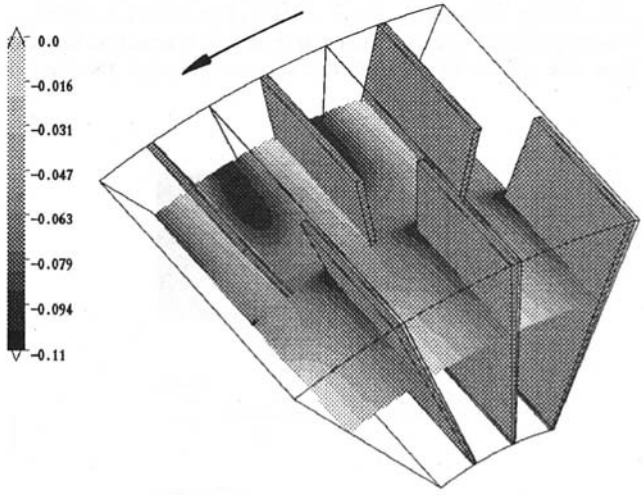


**Fig. 7(*b*) Reduced pressure for the case of Fig. 7(*a*)**

Due to the periodicity of the rotation of the turbine runner in relation to the pump impeller the flow is periodic. Figure 6 shows the time history of the moment of momentum over a time period for Re $= 6.7 \cdot 10^6$ and the slip $s = 0.03$ and 0.4, respectively. In both cases of slip minimum moments are obtained when turbine blades come to alignment with the pump blades. In this case the interference between the vanes and the influence of the impact of fluid with the next row of turbine blade are minimum.

For the case of $s = 0.03$ (Fig. 6(*a*)) the amplitude is approximately 8 percent of the average value whereas for $s = 0.4$ the amplitude becomes 20 percent of the average value. If the amplitude is a measure of the degree of unsteadiness, it increases with the slip. For small slip ($s = 0.03$) the local change of momentum with time is small.

The influence of the unsteady part on $\lambda$ is negligible for very small value of $s$ (Fig. 6(*a*)). For higher slip ($s = 0.4$) the influence of the local unsteadiness is large. This influence manifests itself not only on absolute value but also causes a phase shift. For $s = 0.4$ the local change of instantaneous flow shows substantial influence on moment (Fig. 6) in comparison to $s = 0.03$. With $s = 0.4$ both the absolute value of the maximum

moment as well as the instantaneous changes become noticeable.

Figure 7($a$) shows instantaneous velocity vectors relative to the rotating pump system in the circumferential cross section at the neutral plane ($r = r_N = 0.370$) in a three dimensional representation. The neutral plane denotes the zero velocity point between the entrance flow and the exit flow of a blade channel. The shading of the Fig. 7($b$) denotes the induced pressure. We notice that the fluid flows from the pressure side of the turbine to the suction side of the pump. The flow in the pump is directed radially outward and in the turbine inward.

Figure 8 shows time average velocity vectors in a circumferential cross section ($r/D$ = const.) through the turbine in area of inflow to the turbine. Since the flow from the pump to the turbine is not aligned, the flow tears at the leading edge forming a separation bubble at the suction side of the blade. This separation bubble hinders the circulating flow between the pump and the turbine and reduce the torque. For small $s$ (Fig. 8($a$)) the separated bubble is small, hence its effect on flow is also weak. For large $s$ ($s = 0.4$, Fig. 8($b$)) the bubble is large with a marked influence on flow.

Figure 9 shows the velocity fields in the axial (blade-to-blade) cross sections. The velocity vectors are displayed relative to the angular velocity of the pump. Due to the centrifugal force the main flow is directed radially outward. The Coriolis force, which affects transversally the flow, results the noneven pressure change in the flow. For $s = 0.05$ (Fig. 9($a$)) a secondary vortex (passage vortex) has been therefore formed on the suction side of the blade near the shroud. Through the loss of

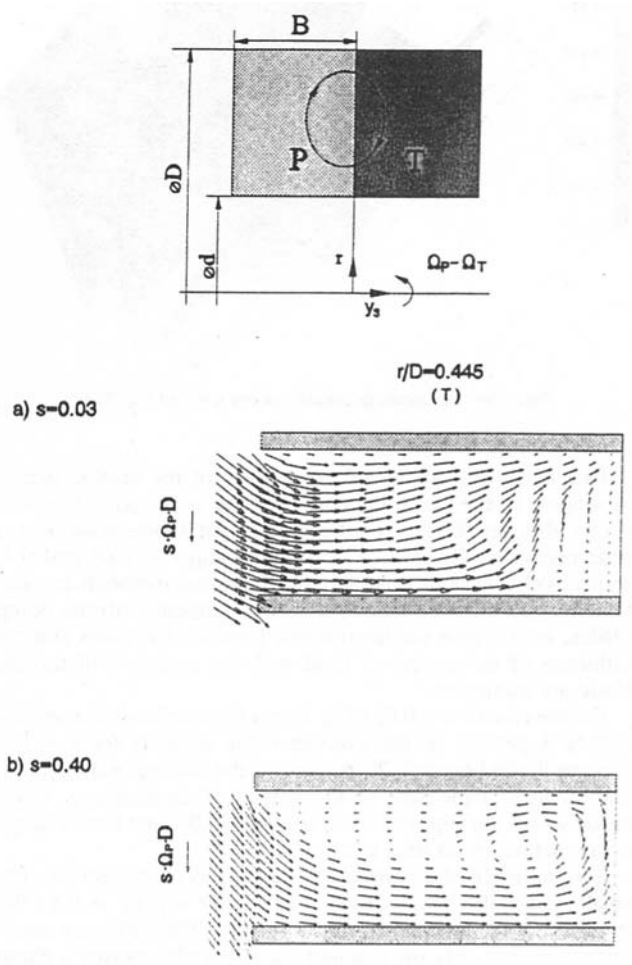


**Fig. 8 Mean velocity field (relative to turbine system) in a circumferential cross-section in the turbine blade for Re = $6.5 \cdot 10^6$, (*a*) $s = 0.03$, (*b*) $s = 0.40$; geometry: $\zeta_d = 0.326$, $\zeta_B = 0.281$, $\zeta_\delta = 0.01$, $Z = 24$**

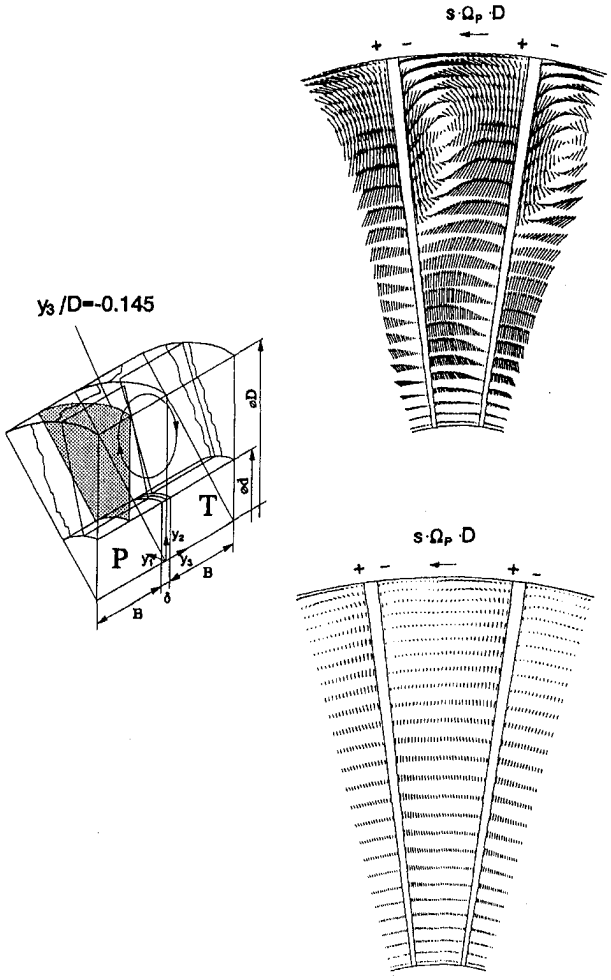


**Fig. 9 Mean velocity fields (relative to pump system) in an axial cross-section for Re = $6.7 \cdot 10^6$ and (*a*) $s = 0.05$, (*b*) $s = 0.40$; ±: pressure and suction sides of the blades; geometry: $\zeta_d = 0.326$, $\zeta_B = 0.281$, $\zeta_\delta = 0.01$, $Z = 24$.**

kinetic energy of the vortex and the mixing course of the vortex with the primary circular flow, the mechanical energy of the fluid is lost, so that the circular flow is delayed and the torque transmission is hindered. For $s = 0.4$ (Fig. 9($b$)) the secondary vortex is hardly visible. In contrast to $s = 0.05$ the pressure difference the turbine and the pump is much larger for $s = 0.4$. This naturally increases the rate of circulation. The coriolis force is not strong enough to divert the fluid to the pressure side, hence no secondary flow appears.

Figure 10 compares computed axial velocity contours with the experimental results in a coupling with 24 vanes for Re = $6.7 \cdot 10^6$ and $s = 0.8$ and 0.4. The experimental results have be obtained by Middelmann (1992). Shaded area indicates flow from the turbine to the pump. Because of different plotting in experiments and numerics the shading appears different. The numbers of the isolines show the ratio of the local velocity $c_m$ and the volume averaged velocity $\bar{c}_m$. The agreement between experiment and numeric is both qualitatively and quantitatively very good. The flow structures for the two cases of slip are qualitatively same. For $s = 0.4$ the maximum $c_{m,\max}$ is 2.9 $\bar{c}_m$. For $s = 0.8$ the flow around the leading edge of the vane is indicated by the change of direction in the pressure side. Figure 10 also shows the formation of the separation zone in the upper area of the turbine vanes. The separated bubble reduces the area for the circulatory flow and thus accelerates the circulatory flow. The position of the neutral lines (0-line) or lines of zero velocity as obtained from experiments and computations agree well.

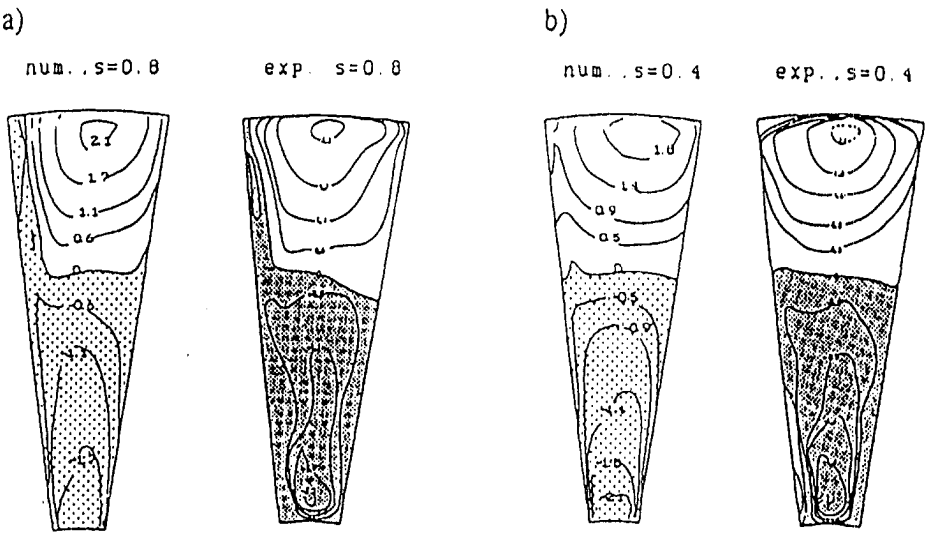


**Fig. 10 Comparison of prediction with experiment of Middelmann (1992): contours of the mean axial velocity in the gap between pump and turbine for Re = $6.7 \cdot 10^6$, *a*) $s = 0.8$, *b*) $s = 0.4$; shaded area: negative velocity direction (from turbine to pump)**

Similar good agreement is found in the position and form of the lines of maximum velocity. However, near differences in the computed and experimental flow structure appear. This is possibly due to the inadequacy of the k-$\epsilon$ turbulence model. The computed flow fields for different slips were used in Eq. (3) to calculate the torque for two configurations one with 24 vanes and the other with 48 vanes. Figure 11 shows the operating curves for $\lambda_m$ against $s$ for $z = 24$ from experiments of Middelmann (1992) and present simulation. We plotted the results of laminar simulation of Kost et al. (1994) for comparison. For the case of $z = 48$, Fig. 12 shows $\lambda_m$ against $s$. In the region of $0 < s \leq 0.4$ the agreement between the experiment and turbulent computations is quite good. The maximum difference is less than 10%. In the region of $0.4 \leq s \leq 1.0$ the difference between the experiment and the turbulent computations can be 20 percent. With large slip, the degree of turbulence and unsteadiness of the flow increase and the k-$\epsilon$-model probably is not any more adequate. Comparison of Figs. 11 and 12 hints that the unsteadiness can be dampened by increasing the number of vanes.

## 5 Concluding Remarks

Flow in fluid couplings has been simulated. The good agreement from the present study and the experiment in both for the local velocity and for the operating characteristics indicates that for the complicated flow in fluid couplings modeling by the standard k-$\epsilon$ turbulence model delivers viable results.

Flow structures in fluid couplings have been analysed to explain the physical process of the torque transmission. The unsteady torque transport shows that for small slip nonsteadiness results from the convective part whereas with large slip local change becomes stronger than the convective part. Increasing the number of vanes one can dampen nonsteadiness.

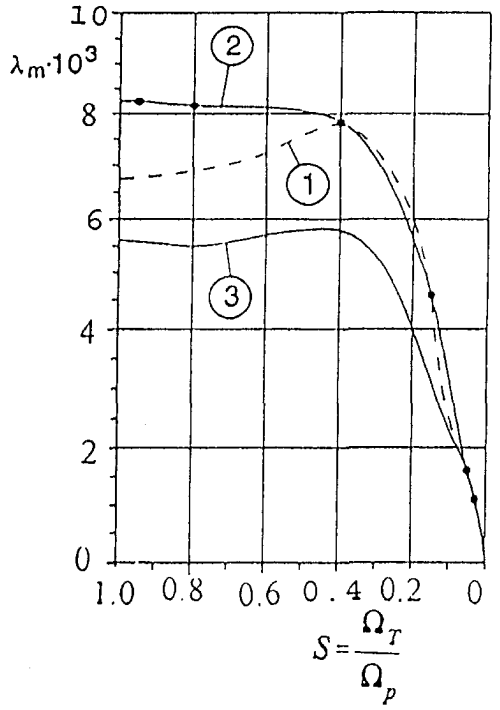


**Fig. 11 Operating characteristics for a coupling with $Z = 24$; $\lambda_m$—mean torque transmission coefficient; geometry: $\zeta_d = 0.326$, $\zeta_B = 0.281$, $\zeta_\delta = 0.01$; 1—experiment of Middelmann (1992), 2—turbulent simulation: Re = $6.7 \cdot 10^6$, 3—laminar simulation of Kost et al. (1994): Re = $6.7 \cdot 10^6$**

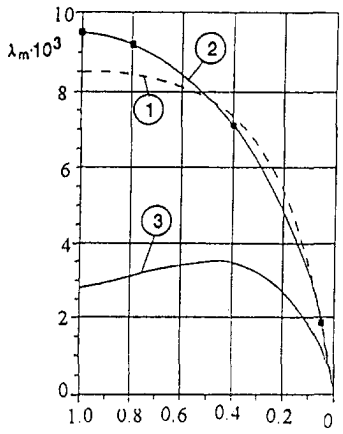


**Fig. 12 Operating characteristics for a coupling with $Z = 48$; geometry: $\zeta_d = 0.326$, $\zeta_B = 0.281$, $\zeta_\delta = 0.01$; 1—experiment of Middelmann (1992), 2—turbulent simulation: Re = $6.7 \cdot 10^6$, 3—laminar simulation of Kost et al. (1994): Re = $6.7 \cdot 10^6$**

Secondary flow leads to loss in torque. Two types of secondary flow may appear. With small slip the vortex in axial cross section is strong. With large slip the in cylindrical cross section becomes important.

## Acknowledgment

The authors gratefully acknowledge this support of the Deutsche Forschungsgemeinschaft.

## References

Bai, L., 1995, "Numerische Untersuchung von turbulenten Strömungen in hydrodynamischen Kupplungen," PhD thesis Ruhr-Universität Bochum, Fortschrittberichte, Reihe 7, Nr. 267, Verlag des Vereins Deutscher Ingenieure, Düsseldorf, Germany.

Bai, L., Fiebig, M., Mitra, N. K., and Kost, A., 1993, "Multigridverfahren zur Berechnung von 3D Strömungen in komplexen Geometrien," *Zeitschrift für angewandte Mathematik und Mechanik,* Vol. 73, pp. T554–T556.

Bai, L., Blomerius, H., Mitra, N. K., and Fiebig, M., 1994, "Numerical Simulation of Unsteady Incompressible 3D Turbulent Flow in Fluid Coupling with Inclined Blades," presented in ASME—Winter Annual Meeting, Chicago, published in DSC—Vol. 55-2, pp. 609–616.

Kost, A., Mitra, N. K., and Fiebig, M., 1994, "Numerical Simulation of 3D Periodic Flow in Fluid Couplings," *Acta Mechanica,* Vol. 4, pp. 199–205.

Khosla, P. K., and Rubin, S. G., 1979, "A Diagonally Dominant Second-Order Accurate Implicit Scheme," *Computers & Fluids,* Vol. 2, pp. 207–209.

Lakshminarayana, B., 1991, "An Assessment of Computational Fluid Dynamic Techniques in the Analysis and Design of Turbomachinery—The 1990 Freeman Scholar Lecture," ASME JOURNAL OF FLUIDS ENGINEERING, Vol. 113, pp. 315–352.

Langlois, H. P., 1979, "Hydrodynamic Adjustable-Speed Drives," *Power Transmission Design,* Vol. 21, pp. 60–62.

Launder, B. E., and Spalding, D. B., 1974, "The Numerical Computation of Turbulent Flow," *Computer Methods in Applied Mechanics and Engineering,* Vol. 3, pp. 269–289.

Middelmann, V., 1992, "Analyse des Systemverhaltens Hydrodynamischer Kupplungen bei Variation der Kreislaufgeometrie," PhD thesis, Ruhr-Universität Bochum.

Rai, M. M., 1989, "Three-Dimensional Navier-Stokes Simulation of Turbine Rotor-Stator-Interaction," *Journal of Propulsion and Power* (American Institute of Aeronautics and Astronautics), Vol. 5, pp. 305–319.

Rhie, C. M., and Chow, W. L., 1983, "Numerical Study of the Turbulent Flow Past an Airfoil with Trailing Edge Separation," *American Institute of Aeronautics and Astronautics Journal,* Vol. 21, pp. 1525–1532.

Stone, H. L., 1968, "Iterative Solution of Implicit Approximations of Multidimensional Partial Differential Equations," *Journal Numerical Analysis* (SIAM), Vol. 5, pp. 530–558.

Van Doormaal, J. P., and Raithby, G. D., 1984, "Enhancement of the SIMPLE Method for Predicting Incompressible Fluid Flows," *Numerical Heat Transfer,* Vol. 7, pp. 147–163.

# Effects of Efficiency Techniques on Accuracy of Dynamic-Overlapped Grids for Unsteady Flows

**Guan-Wei Yen**
Former Graduate Student.

**Oktay Baysal**
Professor and Eminent Scholar.
Fellow ASME

Aerospace Engineering Department,
Old Dominion University,
Norfolk, VA 23529-0247

*There is a strong need for advancements to compute unsteady flows involving moving boundaries and bodies. Currently, there appear to be two dynamic approaches and their variants proposed for this problem: unstructured and domain decomposition methods. The present objective was to further explore the overlapped grids when it was enhanced with several enabling and efficiency techniques. Their effect on the accuracy was studied primarily from a qualitative point of view. Unsteady Euler equations were solved by a characteristic-based alternating-direction-implicit scheme on overlapped subdomains capable of moving with respect to each other. Initially, the errors due to discretization, Courant number, and interpolations, were studied by solving the Riemann problem and comparing with its exact solution. It was concluded, that a second- or higher-order method, temporally and spatially, was needed even in the dynamic interpolation regions. Secondly, the effects of intermediate grids and diagonal inversions were demonstrated by simulating the 2-D flowfield history of a store separating from a wing section along a prescribed trajectory. For computational efficiency, using approximate diagonal inversions for the discrete equations produced less accurate but acceptable results. However, to ease the grid generation, overlaying an intermediate subdomain in a region of high flow gradients had significant impact on the accuracy.*

## Background

A brief review of the literature on computational fluid dynamics (CFD) should reveal its unpreparedness as far as unsteady flows are concerned. This is even more so for unsteady flows involving a complex configuration with its components in relative motion. Beyond and above the issues of algorithms for steady flows, three more constraints become active for unsteady algorithms: 1) time accuracy, 2) time-dependent discretization of the physical domain for moving- or relative-moving-boundary problems, 3) significantly improved computational efficiency. What follows are brief comments on each of these issues.

The accuracy of a CFD method may be obtained either formally by inspecting the leading truncated term in a Taylor expansion, or by a Richardson extrapolation (Celik and Zhang, 1995), or by a systematic evaluation of the truncation error by grid refinement (Roache, 1995). However, since the methods in question here are often used for nonlinear equations on nonuniform grids to resolve nonlinear physical phenomena, such accuracy checking methods may prove to be insufficient. Further, the implementation and accuracy of the boundary conditions may not be fully consistent with the method. Then, a qualitative demonstration of accuracy through comparisons with exact solutions, or experimental data with well established uncertainty limits, or independently obtained numerical benchmark solutions, become very practical. For time accuracy, in particular, these alternatives may either be lacking or some of them may even be irrelevant. As for computational efficiency, since explicit methods are too restrictive in the size of the time steps that they can use, and since most of the implicit CFD algorithms are first-order accurate in time, it is important to study the higher-order accuracy for implicit methods (Pulliam, 1993, Zhang et al., 1994).

For the relative moving boundary problems, currently there appear to be two competing approaches proposed: dynamic unstructured method (Singh and Baysal, 1995) and dynamic domain decomposition method ($D^3M$). When the latter was recently used in simulating a 3-D store separation by Yen and Baysal (1995), an acute need was strongly sensed to further explore some issues related to its accuracy and efficiency. To this end, Meakin (1994) had conducted a series of 2-D computational experiments, but all the subdomains in these cases were forced to engage in the same motion, i.e., no relative motion, and a central finite-difference method was used. Hence, in the present investigation, several enabling and efficiency techniques were studied using $D^3M$ and solving the unsteady Euler equations by a characteristic-based, alternating-direction-implicit, finite-volume scheme on overlapped subdomains capable of moving with respect to each other.

## Synopsis of Methodology

The unsteady, compressible, and inviscid flow equations (Euler) are solved using the implicit, finite-volume, upwind algorithm, described by Thomas et al. (1990) for static bodies, and its extension to relative-moving-boundary problems by Baysal and Yen (1991). The consistency, stability, accuracy, and validation of the "baseline" scheme are well documented in the literature and, therefore, are not repeated herein. Flux-difference splitting is used to construct the formally up to third-order-accurate spatial differences. Time integration is performed by one of the Euler formulas, all of which may be implemented as a two-parameter family (Beam and Warming, 1978). After applying the time linearization, the coefficient matrix is approximately factored, with each factor being solved by a 4-by-4

Contributed by the Fluids Engineering Division of THE AMERICAN SOCIETY OF MECHANICAL ENGINEERS and presented at the ASME/JSME Fluids Engineering Conference, August 13–18, 1995, Hilton Head, SC in *Unsteady Flows 1995*, FED Vol. 216. Manuscript received by the Fluids Engineering Division February 12, 1996; revised manuscript received May 2, 1997. Associate Technical Editor: P. M. Sockol.

block-tridiagonal algorithm. Hence, the "delta" form of the discretized ($\Delta$) Euler equations is,

$$\left[\frac{I}{J\Delta t}+\frac{\theta}{1+\alpha}\left[\Delta_{\xi^1}(\partial_q E_1)\right]\right]\times\left[\frac{I}{J\Delta t}+\frac{\theta}{1+\alpha}\times\left[\Delta_{\xi^2}(\partial_q E_2)\right]\right]\times\Delta Q^n=\left(\frac{I}{J\Delta t}\right)\text{R.H.S.}, \quad (1)$$

where

$$\text{R.H.S.}=-\frac{1}{1+\alpha}\left[\Delta_{\xi^1}E_1+\Delta_{\xi^2}E_2\right]+\frac{\alpha}{1+\alpha}\Delta Q^{n-1}+\vartheta\left[\left(\theta-\frac{1}{2}-\alpha+lf\right)\Delta t^2,\ \Delta t^3,\ \Delta x_1^3,\ \Delta x_2^3\right]. \quad (2)$$

$Q$ and $E$ are the vectors of conserved variables and fluxes, respectively. The last term denotes the order of magnitude of the leading truncated term. Due to the multidimensional nature of the problem, the nonuniform grids, and the boundary condition implementations, the spatial accuracy may not attain its formal value, but it is at least second-order. On the other hand, the temporal accuracy depends on the values of the parameters $\alpha$ and $\theta$, and the magnitude of the neglected terms in the linearization and factorization, which are represented by $lf$. For $\alpha = 0$ and $\theta = 1$, the truncated term is second-order; but for $\alpha = \frac{1}{2}$ and $\theta = 1$, it is $\vartheta[lf\cdot\Delta t^2, \Delta t^3]$. When the second-order flux Jacobians and the product of the first-order flux Jacobians are small, $lf$ tends to zero. Hence, the method approaches temporal second-order accuracy.

A diagonal approximation (Pulliam and Chaussee, 1981) of a spatial factor in Eq. (1) may be obtained as follows:

$$\left[\frac{I}{J\Delta t}+\left[\Delta_{\xi^1}(\partial_q E_1)\right]\right]\cong T_{\xi^1}\left[\frac{I}{J\Delta t}+\left[\Delta_{\xi^1}^{-}\Lambda^{+}+\Delta_{\xi^1}^{+}\Lambda^{-}\right]\right]T_{\xi^1}^{-1} \quad (3)$$

where $\Lambda^{\pm}=(\Lambda\pm|\Lambda|)/2$ are the diagonal eigenvalue matrices and $T^{\pm}$ are the right eigenvectors of the flux Jacobian $A\equiv\partial_q E_1$. Then, due to the repeated eigenvalues, only scalar diagonal inversions, rather than the block inversions, are needed in each direction. Hence, the computational cost should be notably reduced (about 40 percent for single and static grid simulations). However, as it will also be explored with the present results, this approximation may reduce the temporal accuracy and give shock computations a nonconservative feature, that is, slight error in shock speeds.

**Dynamic Overlapped Grids.** The discretized flow equations are solved on a composite grid consisting of overlapped subdomain grids (Steger et al., 1983). These subdomains may be static (Baysal et al., 1991) or in relative motion (Baysal and Yen, 1991). By coupling this method with a trajectory algorithm, the dynamic-overlapped-grids mode of dynamic domain decomposition method, $D^3M$, (Yen and Baysal, 1995) was developed. The dynamic-multiblock and dynamic-zonal grid modes of $D^3M$ were not used in the present work. The motion of each subdomain grid is accounted for by the time-dependent curvilinear coordinate transformations, whereby the grid speeds are also determined:

$$\partial_t\xi^m=-\partial_t x_k\cdot\partial_{x_k}\xi^m,\quad m,k=1,2. \quad (4)$$

The term $\partial_t x_k$ is the grid speed for the physical domain, and it is of primary importance for unsteady aerodynamic problems involving moving boundaries.

Among the important issues in developing $D^3M$ are its accuracy and efficiency. $D^3M$ has several advantages in this regard. First, a subdomain and its cells are not deformed, therefore, the geometric conservation can be preserved (Thomas and Lombard, 1978). Second, this method can virtually calculate unlimited subdomains, and each subdomain may move independent from the others. Third, since the governing equations are written in an inertial frame of reference, all the primitive variables are absolute everywhere and at any time irrespective of the subdomain on which they are computed. Therefore, they can be transferred from one subdomain to another regardless of the relative motion between them. Finally, $D^3M$ may conceivably allow the use of different sets of flow equations and different solution techniques in different subdomains, provided that the interface boundary conditions are properly implemented.

It should be noted that dynamic overlapped grid approaches were independently developed for various applications by others, such as, Meakin (1994), Lijewski and Suhs (1994), Duque et al. (1995), Jordan et al. (1995), and Sahu and Nietubicz (1995).

**On Simulation Error.** The error of a CFD simulation may be due to the following, some of which may not be mutually exclusive: 1) modeling error, 2) dissipation and dispersion components of the discretization (or truncation) error, 3) domain dependency error, 4) time-linearization error, 5) approximate factorization error, 6) interpolation error of the domain decomposition, 7) error related to inappropriate boundary conditions or incomplete convergence, and 8) round-off error. Owing to their relevance to the present results, brief comments only on the dispersion and factorization errors, and a source of interpolation error are discussed next.

Due to the discretization error, simulated unsteady flows may propagate essentially in a dispersive medium. Since there is no converged solution achieved by a time-accurate marching procedure, the phase error can continue to accumulate, resulting in the group velocity of the motion to deviate significantly from its phase velocity. Also, the lack of an accurate method to control its direction causes the phase error to accumulate nonisotropically. Hence, the dispersion error becomes as important as the dissipation error for unsteady flows, mandating higher-order discretizations not only spatially but also temporally.

Factored implicit methods have been widely used because of their memory efficiency and numerical stability, which also has the advantage of rendering the efficiently solvable tridiagonal form. However, the factorization introduces an extra numerical error, which may be of the same order as the discretization error. In Eq. (1), the order of magnitude of $\Delta Q^n$ is $\vartheta(\Delta t)$; but, when a higher gradient is encountered, its order may rise to $\vartheta(1)$ (Beam and Warming, 1978). Consequently, the approximate factorization method may carry the second-order temporal error. Controlling the maximum Courant (CFL) number (around unity) of each cell is suggested in several reports (Ridder and Beddini, 1992, and Baysal et al., 1994) to minimize this error. Also implied in this suggestion is the adverse impact of the factorization on the numerical stability. On the other hand, others (e.g., Pulliam, 1993, Zhang et al., 1994) have suggested a subiteration time stepping procedure to remedy the problem.

An interpolation error arises from the information transfer across the subdomain interfaces. The type of interpolation should be chosen such that the overall accuracy is about the same order as the discretization error. To show this mathematically, consider a 1-D, $n$th-order differential equation,

$$\partial_\xi^n E=R(\xi,E). \quad (5)$$

To solve this problem on a composite grid that consists of two overlapped subdomains, $k$ and $k'$, for which the indices are $i$ and $j$, respectively, the $N_1$th-order-accurate discrete system of equations can be written as follows:

$$(D_+D_-)^{n/2}q_i^k=R_i+\vartheta(\Delta\xi_k^{N_1+1}), \quad (6)$$

where $q_i^k$ is the numerical solution in subdomain $k$. The $N_2$th-

order interpolation to the points in subdomain $k$ from the points in subdomain $k'$ can be represented in the following form:

$$q_i^k = \sum_j \alpha_{i,j}^k \cdot q_j^{k'} + \vartheta(\Delta\xi_{k'}^{N_2+1}) \tag{7}$$

where $q_j^{k'}$ is the numerical solution in subdomain $k'$ and $\alpha$ denotes the interpolation. The goal, therefore, is to make $N_2$ as close to $N_1$ as possible. It can be shown, that an interpolation formula with an overlap width given by $(0.25nN_1 + 1)$ is $N_1$-th-order-accurate, provided that the spatial step sizes are constant in the overlap region and that they are small compared to the width of the overlap region (Chesshire and Henshaw, 1990). Therefore, with the present upwind-biased scheme, to maintain the spatial second-order accuracy representation of scalar and vector quantities in a second-order differential equation (Eq. (1)), *two sets* of interpolation points are needed.

For moving subdomains, the impact of interpolation on temporal error and numerical stability has not been fully studied. One generator of this error is the increased ratio of those cells which receive their update *explicitly* (hence $\Delta t$ time lag) to the total number of cells, since in addition to the physical boundaries, the subdomain interfaces are treated explicitly. For the accuracy of the vector quantities in moving grids, and for relative-moving problems with more than two overlapping subdomains at a given point, there appears to be another source of phase error. This point is illustrated via an example below.

Consider two interpolation points, which belong to two different subdomains ($G_2$ and $G_3$) but close enough to each other to receive data from the same region of a third subdomain ($G_1$). The eigenvalues (characteristic wave directions) at any of these points are

$$\lambda_1 = U = u_k \cdot \partial_{x_k}\xi^m + \partial_t\xi^m$$

$$\lambda_{2,3} = U \pm a_\infty = u_k \cdot \partial_{x_k}\xi^m + \partial_t\xi^m \pm a_\infty. \tag{8}$$

For simplicity, let $m = 1\ (1 - D)$, then, by substituting Eq. (4), $\lambda_1$ is

$$\lambda_1 = U = u_1 \cdot \partial_{x_1}\xi^1 - \partial_t x_1 \cdot \partial_{x_1}\xi^1 = (u_1 - \partial_t x_1) \cdot \partial_{x_1}\xi^1. \tag{9}$$

Now, it is assumed that the velocity $u_1$ is transferred by a second-order interpolation and $\partial_{x_1}\xi^1 \approx 1$, but $G_2$ and $G_3$ have unequal grid speeds, $\partial_t x_1(G_2) \neq \partial_t x_1(G_3)$. Then, from Eq. (9), it can be seen that $\lambda_1(G_2) \neq \lambda_1(G_3)$. This results in the flow properties of these interpolation points to propagate in different directions; that is, a phase shift. Therefore, in addition to a second-order interpolation of the primitive variables, there is the issue of satisfying the correct transfer of grid speeds.

Finally, yet another possible source of error is related to the premise of current flux-difference methods (Thomas et al., 1990): solving the locally one-dimensional Riemann problem, where the directions of numerical fluxes are assumed to be normal to the present cell surfaces. However, if there are two non-similar grid topologies overlapped with each other, then the flow properties computed in different subdomains are likely to propagate in different characteristic directions. This may eventually require a grid-independent Riemann solver (Rumsey et al., 1991), which also would need to be practical to use.

## Demonstrative Cases

**Moving Shock Problem.** The classical Riemann problem of a moving normal shock inside a tube was considered, since it had an exact solution for the shock's amplitude to check dissipation and shock's speed to check dispersion. The nondimensional tube conditions were selected as:

velocity: shock = 2.00, upstream flow = 1.25,
downstream flow = 0.00

ratios across shock: pressure = 4.50, density = 2.67

downstream flow: pressure = 0.714, density = 1.000

Seven cases were selected to study the various effects and some of the computational details were tabulated (Table 1). In A.5–A.7, the Cartesian grid $G_1$ covered the tube's inside, and the much finer Cartesian grid $G_2$ was overlaid on $G_1$ for the shock region. Computations were started at the time when the shock reached the nondimensional axial location $x = 0.4$. The instantaneous pressure distributions along the centerline of the tube after 0.6 nondimensional time units ($t$) are plotted in Fig. 1. At this moment, the calculated exact values of the upstream and downstream pressures were 3.214 and 0.714, respectively, and the shock was at $x = 1.6$.

The adequacy of the global grid $G_1$ was established by comparing A.1 and A.2 and found out that the pressure distributions were almost identical (Fig. 1($a$)). The difference between A.1 and A.3 was their temporal accuracy. Although, there was almost no amplitude error for these cases, the shock location was underpredicted in A.3. Hence, temporal second-order accuracy was deemed necessary for an acceptable dispersion error. To demonstrate the effect of using a greater-than-unity CFL number, the global time step in A.4 was increased to 10 times that of A.1, such that the maximum CFL number was 6.0. Despite its correct prediction of the shock wave location, A.4 showed oscillations to wrongly predict the shock amplitude.

Cases A.5 and A.6 were computed on the same *composite* grid, but with different sets of interpolation points. Using the two-sets in A.5, a second-order data transfer across the subdomain interface (Eq. (7)) appeared to have been achieved (Fig. 1($b$)). Whereas, using one-set of interpolation points in A.6 could not preserve the pressure amplitude within the overlapped subdomain $G_2$.

A comparison of A.1, A.5 and A.7, shown in Fig. 1($c$), demonstrated the accuracy of using static overlapped grids (A.5 versus A.1) and dynamic ($G_2$ moving with the shock) overlapped grids (A.7 versus A.1 and A.5). All the cases displayed a good comparison of the shock speed and amplitude with the exact solution, despite rather benign fluctuations at the overlap region. This suggested that the interpolation error of the static and dynamic overlapped grids was about the same order of magnitude as the discretization error (dissipation and dispersion) of the baseline CFD algorithm.

To scrutinize the dynamic-overlapped grids further, the pressure contours and velocity vectors of A.7 at $t = 0.6$ were examined (Fig. 2). The computed shock wave appeared very close to the exact solution: a normal wave front from the top of the tube to its bottom, with crisper resolution on the finer $G_2$ grid. However, a close up view of the overlap region revealed the minor pressure fluctuations as the shock wave crossed the overlap boundary. This also manifested itself in a nonzero normal velocity component (maximum magnitude of 0.3). This numerical error was largely attributed to the deliberately exaggerated disparity in the sizes of the cells on either side of the interface. The numerical slope of the shock wave crossing the interface had two different values (Fig. 3). Therefore, the higher pressure (coarser mesh) "pushing" the flow into the lower pressure area (finer mesh), generated the physically unexpected normal flow. However, this error did not increase with time.

The unit CPU time and the used memory for each case are also reported in Table 1. The unit processing time decreased by 2 percent for A.2 due to longer data vector lengths (more grid points), but the memory increased almost linearly with the grid size. The time and memory decrease in A.3 were due to the lesser number of terms in Eqs. (1) and (2) for the first-order temporal computations. The additional grid in A.5–A.7 increased the memory and the processing time. Although the increase in time was not significant for the static cases (less than 8 percent), it was so for the dynamic grid case, which more than doubled.

**Table 1 Computational details for the moving shock problem**

| Case | Grid type | Grid size $G_1/G_2$ | $D^3M$ | Sets of IP | Accuracy $\vartheta(\Delta t)$ | $(\Delta x)_{\min}$ | $(\mathrm{CFL})_{\max}$ | CPU time $\mu$s/step/cell | Memory (megabytes) |
|---|---|---|---|---|---|---|---|---|---|
| A.1 | SC | 205*51 | n/a | n/a | 2 | .010 | 0.6 | 5.3 | 6.4 |
| A.2 | SC | 301*101 | n/a | n/a | 2 | .005 | 0.6 | 5.2 | 18.4 |
| A.3 | SC | 205*51 | n/a | n/a | 1 | .010 | 0.6 | 5.2 | 5.6 |
| A.4 | SC | 205*51 | n/a | n/a | 2 | .010 | 6.0 | 5.3 | 6.4 |
| A.5 | TC | 205*51/141*51 | SO | 2 | 2 | .007 | 0.8 | 5.7 | 11.2 |
| A.6 | TC | 205*51/141*51 | SO | 1 | 2 | .007 | 0.8 | 5.6 | 11.2 |
| A.7 | TC | 205*51/141*51 | DO | 2 | 2 | .007 | 0.8 | 11.0 | 12.0 |

SC single Cartesian, TC two Cartesian, SO static overlapped, DO dynamic overlapped, IP interpolation points.

**2-D Store Separation From a Wing Section.** To study the numerical errors associated with *relative-moving* overlapped grids as well as the approximate diagonalization (Eq. (3)), subdomain grids with different topologies were overlapped for a hypothetical 2-D store separation problem (a vertical plane from the 3-D configuration given by Yen and Baysal, 1995), and moved with a prescribed 3-DOF motion (streamwise and normal translations, and pitching), which was intentionally exaggerated:

$$x = u \cdot t = 0.1t, \quad y = v \cdot t = -0.3t, \quad \theta = \omega \cdot t = 0.1t \quad (10)$$

The freestream was transonic at Mach number 0.95. Some computational details for the numerical cases are provided in table 2. The composite grid of B.1 and B.2 consisted of two subdomains: an $O$-type moving grid for the store ($G_3$), which was overlapped on a $C$-type global grid ($G_1$) that was generated for

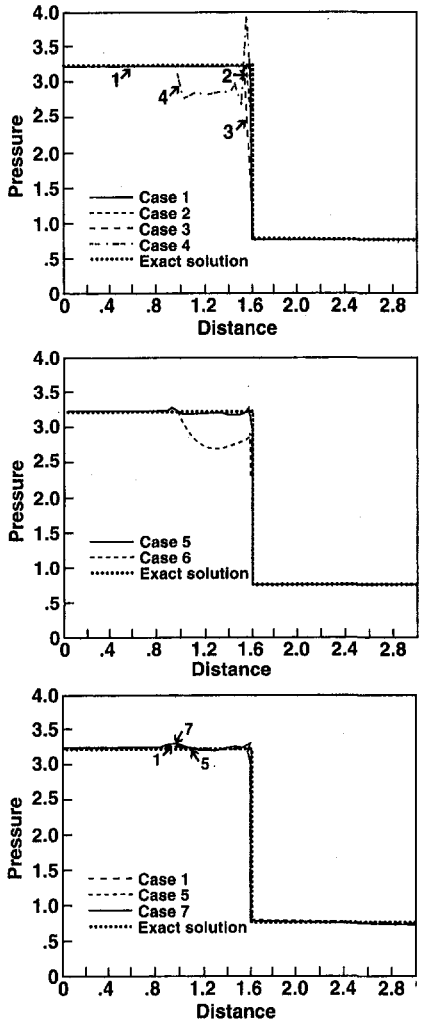


Fig. 1 Comparison of normalized pressure for moving shock to show effects of: (*a*) grid refinement, order of temporal accuracy and CFL number; (*b*) sets of interpolation points; (*c*) static and dynamic overlapping. $M_s = 2$, $M_1 = 1.25$, $p_2/p_1 = 4.5$.

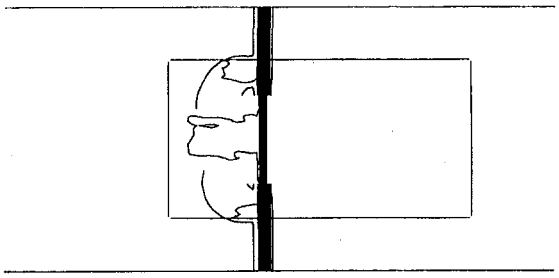

Fig. 2(*a*)

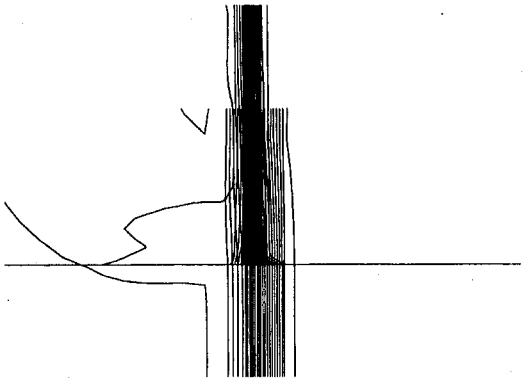

Fig. 2(*b*)

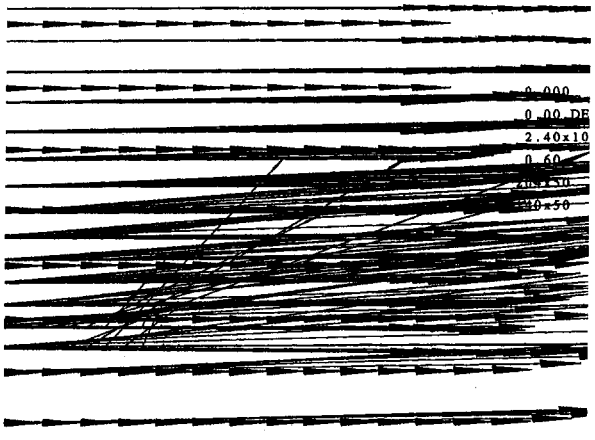

Fig. 2(*c*)

Fig. 2 An instant ($t = 0.7$) of moving shock computed on dynamic overlapped grids (case A.7). (*a*) Pressure contours. Overlaid finer grid is outlined. (*b*) Close up of the shock crossing the outer boundary of overlap. (*c*) Close up of velocity vectors at shock crossing outer boundary of overlap. $M_s = 2$, $M_1 = 1.25$, $p_2/p_1 = 4.5$.

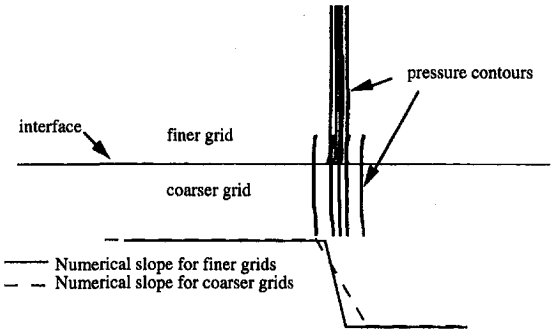


**Fig. 3 Close up of pressure contours and shock slope computed on coarser global grid and finer overlaid grid (case A.7). $M_s = 2$, $M_1 = 1.25$, $p_2/p_1 = 4.5$.**

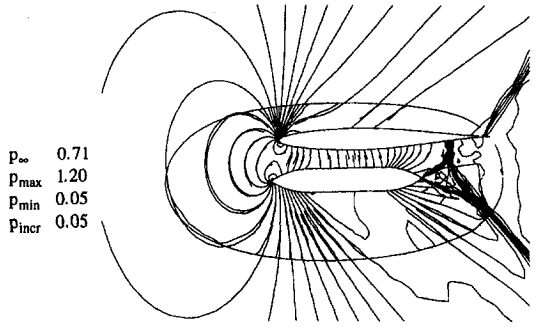


**Fig. 4 Normalized pressure contours of steady flow from case B.1 (two grids and block inversions). Overlaid store grid is outlined. $M_\infty = 0.95$.**

the airfoil. The radii of $G_1$ and $G_3$ were 85 and 3 store diameters ($d$), respectively. The composite grid of B.3 and B.4 had an additional static subdomain ($G_2$), often used to ease grid generation and enhance the interpolation. Hence, this $24.7d$ by $18.7d$ Cartesian grid served as the intermediate grid. Note that the interpolation points for grids $G_2$ and $G_3$ were intentionally put very close to each other near the lower surface of the airfoil, so that any interpolation error in the high gradient region would be accentuated (Eq. (9)). Although a formal grid refinement study is not reported herein, the adequacy of the grids were previously established by Newman and Baysal (1992), when the 3-D, steady-state solutions were successfully compared with the experimental data for this configuration. Starting with the freestream conditions, the computations were marched with local time steps to obtain converged solutions for the steady flow. Then, the computations were continued using global time steps.

For the *steady* flow obtained by *block inversions* on two subdomains (B.1), the normalized pressure contours are shown in Fig. 4, and the surface pressure coefficient ($C_p$) distributions are shown in Fig. 5. Their counterpart plots, obtained by *diagonal inversions* (B.2 not shown here for brevity) requiring 40 percent less time, were virtually identical. Therefore, as also indicated by Pulliam and Chaussee (1981), for converged steady computations, approximate diagonal inversions were deemed to yield comparable accuracy to the block inversions, even with the overlapped grids.

After $4t$ of separation, the instantaneous surface $C_p$ distributions of the unsteady flow from B.1 and B.2 are compared in Fig. 6. For these two cases, it was observed that the off-surface flow structures and the $C_p$ values on the airfoil were mostly similar, including the shock's location and the amplitude. However, the $C_p$ differential between the store's upper and lower surfaces, as predicted by B.1, was smaller than that of B.2, yet the peaks were still matched well. Hence, it was concluded that the two methods, which produced similar steady-state solutions, had differences, attributable to the diagonal inversions, in their dynamic-grid solutions at certain instants.

In B.3 and B.4, both of which employed the *intermediate subdomain* $G_2$ but the latter with the diagonal inversions, the *steady* flow predictions were quite similar to each other. However, the normalized pressure contours of the off-surface flow from B.3 (Fig. 7), when compared to B.1 (Fig. 4), revealed a spurious interaction of the tail shocks. That is, in addition to the predicted physical refraction, a numerical refraction was obtained. Although small, differences between the $C_p$ distributions of B.1 and B.3 (Fig. 5) were also observed and attributed to the use of intermediate subdomain. This might be due in part to the donor and recipient cells of the interpolation having highly discrepant areas (note that interpolations were not area weighted), and in part to the use of a characteristic-based scheme, where the differences in cell wall normals could translate into discrepant numerical flux directions (Rumsey et al., 1991).

After $4t$ of separation, the instantaneous pressure contours of the *unsteady* flows from B.3 and B.4 are presented in Figs. 8 and 9, respectively. The corresponding instantaneous surface $C_p$ distributions are compared in Fig. 10 to observe the com-

**Table 2 Computational details for the 2-D store separation problem**

| Case | Grid size $G_1/G_2/G_3$ | Matrix inversions | CPU time $\mu$s/step/cell | Memory (megabytes) |
|---|---|---|---|---|
| B.1 | 7479/3201/0 | 4 × 4 blocks* | 43.8 | 4.8 |
| B.2 | 7479/3201/0 | diagonal** | 28.2 | 4.8 |
| B.3 | 7479/3969/3201 | 4 × 4 blocks | 53.7 | 6.4 |
| B.4 | 7479/3969/3201 | diagonal | 39.3 | 6.4 |

* eq. (1) ** eq. (3).

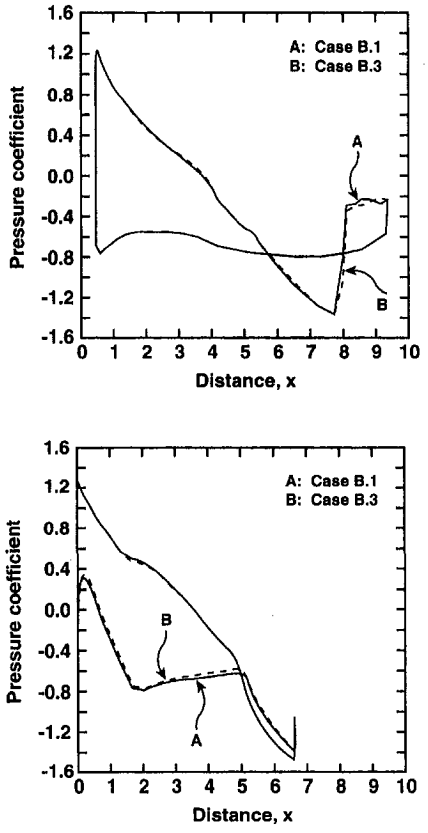


**Fig. 5 Pressure coefficient distributions of steady flow from cases B.1 (two grids and block inversions) and B.3 (three grids and block inversions): (*a*) airfoil surface, (*b*) store surface. $M_\infty = 0.95$.**

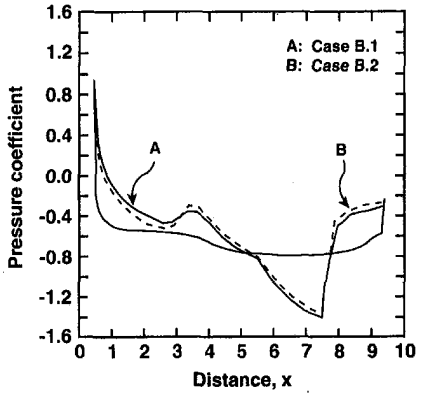


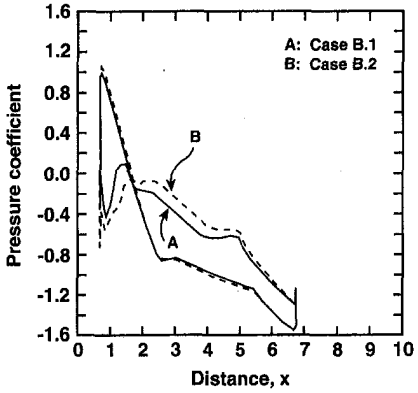


Fig. 6 Pressure coefficient distributions of unsteady flow at $t = 4$ from cases B.1 (two grids and block inversions) and B.2 (two grids and diagonal inversions): (*a*) airfoil surface, (*b*) store surface. $M_\infty = 0.95$.

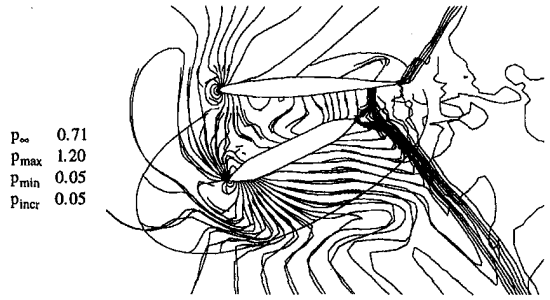


Fig. 9 Normalized pressure contours of unsteady flow at $t = 4$ from case B.4 (three grids and diagonal inversions). Overlaid store grid is outlined. $M_\infty = 0.95$.

pounded effect of diagonal inversion and intermediate subdomain. The off-surface flows looked quite similar to each other (Figs. 8 and 9), but the inboard flows had differences from those predicted in B.1. This difference was again attributed to the use of the intermediate grid. Interestingly, however, the spurious shock-shock refraction that was seen at the steady-state (Fig. 7), disappeared during the separation, at least for the instant shown (Figs. 8 or 9). This was attributed to the fact that the interpolation points of $G_3$, along with the store, had moved away from the airfoil, such that they were no longer coincident or very close to those of $G_2$.

As for the surface flows, the corresponding $C_p$ distributions (Fig. 10) were by and large similar to those of B.1 and B.2 (Fig. 6). The adverse effect of approximate diagonal inversions, when the intermediate grid was present (Fig. 10), appeared quite similar to what was observed with the two-subdomain cases (Fig. 6). That is, $C_p$ differential between the store's upper

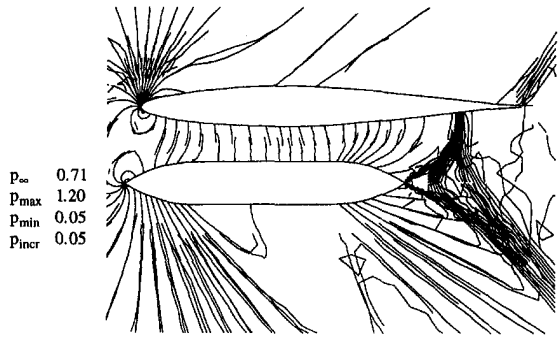


Fig. 7 Normalized pressure contours of steady flow from case B.3 (three grids and block inversions). $M_\infty = 0.95$.

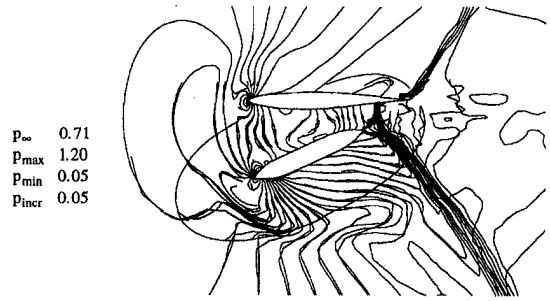


Fig. 8 Normalized pressure contours of unsteady flow at $t = 4$ from case B.3 (three grids and block inversions). Overlaid store grid is outlined. $M_\infty = 0.95$.

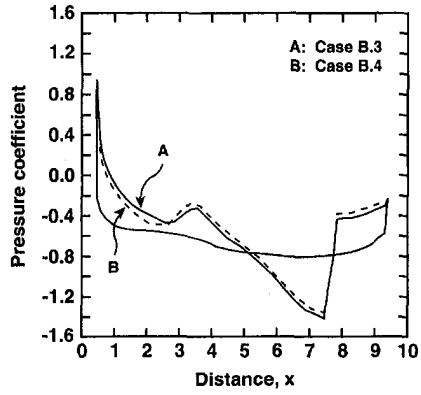


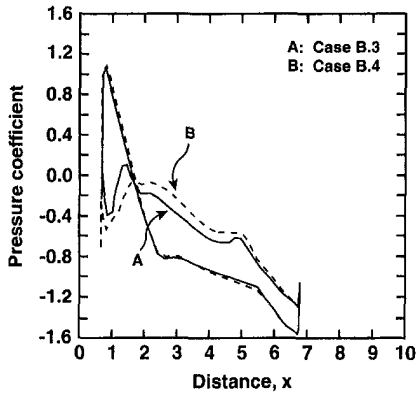


Fig. 10 Pressure coefficient distributions of unsteady flow at $t = 4$ from cases B.3 (three grids and block inversions) and B.4 (three grids and block inversions): (*a*) airfoil surface, (*b*) store surface. $M_\infty = 0.95$.

and lower surfaces as predicted by B.3, was smaller than that of B.4, but the peaks were matched. Therefore, the diagonal inversions caused the same type of inaccuracy and the existence of the intermediate grid could not alter this.

Finally, the CPU time savings in B.4 was 27 percent due to the diagonal inversions. Considering all the cases, it was observed that the savings decreased as the computations became dynamic and as the number of subdomains increased. As expected, the memory increased with the number of subdomains, that is, with more grid points.

## Conclusions

The overlapped-grid mode of a recently developed dynamic-domain-decomposition methodology ($D^3M$), and using several enabling and efficiency techniques, was studied. Two demonstrative problems were computed by a characteristic-based alternating-direction-implicit scheme, to understand the impact of such measures on the accuracy, primarily from a qualitative point of view. Initially, the effects of grid refinement, order of time accuracy, greater-than-one CFL number, number of interpolation points, and static and dynamic overlapping, were demonstrated by computing a moving shock (Riemann) problem. The results suggested the following to achieve an acceptable accuracy: two sets of interpolation points, temporally and spatially second- or higher-order method, for factored implicit methods, CFL number restricted more than what is dictated by the stability.

For the methodology employed, the effects of approximate diagonal inversions, motivated by its computational efficiency, and overlaying more than two subdomains in a region of high flow gradients, motivated by the ease of grid generation that it offered, were demonstrated. This was done by simulating the 2-D flowfield history of a store separating from a wing section along a prescribed trajectory. The results suggested that: the use of approximate diagonal inversions produced less accurate but acceptable results; overlaying an intermediate subdomain in a region of high flow gradients could produce nonphysical results.

Although the present results should contribute to the understanding of the impact on accuracy by the methodology described, more systematic studies on the accuracy of such methods are deemed essential. Another equally important issue would be to reduce the increase in the processing time due to the proposed methods for the moving body problems. Inevitably, the challenge is to do the latter without a significant sacrifice of the former.

## Acknowledgment

This work was supported by NASA Langley Research Center Grant NAG-1-1150. Technical monitor was David S. Miller.

## References

Baysal, O., Fouladi, K., and Lessard, V. R., 1991, "A Multigrid and Upwind Viscous Flow Solver on Three-Dimensional Overlapped and Embedded Grids," *AIAA Journal*, Vol. 29, No. 4, pp. 903–910.

Baysal, O., and Yen, G. W., 1991, "Kinematic Domain Decomposition to Simulate Flows Past Moving Objects," AIAA-91-0725, 29th Aerospace Sciences Meting, Reno, NV.

Baysal, O., Yen, G. W., and Fouladi, K., 1994, "Navier-Stokes Computations of Cavity Aeroacoustics with Suppression Devices," ASME *Journal of Vibration and Acoustics*, Vol. 116, No. 1, pp. 105–112.

Beam, R. M., and Warming, R. F., 1978, "An Implicit Factored Scheme for the Compressible Navier-Stokes Equations," *AIAA Journal*, Vol. 16, No. 4, pp. 393–402.

Celik, I., and Zhang, W. M., 1995, "Calculation of Numerical Uncertainty using Richardson Extrapolation," ASME JOURNAL OF FLUIDS ENGINEERING, Vol. 117, No. 3, pp. 439–445.

Chesshire, G., and Henshaw, W. D., 1990, "Composite Overlapping Meshes for the Solution of Partial Differential Equations," *Journal of Computational Physics*, Vol. 90, No. 1, pp. 1–64.

Duque, E. P. N., Biswas, R., and Strawn, R. C., 1995, "A Solution Adaptive Structured/Unstructured Overset Grid Flow Solver with Application to Helicopter Rotor Flows," AIAA Paper 95-1766, *Proceedings of 13th Applied Aerodynamics Conference*, San Diego, CA, pp. 13–21.

Jordan, J. K., Suhs, N. E., Thoms, R. D., Tramel, R. W., Fox, J. H., and Erickson, Jr., J. C., 1995, "Computational Time-Accurate Body Movement: Methodology, Validation and Application," AEDC-TR-94-15, Arnold Engineering Development Center, Tullahoma, TN.

Lijewski, L. E., and Suhs, N. E., 1994, "Time-Accurate Computational Fluid Dynamics Approach to Transonic Store Separation Trajectory Prediction," *Journal of Aircraft*, Vol. 31, No. 4, pp. 886–891.

Meakin, R. L., 1994, "On the Spatial and Temporal Accuracy of Overset Grid Methods for Moving Body Problems," AIAA-94-1925, *12th AIAA Applied Aerodynamics Conference*, pp. 858–871.

Newman, J. C. III, and Baysal, O., 1992, "Transonic Solutions of a Wing/Pylon/Finned-Store Using Hybrid Domain Decomposition," AIAA-92-4571 (revised) *Proceedings of AIAA Atmospheric Flight Mechanics Conference*, Hilton Head SC, pp. 592–598.

Pulliam, T. H., 1993, "Time Accuracy and the Use of Implicit Methods," AIAA-93-3360, *11th AIAA Computational Fluid Dynamics Conference*, Orlando, FL, pp. 685–693.

Pulliam, T. H., and Chaussee, D. S., 1981, "A Diagonal Form of an Implicit Approximate Factorization Algorithm," *Journal of Computational Physics*, Vol. 39, pp. 347–363.

Ridder, J. P., and Beddini, R. A., 1992, "Temporal and Acoustic Accuracy of an Implicit Upwind Method for Ducted Flows," *AIAA Journal*, Vol. 29, No. 11, pp. 1860–1867.

Roache, P. J., 1995, "Perspective: A Method for Uniform Reporting of Grid Refinement Studies," ASME JOURNAL OF FLUIDS ENGINEERING, Vol. 116, pp. 405–413.

Rumsey, C. L., van Leer, B., and Roe, P. L., 1991, "A Grid-Independent Approximate Riemann Solver with Applications to the Euler and Navier-Stokes Equations, AIAA-91-0239, 29th Aerospace Sciences Meeting, Reno, NV.

Sahu, J., and Nietubicz, C. J., 1995, "Application of Chimera Technique to Projectiles in Relative Motion" *Journal of Spacecraft and Rockets*, Vol. 32, No. 5, pp. 795–800.

Singh, K. P., and Baysal, O., 1995, "3D Unstructured Method for Flows Past Bodies in 6-DOF Relative Motion," *6th International Computational Fluid Dynamics Conference* Hafez and Oshima, eds., Vol. 3, Lake Tahoe, NV, pp. 1161–1168.

Steger, J. L., Dougherty, F. C., and Benek, J. A., 1983, "A Chimera Grid Scheme," *Advances in Grid Generation*, Ghia and Ghia, eds., FED-Vol. 5, ASME, New York, NY, pp. 59–69.

Thomas, J. L., Krist, S. T., and Anderson, W. K., 1990, "Navier-Stokes Computations Vortical Flows Past Low Aspect Ratio Wings," *AIAA Journal*, Vol. 28, No. 2, pp. 205–212.

Thomas, P. D., and Lombard, C. K., 1979, "The Geometric Conservation Law—a Link Between Finite Difference and Finite Volume Methods of Flow Computation on Moving Grids," *AIAA-Journal*, Vol. 17, No. 10, pp. 1030–1037.

Yen, G. W., and Baysal, O., 1995, "Computing Store Separation and its 6-DOF Trajectory using 3-D Dynamic Domain Decomposition Method," *Unsteady Flows 1995*, Keith, Tsukamoto, Baysal, Wei, eds., FED Vol. 216, ASME, New York, NY, pp. 21–28.

Zhang, X. D., Trepanier, J. Y., Reggio, M., and Camarero, R., 1994, "A New Local Time Stepping Approach for the Unsteady Euler Equations," AIAA-94-0525, 32nd Aerospace Sciences Meeting, Reno, NV.

# Numerical Experiments on Application of Richardson Extrapolation With Nonuniform Grids

**Ismail Celik**
Department of Mechanical and Aerospace Engineering, West Virginia University, Morgantown, WV

**Ozgur Karatekin**
Aeronautical Engineering Department, Middle East Technical University, Ankara, Turkiye

*Some unresolved problems related to Richardson extrapolation (RE) are elucidated via examples, and possible remedies are suggested. The method is applied to the case of turbulent flow past a backward facing step using nonuniform grid distributions. It is demonstrated that RE can be used to obtain grid independent solutions using the same grid refinement factors in both coordinate directions. The use of generalized wall functions together with the standard k-ϵ model seems to work well even if the grid refinement extends into the viscous sublayer. In addition, the grid convergence index and other standard uncertainty measures are compared, and a new uncertainty measure is suggested which seems to be a better indicator for the grid convergence error.*

## Introduction

In their earlier studies Celik and Zhang (1993, 1995) have applied Richardson extrapolation to some simple turbulent flow calculations and reported successful results. Demuren and Wilson (1994) reported successful applications of the same method to laminar, separated flows. Celik and Zhang (1995) used uniform grid distributions with wall functions to bridge the viscous sublayer. The first point in the calculation domain was carefully located such that it remained mostly within the log-law region. Several questions remained unanswered in these earlier studies. Some of the relevant questions are:

(*i*) Can we apply the Richardson extrapolation for cases with oscillatory convergence? (*ii*) Can this method be applied with nonuniform grids? What would be a representative grid size parameter? (*iii*) What would the error be if the first grid point remained in the sub-layer? (*iv*) How well would the method work when arbitrary grid refinement factors are used? (*v*) How can one ensure that the grids used are actually in the asymptotic range? Asymptotic range is used in the sense that the grid size is such that the higher order terms in the Taylor expansion are dominated by the leading order term.

In this study, answers are sought to some of the above questions with regard to application of Richardson extrapolation to turbulent flow calculations. A well-documented commercial code, namely, PHOENICS (Ludwig et al., 1989) is used to perform the numerical experiments. This code uses a hybrid of the first order upwind scheme, and the second order central differencing scheme, hence the theoretical order of the method should be between 1 and 2. The turbulent flow example is the flow over a backward facing step which is extensively studied in the literature (see e.g., Speziale and Thangam, 1992; Thangam and Speziale, 1992; Karniadakis et al., 1989; and Avva et al., 1988) for which grid independent solutions are also available. The experiments performed by Kim, et al. (1980) are used as a guide for the numerical computations. A detailed comparison with experimental results is avoided to keep the scope of the paper focused on Richardson extrapolation. The standard *k-ϵ* turbulence model is used for closure. The objective is to seek answers to the above mentioned questions, focusing in particular to application of RE with nonuniform grids.

## Theory

Assuming that the dependent variable $F$ is a continuous and differentiable function of a representative grid size, $h$, it can be shown that (Richardson, 1910), for an arbitrary grid size, $h$, the error $E_h$, is given by

$$E_h = F_{\text{exact}} - F_h = C_1 h + C_2 h^2 + C_3 h^3 + \ldots \quad (1)$$

Keeping only the leading term in the asymptotic range (i.e., when $h$ is small) and replacing $F_{\text{exact}}$ by $F_{\text{ext}}$, the following three equations can be written

$$F - F_1 = C(a_1 h)^n \quad (2a)$$

$$F - F_2 = C(a_2 h)^n \quad (2b)$$

$$F - F_3 = C(a_3 h)^n \quad (2c)$$

to determine the three unknowns, namely, the coefficient $C$, the apparent order of the method, $n$, and the extrapolated value $F = F_{\text{ext}}$ to zero grid size. Here $a_1$, $a_2$, and $a_3$ are the grid refinement or coarsening factors defined as, $a_i = h_i/h_{\text{ref}}$, the ratio of the grid size, $h$, to the size of a reference grid size, $h_{\text{ref}}$. Without loss of generality, one of the factors $a_i$ can be taken as unity hence making that grid the reference grid; in this paper we take $a_1 = 1$. Solving the above equations for the three unknowns yields

$$n = |\ln [(F_2 - F_3)/(F_1 - F_2)]/\ln (a_2) - f(n)| \quad (3a)$$

$$f(n) = \ln [(a_3/a_2)^n - 1)/(a_2^n - 1)])/\ln (a_2) \quad (3b)$$

$$F_{\text{ext}} = (a_2^n F_1 - F_2)/(a_2^n - 1) \quad (3c)$$

The absolute value in Eq. (3*a*) is necessary in order to ensure extrapolation towards decreasing $h$. Otherwise, the solution allows negative values of $n$ and the extrapolated value, $F_{\text{ext}}$ is on the increasing $h$ side. For oscillatory convergence where the error decreases with an alternating sign, the argument $(F_2 - F_3)/(F_1 - F_2)$ is less than zero. For these situations Eq. (2*b*) can be written with a minus sign on the r.h.s. without loss of generality assuming that $C$ is constant. Then Eqs. (3(*a*)–(*b*) are modified as

Contributed by the Fluids Engineering Division for publication in the JOURNAL OF FLUIDS ENGINEERING. Manuscript received by the Fluids Engineering Division February 6, 1996; revised manuscript received January 7, 1997. Associate Technical Editor: P. M. Sockol.

Table 1 Key parameters and the cases investigated using the standard $k$-$\epsilon$ model

| Case # | Grid ($NX \times NY$) | $Y2 \times 10^3$ | $x_R/H$ | $a_i = Y2(i)/Y2(6)$ | $a_i = NY(6)/NY(i)$ |
|---|---|---|---|---|---|
| 1 | 25 × 20 | 1.1750 | 4.765 | 10.271 | 6.0 |
| 2 | 35 × 28 | 0.7590 | 5.260 | 6.635 | 4.286 |
| 3 | 50 × 40 | 0.4774 | 5.636 | 4.173 | 3.0 |
| 4 | 75 × 60 | 0.2818 | 5.863 | 2.463 | 2.0 |
| 5 | 100 × 80 | 0.1939 | 5.972 | 1.695 | 1.5 |
| 6 | 150 × 120 | 0.1144 | 6.063 | 1.0 | 1.0 |

$$n = |\ln [(F_3 - F_2)/(F_1 - F_2)]/\ln (a_2) - f(n)| \quad (4a)$$

$$f(n) = \ln [(a_3/a_2)^n + 1)/(a_2^n + 1)])/\ln (a_2) \quad (4b)$$

If $a_3/a_2 \neq a_2$, Eqs. $(3a)-(3c)$ need to be solved iteratively.

As it shall be shown later in the text, even if the solutions converge to grid independent profiles, sometimes (usually at some discrete points of a field data) the calculated apparent order is quite unrealistic and this leads to unrealistic extrapolated values. To avoid this $n$ must be bounded within its theoretical limits, e.g., within 1 and 2 for the hybrid scheme used in the present numerical simulations.

## Computational Details

**Turbulence Model.** The standard $k$-$\epsilon$ model is used; here $k$ is the turbulent kinetic energy and $\epsilon$ is the dissipation rate of $k$. The model constants with the standard notation are: $\kappa = 0.435$, $E = 9.0$ (wall roughness parameter), $C_\mu = 0.09$ ($= C_d C'_\mu$; $C_d = 0.1643$, $C'_\mu = 0.5478$), $C_{1\epsilon} = 1.44$, $C_{2\epsilon} = 1.92$, $\sigma_k = 1.0$, $\sigma_\epsilon = 1.314$.

**Grid Distribution.** The calculation domain ($-4H \leq x \leq 16\,H$; $0 \leq y \leq 4H$) is divided into two regions, namely the step region, $-4H < x < 0$, $H < y < 3H$, and the channel region, $0 < x < 16H$, $0 < y < H$. Here $H$ is the step height, $x$ is the axial direction, and $y$ is the transverse direction perpendicular to the channel walls. In the step region the grid is distributed uniformly in the $x$-direction. In the $y$-direction a nonuniform, power law grid distribution is used with a power of 1.4 expanding from both walls toward the center symmetrically. In the channel region the grid in both directions is nonuniform. In the $x$-direction a continuously expanding grid with a power of 1.1 is used. In the $y$-direction the grid is distributed symmetrically with a power of 1.3. The power-law grid distribution is given by $\eta_j = [(j - j_{\text{first}})/(j_{\text{last}} - j_{\text{first}})]^{\text{power}}$ inside a normalized region extending from 0 to 1. The number of grids is distributed such that there are NX/5, NY/2 grid in the step region, and 4(NY/5) and NY/2 cells in the channel region, NX and NY being the total number of grids in the $x$- and the $y$-directions, respectively. It should be emphasized that the grids in the $x$- and $y$-directions are distributed in such a way that a grid refinement factor defined by

$$a_i = NF/N(i) \quad (5)$$

remained same in both directions: here $NF$ is the number of grid points for the finest grid, and $N(i)$ is the number of grids for case $(i)$. This seems to be, at least for the present application, a consistent grid refinement parameter for nonuniform grids. In general, one has to be cautious in distributing the additional number of grids. Preferably, the local grid stretching coefficients should remain the same, i.e. the grids should have the property of geometric similarity.

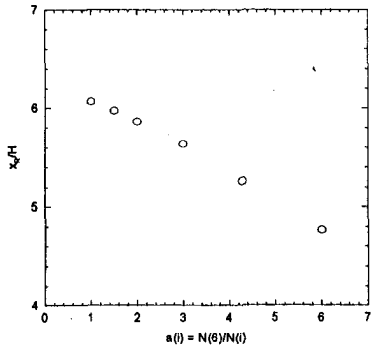


Fig. 1 Variation of reattachment length with grid refinement factor

**Inlet Condition.** A uniform velocity distribution in the axial direction ($U$-velocity) is prescribed as $U = U_{\text{in}} = 13.0$ m/s. The $V$ component in the transverse direction is set equal to zero. The turbulent kinetic energy, $k$, and the dissipation rate, $\epsilon$ profiles, are also uniform at the inlet which are calculated according to

$$k_{\text{in}} = 0.018U_{\text{in}}^2/4;\ \epsilon_{\text{in}} = 0.1643k_{\text{in}}^{3/2}/(0.09H)$$

**Wall Boundaries.** The generalized wall function approach (Rosten and Worrell, 1988; Launder and Spalding, 1974) is used where the logarithmic law of the wall for the velocity component parallel to the wall is written in terms of the turbulent kinetic energy, $k$, representing the wall velocity scale via the relation $k = U^{*2}/\sqrt{C_\mu}$, $U^*$ being the wall friction velocity; $k$ is deduced from the regular transport equation, in which the production term for the near wall cells is calculated by an analytic integration based on the wall-shear stress. The dissipation rate for these cells is fixed at an average value obtained by analytical integration. If $y^+ = U^* y/\nu < 11.5$ then $U$, $k$ and $\epsilon$ are extrapolated to their wall values based on viscous sublayer constraints.

**Iteration Convergence.** False time relaxation method is used in calculating the steady state solutions iteratively. For this, the time step is adjusted to provide the appropriate relaxation while marching toward a steady-state solution. The iteration convergence criteria used is that there was less than 0.1 percent change in 1000 iterations in the value of dimensionless reattachment length, $x_R/H$. The integral sum of the residuals for the $U$-momentum equation were all less than $3.56E$-04, those for the coarse grid solutions being much less. The residu-

Table 2 Results of Richardson extrapolation: using $a_i = NY(6)/NY(i)$

| Cases used | $n$ | $(x_R/H)_{\text{ext}}$ | $a_1$, $a_2$, $a_3$ |
|---|---|---|---|
| 3, 2, 1 | 0.97 | 6.55 | 1.0, 1.429, 2.0 |
| 4, 3, 2 | 1.67 | 6.10 | 1.0, 1.5, 2.143 |
| 5, 4, 3 | 1.11 | 6.26 | 1.0, 1.333, 2.0 |
| 6, 5, 4 | 1.53 | 6.17 | 1.0, 1.5, 2.0 |
| 5, 3, 1 | 1.37 | 6.18 | 1.0, 2.0, 4.0 |
| 6, 4, 2 | 1.37 | 6.19 | 1.0, 2.0, 4.286 |

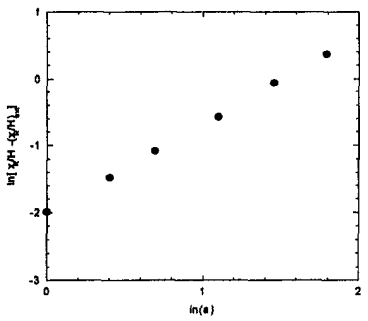


Fig. 2 Variation of error with grid refinement factor

als for the continuity equation were approximately an order of magnitude less than those for the $U$-momentum equation. Residuals for the other variables were not monitored.

**Influence of the Domain Size.** Thangam and Speziale (1992) reported that in their calculations the channel length downstream of the step would have to be at least $30H$ in order to reduce domain dependency errors below acceptable values. In the present calculations the outlet was located at $16H$ down stream of the step; calculations with $30H$ did not show any significant variation in the results. More specifically, the change in the reattachment length was less than 1.0 percent. The inlet boundary was located at $-4H$ upstream of the step. Calculations with $-5H$ did show some influence but this difference was sufficiently small and it should not render the conclusions made below.

**Interpolation.** Application of Richardson extrapolation using various grids requires interpolation of fine grid result to coarse grid nodes. This interpolation process should be done with care such that the interpolation errors do not pollute the accuracy of the over all calculation procedure. This was accomplished by using a third order Newton's divided difference polynomial for interpolation in a pseudo one-dimensional manner, first in the $x$-direction to obtain profiles at desired $x$-locations, and subsequently in the $y$-direction.

**Description of the Cases Studied.** The flow problem is analogous to the case which was studied experimentally by Kim et al. (1980) which is the well known case of turbulent flow past a backward facing step. For the present simulations the Reynolds number based on the step height is $1.5 \times E05$, the kinematic viscosity is $3.302E\text{-}06$ m$^2$/s, the density is 1.0 kg/m$^3$, the step height, $H$, is 0.0381 m and the channel width is $3H$. Six different (but similar) grid distributions with almost arbitrary grid refinement factors were used to investigate the feasibility of Richardson extrapolation when applied with non-uniform grid distributions. The key parameters for the cases investigated are listed in Table 1.

## Results and Discussion

The reattachment length, $x_R$, was calculated by finding the location of zero axial velocity at the first grid node inside the calculation domain. A third order Newton's divided difference polynomial was used for interpolation purposes. It should be noted that using the values of axial velocity at the first grid node introduces a local first-order error in $x_R$ (Roache, 1996; see also later discussion). However, extrapolating the axial velocity to the axis and looking for a zero value is not practical because the velocity must be zero everywhere at the wall to satisfy the no slip condition. Looking for zero derivative of the velocity will also introduce unwanted errors in the calculation of $x_R$. The results for various grid distributions are listed in Table 1 and $x_R/H$ is plotted against the grid refinement factor, $a_i$, in Fig. 1. It is seen that as the grid is refined the asymptotic value of $x_R/H$ approaches a grid independent value of 6.2. A grid independent value of 6.25 was reported by Avva et al. (1988) and Thangam and Speziale (1992) for the standard $k$-$\epsilon$ model. When the inlet profiles are prescribed according to experiments (results not shown here) the asymptotic value of $x_R/H$ improves somewhat and a value of 6.25 does seem to be a grid independent solution obtained in this study by extrapolation. In Table 2 the results of Richardson extrapolation using the dimensionless reattachment length as the dependent variable, $F$, is shown for a combination of grids. In all cases except one, the extrapolated value is close to 6.2. As it is seen in Fig. 1 the reattachment length appears to reach a grid independent values of 6.2. Table 2 also shows that the calculated apparent order "$n$" of the numerical methods is between 1. and 2. with an average value of 1.3. This conclusion is further confirmed by Fig. 2 where the error defined by Eq. (1) is plotted against the grid refinement factor in a log-log scale. In this figure the slope of the straight line passing through the shown points represents an average order for the numerical scheme utilized, which is found to be about 1.3 in close agreement with Table 2. All this indicates that the reattachment length can be determined to an order greater than or equal to one which is consistent with the overall apparent order of the computations in spite of the fact that a first order error may be introduced by using the velocity at the first grid node in calculating $x_R$.

The results of Richardson extrapolation using the ratios of cell sizes near the wall as grid refinement factors showed that the extrapolated values did not change, even though the values of $n$ were considerably smaller compared to those seen in Table 2. Here we use the grid refinement factors calculated from the overall number of grid nodes (Eq. (5)) as suggested by Roache (1994), rather than calculating them from the actual local cell sizes which are cumbersome to calculate when nonuniform grids are used. Since the extrapolated values of the variables are of primary importance, the use of grid refinement factors defined by Eq. (5), which do not change for similar grid distributions (e.g., grids generated with the same power functions as in the present case) should not affect the generality of the procedure.

The extrapolated $Cp$ profiles using various grid combinations are shown in Fig. 3. The pressure coefficient converges to an approximately grid independent profile beyond $100 \times 80$ grid (Case 5). The variation band among the extrapolated values is within $-0.03$ to $+0.03$. The relative error is not a realistic indicator in this case because the magnitude of $Cp$ values are close to zero over a large domain. It is noteworthy to see that the extrapolated $Cp$ values using the coarser grids (Cases 4, 3, and 2) are in close agreement with those obtained from the finer grids, e.g., Cases 6, 4, and 2. Even when cases 3, 2, and 1 (the coarsest grids) are used, the extrapolated $Cp$ profile is in close agreement with the grid independent one, except maybe a few points near minimum pressure. The scatter near $x = 0$ is

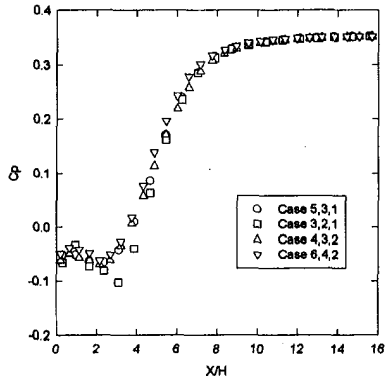


Fig. 3 Extrapolated $C_p$ on step side wall

Table 3 Richardson extrapolation applied to velocity profile at $x_R/H = 8.0$

| J | y(m) | U (Case 2) | U (Case 4) | U (Case 6) | U (Extra.) | n |
|---|---|---|---|---|---|---|
| 1 | 7.58e-4 | 2.6117 | 2.6421 | 2.2292 | 2.2511 | 4.1563 |
| 2 | 2.62e-3 | 3.5591 | 2.8328 | 2.4820 | 2.0555 | 0.8658 |
| 3 | 5.03e-3 | 3.6609 | 3.0081 | 2.7705 | 2.5980 | 1.2496 |
| 4 | 7.76e-3 | 3.8383 | 3.2701 | 3.1108 | 3.0326 | 1.6029 |
| 5 | 0.0108 | 4.1014 | 3.6229 | 3.5225 | 3.4888 | 1.9931 |
| 6 | 0.0139 | 4.4592 | 4.0729 | 4.0193 | 4.0082 | 2.5479 |
| 7 | 0.0173 | 4.9196 | 4.6254 | 4.6102 | 4.6091 | 3.8671 |
| 8 | 0.0208 | 5.4751 | 5.2682 | 5.2846 | 5.2831 | 3.3542 |
| 9 | 0.0242 | 6.0909 | 5.9624 | 6.0042 | 5.9933 | 1.5085 |
| 10 | 0.0273 | 6.7312 | 6.6714 | 6.7339 | 6.7034 | 0.0664 |
| 11 | 0.0303 | 7.3702 | 7.3698 | 7.4492 | 7.4491 | 8.8496 |
| 12 | 0.0331 | 7.9781 | 8.0283 | 8.1213 | 8.2037 | 1.0891 |
| 13 | 0.0355 | 8.5185 | 8.6100 | 8.7136 | 9.1124 | 0.3333 |
| 14 | 0.0373 | 8.9277 | 9.0514 | 9.1629 | 22.574 | 0.0119 |
| 15 | 0.0393 | 9.3676 | 9.5073 | 9.6220 | 10.752 0 | 0.1396 |
| 16 | 0.0426 | 10.0310 | 10.1520 | 10.2610 | 18.571 0 | 0.0187 |
| 17 | 0.0472 | 10.4960 | 10.6190 | 10.7010 | 10.943 0 | 0.4218 |
| 18 | 0.0526 | 10.6050 | 10.7250 | 10.7880 | 10.885 0 | 0.7316 |
| 19 | 0.0587 | 10.6270 | 10.7480 | 10.8110 | 10.901 0 | 0.7648 |
| 20 | 0.0653 | 10.6410 | 10.7670 | 10.8320 | 10.922 0 | 0.7836 |
| 21 | 0.0725 | 10.6530 | 10.7870 | 10.8550 | 10.946 0 | 0.8018 |
| 22 | 0.0799 | 10.6620 | 10.8060 | 10.8790 | 10.973 0 | 0.8189 |
| 23 | 0.0871 | 10.6570 | 10.8170 | 10.8950 | 10.991 0 | 0.8545 |
| 24 | 0.0937 | 10.6120 | 10.7960 | 10.8780 | 10.963 0 | 0.9718 |
| 25 | 0.0998 | 10.4340 | 10.6530 | 10.7190 | 10.755 0 | 1.4990 |
| 26 | 0.1052 | 9.8277 | 9.9863 | 9.8995 | 9.9309 | 0.8185 |
| 27 | 0.1098 | 8.4811 | 8.4440 | 8.1854 | 8.1526 | 3.1498 |
| 28 | 0.1131 | 6.4440 | 6.6461 | 6.1345 | 6.2718 | 1.4469 |

partly due to interpolation errors. Similar comments apply to the pressure distribution along the wall opposite to the step (not shown here).

Richardson extrapolation was applied to calculate extrapolated velocity profiles, for various cases. An example is shown in Table 3 where the profiles at $x/H = 8.00$ for Cases 6, 4, and 2 are given along with the extrapolated profile and the calculated apparent order. In this Table the convergence at points 1, 10, and 26 are examples for oscillatory convergence. It is seen that at some points the calculated apparent order, such as 3.87, 0.012, and 3.15 at grid nodes 7, 14, and 27, respectively, are unrealistic (note that this is one of the worst cases). These lead to unrealistic extrapolated values, e.g., 22.57 m/s at grid node 14. Such irregularities are bound to happen, especially for axial velocity profiles as illustrated by Celik and Zhang (1993) in more detail. It may be tempting to conclude that the numerical solution is still not in the asymptotic range. However, this does not seem to be the case, because all indications are that as grid is refined from Case 1 to Case 6 the velocity profiles seem to converge to a grid independent profile as it is seen in Fig. 4, in addition to the clear indication of grid convergence seen in the variation of the reattachment length (see Fig. 1) which is calculated using axial velocity profiles. The same conclusion may not be valid for the turbulent quantities, i.e., $k$ and $\epsilon$, since these are more sensitive the changes in the grid. To avoid such unrealistic behavior, here it is proposed that the calculated val-

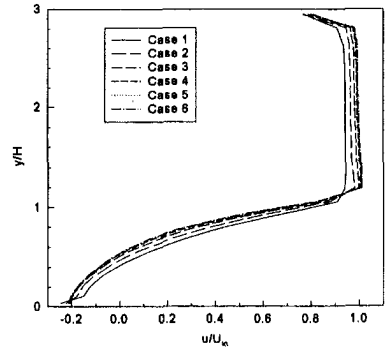


Fig. 4 Convergence of velocity profiles at $x/H = 2.67$

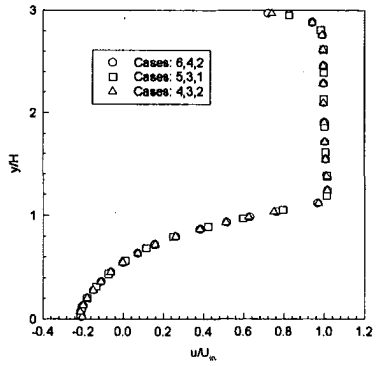


Fig. 5 Comparison of extrapolated velocity profiles at $x/H = 2.67$

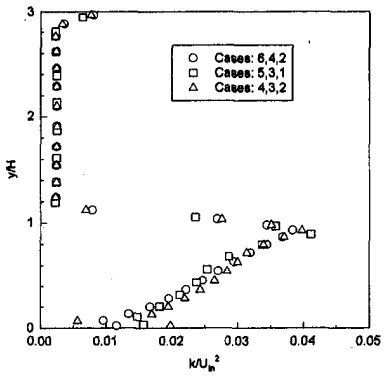


**Fig. 6 Comparison of extrapolated $k$-profiles at $x/H = 2.67$**

ues of $n$ be bounded such that it is always between 1 and 2 which are the minimum and maximum theoretical values for the present numerical scheme. This practice is only valid for mixed-order methods such as the presently used hybrid scheme. When this procedure is applied, Richardson extrapolation seem to work well (see Fig. 5). Grid independent profiles (except may be for $k$ and $\epsilon$) at $x/H = 2.67$ could be obtained from grids as coarse as $75 \times 60$. In practice, this should lead to significant computational savings. Typically $200 \times 100$ grid is necessary for grid independent solution for all dependent variables (Thangam and Speziale, 1992; Thangam and Hur, 1991).

The extrapolated kinetic energy profiles at $x/H = 2.67$ are shown in Fig. 6. Again a reasonably good agreement is obtained among all extrapolated profiles. The error margins for the $k$-profiles are larger compared to the $U$-profiles, indicating the more sensitive behavior of the kinetic energy calculations as mentioned above. The error margins among the extrapolated profiles is within $-0.005$ to $+0.005$, the maximum errors being in the near wall region as it is expected. Similar results were observed for the profiles at other locations.

**Grid Convergence Index.** Figure 7 shows various uncertainty (or error) measures for the computed reattachment length, as a function of the grid refinement factor. The usual error measure is the approximate relative error defined for any two grids by

$$e_a = (F_c - F_f)/F_f \tag{6}$$

where $F_f$ is the solution computed with the fine grid, and $F_c$ is the solution computed with the coarse grid. The true relative error, $e_t$, is computed using the grid independent solution, $F_{\text{ref}}$, from

$$e_t = (F_{\text{ref}} - F_h)/F_{\text{ref}} \tag{7}$$

Another uncertainty measure (an error band) is the grid convergence index, GCI, suggested by Roache (1994), for fine grid solution

$$\text{GCI}_f = 3(F_c - F_f)/[(r^n - 1)F_f] \tag{8a}$$

where $r$ is the grid refinement factor between the coarse grid and the fine grid ($r > 1$). It can be shown that (see Appendix A)

$$\text{GCI}_f = 3e_a/(r_i^n - 1);\ r_i = a_{i+1}/a_i \tag{8b}$$

It is seen from Fig. 7 that the approximate relative error measure (Eq. (6)) underestimates the true relative error, $e_t$. Whereas, the GCI (Eq. (8)) calculated using both the minimum ($n = 1$), and maximum ($n = 2$) values of $n$, significantly over estimates the error as it was originally intended to be so (see Roache, 1994, for a discussion). Although overestimation is a desirable feature so that the uncertainty measure is a conservative estimate, the degree of overestimation should not be too much to cause excessive suspicion, and hence unnecessary grid refinement, particularly for studies involving more than three grids. To this end we suggest here a new uncertainty measure using the extrapolated value of the quantity in question with the minimum values of $n$ (i.e., $n = 1$, linear extrapolation), defined by

$$e_{\text{ext}} = (F_{\text{ext}} - F_h)/F_{\text{ext}} \tag{9a}$$

where $F_{\text{ext}}$ is calculated using Eq. (3c). $F_{\text{ext}}$ and $F_{\text{ref}}$ may differ in that the first is the solution extrapolated to zero grid using any two grids (Eq. (3c)), and $F_{\text{ref}}$ is the "truly" grid independent solution. It can be shown (see Appendix A) that $\text{GCI}_f$ and $e_{\text{ext}}$ can be expressed in terms of each other for $n = 1$ as

$$e_{\text{ext}} = [(r - 1)/(r - F_c/F_f)]\text{GCI}_f/3 \tag{9b}$$

It is shown in Fig. 7 that this new measure very closely approximates the actual relative error, and it is slightly conservative. It is suggested that Eqs. (6) or (9) be used as an approximate measure of the grid convergence error in studies focusing on numerical aspects of computational fluid dynamics. Either of these error measures can also be used to determine whether the computations are in the asymptotic range.

It should be noted that special precaution is required in interpolation and extrapolation, because small changes in the dependent variable leads to significant changes in the calculated apparent order "$n$."

## Conclusions

Remedies were found to some problems relevant to the application of Richardson extrapolation (RE) using nonuniform grids to turbulent separated flows. These were illustrated by applying the method to the case of turbulent flow past a backward facing step. The feasibility of the grid convergence index (GCI) suggested by Roache (1994) was also investigated. The following conclusions can be made based on the results of the present study:

The apparent order of the numerical scheme must always be taken as the positive roots of the asymptotic equations. Otherwise the extrapolation is towards the wrong direction, i.e., toward coarser grid. In case of oscillatory convergence, the trunca-

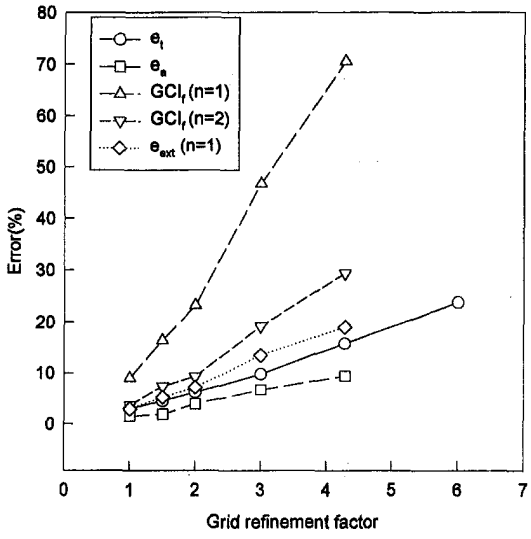


**Fig. 7 Variation of various uncertainty estimates with grid refinement factor**

tion error is allowed to change sign keeping the coefficient still constant. This gives a new set of equations to be solved, but it works. In spite of all these fixes, the method may still give unrealistic exponents and, hence, unreasonable extrapolated values (at some discrete points) especially in cases where the change in the dependent variable is very small. This can be avoided by limiting the apparent order used in the extrapolations to its theoretical range, but then the generality of the method is reduced by assuming rather than calculating the value of $n$.

When the method is applied to the case of flow over a backward facing step, with all of the above precautions, it gave excellent results in case of reattachment length, good results for the axial component of the velocity, but only fair results for the turbulent kinetic energy. However, the user must be very careful, since there may be many pitfalls in application of RE to other flow problems.

Significant computational "savings" (i.e., reduction in number of grid points) can be achieved by extrapolating the grid dependent solutions to "zero" grid size. A reduction by a factor of $2^{-1/2}$ in each coordinate direction is possible which can lead to as much as 180 percent savings in 3D computations.

In particular, this study showed that RE works with nonuniform grids with the same grid refinement factors used in both coordinate directions. The grid refinement does not have to be made by grid halving as noted by Roache (1994). The grid refinement factor defined by Eq. (5) seems to be a good representative grid size parameter for nonuniform but similar grid distributions.

The GCI suggested by Roache (1994) overestimated the uncertainty excessively as it was originally designed to do so with the idea that GCI is an error band not an error estimator. The relative error which is calculated using the extrapolated values (with $n = 1$) of the dependent variable in question seems to be a much realistic measure of the grid convergence error. This suggests that a factor of one rather than three should be used in GCI in rigorous grid convergence studies.

## Acknowledgment

The authors wish to thank all reviewers of this paper for their comments. In particular they extend their sincere appreciation of the open comments and criticism by Patrick J. Roache as a result of which the present version has become much better in quality compared to the first version.

## References

Avva, R. K., Kline, S. J., and Ferziger, J. H., 1988 "Computation of the Turbulent Flow Over a Backward-Facing Step Using the Zonal Modeling Approach," Stanford University, TR TF-33, Stanford CA. Also AIAA Paper 88-0611, Jan.

Celik, I. and Zhang, W-M., 1993 "Application of Richardson Extrapolation to Some Simple Turbulent Flow Calculations," *Proceedings of the Symposium on Quantification of Uncertainty in Computational Fluid Dynamics,* I. Celik et al., eds., ASME Fluids Engineering Division Spring Meeting, Washington D.C., June 20–24, p. 29.

Celik, I. and Zhang, W-M. 1995 "Calculation of Numerical Uncertainty Using Richardson Extrapolation: Application to Some Simple Turbulent Flows Calculations," ASME JOURNAL OF FLUIDS ENGINEERING, Vol. 117, No. 3, pp. 439–445.

Celik, I. and Karatekin, O., 1995 "Numerical Experiments on Application of Richardson Extrapolation to a Turbulent Flow with Separation," Proc. of the forum on "Quantification of Uncertainty in Computational Fluid Dynamics," ASME/JSME Fluids Engineering Conference, Hilton Head, SC, Aug. 13–18.

Demuren, A. O. and Wilson, R. V., 1994 "Estimating Uncertainty in Computations of Two-Dimensional Separated Flows," ASME JOURNAL OF FLUIDS ENGINEERING, Vol. 116, No. 2, pp. 216–220.

Karniadakis, G., Yakhot A., Rakip, S., Orzag, S. A., and Yakhot, V., 1989 "Spectral Element-RNG Simulations of Turbulent Flows in Complex Geometries," *Proceedings of 7th Symposium on Turbulent Shear Flows,* Paper 7.2, Stanford University Press.

Kim, J., Kline S. J., and Johnston J. P., 1980 "Investigation of Reattaching Turbulent Shear Layer: Flow Over a Backward-Facing Step," ASME JOURNAL OF FLUIDS ENGINEERING, Vol. 102, p. 302.

Launder, B. E. and Spalding, D. B., 1974, "The Numerical Computation of Turbulent Flow," *Computational Methods in Applied Mechanics and Engineering,* Vol. 3, pp. 269–289

Ludwig, J. C., Qin, H. Q., and Spalding, D. B., 1989, *The PHOENICS Reference Manual,* CHAM TR/200, CHAM Limited, Bakery House, 40 High Str., Wimbledon Village, London SW195AU, England.

Richardson, L. F., 1910, "The Approximate Arithmetic Solution by Finite Differences of Physical Problems Involving Differential Equations, with Application to Stresses in a Masonry Dam," *Transactions of the Royal Society of London,* Series A., Vol. 210, pp. 307–357.

Roache, P. J., 1994, "Perspective: A Method for Uniform Reporting of Grid Refinement Studies," ASME JOURNAL OF FLUIDS ENGINEERING, Vol. 116, pp. 405–413.

Roache, P. J., 1996, Private Communication

Rosten, H. I. and Worrell, J. K., 1988, "Generalized Wall Functions for Turbulent Flow," Cham Ltd., Bakery House, High Street, Wimbledon, London SW19 5AU, England.

Speziale C. G. and Thangam, S., 1992, "Analysis of an RNG Based Turbulence Model for Separated Flows," *International Journal of Engineering Science,* Vol. 30, No. 10, pp. 1379–1388.

Thangam, S. and Speziale, C. G., 1992, "Turbulent Flow Past a Backward Facing Step: A Critical Evaluation of Two-Equation Models," *AIAA Journal,* Vol. 30, No. 5, pp. 1314–1320.

Thangam, S. and Hur, N., 1991, "A Highly Resolved Numerical Study of Turbulent Separated Flow Past a Backward-Facing Step," *International Journal of Engineering Science,* Vol. 29, No. 5, pp. 607–615.

## APPENDIX A

### The Relations Among Various Notations Used in This Paper

This Appendix explains the relationship between various error measures and indices used in the main text of the paper.

The factor $a_i$ used in this paper and listed in Table a.1 (see also Table 1) is called the grid index and defined with respect to a reference grid size, $h_{\text{ref}}$, as follows:

$$a_i = h_i / h_{\text{ref}} \tag{a.1}$$

where $h_i$ is the grid size of the "$i$"th grid. By this definition if $a_i > 1.0$ (i.e., $h_{\text{ref}}$ = finest grid size) the subsequent grids are coarser by a factor of $a_i$; for $a_i < 1.0$ (i.e. $h_{\text{ref}}$ = coarsest grid size) the subsequent grids are finer by a factor of $a_i$. The grid refinement ratio, $r$, used by Roach (1994) is defined as

$$r = h_c / h_f \tag{a.2}$$

where the subscripts $c$ and $f$ denote coarse grid and fine grid, respectively. These two indices are not necessarily the same. Only in the case where $h_{\text{ref}}$ is taken to be the smaller of the two subsequent grid sizes, $a$ and $r$ will be the same. The grid factor $a$ is a more general index in that it can represent both grid coarsening and grid refinement, and it is not necessary to know the actual grid size to compute it. That is if only the total number of grids are reported for each grid, this parameter can be calculated (see Eq. (5)).

In the present paper $h_{\text{ref}}$ is taken to be the finest grid size, hence $a_i > 1$ and it is related to $r$ by

$$r_i = (a_{i+1}/a_i);\ i = 1, 2, 3, \ldots \tag{a.3}$$

For example, for $i = 2$, $a_3 = h_3/h_1$, $a_2 = h_2/h_1$, $r_2 = a_3/a_2 = h_3/h_2 = 1.333$ (see Table a.1)

**The Relation Between $e_{\text{ext}}$ and $\text{GCI}_f$.** The relative error, $e_{\text{ext}}$, based on an extrapolated solution, is defined by Eq. (9), which is

**Table a.1 Summary of data used for Fig. 7**

| $a_i$ | $x_R/H$ | $e_t$ | $e_a$ | $GCI_f$ ($n = 1$) | $GCI_f$ ($n = 2$) | $e_{\text{ext}}$ | $r$ |
|---|---|---|---|---|---|---|---|
| 1.000 | 6.063 | 2.990 | 1.500 | 9.00 | 3.60 | 2.91 | 1.5000 |
| 1.500 | 5.972 | 4.450 | 1.830 | 16.40 | 7.40 | 5.19 | 1.3330 |
| 2.000 | 5.863 | 6.190 | 3.870 | 23.20 | 9.30 | 7.19 | 1.5000 |
| 3.000 | 5.636 | 9.800 | 6.670 | 46.70 | 19.20 | 13.47 | 1.4287 |
| 4.286 | 5.260 | 15.800 | 9.410 | 70.60 | 29.40 | 19.05 | 1.4000 |
| 6.000 | 4.765 | 23.760 | | | | | |

$$e_{ext} = (F_{ext} - F_h)/F_{ext} \quad \text{(a.4)}$$

where $F_h$ represents a solution at a given size $h$, and $F_{ext}$ is the solution obtained by Richardson extrapolation (i.e., Eq. (3.*c*)) using $n = 1$ and two grids including the grid with size $h$. Let $h = h_1$ be the smaller grid size, and $h_2$ the coarser, and let $h_{ref} = h_1$, then it follows that $a_1 = 1$, $r = a_2$, and from Eq. (3.*c*), with $n = 1$, we obtain

$$F_{ext} = (rF_f - F_c)/(r - 1) \quad \text{(a.5)}$$

Substituting Equation (a.5) in to (a.4) with $F_h = F_f$ and simplifying yields

$$e_{ext} = [1/(r - F_c/F_f)][(F_f - F_c)/F_f] \quad \text{(a.6)}$$

When this is compared with the $GCI_f$ proposed by Roache (1994, Eqs. (7) and (10) of the original reference) it is seen that, for $n = 1$

$$e_{ext} = [(r - 1)/(r - F_c/F_f)]GCI_f/3 \quad \text{(a.7)}$$

It should be noted that $GCI_f$ will be three times $e_{ext}$ only when $F_c = F_f$, indicating fully converged (grid independent) solutions. For example, for $i = 5$, $r = 1.4$, $F_f = 5.26$, $F_c = 4.765$, then $e_{ext} = 0.81\ GCI_f/3 = 19.05$. Similarly, for the approximate relative error $e_a$ defined by Eq. (6), it can be shown that (for $n = 1$)

$$e_a = (r - 1)GCI_f/3 \quad \text{(a.8)}$$

**M. Z. Hasan**
Associate Professor.

**Y. Mitsutake**
Research Associate.

**M. Monde**
Professor.

Department of Mechanical Engineering,
Saga University,
1 Honjo-machi, Saga-shi
Saga 840, Japan

# Shape of an Annular Liquid Jet

*Analytical and experimental studies have been done to determine the shape of a vertical, axisymmetric, annular liquid jet. From a balance of the surface, pressure, gravity, and inertia forces, a nonlinear, second-order, ordinary differential equation is obtained for the shape of the annular jet. This equation is solved numerically by the Runge-Kutta-Nyström method. An annular jet either converges (closes), diverges, or maintains (theoretically) its original radius depending upon the magnitude of the difference between the inside and outside pressure. This corresponds to, in terms of a dimensionless pressure $\bar{p}$, whether $\bar{p}$ is less than, greater than, or equal to 2. An experiment has been performed to verify the analytical solution. The jet velocity, inside pressure and other parameters have been varied to obtain different shapes of the jet, both closing and diverging. Good agreement with the analytical prediction is found.*

## 1 Introduction

Liquid jets in the forms of simple and annular jets and water bells have been studied for a long time, more than one hundred years. Many studies have dealt with the geometric shape of the liquid jets. Annular liquid jets have been studied by Baird and Davidson (1962), Binnie and Squire (1941), and Boussinesq (1869). The closing length of an annular liquid jet has been studied by Hoffman et al. (1980). Water bells have been studied by Dumbleton (1969), Lance and Perry (1953), Shoji (1973), and Taylor (1959).

There are many actual and suggested applications of liquid jets. Enhancement of heat transfer with impinging liquid jets is well known. An interesting suggestion for the use of annular, liquid-metal jets to act as a renewable first wall and blanket for inertial confinement fusion (ICF), or laser fusion, power reactors was made in the late seventies by Hoving (1976) and Maniscalo et al. (1977). The required annular jet parameters for this application would appear formidable: jet thickness, about half a meter; and jet radius and closing length, a few meters. The closing length of such a thick liquid jet can be in the kilometers (Hoving, 1977). Annular liquid jets have other more practical applications such as the formation of spherical shells (Kendall, 1986), acoustic barriers (Walker and East, 1984), and spray technology (Lefebvre, 1989, and Masters, 1985). Instability and breakup of an annular jet is of primary interest in such applications. Many studies have addressed the instability and breakup of annular liquid jets, two recent studies being those by Meyer and Weihs (1987) and Shen and Li (1996). Since surface force is an important parameter in determining the shape of an annular jet, an accurate theoretical prediction of the jet profile or its closing length coupled with experimental observation can be a tool for determining the surface tension of liquids.

The numerical method suggested by Boussinesq (1869) for working out the shape of an annular liquid jet from the basic momentum equation is cumbersome, as pointed out by Baird and Davidson (1962). Several studies have made various assumptions to obtain simplified equations for the annular jet shape. Among the simplifying assumptions are the following.

1. The effect of gravity is negligible.
2. The radius of axial curvature is much larger than the jet meridian radius.
3. The jet velocity is high and the closing length is large such that the jet surface can be considered to be nearly vertical.
4. Pressures inside and outside the annular jet are equal.

Binnie and Squire (1941) have solved for the jet profile using all of these four assumptions. Baird and Davidson (1962) have used the first three assumptions while allowing for pressure difference between the inside and outside of the annular jet. The third and fourth assumptions have been used by Hoffman et al. (1980) in estimating the closing length of an annular liquid jet. Tuck (1982) conducted an analytical and numerical study of annular water jets with and without the effect of gravity. However, he neglected the surface tension effect.

The objectives of the present work are to analytically solve for the shape of a vertical annular liquid jet without the four assumptions mentioned above, and to verify the analytical prediction by experimental observation. The analytical solution is presented in Section 2 where the governing differential equation for the shape of the jet is obtained and numerically solved to show the effects of the various parameters. Section 3 describes the experimental apparatus and experimental results. The analytical and experimental results are compared in Section 4. The concluding remarks are given in Section 5. The present work does not address the issue of instability on the shape or closing length of an annular liquid jet.

## 2 Analytical Solution

The shape of an annular liquid jet will be determined by the initial jet radius $R_o$, initial jet thickness $\delta_o$, density of the liquid $\rho$, its surface tension $\sigma$, initial average liquid velocity $u_m$, acceleration due to gravity $g$, and the pressure difference between inside and outside the jet $\Delta p$. If $r$ is the jet radius at any axial position $x$, then a functional relationship for $r$ can be written as

$$r = f(x, R_o, \delta_o, u_m, g, \rho, \Delta p, \sigma). \quad (1)$$

It can be shown by dimensional analysis that

$$\bar{r} = f_1(\bar{x}, \bar{\delta}_o, \bar{p}, \mathrm{Fr}, \mathrm{Bo}), \quad (2)$$

where the bar signifies that the parameter is dimensionless, and Bo and Fr are, respectively, the Bond and Froude numbers.

The forces that determine the shape of an annular liquid jet are gravity force, surface tension force, inertia force, pressure force, and friction force. Figure 1 shows a schematic of a closing circular, annular liquid jet. The annular jet has two free surfaces, outer and inner. At the exit of the annular nozzle, the mean radius of the jet is $R_o$ and its thickness is $\delta_o$. The axial distance

Contributed by the Fluids Engineering Division for publication in the JOURNAL OF FLUIDS ENGINEERING. Manuscript received by the Fluids Engineering Division June 3, 1996; revised manuscript received March 19, 1997. Associate Technical Editor: P. W. Bearman.

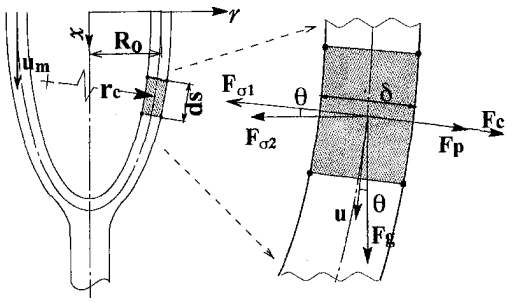


**Fig. 1 Schematic of a closing annular jet showing the coordinates, parameters, and forces on a jet element. $F_c$, $F_g$, $F_p$, $F_{\sigma 1}$, and $F_{\sigma 2}$ are, respectively, centrifugal (inertia), gravity, pressure, surface (axial curvature), and surface (meridian curvature) forces**

$x$ is measured from the exit of the annular nozzle. At $x = 0$, the average liquid velocity is denoted by $u_m$. The pressures inside and outside of the jet are denoted by $p_i$ and $p_o$, respectively. The direction of acceleration due to gravity $g$ is along $x$. The jet closes at a distance $x = L$ when it is converging.

Because of the two curvatures, one around the axis (meridian) and the other along the axis, there are two surface forces acting along the centers of these two curvatures. A small element with the forces acting on it is shown in Fig. 1. The element is located at an axial position $x$ where the mean jet radius is $r$. The forces acting on the element are given by the following equations.

$$F_g = (2\pi rds)\delta\rho g$$

$$F_{\sigma 1} = (2\pi rds)\frac{2\sigma}{r_c}$$

$$F_{\sigma 2} = (2\pi rds)\frac{2\sigma}{r}$$

$$F_c = (2\pi rds)\delta\rho\frac{u^2}{r_c}$$

$$F_p = (2\pi rds)\Delta p \qquad (3)$$

Here $F_g$, $F_{\sigma 1}$, $F_{\sigma 2}$, $F_c$, and $F_p$ are, respectively, the gravity force, surface force due to the axial curvature, surface force due to meridian curvature, inertia force (centrifugal), and pressure force. The length of the element is $ds$ along the axial curvature and its thickness is $\delta$. The density and surface tension of the liquid are denoted by $\rho$ and $\sigma$, respectively. The average liquid velocity in the element is $u$ and the radius of the axial curvature is $r_c$. The pressure difference between inside and outside is $\Delta p = (p_i - p_o)$.

Neglecting any friction loss, the liquid velocity at any $x$ is given by

$$u = \sqrt{(u_m^2 + 2gx)}. \qquad (4)$$

Axial curvature will not affect the jet velocity since gravity is the only external force and $x$ is measured along gravity, not jet profile. However, to include the effect of air drag or any other friction force, the above equation will have to be modified. The jet thickness at any $x$ can be obtained from continuity condition. It is given by

$$\delta = \frac{u_m R_o \delta_o}{ur}. \qquad (5)$$

Now, by force balance in the direction of the local radius of the axial curvature, we get

$$\frac{r}{r_c\cos\theta} + 1 - \frac{r\rho g\delta}{2\sigma}\tan\theta - \frac{u^2 r\rho\delta}{2\sigma}\frac{1}{r_c\cos\theta} - \frac{\Delta p r}{2\sigma\cos\theta} = 0 \qquad (6)$$

where $\theta$ is the angle between the direction of gravity and tangent to the local axial curvature. Boussinesq (1869) used Eq. (6) directly, together with Eqs. (4) and (5), to numerically solve for the jet profile. Using the initial values, $r_c$ is calculated from Eq. (6). Now a small step change in $\theta$ is applied to give new values of $r$ and $x$, and hence $u$ and $\delta$ from Eqs. (4) and (5), respectively. With these new values, $r_c$ can be recalculated, and the process continued to find the shape of the jet. This method is obviously cumbersome and the accuracy may also be questionable.

An ordinary differential equation for the jet radius $r$ can be obtained by a straightforward manipulation of Eq. (6). Denoting differentiation with respect to $x$ by prime, $\tan\theta$, $\cos\theta$, and $r_c$ in above equation can be written as

$$\tan\theta = r',$$

$$\cos\theta = \frac{1}{\sqrt{1 + (r')^2}}, \quad \text{and}$$

$$\frac{1}{r_c} = -\frac{r''}{[1 + (r')^2]^{3/2}}. \qquad (7)$$

Equation (7) is substituted in Eq. (6) and the resulting equation and Eqs. (4) and (5) are nondimensionalized by substituting

## Nomenclature

$d_i$ = initial inner diameter of the annular jet
$d_o$ = initial outer diameter of the annular jet
$f$ = signifies functional relationship
$F_c$, $F_g$, $F_p$, $F_{\sigma 1}$, $F_{\sigma 2}$ = forces due to inertia, gravity, pressure difference, surface tension (axial), and surface tension (meridian)
$g$ = acceleration due to gravity
$h$ = uniform step size along $x$ in numerical solution
$L$ = closing length of a converging jet
$p_i$ = jet inside pressure
$p_o$ = jet outside pressure
$R_o$ = initial mean jet radius, $(d_o + d_i)/2$
$r$ = mean jet radius at any $x$
$r_c$ = radius of the axial curvature
$u$ = average jet velocity at any $x$
$u_m$ = initial mean jet velocity
$x$ = axial distance measured from the exit of the annular tube
$\delta$ = jet thickness at any $x$
$\delta_o$ = initial jet thickness, $(d_o - d_i)/2$
$\rho$ = density of the jet liquid
$\sigma$ = surface tension of the jet liquid
$\theta$ = angle between the directions of jet velocity and gravity
$\bar{x}$, $\bar{r}$, $\bar{\delta}_o$, $\bar{\delta}$, $\bar{u}$ = $x/R_o$, $r/R_o$, $\delta_o/R_o$, $\delta/R_o$, $u/u_m$
$ds$ = length of a jet element along the jet velocity, Fig. 1
$\Delta p = (p_i - p_o)$
$\bar{p} = \Delta p/(\sigma/R_o)$
Bo = Bond number, $(\rho g R_o^2)/\sigma$
Fr = Froude number, $u_m^2/(gR_o)$
We (=Fr Bo) = Weber number, $(\rho R_o u_m^2)/\sigma$

$\bar{x} \rightarrow x/R_o$, $\bar{r} \rightarrow r/R_o$, $\bar{\delta} \rightarrow \delta/R_o$, $\bar{u} \rightarrow u/u_m$, and $\bar{p} \rightarrow \Delta p/(\sigma/R_o)$. The final equations for the liquid velocity, jet thickness, and jet radius become, respectively,

$$\bar{u} = \sqrt{1 + \frac{2\bar{x}}{\mathrm{Fr}}}, \tag{8}$$

$$\bar{\delta} = \frac{\delta_o}{\bar{r}\sqrt{\left(1 + \frac{2\bar{x}}{\mathrm{Fr}}\right)}}, \quad \text{and} \tag{9}$$

$$\bar{r}''\left[\frac{\mathrm{We}\,\bar{\delta}_o}{2}\sqrt{1 + \frac{2\bar{x}}{\mathrm{Fr}}} - \bar{r}\right] - \left[1 + (\bar{r}')^2\right] \times \left[\frac{\mathrm{Bo}\,\bar{\delta}_o}{2\sqrt{1 + \frac{2\bar{x}}{\mathrm{Fr}}}}\bar{r}' + \frac{\bar{p}\,\bar{r}}{2}\sqrt{1 + (\bar{r}')^2} - 1\right] = 0. \tag{10}$$

In these equations, $\mathrm{Fr} = u_m^2/(gR_o)$, $\mathrm{Bo} = \rho g R_o^2/\sigma$, and $\mathrm{We} = \rho R_o u_m^2/\sigma$ are, respectively, the Froude, Bond, and Weber numbers. The initial conditions are: at $\bar{x} = 0$, $\bar{r} = 1$, and $\bar{r}' = 0$.

Equation (10) describes the shape of an axisymmetric, vertial, annular liquid jet. This is a nonlinear, second-order, ordinary differential equation with initial conditions. The thickness of the jet at any axial location is given by Eq. (9). Whether the jet closes, maintains constant radius, or diverges will determine whether the thickness will increase, remain more or less constant (aside from a slight decrease due to the velocity increase), or decrease.

The condition for constant jet radius can be obtained from Eq. (10) by putting $\bar{r} = 1$ and $\bar{r}' = \bar{r}'' = 0$. This gives $\bar{p} = 2$, which in dimensional form is

$$\Delta p = \frac{2\sigma}{R_o}. \tag{11}$$

This implies that $F_p = F_{\sigma 1}$, and that the jet will not close and will maintain its initial radius when the pressure force balances the meridian surface forces.

This analysis does not deal with the stability of the annular jet. The assumptions for this theoretical solution are the following.

- The annular jet is vertical and hence axisymmetric.
- There is no energy loss due to friction with the surrounding medium.
- Jet radius is always very large compared with its thickness, i.e., $r \gg \delta$.
- The velocity profile relaxes quickly upon exit from the nozzle and does not affect the shape of the jet.

The third assumption allows one to take the mean jet radius to represent the inner and outer surface radii. This, however, is not true near the end when the jet is closing and may introduce error in the theoretical prediction. However, comparison with experimental data show that this error is small. The main benefit of this assumption is that it is not necessary to know for a converging jet the closing radius of the inner surface. The assumption of zero closing radius will introduce a singularity in calculating the meridian surface force $F_{\sigma 2}$.

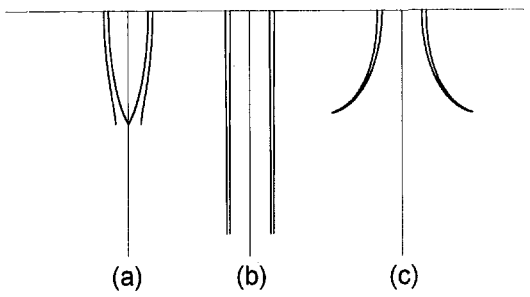


Fig. 2 Effect of pressure on the shape of an annular liquid jet for We = 100. (*a*) $\bar{p}$ = 1.0, (*b*) $\bar{p}$ = 2.0, and (*c*) $\bar{p}$ = 4.0

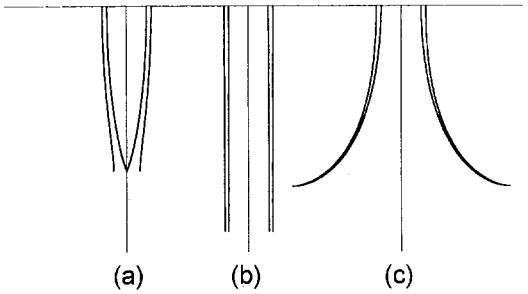


Fig. 3 Effect of pressure on the shape of an annular liquid jet for We = 200. (*a*) $\bar{p}$ = 1.0, (*b*) $\bar{p}$ = 2.0, and (*c*) $\bar{p}$ = 4.0

Experiments with a very short annular nozzle can be conducted to eliminate the last assumption. With a very short nozzle, there will not be enough time for the velocity profile to develop, and the velocity profile will be nearly flat. The present analysis does not use any of the four assumptions mentioned in Section 1 and used in the previous studies for predicting the shape of an annular liquid jet.

The nonlinear, second-order, ordinary differential equation, Eq. (10), together with the two initial conditions constitute an initial-value problem. By rewriting this equation in the form $\bar{r}'' = f(\bar{x}, \bar{r}, \bar{r}', \bar{\delta}_o, \bar{p}, \mathrm{We}, \mathrm{Bo}, \mathrm{Fr})$, it can readily be solved numerically by the Runge-Kutta-Nyström method (Kreyszig, 1988 and Nyström, 1925). The Runge-Kutta-Nyström method is a fourth-order method.

The numerical solution is started with $\bar{r} = 1$ and $\bar{r}' = 0$ at $\bar{x} = 0$. A small but uniform step change $h$ in $\bar{x}$ is taken. After each step increase in $\bar{x}$, the new values of $\bar{r}$ and $\bar{r}'$ are obtained by the numerical solution. At each $\bar{x}$, the new values of $\bar{u}$ and $\bar{\delta}$ are also obtained from the Eqs. (8) and (9), respectively. For a converging jet, calculation is terminated when $r$ becomes equal to $\delta/2$. At this point, $x$ is equal to the closing length. For a diverging jet, the solution is terminated either at a preselected axial distance or when the jet becomes horizontal. Since the Runge-Kutta-Nyström method is of fourth order, halving $h$ reduces the truncation error to one-sixteenth, and convergence to the correct solution is very quickly obtained.

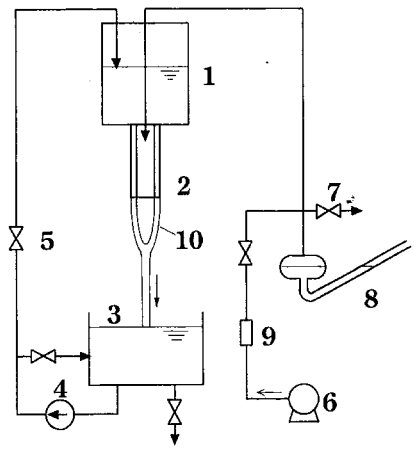


Fig. 4 A schematic of the experimental apparatus. 1-upper tank, 2-annular tube, 3-lower tank, 4-liquid pump, 5-flow control valve, 6-compressor, 7-pressure relief valve, 8-inclined-tube manometer, 9-pressure regulator, and 10-annular jet (converging)

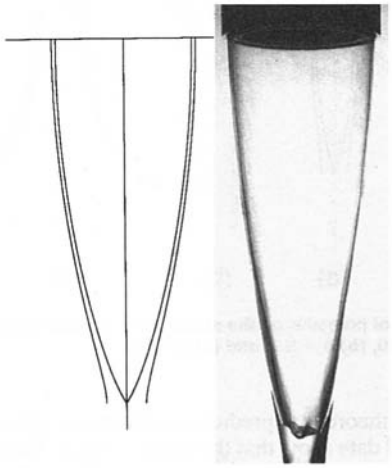

Fig. 5 Comparison of the photograph and theoretical prediction of a converging jet: water, $d_o$ = 37 mm, $d_i$ = 35 mm, $u_m$ = 1.39 m/s, $\Delta p$ = 2.32 Pa

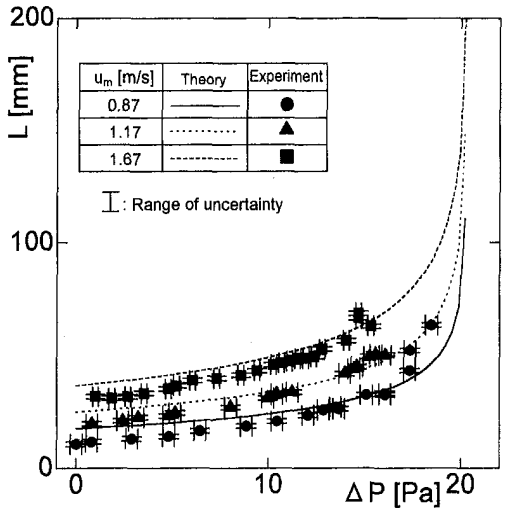


Fig. 7 Comparison of closing length with theoretical prediction for converging jets: water, $d_o$ = 15 mm, $d_i$ = 13 mm, ($\delta_o$ = 1 mm), $u_m$ = 0.87, 1.17, 1.67 m/s

The effects of pressure and We on the shape of an annular jet are shown in Figs. 2 and 3 for We 100 and 200, respectively. The liquid is water and the initial jet outside diameter and thickness are, respectively, 1 cm and 1 mm. For $\bar{p}$ = 1.0, the jet converges, and it diverges for $\bar{p}$ = 4.0. The radius of the jet remains constant at the initial radius for $\bar{p}$ = 2.0. The jet thickness changes with axial distance corresponding to the changes of radius and velocity, as required by continuity. Weber number can be doubled, keeping other parameters constant, either by increasing initial jet velocity to $\sqrt{2}u_m$ or halving the liquid surface tension. The jet shape is the same for either case.

## 3 Experimental Investigation

The theoretical analysis presented in the previous section has a few assumptions. In order to verify the accuracy of theoretical prediction, an experimental study was undertaken. In this section, the experimental apparatus and results are presented.

Figure 4 shows the experimental apparatus which produces a circular, annular liquid jet and allows variation of the parameters affecting the jet shape. The jet issues from the annular space between two concentric tubes marked 2 in the figure. The initial radius and thickness of the jet are varied by choosing appropriate diameters of the inner and outer tubes. The annular nozzle is connected to the upper tank 1 from which the liquid escapes by gravity and collects in the lower tank 3. The initial jet velocity (at the exit of the annular nozzle) is varied by varying the liquid head in the upper tank by means of the liquid pump 4 and valve 5. A pressure difference between the inside and outside of the jet can be maintained and varied by using the compressor 6 and pressure regulator 9. The pressure differential, which is quite small, is measured by the inclined-tube manometer 8, which uses immiscible water and alcohol as the barometric fluids. Two inclination angles were used, giving two magnification factors, 5 and 10, for the inclined manometer. The manometer could be read with 0.5 mm accuracy. The valve 7 vents to the atmosphere; it is used for resetting the pressure inside the jet. The annular nozzle is made of commercial brass tubes. The two tubes are connected at the upper ends only and the tube length is large compared with the hydraulic diameter to minimize entry effects.

For the different annular nozzles, calibration of liquid jet exit velocity against the head in the upper tank was done by actual measurement of the amount of liquid flow in a fixed time. Because of the various losses, a simple application of the Bernoulli's equation does not give the exit velocity accurately. Maximum error in measuring the average exit velocity was estimated to be less than 2 percent. Photographic observations were made for comparison of the overall shape of the converging and diverging jets with theoretical prediction. For a converging jet, the closing length is the axial distance from the exit of the annular nozzle to the point where the jet closes. This closing

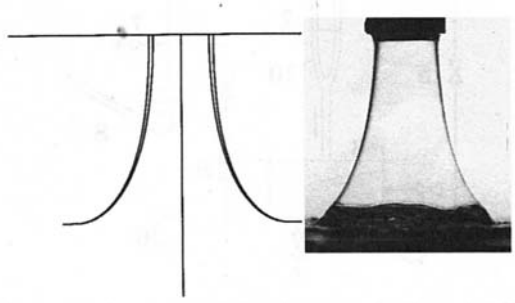

Fig. 6 Comparison of the photograph and theoretical prediction of a diverging jet: water, $d_o$ = 15 mm, $d_i$ = 13 mm, $u_m$ = 1.15 m/s, $\Delta p$ = 26.6 Pa

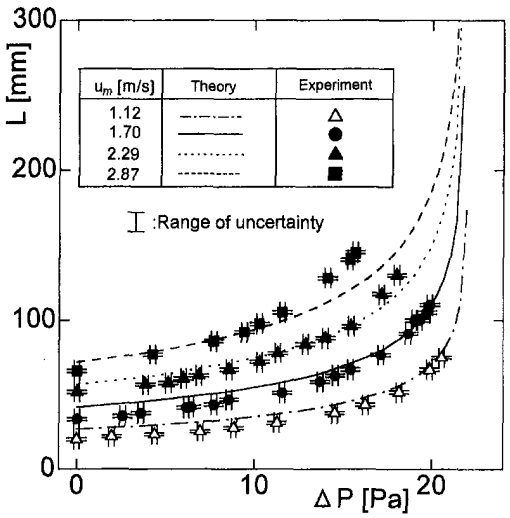


Fig. 8 Comparison of closing length with theoretical prediction for converging jets: water, $d_o$ = 15 mm, $d_i$ = 12 mm, ($\delta_o$ = 1.5 mm), $u_m$ = 1.12, 1.7, 2.29, 2.87 m/s

length increases with the increase in jet velocity, inside pressure, jet thickness and initial radius; it decreases with the increase in surface tension. This closing length was measured for different values of these parameters for comparison with the present theory. The measurement was made against a scale set close to the jet taking care to avoid any parallax error.

To maintain a higher pressure inside a diverging jet, a flat plate was held at bottom of the jet. The divergence of the jet increases with the increase in inside pressure. For diverging jets, the radius at a specific axial distance was measured for comparison with theory. This radius could not be measured easily during the experiment as a scale could not be placed in the plane of this radius. A scale drawn on the flat plate could not be satisfactorily used either because of the disturbance of the jet surface due to the impact with the plate. Therefore, this radius measurement was taken from photographs of diverging jets.

According to the theoretical prediction, an annular jet will maintain its initial radius when the dimensionless pressure difference $\bar{p} = 2$. However, it was not possible to make the closing length substantially long by trying to approach $\bar{p} = 2$; the jet becomes unstable and intermittent breaks occur on the surface, thus preventing the attainment of $\bar{p} = 2$. This instability of the annular liquid jet needs further study.

In the next section, experimental observation is compared with theoretical prediction to determine the accuracy of the theory. It is estimated from an error analysis that the error bar on the experimental data is about 10 percent. The sources of error are inaccuracy in liquid properties (density and surface tension) and error in measuring the initial jet size (radius and thickness), initial velocity, and differential pressure.

## 4 Comparison of Theory With Experiment

The overall shapes of a converging and a diverging jet are compared with the theoretical prediction in Figs. 5 and 6, respectively. It can be seen that the present theory predicts well the overall shape of both converging and diverging jets. However, the closing of the converging jet does not appear as smooth as in the theoretical prediction. This is to be expected as the assumption that the jet radius is much larger than the jet thickness is not valid near the closing point. This limitation is absent for a diverging jet, and the theoretical prediction match better the experimental observation.

Figure 7 compares the closing lengths of converging water jets from theory and experiment for $d_o = 15$ mm, $\delta_o = 1$ mm and three initial jet velocities: 0.87, 1.17, and 1.67 m/s. The theoretical prediction is good. At $\bar{p} = 2$, theory predicts the closing length to be infinite. It was not possible in the experiment to approach $\bar{p} = 2$. A few data near this value for $u_m = 0.87$ m/s show larger error. In general, the theoretical prediction for the closing length is somewhat greater than the experimental observation. This is to be expected, and it has resulted from the invalidity of the assumption of $\delta \ll r$ near the closing point.

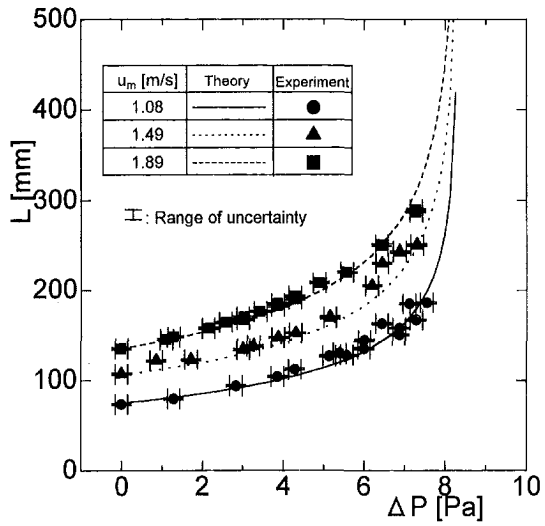


Fig. 9 Comparison of closing length with theoretical prediction for converging jets: water, $d_o = 37$ mm, $d_i = 34$ mm, ($\delta_o = 1.5$ mm), $u_m = 1.08$, 1.49, 1.89 m/s

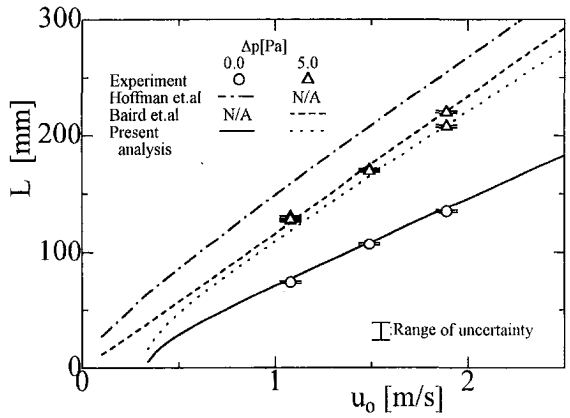


Fig. 10 Comparison with the approximate analyses of Baird and Davidson (1962) and Hoffman et al. (1980) for converging water jets with $d_o = 37$ mm, $d_i = 34$ mm, ($\delta_o = 1.5$ mm)

The same comparison as in Fig. 7 is shown in Fig. 8 for $d_o = 15$ mm, $\delta_o = 1.5$ mm, and $u_m = 1.12$ to 2.29 m/s, and in Fig. 9 for $d_o = 37$ mm, $\delta_o = 1.5$ mm, and $u_m = 1.08$ to 1.89 m/s. The accuracy of theoretical prediction in these two figures is similar to that in Fig. 7.

Figure 10 compares the approximate analyses of Baird and Davidson (1962) and Hoffman et al. (1980) with the present theory and experimental data. In the former reference, $\Delta p \neq 0$ and in the latter $\Delta p = 0$. The present analysis and Baird and Davidson's analysis agree with the experimental data well. The prediction of closing length by Hoffman et al. is much higher than experimental data. This is to be expected as the effect of axial curvature is neglected in their analysis. These two analyses differ greatly from the present analysis in predicting the closing length at low velocities. This is again due to the assumption that $r_c \gg r$ by Baird and Davidson and $r_c = \infty$ by Hoffman et al., which are increasingly in error when the jet closing distance is small due to low velocity and/or small $\Delta p$. In fact, the jet collapses quickly after exiting from the nozzle at sufficiently low velocities. For short closing lengths, $r_c$ is small and comparable to $r$.

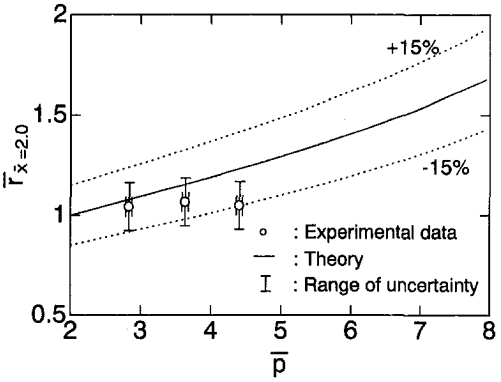


Fig. 11 Comparison of experimentally obtained $\bar{r}$ at $\bar{x} = 2.0$ with theoretical prediction for diverging jets: water, $d_o = 15$ mm, $d_i = 12$ mm, $u_m = 1.10$ m/s

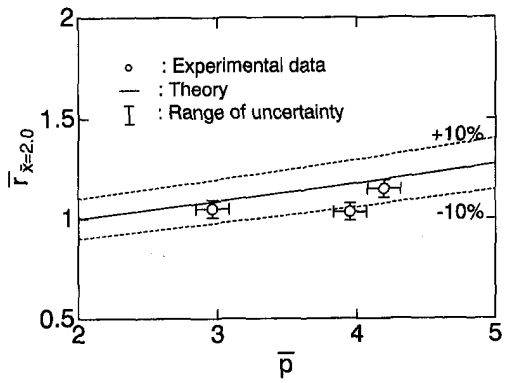


**Fig. 12 Comparison of experimentally obtained $\bar{r}$ at $\bar{x} = 2.0$ with theoretical prediction for diverging jets: water, $d_o = 37$ mm, $d_i = 35$ mm, $u_m = 1.39$ m/s**

In the last two Figs. 11 and 12, dimensionless jet radius at the dimensionless axial distance of 2 is compared with theoretical predictions for diverging jets with $d_o = 15$ mm, $\delta_o = 1.5$ mm and $u_m = 1.1$ m/s, and $d_o = 37$ mm, $\delta_o = 1$ mm and $u_m = 1.39$ m/s, respectively. The number of data points are few here since they had to be taken from photographic observations. The accuracy of theoretical prediction is good, within $\pm 10$ percent for the larger jet and $\pm 15$ percent for the smaller jet.

## 5 Conclusions

The shape of annular jets can be described with good accuracy by Eq. (10), which is a nonlinear, second-order, ordinary differential equation and has been derived by a force balance. It was derived by a straightforward manipulation of the force balance equation first proposed by Boussinesq (1869). The jet converges when the pressure due to the meridian surface tension is greater than the difference between the inside and outside pressures ($p_i - p_o$) and diverges when it is smaller. The present theory predicts well the shape of both converging and diverging jets, the accuracy being $\pm 15$ percent. The invalidity of the assumption that the jet thickness is always much smaller than jet radius near the point of closure of a converging jet does not appear to affect the theoretical prediction significantly.

Theoretically, an annular jet will maintain its initial radius if the meridian surface force is just balanced by the difference between the inside and outside pressure. However, it was not possible to approach this magnitude of pressure difference and obtain a long converging jet. Instability leading to breaks on the jet surface always appeared and did not allow any further increase of the inside pressure. This needs further study.

The average velocity is used as the jet velocity in the theoretical analysis. Since the velocity profile relaxes fairly quickly (Lienhard, 1968), the use of the average velocity seems to be acceptable, as is indicated by the good agreement with experiment. A comparison with the data obtained with a very short annular nozzle would verify this observation. The effect of friction with the air is also negligible for the relatively low velocities in the present experiment.

A flowing liquid-metal blanket for ICF reactors using a single jet is obviously impractical, the closing length would be very long (Hoving, 1977). However, multiple concentric annular jets with negative pressure difference to shorten the closing length might be feasible for such an application. Jet instability limiting the closing length is probably an important consideration for this configuration. There may be other ICF-specific feasibility issues, such as how to provide for the penetration of multiple laser beams.

Future work on annular liquid jets should focus on the effects of stability and friction drag on jet shape and closing length, analysis of a nonvertical jet, and the possibility of realizing a multi-layered liquid blanket for application to ICF reactors.

## Acknowledgment

The authors would like to acknowledge the contributions of Mr. Takahiro Shiki and Mr. Masanori Hayashi in building the experimental facility and collecting data.

## References

Baird, M. H. I., and Davidson, J. F., 1962, "Annular Jets, Part I," *Chemical Engineering Science,* Vol. 17, p. 467.

Binnie, A. M., and Squire, H. B., 1941, "Liquid Jets of Annular Cross-Section," *The Engineer,* London, Vol. 171, p. 236, 1941.

Boussinesq, J., 1869, *J. Comptes Rendus de l'Academie des Sciences,* Paris, Vol. 69. p. 128.

Dumbleton, J. H., 1969, "Effect of Gravity on the Shape of Water Bells," *Journal of Applied Physics,* Vol. 40, No. 10, p. 3950.

Hoffman, M. A., Takahashi, R. K., and Monson, R. D., 1980, "Annular Liquid Jet Experiments," ASME JOURNAL OF FLUIDS ENGINEERING, Vol. 102, p. 344.

Hoving, J., 1976, "First Wall Response to Energy Deposition in Conceptual Laser Fusion Reactors," Lawrence Livermore Laboratory Report, UCRL-77588, Feb.

Hoving, J., 1977, "Stability of a Flowing Circular Annular Liquid Curtain," Internal Memo SS&A-77-108, Lawrence Livermore Laboratory, Aug.

Kendall, M. J., 1986, "Experiments on Annular Liquid Jet Instability and on the Formation of Liquid Shells," *Physics Fluids,* Vol. 29, p. 2086.

Kreyszig, E., 1988, *Advanced Engineering Mathematics,* 6th ed. Wiley, New York.

Lance, G. N., and Perry, R. L., Dec., 1953, "Water Bells," *Proceedings of the Physical Society,* Vol. B66, No. 397B, London, p. 1067.

Lefebvre, A. H., 1989, *Atomization and Sprays,* Hemisphere, New York.

Lienhard, J. H., 1968, "Effects of Gravity and Surface Tension Upon Liquid Jets Leaving Poiseuille Tubes," ASME *Journal of Basic Engineering,* p. 262.

Maniscalco, J. A., Meir, W. R., and Monsler, M. J., July, 1977, "Conceptual Design of a Laser Fusion Powerplant," Lawrence Livermore Laboratory Report, UCRL-79652.

Masters, K., 1985, *Spray Drying Handbook,* 4th ed., Wiley, New York.

Meyer, J., and Weihs, D., 1987, "Capillary Instability of an Annular Liquid Jet," *Journal of Fluid Mechanics,* Vol. 179, p. 531.

Nyström, E. J., 1925, *Acta Soc. Sci. Fennicae,* Vol. 50.

Shen, J., and Li, X., 1996, "Instability of an Annular Viscous Liquid Jet," *Acta Mechanica,* Vol. 114, p. 167.

Shoji, M., 1973, "Study of Free Liquid Film Flow," *Trans. JSME* (in Japanese), Vol. 39, No. 321, p. 1568.

Taylor, G., 1959, "The Dynamics of Thin Sheets of Fluid, Part I—Water Bells," *Proc. Royal Society,* Vol. 253, London, pp. 289–295.

Tuck, E. O., 1982, "Annular Water Jets," IMA *Journal of Applied Mathematics,* Vol. 29, pp. 45–58.

Walker G., and East, R. A., 1984, "Shock Tube Studies of a Water Sheet Inertial Energy Absorber to Reduce Blast Overpressure," *Proc. Symp. Shock and Blast Wave Phenomena,* Paper C-2, p. 16, Cranfield, England.

# Air Entrainment in the Developing Flow Region of Plunging Jets—Part 1: Theoretical Development

**P. D. Cummings**
Maritime Engineer,
Kinhill Engineers,
299 Coronation Drive,
Brisbane QLD 4064,
Australia

**H. Chanson**
Senior Lecturer,
Fluid Mechanics,
Hydraulics and Environmental Engineering,
Department of Civil Engineering,
The University of Queensland,
Brisbane QLD 4072,
Australia

*Air-water bubbly flows are encountered in many engineering applications. One type of air-water shear flows is the developing flow region of a plunging jet. The mechanisms of air entrainment by plunging liquid jets are discussed in the light of new experimental evidence. Then the air bubble diffusion is analyzed analytically in the near-flow field of both circular and two-dimensional plunging jets. The theoretical developments are compared with existing circular plunging jet data and new experiments performed with a two-dimensional vertical supported jet. The study highlights two mechanisms of air entrainment at the plunge point depending upon the jet impact velocity and results suggest that the dispersion of air bubbles within the shear layer is primarily an advective diffusion process.*

## Introduction

When a water jet impinges a pool of water at rest, air bubbles may be entrained and carried away below the pool free surface (Figs. 1 and 2). This process is called plunging jet entrainment.

In chemical engineering, plunging jets are used to stir chemical as well as to increase gas-liquid transfer (e.g., McKeogh and Ervine, 1981, Bin, 1993). In sewage and water treatment plants, aeration cascades combine the effects of flow aeration and high turbulence level, enhancing the mass transfer of volatile gases (e.g., oxygen, nitrogen, volatile organic compounds). Plunging jet devices are used also in industrial processes (e.g., bubble flotation of minerals). Planar plunging jets are observed at weir spillways and overfalls. Some similarity between the planar plunging jet and the jet of a plunging breaking wave in the ocean was noted by several authors (e.g., Coles, 1967, Longuet-Higgins, 1982). A related case is the continuous impingement of a solid surface into a liquid pool and the associated air entrainment (e.g., Burley and Jolly, 1984). Despite the wide range of applications, few studies investigated air bubble entrainment in the developing shear layer of plunging jets.

At a plunging jet, the near-flow field (below the impingement point) is characterised a developing shear layer with some momentum transfer between the high-velocity jet core and the receiving pool of water, at rest at infinity (Fig. 1). In presence of air entrainment, an air bubble diffusion layer takes places (Figs. 1 and 2). The air diffusion layer may not coincide with the momentum shear layer. Further downstream the jet flow becomes fully-developed.

In the present paper and its companion (Cummings and Chanson, 1997), the authors investigate the air bubble entrainment in the developing region of plunging jet flows. New experiments were performed with a vertical supported jet (Fig. 2, Table 1). The results provide new information on the air entrainment mechanisms, the advective diffusion of air bubbles, the momentum exchange process, and the distributions of chord lengths of entrained bubbles. The mechanisms of air entrainment and air bubble diffusion are discussed in this paper. The experimental apparatus, velocity distributions and the chord length data are described in the companion paper. It is the purpose of these two papers to assess critically the overall state of this field, to present new analysis and experimental results, to compare these with existing data, and to present new compelling conclusions regarding momentum and air concentration development of jet-entrained gas-liquid flows. These conclusions will bring together the behavior of both axisymmetric and planar jets impinging on free surfaces.

Contributed by the Fluids Engineering Division for publication in the JOURNAL OF FLUIDS ENGINEERING. Manuscript received by the Fluids Engineering Division December 5, 1995; revised manuscript received April 1, 1997. Associate Technical Editor: O. C. Jones.

## Background

Several researchers (see bibliographic review by Bin, 1993) showed interest in circular plunging jets. Numerous experiments were performed with small circular jets (typically $\varnothing_1 < 5$ mm). Most researchers investigated qualitatively the air entrainment process.

Several studies showed that air entrainment takes place when the jet impact velocity exceeds a characteristic velocity. And the jet length and jet turbulence level both affect the quantitative value of that characteristic velocity (see next section). The mechanisms of air entrainment depends upon the jet velocity at impact, the physical properties of fluid, the jet nozzle design, the length of free-falling jet and the jet turbulence (Bin, 1993).

Some studies, in particular the thesis of Van de Sande (1974), McKeogh (1978), Van de Donk (1981), and Evans (1990), contributed significantly to our present understanding of the entrainment/entrapment process of air at the impingement point. Unlikely only a small number of studies investigated the flow field below the impingement point: e.g., McKeogh and Ervine (1981), Van de Donk (1981) and Bonetto and Lahey (1993). McKeogh and Ervine (1981) and Van de Donk (1981) recorded air concentration profiles and velocity distributions primarily in the fully-developed flow region, while Bonetto and Lahey (1993) presented results obtained in both the developing and fully-developed flow regions.

Two-dimensional plunging jet flows received much less attention. Some studies (Goldring et al., 1980, Sene, 1988) were performed with supported jets to investigate the flow patterns but no information is available on the distributions of air content and velocity below the impingement point.

Bin (1993) highlighted the lack of information on the velocity profiles and air content distributions in the vicinity of the impingement point and in the near-flow field.

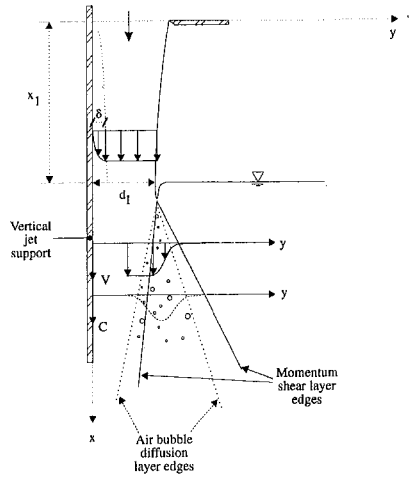


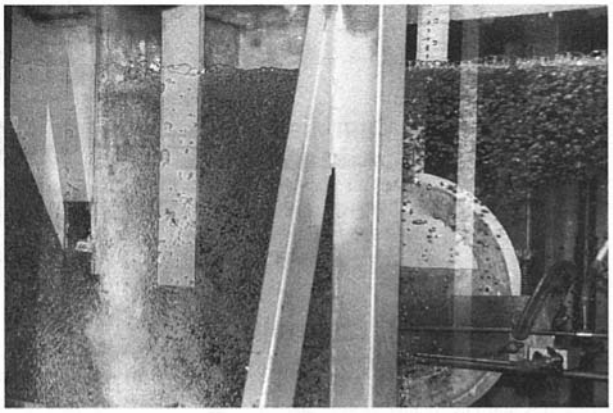

**Fig. 2 Photograph of air bubble entrainment at a vertical supported jet (side view). The support in on the left. The air bubble diffusion layer is clearly seen with the white downward diffusion cone. On the right note the rising air bubbles. $V_1$ = 6.14 m/s.**

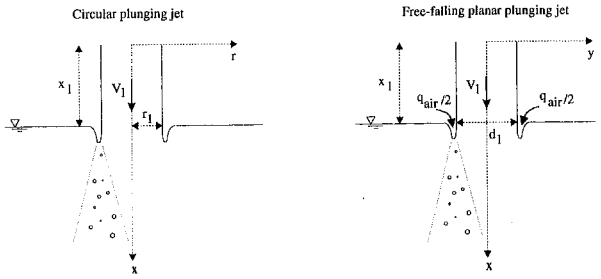


**Fig. 1 Sketch of air entrainment at a vertical supported jet, a circular plunging jet and a free-falling two-dimensional plunging jet**

## Mechanisms of Air Bubble Entrainment

In a plunging jet situation, air bubbles start to be entrained when the jet impact velocity $V_1$ exceeds a critical value. Dimensional analysis suggests that this critical velocity is a function of the fluid properties, the turbulence characteristics (velocity and length scales) and the angle of the jet with the free-surface. For the vertical supported jet experiment, the authors observed air bubble entrainment for $V_1 > 1.1$ to 2.0 m/s when the jet turbulence intensity at impact Tu varies from 1.3 down to 0.3 percent. With vertical circular plunging jets, McKeogh (1978) and Ervine et al. (1980) observed air entrainment for $V_1 > 0.8$ m/s when the turbulence intensity at the jet nozzle was larger than 3 percent, and they noticed larger inception velocities at lower turbulence levels at nozzle.

When air bubbles are entrained, visual and photographic observations obtained during the present series of experiments indicate two major air entrainment process. For low velocities (i.e., $V_1 < 2$ m/s), air bubble entrainment was observed to be caused by the pool of water being unable to follow the undulations of the jet surface and small air pockets are formed. Air enters the flow following the passage of these disturbances through the interface between the jet and the receiving fluid (Fig. 3(*a*)). High-speed videocamera images indicates that most bubbles are entrained as individual bubbles and air pockets, which are subsequently broken up into smaller size bubbles.

For large jet impact velocities (i.e., $V_1 > 3$ to 8 m/s), experiments on both circular (Van de Sande and Smith 1973) and

## Nomenclature

$C$ = air concentration defined as the volume of air per unit volume of air and water; it is also called void fraction
$D_t$ = turbulent diffusivity ($m^2/s$)
$D^\#$ = dimensionless turbulent diffusivity: $D^\# = D_t/(VY)$; $D^\# = D_t/(V_1 d_1)$ for two-dimensional shear flow and $D^\# = D_t/(V_1 r_1)$ for circular jet
$d$ = flow depth or jet thickness (m) measured perpendicular to the flow direction
$d_1$ = jet thickness (m) at the impact with the receiving pool of liquid
$g$ = gravity constant: $g = 9.80$ m/s$^2$ in Brisbane, Australia
$I_0$ = modified Bessel function of the first kind of order zero
$Q_{air}$ = air discharge ($m^3/s$)
$Q_w$ = water discharge ($m^3/s$)
$q_{air}$ = air discharge per unit width ($m^2/s$)
$q_w$ = water discharge per unit width ($m^2/s$)
$r$ = radial distance (m) from the jet centerline
$r'$ = radial coordinate (m)
$r_1$ = jet radius (m) at impact
Tu = turbulence intensity defined as: Tu = $u'/V$
$Tu_0$ = turbulence intensity measured at jet nozzle
$u$ = dimensionless variable
$u'$ = root mean square of longitudinal component of turbulent velocity (m/s)
$V$ = velocity (m/s)
$V_1$ = mean flow velocity (m/s) at jet impact
$W$ = channel width (m)
$x$ = distance along the flow direction (m)
$x_1$ = distance (m) between the channel intake and the impact flow conditions
$Y$ = characteristic flow depth or flow thickness (m) normal to the flow direction
$y$ = distance (m) measured normal to the flow direction
$\delta$ = boundary layer thickness (m) defined in term of 99% of the maximum velocity
$\delta_{al}$ = thickness (m) of the air sheet set into motion by a high-velocity plunging jet (Fig. 3)
$\theta$, $\theta'$ = radial angular coordinate
$\varnothing$ = diameter (m)

### Subscript

air = air flow
$w$ = water flow
1 = impact flow conditions

**Table 1 Experimental flow conditions of vertical plunging jets**

| Ref. (1) | Run (2) | $q_w$ m²/s (3) | $V_1$ m/s (4) | $x_1$[(a)] m (5) | Comments (6) |
|---|---|---|---|---|---|
| McKeogh and Ervine (1981) | | | | | Circular jet. |
| | | | 3.13 | | Fig. 6. $\varnothing_1$ = 0.009 m. $Tu_0$ = 5%. |
| | | | 3.9 | | Fig. 8 and 9. $\varnothing_1$ = 0.009 m. $Tu_0$ = 1%. |
| | | | 2.5 | | Fig. 9. $\varnothing_1$ = 0.009 m. $Tu_0$ = 1%. |
| | | | 3.3 | | Fig. 9. $\varnothing_1$ = 0.009 m. $Tu_0$ = 1%. |
| Van de Donk (1981) | | | | | Circular jet. |
| | VDD1 | | 4.463 | 0.20 | Fig. 3.22. $\varnothing_1$ = 0.0057 m. |
| | VDD2 | | 10.19 | 0.20 | Fig. 3.23. $\varnothing_1$ = 0.0059 m. |
| Bonetto and Lahey (1993) | | | | | Circular jet. |
| | B11 | | 6.18 | 0.03 | Fig. 11. $\varnothing_1$ = 0.0051 m. |
| | B13 | | 8.91 | 0.03 | Fig. 13. $\varnothing_1$ = 0.0051 m. |
| | B16 | | 5.27 | 0.01 | Fig. 16. $\varnothing_1$ = 0.0051 m. |
| Chanson (1995a) | | | | | Two-dimensional supported jet. $W$ = 0.269 m. |
| | F1 | 0.024 | 2.36 | 0.090 | $d_1$ = 0.0102 m. Tu = 1.70%. |
| | F2 | 0.048 | 4.06 | 0.090 | $d_1$ = 0.0118 m. Tu = 1.50%. |
| | F3 | 0.072 | 5.89 | 0.090 | $d_1$ = 0.0122 m. Tu = 0.74%. |
| | F4 | 0.096 | 8.0 | 0.090 | $d_1$ = 0.012 m. |
| | F5 | 0.108 | 9.0 | 0.090 | $d_1$ = 0.012 m. |
| Present study | | | | | Two-dimensional supported jet. $W$ = 0.269 m. |
| | 2-m/s | 0.0240 | 2.39 | 0.0875 | $d_1$ = 0.010 m. Tu = 1.6%. |
| | 6-m/s | 0.0720 | 6.14 | 0.0875 | $d_1$ = 0.0117 m. Tu = 0.75%. |

Notes:
(a): Longitudinal distance between the nozzle and the free-surface pool.
Tu: Jet turbulence intensity at impact.
$Tu_0$: Turbulent intensity measured at jet nozzle.

planar (authors' experiments) plunging jets indicate a qualitative change in the air entrainment process. A thin sheet of air, set into motion by shear forces at the surface of the jet, enters the flow at the impact point (Fig. 3(*b*)). The air sheet behaves as a ventilated cavity (e.g., Michel, 1984): the length of the air layer fluctuates considerably and air pockets are entrained by discontinuous "gusts" at the lower end of the air layer (Fig. 3). The elongated air sheet is intermittently broken by a "re-entrant jet" mechanism. Visual observations and conductivity probe measurements show clearly that some air is entrained in the form of elongated pockets. For jet velocities between 3 and 6 m/s, the authors observed air sheet thickness $\delta_{al}$ of about 0.5 to 5 mm. The jet velocity at which the air layer appears is an inverse function of jet turbulence: i.e., for 'smooth' jets, the air sheet will appear at larger velocities than for 'rough' jets.

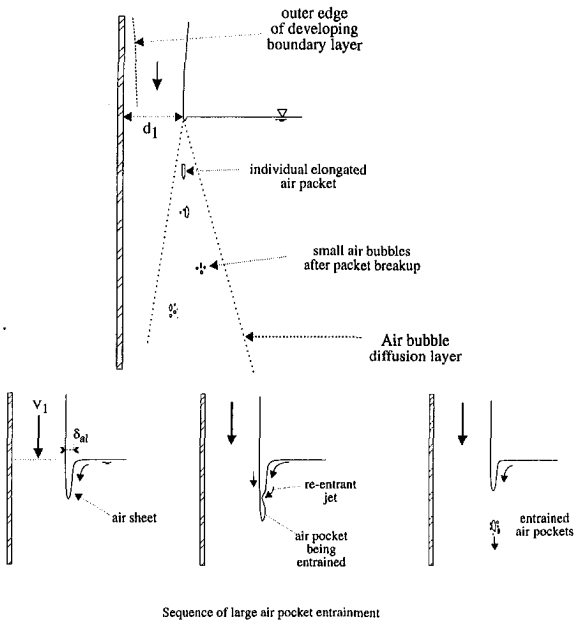


**Fig. 3 Sketch of air entrainment at a vertical supported jet. (*a*) Low-velocity air entrainment mechanism; (*b*) high-velocity air entrainment process**

The observations of air sheet thickness can be compared with the analysis of Lezzi and Prosperetti (1991) and Bonetto et al. (1994) (Table 2). The former suggested that the instability responsible for air entrainment is caused by gas viscosity while the latter study assumed that gas entrainment is induced by a Helmholtz-Taylor instability. The analysis of Bonetto et al. (1994) seems to fit better the authors' observations (Table 2). But additional data are required to confirm this point.

## Analysis of the Air Bubble Diffusion Process

The air bubble diffusion at a plunging liquid jet is a form of advective diffusion. For a small control volume, the continuity equation for air in the air-water flow is:

$$\text{div}\,(C\vec{V}) = \text{div}\,(D_t\,\vec{\text{grad}}\,C) \qquad (1)$$

where $D_t$ is the turbulent diffusivity. Equation (1) implies a constant air density (i.e. neglecting compressibility effects), it neglects buoyancy effects and is valid for a steady flow situation.

Considering a *circular plunging jet,* assuming an uniform velocity distribution, for a constant diffusivity (in the radial direction) independent of the longitudinal location and for a small control volume delimited by streamlines (i.e., stream tube), Eq. (1) becomes a simple diffusion equation:

$$\frac{V_1}{D_t}\frac{\partial C}{\partial x} = \frac{1}{r}\frac{\partial}{\partial r}\left(r\frac{\partial C}{\partial r}\right) \qquad (2)$$

where $x$ is the longitudinal direction, $r$ is the radial direction, and the diffusivity term $D_t$ averages the effects of the turbulent diffusion and of the longitudinal velocity gradient. The boundary conditions of the axisymmetric problem are: $C(x < x_1, r) = 0$ and a circular source of total strength $Q_{air}$ at $\{x - x_1 = 0, r = r_1\}$.

The problem can be solved analytically by applying a superposition method. At each position $\{x, r, \theta'\}$, the diffusion

**Table 2 Thickness of air sheet set into motion in high-velocity two-dimensional plunging jet**

| Reference (1) | $\delta_{al}$ $V_1$ = 2.4 m/s (2) | $V_1$ = 3 m/s (3) | $V_1$ = 6 m/s (4) | $V_1$ = 9 m/s (5) | Comments (7) |
|---|---|---|---|---|---|
| *Experimental data* | | | | | |
| Present data | N/A | | 0.5 to 5 mm | | Two-dimensional jet. |
| *Analysis* (*) | | | | | |
| Lezzi and Prosperetti (1991) | 0.065 mm | 0.06 mm | 0.04 mm | 0.03 mm | |
| Bonetto et al. (1994) | 0.65 mm | N/A | N/A | 6.6 mm | Calculations deduced from the measured air entrainment flux. |

Note:
(*) Calculations applied to two-dimensional plunging jet.

equation is solved for each point source of strength $\delta q_{air}$ located at $\{0, r_1, \theta_1'\}$. The contribution of each point source is:

$$\delta C = \frac{\delta q_{air} r_1 \delta\theta_1'}{4\pi D_t (x - x_1)} \exp\left(-\frac{V_1}{4D_t(x - x_1)} r'^2\right) \quad (3)$$

where $r'^2 = (r\cos\theta' - r_1\cos\theta_1')^2 + (r\sin\theta' - r_1\sin\theta_1')^2$, and $\{r, \theta'\}$ and $\{r_1, \theta_1'\}$ are the polar coordinates of the current point and of the point source respectively. The general solution of the air bubble diffusion equation is solved by superposing all the point sources:

$$C = \int_0^{2\pi} \delta C d\theta_1' \quad (4)$$

and using the definition of the air flow rate:

$$Q_{air} = 2\pi r_1 \delta q_{air} \quad (5)$$

The solution of the air bubble diffusion becomes:

$$C = \frac{Q_{air}}{Q_w} \frac{1}{4D^{\#}\dfrac{x - x_1}{r_1}} \exp\left(-\frac{1}{4D^{\#}} \frac{\left(\dfrac{r}{r_1}\right)^2 + 1}{\dfrac{x - x_1}{r_1}}\right) \times I_0\left(\frac{1}{2D^{\#}} \frac{\dfrac{r}{r_1}}{\dfrac{x - x_1}{r_1}}\right) \quad \text{Circular plunging jet} \quad (6)$$

where $I_0$ is the modified Bessel function of the first kind of order zero[1] and $D^{\#} = D_t/(V_1 r_1)$.

Considering a *two-dimensional free-falling jet,* the air bubbles are supplied by point sources located at $\{x = x_1, y = +d_1/2\}$ and $\{x = x_1, y = -d_1/2\}$ in the two-dimensional plane. Assuming an uniform velocity distribution, for a diffusion coefficient independent of the transverse location and for small control volume $\{dx, dy\}$ limited between two streamlines, the continuity equation (Eq. (1)) becomes a simple diffusion equation:

$$\frac{V_1}{D_t}\frac{\partial C}{\partial x} = \frac{\partial^2 C}{\partial y^2} \quad (7)$$

where $y$ is the distance normal to the jet centerline or jet support (Fig. 1). The boundary conditions of the two-dimensional free-jet flow are: $C(x < x_1, y) = 0$ and two point sources of equal strength $\{0.5Q_{air}/W\}$ located at $\{x_1, +d_1/2\}$ and $\{x_1, -d_1/2\}$.

[1] $I_0(u) = 1 + (u^2/2^2) + (u^4/2^2{*}4^2) + (u^6/2^2{*}4^2{*}6^2) + .$

The problem can be solved by superposing the contribution of each point source. The solution of the diffusion equation is:

$$C = \frac{1}{2}\frac{Q_{air}}{Q_w} \frac{1}{\sqrt{4\pi D^{\#}\dfrac{x - x_1}{d_1}}} \left(\exp\left(-\frac{1}{4D^{\#}} \frac{\left(\dfrac{y}{d_1} - 1\right)^2}{\dfrac{x - x_1}{d_1}}\right) + \exp\left(-\frac{1}{4D^{\#}} \frac{\left(\dfrac{y}{d_1} + 1\right)^2}{\dfrac{x - x_1}{d_1}}\right)\right)$$

two-dimensional free-falling plunging jet (8*a*)

where $Q_{air}$ is the volume air flow rate and $d_1$ is the thickness of the free-jet at impact. $D^{\#}$ is a dimensionless diffusivity: $D^{\#} = D_t/(V_1 d_1)$.

Considering a *two-dimensional supported jet,* the air bubbles are supplied by a point source located at $\{x = x_1, y = +d_1\}$ in the two-dimensional plane and the strength of the source is $Q_{air}/W$. The diffusion equation can be solved by applying the method of images and assuming an infinitesimally long support. It yields:

$$C = \frac{Q_{air}}{Q_w} \frac{1}{\sqrt{4\pi D^{\#}\dfrac{x - x_1}{d_1}}} \left(\exp\left(-\frac{1}{4D^{\#}} \frac{\left(\dfrac{y}{d_1} - 1\right)^2}{\dfrac{x - x_1}{d_1}}\right) + \exp\left(-\frac{1}{4D^{\#}} \frac{\left(\dfrac{y}{d_1} + 1\right)^2}{\dfrac{x - x_1}{d_1}}\right)\right)$$

two-dimensional supported plunging jet (8*b*)

where $Q_{air}$ is the volume air flow rate, $D^{\#}$ is a dimensionless diffusivity: $D^{\#} = D_t/(V_1 d_1)$. Note that $d_1$ is the thickness of the supported jet at impact.

*Remarks.* Equations (6), (8*a*), and (8*b*) are new analytical solutions of the advective diffusion of air bubbles (Eq. (1)). The two-dimensional and axisymmetrical solutions differ however because of the boundary conditions and of the integration method.

Note first that Eqs. (6), (8*a*), and (8*b*) are three-dimensional solutions of the diffusion equation. They are valid in both the developing bubbly region and in the fully-aerated flow region. For circular plunging jet and two-dimensional free jets, the core

of the jet (i.e., $r = 0$, $y = 0$) becomes aerated, respectively, for:

$$\frac{D_t(x - x_1)}{V_1 r_1^2} > 0.039$$

fully-aerated jet flow region [$C(r = 0) > 0.01$] (9$a$)

$$\frac{Q_{air}}{Q_w} \frac{\exp\left(-\frac{1}{4D^\#}\frac{1}{\frac{x - x_1}{d_1}}\right)}{\sqrt{4\pi D^\# \frac{x - x_1}{d_1}}} > 0.01$$

fully-aerated jet flow region [$C(y = 0) > 0.01$] (9$b$)

Note also that the solutions of two-dimensional plunging jet flows (Eq. (8$a$) and (8$b$)) derive from a classical solution of the two-dimensional advective diffusion equation (e.g., Crank, 1956, Fischer et al., 1979). In the developing air bubble diffusion layers (i.e., $C\ (y = 0) = 0$), Eqs. (8$a$) and (8$b$) can be approximated, respectively, by:

$$C = \frac{1}{2}\frac{Q_{air}}{Q_w} \frac{1}{\sqrt{4\pi D^\# \frac{x - x_1}{d_1}}} \exp\left(-\frac{1}{4D^\#}\frac{\left(\frac{y}{d_1} - 1\right)^2}{\frac{x - x_1}{d_1}}\right)$$

free jet (10$a$)

$$C = \frac{Q_{air}}{Q_w} \frac{1}{\sqrt{4\pi D^\# \frac{x - x_1}{d_1}}} \exp\left(-\frac{1}{4D^\#}\frac{\left(\frac{y}{d_1} - 1\right)^2}{\frac{x - x_1}{d_1}}\right)$$

supported jet (10$b$)

Note further that the analytical developments imply a constant diffusion coefficient $D_t$, where $D_t$ averages the effects of turbulent dispersion and streamwise velocity gradient. Such an assumption does not reflect the real nature of the turbulent shear layer not the existence of vortical structures (e.g., Fig. 4($a$), Chanson, 1995b). Nevertheless, the agreement between experiments and theory is within the accuracy of the instrumentation, suggesting that the air bubble diffusion process is little affected by the turbulent shear flow.

Additional details of the calculations were presented in Chanson (1995a).

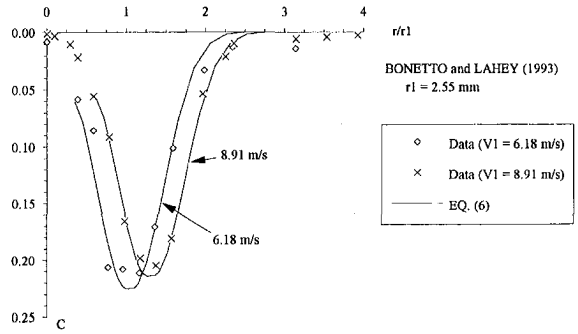


**Fig. 4 Air bubble diffusion in the developing shear region of circular jet. Comparison between Eq. (6) and experimental data (Bonetto and Lahey, 1993).**

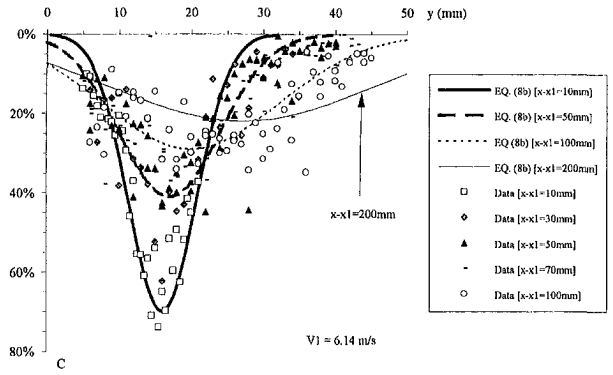


**Fig. 5 Distributions of air concentration in the developing flow region of vertical supported plunging jets. Comparison between Eq. (8$b$) and experimental data (present study: impact velocity $V_1$ = 6.14 m/s).**

## Results and Discussion

**Comparison With Experimental Data.** Equations (6) and (8$b$) have been compared successfully with experimental data (Van de Donk, 1981; Bonetto and Lahey, 1993; Chanson 1995a, Present study). Details of the experimental flow conditions are listed in Table 1. Figures 4 and 5 show some examples.

Figure 4 compares Eq. (6) with the recent data of Bonetto and Lahey (1993) while Chanson's (1995a) data are compared with Eq. (8$b$). Both Figs. 4 and 5 show a good agreement between experimental data and analytical solutions of the advective diffusion equation.

Note that Eq. (8$a$) cannot be verified in the fully-aerated flow region (i.e., $C\ (y = 0) > 0$) because of the absence of experimental data.

**Discussion.** Downstream of the entrainment point, the distributions of air content exhibit a distinctive shape (Figs. 4 and 5) which can be modelled by an advective diffusion equation. The analytical integration of Eq. (1) provides three-dimensional solutions (Eqs. (6), (8$a$), (8$b$)) which are valid in both the developing bubbly region and in the fully-aerated flow region.

Three parameters characterise the advective diffusion solutions (Eqs. (6) and (8)): the air flow rate $Q_{air}/Q_w$, the dimensionless diffusivity $D^\#$ and eventually the location of the symmetry line of the air content profile. For the experiments of Van de Donk (1981), Chanson (1995a) and the authors, the data and analytical solutions were best fitted with the air flow rate and the diffusivity being constants independent of the longitudinal position ($x - x_1$). For the authors' experiments, the air flow rate was calculated from the continuity equation for air as $q_{air} = \int_0^\infty CVdy$ where $C$ and $V$ are local values (Cummings and Chanson 1997). Such results and the close agreement between data and analytical solutions suggest that the diffusion of air bubbles below the impingement point is primarily an advective diffusion process.

Note that the data of Bonetto and Lahey (1993) could not be checked in details because of the insufficient number of data.

The authors wish to emphasize that Eqs. (6) and (8) are not valid very-close to the entrainment point. At the impingement point, the air entrainment/entrapment process cannot be simply modelled by an advective diffusion mechanism. For the authors' experiments, Eq. (8) and experimental data were in good agreement for ($x - x_1$) $\geq$ 20 mm.

## Conclusion

The authors have investigated the mechanisms of air entrainment at plunging liquid jets. They performed new measurements in a large vertical supported jet experiment ($0.3 < V_1 < 9$ m/

s). The flow field below the impingement point was investigated with conductivity probes and high-speed pictures.

1 Air bubble entrainment is observed when the jet impact velocity becomes larger than a critical value of about 1.1 to 2.0 m/s for the two-dimensional vertical jet experiment.

2 At the plunge point, two mechanisms of air entrainment can be observed: individual bubble entrainment at low-jet velocity (i.e. $V_1 < 2$ m/s), and a ventilated-cavity mechanism at high-velocities (i.e., $V_1 > 3$ to 8 m/s).

3 Below the impingement point, the air concentration profiles follow closely new analytical solutions of the diffusion equation for both circular plunging jets (Eq. (6)) and two-dimensional plunging jets (Eq. (8)). The close agreement between data and theory suggests that the dispersion of air bubbles within the shear layer is primarily an advective diffusion process.

In a companion paper (Cummings and Chanson, 1997), the velocity field will be described and bubble chord length distributions will be presented.

## Acknowledgments

The authors want to thank particularly Professor C. J. Apelt, University of Queensland who supported this project since its beginning. They acknowledge the support of the Department of Civil Engineering at the University of Queensland which provided the experimental facility and the financial support of Australian Research Council (Ref. No. A89331591). The first author was supported by an Australian Postgraduate Award during his Ph.D. thesis.

The authors appreciate the helpful comments of the anonymous reviewers and of the associated technical editor, Professor O. C. Jones.

## References

Bin, A. K., 1993, "Gas Entrainment by Plunging Liquid Jets," *Chemical Engineering Science,* Vol. 48, No. 21, pp. 3585–3630.

Bonetto, F., and Lahey, R. T. Jr., 1993, "An Experimental Study on Air Carryunder due to a Plunging Liquid Jet," *International Journal of Multiphase Flow,* Vol. 19, No. 2, pp. 281–294. Discussion: Vol. 20, No. 3, pp. 667–770.

Bonetto, F., Drew, D., and Lahey, R. T. Jr., 1994, "The Analysis of a Plunging Liquid Jet—The Air Entrainment Process," *Chemical Engineering Communication,* Vol. 130, pp. 11–29.

Burley, R., and Jolly, R. P. S., 1984, "Entrainment of Air into Liquids by a High Speed Continuous Solid Surface," *Chemical Engineering Science,* Vol. 39, No. 9, pp. 1357–1372.

Chanson, H., 1995a, "Air Bubble Entrainment in Free-surface Turbulent Flows. Experimental Investigations." Report CH46/95, Dept. of Civil Engineering, University of Queensland, Australia, June, 368 pages.

Chanson, H., 1995b, "Air Entrainment in Two-dimensional Turbulent Shear Flows with Partially Developed Inflow Conditions," *International Journal of Multiphase Flow,* Vol. 21, No. 6, pp. 1107–1121.

Coles, K. A., 1967, *Heavy Weather Sailing,* Adlard Coles, London, UK, 303 pages.

Crank, J., 1956, *The Mathematics of Diffusion,* Oxford University Press, London, UK.

Cummings, P. D., and Chanson, H., 1997, "Air Entrainment in the Developing Flow Region of Plunging Jets. Part 2," ASME JOURNAL OF FLUIDS ENGINEERING, published in this issue pp. 603–608.

Ervine, D. A., McKeogh, E. J., and Elsawy, E. M., 1980, "Effect of Turbulence Intensity on the rate of Air Entrainment by Plunging Water Jets," *Proceedings of the Institution of Civil Engineers,* Part 2, June, pp. 425–445.

Evans, G. M., 1990, "A Study of a Plunging Jet Bubble Column," Ph.D. thesis, Univ. of Newcastle, Australia.

Fischer, H. B., List, E. J., Koh, R. C. Y., Imberger, J., and Brooks, N. H., 1979, *Mixing in Inland and Coastal Waters,* Academic Press, New York, USA.

Goldring, B. T., Mawer, W. T., and Thomas, N., 1980, "Level Surges in the Circulating Water Downshaft of Large Generating Stations," *Proceedings of 3rd International Conference on Pressure Surges,* BHRA Fluid Eng., F2, Canterbury, U.K., pp. 279–300.

Lezzi, A. M., and Prosperetti, A., 1991, "The Stability of an Air Film in a Liquid Flow," *Journal of Fluid Mechanics,* Vol. 226, pp. 319–347.

Longuet-Higgins, M. S., 1982, "Parametric Solutions for Breaking Waves," *Journal of Fluid Mechanics,* Vol. 121, pp. 403–424.

McKeogh, E. J., 1978, "A Study of Air Entrainment using Plunging Water Jets," Ph.D. thesis, Queen's University of Belfast, UK, 374 pages.

McKeogh, E. J., and Ervine, D. A., 1981, "Air Entrainment rate and Diffusion Pattern of Plunging Liquid Jets," *Chemical Engineering Science,* Vol. 36, pp. 1161–1172.

Michel, J. M., 1984, "Some Features of Water Flows with Ventilated Cavities," ASME JOURNAL OF FLUIDS ENGINEERING, Sept., Vol. 106, p. 319.

Sene, K. J., 1988, "Air Entrainment by Plunging Jets," *Chemical Engineering Science,* Vol. 43, Bo. 10, pp. 2615–2623.

Van de Donk, J., 1981, "Water Aeration with Plunging Jets." Ph.D. thesis, TH Delft, The Netherlands, 168 pages.

Van de Sande, E., 1974, "Air Entrainment by Plunging Water Jets," Ph.D. thesis, TH Delft, The Netherlands, 123 pages.

Van de Sande, E., and Smith, J. M., 1973, "Surface Entrainment of Air by High Velocity Water Jets," *Chemical Engineering Science,* Vol. 28, pp. 1161–1168.

# Air Entrainment in the Developing Flow Region of Plunging Jets—Part 2: Experimental

## (Data Bank Contribution)*

**P. D. Cummings**
Maritime Engineer,
Kinhill Engineers,
299 Coronation Drive,
Brisbane QLD 4064,
Australia

**H. Chanson**
Senior Lecturer,
Fluid Mechanics,
Hydraulics and Environmental Engineering,
Department of Civil Engineering,
The University of Queensland,
Brisbane QLD 4072,
Australia

*When a water jet impinges a pool of water at rest, air bubbles may be entrained and carried away below the pool free surface: this process is called plunging jet entrainment. The study presents new experimental data obtained with a vertical supported jet. Distributions of air concentration and mean air-water velocity, and bubble chord length distributions measured in the developing shear layer are presented. The results indicate that the distributions of void fraction follow closely analytical solution of the diffusion equation. Further, the momentum shear layer and the air bubble diffusion layer do not coincide. Chord length data show a wide range of air bubble sizes and overall the experimental results suggest strong interactions between the entrained air bubbles and the momentum transfer mechanisms.*

## Introduction

When a falling nappe impinges a pool of water, air bubbles are entrained at the intersection of the jet with the receiving waters (Fig. 1). Large numbers of air bubbles are entrained into the turbulent shear flow. This process is called plunging jet entrainment. Plunging jet applications include plunging jet columns, drop structures along waterways, cooling system in power plants, plunging breakers and waterfalls.

In a first paper (Cummings and Chanson, 1997), the authors reviewed the current knowledge on the plunging jet entrainment. They showed that most researchers studied circular jets of small sizes, and few experiments described quantitatively the flow field below the free-surface of the receiving pool. It is the purpose of this paper to present new experimental results obtained with a vertical supported plunging jet. First, the experimental apparatus is described in details. Then experimental results of air concentration, mean air-water velocities, and chord length distributions are presented. In a later part, the results are discussed and compared with other data.

## Experimental Apparatus

**Plunging Jet Apparatus.** The experimental apparatus consists of a fresh water planar jet issuing from a 0.269-m × 0.012-m slot nozzle and plunging into a 0.3-m wide (Fig. 1). The receiving channel is 1.8-m deep with glass walls (10-mm thick). The supported-jet nozzle is made of 6-mm thick PVC with lateral perspex windows for flow visualisation. The jet support length is 0.35 m and the angle of the support with the horizontal was 89-degrees for all experiments. The water supply (Brisbane tap water) comes from a constant-head tank with a constant water level of 12.9 m above the nozzle. The experiment provides average jet velocities from 0.3 to 9 m/s.

The discharge was measured with orifice meters. The error on the discharge measurement was less than 1%.

**Instrumentation.** In the free-falling jet, clear water jet velocities and turbulent velocity fluctuations (in clear-water flows) were measured with a Pitot tube connected to a pressure transducer (Validyne™ DP15, diaphragm ranges 2.2 to 22 kPa, accuracy 0.25 percent of full-scale). The transducer was scanned at 500 Hz and the accuracy of the clear-water velocity data was normally estimated as: $\Delta V/V$ = one percent. At very-low velocity (e.g., $V < 0.5$ m/s), measurements with the Pitot tube oriented vertically could mount up to 15 percent.

Two conductivity probes were used to record the air-water flow characteristics. A single-tip conductivity probe (inner electrode ∅: 0.35 mm, outer electrode ∅: 1.42 mm) was used to perform air concentration measurements only. A two-tip conductivity probe was used to record simultaneously the air concentration and air-water velocity. The two tips were aligned in the direction of the flow. Each tip is identical and has an internal concentric electrode ($\varnothing = 25$ $\mu$m, Pt) and an external stainless steel electrode of 200 $\mu$m diameter. Both conductivity probes are excited by an air bubble detector (Ref. AS25240). This electronic system was designed with a response time less than 10 $\mu$s and it was calibrated with a square wave generator. Most measurements were recorded with a scan rate of 40 kHz per channel. The analysis of conductivity probe data provided the void fraction (i.e., air concentration), mean air-water interface velocity and chord length distributions at various positions within the developing shear layer.

The error on the air concentration (void fraction) measurements was estimated as: $\Delta C/C = 2$ percent for $5 < C < 95$ percent, $\Delta C/C \sim 0.001/(1 - C)$ for $C > 95$ percent, and $\Delta C/C \sim 0.001/C$ for $C < 5$ percent. The mean air-water velocities, recorded using the double-tip conductivity probe, were computed with a cross-correlation technique. The analysis of the velocity field and chord length distributions implies no slip between the air and water phases. The error on the mean air-water velocity measurements was estimated as: $\Delta V/V$ = five percent for $5 < C < 95$ percent. $\Delta V/V = 10$ for $1 < C < 5$ and $95 < C < 99$ percent. With the two-tip conductivity probe, the minimum detectable bubble chord length was about 100 $\mu$m

* Data have been deposited to the JFE Data Bank. To access the file for this paper, see instructions on p. 738 of this issue.

Contributed by the Fluids Engineering Division for publication in the JOURNAL OF FLUIDS ENGINEERING. Manuscript received by the Fluids Engineering Division December 5, 1995; revised manuscript received April 11, 1997. Associate Technical Editor: O. C. Jones.

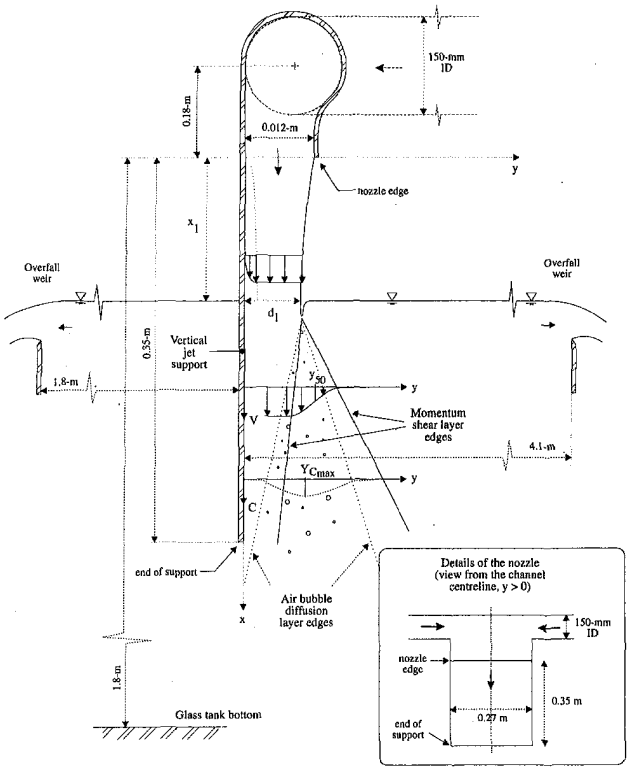


**Fig. 1 Sketch of the vertical supported jet experiment**

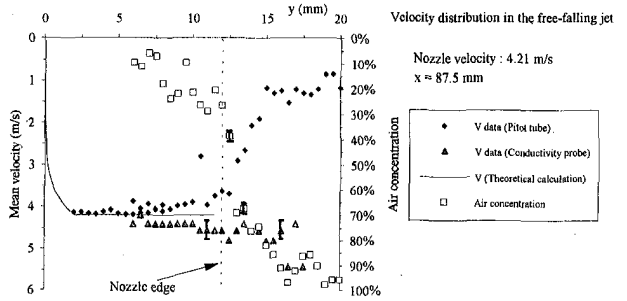


**Fig. 2(*a*) Nozzle velocity: 4.21 m/s**

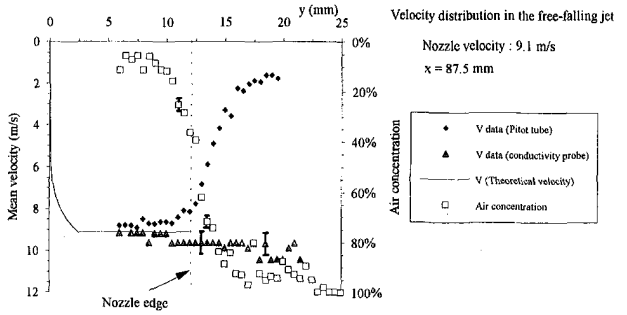


**Fig. 2(*b*) Nozzle velocity: 9.1 m/s**

**Fig. 2 Distributions of air concentration and mean air-water velocity the free-falling jet—comparison between experimental data and calculations**

in a 1-m/s flow and 450 $\mu$m in a 9-m/s jet based upon a data acquisition frequency of 40 kHz per channel.

Measurements were taken on the channel centreline. The displacement of the probes in the direction normal to the jet support and along the jet direction were controlled by two identical scale-verniers. The error in the longitudinal and perpendicular positions of the probes is less than 0.25 mm in each direction.

Additional measurements were performed using high speed photographs with a flash speed of 33 $\mu$s (e.g., Chanson and Cummings, 1994) and high-speed video camera images with a shutter speed of 500 $\mu$s.

**Calibration and Validation of the Measurement Techniques.** Several calibration tests were performed to compare the single-tip and double-tip conductivity probes. Identical experiments were performed with both the single-tip and conductivity probes. In each case, identical air concentration data were observed (within the accuracy of the data) suggesting that the probe diameter has little effect on the void fraction measurement.

To validate the double-tip probe measurement technique, measurements were performed within the free-falling supported jet (i.e., $x < x_1$). Velocities were recorded using both the dual tip conductivity probe and Pitot tube. The tips of each probe were located at the same location for comparison. The data were compared with theoretical calculations: ideal-fluid flow calculation outside of the boundary layer and power law velocity distribution within the developing turbulent boundary layer. Figure 2 presents typical results. The agreement between the two probes and the theoretical calculation are within the accuracy of the measurement techniques.

## Nomenclature

$C$ = air concentration defined as the volume of air per unit volume of air and water; it is also called void fraction
$C_{max}$ = maximum air concentration in the air bubble diffusion layer
$D_t$ = turbulent diffusivity ($m^2/s$)
$D^{\#}$ = dimensionless turbulent diffusivity: $D^{\#} = D_t/(V_1 d_1)$ for two-dimensional shear flow
$d$ = flow depth or jet thickness (m) measured perpendicular to the flow direction
$d_1$ = jet thickness (m) at the impact of a supported plunging jet with the receiving pool of liquid
$g$ = gravity constant: $g = 9.80$ m/s$^2$ in Brisbane, Australia
$K$ = integration constant in Goertler's (1942) solution of the motion equation in a free shear layer
$Q$ = volume discharge ($m^3/s$)
$q$ = volume discharge per unit width ($m^2/s$)
$u$ = dimensionless variable
$V$ = velocity (m/s)
$V_1$ = mean flow velocity (m/s) at jet impact
$W$ = channel width (m)
$x$ = distance along the flow direction (m)
$x_1$ = distance (m) between the channel intake and the impact flow conditions
$y$ = distance (m) measured normal to the flow direction
$Y_{C_{max}}$ = distance (m) normal to the bottom where $C = C_{max}$
$y_{50}$ = distance (m) normal to the flow direction where $V = 0.5V_1$
$\nu_T$ = eddy viscosity ($m^2/s$) or momentum exchange coefficient
$\omega$ = vorticity ($s^{-1}$)
$\varnothing$ = diameter (m)
$\Delta$ = error

### Subscript

air = air flow
$w$ = water flow
$x$ = component in the $x$-direction
$y$ = component in the $y$-direction
1 = impact flow conditions

Further comparisons between Pitot tube and conductivity probe data were performed during each experiment. Velocities were recorded as close as possible of the support, and the data were compared successfully with the ideal-fluid flow velocity deduced from the continuity and Bernoulli equation. Typical results are shown in Figs. 3 and 4. Additional verifications were conducted by checking the continuity equation for water at each cross-section (i.e., $q_w = \int_0^\infty (1 - C)Vdy$).

**Experimental Flow Conditions.** A large number of experiments were performed with jet impact velocities ranging from 0.5 to 9 m/s. The entire flow characteristics were recorded for two jet velocities (Table 1). For most experiments, the vertical jet impacted the receiving pool of water at 0.09-m below the jet nozzle. The impact flow conditions were not fully-developed and the ratio of the boundary layer thickness over jet thickness $\delta/d_1$ was less than 0.2.

During the experiments, the plunging jet was unsteady and fluctuating while the probes were fixed and did not follow the fluctuations of the flow (e.g., fluctuations of pool free-surface). As a result, the data (e.g., Figs. 3 and 4) exhibit a greater scatter than the probe accuracy, reflecting the unsteady fluctuating nature of the investigated flow.

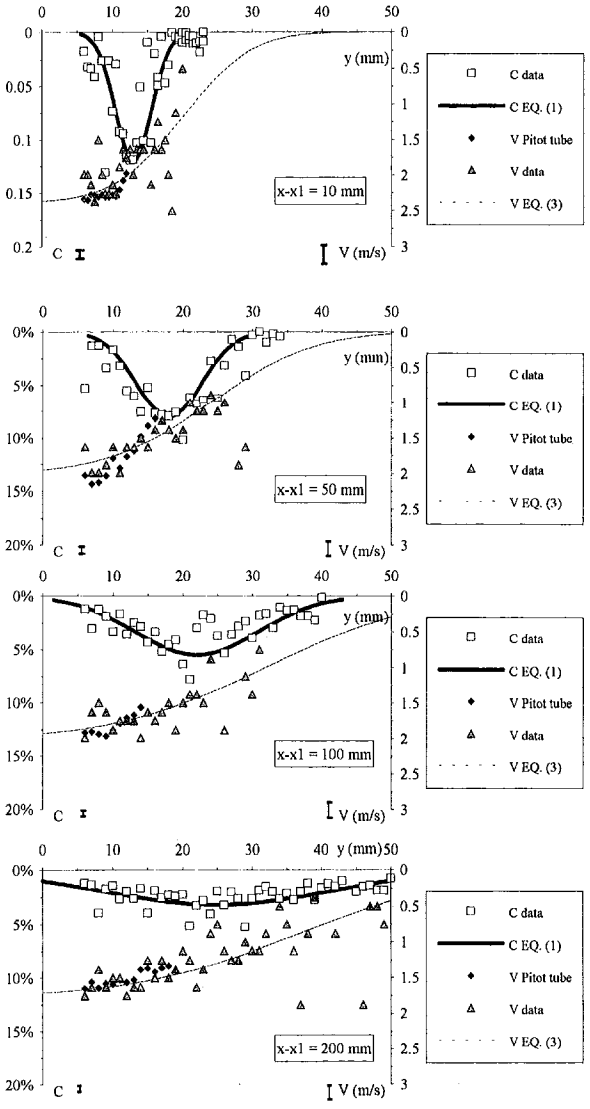


**Fig. 3 Distributions of air concentration and mean air-water velocity in the developing flow region of vertical supported plunging jets—comparison between Eqs. (1) and (3) and experimental data (impact velocity $V_1$ = 2.39 m/s)**

Full details of the experimental apparatus and instrumentation, and experimental results are reported in Cummings (1996). An earlier series of experiments performed in the same facility was reported in Chanson (1995).

## Experimental Results and Discussion

**Air Concentration Distributions.** Figures 3 and 4 present some experimental results for two jet impact velocities and at several locations below the impingement point. Both air concentration and velocity profiles are plotted as functions of the distance normal to the jet support.

For a two-dimensional supported jet, the air concentration data followed closely an analytical solution of the diffusion equation (Cummings and Chanson, 1997):

$$C = \frac{Q_{air}}{Q_w} \frac{1}{\sqrt{4\pi D^* \frac{x - x_1}{d_1}}} \left( \exp\left( -\frac{1}{4D^*} \frac{\left(\frac{y}{d_1} - 1\right)^2}{\frac{x - x_1}{d_1}} \right) + \exp\left( -\frac{1}{4D^*} \frac{\left(\frac{y}{d_1} + 1\right)^2}{\frac{x - x_1}{d_1}} \right) \right) \quad (1a)$$

where $C$ is the air concentration defined as the volume of air per unit volume of air and water, $x$ is the longitudinal jet direction, $x_1$ is the impact point location, $y$ is the normal direction, $d_1$ is the impact jet thickness of supported jet, $Q_{air}$ is the volume air flow rate and $D^*$ is a dimensionless diffusivity ($D^* = D_t/(V_1 d_1)$ for vertical supported jet). Equation (1$a$) was compared successfully with experimental data (e.g., Figs. 3 and 4).

In the developing air-water flow region (i.e., $C$ ($y$ = 0) = 0), Eq. (1$a$) can be simplified as:

$$C = \frac{Q_{air}}{Q_w} \frac{1}{\sqrt{4\pi D^* \frac{x - x_1}{d_1}}} \exp\left( -\frac{1}{4D^*} \frac{\left(\frac{y}{d_1} - 1\right)^2}{\frac{x - x_1}{d_1}} \right)$$

developing air-water flow region (1$b$)

**Mean Air-Water Velocity Distributions.** Downstream of the intersection of the free-falling jet with the receiving pool of water, a free-shear layer develops (Fig. 1). For monophase flows, Goertler (1942) solved the equation of motion for a plane shear layer assuming a constant eddy viscosity $\nu_T$ across the shear layer:

$$\nu_T = \frac{1}{4K^2} (x - x_1) V_1 \quad (2)$$

where $K$ is a constant. The solution in the first approximation yields (Rajaratnam, 1976, Schlichting, 1979):

$$\frac{V}{V_1} = \frac{1}{2} \left( 1 + \text{erf}\left( \frac{K(y - y_{50})}{x - x_1} \right) \right) \quad (3)$$

where $y_{50}$ is the location where $V = V_1/2$ and erf is the error function:

$$\text{erf}(u) = \frac{2}{\sqrt{\pi}} \int_0^u \exp(-u^2) du \quad (4)$$

Equation (3) is an analytical solution of the motion equation developed for two-dimensional monophase flow. In air-water flows, the presence of air bubbles within the shear

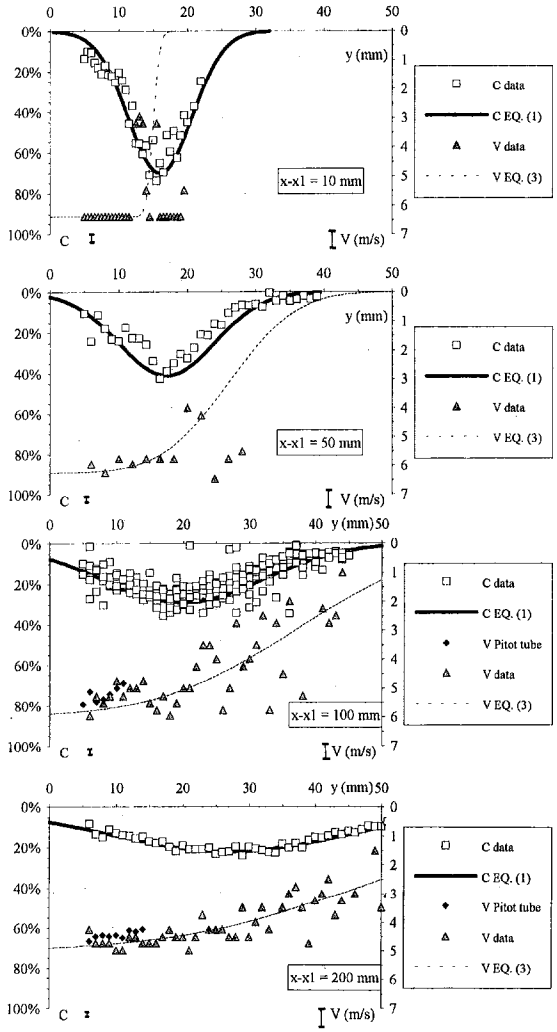


**Fig. 4 Distributions of air concentration and mean air-water velocity in the developing flow region of vertical supported plunging jets—comparison between Eqs. (1) and (3) and experimental data (impact velocity $V_1$ = 6.14 m/s).**

layer is expected to affect the shear flow which in turn affects the diffusion of air bubbles. In Figs. 3 and 4 the mean velocities of the air-water mixture (experimental data) are compared with Eq. (3). Figures 3 and 4 indicate that the air-water velocity profiles have the same shape as in monophase flows.

In the air-water shear layer of vertical supported jets, the authors estimated $K = 10.6$ and 6.3 for $V_1 = 2.39$ and 6.14 m/s, respectively. In comparison, for monophase shear flows, Rajaratnam (1976) and Schlichting (1979) deduced $K = 11$ and 13.5. As the rate of expansion of the shear layer is proportional to $1/K$, the new results suggest that the air bubbles cause an increase in the expansion rate for the 6.14-m/s jet.

*Remarks.* In Figs. 3 and 4, the velocity conductivity probe data are compared with Pitot tube measurements in the low air content region close to the support.

Note also that, during the experiments, the plunging jet was unsteady and the free-surface level fluctuating while the probes were fixed to the channel. Hence, the experimental results (e.g., Figs. 3 and 4) exhibit more scatter than the accuracy of the probes.

**Chord Length Distributions.** At each position $\{x, y\}$ below the entrainment point, the chord length[1] distributions were also computed. A dual tip conductivity probe, used to measure air bubble size characteristics, detects only the bubble chord lengths. If the bubbles are small (i.e. less than 0.1 mm), the bubble diameter probability distribution can be deduced from the bubble chord probability distribution by assuming that all the bubbles are spherical or ellipsoidal (e.g., Herringe and Davis, 1976, Clark and Turton, 1988). In the present bubbly free-shear-layer flow, video pictures and still camera photographs showed the entrainment of large bubbles with a large variety of shapes (Cummings, 1996). For these reasons only the bubble chord data are presented here.

In Fig. 5 the bubble chord probability histograms are shown. The histogram columns represent each the probability of a bubble chord length in one millimetre intervals (e.g., the probability of a chord length from 2.0 to 3.0 mm is represented by the column labeled 3). The histograms describe all the bubble detected across the shear layer width at depths $(x - x_1) = 10$, 50, 100 and 200 mm.

First, note the broad range of bubble chord lengths: i.e., from less than 0.1 mm to more than 30 mm. The observations of bubble chord length indicated consistently a broad range of bubble sizes, extending over several orders of magnitude.

Second, Figs. 5(*a*) and 5(*b*) show clearly the existence of large chord-length bubbles at $(x - x_1) = 10$-mm (i.e., very close to the entrainment point). Further downstream (i.e., $(x - x_1) = 100$ to 200 mm), most large chord length bubbles have disappeared presumably by a bubble breakage process in the turbulent shear flow. This bubble breakage is confirmed by high speed video and photographic observations, showing that the bubbles can be entrained in the form of elongated air packets which break later within the free shear layer. Bubble detrainment is unlikely to account for the disappearance of the larger bubbles so close to the entrainment point.

**Discussion.** For a two-dimensional shear layer, the vorticity $\omega$ can be deduced from the velocity profile (Eq. (3)) by neglecting the term $\partial V_y/\partial x$. In dimensionless terms, it yields:

$$\frac{\omega d_1}{V_1} = -\frac{1}{2}\frac{d_1}{V_1}\frac{\partial V_x}{\partial y} = -\frac{1}{2}\frac{1}{\sqrt{4\pi\,\dfrac{\nu_T}{V_1 d_1}\,\dfrac{x - x_1}{d_1}}} \times \exp\left(-\frac{1}{4\,\dfrac{\nu_T}{V_1 d_1}}\,\frac{\left(\dfrac{y - y_{50}}{d_1}\right)^2}{\dfrac{x - x_1}{d_1}}\right) \quad (5)$$

Equation (5) is very similar to Eq. (1*b*). It implies that, for plane shear layers, the advective diffusion of vorticity is of similar shape as that of air bubble (Eqs. (1*a*) and (1*b*)). The diffusion processes of air bubbles and vorticity are primarily defined by their dimensionless diffusivity (i.e., $D_t/(V_1 d_1)$ and $\nu_T/(V_1 d_1)$, respectively) and their axis of symmetry (i.e., $Y_{C_{max}}$ and $y_{50}$, respectively).

*Air Diffusion Layer and Momentum Shear Layer.* First it is important to note that the momentum shear layer (as described by the mean air-water velocity field) does not coincide with the air bubble diffusion layer. Further, with vertical supported plunging jets, the new experiments showed consistently that 1—the momentum shear layer is shifted outwards (away from the support) in comparison with monophase shear flows, and that 2—$y_{50} > Y_{C_{max}}$ where $Y_{C_{max}}$ is the location where the air

[1] Length of the straight line connecting the two intersections of the air-bubble free-surface with the tip of the probe as the bubble is transfixed by the probe sharp-edge.

**Table 1 Experimental values of turbulent diffusivity and eddy viscosity at vertical supported jets**

| Ref. (1) | Run (2) | $V_1$ m/s (3) | $d_1$ m (4) | $x_1$ m (5) | $\frac{q_{air}}{q_w}$ (6) | $\frac{D_t}{V_1 d_1}$ (7) | $\frac{\nu_T}{V_1 d_1}$ (8) | Comments (9) |
|---|---|---|---|---|---|---|---|---|
| Chanson (1995) | F1 | 2.36 | 0.0102 | 0.090 | N/A | 0.039 | N/A | Two-dimensional supported jet. $W$ = 0.269 m. |
| | F2 | 4.06 | 0.0118 | 0.090 | N/A | 0.018 | N/A | |
| | F3 | 5.89 | 0.0122 | 0.090 | N/A | 0.037 | N/A | |
| | F4 | 8.0 | 0.012 | 0.090 | N/A | 0.061 | N/A | |
| | F5 | 9.0 | 0.012 | 0.090 | N/A | 0.053 | N/A | |
| Present study | 2-m/s | 2.39 | 0.010 | 0.0875 | 0.057 | 0.039 | 0.011 | Two-dimensional supported jet. $W$ = 0.269 m. |
| | 6-m/s | 6.14 | 0.0117 | 0.0875 | 0.543 | 0.038 | 0.027 | |

Notes:
N/A: not available.
$q_{air} = \int_0^\infty CVdy$, where both $C$ and $V$ were measured locally.
$W$: plunging jet width.

concentration is maximum (i.e. $C = C_{max}$) at a given cross-section (Fig. 1).

For monophase flows, Rajaratnam (1976) quoted:

$$\left(\frac{y_{50} - d_1}{x - x_1}\right)_{monophase} = +0.041 \quad \text{monophase shear layer} \quad (6)$$

while the authors' results suggest that:

$$\left(\frac{y_{50} - d_1}{x - x_1}\right)_{air\text{-}water} = +0.226 + 0.024V_1$$

air-water shear layer (7)

where $V_1$ is in m/s. In comparison, the symmetry line of air bubble diffusion layer (i.e. $y = Y_{C_{max}}$) was estimated as:

$$\left(\frac{Y_{C_{max}} - d_1}{x - x_1}\right)_{air\text{-}water} \sim +0.10$$

(Chanson, 1995, $2 < V_1 < 9$ m/s) (8)

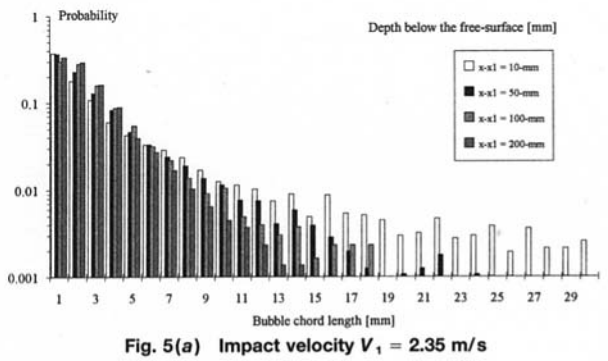


Fig. 5(*a*) Impact velocity $V_1$ = 2.35 m/s

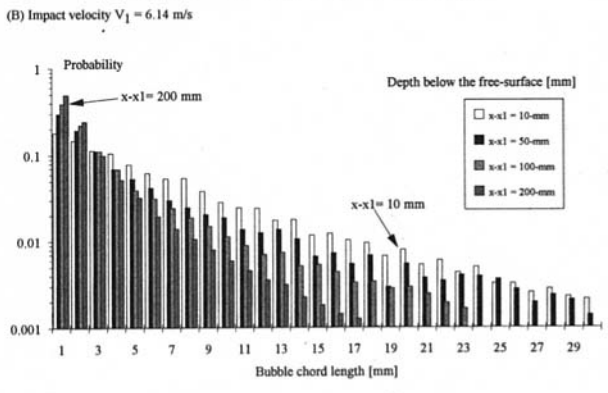


Fig. 5(*b*) Impact velocity $V_1$ = 6.14 m/s

**Fig. 5 Bubble chord length probability histogram for a vertical supported jet at various cross-sections below the entrainment point**

Basically the present air-water flow data (Eqs. (7) and (8)) imply that the symmetry lines of monophase shear layer, air diffusion cone and air-water shear layer satisfy: $(y_{50})_{monophase} < Y_{C_{max}} < (y_{50})_{air\text{-}water}$.

*Turbulent Diffusivity and Eddy Viscosity.* There is little information on the turbulent diffusivity. Chanson (1995) reported some air bubble diffusivity values. These results are compared with the authors' results in Table 1. Momentum exchange coefficients observed in the air-water shear layer are reported also. In each case, the values of $D_t$ and $\nu_T$ were determined from the best fit of the data (Table 1).

For the small number of results presented in Table 1, it is worth noting that the dimensionless turbulent diffusivity and eddy viscosity are of the same order of magnitude. Further the turbulent diffusivity of air bubbles tends to be larger than the momentum exchange coefficient for the two series of experiments (Table 1, columns 6 and 7).

## Overall Discussion of Plunging Jet Flows

Plunging jet entrainment takes place when the jet impact velocity exceeds a critical velocity. This characteristic velocity is a function of the jet turbulence. For small jet velocities (larger than the critical velocity), air is entrained in the form of individual air pockets and bubbles. At larger jet velocities, large air packets are entrained and broken up subsequently in the shear flow.

The near-flow field is characterized by a developing shear layer and an air diffusion layer (Fig. 1). New experimental results with the vertical supported jet have shown that these layers do not coincide. Below the impingement point, the air entrainment is primarily an advection-diffusion process (Cummings and Chanson, 1997). And most air is entrained in the region of high-velocity ($y < y_{50}$). Although the velocity distribution has the same shape as for monophase flows, its quantitative parameters ($\nu_T$, $y_{50}$) are affected by the air entrainment process.

The interactions between the air bubble diffusion and the shear flow are significant. The presence of bubbles within the shear layer modifies the momentum transfer between the high-velocity jet core and the surrounding fluid (at rest at infinity). And the turbulent shear flow contributes to the bubble breakage, leading to a broad spectrum of bubble sizes in the shear layer (Fig. 5).

## JFE Data Bank Contribution

Plunging jet experiments were performed using a two-dimensional vertical supported jet facility. The apparatus consists of a glass tank with a depth of 1.8 m, a width of 0.30 m and a length of 3.6 m. A PVC rotatable slot nozzle supplies a planar supported jet, 0.27 m wide and 0.012 m thick. The length of

the plate that supported the jet was 0.35 m and its inclination with the horizontal was 89 degrees for all experiments. The water supply comes from a constant head tank, which has a constant water level of 12.9 m above the nozzle.

A summary of the experiments is presented in section 2 before the full set of data (Sections 3 and 4). The full set of experimental data was first published in: Chanson, H., 1995, "Air bubble Entrainment in Free-Surface Turbulent Flows. Experimental Investigations," Report CH 46/95, Department of Civil Engineering, University of Queensland, Australia, June, 368 pages (ISBN 0 86776 611 5).

## Conclusion

New experiments were performed in the developing flow region of a vertical supported plunging jet. The air-water shear flow was investigated. The main results of the study are:

1 In two-dimensional plunging jet flows, the distributions of air concentration follow closely analytical solutions of the diffusion equation (Cummings and Chanson, 1997). And the velocity profiles have the same shape (Eq. (3)) as monophase flows. But the data show that the rate of spread of the shear layer is enhanced by the entrained bubbles for the 6.1-m/s jet experiment.

2 The results show consistently that the air bubble diffusion and momentum exchange layers do not coincide. The momentum shear layer is shifted away from the jet support compared to monophase flows, and air bubble diffusion takes place predominantly in the inner part of the shear layer: i.e., $Y_{C_{max}} < y_{50}$.

3 Chord length data show a broad range of entrained bubble sizes. The measurements show also the entrainment of some large air pockets which are subsequently broken into smaller air bubbles as they are entrained within the shear flow.

Overall, the developing flow region of plunging jets is subjected to strong interactions between the entrained air bubbles and the momentum transfer mechanism.

## Acknowledgments

The authors want to thank particularly Professor C. J. Apelt, University of Queensland who supported this project since its beginning. They acknowledge the support of the Department of Civil Engineering at the University of Queensland which provided the experimental facility and the financial support of Australian Research Council (Ref. No. A89331591). The first author was supported by an Australian Postgraduate Award during his Ph.D. thesis.

The authors appreciate the helpful comments of the anonymous reviewers and of the associated technical editor, Professor O. C. Jones.

## References

Chanson, H., and Cummings, P. D. (1994). "An Experimental Study on Air Carryunder due to Plunging Liquid Jet—Discussion," *International Journal of Multiphase Flow,* Vol. 20, No. 3, pp. 667–770.

Chanson, H., 1995, "Air Bubble Entrainment in Free-surface Turbulent Flows. Experimental Investigations." Report CH46/95, Dept. of Civil Engineering, University of Queensland, Australia, June, 368 pages.

Clark, N. N., and Turton, R., 1988, "Chord Length Distributions Related to Bubble Size Distributions in Multiphase Flows," *International Journal of Multiphase Flow,* Vol. 14, No. 4, pp. 413–424.

Cummings, P. D., 1996, "Aeration due to Breaking Waves," Ph.D. thesis, Dept. of Civil Engrg., University of Queensland, Australia.

Cummings, P. D., and Chanson, H. 1997, "Air Entrainment in the Developing Flow Region of Plunging Jets. Part 1," ASME JOURNAL OF FLUIDS ENGINEERING, published in this issue pp. 597–602.

Goertler, H., 1942, "Berechnung von Aufgaben der freien Turbulenz auf Grund eines neuen Näherungsansatzes," *Zeitschrift für angewandete Mathematik und Mechanik,* Vol. 22, pp. 244–254 (in German).

Herringe, R. A., and Davis, M. R., 1976, "Structural Development of Gas-Liquid Mixture Flows," *Journal of Fluid Mechanics,* Vol. 73, pp. 97–123.

Rajaratnam, N., 1976, *Turbulent Jets,* Elsevier Scientific, Development in Water Science, 5, New York.

Schlichting, H., 1979, *Boundary Layer Theory,* McGraw-Hill, New York, 7th edition.

**C. Crnojevic**
Assistant Professor,
Laboratory of Fluid Mechanics,
University of Valenciennes,
Valenciennes, France

**G. Roy**
Research Associate,
School of Engineering,
Université de Moncton,
Moncton, Canada

**A. Bettahar**
Assistant Professor,
University of Chlaif, Algeria

**P. Florent**
Professor,
Laboratory of Fluid Mechanics,
University of Valenciennes,
Valenciennes, France

# The Influence of the Regulator Diameter and Injection Nozzle Geometry on the Flow Structure in Pneumatic Dimensional Control Systems

*The present paper describes an experimental investigation of the various parameters affecting the operation of industrial pneumatic controllers based on the jet nozzle principle. A test rig was built to monitor supply pressure, air temperature, airflow characteristics, and the static pressure distribution over the flat plate on which the jet impinges. The results demonstrate the existence of a low pressure, separated flow zone, subject to fouling, which subsequently was eliminated by appropriate changes of the injection nozzle geometry. The previous experimental findings were also confirmed by numerical simulation of the flow. Experimental results also show that the internal diameter of the regulator, situated inside the measuring branch, has an important influence on the sensitivity of the apparatus, as well as influencing its range.*

## 1 Introduction

The pneumatic dimensional control method is a widely used process in numerous industrial metrology applications throughout the world. The principle behind the method is in fact quite simple. If air under constant pressure ($p_{al}$ = const.) flows through two orifices, A and B placed in series (Fig. 1), the static pressure $p$ in the chamber between the two orifices is a function of the ratio of their two areas (Wattebot, 1937). If the area of the orifice A is fixed, and the exit of nozzle B is situated at a small distance $\delta$ from a nearby plate, the pressure $p(\delta)$ in the intermediate cavity is a function of $\delta$, and through calibration can be used to measure or control $\delta$. In order to improve the accuracy, Fortier (1950) introduced the differential measuring system illustrated in Fig. 2, consisting of two branches; one used as a reference and the other for measurement purposes. In this layout, the flow in the nozzles A and C is choked (Mach number = 1), with subsonic flow through nozzles B and D. Depending on the area ratios $A_A/A_B$ and/or $A_C/A_D$, it is possible to have any one of the following four flow regimes: subsonic at both A and B, subsonic at A and sonic at B, sonic at A and subsonic at B, or sonic at both A and B. According to Molle (1955 and 1956), one can use the pressure ratios $p_{al}/p(\delta)$ or $p(\delta)/p_a$ to discriminate the flow regimes in the nozzles. In the present paper, we will study the case shown in figure 3, where the flow is subsonic at A and sonic at B with $\delta \leq D^2/4d$. The case where $\delta > D^2/4d$, with sonic and subsonic flows respectively at A and B, has also been investigated, but the results are not presented here. The principal objective of the present work was to investigate the influence of the injection nozzle geometry and the characteristics of certain important elements in the pneumatic control system affecting the quality of the measurements.

## 2 Experimental Setup

**2.1 Description of the Apparatus.** In order to investigate the effects of the nozzle geometry and the regulator diameter found inside a typical industrial pneumatic controller, the experimental setup illustrated in figure 3 was used. This installation included a compressed air source (AL), a pressure regulator (RP), the pneumatic control unit (AP) and an injection nozzle (B). The control unit (AP) consisted of two branches; the measurement branch with pressure $p_m$ and the reference branch with pressure $p_r$. The pressure difference $\Delta p = p_m - p_r$ was measured with a differential pressure transducer. A simple calibration provided the relationship between $\Delta p$ and the distance $\delta$ between the nozzle and the flat plane. The reference branch remained closed during the measurement phase and flowmeter (FM) was only used to investigate the characteristics of the measurement branch. Electronic pressure transducers (CP) and thermocouples (TC) were used respectively to record the static pressures on the flat plate and the stagnation temperatures. Pressure and temperature values were measured in the fully developed regions in sections 1-1, 2-2, and 3-3. A 0.2 mm diameter pressure tap on the moveable flat plate was connected to a pressure transducer to determine the wall pressure distribution over the plate. The vertical and horizontal displacements of the nozzle and the plate were made using a small milling machine, with the corresponding movements monitored by two displacement transducers (DV) and (DH). The positioning accuracy of this traverse system is $\pm 1$ $\mu$m both horizontal and vertical directions. The latter were connected to two ETAMIC electronic measurement systems, with digital displays, capable of detecting displacements of the order of a micron. The regulator diameter ranged from 0.5 to 2 mm, and all the measurements were carried out using a standard nozzle with an internal diameter ($d$) of 2 mm and an external diameter ($D_s$) of 4 mm.

The random uncertainty estimate for the measurements presented in this paper was less then 1 percent for pressure, 5 percent for volumetric air flow rate, and 0.5 percent for temperature.

**2.2 Flow Conditions.** The volume flow rate, $\dot{V}$, was measured in litres per minute, which gave the mass flow rate $\dot{m} = \rho\dot{V}$, when multiplied by the air density drop "normal conditions." At the measuring stations, the static pressure $p$ and the total temperature $T_o$ were recorded for a given airflow. With

Contributed by the Fluids Engineering Division for publication in the JOURNAL OF FLUIDS ENGINEERING. Manuscript received by the Fluids Engineering Division February 16, 1995; revised manuscript received January 28, 1997. Associate Technical Editor: M. M. Sindir.

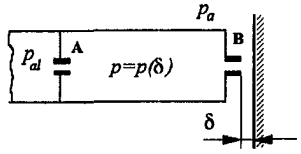


Fig. 1 Simple apparatus of Wattebot (1937)

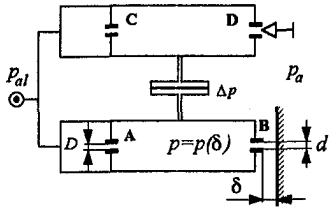


Fig. 2 Differential apparatus of Fortier (1950)

this date, it was possible to calculate the static temperature, velocity and Mach number from the following relationships:

$$T_o = T + v^2/2c_p, \tag{1}$$

$$p_a + p = \rho RT, \tag{2}$$

$$\dot{m} = \rho v d^2\pi/4, \tag{3}$$

and

$$T = \frac{1}{2a}(\sqrt{1 + 4aT_o} - 1), \tag{4}$$

$$v = \frac{4\dot{m}}{d^2\pi}\frac{RT}{p_a + p}, \tag{5}$$

$$M = \frac{v}{\sqrt{\kappa RT}}, \tag{6}$$

where

$$a = \frac{R}{2}\frac{\kappa + 1}{\kappa}\left[\frac{4\dot{m}}{d^2\pi(p_a + p)}\right]^2.$$

From the resulting velocity, temperature and Mach number data, with different supply pressures, and for flows with tube diameters varying from 6 to 8 mm, we were able to draw the following conclusions:

(1) The velocities and Mach numbers throughout the apparatus were low, so that flow could be considered as incompressible.

(2) Differences between the total and static temperatures were negligible, because of the low velocities.

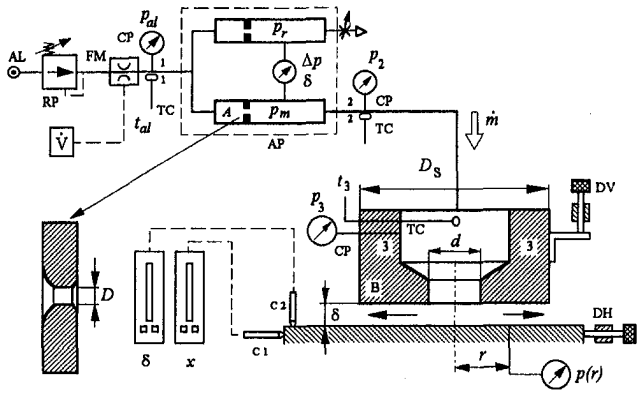


Fig. 3 Experimental setup

(3) No significant temperature change was noted along the tubes, so the airflow could be considered to be isentropic.

## 3 Wall Pressure Distribution in the Flat Plate

As the air exiting the injection nozzle hits the flat plane, important changes occur in the velocity and pressure fields. An analysis of the possible resulting flow structure between the nozzle and the plate, based on the wall pressure distributions, is presented in the present section. Figures 4 and 5 show the wall pressure distributions on the flat plane, produced by the impinging jet, for cases using a standard nozzle with a regulator diameter of 1 mm. The supply pressures were $p_{al}$ = 2 and 3 bars, with varying $\delta$ and $\delta < D^2/4d$. The area ($A_e = d\pi\delta$) at the entrance (e-e) of the space between the nozzle and the flat plane is smaller then the nozzle exit area ($A_B = d^2\pi/4$, where $d$ = 2 mm). As a result, the airflow is accelerated and one observes a corresponding pressure drop, with a minimum value $p_{\min}$ reached at the section c-c. Here the air velocity achieves a maximum value corresponding to the local speed of sound. This section is known as the critical section. Its position is denoted by the radial coordinate $r^*$ and depends on both the supply pressure $p_{al}$ and the distance $\delta$, as shown is Figs. 6 and 7. In pneumatic dimensional control applications ($80 \le \delta \le 200$ $\mu$m), the critical section is found to be situated at a distance corresponding to the half-height of the standard nozzle. From the figures, it can be seen that the position of this critical section is displaced toward the periphery of the nozzle as the height $\delta$ increases. After a certain value of $\delta$, for example $\delta$ = 1250 $\mu$m for $p_{al}$ = 3.5 bars as shown in Fig. 7, the minimum pressure section is found to be situated outside the injection nozzle frontal area. In this case, a recirculation bubble is found between the nozzle and the flat plate and a second bubble outside the nozzle (Fig. 4). For values of $\delta$ greater than a certain value, for example $\delta$ = 1600 $\mu$m for $p_{al}$

## Nomenclature

$A$ = area
$c_p$ = constant pressure specific heat
$d$ = injection nozzle inner diameter
$D$ = regulator diameter
$M$ = Mach number
$\dot{m}$ = mass airflow
$p$ = static gauge pressure
$p_a$ = atmospheric pressure
$p_{al}$ = supply gauge pressure
$r$ = radial coordinate
$r^*$ = position of critical section
$R$ = ideal gas constant
Re = Reynolds number
$s$ = pneumatic sensitivity
$T$ = fluid temperature
$v$ = velocity
$\dot{V}$ = volumetric airflow
$\delta$ = distance separating nozzle and flat plate
$\kappa$ = specific heat ratio
$\mu$ = flow coefficient
$\nu$ = kinematic viscosity
$\rho$ = density
$\psi$ = contraction coefficient

**Subscripts**

$o$ = stagnation conditions
1 = upstream
2 = downstream
$r$ = reference value

**Subscripts**

* = value in critical cross-sectional area

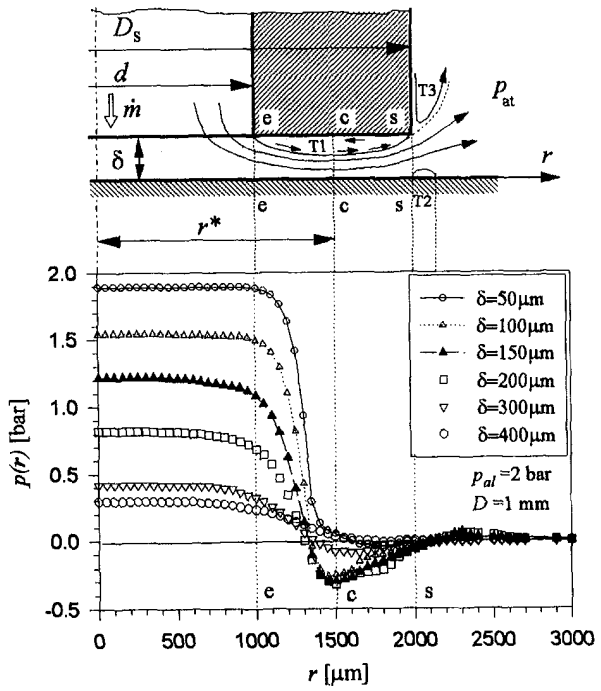


Fig. 4 Wall pressure distribution on a flat plate with $p_{al}$ = 2 bar (uncertainty in $p(r)$ is ±1 percent)

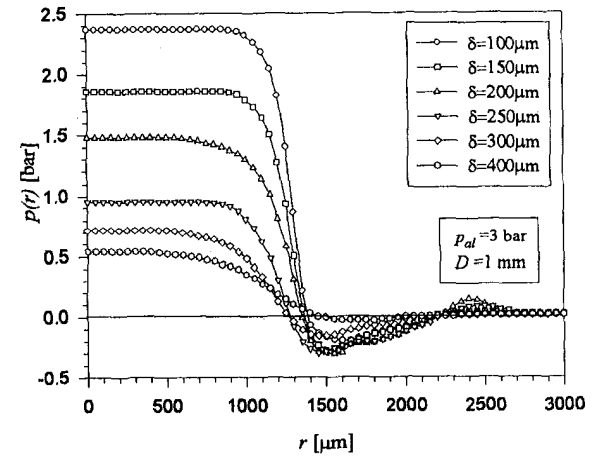


Fig. 5 Wall pressure distribution on a flat plate with $p_{al}$ = 3 bar (uncertainty in $p(r)$ is ±1 percent)

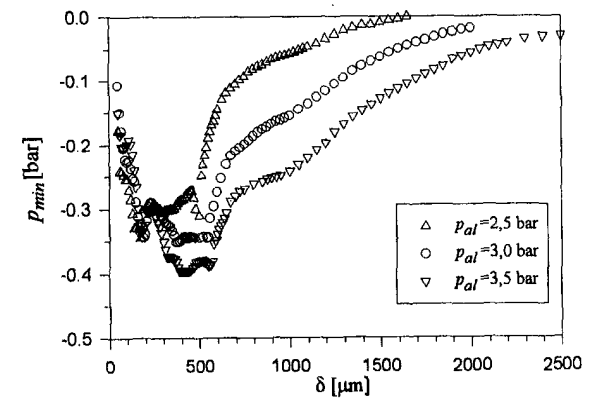


Fig. 6 The minimum pressure $p_{min}$ as a function of $\delta$ (uncertainty in $p_{min}$ is ±1 percent)

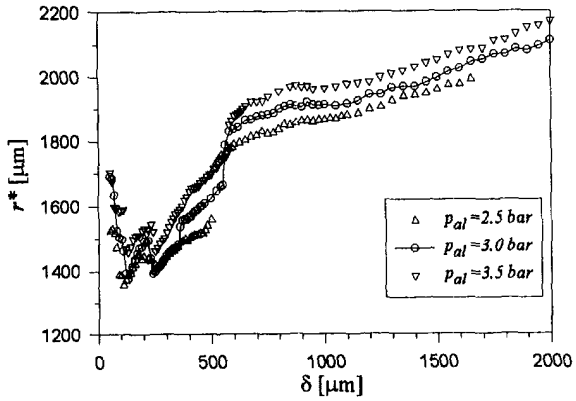


Fig. 7 Position of the critical section

= 2.5 bars in Fig. 6, the low pressure zone on the flat plate completely disappears.

As the distance $r$ increases, the radial area $A(r) = 2\pi r\delta$ of the space between the nozzle and the flat plate increases. However, the airflow does not necessarily use this entire area to pass in the space between the two surfaces. In fact, the acceleration of the airflow causes a recirculation bubble T1 (Fig. 4) between sections (e-e) and (c-c) which reduces the airflow area from $A_e$ to $A^*$. Therefore, between these sections, the flow possesses the characteristics of flow in a convergent section where $A^* \leq A_e$. A height contraction coefficient of $\delta^*/\delta < d/2r^* \approx 0.667$, was found, when $r^* = 1500$ $\mu$m.

Downstream of the critical section c-c, the pressure increases and the velocity decreases. This state of affairs continues until the exit section (s-s) is reached. Therefore, in this region, the flow has the characteristics of flow in a divergent section. At the exit section, a sudden expansion is encountered where atmospheric pressure conditions exist. Since the airflow cannot follow the sharp contours, two more circulation bubbles are formed, one on the flat plate (T2) and the other on the external, vertical lip of the nozzle (T3). The wall pressure distributions shown in Figs. 4 and 5 indicate the presence of the recirculation zone (T2) in this particular area. This relatively small bubble (~150 to 200 $\mu$m) depends on the supply pressure and the distance $\delta$. In fact, it disappears when $\delta$ is greater than 400 $\mu$m. These recirculation zones (T1 and T2) can cause annular deposits of oil and dirt on the surfaces and are affected by the injection nozzle geometry.

## 4 Influence of Supply Pressure and Injection Nozzle Geometry

**4.1 Experimental Results.** Wall pressure distributions are shown in figure 8 for the cases of $\delta$ = 150 $\mu$m and $p_{al}$ = 1, 2 and 3 bars. The results show that the size of the low pressure area, or recirculation zone, is not greatly affected by the supply pressure.

Figure 9 shows wall distributions for three different nozzle geometries for a given $\delta$ and supply pressure. The different geometries include a standard nozzle (NS), a bevelled edge nozzle with a small level frontal area (N1) and a sharp bevelled edge without any frontal area (N2). Indeed, if the level frontal area is completely eliminated, the low pressure area disappears. This means that the nozzle geometry is very important and controls the position of the recirculation zone. The elimination of the low pressure area offers important benefits in an industrial pneumatic dimensional control system by reducing the risk of oil and dirt deposits.

**4.2 Numerical Simulation for Incompressible Flow.** As the space between the nozzle and the flat plate is quite restricted, the only measurable quantity is the wall pressure distribution

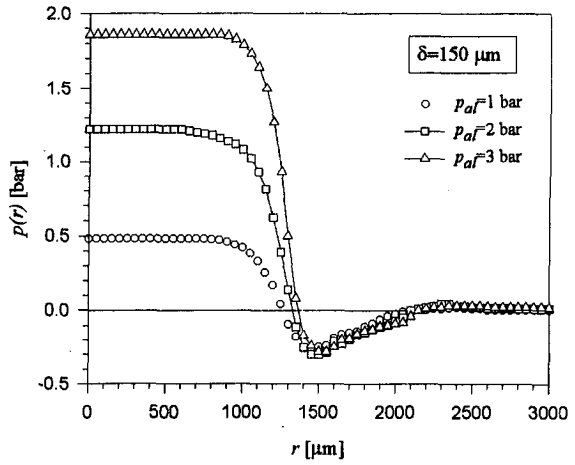


**Fig. 8 Wall pressure distribution on the flat plate for various supply pressures (uncertainty in $p(r)$ is ±1 percent)**

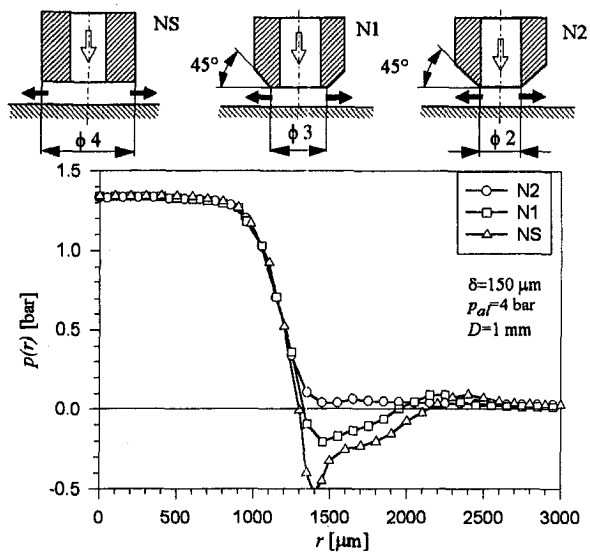


**Fig. 9 Wall pressure distribution on the flat plate for various nozzle geometries (uncertainty in $p(r)$ is ±1 percent)**

on the flat plate. Therefore, information regarding the entire flow field can only be obtained by means of numerical methods. For the present paper, the flow was calculated using the SIMPLER method (cf. Patankar, 1980). The flow was considered to be laminar, incompressible, isentropic, and symmetrical. This type of flow is governed by the Navier-Stokes equations, together with the continuity equation, written in cylindrical coordinates. The effects of various boundary conditions were tested, particularly in areas where the no-slip condition cannot be applied, and the results showed that the results in the main region of interest were not greatly affected. Results presented in this paper are based on an 82 × 172 non-uniform grid in the axial and radial directions respectively. Numerical accuracy for evaluation of all flow quantities is $10^{-4}$ and has been achieved after nearly 4000 iterations. For all cases presented here, the Reynolds number of the flow, defined by:

$$\mathrm{Re} = 4\dot{V}/\pi\nu d, \qquad (7)$$

was set at 1400. All other dimensions were chosen to match those found in typical pneumatic dimensional control applications. The calculated general flow patterns and wall pressure

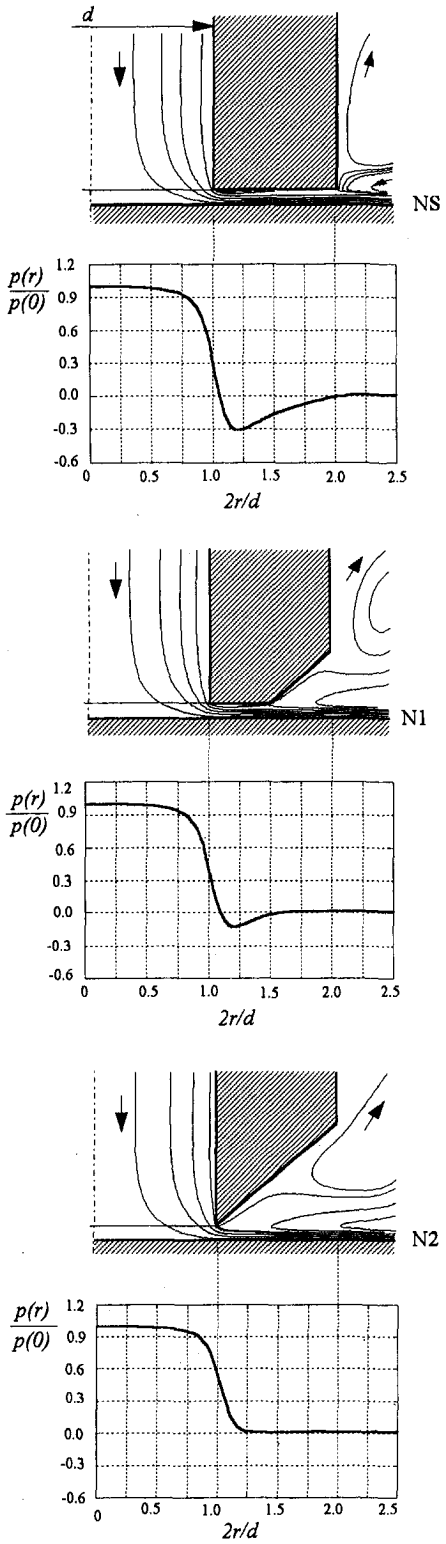


**Fig. 10 Flow structure and wall pressure distributions for NS, N1, and N2 nozzles**

distributions are illustrated in Fig. 10, and the axial velocity profiles in Fig. 11, for the three different types of nozzle geometry. The recirculation zones can be clearly seen in the flow patterns for the cases of the standard nozzle and the bevelled edge nozzle with the frontal level area. Figure 12 illustrates the good agreement between the present numerical results and the experimental wall pressure distributions.

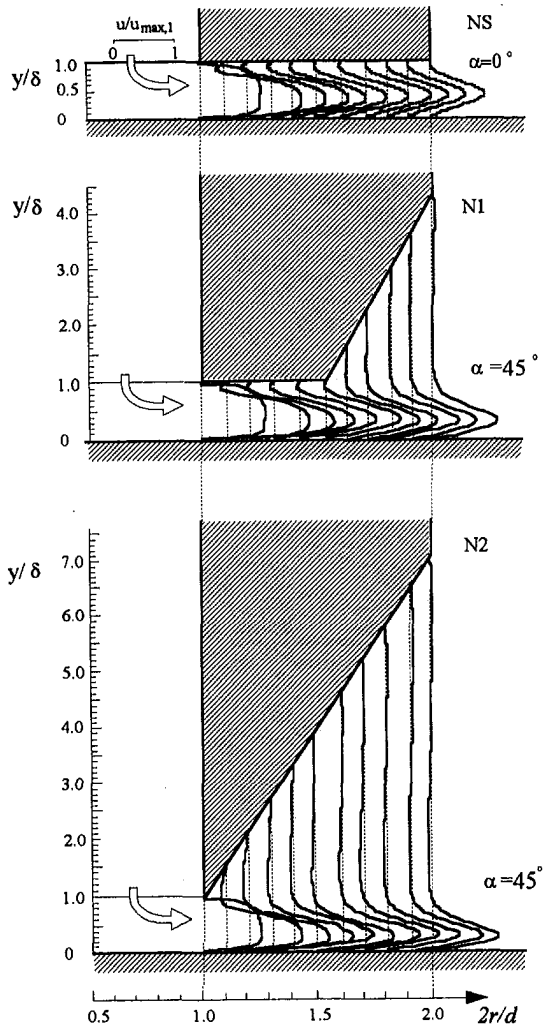


Fig. 11 Velocity profiles

Comparing Figs. 9 and 12, it would appear that the geometry is more critical than the flow regime.

## 5 Influence of Regulator Diameter and Supply Pressure

The standard regulator found in dimensional control equipment (Fig. 3) has a convergent shaped inlet and a cylindrical section. The ratio of the diameters ($D/d$) of the inner chamber and the nozzle outlet has a great influence on the position of the critical section, where the flow is choked, as well as on the sensitivity of the instrument.

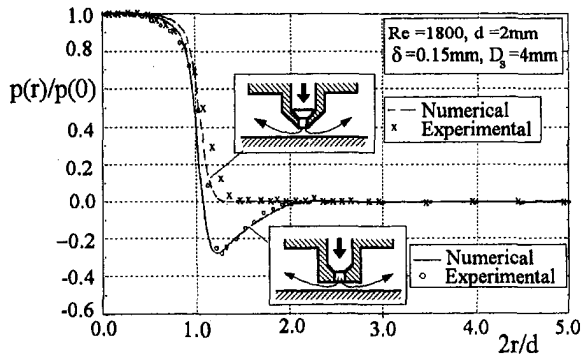


Fig. 12 Numerical results and experimental data for wall pressure distribution (uncertainty in $p(r)/p(0)$ is ±2.5 percent)

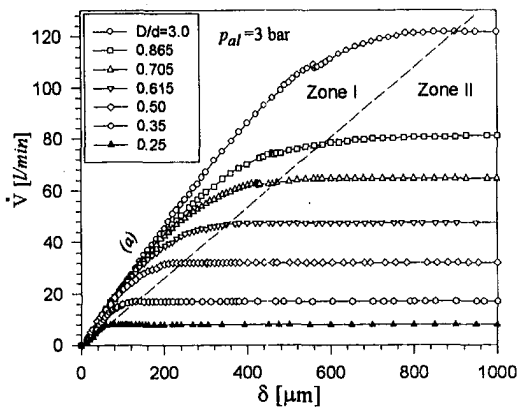


Fig. 13 Flow rate as a function of $\delta$ for different regulator diameters (uncertainty in $\dot{V}$ is 5 percent)

Volume flow rates for different ratios $D/d$ and varying distances $\delta$ are shown in Fig. 13. Looking at these curves, one can see that two distinct flow zones exist: in zone I the flow rate varies and in zone II it is constant. Zone I corresponds to the flow regime where the volume flow rate increases with the distance $\delta$. In this case sonic flow occurs in region between the nozzle and the flat plate. Zone II, on the other hand, corresponds to the case where choked, sonic flow occurs in the regulator, which thus fixes the flow rate. This is outside the pneumatic control range.

Figure 14 illustrates the variations in flow rate as a function of the height $\delta$, for a regulator of ratio $D/d = 0.5$ and for different supply pressures. This figure clearly shows that the supply pressure has an important influence on the flow rate. This flow rate is proportional to the absolute supply pressure in zone II. However, the supply pressure has no influence on the critical distance (cf. Fig. 14; $\delta_{cr} = 220$ $\mu$m) at which the flow rate becomes constant.

The variation in pressure at the stagnation point on the flat plate as a function of the distance $\delta$ for different values of the ratio $D/d$ is shown in Fig. 15 for a supply pressure $p_{al} = 3$ bars. The fact that the pressure difference is a function of the distance $\delta$ forms the basis of the construction of pneumatic dimensional control systems such as the one shown in Fig. 3. For practical purposes, the linear section of the pressure curve is used; for example, the interval $60 \leq \delta \leq 240$ $\mu$m, for the ratio $D/d = 0.5$. Figure 15 illustrates the fact that as the ratio $D/d$ decreases, the pressure loss in the measurement branch

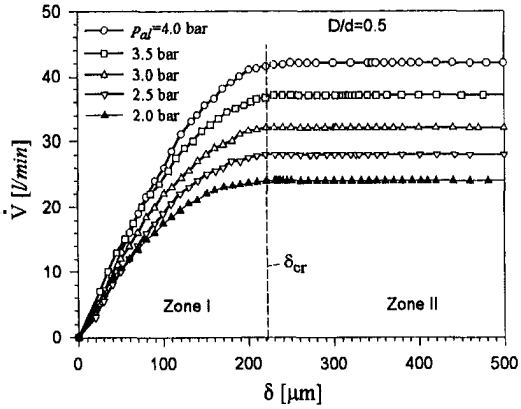


Fig. 14 Flow rate versus distance $\delta$ and for various supply pressures (uncertainty in $\dot{V}$ is 5 percent)

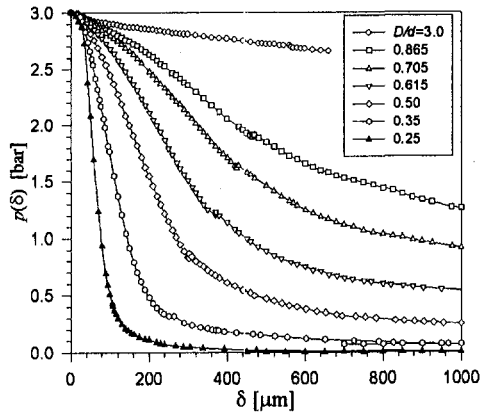


**Fig. 15 Stagnation pressure for various regulator diameters and $p_{al}$ = 3 bar (uncertainty in $p(\delta)$ is ±1 percent)**

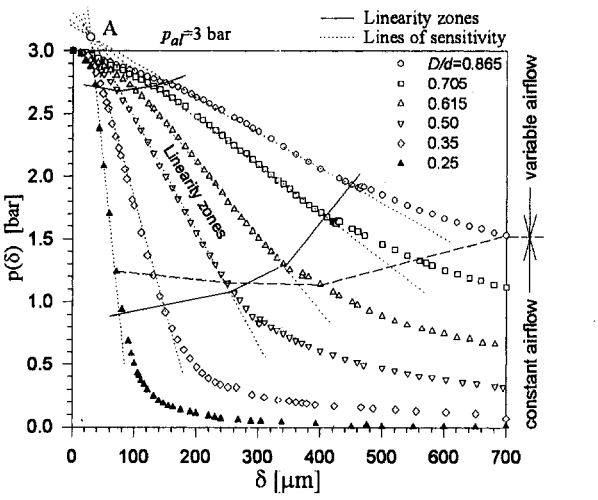


**Fig. 17 Linearity zones: constant and variable airflow diagram (uncertainty in $p(\delta)$ is ±1 percent)**

increases, as does the slope of the $p = p(\delta)$ curve. Figure 16 shows the change in the stagnation pressure on the flat plate, with $D/d = 0.5$, for different supply pressures. The figure shows that increasing the supply pressure increases the sensitivity of the instrument.

**5.2 Pneumatic Sensitivity.** Using the linear section of any of the curves illustrated in Fig. 15, one can define the pneumatic sensitivity by the following expression:

$$s = \Delta p/\Delta\delta \tag{8}$$

where $\Delta p$ and $\Delta\delta$ are, respectively, the pressure and distance differences corresponding to the linear part of the curve. It will be noticed from Fig. 17 that, for cases with regulators, all the linear parts of the curves extrapolate to, and pass through, the same point A. Also the figure clearly illustrates the region where the pressure curves are linear. In addition it can be seen that, as the ratio $D/d$ increases, the slope of the pressure curve $p = p(\delta)$ decreases, indicating a reduction in sensitivity. The variations in sensitivity, as a function of $D/d$, are shown in Fig. 18, underlining the fact that the instrument is more sensitive for small values of $D/d$. It is clear that the ratio $D/d$ has an important influence on the pneumatic sensitivity of the instrument. It should be noted that the type of flow, whether subsonic or sonic, at the regulator level, and the restriction formed by the frontal surface of the nozzle and the flat plate, are also important factors influencing the sensitivity of the equipment.

The variable and constant airflow zones are also shown in Fig. 17. The zone between the constant flow region and the highly sensitive linear zone becomes larger with decreasing $D/d$. The same thing occurs in the region past the transition zone, indicating that the flow becomes constant more rapidly as $D/d$ becomes smaller.

**5.3 Flow Coefficient in the Measurement Branch.** In the case of an isentropic airflow, the theoretical mass flow rate at the critical section is given by the following expression:

$$\dot{m}^* = A^* f \frac{p_o}{\sqrt{T_o}} = \psi A_B f \frac{p_o}{\sqrt{T_o}}, \tag{9}$$

where $A^* = 2r^*\pi\delta^*$ is the critical cross-section area, and

$$f = \sqrt{\frac{\kappa}{R}}\left(\frac{2}{\kappa+1}\right)^{(\kappa+1)/(2(\kappa-1))}.$$

The section area $A^*$ varies and depends on the height $\delta$. The airflow can be expressed in terms of the exit section area $A_B$, where $\psi$ is the contraction coefficient which depends on $\delta$. Since there is a pressure loss in the measurement branch, Eq. (9) must be corrected by the velocity coefficient $\varphi$. The product of these two coefficients can be represented by a single flow coefficient: $\mu = \varphi\psi$. Introducing this coefficient, the mass flow rate can be calculated from the following expression:

$$\dot{m} = \mu \cdot \frac{d^2\pi}{4} f \frac{p_o}{\sqrt{T_o}}. \tag{10}$$

Knowing the true and theoretical mass flow rates, it is quite simple to determine the flow coefficient in the measurement

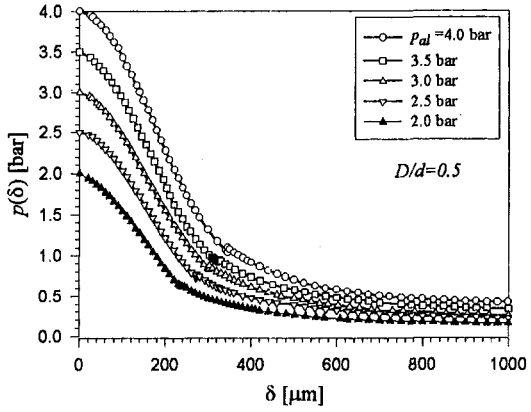


**Fig. 16 Stagnation pressure for various supply pressures with $D$ = 1 mm (uncertainty in $p(\delta)$ is ±1 percent)**

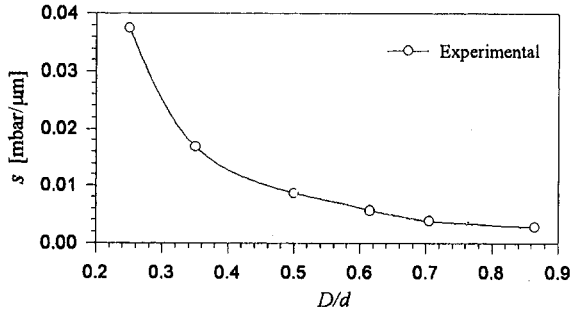


**Fig. 18 Pneumatic sensitivity as a function of the diameter ratio $D/d$**

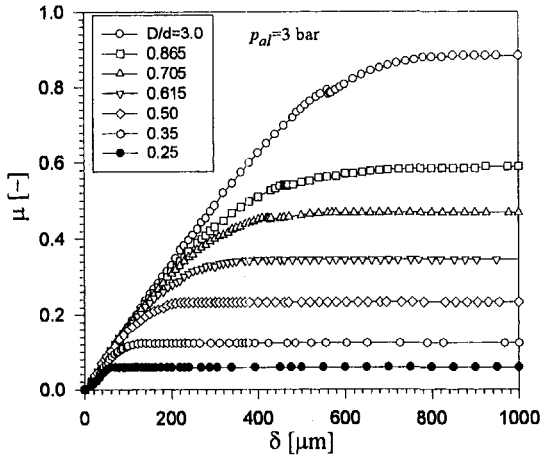


**Fig. 19 Flow coefficient in the measurement branch (uncertainty in $\mu$ is 5.11 percent)**

branch $\mu = \dot{m}/\dot{m}^*$. Figure 19 illustrates the variations in the flow coefficient $\mu$ as a function of the regulator diameter ratio $D/d$ and the height $\delta$. This figure shows that, as the ratio $D/d$ increases, the pressure loss in the measurement branch decreases and the value of the flow coefficient increases. Without any regulator in the measurement branch, the flow coefficient becomes simply the flow coefficient of the injection nozzle. For very large distances separating the nozzle and the flat plate ($\delta \geq 800$ $\mu$m), the flow coefficient becomes constant and takes on the asymptotic value of $\mu = 0.883$, corresponding to a convergent shaped nozzle.

## 6 Pressure Discontinuity

As seen in Figs. 13, 15, and 16, pressure discontinuities exist outside the pneumatic dimensional control domain of application. By enlarging part of Fig. 16, we obtain Fig. 20. This figure clearly illustrates the existence of discontinuities in the pressure curves. These are in the form of sharp increases occurring over very short distances ($0 \leq \Delta\delta \leq 1$ mm). The existence of these "jumps" was first noted by Markow (1971), however no concrete explanation was given. This discontinuity seems to be caused by an oblique shock wave which is created at the exit section near the flat plate (cf. Fig. 20). The volume over which the pressure jump occurs is very small, therefore, it is practically impossible to give the exact position of the shock wave. Furthermore, apart from the wall pressure, measurements

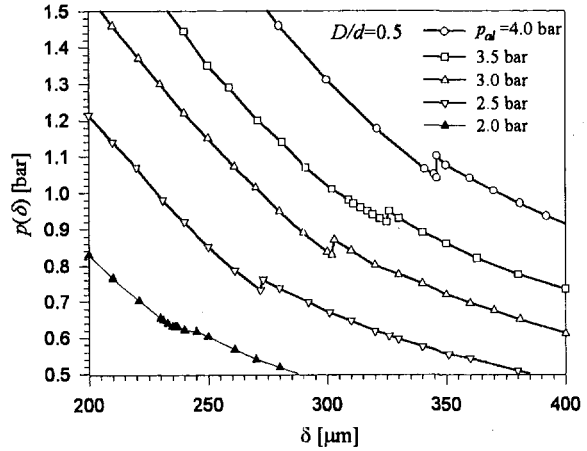


**Fig. 20 Pressure jump (uncertainty in $p(\delta)$ is ±1 percent)**

are practically impossible in the restricted space under the head. When an airflow passes through a shock wave, the flow is decelerated and the Mach number decreases from $M_1$ to $M_2$. These Mach numbers can be determined using the well known expressions:

$$M_1 = \sqrt{1 + \frac{\kappa + 1}{2\kappa}(p_2/p_1 - 1)}, \quad (11)$$

$$M_2 = \sqrt{1 + \frac{\kappa + 1}{2\kappa}(p_1/p_2 - 1)}, \quad (12)$$

where the subscripts 1 and 2 represent the upstream and downstream states respectively. Experimental results show that the ratio of the downstream and upstream absolute pressures, $p_2/p_1$, varies from 1.0018 to 1.029. These values correspond to Mach numbers $M_1 = 1.0008$ to 1.0125 and $M_2 = 0.9992$ to 0.9877, representing a "weak" shock. The creation of this shock wave causes a slight increase in the pressure loss, creating a small decrease in the airflow in the measurement branch.

## 7 Conclusion

For values of $\delta$ inside the industrial pneumatic dimensional control range, low pressure areas were found to exist, corresponding to recirculation zones. In the section corresponding to the recirculation zone, between the frontal surface of the nozzle and the flat plate, a section of minimum pressure and maximum (sonic) velocity was found. In order to improve the reliability of the control system, it is necessary to eliminate this low pressure area. This can be accomplished by reducing the level frontal area of the injection nozzle. If this level area is completely eliminated, then so is the low pressure recirculation zone and the critical flow is found at the outlet section $A_e = d\pi\delta$.

If the flow is compressible in the measurement branch, the sonic section corresponds to the minimum section area which depends on the height $\delta$. For small values of $\delta$, the critical section ($A^* = r^*\pi\delta^* < D^2\pi/4$) is situated between the nozzle and the flat plate surface. In this case the airflow is a function of the distance $\delta$. As this distance is increased, the critical section moves upstream into the regulator because its section becomes equal to the minimal area section ($A^* > D^2\pi/4$).

The pneumatic sensitivity and the industrial application range can be adjusted by the regulator diameter which sets the slope of the pressure curves. When the regulator diameter is reduced, the sensitivity of the controller increase but the range is reduced. However, for a fixed regulator diameter, the measurement range is not a function of the supply pressure.

The flow coefficient, $\mu$, of the measurement branch depends on the regulator diameter $D$. A reduction in the diameter $D$ causes a reduction in the flow coefficient as well, signifying that the difference between the real and isentropic flows is becoming more importance.

## References


Bettahar, A., 1994, "Application of the Radial Flow in the Pneumatic Dimensional Control (in French)," Ph. thesis, University of Valenciennes, France.

Fortier, M., 1950, "Industrial Application of the Compressible Flow with Critical Velocity (in French)," *Revenu haleur et Industrie,* No. 299, p. 145.

Markow, B. N., 1971, "Pneumatic Dimensional System with the Measuring Nozzle (in German)," *Feinerätetechnik,* 20. Jg. Helt 4., pp. 160–161.

Molle, R., 1955, "Comparison of the Incompressible et Compressible Flow Applied in Pneumatic Metrology (in French)," *Journal of Microtecnic,* Vol. X, No. 1, pp. 16–25.

Molle, R., 1956, "The Contemporary Tendencies in the Pneumatic Amplification (in French)," *Journal of Microtecnic,* Vol. X, No. 4., pp. 167–179.

Patankar, S. V., 1980, *Numerical Heat Transfer and Fluid Flow,* McGraw-Hill, New York.

Roy, G., Crnojevic, C., Bettahar, A., Florent, P., and Vo-Ngoc, D., 1994, "Influence of Nozzle Geometry in Radial Flow Applications," *International Conference on Fluid and Thermal Energy Conversion, Proc.,* Vol. 1, pp. 363–368, Bali, Indonesia.

Wattebot, L., 1937, "Principles of the Pneumatic Amplification (in French)," *Journal of Mechanics,* pp. 70–72.

**A. Youcefi**[1]
Maître de Conférences à l'Université des Sciences et de la Technologie d'Oran.

**D. Anne-Archard**[2]
Chargée de Recherche, Centre National de la Recherche Scientifique.

**H. C. Boisson**
Directeur de Recherche, Centre National de la Recherche Scientifique.

**M. Sengelin**
Ingénieur de Recherche, Centre National de la Recherche Scientifique.

Institut de Mécanique des Fluides,
U.M.R. CNRS/INPT-UPS 5502,
Avenue du Professeur Camille Soula,
31400 Toulouse, France

# On the Influence of Liquid Elasticity on Mixing in a Vessel Agitated by a Two-Bladed Impeller

*The experimental study of the velocity field and power consumption has been conducted in a mixing vessel equipped with a two-bladed impeller for a viscoelastic fluid and Newtonian and non-Newtonian inelastic fluids for comparison. The results are interpreted in the light of a numerical simulation using a finite element method for an "Oldroyd B" fluid. Both numerically and experimentally a significant influence of elasticity is found for an effective Reynolds number greater than a threshold value $Re^* = 5$ to 7. Above this value, the power number is increased and the velocity field deeply modified. This behavior is mainly related to elasticity of the fluid.*

## 1 Introduction

In many industrial fluid mixing operations, the liquid raw materials, products, and intermediates are rheologically complex. Numerous examples can be found in the polymer based industries (manufacturing and processing of synthetic rubbers, plastics, fibers, resins, paints, coatings and adhesives), food-processing industries, biochemical operations or in the manufacturing of detergents. The most frequently occurring anomalies in the fluid behavior are shear-dependent viscosity and viscoelasticity. The viscosity is considered as the most important rheological function, and it is a common practice to classify the fluids in two categories for which different technologies are used for mixing: the low-viscosity fluids, which imply turbulent flows and the high-viscosity fluids, which are limited to laminar flows in practice and that we study here. The rheological behavior of industrial fluids is generally complex and viscoelastic properties are often exhibited. Little is known about the nature of the mixing process or the impact of rheological complexities, and particularly about the effect of elastic properties on mixing performance. As viscoelastic fluids are to be more and more employed in industry, it is important to get a better understanding of hydrodynamics in mixing systems when viscoelasticity is involved. This will lead to improve efficiency by making mixing systems suitable for viscoelastic fluids. Although the oldest results on the influence of viscoelasticity on mixing efficiency show some discrepancy, works in the last 15 years agree on a negative influence on it. We should quote the results of Höcker et al. (1981) for a flat blade disk agitator, Brito de la Fuente et al. (1990), Leuliet et al. (1992) and Carreau et al. (1993) for an helical ribbon impeller, and Youcefi et al. (1992.a) for a paddle impeller. These authors always noted a marked increase of power consumption with viscoelasticity beyond a Reynolds number threshold, even when influence on mixing time was weak when studied. All these studies were concerned with global measurements and no connection has been made with local hydrodynamics.

This paper deals with the flow in a cylindrical vessel agitated by a two-bladed impeller, a simple geometrical situation which allows both numerical and experimental approaches. This agitator is not of common use in industry but it is chosen as a basic case that can be extended to anchor or barrier agitators. It is nevertheless sufficiently complex to involve the main dynamic features of these flows. The studied regime is limited to moderate agitator speeds in order to avoid transition to turbulence and noticeable 3-D effects. This was verified experimentally and taken as an hypothesis for the numerical simulation. The aim of this paper is to study the hydrodynamical field under the conjugate influence of inertia and viscoelasticity, and to relate it to the power consumption in the mixer.

The experiments were conducted with a typical polyacrylamide solution using hot film anemometry in order to determine the velocity field. Power consumption was measured by means of a torquemeter on the same plant. As pointed out by the rheological study, the modifications in the flow properties can be attributed to viscoelasticity but also to nonlinear pseudoplastic behavior. By means of a numerical analysis conducted by Anne-Archard and Boisson (1995), it is possible to isolate in a similar situation the effects of elasticity alone for an "Oldroyd-B" fluid (corresponding to a nonpseudoplastic viscoelastic fluid). Comparison of these approaches allows to bring some interesting insight in the flow organization.

The paper is organized in four sections: (*i*) description of the test fluids used and their rheological properties; (*ii*) experimental apparatus; (*iii*) numerical simulation used for comparison; and (*iv*) experimental and numerical results in the vessel concerning velocity fluids and power consumption. The qualitative effects of viscoelasticity are revealed by the comparison between the actual experimental fluid and the ideal simulation.

## 2 Test Fluids for Experiments

Without taking into account time-dependent behavior, there are mainly three classes of fluids: the Newtonian ones, the non-Newtonian but inelastic ones, and the viscoelastic ones. Fluids of the second class have thus no elastic properties (such as nonzero storage modulus) but exhibit a nonconstant shear viscosity: they are pseudoplastic (or seldom shear-thickening).

[1] Present address: Institut de Genie Mécanique, Université des Sciences et de la Technologie d'Oran, B.P. 1505 Oran El Menaouor, Oran, Algerie.

[2] Correspondence should be addressed to Dr. Anne-Archard.

Contributed by the Fluids Engineering Division for publication in the JOURNAL OF FLUIDS ENGINEERING. Manuscript received by the Fluids Engineering Division July 6, 1995; revised manuscript received March 27, 1997. Associate Technical Editor: J. A. C. Humphrey.

Most of the viscoelastic fluids of our third category have also pseudoplastic properties. One can study specific viscoelastic behavior either with a nonpseudoplastic viscoelastic fluid, such as the one discovered by Boger (1977), or by comparing measurements among the three classes of fluids in identical physical situations.

For practical reasons, we have adopted the second approach, so experiments were conducted with:

($a$) a viscous Newtonian fluid: glycerol,
($b$) two non-Newtonian but inelastic fluids: the first one without yield stress: a 1.5 percent (by weight) aqueous solution of Carboxymethylcellulose (CMC in abbreviated form), the second one with a yield stress: a 2.0 percent (by weight) aqueous solution of carbopol 940,
($c$) viscoelastic fluids: 0.4 and 1 percent aqueous solutions of polyacrylamide (S. N. Floerger AN934SH, PAA in abbreviated form).

**2.1 Rheological Models.** If we decompose the stress tensor $\boldsymbol{\sigma}$ in the isotropic pressure $p$ associated to the unit tensor $I$, and in the extra-stress tensor $\boldsymbol{\tau}$ such as:

$$\boldsymbol{\sigma} = -p\mathbf{I} + \boldsymbol{\tau}, \tag{1}$$

the constitutive equation connects the rate of deformation tensor $D$ to the extra-stress tensor $\boldsymbol{\tau}$. For a large class of inelastic fluids including the ones studied here, this constitutive relationship can be expressed as a generalized Newtonian relationship:

$$\boldsymbol{\tau} = 2\eta(\mathbf{D})\mathbf{D}, \tag{2}$$

where $\eta(\mathbf{D})$ is the shear viscosity. In the case of a Newtonian fluid, this viscosity is constant hence yields a purely isotropic behavior for the fluid. In the case of 2-D flow with prefered direction, say $x$, this law is expressed in terms of a relationship between shear stress $\tau_{xy}$ and shear rate $\dot{\gamma} = \partial U/\partial y$, where $U$ is the $x$-component of the velocity.

For a viscoelastic behavior, one needs more sophisticated laws between tensors $\boldsymbol{\tau}$ and $\mathbf{D}$ and their derivatives, introducing in particular the evanescent memory which is a characteristic of such fluids. Our polymer solutions are isotropic ones in the usual macroscopic sense although they can give rise to some kind of anisotropy which is called "flow induced" (Lodge, 1964) and which is taken into account by means of complex tensorial dependence in the rheological equation of state (see Section 4).

**2.2 Viscous Properties.** The main characteristic of a fluid is its dynamical viscosity $\eta$, which is used to define the Reynolds number in presence of inertia effects. CMC and PAA solutions are pseudoplastic fluids and variations of $\eta$ are well correlated over the shear rate range $10^{-2}$ to $10^{3}$ s$^{-1}$ by a power law model:

$$\tau_{xy} = m\dot{\gamma}^n \tag{3}$$

$m$ is the fluid consistency index and $n$ the flow behavior index. For such a system, the apparent viscosity $\eta_a$ is then:

$$\eta_a = m\dot{\gamma}^{n-1} \tag{4}$$

Equation (3) should be modified for Carbopol solution because of the yield-stress. This law is known as Herschel-Bulkley model:

$$\tau_{xy} = \tau_0 + m\dot{\gamma}^n \tag{5}$$

Adjustment of these different parameters for our test fluids was made using a Carri-Med controlled stress rheometer CS 100 with a cone and plate geometry (gap angle: 2 degrees, diameter: 40 mm). The controlled temperature was fixed to 20°C ± 0.2°C. Viscous properties for all test fluids are listed in Table 1.

**Table 1 Rheological properties of tested fluids (the estimated uncertainty in $m$- and $\tau_0$-measurement is ≤ ±3%, and ≤ ±5% for the index $n$)**

| Solution | | $m$ (Pa·s$^n$) | $n$ (−) | $\tau_0$ (Pa) |
|---|---|---|---|---|
| Glycerol | Newtonian | 1.28 | 1 | 0 |
| CMC 1.5% | pseudoplastic | 13.9 | 0.47 | 0 |
| Carbopol 2% | pseudoplastic | 3.2 | 0.63 | 91.2 |
| PAA 0.4% | viscoelastic | 0.93 | 0.35 | — |
| PAA 1% | viscoelastic | 10.43 | 0.21 | — |

The Reynolds number Re for a Newtonian fluid in a stirred tank is usually defined as:

$$\mathrm{Re} = \frac{\rho N D_a^2}{\eta} \tag{6}$$

where $\rho$ is the fluid density, $N$ the rotation frequency of the impeller, $D_a$ the impeller diameter, and $\eta$ the dynamic viscosity. For non-Newtonian fluids, pseudoplasticity should be taken into consideration and an effective Reynolds number Re′ based on the apparent viscosity $\eta_a$ is used. Assuming a power law for viscosity versus shear rate, $\eta_a$ obeys Eq. (4) in which $\dot{\gamma}$ is a representative shear rate for the flow in the vessel. This last one is estimated according to the largely used theory of Metzner and Otto (1957), i.e., it is assumed to be proportional to the impeller speed $N$:

## Nomenclature

$C$ = torque, N.m
$C_o$ = vacuum torque, N.m
$\mathbf{D}$ = rate of deformation tensor
$D_a$ = impeller diameter, m
$d_a$ = shaft diameter, m
$H$ = height of two-bladed impeller, m
$\mathbf{I}$ = unit tensor
$J$ = elastic compliance, Pa$^{-1}$
$J_o$ = instantaneous compliance, Pa$^{-1}$
$J_i$ = spring compliance, Pa$^{-1}$
$K$ = Metzner-Otto constant
$m$ = power law parameter, Pa.s$^n$
$n$ = power law index
$N$ = impeller rotational speed, rev/s
$p$ = pressure
$P$ = power consumption, Watt
$r$ = radial coordinate (adimensional)
$T$ = vessel diameter, m
$V$ = velocity field (vectorial)
$V_r$, $V_\theta$, $V_z$ = nondimensional radial, tangential and axial velocity
$V_{\mathrm{ref}}$ = reference velocity
$\dot{\gamma}$ = shear rate, s$^{-1}$
$\delta$ = loss angle: phase difference between stress and strain in small amplitude oscillatory shear flow
$\eta$ = dynamic viscosity, Pa.s
$\eta_o$ = shear viscosity (Oldroyd 'B' law)
$\eta_a$ = apparent viscosity, Pa.s
$\theta_i$ = retardation time (Kelvin-Voigt model), s
$\lambda$, $\lambda_r$ = characteristic times (Oldroyd 'B' law)
$\rho$ = liquid density, kg.m$^{-3}$
$\boldsymbol{\sigma}$ = stress tensor, Pa
$\boldsymbol{\tau}$ = extra-stress tensor, Pa
$\tau_0$ = yield stress, Pa
$\tau_{xy}$ = shear stress, $x$-$y$ component of $\tau$

**Dimensionless Number**

$E$ = elasticity number
$Np$ = power number
Re = Reynolds number
Re′ = effective Reynolds number

**Table 2 Viscoelastic parameters for PAA solutions (uncertainty measurements: $\theta_0$, $J_0$: ±3%, $\theta_1$, $J_1$: ±5%, $\theta_2$, $J_2$ ±15%)**

| $C$ (%) | $J_0$ | $\theta_0$ | $J_1$ | $\theta_1$ | $J_2$ | $\theta_2$ |
|---|---|---|---|---|---|---|
| 0.4 | 0.038 | 3.04 | 0.499 | 16.87 | 0.131 | 1.99 |
| 1.0 | 0.020 | 3.61 | 0.191 | 24.72 | 0.080 | 5.07 |

$$\dot{\gamma} = K.N \tag{7}$$

$K$ is an experimentally determined constant which is essentially function of geometry. The relation (7) has been broadly verified with Newtonian fluids. Some studies with non-Newtonian inelastic fluids mention a weak dependence of $K$ upon the power-law index $n$ (Hiraoka et al. for a paddle impeller, 1979). Nevertheless, a constant value for $K$ is commonly assumed (Takahashi et al., 1989; Bertrand and Couderc, 1985; Shamlou and Edwards, 1985). Then a constant value of $K$ equal to 7.54 ± 8% is taken for our experimental apparatus. This allows evaluation of the effective Reynolds number as:

$$\mathrm{Re}' = \frac{\rho N^{2-n} D_a^2}{m K^{n-1}} \tag{8}$$

**2.3 Elastic Properties.** The phase shift between shear stress and deformation in a small amplitude oscillatory experiments reveals the elastic character of Polyacrylamide solutions. The characterization of viscoelastic properties of PAA solutions was performed using a creep experiment and a generalized "Kelvin-Voigt" model was fitted, whose creep function is given by:

$$J(t) = J_0 + \sum_{i=1}^{n} J_i\left(1 - \exp\left(-\frac{t}{\theta_i}\right)\right) + J_0 \frac{t}{\theta_0} \tag{9}$$

Oscillatory flow and creep recovery measurements were carried out using the Carri-Med rheometer. The analysis of the data was conducted according to the so-called "Inokuchi" method (Couaraze and Grossiord, 1985). This investigation shows that the viscoelastic response could be adequately described by assuming two retardation processes ($n = 2$). All these parameters were fitted for six different PAA solutions whose concentrations vary from 0.4 to 2 percent. The decrease of the compliances $J_i$ when concentration is increased shows that elasticity grows with concentration. The parameters for both fluids presented in the following are listed in Table 2.

## 3 Experiments

**3.1 Experimental Apparatus.** The experimental apparatus is shown schematically in Fig. 1. The vessel is a cylindrical flat-bottomed plexiglass non baffled tank. It has a diameter of 300 ± 0.2 mm and a height of 0.50 m. In the present study a two-bladed impeller, which dimensions are given in Table 3, is used. The height of the liquid in this tank is equal to the diameter of the vessel. The diameter of the two-bladed impeller is half of the vessel diameter. The impeller was built in polished stainless steel and mounted centered on the axis of the vessel. It is driven by a variable speed electric motor (Leroy-Somer MVS-25 model, France) with a maximum speed of 2000 rev.mn$^{-1}$. The rotational speed of the motor shaft is measured using a digital tachometer (Bioblock Scientific DT 2234). The torquemeter, allowing power measurements, as well as the anemometer used for local velocity measurements are connected to a data acquisition system.

The uncertainties in angular velocity $N$ and density $\rho$ are estimated at 1 percent and 0.2 percent, respectively. These values, together with previously given uncertainties, lead to total uncertainty on Reynolds number calculation equal to 4.5 percent

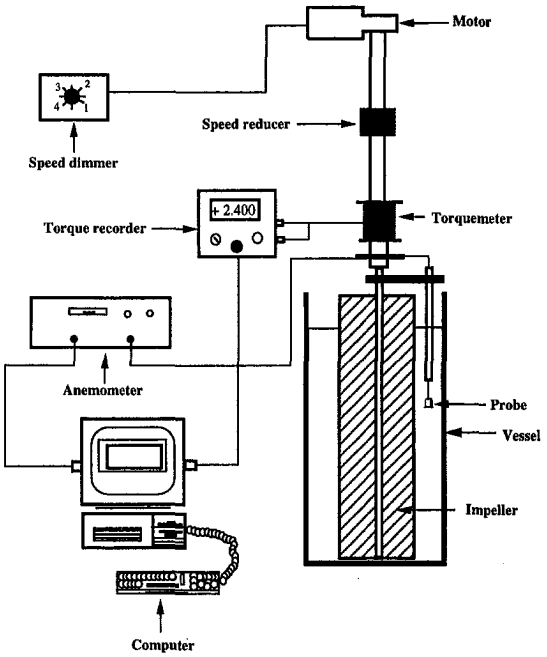


**Fig. 1 Experimental apparatus**

in Newtonian case (relation (6) for glycerol) and between 8 and 11.5 percent in non-Newtonian case (relation (8)), depending on the index $n$.

**3.2 Power Measurement.** The power consumption $P$ is determined by torque measurement on the shaft. The torque $C$ is measured using a noncontact strain gauge torquemeter of type HBM-T30FN for torque up to 50 N.m. The power required for mixing is then calculated:

$$P = 2\pi N(C - C_0) \tag{10}$$

where $C_0$ is the unloaded torque. The power consumption is a function of the system geometry, rheological properties of the fluid and kinematic variables, namely the rotation speed $N$. It is customary to present these results by plotting the dimensionless power number $Np$ as a function of the Reynolds number. It is defined as:

$$Np = \frac{P}{\rho N^3 D_a^5} \tag{11}$$

The estimated uncertainty on torque measurements is estimated to 2 percent and to less than 8.5 percent on the power number.

**3.3 Velocity Profiles Measurement.** Local measurements of the velocity components are carried out inside the tank using hot film anemometry (Dantec 55R11). The probe is rotating in the flow with the agitator. This technique is a practical compromise with respect to accuracy when one has to deal with large agitators and nontransparent fluids. It was used previously for this purpose by Bertrand and Couderc (1985), Soliman and Bertrand (1986), and Youcefi et al. (1991). Following a procedure identical to these previous studies, the film was calibrated in the corresponding fluid at rest inside a circular channel of square section in which the probe is translated with

**Table 3 Impeller characteristics**

| $D_a$ (mm) | $D_a/T$ (−) | $H$ (mm) | $d_a$ (mm) |
|---|---|---|---|
| 150 ± 0.1 | 0.5 | 500 ± 1 | 14 ± 0.1 |

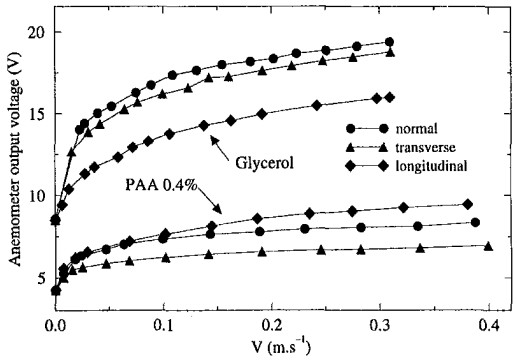


**Fig. 2 Calibration curves for the probes**

a controlled angular velocity. Three positions of the probe were selected with respect to the flow direction: normal (along $r$-axis), transverse (along $z$-axis), and longitudinal (along $\theta$-axis). Examples of the calibration curves are represented in Fig. 2. It appears that the level of energy exchanged with the flow is lower in the viscoelastic case than in the Newtonian case. Furthermore, the behavior for the viscoelastic fluid is different from the one observed with inelastic fluids. In opposition to the latter, the thermal energy obtained for the film aligned with the flow direction is greater than for the film normal to the flow. Experimental results from Smith et al. (1967) and from Piau (1974, 1980) showing strong modifications on the flow pattern around a circular cylinder, confirm that the transfer in such fluids is less efficient on obstacles submitted to an incoming normal flow. For these reasons the calibration has to be done even more carefully in this case and for each tested solution.

The calibration is realized with an error less than 3 percent but one must also take account of the drift during the measurement time and the misalignment of the probe. It can be evaluated to 5 percent owing to frequent readjustment during the experiments. For each measurement point, the response of the probe for the three positions is processed to provide the three components of the velocity. In the mixing vessel, the vertical component along Oz has been found negligible, that is to say, inside the limit of 5 percent of the tangential velocity. This finding confirms the hypothesis of 2D flow adopted in the simulation. The radial velocity is also smaller than the tangential one and for this component the error is more important and can reach 15 to 20 percent. We will not present this component in the sequel and we will concentrate our attention on the tangential velocity which drives most of the dynamics although it cannot be said that this flow is only tangential. The time signals of the anemometer show a periodic variation (Youcefi, 1983) due to unbalanced load on the axis of rotation. The variations correspond to 1 to 2 percent of the output voltage of the anemometer. From the inspection of this signal it can also be concluded that turbulence if exists is small and in all case less than 0.6 percent of the maximum velocity in the vessel. Altogether the error on the calculated tangential velocity can be evaluated to 7 percent, a value which is high but still fairly acceptable owing to the difficulty of the measurements.

## 4 Numerical Simulation of Viscoelastic Flow

Concurrently with the experimental study, a 2-D numerical simulation was conducted on a similar geometry. The 2-D approximation is actually considered as a good one justified by experimental measurements. Numerous difficulties are encountered in numerical simulation of viscoelastic fluids which are mainly related to the number of variables (six scalar fields in 2-D) related by a system of non-linear coupled partial derivative equations of mixed type elliptic-hyperbolic (Joseph et al., 1985, Keunings, 1988). The choice of this configuration is particularly suitable for a comparative study.

The fluid is described by an Oldroyd "B" law which is a viscoelastic but non pseudoplastic model with a constant shear viscosity $\eta_0$. Thus the numerical simulation is able to treat separately the specific effects of viscoelasticity and provides complementary means to compare the elastic and non elastic fluids mentionned in Section 2. This law is expressed as follows:

$$\boldsymbol{\tau} + \lambda \overset{\nabla}{\boldsymbol{\tau}} = 2\eta_0(\mathbf{D} + \lambda_r \overset{\nabla}{\mathbf{D}}) \tag{12}$$

where the symbol $\nabla$ holds for the upper-convected derivative:

$$\overset{\nabla}{\boldsymbol{\tau}} = \frac{\partial \boldsymbol{\tau}}{\partial t} + (\nabla.V)\boldsymbol{\tau} - \nabla V.\boldsymbol{\tau} - \boldsymbol{\tau}.\nabla V^T \tag{13}$$

which confers objectivity to the rheological law (Bird, 1977).

The elasticity of the fluid is proportional to $\lambda$ which is a relaxation time. $\lambda_r$ is the retardation time and a zero-value gives the well-known upper-convected Maxwell model; $\lambda_r = \lambda$ is a more complex form of the Newtonian law. Then for significantly elastic fluids $\lambda_r$ must be smaller than $\lambda$. The retardation time $\lambda_r$ induces a purely viscous term in the momentum equation and has thus a stabilizing effect on the numerical results (Joseph et al., 1985). As in numerous numerical simulations, we have adopted the commonly constant ratio used for the characteristic times, which is $\lambda_r/\lambda = \frac{1}{9}$ (Keunings, 1988; Bird et al. 1977 (Section 8.1); Fortin and Fortin, 1990; Marchal and Crochet, 1987). Note that introducing $\lambda_r$ in such a way that $\lambda_r/\lambda$ remains small does not change the nature of the rheological characteristics of the model.

The studied flow is governed by a set of coupled partial differential equations: the constitutive equation and the continuity and momentum equations:

$$\nabla.V = 0 \tag{14}$$

$$\rho\left(\frac{\partial V}{\partial t} + (V.\nabla)V\right) - \nabla.\boldsymbol{\tau} + \nabla p = 0 \tag{15}$$

Equation (15) is then expressed in a rotating frame bound to the impeller introducing centrifugal and Coriolis forces. This allows the problem to be a steady one. Results are then expressed in a fixed frame in a post-processing stage. Nevertheless, the flow is simulated by an unsteady finite element method converging to a final steady-state. This time marching approach contributes to a good convergence of the decoupled procedure used for the hydrodynamic and constitutive equations. A more detailed presentation of the method can be found in a previous work (Anne-Archard and Boisson, 1995). Dimensionless equations naturally introduce the Reynolds number defined as in experimental case (see Eq. (6)), and a dimensionless group E called Elasticity number which is characteristic of the elasticity of the fluid, independently of flow conditions:

$$\mathrm{E} = \frac{\lambda\eta_0}{\rho D_a^2} \tag{16}$$

Numerical simulations are carried out for Reynolds number up to 10. The typical difficulties encountered in such computation of viscoelastic flows involve a practical upper limit to the Elasticity number at about 2.5 in very low inertia flow (Re = 0.1), and at lower values of about 0.021 at Re = 10. Use of special techniques as streamline upwinding for the constitutive equation and subelements for stresses (Marchal and Crochet, 1987, Anne-Archard and Boisson, 1995) were necessary to achieve this performance. The convergence criterion in the iterative time approach procedure is based on the ratio of the maximum absolute difference of the values of any variable at two successive time steps, to the value at this time step. In the less favorable case (i.e., for high elasticity number), a value of $10^{-2}$

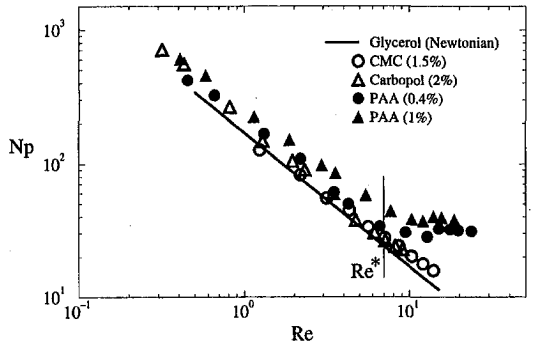


Fig. 3 Evolution of the power number *Np* versus the Reynolds number for all the test fluids. Experimental results. Uncertainty of data: Re: ±4.5%, Re′: ±8% (Carbopol), ±9% (CMC), ±10% (PAA 0.4%), ±11.5% (PAA 1%), *Np*: ±8.5%.

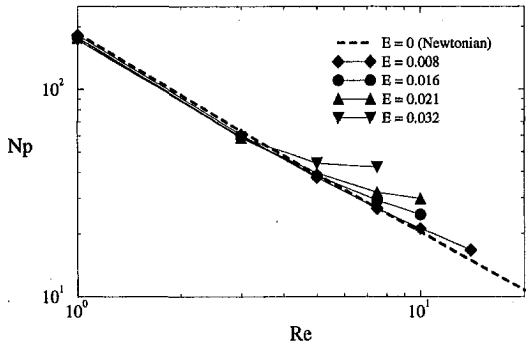


Fig. 4 Evolution of the power number *Np* versus the Reynolds number for three Oldroyd-type fluids. Numerical results

was used. Note that this process is governed by the stresses, so that this relative deviation for velocity field is currently $10^{-4}$. Mass conservation is verified to within 0.1 percent in most cases, 0.6 percent for the highest elasticity number.

## 5 Results and Discussion

A Reynolds number range of 0.3 to 36 was explored for the power consumption measurements, but velocity measurements were possible only for Re or Re′ greater or equal to 5. Flow visualizations indicate that end effects at the top and the bottom of the vessel are reduced to small regions when compared to the whole domain, confirming the 2-D character of the flow. In the central zone, the three components of the velocity field were measured and clearly confirm the two-dimensional character of the flow, i.e., negligible axial velocity $V_z$ compared to tangential one $V_\theta$ (see Section 3.3). This was observed for both Newtonian and viscoelastic fluids.

Experimental as well as numerical results are presented in dimensionless form, using the vessel radius, $T/2$ and the quantity $V_{\text{ref}} = \pi NT$ as references for length and velocity, respectively. $V_\theta$ indicates the dimensionless value of the tangential velocity and $r$ is also the dimensionless radial coordinate. For the presentation of the results, "impeller plane" will indicate the plane of the shaft and the diameter of the vessel containing the impeller. Similarly, "median plane" is the perpendicular plane to the impeller plane through the shaft. These planes are fixed in a frame rotating with the agitator.

**5.1 Results for Power Number.** Experimental results for power number versus Reynolds number are presented in Fig. 3. These results clearly show two different behaviors: for Newtonian and pseudoplastic inelastic fluids, the power number linearly decreases with Reynolds number in logarithmic coordinates. Moreover, the three curves for Newtonian, pseudoplastic fluids with and without threshold almost superimpose. This is obtained by taking into account pseudoplasticity for the effective Reynolds number Re′ (Eq. (8)) (Youcefi et al., 1992a, Carreau et al., 1993).

Viscoelastic fluids (PAA solutions) do not follow this linear law: a threshold Re* clearly appears in the vicinity of Re = 7. As long as Reynolds number is less than Re*, these measurements of power consumption show a behavior similar to inelastic fluids. Beyond Re* the power number significantly increases and departs from the Newtonian reference. This behavior is then a typically viscoelastic one, which does not appear in weakly inertial flow.

By the numerical simulation we can determine velocity and stress fields, thus compute the power $P$:

$$P = \int_\Omega \tau : \nabla V dv \qquad (15)$$

Numerical results for power number are presented in Fig. 4 in logarithmic coordinates, as in experimental case, and for three different elasticity numbers. The Reynolds number range on this graph varies from 1 to 10 for a better legibility, but comparison in the whole Reynolds number range (i.e., 0.1 to 10) between experimental and numerical results clearly shows a very good agreement in the Newtonian case. A behavior similar to the experimental results is observed in this figure for the viscoelastic case with a change of slope of the curves beyond the threshold $\text{Re}_n^*$. This numerical threshold lies between 5 and 6 and is then comparable to the experimental one. The numerical simulation reproduces the behavior below the threshold both qualitatively and quantitatively for Newtonian as well as for viscoelastic fluids. Beyond this threshold, viscoelasticity induces an increase in power consumption with respect to Newtonian fluids. The model used for this simulation only provides a qualitative trend for this increase.

**5.2 Results for Velocity Field.** In the previous section of this paper, the effect of viscoelasticity on global parameters and namely on the power consumption was addressed. The local study of hydrodynamics provides a complementary point of view on the problem and gives a better understanding of the modifications involved by the viscoelasticity. In our experiments, in order to obtain an acceptable accuracy it is necessary to impose a sufficient rotation speed, specially in the viscoelastic case and Re′ must be greater or equal to 5.

Taking the Newtonian case as a reference, velocity measurements were first conducted with glycerin solutions. The results are consistent with the ones of Bertrand (1983) and with our numerical simulation as already shown by Youcefi et al. (1992.b): the dispersion in the results is less than 5 percent. The first tangential velocity profiles $V_\theta$ in the impeller plane (Fig. 5) are presented for a Reynolds number equal to 5. Of course the linear growth in these curves corresponds to the solid rotation of the impeller and the measurements are only possible in the gap between the tip of the blade and the vessel wall. In

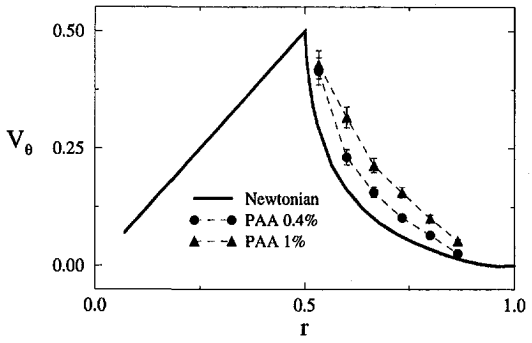


Fig. 5 Tangential velocity in the impeller plane. Effective Reynolds number: Re′ = 5. Uncertainty on Newtonian reference: 5%

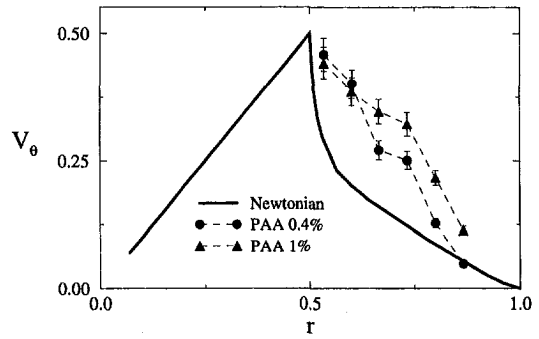


**Fig. 6 Tangential velocity in the impeller plane. Effective Reynolds number: Re′ = 30. Uncertainty on Newtonian reference: 5%.**

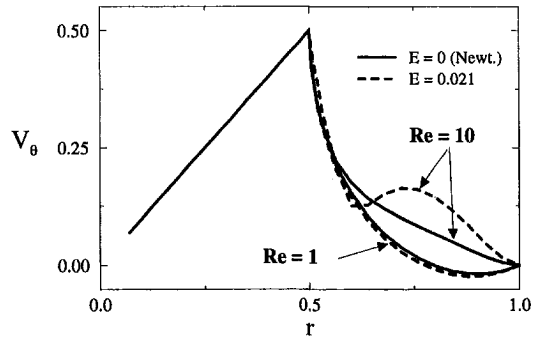


**Fig. 7 Comparison of tangential velocities for Newtonian and Oldroyd-type fluids in the impeller plane**

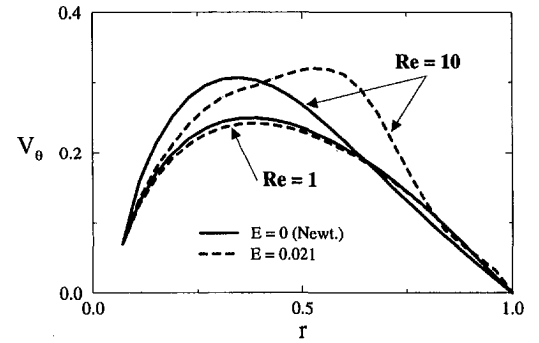


**Fig. 8 Comparison of tangential velocities for Newtonian and Oldroyd-type fluids in the median plane of the impeller**

this figure, the Newtonian case is plotted and serves as a reference. The experimental points for PAA solutions are connected by straight lines. Although this Reynolds number of 5 is slightly less than the value proposed for the threshold from the experimental curves of $Np$, significant differences exist between the results for Newtonian and viscoelastic fluids. These differences are normally increasing with concentration of PAA, i.e., with elasticity. Figure 6 is similar to Fig. 5 but corresponds to Re or Re′ equal to 30. We notice that inertia increases the gap between Newtonian and viscoelastic results. Moreover, the conjugate effects of inertia and viscoelasticity modify the shape of the velocity profiles and higher tangential velocities are obtained in the central part of the gap. A larger flow rate is then pumped by the blade, which is consistant with the larger power consumption observed in this case.

Numerical simulation can supply for the lack of experimental results in low inertia flows. In Figs. 7 and 8 are represented the numerical tangential velocity profiles for two Reynolds numbers on both sides of the threshold $Re_n^*$. These figures display the values, respectively, on the impeller plane and on the median plane. These results clearly indicate two different behaviors: in low inertia flow (Re = 1), the velocity field is weakly affected by elasticity: a very small decrease of $V_\theta$ is noticed. On the contrary, moderate inertia effects (Re = 10) lead to serious differences between Newtonian and viscoelastic fluids. The shape of the velocity profile is largely affected, with emergence of a point of inflection, and a large increase of $V_\theta$ in the gap between the tip of the blade and the vessel wall.

## 6 Conclusion

This study is dedicated to hydrodynamics and global energetics of a mixing process in viscoelastic fluids. It has been conducted in a fairly simple geometrical configuration namely, a nonbaffled mixing tank equipped with a paddle impeller. The flow was shown to be a 2-D one and this allows qualitative comparison with a numerical simulation using the Oldroyd 'B' rheological model.

Two original aspects have been developed through this study. The first one consists of direct measurements of the local velocity field in such a system. Despite of the existence of previous works on agitated mixing vessels filled up with viscoelastic fluids, it is worthwhile noticing that experimental data on the velocity field were not available before this work. In fact, classical methods cannot be easily applied to such fluids: for instance, the hot film anemometer used here does not behave as in the inelastic fluids. The second aspect of this study is directed toward the discussion of the effect of the fluid elasticity on the process. Actually, in all existing case, except for the very peculiar Boger fluid, viscoelasticity is associated to shear-thinning and it is difficult to separate both effects from each other. This is done here experimentally by using the three categories of fluids, namely, Newtonian fluid, inelastic shear-thinning ones, and viscoelastic ones. In contrast, Oldroyd model does not introduce the shear-thinning effect and can show the effect of elasticity on constant viscosity fluid although in our case only qualitative conclusion can be drawn from the simple theoretical model used.

The data on the power number versus the Reynolds number collapse on a single curve for every nonelastic fluid tested whether Newtonian or shear-thinning. This is also the situation for elastic fluids below a given threshold of the Reynolds number. Beyond this value, the increase in elasticity of the fluid induces a significant raise of the power number and a departure from the previous correlation. The numerical simulation support this point of view: in this case, there is no shear-thinning effect in the Oldroyd 'B' fluid and the observed raise, that corresponds roughly to the observed value in the experiments, is only due to the conjugate effects of inertia and viscoelasticity.

The measurements and the computation of the local velocity field show that the change in shape of velocity profiles can explain the change in the power number behavior and this change cannot be attributed to the onset of turbulence as claimed by some authors, but should be attributed to elasticity of the fluid. As far as the hydrodynamics is changed one must expect some changes in the mixing efficiency and work are still in progress on this aspect.

As viscoelasticity is observed in many industrial fluids and applications, it will be of great interest to extend the study presented here to more complex mixing flows, i.e., to 3-D flows as those generated in the most commonly used mixing systems for highly viscous fluids. Furthermore, numerical prediction of such flows can be improved using more performant rheological laws. Insofar as industrial processes are usually confronted to elastic behavior, the knowledge of hydrodynamics, together with simulation of mixing flows for complex fluids, will thus lead to increased efficiency.

## Acknowledgments

The authors are thankful to "Centre National Universitaire Sud de Calcul" for a support in CPU time for numerical simulation, under account C00045-IMF1282. They also thank Professor Rémi Gaudu who initiated this work.

## References

Anne-Archard, D., and Boisson, H. C., 1995, "A Finite Element Simulation of the Cross-Effects of Viscoelasticity and Inertia in an Agitated Vessel," *International Journal for Numerical Methods in Fluids,* Vol. 21, pp. 75–90.

Bertrand, J., and Couderc, J. P., 1985, "Evaluation of the Power Consumption in Agitation of Viscous Newtonian or Pseudoplastic Liquids by Two-Bladed, Anchor or Gate Agitator," *Chemical Engineering Research and Design,* Vol. 63, pp. 259–263.

Bertrand, J., 1983, "Agitation de fluides visqueux. Cas de mobiles à pales, d'ancres et de barrières," Thèse de Doctorat d'Etat de l'Institut National Polytechnique de Toulouse, France.

Bird, R. B., Armstrong, R. C., and Hassager, O., 1977, *Dynamics of Polymeric Liquids. Vol. 1: Fluid Mechanics,* Wiley, New York.

Boger, D. V., 1977, "A Highly Elastic Constant Viscosity Fluid," *Journal of Non-Newtonian Fluid Mechanics,* Vol. 3, pp. 87–91.

Brito de la Fuente, E., Leuliet, J. C., Choplin, L., and Tanguy, P. A., 1990, "Mixing and Circulation Times in Rheologically Complex Fluids," *Institution of Chemical Engineers Symposium Series No. 121,* pp. 75–96.

Carreau, P. J., Chhabra, R. P., and Cheng, J., 1993, "Effects of Rheological Properties on Power Consumption with Helical Ribbon Agitators," *American Institute of Chemical Engineers Journal,* Vol. 39, No. 9, pp. 1421–1430.

Couaraze, G., and Grossiord, J. L., 1985, "Initiation à la rhéologie," Lavoisier Tech. et Doc., Paris.

Fortin, A., and Fortin, M., 1990, "A Preconditioned Generalized Minimal Residual Algorithm for the Numerical Solution of Viscoelastic Flows," *Journal of Non-Newtonian Fluid Mechanics,* Vol. 36, pp. 277–288.

Höcker, H., Langerg, G., and Werner, U., 1981, "Power Consumption of Stirrers in non-Newtonian Liquids," *German Chemical Engineering,* Vol. 4, pp. 113–123.

Joseph, D. D., Renardy, M., and Saut, J. C., 1985, "Hyperbolicity and Change of Type in the Flow of Viscoelastic Fluids," *Archive for Rational Mechanics and Analysis,* Vol. 27, pp. 213–251.

Keunings, R., 1988, "Simulation of Viscoelastic Fluid Flow," *Fundamentals of Computer Modeling for Polymer Processing,* C. L. Tucker Edition, Verlag, Munich.

Leuliet, J. C., Brito de la Fuente, E., and Choplin, L., 1992, "Mélanges de Fluides élastiques avec un agitateur à ruban hélïcoidal," *Entropie,* Vol. 28, No. 171, pp. 53–58.

Lodge, A. S., 1964, *Elastic Liquids,* Academic Press, London.

Marchal, J. M., and Crochet, M. J., 1987, "A New Mixed Finite Element Method for Calculating Viscoelastic Flow," *Journal of Non-Newtonian Fluid Mechanics,* Vol. 26, pp. 77–114.

Metzner, A. B., and Otto, R. E., 1957, "Agitation of non-Newtonian Fluids," *American Institute of Chemical Engineers Journal,* Vol. 3, No. 1, pp. 3–10.

Piau, J. M., 1974, "Ecoulement des solutions diluées d'un polyoxyéthylène autour des cylindres à base circulaire," *Comptes Rendus à l'Académie des Sciences de Paris,* Série B, Vol. 278, pp. 493–495.

Piau, J. M., 1980, "A Characteristic Length for Dilute Drag Reducing Polymer Solutions: Measurements Using Hot Film Anemometers," *Rheologica Acta,* Vol. 19, pp. 724–730.

Shamlou, P. A., and Edwards, M. F., 1985, "Power Consumption of Helical Ribbon Mixers in Viscous Newtonian and non-Newtonian Fluids," *Chemical Engineering Science,* Vol. 40, No. 9, pp. 1773–1781.

Smith, K. A., Merril, E. W., Mickley, H. S., and Virk, P. S., 1967, "Anomalous Pitot Tube and Hot Film Measurements in Dilute Polymer Solutions," *Chemical Engineering Science,* Vol. 22, pp. 619–626.

Soliman, M., and Bertrand, J., 1986, "Agitation by Helical Ribbons: Power Consumption, Mixing Time and Local Velocities," *Proceedings of World Congress III of Chemical Engineering,* Tokyo, pp. 398–400.

Youcefi, A., Gaudu, R., Bertrand, J., Anne-Archard, D., and Sengelin, M., 1992a, "Mechanical agitation of viscoelastic fluids by a two-bladed stirrer," *Proceedings of the 1992 Institution of Chemical Engineers Research Event,* Manchester, U.K., pp. 377–379.

Youcefi, A., Anne-Archard, D., Boisson, H. C., Sengelin, M., Bertrand, J., 1992b, "Etude numérique et expérimentale de l'écoulement d'un fluide viscoélastique autour d'un agitateur bipale en cuve agitée," *Collection Récents Progrès en Génie des Procédés,* Lavoisier, Paris, Vol. 6, No. 19, pp. I.1–I.8.

**K. J. Myers**
Associate Professor.

**R. W. Ward**
Graduate Student.

Chemical and Materials Engineering,
University of Dayton,
Dayton, OH 45469-0246

**André Bakker**
Technical Director,
Chemineer, Inc.,
Dayton, OH 45401-1123

# A Digital Particle Image Velocimetry Investigation of Flow Field Instabilities of Axial-Flow Impellers

*Digital particle image velocimetry (DPIV) has been used to examine the flow field in a vessel agitated by an axial-flow impeller in turbulent operation. Both a pitched-blade turbine and a high-efficiency impeller were studied. Time series analysis indicates that the flow field is not steady; rather, it is subject to transients with frequencies well below the blade passage frequency (periods ranging from 40 to over 300 impeller revolutions have been observed). This result has important implications for computational modeling because current descriptions of agitated vessels are based upon time-averaged flow fields with superimposed turbulence. This modeling approach may not accurately capture the mixing associated with the low-frequency phenomena observed in this study.*

## Introduction

Mechanically agitated vessels are in widespread use in the chemical processing and allied industries. Their diverse array of applications includes storage tanks, blending operations, crystallization, fermentation, and as chemical reactors. Design of agitators has traditionally relied on qualitative rules of thumb and past experience. However, with the increasing availability of enhanced computational and experimental techniques, there is a growing emphasis on understanding the fundamentals of agitated vessel performance. In many instances the success or failure of an agitator can be directly related to the flow in the vessel and how it impacts physical and chemical transformations.

It is becoming apparent that the flow fields in agitated vessels are not invariant. Rather, they are influenced by Reynolds number (Wang et al., 1995) and geometry (Kresta and Wood, 1993). Further, there is growing evidence that the flow fields produced by axial-flow impellers are time-dependent, exhibiting transients with frequencies considerably less than those associated with small-scale turbulence and blade passage. In this work, digital particle image velocimetry (DPIV) is used to characterize low frequency transients in the flow fields produced by axial-flow impellers.

## Studies of Flow Pattern Instability

Numerous recent publications have demonstrated that the flow field produced by an axial-flow impeller is not truly steady, but rather is subject to instabilities with time scales that are substantially longer than those associated with blade passage and small-scale turbulence. Single-phase flow patterns of various axial-flow impellers have been studied by several methods. Chapple and Kresta (1993) used tuft visualization to study the stability of the flow patterns produced by a three-blade hydrofoil impeller and a pitched-blade turbine. They also characterized the influence of geometric parameters such as impeller off-bottom clearance, impeller diameter, and number of baffles on flow pattern stability. Brůha et al. (1994, 1995) identified time dependence in the flow pattern of a pitched-blade turbine using a mechanical measuring device. They found that the frequency of transition in the flow pattern is linearly related to the speed of impeller rotation, but is much slower than the speed of impeller rotation. Winardi and Nagase (1991) used a combination of flow visualization techniques to examine the flow patterns produced by a marine propeller. They described the observed flow patterns as quick return, full circulation, and intermediate circulation. They measured the lifetime distribution of these patterns and found that the flow pattern changes were random in their order and that the lifetime of a given flow pattern could range from half a second to several minutes. Using laser Doppler velocimetry (LDV) Bakker and Van den Akker (1994a) found that in the upper portions of a vessel agitated by a pitched-blade turbine the axial velocity exhibited bimodal and trimodal distributions. This behavior suggests that the flow in this region is not stable, perhaps oscillating between a number of quasi-stable flows.

A few process-oriented investigations have also indicated the unstable nature of the flow patterns produced by axial-flow impellers. Haam et al. (1992) found that the magnitude of the interphase (vessel to inside wall) heat transfer coefficient in an agitated vessel is periodic in nature. They attributed the oscillations in the heat transfer coefficient to the slow (relative to the impeller speed) precession of an axial vortex around the vessel. Bakker and Van den Akker (1994b) observed periodic fluctuations in the local gas holdup for systems agitated with axial-flow impellers. Again, the frequency of the fluctuations were slow relative to the speed of impeller rotation. As in Haam et al.'s heat transfer study, this behavior was attributed to an asymmetric flow pattern caused by complex nonstationary vortex motion. Thus, both fundamental and process studies have established the unstable nature of the flow fields produced by axial-flow impellers. The observed instabilities have exhibited a wide range of frequencies, with many instabilities occurring over a time scale much longer than that associated with impeller rotation or blade passage. However, characterization of these instabilities is incomplete and very little is known about their origin and influence on mixing performance.

## The DPIV Technique

Digital particle image velocimetry (DPIV) combines the optical flow characterization technique of particle image velocime-

Contributed by the Fluids Engineering Division for publication in the JOURNAL OF FLUIDS ENGINEERING. Manuscript received by the Fluids Engineering Division April 2, 1996; revised manuscript received December 5, 1996. Associate Technical Editor: P. W. Bearman.

try (PIV) with digital image processing to yield a rapid, nonintrusive method to study flow fields. Like many other velocimetry techniques, DPIV requires seeding the flow with particles that mimic the motion of the liquid. In the case of DPIV, these particles fluoresce when exposed to light of a characteristic wavelength. This light is provided by a laser whose output is manipulated into a light sheet that illuminates a plane of the flow field to be studied. To increase processing speed, rather than using photographic techniques, DPIV captures the images of the fluorescent particles digitally with a charge coupled device (CCD) camera.

To obtain fluid velocities, two images of the seeded flow field are captured digitally at successive points in time, and comparison of these images allows the velocity field in the system to be constructed. To do this, the flow field is divided into smaller interrogation regions that are considered individually. Rather than tracking individual particles, cross correlation is used to obtain the average particle displacement of the ensemble of particles in an interrogation region from the successive flow field images. Computationally, cross correlation is achieved with two-dimensional signal processing techniques whose speed is enhanced through the use of fast Fourier transforms. The fluid velocity is then calculated assuming linear displacement over the time interval between the successive images.

Willert and Gharib (1991) have described DPIV in greater detail, focusing on the cross correlation technique and its implementation. The accuracy of DPIV relies on experimentation under appropriate conditions. These include a minimum particle displacement of two particle diameters, a maximum particle displacement of twenty-five percent of the interrogation region dimension, minimal out-of-plane displacement, and a minimum of five particles in an interrogation region to ensure accurate velocity measurements.

## Experimental Apparatus and Procedures

The DPIV apparatus used in this study is a commercial system acquired from Dantec Measurement Technology. Figure 1 illustrates the primary components of the apparatus. A continuous argon-ion laser is the light source. A light sheet probe equipped with a prism converts the beam into a nominal 0.01 meter thick light sheet. Background laser reflections are virtually eliminated with an optical cutoff filter. The thick light sheet used in this study reduces the effects of tangential motion that carries particles in and out of the plane of study. This effect is particularly significant in the impeller region where the tangential velocities are higher than in the rest of the vessel. The flow is seeded with approximately 5000 80-micron diameter fluorescent spheres in the illuminated plane. The CCD camera is placed 1.8 m from the plane of the light sheet. Placement of the CCD camera far from the plane of study minimizes errors in determination of the axial and radial velocities due to tangential movement of particles within the rather thick light sheet. The CCD camera captures a 512 by 480 pixel image of the flow field. This image is divided into either 16 by 16 or 32 by 32 pixel interrogation regions, depending on the expected velocities. An 8 pixel step size between adjacent interrogation regions is used, resulting in fifty percent or seventy-five percent overlap, respectively. The two-dimensional DPIV flow field is then represented by a discrete flow field containing approximately 3000 velocity vectors. Oversampling the velocity field by overlapping the interrogation regions provides more velocity vectors which aids in the removal of velocity outliers, reinterpolation, and smoothing of the velocity field, all of which improve the accuracy of the measurements.

The diameter of the cylindrical, flat-bottomed plexiglass vessel used in this work was 0.292 meters. This vessel was placed in a square plexiglass tank filled with water to reduce optical distortion. The vessel was equipped with four vertical baffles that were evenly spaced about the periphery of the vessel. The baffle widths were equal to one-twelfth of the vessel diameter. The baffles were offset from the vessel wall by a distance equal to one-sixth of the baffle width. The liquid used was water and the liquid level was equal to the tank diameter ($H/T = 1$). The three-dimensional, cylindrical vessel could be rotated relative to the laser light sheet so that data could be taken in any vertical plane. For some experiments the plane of study was located midway between the baffles, while for other experiments a plane slightly in front of the plane between two baffles was studied.

Two impellers were studied (refer to Fig. 1). The first was the P-4, a four-bladed, forty-five degree pitched-blade turbine with a diameter of 0.102 meters ($D/T = 0.35$). The width of the impeller blades was one-fifth of the impeller diameter ($W/D = 0.20$). This impeller was studied at off-bottom clearances of 0.134 meters ($C/T = 0.46$, $C/D = 1.31$) and 0.097 meters ($C/T = 0.33$, $C/D = 0.94$). The second impeller studied was

## Nomenclature

$C$ = impeller off-bottom clearance, measured from the lowest point on the impeller to the vessel base (m)
$D$ = impeller diameter (m)
$f, f_l$ = frequency of large-scale flow pattern fluctuations ($s^{-1}$)
$H$ = total liquid depth (m)
$N$ = agitation speed (revolutions per second, $s^{-1}$)
$P(f_l)$ = power spectral density of the spatially-averaged vorticity-time record (−)
$S$ = ratio of velocity standard deviation to time-averaged velocity (−)
$t$ = time (s)
$T$ = vessel diameter (m)
$u$ = velocity in the $x$-direction (m/s)
$v$ = velocity in the $y$-direction (m/s)
$\mathbf{v}$ = velocity vector (m/s)
$W$ = impeller blade width (m)
$W_l$ = discrete Fourier transform of the spatially-averaged vorticity-time record (−)
$y$ = distance above the vessel base (m)
$\nu$ = kinematic viscosity ($m^2/s$)
$\sigma$ = standard deviation in the velocity (m/s)
$\boldsymbol{\omega}$ = vorticity vector ($s^{-1}$)

### Subscripts

$i$ = index for $x$-direction (−)
$I$ = total number of interrogation regions in the $x$-direction (−)
$j$ = index for $y$-direction (−)
$J$ = total number of interrogation regions in the $y$-direction (−)
$k$ = flow field number in the time series (−)
$K$ = total number of flow fields in the time series (−)
$l$ = frequency index
$z$ = indicates $z$ coordinate (−)

### Operators

$\nabla$ = vector differential operator ($m^{-1}$)
$X$ = vector cross product operator (−)
$\Sigma$ = summation operator (−)
$\langle\ \rangle$ = area average operator (−)
$\bar{\ }$ = time average operator (−)
$\Delta$ = difference operator (−)

### Acronyms

CCD = charge coupled device
DPIV = digital particle image velocimetry
LDV = laser Doppler velocimetry
PIV = particle image velocimetry
PSD = power spectral density

Figure 1 (top)

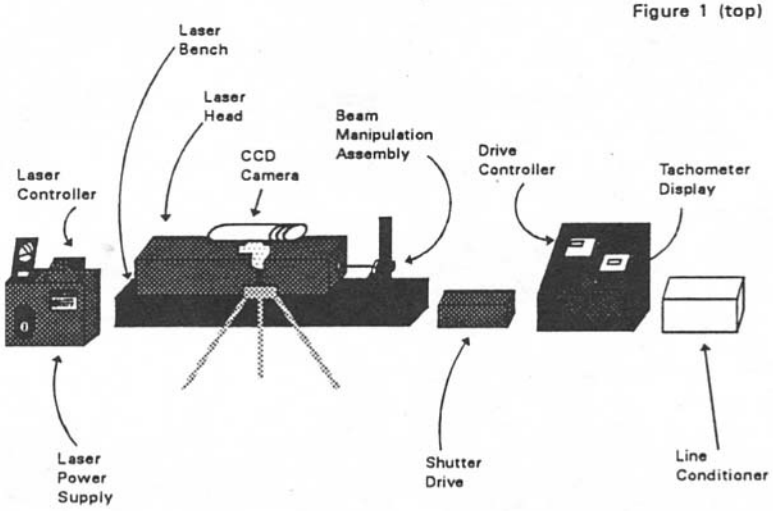


Figure 1 (middle)

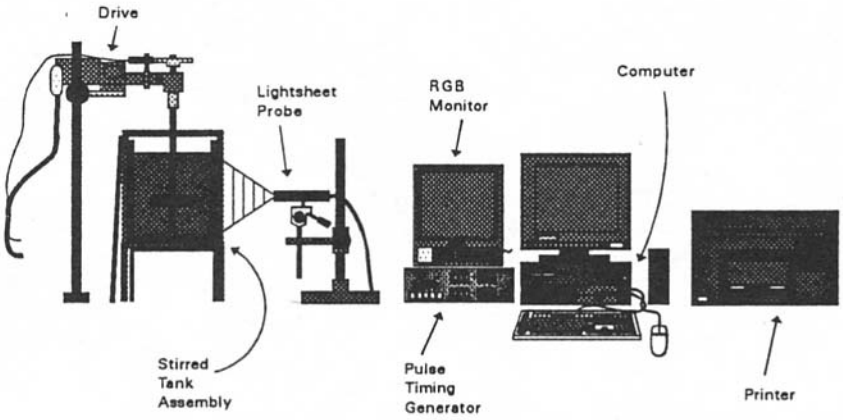


Figure 1 (bottom)

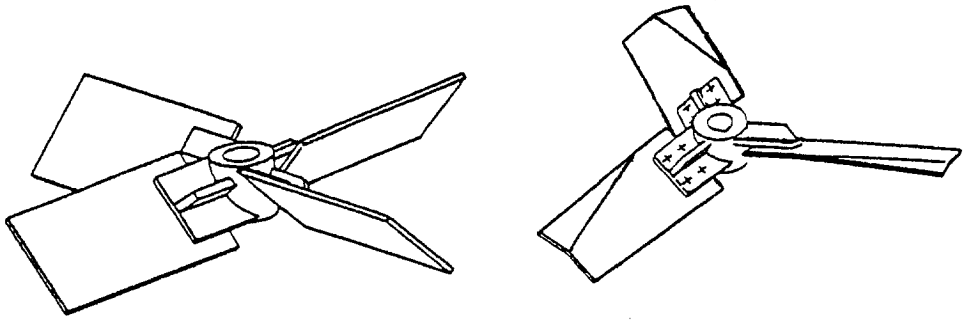

**Fig. 1 Experimental apparatus: laser, controls, and CCD camera (top), vessel and computing hardware (center), and impellers studied (bottom)**

a high-efficiency impeller, a Chemineer HE-3 of standard construction with a diameter of 0.114 meters ($D/T = 0.39$). This impeller was studied only at an off-bottom clearance of 0.097 meters ($C/T = 0.33$, $C/D = 0.84$). Operation at speeds of either 0.6 or 1 $s^{-1}$ (36 or 60 rpm) yielded impeller Reynolds numbers ($ND^2/\nu$) ranging from 6,190 to 13,100, the lower end of the turbulent regime.

The successive images for DPIV analysis were captured using a time delay of 0.033 seconds between the images (this corresponds to the standard video timing rate). This delay was appropriate for the relatively low velocities encountered in this work. The highest impeller tip speed used was 0.36 m/s, and the maximum fluid velocities would be only a fraction of this value. Further, a series of image pairs was taken to study the transient behavior of the flow field. Series of either 64 or 1024 image pairs were taken. The successive image pairs were separated by a time delay of approximately 11 seconds for the 64 image pair series and 1.3 seconds for the 1024 image pairs series. This yielded time records of 700 or 1330 seconds (11.7 or 22.2 minutes). Time series analysis was performed only on the data sets obtained with the faster sampling rate (with a delay of 1.3 seconds between successive image pairs). Since this sampling rate is approximately 30 times faster than the fastest transients observed in the flow field, aliasing errors are not likely to be significant. To further verify that aliasing did not influence the results and that the observed changes in flow pattern were not associated with blade passage, a set separate of experiments was performed. These experiments used a much shorter time delay of 0.167 seconds between successive image pairs. These results are discussed in the section Blade Passage Effects.

## Data Analysis

Computational options following measurement of the series of two-dimensional velocity fields include calculation of the time-averaged velocity field, calculation of quantities such as vorticity and the standard deviation in the velocity, and the construction of one-dimensional time series.

The time-averaged velocity components at a point $i, j$ in the flow field are calculated in the following manner.

$$\bar{u}_{i,j} = \frac{1}{K}\sum_{k=1}^{K} u_{i,j,k} \quad \bar{v}_{i,j} = \frac{1}{K}\sum_{k=1}^{K} v_{i,j,k} \tag{1}$$

Here $u$ and $v$ are the velocities in the $x$-direction and the $y$-direction, respectively, $i$ and $j$ denote the $x$ and $y$ locations in the flow field, $k$ denotes the $k$th flow field in the time series, and $K$ is the total number of near-instantaneous flow fields measured. Note that the cylindrical coordinates, with radial, tangential, and axial components, typically used to describe flow in agitated vessels have been replaced by a planar coordinate system since the DPIV technique provides a near-instantaneous, two-dimensional flow field in the plane illuminated by the laser light sheet. In this planar coordinate system, the $x$ coordinate replaces the radial coordinate and the $y$ coordinate replaces the axial coordinate (with the $y$ position measured relative to the base of the vessel). The $z$ coordinate, which will be important relative to the calculation of vorticity, is normal to the illuminated plane of study.

The standard deviation in the velocity at any point in the flow field, $\sigma_{i,j}$, can also be calculated.

$$\sigma_{i,j} = \sqrt{\frac{1}{K}\sum_{k=1}^{K}(u_{i,j,k}^2 + v_{i,j,k}^2) - \frac{1}{K^2}\left(\sum_{k=1}^{K}(u_{i,j,k}^2 + v_{i,j,k}^2)^{1/2}\right)^2} \tag{2}$$

This velocity standard deviation is a measure of the energy contained in the fluctuating velocities in the flow field. The ratio of the standard deviation and the magnitude of the average velocity, often termed the coefficient of variation,

$$S_{i,j} = \frac{\sigma_{i,j}}{\sqrt{\bar{u}_{i,j}^2 + \bar{v}_{i,j}^2}} \tag{3}$$

provides an indication of the local stability of the flow.

Vorticity is the curl of the velocity vector ($\boldsymbol{\omega} = \nabla \times \mathbf{v}$) and characterizes the rotation of fluid elements in the flow field. Vorticity is a vector with a characteristic direction normal to the plane in which rotation occurs (as determined by the right-hand rule). For a two-dimensional flow field such as that obtained by DPIV, this directional aspect can simply be described by the sense (sign) of the vorticity. Positive vorticity (directed out of the plane of observation) corresponds to counterclockwise rotation while negative vorticity (directed into the plane of observation) corresponds to clockwise rotation. Given a near-instantaneous, two-dimensional ($x$-$y$) velocity field at time step $k$, the $z$-component of vorticity at the point $i, j$ in the flow field

$$(\omega_{i,j,k})_z = \frac{\partial v_{i,j,k}}{\partial x} - \frac{\partial u_{i,j,k}}{\partial y} \tag{4}$$

can be calculated from the discrete velocity fields using finite difference approximations of the derivatives. The spatially-averaged vorticity of the $k$th near-instantaneous velocity field, $\langle\omega\rangle_k$, is calculated as follows.

$$\langle\omega\rangle_k = \frac{1}{I \cdot J}\sum_{i=1}^{I}\sum_{j=1}^{J}(\omega_{i,j,k})_z \tag{5}$$

This yields a one-dimensional time series of the spatially-averaged vorticity of the near-instantaneous velocity fields. As will be seen, the spatially-averaged vorticities of near-symmetric flow fields are approximately zero, while the spatially-averaged vorticities of asymmetric flow fields have large magnitudes. A high positive spatially-averaged vorticity indicates that there are more (or larger) counterclockwise circulation loops, while a high negative spatially-averaged vorticity indicates that there are more (or larger) clockwise circulation loops.

The time series of the spatially-averaged vorticity is then further analyzed by calculating the power spectral density function (PSD), $P(f_l)$, which identifies the dominant frequencies of the time series. The power spectral density is determined from the discrete Fourier transform of the spatially-averaged vorticity, $W_l$.

$$W_l = \sum_{k=0}^{K-1}\langle\omega\rangle_k e^{2\pi ikl/K} \quad l = 0, \ldots, K-1 \tag{6}$$

$$P(f_l) = \frac{1}{K^2}[|W_l|^2 + |W_{K-l}|^2]$$

$$l = 1, 2, \ldots, \left(\frac{K}{2} - 1\right) \quad f_l = \frac{1}{K\Delta t} \tag{7}$$

$f_l$ represents frequency (note that $i^2 = -1$ in Eq. (6), not the $x$-direction index as in other equations). The discrete Fourier transform is calculated using a fast Fourier transform (FFT) algorithm after applying a Welch window to the time series of $\langle\omega\rangle_k$. These algorithms are described by Press et al. (1992).

## Comparison of DPIV and LDV Data

Since the DPIV technique has not been previously used to study flow fields in agitated vessels, a comparison between DPIV and a more traditional measurement technique is warranted. Figure 2 compares the time-averaged (over the series of 64 image pairs) DPIV flow field with the LDV flow field reported by Lee (1994). Lee's data was taken in a 0.145-meter diameter vessel, and all length ratios (D/T, C/T, H/T, etc.) were approximately equal to those of this study. The DPIV flow field was obtained at a speed of 0.6 $s^{-1}$ (36 rpm; impeller Reynolds number of 6,190), while Lee's data was taken at a speed of 8.33 $s^{-1}$ (500 rpm; impeller Reynolds number of 21,500). The LDV data was taken in the plane of two baffles. Since light scattering by the baffles prevents data acquisition in

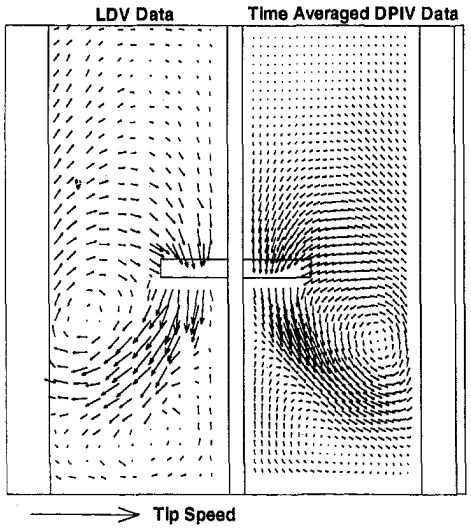


**Fig. 2 Comparison of the normalized time-averaged velocity fields of a pitched-blade turbine as determined by LDV (left) and DPIV (right)**

the baffle plane, DPIV data was taken directly in front and behind the baffle plane and averaged to yield an approximation of the baffle plane behavior. Both flow fields of Fig. 2 have been normalized with respect to impeller tip speed to account for the differences between the absolute velocities of the two experimental systems. The areas of the flow fields have also been scaled to the same size for this side-by-side comparison.

The two flow fields of Fig. 2 demonstrate good qualitative agreement between the DPIV and LDV measurement techniques. Previously, Fasano and Bakker (1993) have shown that the velocity fields determined by PIV are comparable to those predicted by computational fluid mixing simulation with LDV-prescribed impeller boundary conditions. The highest velocities in both flow fields are in the impeller outflow which has a relatively large radial velocity component. This flow impinges on the vessel wall which leads to reversed (radially inward) flow at the base of the vessel. Thus, the overall flow field can be described as a double figure eight, with flow loops beside and below the impeller. One qualitative difference between the two flow fields is the location of the centers of the circulation loops. This may be due to small differences in the geometries of the two experimental systems. In particular, the DPIV vessel of this study had a small gap between the wall and the baffles, while the vessel of Lee's LDV study used baffles that were flush with the wall.

Figure 3 is a more quantitative comparison of the axial and radial velocities measured by the DPIV and LDV techniques. Again, all velocities are normalized with respect to impeller tip speed. $y$ represents the distance between the measurement point and the base of the vessel, and $H$ represents the total liquid height. Also, negative axial velocities are directed downwards in the vessel. Although there are differences in the velocities determined by the two techniques, the quantitative agreement is reasonable except for the highest velocities in the impeller outflow region ($y/H = 0.4$). The magnitudes of these highest velocities are greater for LDV than for DPIV. The lower velocities of DPIV may be due to out-of-plane movement of the fastest particles caused by the tangential flow in the impeller discharge. Also, the LDV technique may have a bias towards higher velocities since during a certain time period more particles will pass through the measurement volume if the velocity is high than when the velocity is low (Lee, 1994).

The accuracy of the DPIV data in the impeller outflow region can be improved by limiting the effect of out-of-plane particle displacement by using shorter time delays between the two digital images that are used to construct the flow field. However, this leads to inaccuracies in measuring the lower velocities outside of the impeller outflow region because the small displacements of these particles would not be accurately measured given the spatial resolution of the digital technique. Since the entire flow field is required for the following instability analysis, a compromise is necessary. However, given the differences observed between the LDV and DPIV techniques, a direct comparison of these methods on the same agitated vessel is warranted (recall that two different vessels were used in the present comparison).

## DPIV Study of Flow Instability

The DPIV flow pattern shown in Fig. 2 is the average of 64 near-instantaneous flow fields taken over a period of 700 seconds (11.7 minutes). The DPIV flow pattern and that found by LDV are clearly very similar. However, as shown in Fig. 4, the near-instantaneous flow fields determined by DPIV are more complex than the time-averaged flow field of Fig. 2. In general, any near-instantaneous flow field may look very little like the time-averaged flow field. The following study of flow pattern instability was performed at a speed of 1 $s^{-1}$ (60 rpm), with

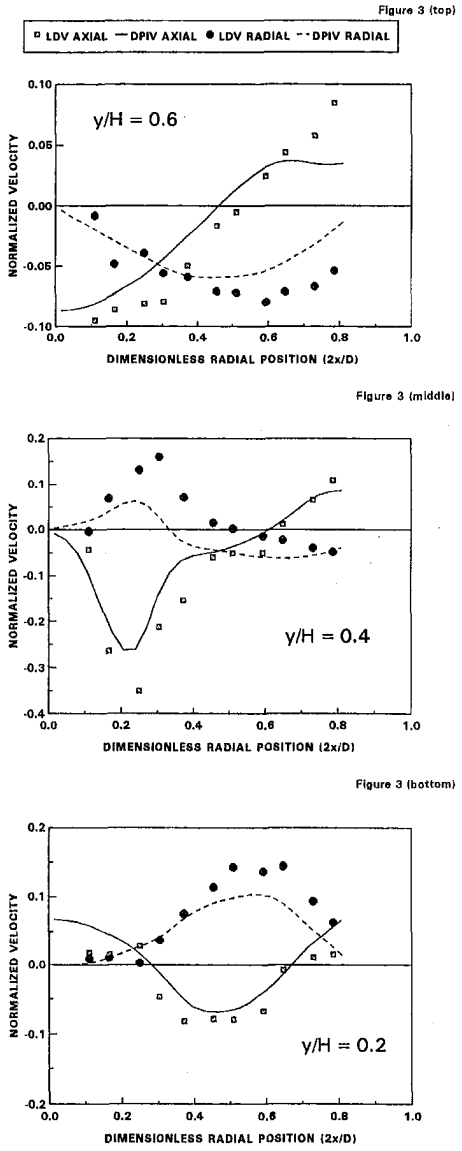


**Fig. 3 Comparison of LDV and DPIV normalized time-averaged velocities: $y/H = 0.6$ (top), $y/H = 0.4$ (center), and $y/H = 0.2$ (bottom)**

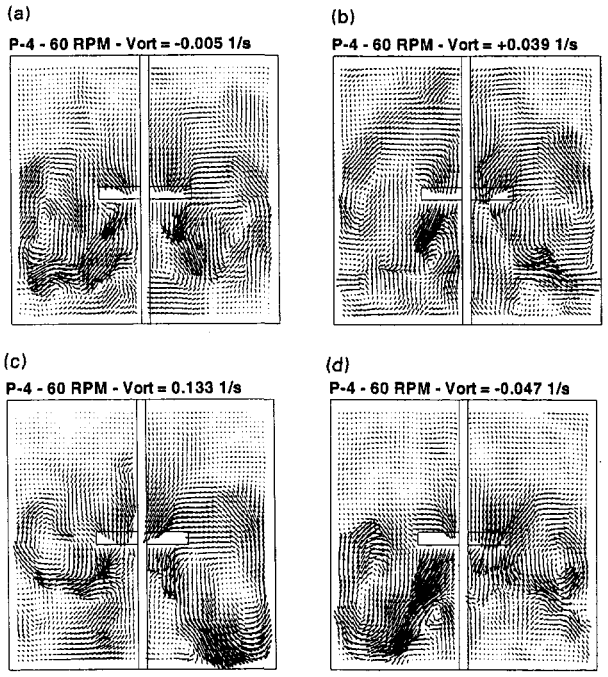


**Fig. 4 Near-instantaneous DPIV velocity fields: (*a*) symmetric; (*b*) near symmetric with less structure; (*c*) and (*d*) asymmetric**

the plane of study being located midway between the baffles for the pitched-blade turbine and slightly in front of the baffle plane for the HE-3 impeller. A series of 1024 near-instantaneous flow fields was obtained over a period of 1330 seconds (22.2 minutes). The instability of the flow field introduces the problem of analyzing this transient phenomenon, and a number of approaches were considered.

The spatially-averaged velocity in the plane of study was found to fluctuate with time, with some fluctuations being greater than ten percent of the mean (time-averaged) velocity. Figure 5 presents the standard deviation of velocity, $\sigma$, and the ratio of the velocity standard deviation to the time-averaged velocity, $S$ (again with the pitched-blade turbine at $C/T = 0.46$; the corresponding time-averaged DPIV velocity field was previously presented in Fig. 2). The standard deviation of velocity can be seen to be largest in the impeller outflow. However, since the velocities are also high in this region, the relative instability of the flow (as expressed by the ratio of the velocity standard deviation to the time-averaged velocity) is rather low in this region. There are three regions of the flow field that are particularly unstable. The first region is near the liquid surface where the velocities are very low and the flow direction is not well-defined (i.e., the flow changes direction, typically being directed radially-inward, but sometimes being directed radially-outward). A second region of flow instability is the center of rotation in the upper flow loop of the flow field. Although the standard deviation of velocity is low in this region, the velocities are also low. This, and the mobile nature of the center of rotation make this region unstable. The third region of instability is the boundary between the upper and lower flow loops, including the region where the wall meets the base of the vessel. The velocities in this region are high, indicating that the boundary between the flow loops is mobile, similar to the center of rotation of the upper flow loop.

The parameter that yielded the best analysis of the transient flow field was vorticity. Figure 6 is a plot of the vorticity field associated with the time-averaged DPIV velocity field of Fig. 2 (the pitched-blade turbine with $C/T = 0.46$). This field has four regions of high vorticity. The discharge flow to the right of the impeller rotates counterclockwise, and therefore has a

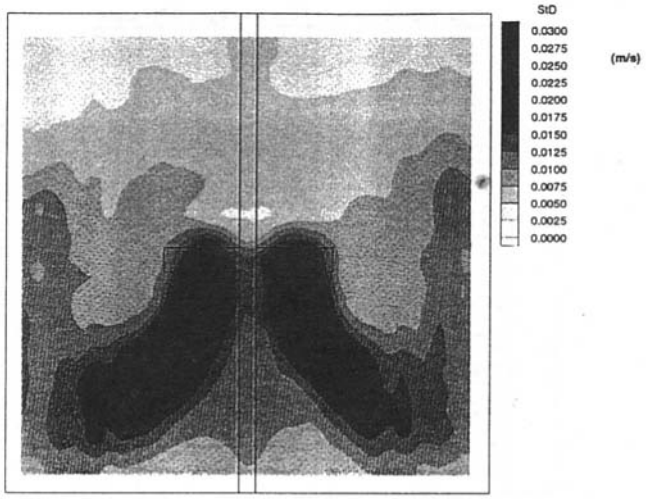


**Fig. 5(*a*) Velocity standard deviation of the pitched-blade turbine**

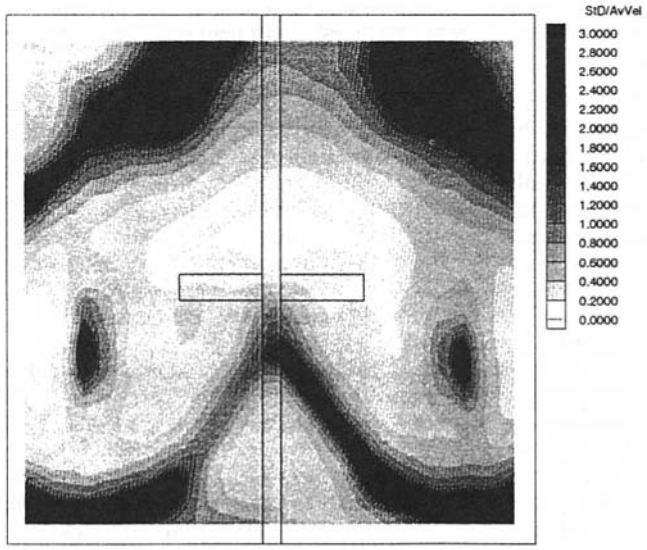


**Fig. 5(*b*) Ratio of the velocity standard deviation to the time-averaged velocity of the pitched-blade turbine**

positive vorticity. Conversely, the discharge flow to the left of the impeller rotates clockwise and has a negative vorticity. The flows returning to the impeller from below also have high vorticity. The flow to the right rotates clockwise and has a negative

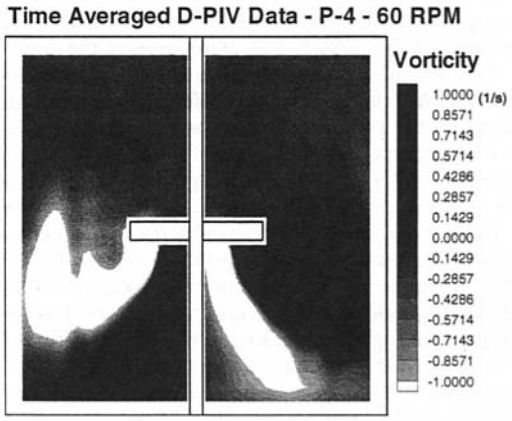


**Fig. 6 Vorticity field corresponding to the time-averaged DPIV velocity field of Fig. 2**

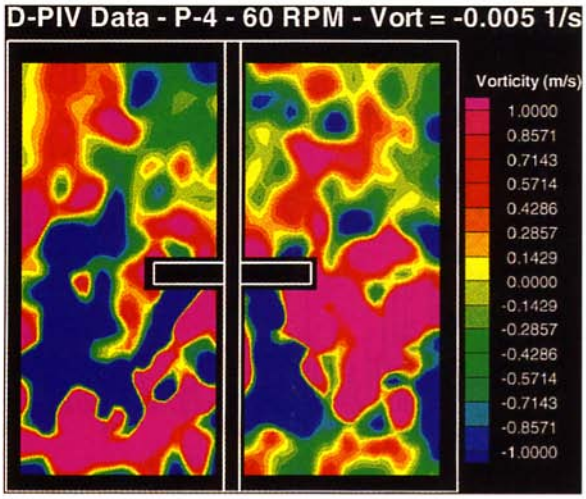


Fig. 7(*a*)

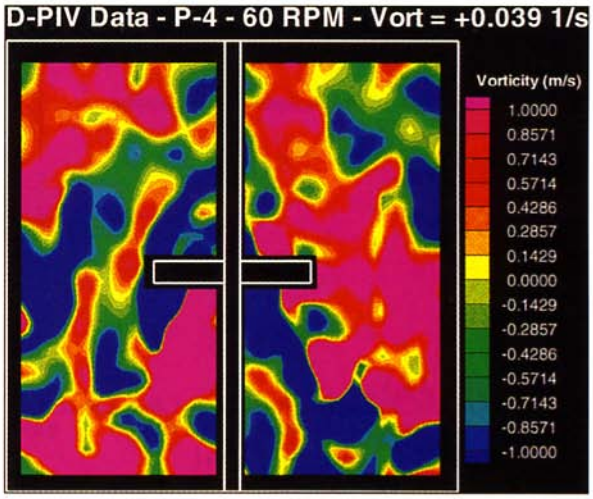


Fig. 7(*b*)

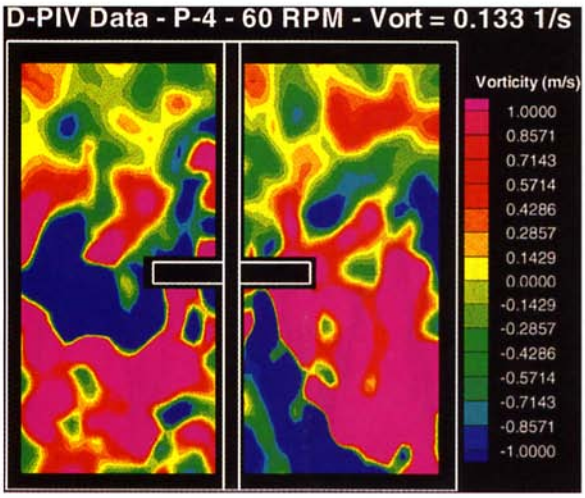


Fig. 7(*c*)

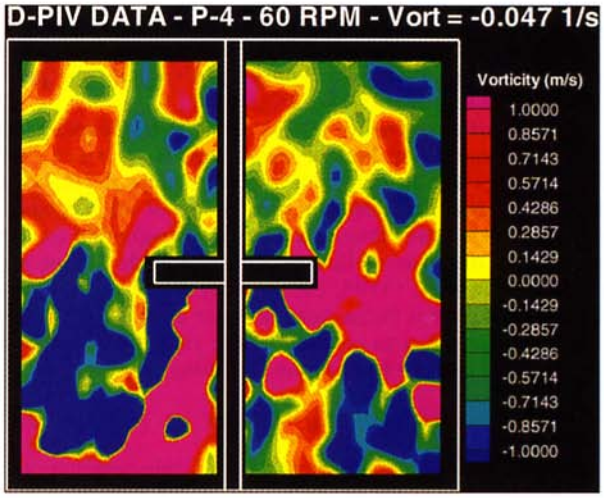


Fig. 7(*d*)

**Fig. 7 Vorticity fields corresponding to the near-instantaneous DPIV velocity fields of Fig. 4**

vorticity, and the flow to the left rotates counterclockwise and has a positive vorticity.

Figure 7 presents the near-instantaneous vorticity fields corresponding to the velocity fields of Fig. 4. The spatially-averaged vorticity of Fig. 7(*a*) is approximately zero because the near-instantaneous flow field is nearly symmetric (refer to Fig. 4(*a*)). The flow field of Fig. 4(*b*) is nearly symmetric, but less structured than that of Fig. 4(*a*). In this case the spatially-averaged vorticity has a relatively small magnitude, but is not zero (refer to Fig. 7(*b*)). The near-instantaneous velocity field of Fig. 4(*c*) has a large positive spatially-averaged vorticity because the large region of positive vorticity to the right of the impeller dominates the smaller region of negative vorticity to the left of the impeller (refer to Fig. 7(*c*)). Conversely, the spatially-averaged vorticity of the near-instantaneous flow field of Fig. 4(*d*) is negative because the large region of negative vorticity to the left of the impeller dominates the smaller region of positive vorticity to the right of the impeller (refer to Fig. 7(*d*)).

A portion of the time record of the spatially-averaged vorticity is shown in Fig. 8 (note that only 200 out of a total of more than 1200 seconds is shown to avoid compression of the data that obscures the oscillations between periods of positive and

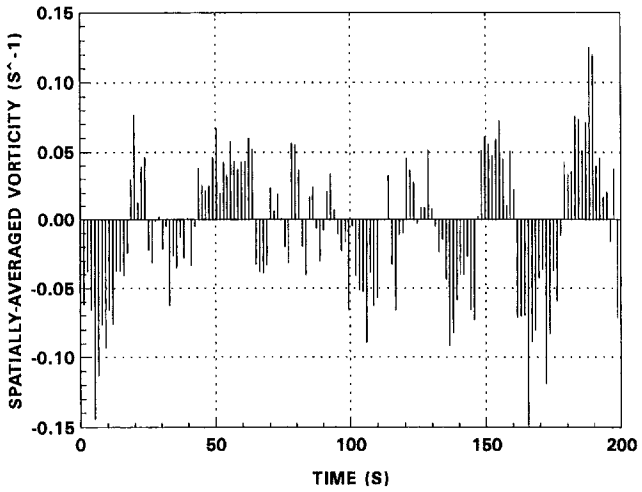


**Fig. 8 Time record of the spatially-averaged vorticity of the pitched-blade turbine (*C*/*T* = 0.46)**

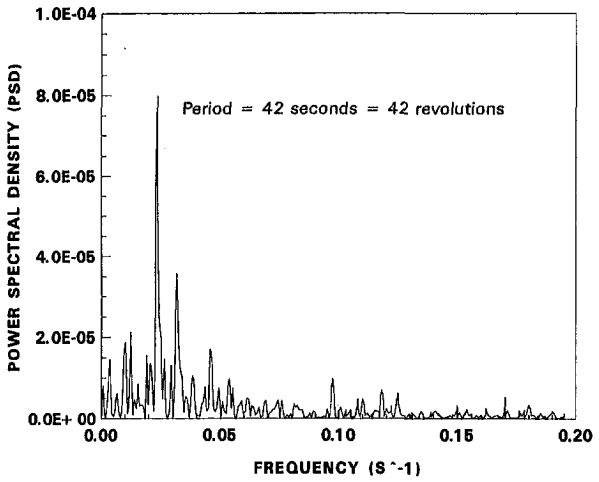


Fig. 9 Power spectral density (PSD) of the time record of the spatially-averaged vorticity of the pitched-blade turbine ($C/T = 0.46$)

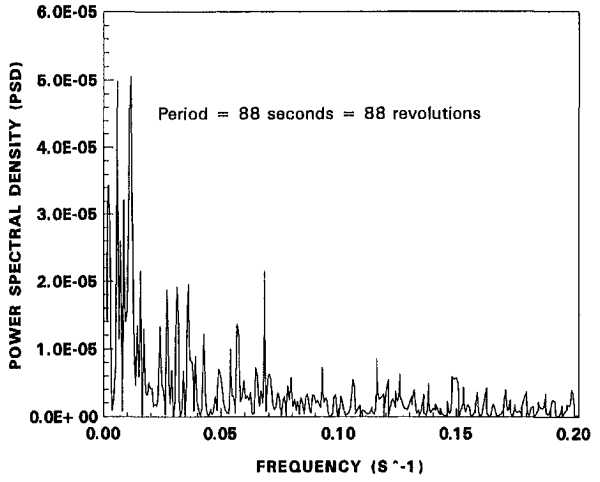


Fig. 11 Power spectral density of the time record of the spatially-averaged vorticity of the pitched-blade turbine at a lower off-bottom clearance ($C/T = 0.33$)

negative vorticity). Although the periods vary, including some very quick oscillations, there is a rather ordered oscillation between periods of positive spatially-averaged vorticity and periods of negative spatially-averaged vorticity.

The power spectral density (PSD) of the spatially-averaged vorticity, obtained using Fourier transforms, is shown in Fig. 9. This indicates that the dominant frequency of the fluctuations is 0.025 $s^{-1}$ (which corresponds to a period of 40 seconds). This frequency is lower than, but of similar magnitude as, the frequencies of macro-instability of a pitched-blade turbine reported by Brůha et al. (1994, 1995). They found that the frequency of flow pattern fluctuations in water at an impeller off-bottom clearance equal to one-half of the vessel diameter ($C/T = 0.5$) could be correlated in the following manner.

$$f = -0.032 + 0.040N \tag{8}$$

For the impeller speed of this work (1 $s^{-1}$), this equation predicts a frequency of 0.008 $s^{-1}$ (a period of 125 seconds). The disagreement between the predicted frequency and the experimental value is most likely due to extrapolation of the equation (i.e., the slower speed of this study relative to those used by Brůha et al. (1 $s^{-1}$ relative to 3.33 to 8.33 $s^{-1}$)). Also, the pitched-blade turbine of this study had four blades, while that used by Brůha et al. had six blades.

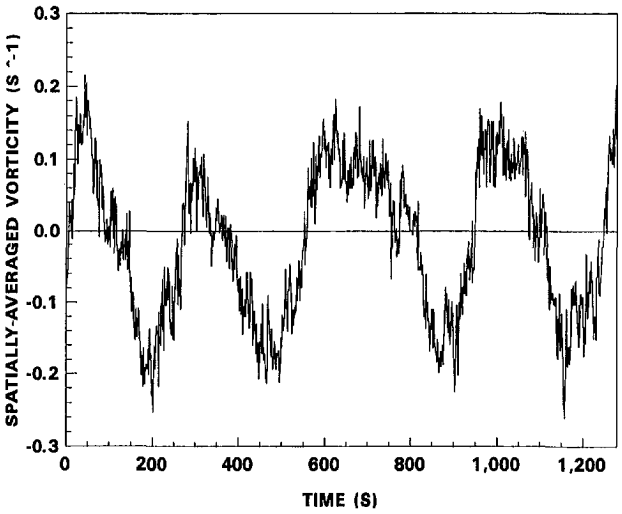


Fig. 12 Time record of the spatially-averaged vorticity of the high-efficiency impeller ($C/T = 0.33$)

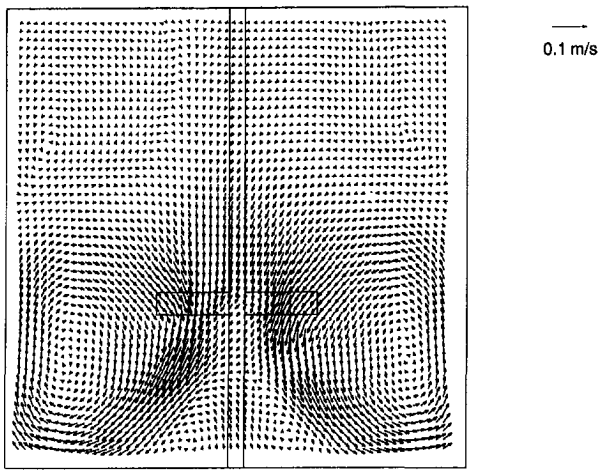


Fig. 10 Time-averaged velocity field of the pitched-blade turbine at a lower off-bottom clearance ($C/T = 0.33$)

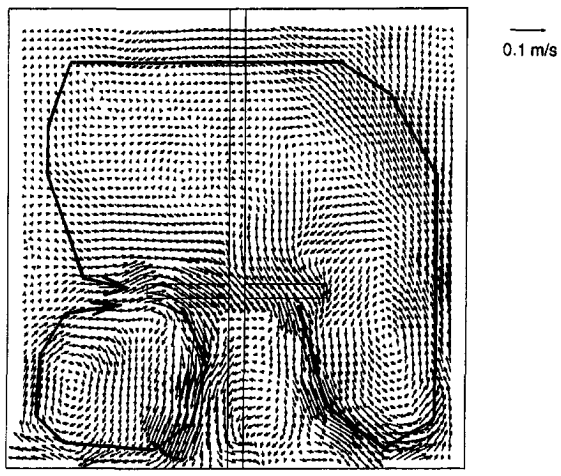


Fig. 13 Near-instantaneous velocity field of the high-efficiency impeller illustrating quick return and full circulation flow loops

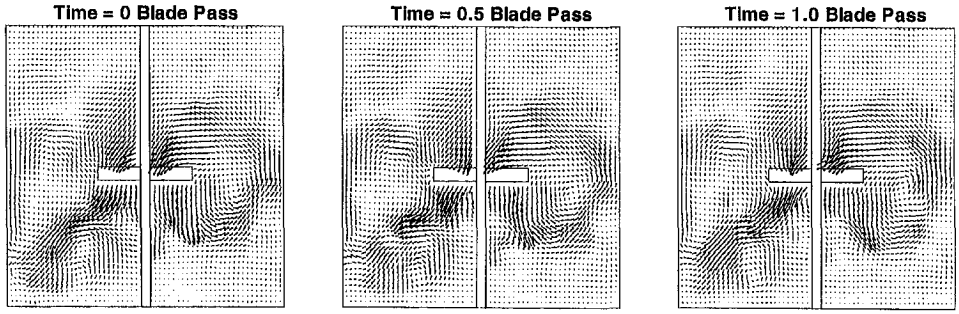


**Fig. 14 Near-instantaneous velocity fields of the pitched-blade turbine taken during blade passage**

The time-averaged velocity field of the pitched-blade turbine at the lower clearance ($C/T = 0.33$; also at a rotational speed of 1 $s^{-1}$) is shown in Fig. 10. In this instance the discharge flow reaches the base of the vessel rather than impinging on the vessel wall as was observed at the higher off-bottom clearance ($C/T = 0.46$). However, there is a small region of upflow directly below the impeller. This flow field is more typical of axial-flow impellers. The power spectral density of the spatially-averaged vorticity of the pitched-blade turbine at this lower clearance is shown in Fig. 11. In this instance, the maximum in this function is not well-defined, but peaks are found at frequencies of 0.0114 and 0.0071 $s^{-1}$ (periods of 88 and 141 seconds, respectively). The lack of a clear maximum in the power spectral density of the spatially-averaged vorticity may indicate that the flow field of the pitched-blade turbine is more stable at the lower clearance. This would agree with visual observation of the flow and the results of Chapple and Kresta (1993). Also, these peak frequencies are more comparable to those observed by Brůha et al. (1994, 1995).

The time-averaged velocity field of the HE-3 impeller (studied at a rotational speed of 1 $s^{-1}$ and $C/T = 0.33$), is very similar to that of the pitched-blade turbine at the lower clearance (refer to Fig. 10). However, the time-averaged velocity field of the HE-3 impeller is more axial than that of the pitched-blade turbine, with no region of upflow directly below the impeller. The time record of the spatially-averaged vorticity of the HE-3 flow field is shown in Fig. 12. This vorticity time series and the corresponding power spectral density (not shown in a figure) indicate that a very clear peak frequency occurs at 0.00301 $s^{-1}$ (a period of 332 seconds).

The periodicity in the flow field of the HE-3 impeller is far more apparent than that of the pitched-blade impeller. The period is also much longer. As illustrated in Fig. 13, visual inspection of the near-instantaneous velocity fields of the HE-3 impeller gives insight into this phenomenon. This particular flow field can be seen to be highly asymmetric which is indicated by a large positive vorticity. In the terminology of Winardi and Nagase (1991) this flow field exhibits quick return (the short flow loop below and to the left of the impeller) and full circulation (the long flow loop to the right of the impeller that crosses the top of the vessel and returns to the upper left of the impeller). Visual observation of the flow indicates that this flow asymmetry is very persistent, if not permanent, and slowly precesses around the vessel.

## Blade Passage Effects

A concern that arises when studying transient phenomena in agitated vessels is the effect of blade passage on the flow field. Since the periods of the transients observed in this study are much longer than those associated with blade passage, it is unlikely that the transients are due to blade passage. However, if the asymmetry in the flow fields would arise from the high frequency blade passage, they might still show up as low frequencies in the current measurements due to aliasing. To experimentally validate that the observed asymmetries are not related to blade passage, near-instantaneous velocity fields were obtained with the pitched-blade turbine ($C/T = 0.46$) during blade passage through the plane of study (this requires a significantly faster sampling frequency than used in the preceding analysis). Three of these velocity fields taken during one blade passage are shown in Fig. 14. Although there are minor differences in the flow fields, it is apparent that blade passage does not strongly influence the asymmetries present in the flow field.

## Conclusions

Comparison of DPIV and LDV velocity fields indicates that digital particle image velocimetry is a reliable technique for studying flow in agitated vessels. A novel application of DPIV to the study of instability in the flow fields produced by a pitched-blade turbine and a high-efficiency impeller illustrates the further potential of the DPIV technique. Specifically, time series analysis of the spatially-averaged vorticity of the flow fields of these impellers indicates that transients with time scales corresponding to forty to over three hundred impeller revolutions are present. Further, these transients were found to not depend on impeller blade passage. These results have important implications for computational modeling because descriptions of agitated vessels that are based on time-averaged flow fields with superimposed turbulence may not accurately capture the mixing associated with these low-frequency phenomena. Future studies will include further characterization of the transients, specifically the influence of impeller type, system geometry, and operating conditions. It is also critical that the origins of the transients and their influence on mixing performance, subjects that have previously received little attention, be the focus of future work.

## Acknowledgments

We would like to thank Cassian Lee of The Dow Chemical Company for providing the LDV data of Figs. 2 and 3. Also, we acknowledge the assistance of Julian B. Fasano and James W. Nordmeyer of Chemineer, Inc. in the completion of this work.

## References

Bakker, A., and Van den Akker, H. E. A., 1994a, "Single-Phase Flow in Stirred Reactors," *Trans IChemE,* Vol. 72, Part A, pp. 583–593.

Bakker, A., and Van den Akker, H. E. A., 1994b, "Gas-Liquid Contacting with Axial Flow Impellers," *Trans IChemE,* Vol. 72, Part A, pp. 573–582.

Brůha, O., Fořt, I., and Smolka, P., 1994, "Flow Transition Phenomenon in an Axially Agitated System," *Proceedings of the Eighth European Conference on Mixing* (IChemE Symposium Series Number 136), pages 121–128, Cambridge, United Kingdom, Sept. 21–23.

Brůha, O., Fořt, I., and Smolka, P., 1995, "Phenomenon of Turbulent Macro-Instabilities in Agitated Systems," *Collect. Czech. Chem. Commun.,* Vol. 60, pp. 85–94.

Chapple, D., and Kresta, S., 1993, "The Effect of Geometry on the Stability of Flow Patterns in Stirred Tanks," paper presented at Mixing XIV, Santa Barbara, California, June 20–25.

Fasano, J. B., and Bakker, A., 1993, "Particle Image Velocimetry: 2-D Velocity Fields for Agitated Tanks for the Six Bladed Disc and the Four Bladed 45° Pitched Impellers," paper presented at Mixing XIV, Santa Barbara, CA, June 20–25.

Haam, S., Brodkey, R. S., and Fasano, J. B., 1992, "Local Heat Transfer in a Mixing Vessel Using Heat Flux Sensors" *Industrial and Engineering Chemistry Research,* Vol. 31, No. 5, pp. 1384–1391.

Kresta, S. M., and Wood, P. E., 1993, "The Mean Flow Field Produced by a 45° Pitched Turbine: Changes in the Circulation Pattern Due to Off Bottom Clearance," *Canadian Journal of Chemical Engineering,* Vol. 71, pp. 42–53.

Lee, C., 1994, private communication with A. Bakker.

Press, W. H., Teukolsky, S. A., Vetterling, W. T., and Flannery, B. P., 1992, *Numerical Recipes in Fortran: The Art of Scientific Computing,* Cambridge University Press.

Wang, M.-H., Calabrese, R. V., and Bakker, A., 1995, "Effect of Reynolds Number on the Flow Generated by Pitched Blade and High Efficiency Turbines," presented at Mixing XV (15th Biennial North American Mixing Conference), Banff, Alberta, Canada, June 18–23.

Willert, C. E., and Gharib, M., 1991, "Digital Particle Image Velocimetry," *Experiments in Fluids,* Vol. 10, pp. 181–193.

Winardi, S., and Nagase, Y., 1991, "Unstable Phenomenon of Flow in a Mixing Vessel with a Marine Propeller," *Journal of Chemical Engineering of Japan,* Vol. 24, No. 2, pp. 243–249.

**Hiromu Tsurusaki**
Associate Professor,
Department of Mechanical Engineering,
Fukuyama University,
Fukuyama, Hiroshima, Japan

**Yoshinobu Tsujimoto**
Professor.

**Yoshiki Yoshida**
Associate Professor.

Department of Mechanical Engineering,
Osaka University,
Toyonaka, Osaka, Japan

**Koichi Kitagawa**
Senior Research Engineer,
Toshiba, Co., Ltd.,
Yokohama, Kanagawa, Japan

# Visualization Measurement and Numerical Analysis of Internal Flow in Cross-Flow Fan

*Measurements of the internal flow velocity distributions in a cross-flow fan were made by particle-tracking velocimetry (PTV). The flow paths (pathlines) were photographed using a digital camera and analyzed using a computer program developed by Tsurusaki and Urata (1989) in order to obtain the velocity distributions. From the velocity distributions, the vorticity distributions were calculated and the vorticity supply and diffusion in the eccentric vortex region was discussed based on an axisymmetric vortex model. A numerical simulation was carried out using a random walk model. The work done by the impeller was also discussed based on the measured velocity distributions.*

## Introduction

Cross-flow fans (CFF) are widely used for industrial equipments and household electric appliances like air curtains, air conditioners, and heaters. A design method for CFFs, however, has not yet been well established because of the complexity of the internal flow. The structure of the internal flow can be divided into two regions. One region is composed of completely closed streamlines and is termed the "eccentric vortex or recirculating region." The other region consists of inflow and outflow and is called here the "through-flow region."

Many experimental and theoretical studies have been conducted in order to improve CFF performance. Porter and Markland (1970) measured the internal flow using a hot-wire probe and flow visualization, and obtained useful information pertaining to casing design. Murata and Nishihara (1975) also studied the effect of the casing on CFF performance, and derived a relationship between the performance curve and the internal flow condition. Mazur and Singh (1987) classified the energy loss in the CFF based on measurements of the flow velocity. Ilberg and Sadeh (1965), and Ikegami and Murata (1966) developed basic theories regarding the eccentric vortex structure in CFFs.

Concerning the generation of the eccentric vortex, Yamafuji (1975) observed the internal flow and showed that the eccentric vortex was closely related to vortices shed from the impeller blades. Lajos (1975) derived a quantitative relationship between the blade circulation and the shed vortex strength from flow measurements. It must be true that the vorticity is supplied into the recirculating region by the impeller. However, there should be a mechanism which "removes" the vorticity from the recirculating region: otherwise the vorticity accumulates and eventually the flow breaks down. In numerical simulations of CFF flow, such as those by Okamoto et al. (1991), Takushima and Iizuka (1992), and Kitagawa et al. (1992), it is assumed that shed vortices "decay."

In the present paper, we postulate that the strength of the eccentric vortex is determined by the mechanisms of vorticity supply from the blades and vorticity diffusion from the recirculating region. This area has not been studied before. The experimental results are used to study the diffusion process as well as the work done by the impeller in the recirculating and through-flow regions.

## Experimental Apparatus and Method of Measurement

**Experimental Apparatus.** A transparent CFF model is installed in a rectangular water tank (700 × 700 × 280 mm) made of acrylic resin, as shown in Fig. 1. The top of the CFF is covered by a transparent plate in order to maintain two-dimensional flow. The CFF casing and the impeller specifications are shown in Fig. 2 and Table 1, respectively. The impeller is driven by a motor attached to the bottom plate of the tank. The flow rate is adjusted using perforated plates at the inlet and the outlet of the casing.

Particle-tracking velocimetry (PTV) is used to measure the internal flow of the CFF. Silver polystyrene particles 0.7 mm in diameter are used as tracers, and the density of water in the tank is adjusted so that it is equal to the particle density by adding salt to the water. Halogen lamps at points $H_1$, $H_2$, and $H_3$ are used as light sources as shown in Fig. 1. The halogen lamps illuminate the measurement section, which is perpendicular to the impeller shaft, through red cellophane films and a slit 6 mm wide. Flash units are placed at points $S_1$ and $S_2$, as shown in Fig. 1. Red cellophane films are attached to the lens of $S_2$. These flash units are connected to a digital camera through a delay circuit.

**Method of Measurement.** The CFF flow field is very sensitive to obstacles. Therefore, measurements using a probe should be carried out carefully. Here, PTV has an advantage over other methods involving a probe. However, few studies have been carried out using PTV in a CFF flow field.

Flow velocity measurements are carried out at the midpoint of the impeller width. The rotational speed of the impeller is maintained at 50 ± 0.5 rpm.

The measurement section is illuminated by red light from the halogen lamps. $S_1$ emits a flash of white light immediately after the shutter of the digital camera opens, $S_2$ emits a flash of red light after 19.7 ms, and then the shutter closes. A pathline image is composed of a bright white initial point, a bright red terminal

Contributed by the Fluids Engineering Division for publication in the JOURNAL OF FLUIDS ENGINEERING. Manuscript received by the Fluids Engineering Division February 1, 1996; revised manuscript received December 4, 1996. Associate Technical Editor: J. A. C. Humphrey.

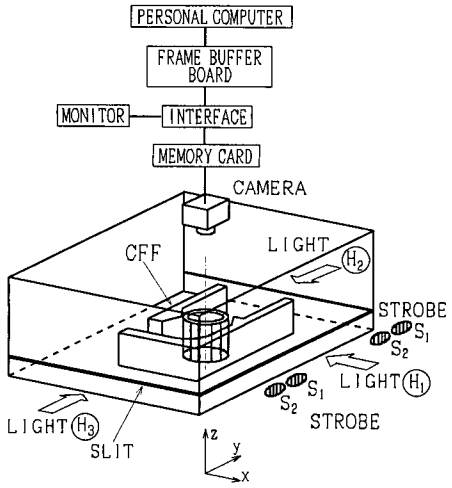


**Fig. 1 Experimental apparatus for water flow visualization**

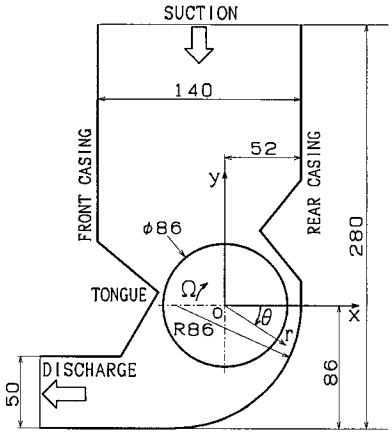


**Fig. 2 Casing of cross-flow fan**

point and a red line between these two points. As shown in Fig. 1, the pathline images are stored in the memory of the digital camera, then transferred to the color frame buffer board (640 × 400 pixels, 256 intensity levels) of a personal computer. The image data are recorded on a hard disk.

**Table 1 Impeller specifications**

| | |
|---|---|
| Outer diameter | 86 mm |
| Inner diameter | 68 mm |
| Number of blades | 38 |
| Blade angle | $\beta_1 = 100°$ $\beta_2 = 20°$ |
| Blade height | 72 mm |

The CFF flow field is divided into five or six regions, and about fifty pictures are taken for each region. The velocities obtained from these pictures at different times are superposed and averaged in order to obtain an ensemble averaged flow field. The flow field is reconstructed from the divided regions.

## Data Processing

**Analysis of Pathline Image.** The initial and terminal points of the pathlines are determined based on the intensity of the pixels which comprise the pathline using a computer program developed by Tsurusaki and Urata (1989). The velocity is calculated from the measured distance between these two points and the measurement time. The initial point is determined based on the criteria that the total intensity of R (red), G (green), and B (blue) lights is higher than a threshold value, and the intensities of R, G, and B are almost the same. The terminal point is determined based on the criterion that the intensity of R is higher than a threshold value. These threshold values are determined empirically.

**Analysis of Velocity Field.** To analyze the velocity field, a square grid system with a mesh width of 7 mm (8% of the impeller diameter) is used. The velocity at a grid point is obtained by averaging the velocity data within the grid. The values of the stream function and vorticity are determined by integrating and differentiating the velocities, respectively. The flow coefficient of the CFF is defined as

$$\phi = Q/u_2 d_2, \tag{1}$$

where $Q$ is the flow rate per unit axial length determined by integrating the normal velocities at the CFF inlet (see Fig. 2, Suction).

**Representation of Impeller.** To facilitate the calculation of vorticity supply into the recirculating region, the impeller is represented by a circular actuator with radius $r_m = (r_1 + r_2)/2$. Since there should be no normal velocity difference across

## Nomenclature

$d_2$ = outer diameter of impeller
$Q$ = flow rate per unit axial length
$r$ = radial distance from impeller center
$R$ = radial distance from eccentric vortex center
$s$ = vorticity source strength
$T$ = moment
$u$ = peripheral velocity of impeller
$v$ = velocity of fluid
$\gamma$ = vortex sheet strength of actuator impeller
$\Gamma$ = eccentric vortex circulation (plus sign denotes impeller rotation direction)
$\Delta\Gamma_v$ = shed vortex circulation (plus sign denotes impeller rotation direction)
$\Delta H$ = local head of impeller
$\Delta\Psi$ = local head coefficient of impeller
$\theta$ = impeller peripheral coordinate
$\Theta$ = eccentric vortex peripheral coordinate
$\nu$ = kinematic viscosity
$\nu^*$ = effective kinematic viscosity
$\rho$ = density of fluid
$\tau$ = shearing stress
$\phi$ = flow coefficient
$\Psi$ = head coefficient
$\omega$ = vorticity
$\Omega$ = angular velocity of impeller

**Subscripts**

$c$ = through-flow
$m$ = midpoint of impeller blade
$p$ = Pitot tube measurement
$r$ = radial direction
$v$ = eccentric vortex
$\theta$ = impeller peripheral coordinate
$\Theta$ = eccentric vortex peripheral coordinate
$\tau$ = shearing stress
1 = impeller inner radius
2 = impeller outer radius

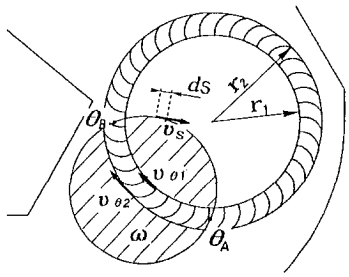


Fig. 3 Explanation of eccentric vortex (hatched area)

the actuator impeller, the actuator can be represented by the vortex distribution

$$\gamma = v_{\theta mo} - v_{\theta mi}, \tag{2}$$

where $v_{\theta mo}$ and $v_{\theta mi}$ are the circumferential velocities on the outer and inner surfaces of the actuator impeller, respectively. These velocities are obtained as follows. First, the velocities at $r = r_2$ and $r = r_1$ are determined by extrapolating the velocities at the grid points. Then, $v_{\theta mo}$ and $v_{\theta mi}$ are estimated by considering angular momentum conservation.

From the law of conservation of circulation, we find that the total circulation shed from the actuator impeller per unit time is

$$\Delta\Gamma_v = -u_m(d\gamma/d\theta)\Delta\theta, \tag{3}$$

where $u_m$ is the peripheral velocity of the actuator impeller.

## Results of Measurements

**Accuracy of PTV.** The accuracy of the PTV used here was examined by comparing the velocities measured using the PTV and a Pitot tube at the CFF exit (see Fig. 2, Discharge). The velocity, averaged over the CFF exit, obtained using the PTV was about 6 percent smaller than that obtained using the Pitot tube.

We now investigate the relationship between the vorticity and circulation in the CFF flow field. The circulation around the eccentric vortex, shown by the hatched circle in Fig. 3, should be equal to the sum of the integral of the vorticity in the hatched area and the impeller blade circulation. This is expressed as

$$\oint v_s ds = \int \omega dA + \int_{\theta_A}^{\theta_B} \gamma r_m d\theta. \tag{4}$$

The left-hand side of Eq. (4) is calculated using the velocities at the grid points, and the first and second terms on the right-hand side are obtained by integrating the measured vorticity and vortex sheet strength, respectively. As shown in Table 2, the experimental results corresponding to the left-hand side of Eq. (4) agree well with those corresponding to the right-hand side. Therefore, we conclude that the PTV is useful and the measurements are internally consistent.

Table 2 Nondimensional circulations (divided by $r_2u_2$)

| $\phi$ | $\oint v_s ds$ | $\int \omega dA$ | $\int_{\theta_A}^{\theta_B} \gamma r_m d\theta$ | $\int \omega dA + \int_{\theta_A}^{\theta_B} \gamma r_m d\theta$ |
|---|---|---|---|---|
| 0.68 | 6.05 ± 0.29 | 2.97 ± 0.45 | 3.13 ± 0.15 | 6.10 ± 0.47 |
| 0.36 | 7.07 ± 0.39 | 3.68 ± 0.86 | 3.62 ± 0.21 | 7.30 ± 0.89 |

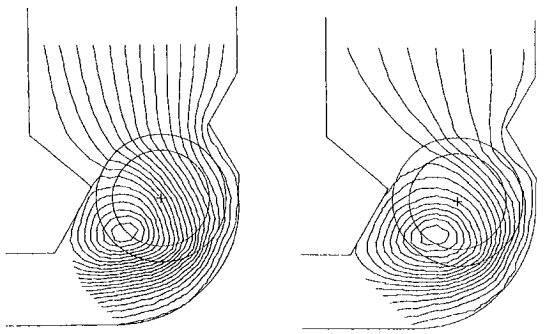

(a) $\phi$ =0.68 (b) $\phi$ =0.36

Fig. 4 Measured streamlines

**Streamlines and Vorticity Distribution.** Figure 4 shows the streamlines obtained from the velocities measured at the grid points, for $\phi$ = 0.68 and 0.36. An eccentric vortex is observed clearly at both flow rates. The center of the eccentric vortex moves towards the rear casing (see Fig. 2), and the area of the recirculating region increases as the flow rate decreases. Figure 5 shows the vorticity distributions. The vorticity is highest at the center of the eccentric vortex, and decreases in the radial direction.

The performance of a CFF depends on the Reynolds number for Re < 5000, where Re = $u_2c/\nu$, and $c$ is a blade chord (Nakamura, 1985). Some commercial CFFs, however, are operated at Re < 3000 due to fan noise problems (Nakamura, 1985). The present experimental results obtained at Re = 2000 will differ from results obtained at different Reynolds numbers. However, the model for vorticity supply and diffusion described in the next section is applicable for different Reynolds numbers.

## Vorticity Supply and Diffusion in Eccentric Vortex

Figure 6 shows the vorticity distributions plotted against radius $R$ along lines 1–6 defined in the illustration. Figures 6($a$) and 6($b$) show that the measured data fall on a single curve irrespective of the directions of lines 1–6. The vorticity decreases linearly from point $R/r_2 = 0$ to point $R/r_2 = 0.4$, but the gradient of that curve changes beyond $R/r_2 = 0.4$. This point is denoted as $R_1/r_2$. In Fig. 6, $R_2$ denotes the radius of a circle with the same area as the measured eccentric vortex (excluding the impeller area).

Here we consider vorticity diffusion using an axisymmetric vortex model which represents the eccentric vortex. As shown in Fig. 7($a$), the vortex model consists of two layers of circular vortices within $0 < R < R_1$ and $R_1 < R < R_2$. The impeller is represented by an actuator with radius $r_m$. In the steady axisym-

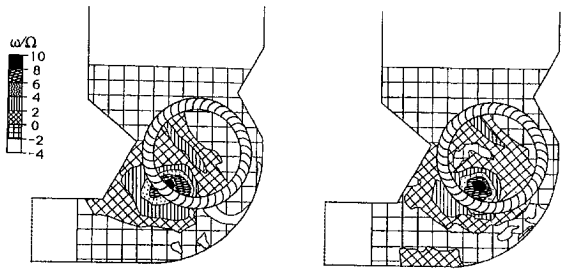


(a) $\phi$ =0.68 (b) $\phi$ =0.36

Fig. 5 Measured vorticity distributions

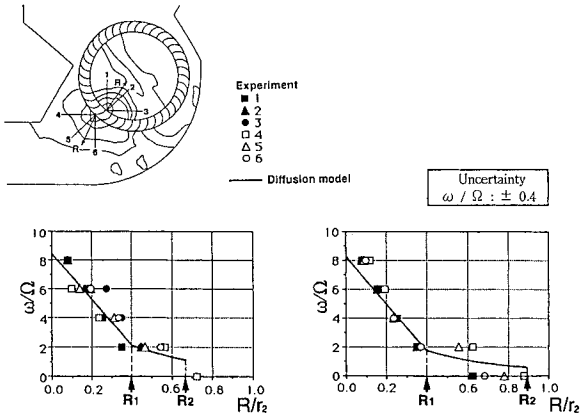


(a) $\phi$ =0.68 (b) $\phi$ =0.36

**Fig. 6 Vorticity distributions**

metric vortex model, the vorticity transport equation is given by

$$(\nu^*/R)\partial(R\partial\omega/\partial R)/\partial R = -s, \quad (5)$$

in the coordinate system $(R, \Theta)$ shown in Fig. 7($a$), where $\nu^*$ is the effective kinematic viscosity and "$s$" is the vorticity source strength or vorticity supply from the impeller.

We now distribute the shed vorticity instantaneously in the dark ring $\Delta R$ as shown in Fig. 7($a$). Then the vorticity source strength "$s$" is given by

$$2\pi R\Delta R \cdot s = 2\Delta\Gamma_v = -2u_m(d\gamma/d\theta)\Delta\theta,$$

where $2\Delta\Gamma_v$ is the total circulation shed from the actuator, and $\Delta\Gamma_v$ is given by Eq. (3).

The measured distribution of $\gamma$, as shown in Fig. 8, is approximated by the broken lines in Fig. 7($b$). Then, from the above equation, the vorticity source strength "$s$" is given by

$$s_1 = (u_m/\pi R)(\gamma_2 - \gamma_3)/2R_1 = A_1/\pi R \quad (0 < R < R_1), \quad (6a)$$

$$s_2 = (u_m/\pi R)(\gamma_1 - \gamma_2 + \gamma_3 - \gamma_4)/2(R_2 - R_1) = A_2/\pi R \quad (R_1 < R < R_2). \quad (6b)$$

Assuming that the vorticity at the eccentric vortex center is finite, the vorticities are obtained from Eqs. (5) and (6) as

$$\omega_1(R) = A_1(R_1 - R)/\pi\nu_1^* + C_1 \quad (0 < R < R_1), \quad (7a)$$

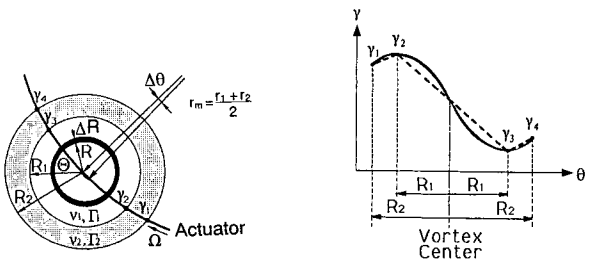


(a) Two-layer model of eccentric vortex (b) Approximation of vortex sheet strength distribution

**Fig. 7 Vorticity diffusion model of eccentric vortex**

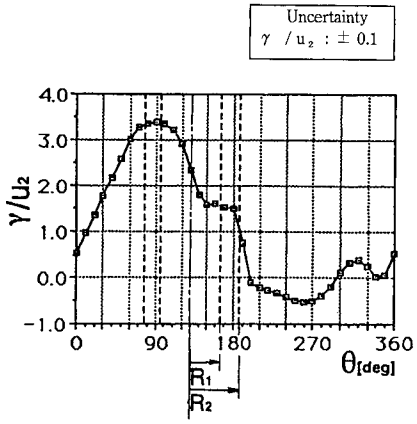


**Fig. 8 Measured vortex sheet strength of actuator ($\phi$ = 0.68)**

$$\omega_2(R) = A_2(R_2 - R)/\pi\nu_2^* + C_2 \ln(R) + C_3 \quad (R_1 < R < R_2). \quad (7b)$$

The unknown factors $\nu_1^*$, $\nu_2^*$, $C_1$, $C_2$ and $C_3$ are determined by the following conditions.

(1) The vorticity transport flux $(2\pi\nu^* R\partial\omega/\partial R)$ is continuous at $R = R_1$.

(2) The vorticity is continuous at $R = R_1$.

(3) The vorticity at $R = R_2$ is given by the value measured (averaged) on the circle at $R = R_2$.

(4) and (5)

Circulations $\Gamma_1$ and $\Gamma_2$ are given by the surface integrals of the vorticity (Fig. 6) measured within the circles with radii $R_1$ and $R_2$ as

$$\Gamma_1 = 2\pi \int_0^{R_1} \omega_1(R)RdR,$$

$$\Gamma_2 = 2\pi \int_{R_1}^{R_2} \omega_2(R)RdR.$$

The measured parameters and effective kinematic viscosity coefficients are tabulated in Table 3. The vorticity distributions given by Eq. (7) are shown by the solid lines in Fig. 6. The peripheral velocity $v_{\Theta v}$ is obtained from Eq. (7) as

$$v_{\Theta v}(R) = (1/R) \int_0^R \omega(R)RdR. \quad (8)$$

The values of $v_{\Theta v}$ obtained using Eq. (8) are shown by the thick solid line in Fig. 9. They are in good agreement with the measured values. The effective kinematic viscosity obtained here is 200–900 times greater than the molecular kinematic viscosity $\nu = 1.31 \times 10^{-6}$ m$^2$/s (water at 10°C). This large value is caused by very strong mixing in the CFF. In the wake of a compressor, Gallimore and Cumpsty (1986) reported that the effective kinematic viscosity was about 400–800 times greater than the molecular kinematic viscosity.

## Numerical Analysis Using Random Walk Model

The two-dimensional potential flow in the CFF is computed using the singularity method as follows. The casing, suction (see Fig. 2) and blades are represented by vortex distributions, and the discharge by a vortex-source distribution. Vortices shed from the blades are represented by point vortices. The strengths of vortices and sources on the boundaries are determined by the following conditions. The normal components of induced velocities are zero at the surfaces of the casing and blades (relative normal velocities), and uniform at suction, and the tangential components are zero at discharge. The details of this method were described by Kitagawa et al. (1992).

Table 3 Measured parameters of eccentric vortex

| $\phi$ | $R_1$ (m) | $R_2$ (m) | $\Gamma_1$ ($m^2$/s) | $\Gamma_2$ ($m^2$/s) | $\nu_1^*$ ($m^2$/s) | $\nu_2^*$ ($m^2$/s) |
|---|---|---|---|---|---|---|
| 0.68 | 0.0172 | 0.0284 | 0.0208 ± 0.0021 | 0.0131 ± 0.0036 | 0.00035 ± 0.00009 | 0.00120 ± 0.0016 |
| 0.57 | 0.0172 | 0.0303 | 0.0225 ± 0.0021 | 0.0166 ± 0.0044 | 0.00035 ± 0.00007 | 0.00098 ± 0.0014 |
| 0.36 | 0.0172 | 0.0381 | 0.0191 ± 0.0021 | 0.0165 ± 0.0081 | 0.00031 ± 0.00012 | 0.00093 ± 0.0015 |
| 0.21 | 0.0172 | 0.0426 | 0.0180 ± 0.0021 | 0.0142 ± 0.0110 | 0.00015 ± 0.00008 | 0.00044 ± 0.0012 |

Here, we introduce the vorticity diffusion effect using the random walk model. A solution of the vorticity diffusion equation for nonconvective and axisymmetric flow is written as

$$\omega = (\Gamma/4\pi\nu t)\exp(-R^2/4\nu t),$$

where $\Gamma$ is the circulation of a point vortex at the origin at time $t = 0$, and $R$ is the distance from the origin. A point vortex at the origin can be considered as a group of many vortices, which diffuse with time. For these vortices, the probability of being within a circle of radius $R$ and that of being within the angular band $\theta$ are expressed as

$$U_1 = \int_0^R \int_0^{2\pi} (\omega/\Gamma) R d\theta dR = 1 - \exp(-R^2/4\nu t),$$

$$U_2 = \theta/2\pi.$$

The vortex location $(R, \theta)$ due to random walk is obtained from the above equations. Here, $t$ is the time elapsed after shedding of a vortex from a blade, and the probabilities $U_1$ and $U_2$ are obtained as uniform random numbers generated by a computer. The location of a shed vortex is determined by convective motion and random walk.

Originally, Chorin (1973) used the random walk model to analyze slightly viscous flow. The flow past a circular cylinder was computed and a good result was obtained for high Reynolds numbers. In contrast, we apply the random walk model for low Reynolds numbers due to large effective kinematic viscosity.

Figure 10 shows the results obtained for $\phi = 0.68$ and 0.36 using an effective kinematic viscosity of $\nu^* = 0.00138$ $m^2$/s, substituting $\nu^*$ for $\nu$, and a Reynolds number of $Re^* = u_2 d_2/\nu^* = 14$. This very large value for the effective kinematic viscosity coincides with the measured values given in Table 3. Reasonable flow fields are obtained using the random walk model at a low Reynolds number. In this computation, a single value of the effective kinematic viscosity is used. This is one advantage of using the random walk model as opposed to the vortex decay model (Kitagawa et al., 1992), in which shed vortices decay with different decay rates for different flow coefficients.

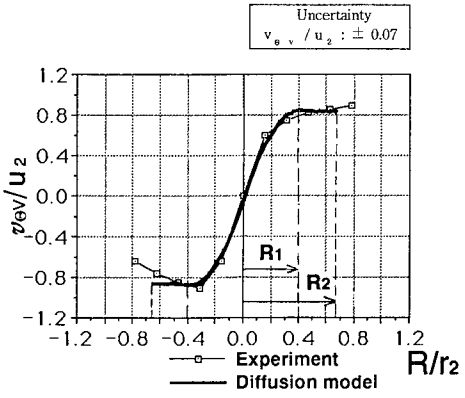


Fig. 9 Measured and computed peripheral velocities as a function of the eccentric vortex coordinate ($\phi = 0.68$)

## Work Done By Impeller

The impeller local head weighted according to the local flow rate, and its nondimensional form (local head coefficient) are defined as

$$\Delta H = (\Delta Q/Q)(u_2 v_{\theta 2} - u_1 v_{\theta 1})/g, \quad (9)$$

where

$$\Delta Q = r_1 v_{r1} \Delta\theta = r_2 v_{r2} \Delta\theta,$$

and

$$\Delta\Psi = \Delta H/(u_2^2/2g). \quad (10)$$

The local head coefficient is calculated from the measured velocity components with $\Delta\theta = 10$ deg here. Figure 11 shows the distributions of the local head coefficient around the impel-

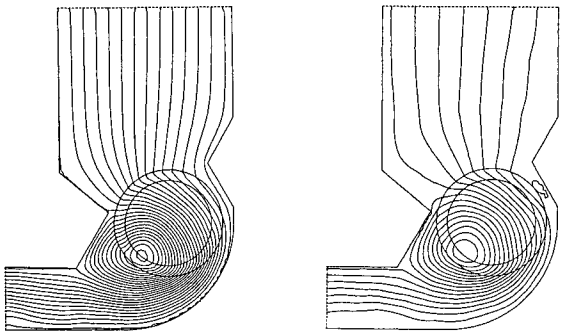

(a) $\phi$ =0.68 (b) $\phi$ =0.36

Fig. 10 Computed streamlines (random walk model, $Re^* = 14$)

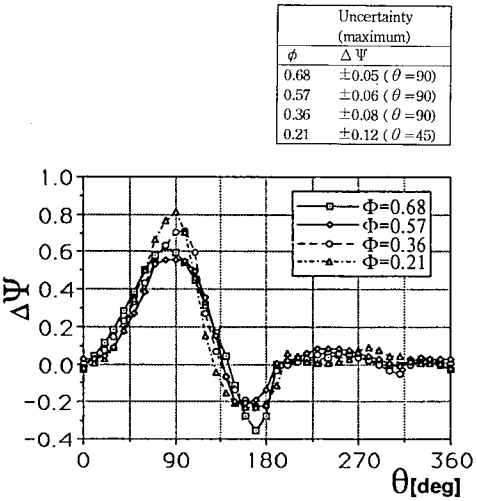


Fig. 11 Local head coefficient distributions

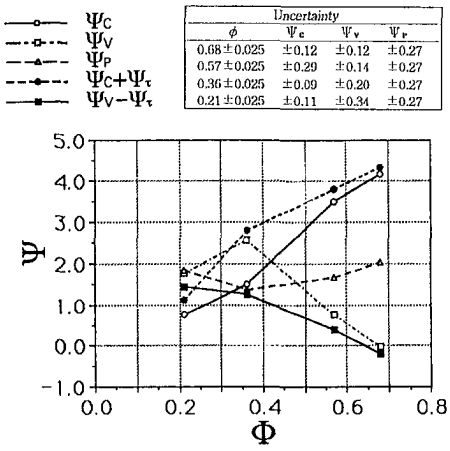


**Fig. 12 Detail of impeller work**

ler. The maximum value appears near the boundary between the through-flow region and the eccentric vortex region.

The work done in the eccentric vortex region and that in the through-flow region are calculated as

$$\Psi_v = \Sigma\Delta\Psi \text{ (eccentric vortex region)},$$

$$\Psi_c = \Sigma\Delta\Psi \text{ (through-flow region)}.$$

The boundary between the above two regions is determined from the measured streamlines. The results are shown in Fig. 12. The work done in the through-flow region is large at high flow rates, and decreases as the flow rate decreases. In contrast, the work done in the eccentric vortex region increases as the flow rate decreases.

At a low flow rate of less than $\phi = 0.36$, the work done, $\Psi_c$, in the through-flow region is smaller than the total head coefficient, $\Psi_p$, obtained from measurements of the total pressure at the CFF inlet and outlet. From this, we conclude that an eccentric vortex transfers its kinetic energy to the through-flow. The moment due to shearing stress at the eccentric vortex surface is written as

$$T = \int_0^{2\pi} \tau R_2^2 d\Theta,$$

where $\tau = -\rho\nu_2^*\{R\partial(v_{\Theta v}/R)/\partial R\}_{R=R_2}$.
The work done by this moment is

$$\Psi_\tau = T(v_{\Theta v}/R)_{R=R_2}/\rho g Q/(u_2^2/2g). \quad (11)$$

The measured velocities (Fig. 9) and effective kinematic viscosity (Table 3) are used in the calculation. The total work $\Psi_c + \Psi_\tau$, shown in Fig. 12, is larger than $\Psi_p$ except at $\phi = 0.21$, where the flow in the CFF is unsteady and three-dimensional.

## Uncertainty Estimation

The uncertainties in the measured data were estimated using a formula for propagation of errors given in ASME PTC19.1-1985. Uncertainty bands are shown in the figures and tables.

## Conclusions

The main results of this study are as follows.

(1) The present PTV technique including the algorithm proposed by Tsurusaki and Urata (1989) is shown to be useful for measurement of the CFF flow field and quantitative analysis of the CFF performance.

(2) The circulation of the impeller blade changes significantly while the blade passes through an eccentric vortex, and the blade supplies vorticity to the eccentric vortex.

(3) The circulation around an eccentric vortex is determined by the vorticity supply due to shed vortices and the diffusion of vorticity which depends on the effective kinematic viscosity. This viscosity is 200–900 times greater than the molecular kinematic viscosity of the working fluid, as is typical in turbulent flows.

(4) The flow fields were simulated using the random walk model and a single value for the effective kinematic viscosity. The value for the effective kinematic viscosity was close to experimental values.

(5) The work done by the impeller in the through-flow region is significantly larger than the work done in the recirculating region at high flow rates, and decreases as the flow rate decreases. An eccentric vortex transfers its kinetic energy to the through-flow and the amount of energy transferred increases as the flow rate decreases.

## Acknowledgments

The authors wish to thank Professor T. Uemura of Kansai University for his helpful suggestion, and Mr. H. Tatsuke and Mr. H. Shimizu, who were graduate students at Osaka University, for their cooperation.

## References

Chorin, A. J., 1973, "Numerical Study of Slightly Viscous Flow," *J. Fluid Mech.*, Vol. 57, No. 4, pp. 785–796.

Gallimore, S. J., and Cumpsty, N. A., 1986, "Spanwise Mixing in Multistage Axial Flow Compressors: Part 1—Experimental Investigation," ASME *Journal of Turbomachinery*, Vol. 108, pp. 2–9.

Ikegami, H., and Murata, S., 1966, "A Study of Cross Flow Fan," Osaka University Technology Reports, Vol. 16, No. 731, pp. 557–578.

Ilberg, H., and Sadeh, W. Z., 1965–66, "Flow Theory and Performance of Tangential Fans," *Proc. Instn. Mech. Engrs.*, Vol. 180, Part 1, No. 19, pp. 481–491.

Kitagawa, K., et al., 1992, "A Numerical Simulation of Cross Flow Fan," *Boundary Elements in Fluid Dynamics*, Computational Mechanics Publications, pp. 3–20.

Lajos, T., 1975, "Investigation of the Flow Characteristics in the Impeller of the Tangential Fan," *Proc. 5th Conf. on Fluid Machinery*, pp. 567–577.

Mazur, J., and Singh, T., 1987, "Momentum Exchanges and Energy Transfers in Cross Flow Fans," ASME Paper No. 87-GT-32.

Murata, S., and Nishihara, K., 1975, "A Study on Cross-Flow Fans," *Trans. JSME*, Vol. 41, No. 347, pp. 2062–2075, ibid., pp. 2076–2089 (in Japanese).

Nakamura, K., 1985, "A Study of High-Performance Cross-Flow Fan based on Internal Flow Analysis," Doctoral thesis, Osaka University (in Japanese).

Okamoto, Y. et al., 1991, "Discrete Vortex Method Analysis of Cross Flow Fan," Prepr. JSME, No. 914-4, pp. 170–172 (in Japanese).

Porter, A. M., and Markland, E., 1970, "A Study of the Cross Flow Fan," *Journal Mechanical Engineering Science*, Vol. 12, No. 6, pp. 421–431.

Takusima, A., and Iizuka, K., 1992, "Numerical Analysis of Cross-Flow Fan by a Clouds-in-Cells Method Combined with the Finite-Element Method," *Trans. JSME*, Vol. 58, No. 545, B, pp. 64–70 (in Japanese).

Tsurusaki, H., and Urata, T., 1989, "A Measuring Method for Three-Dimensional Steady Flow by Digital Image Processing of Pathline Pictures," *Proc. ASME, Flow Visualization*, FED-Vol. 85, pp. 95–100.

Yamafuji, K., 1975, "Studies on the Flow of Cross-Flow Impellers," *Bulletin of the JSME*, Vol. 18, No. 123, pp. 1018–1025.

# Prediction of Flow Behavior and Performance of Squirrel-Cage Centrifugal Fans Operating at Medium and High Flow Rates

**R. J. Kind**
Professor,
Department of Mechanical and Aerospace Engineering,
Carleton University,
Ottawa, Ontario K1S 5B6, Canada
Mem. ASME

*This paper describes a method for predicting flow behavior and performance for centrifugal fans of the squirrel-cage type. The work is directed at improving understanding of the factors affecting performance of these fans. A simulation approach has been adopted. That is, the fan is subdivided into a number of zones (inlet zone, blading zone, volute zone) and the zones are divided into elements. Flow behavior in the zones and elements and interactions between them are modeled using appropriate equations and correlations. The blading correlations make use of new experimental data for high-solidity cascades of bent sheet metal blades, typical of squirrel-cage fans. Predicted fan performance characteristics are in reasonable agreement with experimental results for flow rates at and above the best-efficiency operating point. Although relatively simple, the method recognizes the main flow phenomena and interactions that occur in squirrel-cage fans and it thus represents a substantial advance over what is currently available in the literature. Together with earlier experimental work, development of the method has provided considerable insight into the relative importance of various aspects of flow behavior. The ability to deal with extensive reverse flow through the rotor blading has not yet been incorporated and it is evident that this ability is essential for realistic prediction of flow behavior and performance at below-design flow rates.*

## 1 Introduction

Figure 1 shows a diagram of a squirrel-cage fan. Large numbers of fans of this type are used in applications requiring low noise, small size, relatively high capacity and low cost. They are used as circulating fans in central heating and air-conditioning systems in residences, as blowers in automotive heating/cooling units and in numerous other applications. Many millions of these fans are in use in North American residences. Although typical power consumption is only 0.5 kW, peak efficiency is only about 60 percent so the potential for energy savings is substantial.

A key distinguishing feature of squirrel-cage fans is the large width to diameter ratio, $b/D_2$, of their rotors; $b/D_2$ is typically substantially larger than 0.25 so that the rotor exit area, $\pi D_2 b$, substantially exceeds the inlet eye area, $\pi D_1^2/4$. Uniform flow at rotor exit would thus require the flow to sustain a large deceleration, which it is not normally able to do. Instead the flow separates as sketched in Fig. 2 and is highly nonuniform in the axial direction in the rotor. At relatively low flow rates there is also much nonuniformity in the circumferential direction, with reverse flow through substantial portions of the rotor. Another distinctive feature of squirrel-cage fans is that the rotor generally uses a large number of blades of short chord (about $0.1 D_2$). The blades are generally made of a single thickness of sheet metal and are forward curved to assist in obtaining high capacity at low rotational speeds, and thus with low noise. Efficiency is generally low, typically about 0.6 total-to-total at the best-efficiency operating point.

Kind and Tobin (1990) reviewed the literature and reported on a detailed experimental investigation of the flow in three squirrel-cage fan configurations. The present paper describes a model for predicting flow behavior and performance for squirrel cage fans operating at flow rates near and above the best-efficiency point, that is where there is negligible reverse flow through the rotor. The objective is to gain better insight into flow behavior and to identify the main factors which affect performance. The ultimate goal is to enable design of more efficient fans. Current design methodology is outlined by Eck (1973). It completely ignores the highly nonuniform nature of the flow and does not deal realistically with the volute flow; also it cannot provide performance predictions. Although still relatively simple, the flow model outlined in the present paper goes well beyond that outlined by Eck and achieves reasonably good predictions of performance.

There are no data in the literature for losses and flow turning in cascades of blades such as those used in squirrel-cage fans. The paper reports on experiments carried out to provide such data.

## 2 The Flow Simulation Model

A flow simulation approach has been adopted for analyzing flow behavior and predicting fan performance. That is, the fan is subdivided into several zones and each zone is itself subdivided into a number of discrete elements. Appropriate conservation relations and/or correlations are applied to each element and compatibility relations govern the interactions between elements. Elder and Gill (1985) and Lorett and Gopalakrishnan (1986) have used a similar approach for centrifugal compressors and centrifugal pumps, respectively.

All equations in this paper are expressed in terms of nondimensional variables; the nondimensionalizing parameters are listed under Nomenclature. Incompressible flow is assumed.

**2.1 Discretization Scheme.** The fan is divided into three flow zones, inlet (I), blading (B) and volute (V). The zone boundaries are shown in Fig. 3. Subscripts 1 and 2 denote entry

Contributed by the Fluids Engineering Division for publication in the JOURNAL OF FLUIDS ENGINEERING. Manuscript received by the Fluids Engineering Division September 11, 1996; revised manuscript received March 11, 1997. Associate Technical Editor: B. Schiavello.

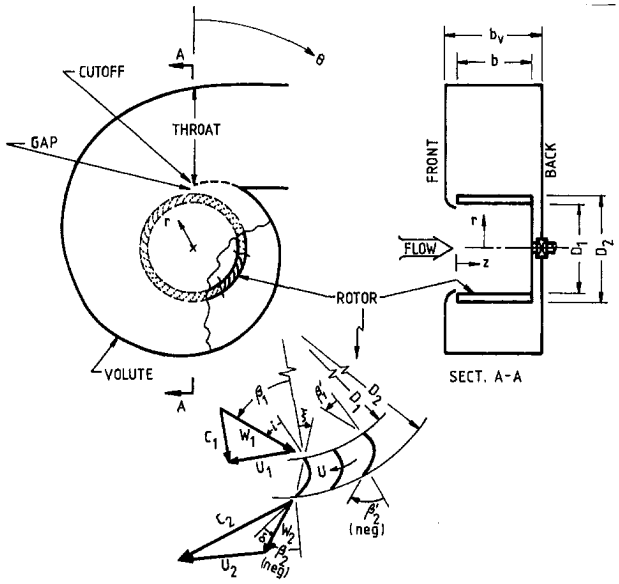


Fig. 1 Diagram of a squirrel-cage fan and velocity triangle notation (all angles except $\beta_2$ and $\beta_2'$ are positive as shown)

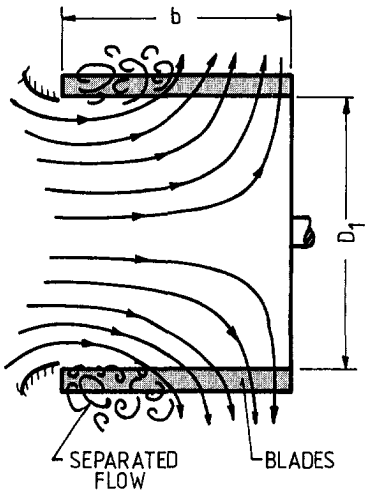


Fig. 2 Sketch of flow into rotor

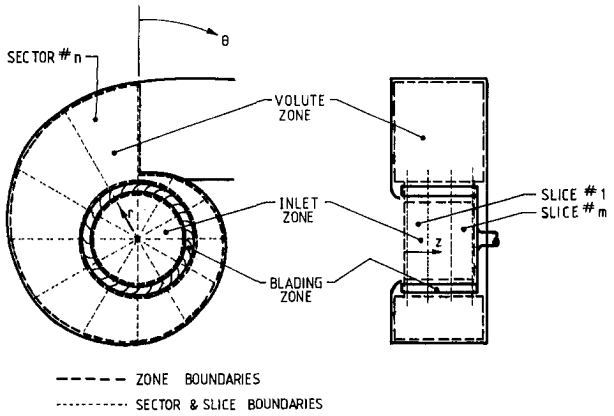


Fig. 3 Discretization scheme

and exit, respectively, of a zone. The boundary between the blading and volute zones, for example, can be designated as either B2 or V1.

The fan is also subdivided axially into "slices" and circumferentially into "sectors," as shown in Fig. 3. Subscripts $i$ and $j$ denote slices and sectors, respectively. If there are $m$ slices and $n$ sectors, the blading zone is thus subdivided into $m \times n$ "elements" and each blading-zone element, for example, has an identifier of the form $B_{ij}$. Values of about 4 and 30 are typically used for $m$ and $n$, respectively.

**2.2 Flow Model, Inlet Zone.** Conditions over the entry (I1) plane are assumed to be uniform, with velocity purely axial. Radial velocity and static pressure over the exit (I2) surface are allowed to vary in both the axial and the circumferential directions, that is from slice to slice and sector to sector; flow rate can vary from sector to sector. Velocity is assumed to be purely radial over the I2 surface. In reality, there is usually some backflow from the casing into the inlet zone in squirrel-cage fans and this tends to impart some preswirl to the incoming flow. The experiments of Kind and Tobin (1990), however, show that backflow and preswirl are negligible for flow rates well above the best-efficiency value and are small near the best-efficiency point. The assumption of purely radial flow at the I2 surface is thus in keeping with the experimental results, provided that the analysis is restricted to conditions with little or no reverse flow, as in this paper. The radial velocity at the I2 surface is prescribed as a function of axial position, $z$. Uniform,

## Nomenclature

$b$, $b_v$ = rotor width, volute width
$C$ = absolute velocity of flow
$c$ = blade chord length
$D_1$, $D_2$ = rotor inlet, rotor exit diameter
$h$ = hydraulic head or water depth in the cascade tests
$i$ = incidence angle, $(\beta_1 - \beta_1')$
$K$ = loss coefficient, see Eq. (3)
$m$, $n$ = number of slices, sectors
$p$ = static pressure/$\rho U_2^2$
$p_t$ = total pressure/$\rho U_2^2$
$Q$ = volume flow rate
$r$, $\theta$, $z$ = radial, tangential, axial coordinates (Fig. 1)
$s$ = blade spacing, $0.5\pi(D_1 + D_2)$/(no. of blades)
$U$ = blade speed
$W$ = relative velocity of flow
$\alpha_v$ = volute wall angle (Fig. 10)
$\beta$, $\beta'$ = relative flow angle, blade angle (Fig. 1)
$\delta$ = deviation angle, $\beta_2 - \beta_2'$
$\epsilon$ = flow deflection angle, $\beta_1 - \beta_2$
$\eta$ = total-to-total efficiency of fan
$\xi$ = stagger angle (Fig. 1)
$\rho$ = fluid density
$\phi$ = nondimensional fan flow coefficient, $Q/U_2D_2^2$
$\psi$ = (total-pressure rise across the fan)/$\rho U_2^2$

### Subscripts

1, 2 = rotor or zone inlet, exit; also inner, outer boundary
*aug* = augmented (see text following Eq. (14 and 16))
B, I, V = blading, inlet, volute zones
*d* = diffusion
*g* = gap flow
*i* = slice index; also incidence
*j* = sector index
*m* = mixing
$r$, $w$, $z$ = radial, whirl, axial velocity components
*S* = blading-exit-flow streamtube

### Superscripts

$\bar{}$ = overbars denote values at volute cross-section centroids

### Nondimensionalizing Parameters

for lengths: $D_2$
for velocities: $U_2$
for pressures: $\rho U_2^2$
for volume flow rates: $U_2D_2^2$

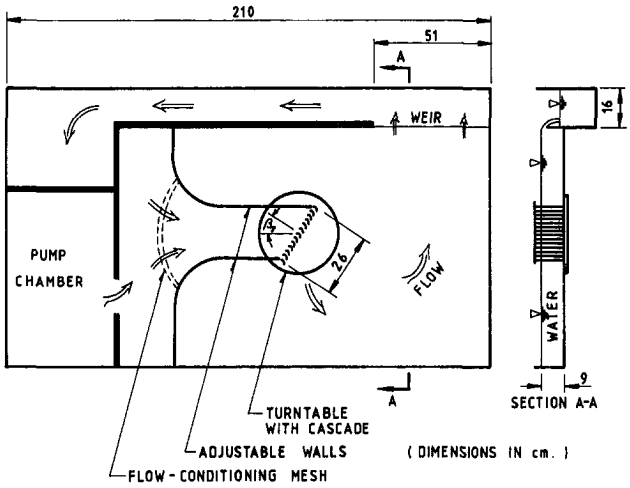


**Fig. 4 Schematic diagram of cascade test apparatus**

linear and step distributions have been tried, with the maximum velocity always at the backplate ($z = b$) of the rotor in recognition of the flow pattern sketched in Fig. 2. Total pressure is assumed to be uniform over the I2 surface at the fan-inlet value minus a small loss proportional to the dynamic pressure at the I1 surface. This is also in keeping with the experimental results. With these assumptions, the velocity and static pressure at any point on the I2 surface can readily be calculated from continuity and Bernoulli relations for any value of sector flow rate.

**2.3 Flow Model, Blading Zone.** A cascade-correlation approach is used to treat the flow through the rotor blading. As outlined earlier, the blading zone is sub-divided into a number of elements. Flow conditions are assumed to be uniform over the inlet ($B1_{ij}$) and exit ($B2_{ij}$) surfaces of each element and the cascade correlation is applied separately to each element of the blading zone.

At the inlet surface of each blading-zone element the flow velocity (purely radial) and the total and static pressure are known from the inlet-zone assumptions and analysis. Average values are used where these parameters vary. The blade speed, $U_1$, is also known. The velocity triangle at element inlet can thus be solved for the relative velocity vector, $W_{1ij}$.

The information required from the cascade correlation is the exit angle of the flow (i.e., the direction of the vector $W_{2ij}$) and the losses incurred by the flow in passing through the blade row. Unfortunately, there is virtually no information in the literature on the performance of the rather unusual cascades used in squirrel-cage fans. Typically the blade profiles are highly cambered thin arcs; they are strongly forward-facing at exit ($\beta_2 \approx -60$ deg) and operate at very large incidence angles ($i \approx 50$ deg), even at the design operating point of the fan. Furthermore, with highly nonuniform and reverse flow through the rotor as possibilities the range of incidence angles can be very large; for example, in the case of reverse flow with a rotor having $\beta_2 = -60$ deg the fluid could well re-enter the rotor with an incidence angle of about $-120$ deg. To supply at least an approximate data base, simple cascade tests were conducted. The emphasis in these tests was on obtaining a wide range of data with a reasonable amount of time and effort.

The cascade tests were done in water flow, using an open surface apparatus shown schematically in Fig. 4. Water depth was about 9 cm and flow velocities were of order 0.2 m/s. The inlet Froude number, $W_1/\sqrt{h_1 g}$, which is analogous to Mach number, was thus about 0.2, which is sufficiently low to ensure that depth changes due to flow accelerations were small. This constraint was necessary to ensure reasonable two-dimensionality of the flow through the cascades. All cascades were made up of circular-arc cambered sheet metal blades having a chord length of 28 mm, a thickness of 0.84 mm and 60 deg camber. Leading and trailing edges were square-cut with sharp edges. Three space/chord ratios, s/c = 0.51, 0.77 and 1.02 were tested. Inflow angle, $\beta_1$, ranged from $-75$ to $+75$ degrees and stagger angle, $\xi$, from $-45$ to 70 degrees so that the full possible range of incidence angles, $i$, was covered. The open top of the apparatus enabled changes to the cascade and flow-channel configurations to be made quickly and easily. Flow visualization was also easy.

The Reynolds number based on blade chord was approximately 6500; the corresponding Reynolds number in the fan tests of Kind and Tobin (1990) was about 35,000, which is typical of squirrel-cage fan operating conditions. Despite the relatively low Reynolds number of the cascade experiments, flow visualization confirmed that the shear layers were always turbulent, as would be expected in view of the square-cut leading edges of the blades. This and the fact that separation locations were generally fixed by blade edges imply that the cascade test results should be representative of full-scale conditions.

The cascade test results were applied to the rotating blade rows of squirrel-cage fans simply by working in the relative reference frame. This procedure neglects the effect of rotation on deviation angle, an effect that occurs because the blade-to-blade passages have an angular velocity in the plane of the flow velocity vectors. An adaptation of the Stodola flow model for slip (e.g., Dixon, 1978) indicates that the magnitude of the rotation effect would only be about one degree for typical squirrel-cage fans because they have many blades and large values of $\beta_2'$.

Flow directions in the cascade tests were determined using 10 cm long cotton threads immersed in the flow and reading their direction angles with rulers and a protractor; angles could be read within about $\pm 5$ degrees. The moderate scatter in the results (Fig. 5) indicates that the method was quite satisfactory for present purposes. The results of Fig. 5 show that the direction, $\beta_2$, of the flow leaving the cascades can be described by the relation

$$\beta_2 = \beta_2' + \delta \tag{1}$$

where $\beta_2'$ is the blade exit angle and $\delta$ is the deviation angle which to a good approximation depends only on incidence angle, $i$, and space/chord ratio, s/c. The data were fitted by the correlation

$$\delta = 15(2s/c)^{0.6} - 0.13i + 0.0007i^2 \tag{2}$$

with $\delta$ and $i$ in degrees. The goodness of fit can be assessed by viewing Fig. 5 where Eq. (2) is plotted together with the data.

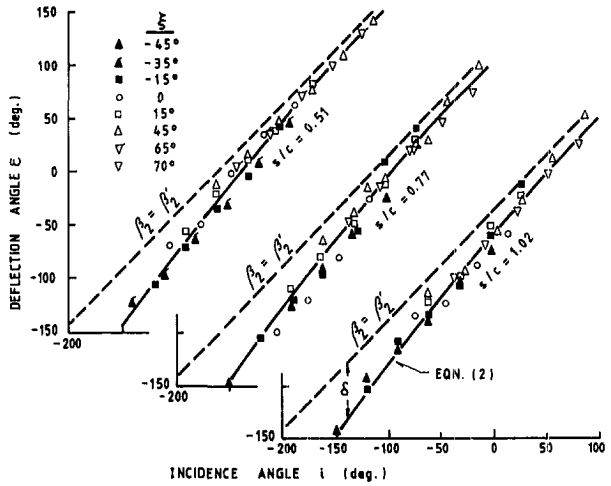


**Fig. 5 Flow deflection angle versus incidence angle for the tested cascade configurations. (sheet metal blades, square-cut edges, 60 deg camber, thickness 0.84 mm, chord 28 mm, $W_1 c/\nu \approx 6500$)**

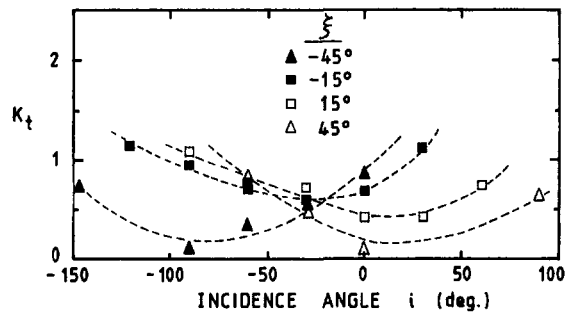


**Fig. 6 Experimental data for total loss coefficient as a function of incidence angle for various stagger angles, s/c = 0.77 (blade parameters as in Fig. 5)**

In the nondimensional notation the total loss coefficient, $K_t$, is defined by

$$K_t = 2(p_{t1} - p_{t2})/W_1^2 \quad (3)$$

In hydraulic flows depth or head is proportional to pressure; therefore for the cascade experiments Eq. (3) can be written as

$$K_t = \Delta h/h_{dyn} + (1 - W_2^2/W_1^2) \quad (4)$$

where $\Delta h$ is the drop in surface elevation or static head of the water across the cascade, $h_{dyn}$ is the dynamic head upstream of the cascade and $W_1$ and $W_2$ are the water mean velocity upstream and downstream of the cascade, respectively. The level drop $\Delta h$ was measured with an accuracy of $\pm 0.05$ mm by means of two micrometers in wells connected to static taps in the floor of the apparatus. $W_1$ and $W_2$ were determined from the continuity equation, the volume flow rate through the cascade being determined by means of a sharp-edged weir (see Fig. 4). Equation (4) can only be used when the Froude number, $W_2/\sqrt{h_2 g}$, at cascade exit is well below unity; when it exceeds unity the jet of water leaving the cascade undergoes a hydraulic jump and the downstream depth read by the micrometer is not representative of cascade-exit conditions. Therefore no loss data are presented for cascade configurations which produced large acceleration of the flow.

Total loss coefficient is plotted against incidence angle in Fig. 6 for s/c = 0.77. The points for each value of stagger angle, $\xi$, are seen to lie on reasonably smooth curves without excessive scatter. This helps inspire confidence in the data. Accuracy of individual $K_t$ values is estimated at $\pm 0.2$. The minima of the various curves in Fig. 6 are found to occur at the incidence angle for which the diffusion coefficient, $K_d$, is minimum. $K_d$ is defined as

$$K_d = 1 - (W_2/W_1)^2 \quad (5)$$

This suggests replotting of the data in the form of Fig. 7. In

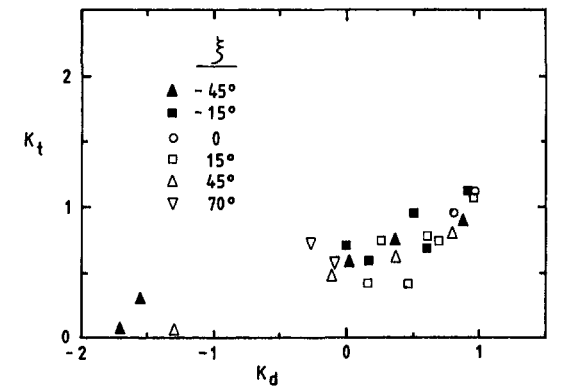


**Fig. 7 Total loss coefficient versus diffusion coefficient, s/c = 0.77 (blade parameters as in Fig. 5)**

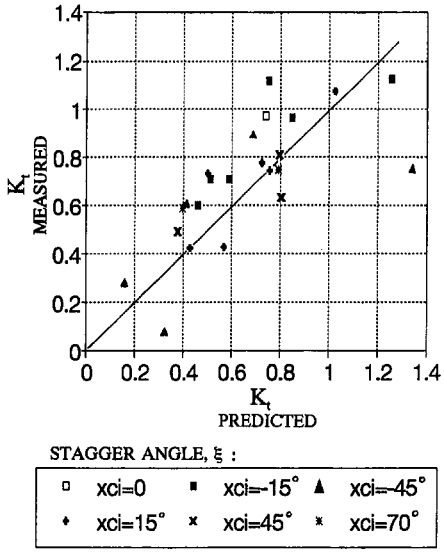


**Fig. 8 Scatter diagram for total loss coefficient correlation, s/c = 0.77**

Fig. 7 the data collapse into a band, with low and high-incidence points tending to fall along the lower and upper margins of the band, respectively. The data for s/c = 0.51, 1.02 exhibit similar behavior although the collapse is not quite as good as seen in Fig. 7. The bands for the different s/c values fall in somewhat different locations. All this indicates that the total pressure losses are mainly governed by the diffusion coefficient and that incidence and space/chord ratio are also significant. The following relation was fitted to the data for the total loss coefficient:

$$K_t = (K_d/4 + 0.5)^{1.7}(c/s)^{0.7} + 0.35(0.01i)^2(1 + 12(s/c - 0.85)^2) + 0.01(c/s) \quad (6)$$

The form of this relation was chosen on the basis of the above discussion. The first two terms represent diffusion and incidence effects, respectively; $i$ is in degrees. The third term represents friction losses in a constant-area passage with a skin friction coefficient of 0.005; this value corresponds to fully developed flow at a Reynolds number based on hydraulic diameter, 2s, of $5 \times 10^4$ which is reasonably typical of full-scale conditions and of the experiments of Kind and Tobin (1990). The third term of Eq. (6) is very small relative to the other terms in the present application and it is included mainly as a matter of form. The loss coefficient values seen in Fig. 7 are unusually high compared to profile loss coefficients for conventional cascades; this reflects the fact that for virtually all incidence angles there are extensive regions of separated flow in the blade-to-blade passages, due to the sharp-cornered thin leading edges of the blades.

Figure 8 compares values predicted by Eq. (6) with measured values of the total loss coefficient, $K_t$, for the s/c = 0.77 data. The root-mean-square of the errors between measured and predicted values of $K_t$ is 0.20 for the s/c = 0.77 data shown in Fig. 8 and 0.35 and 0.19, respectively, for the s/c = 0.51 and 1.02 data. Equation (6) is thus considerably less successful in correlating the s/c = 0.51 data than for the other two s/c values.

The incidence angle for any blading-zone element can be determined from the velocity triangle at element inlet and from the known blading geometry. As is usual for cascades, the difference in direction between the relative velocity leaving the blade row and the blade exit angle is represented by the deviation angle, $\delta$ (see Fig. 1). This is used instead of the slip factor that is normally used for conventional centrifugal impellers whose vane-to-vane passages are relatively long. The deviation angle is found from Eq. (2) and Eq. (1) then gives the exit

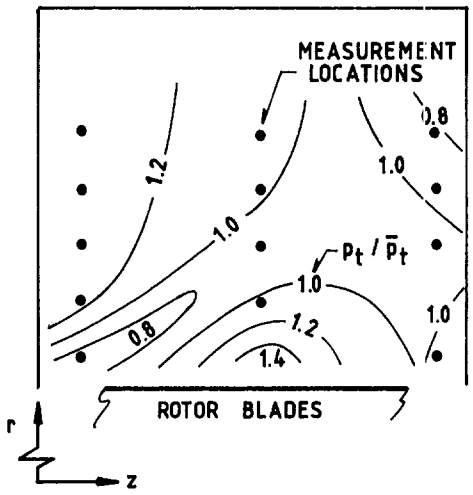


**Fig. 9 Contour plot of total pressure in a volute cross-section plane (R1-C1, $\phi = 0.6$, $\theta = 315°$, $U_2D_2/\nu \approx 3 \times 10^5$)**

angle, $\beta_2$, of the flow, enabling determination of the exit velocity triangle. With the exit velocity triangle established, the well known Euler pump and turbine equation (e.g., Massey, 1979) can be used to calculate the ideal total-pressure rise across any element $ij$ of the blading zone. In non-dimensional form this equation is

$$(\Delta p_{tij})_{\text{ideal}} = (C_{w2} - C_{w1}U_1/U_2) \tag{7}$$

The actual total pressure rise across the element is found by subtracting the losses of Eqs. (3) and (6) from the result of Eq. (7). The static pressure is then obtained by subtracting the absolute dynamic pressure, the absolute velocity, $C_2$, being given by the velocity triangle.

**2.4 Flow Model, Volute Zone.** Flow parameters in the volute are assumed to be uniform in the axial ($z$) direction. Thus the volute is only subdivided into sectors with no axial sub-divisions or slices. The various fluid streams entering a volute sector are assumed to mix rapidly such that total pressure is uniform over volute cross-section planes. Figure 9 shows a contour plot of preliminary experimental data from the apparatus of Kind and Tobin (1990); it indicates that the assumption of uniform total pressure over volute cross-section planes is valid within about ±30 percent.

Figure 10 shows a volute sector. Sector geometry is straightforward. Flow enters any volute sector $j$ from the corresponding blading-zone elements $B_{ij}$ and from the upstream volute sector, $(j - 1)$. Flow leaves the sector through its downstream face. Axial velocity components are assumed to be negligible throughout the volute. All parameters of flow streams entering a volute sector are known from previous calculations. Since total pressure is assumed uniform over cross-section planes, the circumferential or whirl velocity, $C_w$, over the upstream and downstream faces of volute sectors can be assumed to follow the free-vortex relation, that is

$$rC_w = \text{Constant} \tag{8}$$

The calculations for a volute sector must yield the following parameters at the downstream face of the sector: whirl velocity, $C_w$; radial velocity, $C_r$; static pressure; total pressure. This information is found from continuity considerations as follows (refer to Fig. 10).

$$Q_{\text{V}j} = Q_{\text{V},j-1} + \sum_{i=1}^{m} Q_{Bij} \tag{9}$$

$$\bar{C}_{wj} = Q_{\text{V}j}/b_{\text{V}}(r_{\text{V}2j} - r_{\text{V}1j}) \tag{10}$$

$\bar{C}_{wj}$ is the mean whirl velocity on the sector exit plane and is assumed to be the value of $C_w$ at the centroid of the plane. Equation (8) then gives values of $C_w$ at all other radii. The radial velocity is assumed to be given by

$$C_r = C_w \tan(\alpha_{\text{V}}) \tag{11}$$

where $\alpha_{\text{V}}$ is the volute wall angle. Other relations for $C_r$ were also tried; the results are insensitive to assumptions for $C_r$. The value of $C_r$ at blading exit normally differs substantially from that given by Eq. (11) and the difference drives a crossflow which assists rapid mixing in the volute. The angular momentum equation is applied to a control volume coinciding with the volute sector (Fig. 10) to obtain the static pressure, $\bar{p}_j$, at the centroid of the sector's downstream face. The equation takes the nondimensional form:

$$(Q_{\text{V}j}\bar{C}_{wj}\bar{r}_j - Q_{\text{V},j-1}\bar{C}_{w,j-1}\bar{r}_{j-1} - r_{\text{V1}}\sum_{i=1}^{m} Q_{Bij}C'_{wB2ij})$$
$$= b_{\text{V}}[\bar{p}_{j-1}\bar{r}_{j-1}(r_{\text{V2},j-1} - r_{\text{V1}}) + (\bar{p}_{j-1} + \bar{p}_j)(r^2_{\text{V}2j} - r^2_{\text{V}2,j-1})/4$$
$$- \bar{p}_j\bar{r}_j(r_{\text{V2}j} - r_{\text{V1}})] - [\text{wall-friction torque}] \tag{12}$$

where $\bar{r}$ denotes the radius to the centroid of the face. The terms on the left-hand side of Eq. (12) represent the angular momentum fluxes associated with the inflows and outflows shown in Fig. 10. The terms on the right-hand side represent the torques due to the pressures and skin-friction on the surfaces of the control volume of Fig. 10. The only unknown quantity in Eq. (12) is $\bar{p}_j$ which can thus be determined. The wall-friction torque in Eq. (12) is evaluated by assuming, as discussed later, a suitable value of the skin-friction coefficient on the outer and side walls of the volute sector; appropriate mean velocities from Eq. (8) are used to evaluate the shear stress on each wall. Knowing $\bar{p}_j$ from Eq. (12), the nondimensional total pressure at the centroid of the volute sector's exit plane is found from

$$p_{t\text{V}j} = \bar{p}_j + 0.5(\bar{C}^2_{wj} + \bar{C}^2_{rj}) \tag{13}$$

where $\bar{C}_{wj}$ and $\bar{C}_{rj}$ denote the whirl and radial velocity, respectively, at the centroid of the exit plane, found from Eqs. (10) and (11). Using Eqs. (8) and (11) the static pressure at any radius $r$ in the sector exit plane can be found from an equation like Eq. (13).

The mixing process assumed to occur inside the volute sectors implies a total pressure loss. This loss can be calculated by subtracting the total pressure given by Eq. (13) from the mass-flow-weighted mean total pressure of the fluid streams that enter the volute sector. The principle of the above analysis is identical to that of the classical analysis for flow through a sudden enlargement in a duct (e.g., Massey, 1979).

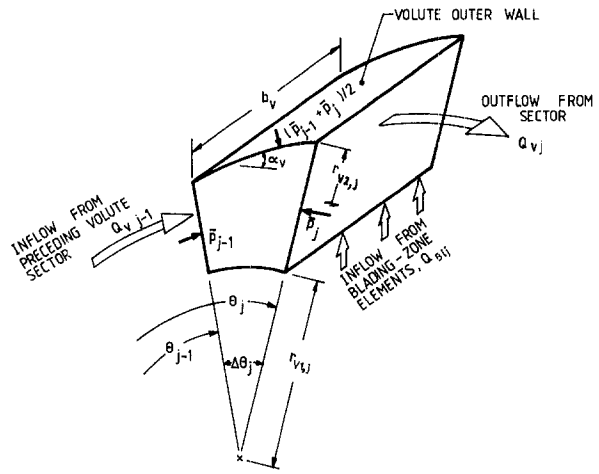


**Fig. 10 Volute sector**

In view of the discussion below regarding Eqs. (14) and (16), the static pressure at blading exit is not necessarily equal to that in the volute at radius $r_{V1}$. Although these static pressures do not appear in Eq. (12), the fluid implicitly assumes the value prevailing in the volute upon entering the volute-sector control volume of Fig. 10. Of course the mechanical energy or total pressure of the fluid should remain constant as it crosses the boundary. The dynamic pressure of the fluid from the blading is modified to enforce this requirement. The flow direction is assumed to remain constant so a modified whirl velocity, $C'_{wB2ij}$, can be determined for use in Eq. (12). This is important to ensuring that the overall losses in the fan are calculated correctly.

**2.5 Compatibility of Blading Flow and Volute Flow.** The flow models outlined in the three preceding subsections enable calculation of element or sector exit flow parameters for any given set of inflow parameters. However, realistic solutions for flow in a fan must satisfy certain compatibility conditions between flow in the inlet, blading and volute zones. For example, the local flow rate from a blading sector must adjust itself such that where it enters the volute it is in equilibrium with its surroundings. One must adopt an overall calculation scheme which enables the various compatibility conditions to be satisfied. This is not entirely straightforward, especially as there is considerable uncertainty about what the most pertinent compatibility conditions are.

In the present work, two main compatibility conditions were imposed:

$$\begin{pmatrix}\text{augmented static pressure at}\\ \text{blading-zone exit, sector } j\end{pmatrix} = \begin{pmatrix}\text{static pressure in}\\ \text{volute at } r_{V1},\ \theta_j\end{pmatrix} \quad (14)$$

$$\begin{pmatrix}\text{static pressure of}\\ \text{gap flow}\end{pmatrix} = \begin{pmatrix}\text{static pressure at}\\ \text{blading-zone exit, first sector}\end{pmatrix} \quad (15)$$

In general, a blading-zone sector contains $m$ elements; mass-flow weighted means of the element-exit pressures and velocities were used for the blading-zone exit parameters which appear in Eqs. (14) and (15). The term "augmented static pressure" in Eq. (14) will be defined below. The term "gap flow" in Eq. (15) refers to the flow through the gap between the cutoff of the volute and the rotor (see Fig. 1). Some of the flow from the final ($j = n$) volute sector recirculates by flowing through the gap into the first volute sector, at the $\theta = 0$ plane.

In centrifugal pumps and fans there is a strong interaction between the rotor and the volute and the volute can have a strong influence on the overall performance characteristics of the machine. This has been discussed by several authors, including Worster (1963), Brownell and Flack (1984), and Lorett and Gopalakrishnan (1986). Equation (14) represents one of the interaction mechanisms, the adjustment of blading sector flow rate to give flow parameters compatible with local conditions in the volute. Conditions in the volute at any circumferential position are mainly determined by the inflows at upstream stations. In general, the static pressure at the rotor/volute interface varies circumferentially. At the nominal design point the rotor and volute are normally matched such that the pressure is circumferentially uniform; at flow rates above (below) the design value the pressure falls (rises) with increasing $\theta$. There is a corresponding static pressure rise (drop) across the gap which decelerates (accelerates) the gap flow. The gap flow thus also plays an important role in the interaction between rotor and volute. In effect it enables the flow rate in the volute to vary less than the delivery flow rate as the fan's operating point is varied. Equation (15) attempts to represent the essential physics which govern the gap flow rate.

Equation (14) is a vague statement of the first compatibility condition because augmented static pressure is as yet undefined. It was originally thought that the static pressure itself was the appropriate parameter for the left hand side of Eq. (14) but this failed to yield any solutions for blading sector flow rates because the blading-exit static pressure was always less than the local static pressure in the volute. Upon reflection this is to be expected. With the typical forward facing blading, the relative flow through the rotor accelerates with an attendant drop in static pressure. The static pressure at blading exit is thus below ambient while that in the volute is usually at least slightly above ambient to meet requirements imposed by the load on the fan. The inescapable conclusion is that the blading-exit flow can somehow enter the volute even if its static pressure is initially less than that in the volute. Since its total pressure is typically well above the volute static pressure it seems reasonable to assume that the blading-exit flow undergoes some diffusion which augments its static pressure during the process of entering the volute.

Under the assumption of rapid mixing in the volute, the fluid from blading sector $j$ must decelerate to the whirl velocity of the volute flow, as given by Eqs. (8), (9), and (10), by the time it reaches the volute-sector exit plane. The associated static pressure rise is assumed to be that given by the classical sudden-enlargement relation (Massey, 1979) minus a loss due to mixing. The loss is assumed to exceed that given by the sudden-enlargement relation because the blading-exit streamtube is not in a duct but is exposed to the surrounding fluid to which it can lose energy by mixing. The relation for the augmented static pressure required in Eq. (14) is, in non-dimensional form:

$$p_{\text{aug},j} = p_{B2j} + C_{wVSj}(C_{wB2j} - C_{wVSj}) - 0.5\,K_m\,(C^2_{wB2j} - C^2_{wVSj}) \quad (16)$$

where $p_{B2j}$ and $C_{wB2j}$ denote the static pressure and whirl velocity at the exit of blading sector $j$ and $C_{wVSj}$ denotes the whirl velocity of the volute flow at the streamtube mean radius at the volute-sector exit plane. This radius is given by

$$r_{Sj} = r_{V1j} + 0.5(r_{V2j} - r_{V2,j-1}) \quad (17)$$

The final term in Eq. (16) is the mixing loss; $K_m$ is an empirical constant, determined as outlined later. It should be noted that Eq. (16) is used only for selecting sector flow rates in conjunction with Eq. (14); it does not enter in any direct way into the evaluation of fan efficiency or pressure rise.

We now turn to the gap flow compatibility condition, Eq. (15). The static pressure, $p_g$, of the gap flow is determined by subtracting the dynamic pressure and a loss from the total pressure just upstream of the gap. That is, in nondimensional terms,

$$p_g = p_{tV,j=n} - 0.5\,C_g^2 - K_g[0.5(C^2_{V1,n} - C_g^2)] \quad (18)$$

where $C_g$ is the velocity of the gap flow, $K_g$ is a gap loss coefficient (discussed below), and $C_{V1,n}$ is the last-volute-sector exit velocity at radius $r_{V1}$. Thus the loss is assumed to be proportional to the dynamic-pressure change sustained by the gap flow. In squirrel-cage fans operating at medium and high flow rates the gap flow will generally be in the forward direction with $C_{V1,n} \geq C_g$. This is because the total pressure upstream of the gap will then tend to be higher than downstream, due to the forward-facing blading and higher flow rate through the blading at $j = n$, and because the static pressure then normally rises across the gap as discussed earlier. The flow is thus expected to decelerate just before passing through the gap and consideration of the likely flow pattern suggests that the gap flow will sustain little if any loss. The gap loss coefficient, $K_g$, was accordingly set to zero in the present work unless otherwise stated. The gap condition, Eqs. (15), (18), is similar to that used by Lorett and Gopalakrishnan (1986).

**2.6 Iterative Calculation Scheme.** The following iterative calculation scheme was eventually adopted for finding solutions which satisfy the flow equations and compatibility conditions.

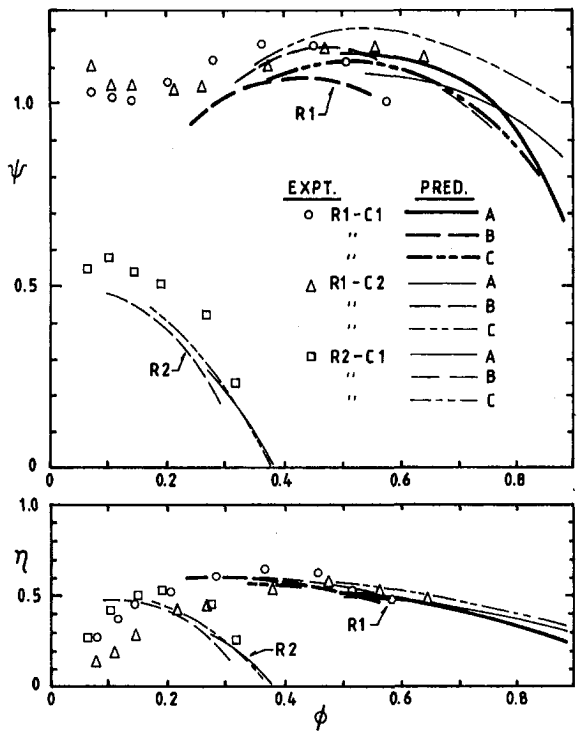


**Fig. 11 Comparison of predicted total-pressure-rise coefficient and total-to-total efficiency with Kind and Tobin (1990) measurements (*A*: blading-sector flow rates satisfy Eq. (14); *B*: circumferentially uniform sector flow rate specified; *C*: sector flow rate specified to vary quadratically, doubling between $\theta = 0$ and $\theta = 360$ deg)**

(*a*) A sector flow rate is assumed for the $j = 1$ sector of the inlet zone. This is subdivided into element flow rates according to the assumed axial distribution of velocity leaving the inlet zone. These element flow rates enter the corresponding blading-zone elements. The blading calculations yield the blading-zone exit conditions which are the first-volute-sector inlet conditions (the $Q_{Bij}$ streams of Fig. 10).

(*b*) A gap velocity, $C_g$, is assumed. The $j = 1$ volute sector flow computations can then be carried out.

(*c*) An inlet and blading sector flow rate is guessed for the $j = 2$ sector and calculations like those of step (*a*) are carried out. The program checks if the compatibility condition, Eq. (14), is satisfied. If it is not, a new sector flow rate is tried, and so on, until Eq. (14) is satisfied. Only solutions where $dp_{aug}/dQ < 0$ are accepted because only they represent a stable condition.

(*d*) Step (*c*) is repeated for all remaining sectors.

(*e*) The program checks if the gap condition, Eq. (15), (18), is satisfied. If it is not, a new value of gap velocity, $C_g$, is tried and steps (*b*) to (*e*) are repeated until Eqs. (15), (18) are satisfied.

Upon completion of steps (*a*) to (*e*) a valid fan operating condition has been obtained. The delivery flow rate is the sum of the sector flow rates through the blading zone. The delivery total pressure is $p_{t,j=n}$. Another operating point can be determined by repeating steps (*a*) to (*e*) with a different value for the flow rate in the $j = 1$ sector.

**2.7 Assumptions for Performance Calculations.** The flow simulation model has been implemented as a computer program. The model allows a range of assumptions for the axial distribution of the flow through the blading sectors and involves a number of coefficients whose values must be specified. The assumptions and values used for the performance predictions of this paper are presented here.

As discussed in the introduction, the incoming flow must separate as sketched in Fig. 2. It is therefore reasonable to assume constant static pressure along the free boundary of the streamtube that enters the blading zone; with the assumption of purely radial flow, the cross-sectional area of this streamtube at blading entry must then equal the inlet area, $\pi D_1^2/4$. The axial distribution of flow through the blading zone would then be a step profile, with zero flow over the front part of the rotor and uniform flow over an axial distance of $D_1/4$. This distribution was used in the present work. A uniform distribution over the full rotor width and a linear distribution from the front to the back were also tried; the uniform distribution gave unrealistically high overall flow rates and results with the linear distribution were not greatly different from those with the step distribution. The step distribution was used because it appears to have the most rational physical basis.

The inlet loss was assumed to be 0.1 of the dynamic pressure at entry to the inlet zone. This is simply a rough estimate; the results are only mildly sensitive to the assumed value. For typical squirrel-cage fans the inlet losses would be mainly due to the flow separation (Fig. 2) that occurs in the inlet zone.

As discussed earlier, the gap loss coefficient was set to zero.

The skin-friction coefficient on the volute walls was assigned the value 0.003. This is consistent with the friction factor value for turbulent flow in a smooth pipe at a Reynolds number of $4 \times 10^5$ based on hydraulic diameter. The volute dimensions and mean circumferential velocity at $\theta = 180°$ in the Kind and Tobin (1990) experiments, which are typical of full-scale conditions, correspond to this value of Reynolds number.

The mixing loss coefficient, $K_m$, of Eq. (16) was assigned the value 0.3 simply because the program produced reasonable results with this value. With substantially lower values the compatibility condition, Eq. (14), was only satisfied for very high sector flowrates and overall solutions were only obtainable for very high fan flow coefficients (e.g., $\phi > 1$). On the other hand, values substantially above 0.3 made it impossible to satisfy Eq. (14). The computed performance results were not overly sensitive to the value of $K_m$, with values in the range 0.25 to

**Table 1 Sensitivity of predicted performance results to various factors**

| Factors | Values | | Results | |
|---|---|---|---|---|
| | Datum | Trial | $\Delta\psi$ | $\Delta\eta$ |
| Inlet loss coefficient | 0.1 | 0 | +0.03 | +0.015 |
| Blading loss, deviation | $K_t$, $\delta$ per Eqs. (6, 2) | $K_t = 0$; $\delta$ per Eq. (2) | +0.47 | +0.25 |
| | $K_t$, $\delta$ per Eqs. (6, 2) | $K_t = 0$; $\delta = 0$ | +0.93 | +0.28 |
| Skin friction coefficient on volute walls | 0.003 | 0 | +0.05 | +0.018 |
| Gap loss coefficient, $K_g$ | 0 | 0.5 | −0.035 | −0.025 |
| Gap velocity, $C_g$ | 1.81 (Eq. (15) satisfied) | 1.4 (Eq. (15) not satisfied) | −0.26 | −0.14 |

Note: The $\Delta\psi$ and $\Delta\eta$ values are the changes in the predicted values for $\psi$ and $\eta$ that result from changing the value of the factor in the left hand column from the datum value to the trial value, while leaving all the other factors at their datum values. The datum case is as follows: assumptions as in sub-section 2.7; sector flow rate specified as circumferentially uniform; $\phi = 0.40$.

0.35 producing similar results. Recall that $K_m$ is used only for selecting sector flow rates, not for pressure-rise or efficiency calculations.

Instead of selecting flow rates through the blading sectors on the basis of the compatibility condition, Eq. (14), the flow rates can simply be specified. Computations were also carried out with the circumferential distribution of sector flow rate specified to be uniform and to increase linearly and quadratically with $\theta$. Of course this approach ignores the physical processes which determine the sector flowrates and the specified ones may be inconsistent with local conditions.

The computed results became insensitive to the number of sectors, $n$, for $n > 20$. All the reported results were obtained with $n = 24$.

## 3 Comparison With Experimental Results

Calculations were done for the three squirrel-cage fan configurations tested by Kind and Tobin (1990). These three configurations were designated R1-C1, R1-C2 and R2-C1; two rotors, R1 and R2, and two casings or volutes, C1 and C2, were involved. Rotor R1 had forward facing blades ($\beta_1' = 0$, $\beta_2' = -65°$) and rotor R2 had radial-exit blades ($\beta_1' = 60°$, $\beta_2' = 0$). Casing C2 had a throat area 1.5 times that of casing C1. Details are available in Kind and Tobin (1990). Figure 11 compares measured and predicted fan performance characteristics for flow rates near and above the best-efficiency values. The agreement between measurements and predictions is within 10 percent for the commercial rotor (R1) configurations and within 20 percent for the R2 configurations. In particular the large performance difference between the R2-C1 configuration and the other two configurations is well predicted. No comparisons are presented for relatively low flow rates because, as mentioned earlier, substantial reverse flow through the rotor occurs under such operating conditions and the flow model is then invalid.

Two sets of predictions are presented in Fig. 11. For one set the flow rates through the blading sectors satisfy the compatibility condition, Eq. (14); for the other set this condition is ignored and the circumferential distribution of flow rate through the blading is simply specified, as outlined above. Solutions for $\phi$ values near the best-efficiency operating point could only be obtained when circumferentially uniform sector flow rate was specified. When sector flow rates were selected on the basis of the compatibility condition the selected flow rates always increased substantially in the $\theta$ direction, yielding relatively high $\phi$ values. This presumably reflects deficiencies in Eq. (16). Where the two sets of predictions overlap, the results differ only slightly. Predicted fan performance thus depends mainly on the mean value of sector flow rate and not on its circumferential distribution.

## 4 Discussion

The good agreement between measured and predicted performance of the three fans suggests that the flow simulation model adequately represents the essential features of the flow in squirrel-cage fans operating at medium and high flow rates.

As mentioned above, it was found necessary to use a specified circumferential distribution of blading sector flow rates in order to obtain results near the best-efficiency operating point. However, as discussed earlier, circumferentially uniform flow through the blading is normally expected at the design point. Also the performance predictions are insensitive to the circumferential distribution of sector flowrate. Therefore this is not a serious practical limitation.

It is interesting to examine the sensitivity of the performance predictions to various factors and assumptions. Table 1 presents some results of this nature for the R1-C1 fan operating at $\phi = 0.4$, that is near its best-efficiency point.

It is clear from Table 1 that inlet losses and volute friction losses are relatively unimportant. Blading losses are, however, very important and are responsible for approximately half of the overall losses. At $\phi$ values within the operating range, the fluid leaving the blading zone undergoes a substantial deceleration upon entering the volute; the other major loss is the 'dump' or sudden-enlargement loss incurred in this process. The flow rate through the gap has a substantial effect on the dump loss because higher gap flow rates mean higher velocities in the volute and thus lower dump losses. This is illustrated by the last entry in Table 1. The gap-loss coefficient can have a significant influence on the gap velocity and flow rate and thus on the fan efficiency. For the second-to-last entry in Table 1 the nondimensional gap velocity that satisfies Eq. (15) is only reduced from 1.81 to 1.75 and the impact on efficiency is minor. However at $\phi = 0.7$ the gap velocity changes from 2.33 to 1.53 and the predicted efficiency from 0.33 to 0.15 These results suggest that it would be worthwhile to explore ways of reducing blading losses and to investigate the effects of varying the gap velocity and flow rate.

## 5 Conclusions

A simulation model of the flow in squirrel-cage fans has been formulated. It gives reasonably good predictions of fan performance at flow rates near and above the best-efficiency operating point and provides considerable insight into what features of flow behaviour are most important. It suggests that attempts to improve efficiency should focus on blading losses and on the gap flow.

A large range of cascade configurations of the type used in squirrel-cage fans were tested. These tests provided hitherto unavailable data for blading losses and flow deflection for use in the fan model.

In its present form the method is unable to calculate fan performance for flow rates well below the best-efficiency value. This capability would require incorporation of methods for dealing with reverse flow through the rotor blading.

## Acknowledgments

Financial support from a Natural Sciences and Engineering Research Council operating grant is gratefully acknowledged. The author also wishes to acknowledge the contributions of graduate student R. Sagi who developed a preliminary version of the computer program and of undergraduate summer students A. Eyvindson, D. Waigh, and J. Dillon who assisted with the cascade tests, data reduction, and computer programming.

## References

Brownell, R. B. Jr., and Flack, R. D. Jr., 1984, "Flow Characteristics in the Volute and Tongue Region of a Centrifugal Pump," ASME Paper No. 84-GT-82.

Dixon, S. L., 1978, *Fluid Mechanics, Thermodynamics of Turbomachinery,* 3rd ed., Pergamon Press, pp. 202–203.

Eck, B., 1973, *Fans,* 1st English ed., Pergamon Press, Oxford, pp. 139–153, 156–184.

Elder, R. L., and Gill, M. E., 1985, "A Discussion of the Factors Affecting Surge in Centrifugal Compressors," ASME *Journal of Engineering for Gas Turbines and Power,* Vol. 107, pp. 497–506.

Kind, R. J., and Tobin, M. G., 1990, "Flow in a Centrifugal Fan of the Squirrel-Cage Type," ASME *Journal of Turbomachinery,* Vol. 112, pp. 84–90.

Lorett, J. A., and Gopalakrishnan, S., 1986, "Interaction Between Impeller and Volute of Pumps at Off-Design Conditions," ASME JOURNAL OF FLUIDS ENGINEERING, Vol. 108, pp. 12–18.

Massey, B. S., 1979, *Mechanics of Fluids,* 4th ed., Van Nostrand Reinhold, pp. 198–199 and 475–476.

Worster, R. C., 1963, "The Flow in Volutes and Its Effect on Centrifugal Pump Performance," *Proc. Inst. of Mech. Engineers,* Vol. 177, pp. 843–875.

# Theoretical Study of Pressure Fluctuations Downstream of a Diffuser Pump Impeller—Part 1: Fundamental Analysis on Rotor-Stator Interaction

**W. Qin**
Engineer,
Yonago Factory,
Awamura Manufacturing Co., Ltd.,
Yomi-cho, Yonago, 683, Japan

**H. Tsukamoto**
Professor,
Faculty of Engineering,
Kyushu Institute of Technology,
Tobata, Kitakyushu, 804, Japan

*A theoretical method was developed to calculate the unsteady flow caused by the interaction between impeller and diffuser vanes in a diffuser pump by using the singularity method. The unsteady flow in the diffuser vane is assumed to be induced by three kinds of unsteady vortices: bound vortices distributed on the impeller blades and diffuser vanes, and free vortices shed from the trailing edge of diffuser vanes. In order to make clear the contribution of each harmonic component of unsteady vortices to unsteady pressure, all the unsteady vortices are expressed in the form of Fourier series. The calculated unsteady pressures downstream of impeller agree well with the corresponding measured ones. Moreover, it was shown that impulsive pressure plays a predominant role for unsteady pressures.*

## Introduction

In a diffuser pump, the centrifugal impeller interferes with its surrounding diffuser vanes and produces pressure fluctuations downstream of the impeller. The magnitude of the pressure fluctuations may be as large as the total pressure rise across the pump in the case of small radial gap between impeller and diffuser vanes (Arndt et al., 1989, 1990; Brennen, 1994; and Tsukamoto et al., 1995). This generates noise and vibration, causing unacceptable levels of stress and adversely affecting structure fatigue life. There has been, therefore, a need for understanding unsteady flow field due to the interaction between the rotating impeller blades and stationary diffuser vanes, i.e., rotor-stator interaction.

The rotor-stator interaction has been investigated intensively for axial flow machines. The unsteady component of the lift might be the same order as the steady component in the case of small gap between the upstream blade trailing edge and the downstream leading edge. One of the earlier theoretical studies of the interaction problem was conducted by Kemp and Sears (1953), who addressed the unsteady loading on thin airfoils by using linearized potential flow techniques. Many theoretical studies subsequent to Kemp and Sears have been carried out for unsteady loading on a cascade of blades due to the rotor-stator interaction. However, there have been few studies on centrifugal machines, the cascades of which constitute circular cascades. Among a few studies on the centrifugal machines Simpson et al. (1967) characterized the noise induced by the interaction in a centrifugal pump by extending Kemp and Sears' results to centrifugal machine. Iino (1981) applied the singularity method to the unsteady pressure in a centrifugal pump impeller. Several attempts have been made to simulate numerically the rotor-stator unsteady flow (Dawes, 1995). In the theoretical point of view, however, we have not reached the stage where we can predict the rotor-stator interaction in centrifugal machines with sufficient accuracy.

Whereas there have been a number of experimental works on the axial machines (Gallus et al., 1980; Dring et al., 1982; Capace and Fleeter, 1989), few of them have been done for centrifugal machines. Flow field investigation in the centrifugal impeller has been made by Krain (1981), Inoue and Cumpsty (1984). Impeller blade pressures were measured by Iino and Kasai (1985), and the experimental research of rotor-stator interaction in a diffuser pump was published by Arndt et al. (1989, 1990) and Tsukamoto et al. (1995). Akin and Rockwell (1994) carried out the work of manipulation of spectral content of wakes and wake-blade interactions, and investigated the flow structure in a radial flow pumping system using high-image-density particle image velocimetry. However, we need more information to provide knowledge on the magnitude of the unsteadiness in flow passage downstream of impeller due to the rotor-stator interaction.

The aim of the present study is to evaluate the magnitude of the unsteady pressure downstream of impeller due to the interaction between rotating centrifugal impeller and stationary diffuser vanes in a diffuser pump by using the singularity method. This complex phenomena may be caused by many factors—potential interaction, wake interaction, unsteady boundary layer, separating vortices, etc. For the purpose of understanding the basic mechanism of rotor-stator interaction in diffuser pumps, in the present study, flow is assumed to be two dimensional, inviscid, incompressible, and cavitation-free, and thus only potential effect will be considered. The present report describes a fundamental analysis on rotor-stator interaction in a diffuser pump. In Part 2 the fundamental unsteady flow analysis will be extended to incorporate volute casing effect and pressure fluctuations due to rotor-stator interaction will be discussed on the effect of flow rate as well as radial gap between impeller and diffuser vanes.

## Analysis

**Flow Model.** In a diffuser pump, which is our main concern, the impeller and diffuser vanes on the stream surface constitute two circular cascades. Unsteady flow analysis can thus be made for two-dimensional circular cascades in relative motion by use of the singularity method. The configuration of

Contributed by the Fluids Engineering Division for publication in the JOURNAL OF FLUIDS ENGINEERING. Manuscript received by the Fluids Engineering Division May 18, 1996; revised manuscript received February 18, 1997. Associate Technical Editor: L. Nelik.

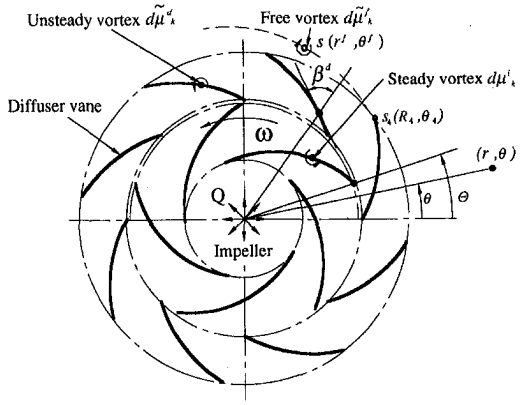


Fig. 1 Analytical model

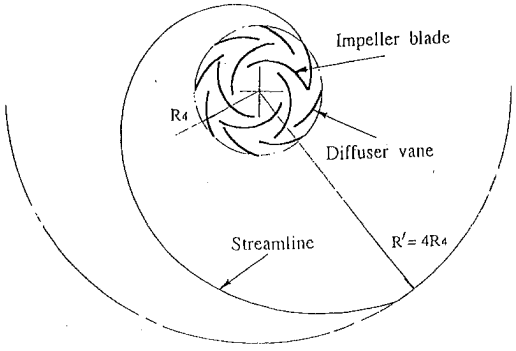


Fig. 2 Streamline extending from the diffuser vane trailing edge at rated flow rate

the circular cascades used in the present unsteady analysis is shown in Fig. 1. These are a rotating circular cascade with $Z^i$ thin blades and its surrounding vaned diffuser cascade with $Z^d$ thin blades. In the present analysis, attention is confined to the unsteady flow field downstream of the impeller. It is assumed that, to calculate the unsteady effects at any given points, it is permissible to neglect the unsteady parts of the vortices on the impeller blades. The unsteady flow downstream of the impeller is assumed to be induced by the three kinds of vortices: steady bound vortices on the rotating impeller blades, $d\mu^i$, unsteady bound vortices on the diffuser vanes, $d\tilde{\mu}^d_k$, and free vortices shed from the diffuser vane trailing edge, $d\tilde{\mu}^f_k$.

**Steady Flow.** Before going into unsteady flow analysis, the steady flow analysis is carried out based on two-dimensional circular cascade theory so as to determine the steady vorticity distributions on the impeller blades, the diffuser vanes, and the steady streamline along which the unsteady free vortices are shed from the diffuser vane trailing edge according to the change in the circulation around the diffuser vane. The steady vortices on impeller blade are expressed as a series in terms of the variable $\phi^i$:

$$\gamma^i ds \equiv d\mu^i(\phi^i) = \{A^i_1(1 + \cos\phi^i) + \sum_{m=2}^{\infty} A^i_m \sin(m-1)\phi^i \sin\phi^i\} \quad (1)$$

where

$$\cos\phi^i = (R_1 + R_2 - 2r^i)/(R_2 - R_1) \quad (2)$$

The steady flow analysis for the impeller is made by neglecting unsteady effect due to the interaction between rotating impeller and stationary diffuser vanes. Unknown coefficients of impeller blade vortices $A^i_m$ can be determined by the boundary condition that there is no flow through the blade surface in the relative system.

In the steady flow analysis downstream of the impeller, the velocity induced by the steady bound vortices on the impeller blades is approximated by the vortex of circulation $Z^i\bar{\Gamma}^i$ on the origin. Therefore, the steady velocity downstream of the impeller is induced by impeller circulation $Z^i\bar{\Gamma}^i$, source on the origin, $Q$, and steady vortices on diffuser vanes. Unknown steady vorticity $d\bar{\mu}^d$ on the diffuser vanes can be determined in a similar manner to the impeller blade vortices by the boundary condition that there is no flow through the blade surface in the stationary system. Figure 2 shows an example of the calculated streamline

## Nomenclature

$A, B$ = coefficients of vortices on impeller blade and diffuser vane
$c$ = symbol of pressure traverse line
$g$ = acceleration of gravity
$H$ = total head rise across pump
$N$ = rotational speed
$l$ = harmonic indices
$N$ = number of vortices
$p$ = static pressure
$p^*$ = relative pressure, $= p - (p_0 + \rho V_0^2/2)$
$Q$ = flow rate per unit passage width
$Q_r$ = rated flow rate
$R, r$ = radius
$s$ = coordinate along the streamline
$T$ = time passing through one pitch of impeller blade
$t$ = time
$t^*$ = nondimensional time, $= t/T$
$u$ = circumferential velocity
$V$ = absolute velocity
$Z$ = number of blades
$\beta$ = angle (see Fig. 1)
$\Gamma$ = circulation, $= \int_{s_1}^{s_2} \gamma^i ds$
$\gamma$ = density of vortex
$\phi$ = coordinate variable along the blade or vane
$\epsilon$ = strength of vortices shed from diffuser vane trailing edge
$\varphi$ = velocity potential
$\Theta$ = angle in relative system (see Fig. 1)
$\theta$ = angle in absolute system (see Fig. 1)
$d\mu$ = vortices element
$\rho$ = fluid density
$\sigma$ = standard deviation of unsteady pressure
$\tau$ = time defined by Eq. (12)
$\Delta\psi$ = nondimensional unsteady pressure, $= \tilde{p}^*/(\rho u_2^2/2)$
$\Delta\psi_{p-p}$ = magnitude of nondimensional unsteady pressure $\Delta\psi$
$|\Delta\psi|$ = amplitude of $\Delta\psi$
$\omega$ = angular velocity of impeller

### Subscripts

0 = reference point at pump center
1, 2 = impeller inlet and outlet
3, 4 = diffuser vane inlet and outlet
$c$ = cosine component
$k$ = $k$th vortex on diffuser vane
$l, m$ = summation indices
$Mt$ = maximum number of $m$
$r$ = radial component
$s$ = sine component
$\theta$ = tangential component

### Superscripts

$d$ = diffuser vane
$f$ = vortices shed from diffuser vane trailing edge
$i$ = impeller
$-$ = steady value
$\sim$ = unsteady value

### Abbreviations

IP = pressure side in impeller
IS = suction side in impeller
DP = pressure side in diffuser
DS = suction side in diffuser

extending from the diffuser vane trailing edge at the rated flow rate. Each streamlines from each trailing edges has an identical line because the steady flow is supposed to be axisymmetric.

**Unsteady Vortices on Diffuser Vanes.** The vortices on the diffuser vanes change with an identical amplitude and a constant phase angle equivalent to the pitch of the diffuser vanes according to the relative movement between the rotating impeller and stationary diffuser vanes. The distribution of vorticity on the $k$th diffuser vane, therefore, can be expressed in the form of an infinite series

$$\tilde{\gamma}_k^d ds \equiv d\tilde{\mu}_k^d = \sum_{l=1}^{\infty} \sin\left[lZ^i\omega\{t - 2\pi(k-1)/(Z^d\omega)\}\right] \times \{A_{sl1}^d(1+\cos\phi^d) + \sum_{m=2}^{\infty} A_{slm}^d \sin(m-1)\phi^d \sin\phi^d + B_{sl}^d \cos\phi^d \sin\phi^d\} d\phi^d + \sum_{l=1}^{\infty} \cos\left[lZ^i\omega\{t - 2\pi(k-1)/(Z^d\omega)\}\right] \times \{A_{cl1}^d(1+\cos\phi^d) + \sum_{m=2}^{\infty} A_{clm}^d \sin(m-1)\phi^d \sin\phi^d + B_{cl}^d \cos\phi^d \sin\phi^d\} d\phi^d \quad (3)$$

where, $l$ is the harmonic index. The coefficients $A^d$ and $B^d$ of each vane are identical, and the variable $\phi^d$ is defined as,

$$\cos\phi^d = (R_4 + R_3 - 2r^d)/(R_4 - R_3) \quad (4)$$

**Unsteady Velocity Downstream of Impeller.** We will consider the unsteady velocity induced by the vortices at the point $(r, \theta)$ in stationary coordinate system. The impeller bound vortices $d\mu^i$ rotate with a rotational speed $\omega$, and thus induce the unsteady velocity given in Fourier series:

$$V_r^i = -\frac{Z^i}{2\pi r}\int_{S_1}^{S_2} \sum_{l=1}^{\infty} \{r^i(s)/r\}^{lZ^i} \times \sin\{lZ^i(\theta - \theta^i(s) - \omega t)\}\gamma^i ds \quad (5)$$

$$V_\theta^i = \frac{Z^i}{2\pi r}\int_{S_1}^{S_2} [1 + \sum_{l=1}^{\infty} \{r^i(s)/r\}^{lZ^i} \times \cos\{lZ^i(\theta - \theta^i(s) - \omega t)\}]\gamma^i ds \quad (6)$$

The velocity induced by the unsteady diffuser vane vortices $d\tilde{\mu}_k^d$ is expressed by

$$\tilde{V}_r^d = -\sum_{k=1}^{Z^d}\int_{S_3}^{S_4} \frac{1}{2\pi r}\frac{(r_k^d/r)\sin(\theta - \theta_k^d)}{(r_k^d/r)^2 + 1 - 2(r_k^d/r)\cos(\theta - \theta_k^d)} \times \tilde{\gamma}_k^d ds \quad (7)$$

$$\tilde{V}_\theta^d = \sum_{k=1}^{Z^d}\int_{S_3}^{S_4} \frac{1}{2\pi r}\frac{1 - (r_k^d/r)\cos(\theta - \theta_k^d)}{(r_k^d/r)^2 + 1 - 2(r_k^d/r)\cos(\theta - \theta_k^d)} \times \tilde{\gamma}_k^d ds \quad (8)$$

The velocity induced by the vorticity shed from the diffuser vane trailing edge, $d\tilde{\mu}_k^f = \tilde{\epsilon}_k^f ds$, is expressed by

$$\tilde{V}_r^f = -\sum_{k=1}^{Z^d}\int_{S_4}^{\infty} \frac{1}{2\pi r}\frac{(r_k^f/r)\sin(\theta - \theta_k^f)}{(r_k^f/r)^2 + 1 - 2(r_k^f/r)\cos(\theta - \theta_k^f)} \times \tilde{\epsilon}_k^f ds \quad (9)$$

$$\tilde{V}_\theta^f = \sum_{k=1}^{Z^d}\int_{S_4}^{\infty} \frac{1}{2\pi r}\frac{1 - (r_k^f/r)\cos(\theta - \theta_k^f)}{(r_k^f/r)^2 + 1 - 2(r_k^f/r)\cos(\theta - \theta_k^f)} \times \tilde{\epsilon}_k^f ds \quad (10)$$

The Helmholz theorem for the conservation of vortices leads to the conclusion that the rate of total circulation change around the diffuser vane is equal to the total shed vortices from the diffuser vane trailing edge within unit time. Thus the strength of the vortices shed from the diffuser vane trailing edge is expressed by

$$\tilde{\epsilon}_k^f(s,t) = -\{1/V(s)\}\frac{d}{dt}\int_{S_3}^{S_4} \tilde{\gamma}_k^d\{t - \tau(s)\} ds \quad (11)$$

where $V(s)$: velocity at the point P($s$), and

$$\tau(s) = \int_{S_4}^{S} ds/V(s) \quad (12)$$

The velocity induced by shed vortices $d\tilde{\mu}_k^f$ can be rewritten by substituting Eqs. (11) and (12) into Eqs. (9) and (10). The radial and circumferential components of resultant velocity induced by the above three kinds of vortices are given by

$$\tilde{V}_r = \tilde{V}_r^i + \tilde{V}_r^d + \tilde{V}_r^f \quad (13)$$

$$\tilde{V}_\theta = \tilde{V}_\theta^i + \tilde{V}_\theta^d + \tilde{V}_\theta^f \quad (14)$$

**Numerical Procedure for Determining Unknown Vortices.** The boundary condition requires that the fluid should flow along the diffuser vane surface. This condition is fulfilled if

$$\tan\beta = V_\theta/V_r \quad (15)$$

The velocity $V$ is divided into the steady and unsteady terms, and then the unsteady terms satisfy the following equation.

$$\tan\beta = \tilde{V}_\theta/\tilde{V}_r \quad (16)$$

Kutta-Joukowski condition is satisfied in the present calculation by applying Eq. (11) into the diffuser vane trailing edge. And the free vorticity shed from trailing edge $d\tilde{\mu}_k^f$ should be equal to the unsteady vorticity $d\tilde{\mu}_k^d$ at diffuser vane trailing edge. That requires

$$d\tilde{\mu}_k^d = d\tilde{\mu}_k^f \equiv \tilde{\epsilon}_k^f ds \quad (17)$$

The *sine* term as well as *cosine* term in Eq. (3) should satisfy the above equation for each harmonic component of unknown unsteady vortices, and then the following two equations can be obtained:

$$\pi lZ^i\omega A_{cl1}^d/U_4 + \pi lZ^i\omega A_{cl2}^d/(2U_4) + 2B_{sl}^d\cos\beta_4^d/(r_4 - r_3) = 0 \quad (18)$$

$$\pi lZ^i\omega A_{sl1}^d/U_4 + \pi lZ^i\omega A_{sl2}^d/(2U_4) + 2B_{cl}^d\cos\beta_4^d/(r_4 - r_3) = 0 \quad (19)$$

In the present analysis, each component of harmonics, $lZ^i\omega(l = 1, 2, \cdots)$, can be calculated independently. The diffuser vane vortices can be expressed as a series from $m = 1$ to $m = Mt$ in Eq. (3), in which the unknown coefficients are $A_{slm}^d$, $A_{clm}^d$ ($m = 1, 2, \cdots$) and $B_{sl}^d$, $B_{cl}^d$ for all the diffuser vanes,

**Table 1 Specifications of test pump**

| | | |
|---|---|---|
| Impeller: | | |
| Outlet radius | $R_2$ | 125 mm |
| Number of vanes | $Z^i$ | 5 |
| Diffuser vane: | | |
| Inlet radius | $R_3$ | 129 mm |
| Outlet radius | $R_4$ | 162.5 mm |
| Number of vanes | $Z^d$ | 8 |
| Volute casing: | | |
| Base circle radius | $R_5$ | 239.4 mm |
| Rating: | | |
| Flow rate | $Q_r$ | 6.21 m³/min |
| Total head | $H$ | 29.2 m |
| Rotational speed | $N$ | 2066 rpm |
| Specific speed | Ns | 410 rpm, m³/min, m |

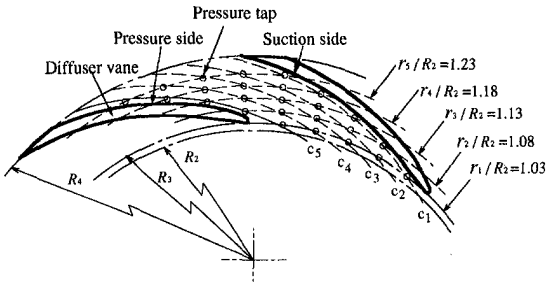


**Fig. 3 Pressure measurement stations for a vaned diffuser passage**

and thus the number of unknown coefficients is $2(Mt + 1)$. To establish a set of linear equations for the unknown variables, the unknown coefficients are specified from the boundary condition Eq. (16) at the $Mt$ points on the diffuser vane. Furthermore, Eqs. (18) and (19) yield two equations, and thus the $2(Mt + 1)$ values of the unknown coefficient of unsteady bound vortices are determined.

**Unsteady Pressure.** Based on the above calculated flow field, the unsteady pressure is calculated using the following unsteady Bernoulli's equation:

$$p/\rho + V^2/2 + (\partial\varphi/\partial t) - \{p_0/\rho + V_0^2/2 + (\partial\varphi_0/\partial t)\} = gH \quad (20)$$

The pressure and velocity terms are divided into steady and unsteady components, and the total head rise through the pump, $H$, is assumed to be steady. Neglecting the small terms, we have the unsteady pressure relative to the total pressure at a reference point:

$$\tilde{p}^*/\rho = -\bar{V}_r\tilde{V}_r - \bar{V}_\theta\tilde{V}_\theta - (\partial\tilde{\varphi}/\partial t) + (\partial\tilde{\varphi}_0/\partial t) \quad (21)$$

In the above equation, the time derivative of velocity potential is expressed by

$$(\partial\tilde{\varphi}/\partial t) = (\partial\tilde{\varphi}/\partial t)^i + (\partial\tilde{\varphi}/\partial t)^d + (\partial\tilde{\varphi}/\partial t)^f \quad (22)$$

$$(\partial\tilde{\varphi}_0/\partial t) = (\partial\tilde{\varphi}_0/\partial t)^i + (\partial\tilde{\varphi}_0/\partial t)^d + (\partial\tilde{\varphi}_0/\partial t)^f \quad (23)$$

where,

$$(\partial\tilde{\varphi}/\partial t)^i = \frac{Z^i\omega(d\mu^i)}{2\pi} \times \sum_{l=1}^{\infty} (r/r^i)^{-lZ^i} \cos\{lZ^i(\theta - \theta^i(s) + \omega t)\} \quad (24)$$

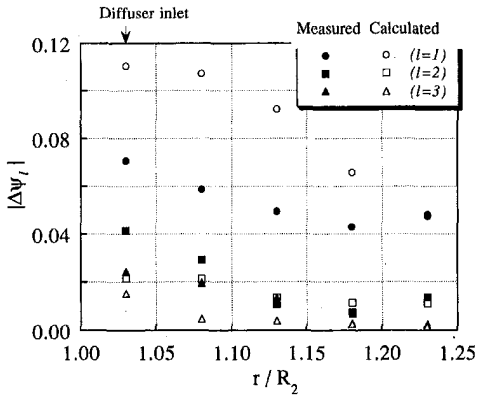


**Fig. 4 Calculated and measured amplitudes for the first three harmonics of unsteady pressure at rated flow rate**

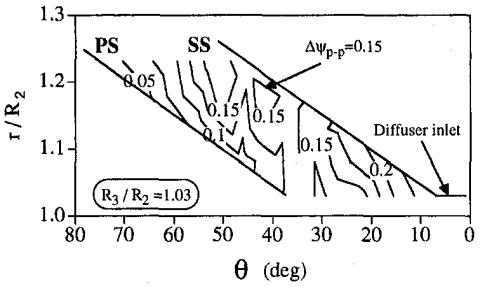


**Fig. 5(*a*) Measured**

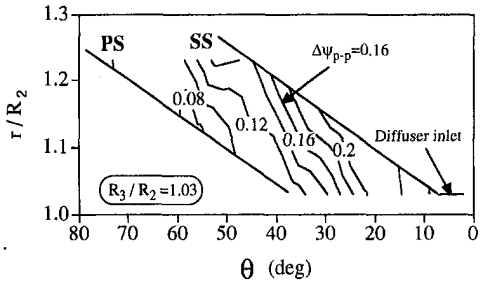


**Fig. 5(*b*) Calculated**

**Fig. 5 Contour map of magnitude $\Delta\psi_{p-p}$ of pressure fluctuations in vaned diffuser passage at rated flow rate; Experimental uncertainty in $\Delta\psi_{p-p}$ = ±7.1 percent**

$$(\partial\tilde{\varphi}/\partial t)^d = \sum_{k=1}^{Z^d} \frac{1}{2\pi} \tan^{-1} \frac{r\sin\theta - r_k^d \sin\theta_k^d}{r\cos\theta - r_k^d\cos\theta_k^d} \frac{\partial\tilde{\mu}_k^d}{\partial t} \quad (25)$$

$$(\partial\tilde{\varphi}/\partial t)^f = \sum_{k=1}^{Z^d} \frac{1}{2\pi} \tan^{-1} \frac{r\sin\theta - r_k^f \sin\theta_k^f}{r\cos\theta - r_k^f\cos\theta_k^f} \frac{\partial\tilde{\varepsilon}_k^f}{\partial t} ds \quad (26)$$

The nondimensional unsteady pressure is divided into two parts, that is, the dynamic pressure, $(\Delta\psi)_\nu$ and the impulsive pressure, $(\Delta\psi)_\varphi$. Then Eq. (21) can be rewritten as

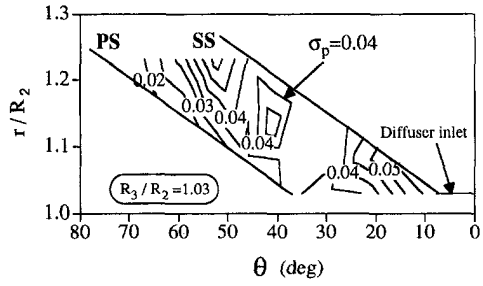


**Fig. 6(*a*) Measured**

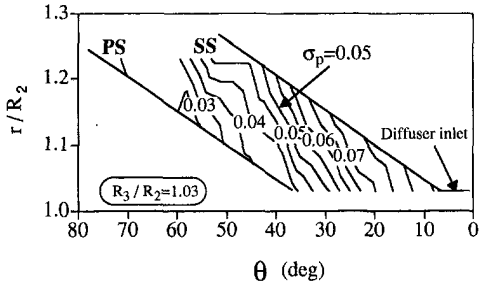


**Fig. 6(*b*) Calculated**

**Fig. 6 Contour map of standard deviation $\sigma$ of pressure fluctuations in vaned diffuser passage at rated flow rate; Experimental uncertainty in $\sigma$ = ±4.4 percent**

$$\Delta\psi = (\Delta\psi)_\nu + (\Delta\psi)_\varphi \tag{27}$$

where

$$\Delta\psi = (\tilde{p}^*/\rho)/(u_2^2/2) \tag{28}$$

$$(\Delta\psi)_\nu = (-\bar{V}_r\tilde{V}_r - \bar{V}_\theta\tilde{V}_\theta)/(u_2^2/2) \tag{29}$$

$$(\Delta\psi)_\varphi = \{-(\partial\tilde{\varphi}/\partial t) + (\partial\tilde{\varphi}_0/\partial t)\}/(u_2^2/2) \tag{30}$$

Moreover, the $(\Delta\psi)_\varphi$ consists of three terms, $(\Delta\psi)^i_\varphi$, $(\Delta\psi)^d_\varphi$, and $(\Delta\psi)^f_\varphi$, which are induced by the three different unsteady vortices, $d\mu^i$, $d\tilde{\mu}^d_k$, and $d\tilde{\mu}^f_k$, respectively.

$$(\Delta\psi)_\varphi = (\Delta\psi)^i_\varphi + (\Delta\psi)^d_\varphi + (\Delta\psi)^f_\varphi \tag{31}$$

The accuracy of present analysis may be affected by number of numerical integration points, the length of streamline from the trailing edge of diffuser vanes, and the number of the harmonics. The calculations are tried for a variety of integration points (maximum 100) and the length of streamline (maximum $R^f = 6R_2$). As a result of the trial, in the present calculation, we have adopted the 40 integration points and the streamline extending to $4R_2$ from the origin, since the differences of the calculated values are found to be small enough to assure a reasonable degree of accuracy under these condition. And the first five harmonics of unsteady pressure were adopted in the calculation because the higher harmonic components are smaller enough to neglect comparing with the fundamental one.

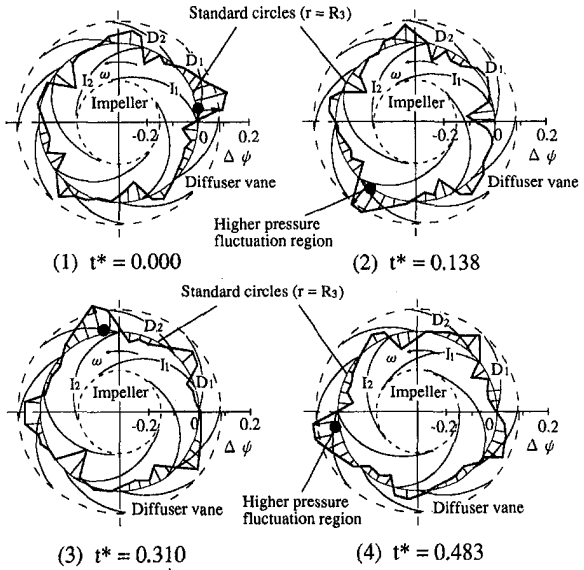


**Fig. 7(*a*) Measured**

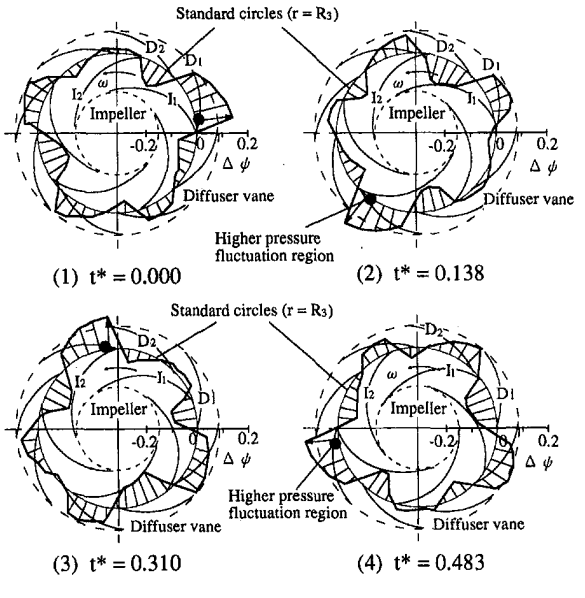


**Fig. 7(*b*) Calculated**

**Fig. 7 Time dependent pressure distribution at vaned diffuser inlet for rated condition; Experimental uncertainty in $\Delta\psi = \pm 7.1$ percent**

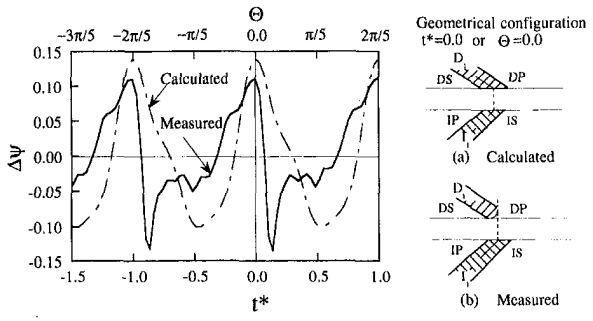


**Fig. 8 Time histories of instantaneous pressure $\Delta\psi$ on the pressure tap $(r_1, c_1)$ at rated flow rate; Experimental uncertainty in $\Delta\psi = \pm 7.1$ percent**

## Discussion

The present calculating method is applied to a test diffuser pump and the calculated pressures are compared with the corresponding experimental ones. Table 1 shows the specifications of the test pump, and the pressure measurement stations are shown in Fig. 3. The experimental uncertainty in flow rate was found to be within 1.6 percent, and the uncertainty for unsteady pressure was within 7.1 percent at diffuser vane passage (Tsukamoto et al., 1995). In the present report, the comparison will be made for the rated condition of the test pump.

**Unsteady Pressure in Diffuser Vane Passage.** Figure 4 shows the calculated and measured amplitudes for the first three harmonic components of the unsteady pressure $|\Delta\psi|$ on the $c_1$ line in the test diffuser passage. The symbols marked by circle, square, and triangle indicate the fundamental, the second, and the third harmonic components of unsteady pressure, respectively. The fundamental harmonic component of unsteady pressure is greater than other higher harmonic ones in the calculated and measured results. And the difference of first harmonic component and higher harmonic ones is larger in calculated results than in the measured ones. That is because the viscosity of fluid is neglected in the present analysis.

Figures 5 and 6 show the blade-to-blade distributions of the magnitude $\Delta\psi_{p-p}$ and the standard deviation $\sigma$ of pressure fluctuations in the test diffuser, respectively. In these figures, $(a)$ and $(b)$ are the measured and calculated results, respectively. The unsteady pressure is found to be larger on the suction side of diffuser vane than on the pressure side at a constant radius, and the unsteady pressure decreases with increasing radius both in measured and calculated results.

Figures 7$(a)$ and $(b)$ show the measured and calculated unsteady pressure distributions at the diffuser vane inlet, respectively. These figures represent the pressure distributions for four different stages in time. While the plots outside and inside the circle of radius $R_3$ indicate the pressure higher and lower than the time-averaged one, respectively. Pressure has a maximum at the instant when an impeller blade encounters a diffuser vane. There can be seen a higher pressure region indicated by a large dot which rotates with the impeller rotation. The calculated results agree well with the experimental ones, and hence the present method may be applicable for the prediction of the unsteady pressure in diffuser vane passage of a diffuser pump.

Figure 8 indicates time history of the instantaneous unsteady pressure $\Delta\psi$ on the pressure tap $(r_1, c_1)$. The $\Theta = 0.0$ means

that the trailing edge of a impeller blade and the leading of a diffuser vane are on the same line radiated from the origin. Because the first harmonic is predominant in the calculated pressure compared with the measured one as shown in Fig. 4, the calculated waveform of pressure changes more smoothly with time than the measured one. That is the reason why the calculated and measured magnitudes of unsteady pressure $\Delta\psi_{p-p}$ shown in Fig. 5 shows better agreement compared with the standard deviation $\sigma$ shown in Fig. 6.

**Contribution of Dynamic and Impulsive Pressures.** In the present singularity analysis in which unsteady flow due to rotor-stator interaction is assumed to be induced by three kinds of vortices in Fourier series, we can classify the contribution of each factor on harmonic components of unsteady pressures. Figure 9 shows the contributions of the individual terms of unsteady pressure in Eqs. (27) and (31) to the first harmonic component at the diffuser inlet. Figures 9($a$) and ($b$) correspond to the suction and pressure side. The impulsive pressure $(\Delta\psi)^i_\varphi$ induced by $d\mu^i$ is a half-cycle out of phase with the dynamic pressure $(\Delta\psi)_\nu$. The impulsive pressure $(\Delta\psi)^f_\varphi$ induced by $d\tilde{\mu}^f_k$, is smaller than other unsteady pressure terms. Therefore, the amplitude of pressure is dependent of the phase difference between the impulsive pressure $(\Delta\psi)^d_\varphi$ and $(\Delta\psi)^i_\varphi$. The larger pressure amplitude at suction side is because the impulsive pressures $(\Delta\psi)^i_\varphi$ and $(\Delta\psi)^d_\varphi$ induced by $d\mu^i$ and $d\tilde{\mu}^d_k$ take smaller phase difference there.

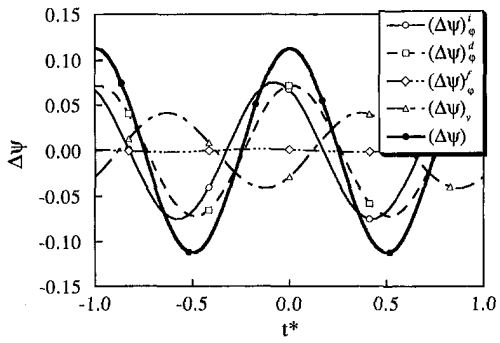


Fig. 9($a$) Suction side; ($r_1$, $c_1$)

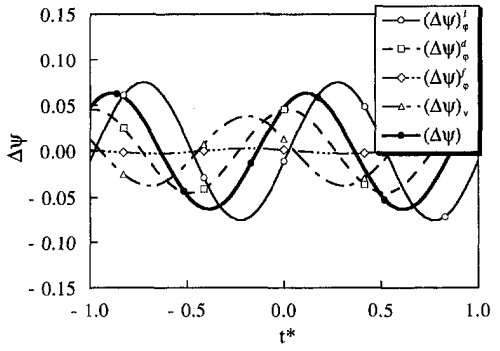


Fig. 9($b$) Pressure side; ($r_1$, $c_5$)

**Fig. 9 Time histories of individual terms for the first harmonic of unsteady pressure at rated flow rate**

## Conclusions

Theoretical analysis has been developed for the unsteady flow due to the interaction between impeller blades and diffuser vanes in the diffuser passage by using the singularity method. The calculated unsteady pressures agree with the corresponding measured ones, and the calculated results showed that the interaction between impeller blades and diffuser vanes is main factor for the pressure fluctuations in the diffuser passage. The fundamental harmonic component of the pressure fluctuations is found to be larger than other ones. And it was found that the influence of impulsive pressure is larger than the unsteady dynamic pressure.

## Acknowledgments

The investigations were carried out in the Department of Mechanical Engineering of Kyushu Institute of Technology and this work was a portion of the first author's dissertation. The authors wish to express their gratitude to Messrs. T. Ito and J. Asakura for their assistance in the preparation of this paper.

## References

Akin, O., and Rockwell, D., 1994 (a), "Actively Controlled Radial Flow Pumping System: Manipulation of Spectral Content of Wakes and Wake-Blade Interactions," ASME *Journal of Turbomachinery,* Vol. 116, pp. 528–537.

Akin, O., and Rockwell, D., 1994 (b), "Flow Structure in a Radial Flow Pumping System Using High-image-Density Particle Image Velocimetry," ASME *Journal of Turbomachinery,* Vol. 116, pp. 528–537.

Arndt, N., Acosta, A. J., Brennen, C. E., and Caughey, T. K., 1989, "Rotor-Stator Interaction in a Diffuser Pump," ASME *Journal of Turbomachinery,* Vol. 111, pp. 213–221.

Arndt, N., Acosta, A. T., Brennen, C. E., and Caughey, T. K., 1990, "Experimental Investigation of Rotor-Stator Interaction in a Centrifugal Pump With Several Vaned Diffusers," ASME *Journal of Turbomachinery,* Vol. 111, pp. 213–221.

Brennen, C. E., 1994, *Hydrodynamics of Pumps,* Concepts ETI, Inc. and Oxford University Press, pp. 196–204.

Capace, N. R., and Fleeter, S., 1989, "Experimental Investigation of Multistage Interaction Gust Aerodynamics," ASME *Journal of Turbomachinery,* Vol. 111, pp. 409–417.

Dawes, W. N., 1995, "A Simulation of the Unsteady Interaction of a Centrifugal Impeller With Its Vaned Diffuser: Fow Analysis," ASME *Journal of Turbomachinery,* Vol. 117, pp. 213–220.

Dring, R. P., Joslyn, H. D., Hardin, L. W., and Wagner, J. H., 1982, "Turbine Rotor-Stator Interaction," ASME *Journal of Engineering for Power,* Vol. 104, pp. 729–742.

Gallus, H., E., Lambertz, J., and Wallmann, Th., 1980, "Blade-Row Interaction in an Axial-Flow Subsonic Compressor Stage," ASME *Journal of Engineering for Power,* Vol. 102, pp. 169–177.

Iino, T., 1981, "Potential Interaction Between a Centrifugal Impeller and a Vaned Diffuser," ASME *Fluid/Structure Interactions in Turbomachinery,* pp. 63–69.

Iino, T., and Kasai, K., 1985, "An Analysis of Unsteady Flow Induced by Interaction Between a Centrifugal Impeller and a Vaned Diffuser," (in Japanese), *Transactions of the Japan Society of Mechanical Engineers,* Vol. 51, No. 471, pp. 154–159.

Inoue, M., and Cumpsty, N. A., 1984, "Experimental Study of Centrifugal Impeller Discharge Flow in the Vaneless and Vaned Diffusers," ASME *Journal of Engineering for Gas Turbines and Power,* Vol. 106, pp. 455–467.

Kemp, N. H., and Sears, W. R., 1953, "Aerodynamic Interference Between Moving Blade Rows," *Journal of the Aeronautical Sciences,* Vol. 20, No. 9, pp. 585–597.

Krain, H., 1981, "A Study on Centrifugal Impeller and Diffuser Flow," ASME *Journal of Engineering for Power,* Vol. 103, pp. 688–697.

Simpson, H. C., Clark, T. A., and Weir, G. A., 1967, "A Theoretical Investigation of Hydraulic Noise in Pump," *Journal of Sound and Vibration,* Vol. 5, No. 3, pp. 456–488.

Tsukamoto, H., Uno, M., Hamafuku, H., and Okamura, T., 1995, "Pressure Fluctuation Downstream of a Diffuser Pump Impeller," The 2nd Joint ASME/JSME Fluids Engineering Conference, *Forum of Unsteady Flow,* FED-Vol. 216, pp. 133–138.

# Theoretical Study of Pressure Fluctuations Downstream of a Diffuser Pump Impeller—Part 2: Effects of Volute, Flow Rate and Radial Gap

**W. Qin**
Engineer,
Yonago Factory,
Awamura Manufacturing Co., Ltd.,
Yomi-cho, Yonago, 683, Japan

**H. Tsukamoto**
Professor,
Faculty of Engineering,
Kyushu Institute of Technology,
Tobata, Kitakyushu, 804, Japan

*The fundamental analysis in the first report was extended to calculate the unsteady flow induced by the interaction between impeller blades and diffuser vanes/volute casing in a diffuser pump. The unsteady flow in the diffuser vane passage, as well as the volute casing, is assumed to be induced by the five kinds of singularities—the bound vortices distributed on the impeller blades, diffuser vanes and volute casing wall, the sources at volute outlet, and the free vortices shed from the trailing edge of diffuser vanes. Calculated unsteady pressures agree with the corresponding experimental data. And the calculated results showed the effects of the flow rate, volute casing and the radial gaps between impeller blade trailing edge and diffuser vane leading edge on the magnitude of unsteady pressure downstream of impeller.*

## Introduction

It is interesting to calculate the pressure fluctuations due to rotor-stator interactions in a diffuser pump, since the magnitude of pressure fluctuations may be as large as the total pressure rise across the pump in the case of small radial gap between impeller and diffuser vanes (Arndt et al., 1989, 1990; Brennen, 1994, and Tsukamoto et al., 1995). There are few practical and analytical methods to provide knowledge on the magnitude of this unsteadiness in flow passage downstream of impeller.

The purpose of the present study is to evaluate the unsteady pressure downstream of the impeller due to the interaction between a rotating centrifugal impeller and stationary structures like vaned diffuser and volute casing. In Part 1, the unsteady flow due to rotor-stator interaction was calculated by using the singularity method (Qin and Tsukamoto, 1997). In the present paper, unsteady flow analysis will be extended to incorporate volute casing effect and calculations will be carried out for the effect of flow rate as well as radial gap between impeller outlet and diffuser inlet.

## Analysis

**Flow Model.** In a diffuser pump, which is our main concern, the impeller and diffuser vanes on the stream surface constitute two circular cascades with volute casing. Unsteady flow analysis can thus be made for two-dimensional circular cascades in relative motion by use of the singularity method similar to the first report (Qin and Tsukamoto, 1997). The configuration of the circular cascades used in the present unsteady analysis is shown in Fig. 1. These are a rotating circular cascade with $Z^i$ thin blades, its surrounding vaned diffuser cascade with $Z^d$ thin blades, and volute casing. The unsteady flow downstream of the impeller is assumed to be induced by five kinds of singularities: steady vortices on the rotating impeller blades, $d\mu^i$, unsteady vortices on the diffuser vanes, $d\tilde{\mu}_k^d$, unsteady free vortices shed from the diffuser vane trailing edge, $d\tilde{\mu}_k^f$, unsteady vortices on the volute casing, $\tilde{\mu}_k^{vc}$, and unsteady sources at the volute outlet, $\tilde{q}_k^{vs}$.

Before going into unsteady flow analysis, the steady flow analysis is carried out in the manner similar to the first report so as to determine the steady singularity distributions on the impeller blades, the diffuser vanes, the volute casing and the steady streamline along which the unsteady free vortices are shed from the diffuser vane trailing edge according to the change in the circulation around the diffuser vane (Qin, 1995). Figure 2 shows an example of the calculated streamline extending from the diffuser vane trailing edge at the rated condition. The unsteady free vortices $d\tilde{\mu}_k^f$ are shed from the diffuser vane trailing edge along these steady streamlines.

**Unsteady Vortices on Diffuser Vanes.** In Part 1, the unsteady vortices on the diffuser vanes were assumed to change with an identical amplitude and a constant phase angle equivalent to the pitch of the diffuser vanes according to the relative movement between the rotating impeller and stationary diffuser vanes. The flow fluctuations, however, are not always identical in amplitude, and do not have a constant phase shift with those in other diffuser passages because of the asymmetric volute casing. The distribution of vorticity on the $k$th diffuser vane, therefore, can be expressed in the form of an infinite series

$$\tilde{\gamma}_k^d ds \equiv \tilde{\mu}_k^d = \sum_{l=1}^{\infty} \sin(lZ^i\omega t)[A_{ksl1}^d(1+\cos\phi^d) + \sum_{m=2}^{\infty} A_{kslm}^d \sin\{(m-1)\phi^d\}\sin\phi^d + B_{ksl}^d \cos\phi^d \sin\phi^d]d\phi^d + \sum_{l=1}^{\infty} \cos(lZ^i\omega t)[A_{kcl1}^d(1+\cos\phi^d) + \sum_{m=2}^{\infty} A_{kclm}^d \sin\{(m-1)\phi^d\}\sin\phi^d + B_{kcl}^d \cos\phi^d \sin\phi^d]d\phi^d \quad (1)$$

where the coefficients $A^d$ and $B^d$ are functions of diffuser vane index $k$. The values of the coefficients are determined from the boundary condition on the individual vanes as described later.

Contributed by the Fluids Engineering Division for publication in the JOURNAL OF FLUIDS ENGINEERING. Manuscript received by the Fluids Engineering Division May 18, 1996; revised manuscript received February 18, 1997. Associate Technical Editor: L. Nelik.

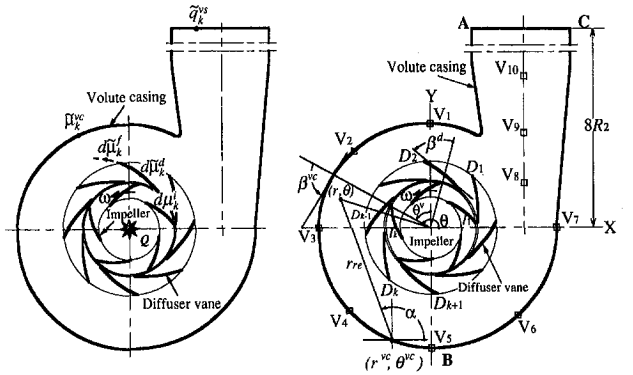


(a) Distribution of singularities (b) definition of geometrical variables

**Fig. 1 Model of diffuser pump**

The unsteady vortices and sources on the volute casing surface are expressed in the form of an infinite series with the same frequency as the vortices on the diffuser vanes, $lZ^i\omega$:

$$\tilde{\mu}_k^{vc} = \sum_{l=1}^{\infty} \{ C_{ksl}^{vc} \sin (lZ^i\omega t) + C_{kcl}^{vc} \cos (lZ^i\omega t) \} \quad (2)$$

$$\tilde{q}_k^{vs} = \sum_{l=1}^{\infty} \{ D_{ksl}^{vs} \sin (lZ^i\omega t) + D_{kcl}^{vs} \cos (lZ^i\omega t) \} \quad (3)$$

**Unsteady Velocity Field.** We will consider the unsteady velocity induced by the vortices at the point $(r, \theta)$ in stationary coordinate system. The velocities induced by the vortices $d\mu^i$, $d\tilde{\mu}_k^d$, and $d\tilde{\mu}_k^f$ are shown in Part 1.

The radial and circumferential components of velocity induced by $\tilde{\mu}_k^{vc}$ and $\tilde{q}_k^{vs}$ on the volute casing are expressed as follows:

$$\tilde{V}_r^{vc} = \sum_{k=1}^{N^{vc}} \left( -\frac{\tilde{\mu}_k^{vc}}{2\pi r_{re}} \sin \alpha \cos \theta + \frac{\tilde{\mu}_k^{vc}}{2\pi r_{re}} \cos \alpha \sin \theta \right) \quad (4)$$

$$\tilde{V}_\theta^{vc} = \sum_{k=1}^{N^{vc}} \left( \frac{\tilde{\mu}_k^{vc}}{2\pi r_{re}} \cos \alpha \cos \theta + \frac{\tilde{\mu}_k^{vc}}{2\pi r_{re}} \sin \alpha \sin \theta \right) \quad (5)$$

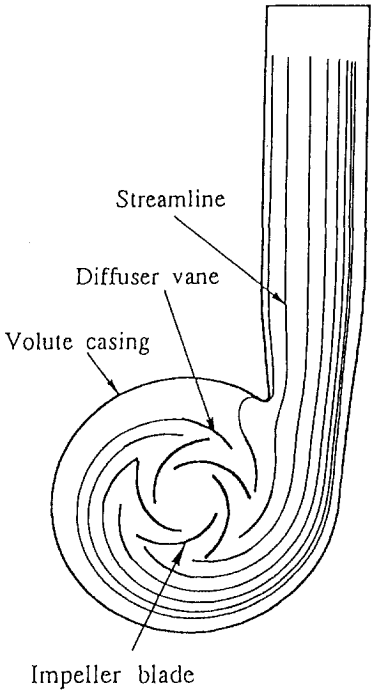


**Fig. 2 Streamline extending from the diffuser vane trailing edge at rated flow rate**

$$\tilde{V}_r^{vs} = \sum_{k=1}^{N^{vs}} \left( \frac{\tilde{q}_k^{vs}}{2\pi r_{re}} \cos \alpha \cos \theta + \frac{\tilde{q}_k^{vs}}{2\pi r_{re}} \sin \alpha \sin \theta \right) \quad (6)$$

$$\tilde{V}_\theta^{vs} = \sum_{k=1}^{N^{vs}} \left( \frac{\tilde{q}_k^{vs}}{2\pi r_{re}} \sin \alpha \cos \theta - \frac{\tilde{q}_k^{vs}}{2\pi r_{re}} \cos \alpha \sin \theta \right) \quad (7)$$

The radial and circumferential components of resultant veloc-

## Nomenclature

$A, B$ = coefficients of vortices on impeller blade and diffuser vane
$C, D$ = coefficients of singularity on volute casing wall
$c$ = symbol of pressure traverse line
$g$ = acceleration of gravity
$H$ = total head rise across pump
$l$ = harmonic indices
$N$ = rotational speed
N = number of vortices
$p$ = static pressure
$p^*$ = relative pressure, $= p - (p_0 + \rho V_0^2/2)$
$Q$ = flow rate per unit passage width
$Q_r$ = rated flow rate
$q$ = source strength at volute casing outlet
$R, r$ = radius
$s$ = coordinate along the streamline
$T$ = time passing through one pitch of impeller blade
$t$ = time
$t^*$ = nondimensional time, $= t/T$
$u$ = circumferential velocity
$V$ = absolute velocity
$Z$ = number of blades
$\alpha, \beta$ = angle (see Fig. 1)
$\Gamma$ = circulation, $= \int_{S_1}^{S_2} \gamma^i ds$
$\gamma$ = density of vortex
$\phi$ = coordinate variable along the blade or vane
$\epsilon$ = strength of vortices shed from diffuser vane trailing edge
$\varphi$ = velocity potential
$\Theta$ = angle at relative system (see Fig. 1)
$\theta$ = angle at absolute system (see Fig. 1)
$d\mu$ = vortices element
$\rho$ = fluid density
$\sigma$ = standard deviation of unsteady pressure
$\tau$ = time defined by $\tau(s) = \int_{S_4}^{S} ds/V(s)$
$\Delta\psi$ = nondimensional unsteady pressure, $= \tilde{p}^*/(\rho u_2^2/2)$
$\Delta\psi_{p-p}$ = magnitude of nondimensional unsteady pressure $\Delta\psi$
$|\Delta\psi|$ = amplitude of $\Delta\psi$
$\omega$ = angular velocity of impeller

### Subscripts

0 = reference point
1, 2 = impeller inlet and outlet
3, 4 = diffuser inlet and outlet
$c$ = cosine component
$k$ = $k$th vortex on diffuser vane
$l, m$ = summation indices
$Mt$ = maximum number of $m$
$r$ = radial component
$re$ = relative value (see Fig. 1)
$s$ = sine component
$\theta$ = tangential component

### Superscripts

$d$ = diffuser vane
$f$ = vortices shed from diffuser vane trailing edge
$i$ = impeller
$vc$ = vortices on volute casing wall
$vs$ = sources on volute casing outlet
$\bar{}$ = steady value
$\tilde{}$ = unsteady value

### Abbreviations

DP = pressure side in diffuser
DS = suction side in diffuser

ity induced by the above five kinds of singularities are given by

$$\tilde{V}_r = \tilde{V}_r^i + \tilde{V}_r^d + \tilde{V}_r^f + \tilde{V}_r^{vc} + \tilde{V}_r^{vs} \quad (8)$$

$$\tilde{V}_\theta = \tilde{V}_\theta^i + \tilde{V}_\theta^d + \tilde{V}_\theta^f + \tilde{V}_\theta^{vc} + \tilde{V}_\theta^{vs} \quad (9)$$

**Numerical Procedure for Determining Unknown Coefficients.** In the present numerical procedure, each component of harmonics, $lZ^i\omega$ ($l = 1, 2, \ldots$), will be calculated independently. The diffuser vane vortices can be expressed as a series from $m = 1$ to $m = Mt$ in Eq. (1), in which the unknown coefficients are $A^d_{kslm}$, $A^d_{kclm}$, $B^d_{ksl}$ and $B^d_{kcl}$ ($m = 1, 2, \ldots, Mt$; $k = 1, 2, \ldots, Z^d$) for all the diffuser vanes, and thus the number of unknown coefficients is $2Z^d(Mt + 1)$. The number of singularities on the volute casing is $N^{vc+vs}$, and then the total number of unknown variables for each component of harmonics is $2Z^d(Mt + 1) + 2N^{vc+vs}$. To establish a set of linear equations for the unknown variables, the unknown coefficients are specified from the boundary condition that requires the fluid should flow along the solid surface at the $Mt$ points on the diffuser vane and $N^{vc+vs}$ points on the volute casing. And the continuity condition of unsteady vorticity at trailing edge yields two equations shown in the first report, and thus the $2Z^d(Mt + 1) + 2N^{vc+vs}$ values of the unknown coefficient of unsteady bound singularities are determined.

**Unsteady Pressure Downstream of Impeller.** The unsteady pressure is calculated using the unsteady Bernoulli's equation. The unsteady pressure relative to the total pressure at a reference point is expressed as

$$\tilde{p}^*/\rho = -\bar{V}_r\tilde{V}_r - \bar{V}_\theta\tilde{V}_\theta - (\partial\tilde{\varphi}/\partial t) + (\partial\tilde{\varphi}_0/\partial t) \quad (10)$$

where the time derivatives of velocity potential include the five terms induced by the five kinds of singularities, and are expressed by

$$(\partial\tilde{\varphi}/\partial t) = (\partial\tilde{\varphi}/\partial t)^i + (\partial\tilde{\varphi}/\partial t)^d + (\partial\tilde{\varphi}/\partial t)^f + (\partial\tilde{\varphi}/\partial t)^{vc} + (\partial\tilde{\varphi}/\partial t)^{vs} \quad (11)$$

$$(\partial\tilde{\varphi}_0/\partial t) = (\partial\tilde{\varphi}_0/\partial t)^i + (\partial\tilde{\varphi}_0/\partial t)^d + (\partial\tilde{\varphi}_0/\partial t)^f + (\partial\tilde{\varphi}_0/\partial t)^{vc} + (\partial\tilde{\varphi}_0/\partial t)^{vs} \quad (12)$$

where,

$$(\partial\tilde{\varphi}/\partial t)^i = \frac{Z^i\omega(d\mu^i)}{2\pi} \times \sum_{l=1}^{\infty} (r/r^i)^{-lZ^i} \cos\{lZ^i(\theta - \theta^i(s) + \omega t)\} \quad (13)$$

$$(\partial\tilde{\varphi}/\partial t)^d = \sum_{k=1}^{Z^d} \frac{1}{2\pi} \tan^{-1} \frac{r\sin\theta - r_k^d \sin\theta_k^g}{r\cos\theta - r_k^d\cos\theta_k^d} \frac{\partial\tilde{\mu}_k^d}{\partial t} \quad (14)$$

$$(\partial\tilde{\varphi}/\partial t)^f = \sum_{k=1}^{Z^d} \frac{1}{2\pi} \tan^{-1} \frac{r\sin\theta - r_k^f \sin\theta_k^f}{r\cos\theta - r_k^f\cos\theta_k^f} \frac{\partial\tilde{\varepsilon}_k^f}{\partial t} ds \quad (15)$$

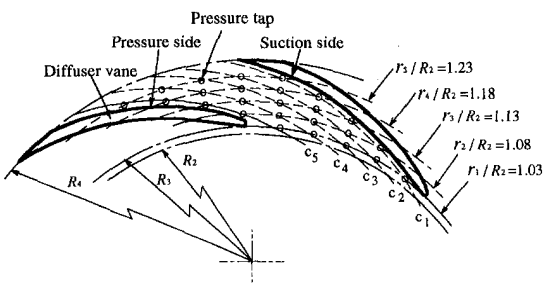


Fig. 3 Pressure measurement stations for a vaned diffuser passage

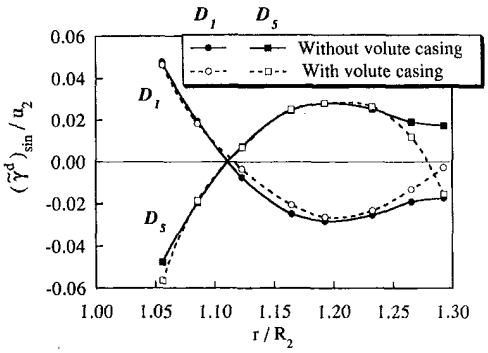


Fig. 4(a) Sine term

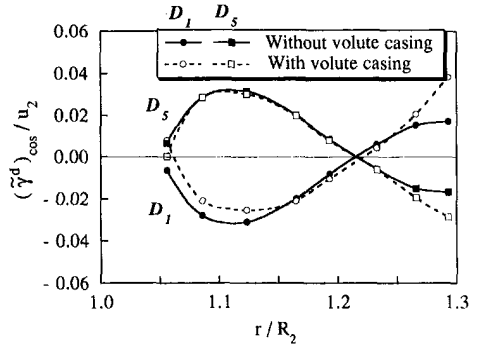


Fig. 4(b) Cosine term

Fig. 4 Effect of volute casing on distribution of the first harmonic of vorticity on diffuser vanes ($R_3/R_2$ = 1.03, $Q/Q_r$ = 1.0)

$$(\partial\tilde{\varphi}/\partial t)^{vc} = \sum_{k=1}^{N^{vc}} \frac{1}{2\pi}(\theta - \theta_k^{vc}) \frac{\partial\tilde{\mu}_k^{vc}}{\partial t} \quad (16)$$

$$(\partial\tilde{\varphi}/\partial t)^{vs} = \sum_{k=1}^{N^{vs}} \frac{1}{2\pi}\{\mathrm{Log}\,(r) - \mathrm{Log}\,(r_k^{vs})\} \frac{\partial\tilde{q}_k^{vs}}{\partial t} \quad (17)$$

The nondimensional unsteady pressure $\Delta\psi$ will be divided in two parts: the dynamic pressure, $(\Delta\psi)_v$ and the impulsive pressure, $(\Delta\psi)_\varphi$. Then Eq. (10) can be rewritten as

$$\Delta\psi = (\Delta\psi)_v + (\Delta\psi)_\varphi \quad (18)$$

where

$$\Delta\psi = (\tilde{p}^*/\rho)/(u_2^2/2) \quad (19)$$

$$(\Delta\psi)_v = (-\bar{V}_r\tilde{V}_r - \bar{V}_\theta\tilde{V}_\theta)/(u_2^2/2) \quad (20)$$

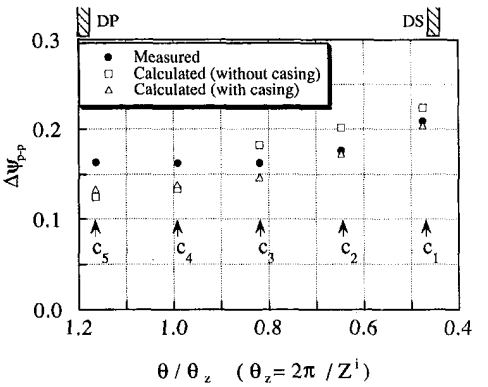


Fig. 5 Effect of volute casing on circumferential distribution of magnitudes of unsteady pressure at a radius of $r_2$ ($R_3/R_2$ = 1.03, $Q/Q_r$ = 1.0); Experimental uncertainty in $\Delta\psi_{p-p}$ = ±7.1 percent

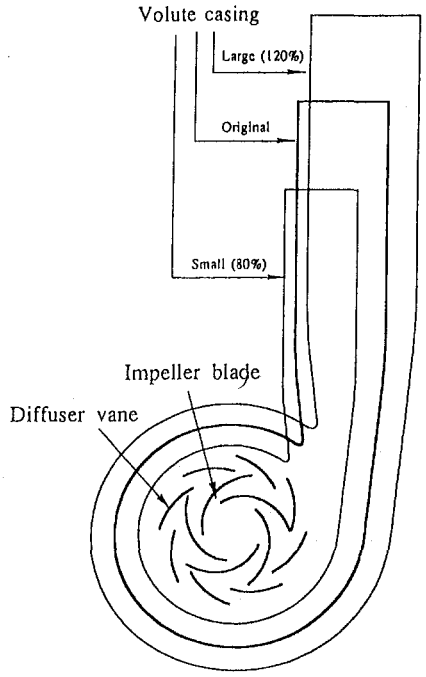


Fig. 6 Schematics of calculated volute casings

$$(\Delta\psi)_\varphi = \{-(\partial\tilde{\varphi}/\partial t) + (\partial\tilde{\varphi}_0/\partial t)\}/(u_2^2/2) \qquad (21)$$

## Discussion

The present calculating method is applied to the same test diffuser pump as the first report and the calculated results are compared with the corresponding experimental data. The calculated and measured unsteady pressures will be shown for the stations in the diffuser passage shown in Fig. 3 and the pressure taps from the $V_1$ to $V_{10}$ on the volute casing illustrated in Fig. 1($b$). The experimental uncertainty in flow rate was found to be within 1.6 percent, and the uncertainty for unsteady pressure was within 7.1 percent at the vaned diffuser passage and volute casing wall (Tsukamoto et al., 1995).

**Effects of Volute Casing.** In order to investigate the influence of volute casing on unsteady pressures, the results calculated by the present method incorporated the volute casing effect are compared with those without the casing effect. Figure 4 shows an example of unsteady vorticity distribution on the diffuser vane. The solid line shows the results without casing effect, and the dotted line does ones with volute casing effect. Figures 4($a$) and ($b$) present the vorticity distribution of *sine* and *cosine* terms of unsteady vortices, respectively, at $t^* = 0.0$ when the geometrical relations of impeller blades to diffuser vanes are shown in Fig. 1.

It can be observed that the phase difference between diffuser vane $D_1$ and $D_5$ is 180 degrees in the case without volute casing. On the other hand, the periodicity in circumferential direction is not kept in the case with volute casing effect, although the effect of the present volute casing is not so significant except at diffuser vane outlet.

Figure 5 shows the circumferential distribution of the magnitude of nondimensional unsteady pressure at a radius of $r_2$ in a passage of diffuser at rated flow rate. In this figure, the triangle, square, and circular marks indicate the calculated results for the case with casing effect, one without casing effect and experimental results, respectively. The circumferential variations of pressure fluctuations are found to be largest near the suction surface of the diffuser vane. It can be also observed that the

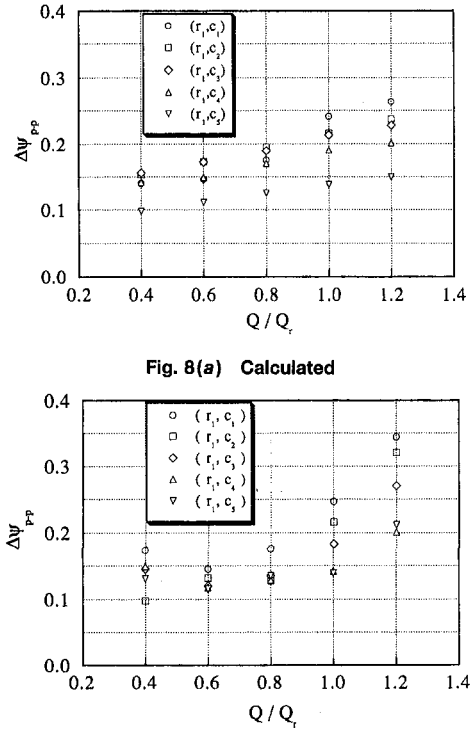


Fig. 8($a$) Calculated




Fig. 8($b$) Measured

Fig. 8 The relation of $\Delta\psi_{p-p}$ at diffuser inlet to flow rate ($R_3/R_2$ = 1.03); Experimental uncertainty in $Q$ = ±1.6 percent and in $\Delta\psi_{p-p}$ = ±7.1 percent

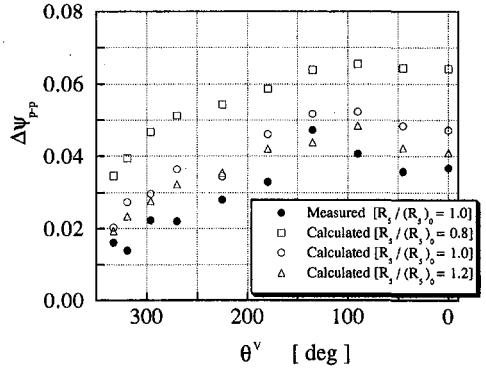


Fig. 7 Effect of volute size on circumferential distributions of magnitudes of unsteady pressures in volute casings ($R_3/R_2$ = 1.03, $Q/Q_r$ = 1.0); Experimental uncertainty in $\Delta\psi_{p-p}$ = ±7.1 percent

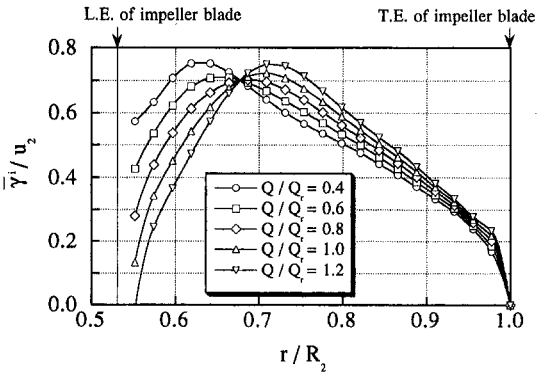


Fig. 9 Dependence of flow rate on distributions of steady vorticity on impeller blades

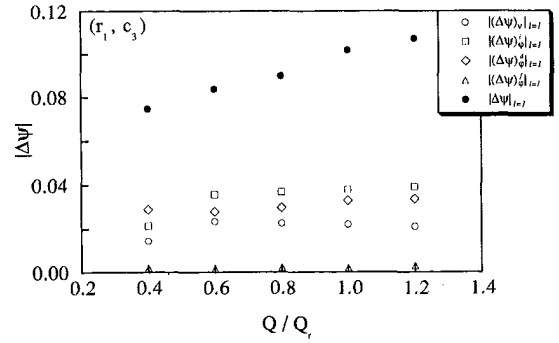


Fig. 10 Variations of individual terms in first harmonic of unsteady pressure at ($r_1$, $c_3$) with flow rate ($R_3/R_2$ = 1.03)

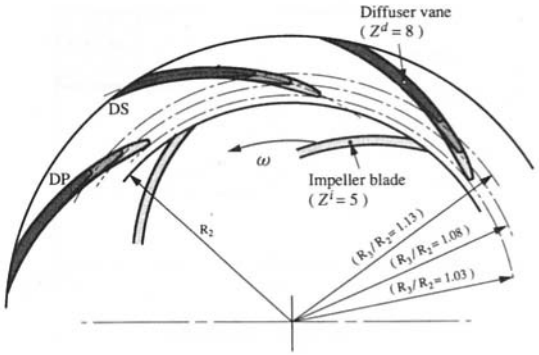


Fig. 11 Schematics of test vaned diffusers

influence of volute casing on unsteady flow is small in the present diffuser vane passage.

Figure 6 illustrates volute casings with the three different sizes. The sizes of the smaller and larger casings are 0.8 and 1.2 times as large as the original one, respectively. In the steady state operational condition, the flow in the volute casing also may be affected by the interaction between impeller blades and diffuser vanes (Tsukamoto et al., 1995). Figure 7 presents the comparison between measured and calculated magnitudes of unsteady pressure $\Delta\psi_{p-p}$ on the three kinds of volute casing. The horizontal axis $\theta^v$ is the angle measured from the cut water along the casing as shown in Fig. 1($b$). The pressure fluctuations on the diffuser pump casing wall are remarkable near the cut water as on the volute pump casing (Imaichi et al., 1980). Calculated results have the same order as the measured ones for the original volute casing, and the magnitude of unsteady pressure is about $\frac{1}{5}$ of the magnitude at the point ($r_1$, $c_1$) near the suction side at the vaned diffuser inlet. Because the unsteady flow in the volute casing depends on the distance between diffuser vane trailing edge and base circle of volute casing, the unsteady pressure on the casing wall increases with the decreasing distance. There are the largest pressure fluctuations in the smaller volute casing, and the value of $\Delta\psi_{p-p}$ at $V_3$ expressed by square symbol is about 130 percent of the value for the original one plotted as a circle.

**Effect of Flow Rate.** Figure 8 presents the distribution of the magnitude of nondimensional unsteady pressure $\Delta\psi_{p-p}$ at the diffuser inlet from ($r_1$, $c_1$) to ($r_1$, $c_5$) for several flow rates. Here, the calculated pressures do not include the volute casing effect. Calculated and measured results have the same tendency which the magnitude of unsteady pressure $\Delta\psi_{p-p}$ increases with the increasing flow rate $Q$ in the case of $Q/Q_r > 0.6$. While the measured $\Delta\psi_{p-p}$ is greater at $Q/Q_r = 0.4$ than that at $Q/Q_r = 0.6$, calculated ones show different tendency. That might be thought to be because the present analysis is based on potential flow analysis, and the present method cannot estimate the complicated unsteadiness in lower flow rate range.

Figure 9 shows the calculated steady vorticity distributions on impeller blade. The distributions of vorticity shift to the trailing edge of impeller blade with increasing flow rate. This means stronger interference effect to downstream of the impeller. Figure 10 shows the contributions of the individual terms of unsteady pressure in Eq. (18) to the first harmonic component at the diffuser inlet ($r_1$, $c_3$). Here, the $(\Delta\psi)_\varphi$ consists of three terms, $(\Delta\psi)^i_\varphi$, $(\Delta\psi)^d_\varphi$, and $(\Delta\psi)^f_\varphi$, which are induced by the three different unsteady vortices, $d\mu^i$, $d\tilde{\mu}^d_k$, and $d\tilde{\mu}^f_k$, respectively.

$$(\Delta\psi)_\varphi = (\Delta\psi)^i_\varphi + (\Delta\psi)^d_\varphi + (\Delta\psi)^f_\varphi \qquad (31)$$

Corresponding to the movement of vorticity on the impeller blades with the increase in flow rate, the terms by the $d\mu^i$ and $d\tilde{\mu}^d$ increase with increasing flow rate. Therefore, the shift of impeller vorticity distributions is the main cause for the increasing unsteady pressure with increasing flow rate.

**Effect of Radial Gap.** It was reported that the radial gaps between impeller blade trailing edge and diffuser vane leading edge are important factor for the unsteady pressure due to the rotor-stator interaction (Arndt et al., 1989, 1990). Calculations were conducted for the three kinds of vaned diffuser with different inlet radii to investigate the effect of gaps between impeller blade trailing edge and diffuser vane leading edge on the unsteady pressure. The specifications and schematics of the test vaned diffuser are shown in Table 1 and Fig. 11, respectively. Calculations were made for the radial gaps of 3, 8, and 13 percent (based on the impeller discharge radius) between impeller discharge and diffuser vane leading edge. Figure 12 shows the calculated and measured magnitudes of unsteady pressure $\Delta\psi_{p-p}$ along the $c_1$ line near the suction side of vaned diffuser. Both calculated and measured $\Delta\psi_{p-p}$ are decreasing with the increase in the radial gap. At the diffuser inlet ($r_1$, $c_1$), the measured $\Delta\psi_{p-p}$ decreases to 55 percent, and calculated one become 30 percent when the radial gaps change from 3 percent to 13 percent. The difference between calculated and measured results is due to the present theoretical method considering only

Table 1 Specifications of test vaned diffusers

| Diffuser no. | Radial clearance $R_3/R_2$ | Inlet angle $\beta_3$ (deg) | Outlet angle $\beta_4$ (deg) | Inlet radius $R_3$ (mm) |
|---|---|---|---|---|
| 1 | 1.03 | 16.97 | 15.44 | 129.0 |
| 2 | 1.08 | 17.49 | 15.44 | 135.0 |
| 3 | 1.13 | 17.59 | 15.44 | 141.0 |

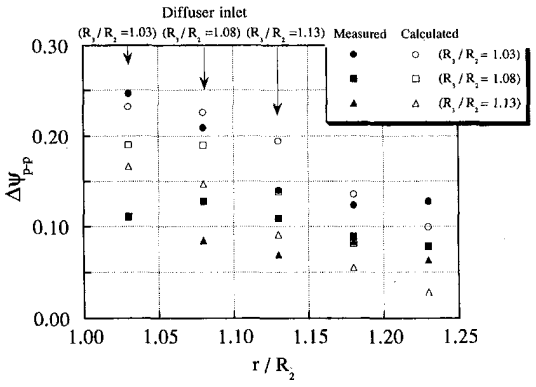


Fig. 12 Effect of radial gap between impeller discharge and diffuser inlet on pressure fluctuation at suction side in diffuser ($Q/Q_r$ = 1.0); Experimental uncertainty in $\Delta\psi_{p-p}$ = ±7.1 percent

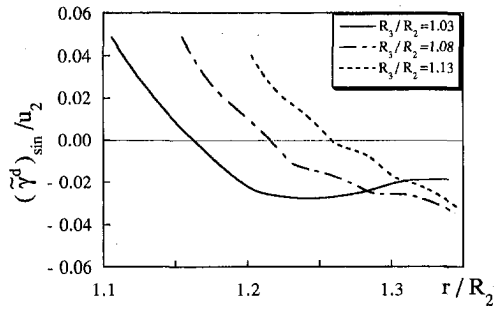


Fig. 13(*a*) Sine term

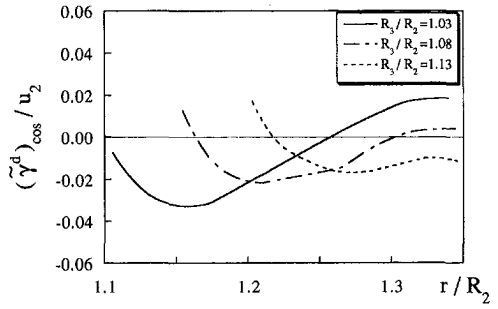


Fig. 13(*b*) Cosine term

**Fig. 13 Variation of unsteady vorticity distributions on diffuser vanes with radial gap between impeller discharge and diffuser inlet ($Q/Q_r$ = 1.0)**

potential interaction. Figure 13 presents the unsteady vorticity $d\tilde{\mu}_k^d$ on the diffuser vane at $t^*$ = 0.0. Because the vorticity distribution shifts to the trailing edge with increasing gap between impeller discharge and diffuser inlet, the interaction between impeller and diffuser is weaken and thus the magnitude of unsteady pressure induced by $d\tilde{\mu}_k^d$ decreases.

## Conclusions

The unsteady pressure downstream of the impeller due to the interaction between impeller blades and diffuser vanes was analyzed for a variety of parameters by using the singularity method incorporated the effect of volute casing. The influence of volute casing on the unsteady pressure in the test vaned diffuser passage is found to be small because of large gap between vaned diffuser and volute casing. Moreover, calculations were carried out to study the effects of flow rate and radial gaps between impeller blade trailing edge and diffuser vane leading edge on the magnitude of unsteady pressure downstream of impeller. As the results of the present study, it was made clear that the magnitude of unsteady pressure $\Delta\psi_{p-p}$ increases with increasing flow rate except lower flow rate range ($Q/Q_r < 0.6$), in both calculated and measured pressures. And the magnitude $\Delta\psi_{p-p}$ decreases 50 percent in measured pressure and 30 percent in calculated one near the suction side at diffuser inlet, when the gap between impeller discharge radius and diffuser inlet radius is increased from 3 percent to 13 percent.

## Acknowledgments

The investigations were carried out in the Department of Mechanical Engineering of Kyushu Institute of Technology and this work was a portion of the first author's dissertation. The authors wish to express their gratitude to Messrs. T. Ito and J. Asakura for their assistance in the preparation of this paper.

## References

Arndt, N., Acosta, A. J., Brennen, C. E., and Caughey, T. K., 1989, "Rotor-Stator Interaction in a Diffuser Pump," ASME *Journal of Turbomachinery,* Vol. 111, pp. 213–221.

Arndt, N., Acosta, A. T., Brennen, C. E., and Caughey, T. K., 1990, "Experimental Investigation of Rotor-Stator Interaction in a Centrifugal Pump With Several Vaned Diffusers," ASME *Journal of Turbomachinery,* Vol. 111, pp. 213–221.

Brennen, C. E., 1994, *Hydrodynamics of Pumps, Concepts* ETI, Inc. and Oxford University Press, pp. 196–204.

Imaichi, K., Tsujimoto, Y., and Yoshida, Y., 1980, "A Two-Dimensional Analysis of the Interaction Effects of Radial Impeller in Volute Casing," *Proceedings of the 10th IAHR Symposium,* Tokyo, Vol. 1, pp. 635–647.

Kemp, N. H., and Sears, W. R., 1953, "Aerodynamic Interference Between Moving Blade Rows," *Journal of the Aeronautical Sciences,* Vol. 20, No. 9, pp. 585–597.

Qin, W., 1995, "Pressure Fluctuations Downstream of Impeller Due to Rotor-Stator Interaction in a diffuser Pump," Ph.D. thesis, Department of Mechanical Engineering, Kyushu Institute of Technology (in Japanese).

Qin, W., and Tsukamoto, 1997, "Theoretical Study of Pressure Fluctuations Downstream of a diffuser Pump Impeller—Part 1: Fundamental Analysis on Rotor-Stator Interaction," ASME JOURNAL OF FLUIDS ENGINEERING, published in this issue pp. 647–652.

Tsukamoto, H., Uno, M., Hamafuku, H., and Okamura, T., 1995, "Pressure Fluctuation Downstream of a Diffuser Pump Impeller," The 2nd Joint ASME/JSME Fluids Engineering Conference, Forum of Unsteady Flow, FED-Vol. 216, pp. 133–138.

# Development and Optimization of Screw Machines With a Simulation Model—Part I: Profile Generation

**N. Stošić**
Professor,
Department of Mechanical Engineering and Aeronautics,
City University,
London EC1V OHB, U.K.

**K. Hanjalić**
Professor,
Faculty of Applied Physics,
Delft University of Technology,
Lorentzweg 1, 2628 CJ Delft,
The Netherlands

*This paper presents a method for the design of twin screw compressors and expanders, which is based on a differential algorithm for defining the rotor profiles and an analytical model of the fluid flow and thermodynamic processes within the machine. Part I of the paper describes the algorithm for screw rotor profile generation. It demonstrates the conjugacy condition which, when solved explicitly, enables a variety of primary arcs to be defined either analytically or by discrete point curves. Its use greatly simplifies the design since only primary arcs need to be specified and these can be located on either the main or gate rotor or even on any other rotor including a rack, which is a rotor of infinite radius. Secondary arcs are then generated automatically from this. By such means any profile combination may be considered. The most efficient were obtained from a combined rotor-rack generation procedure. An example of this combination is given which produces a rotor profile with stiff lobes and a higher throughput than any other known type. Part II describes a mathematical model of the compression and expansion processes within positive displacement machines which has been well proven in its use for the design of reciprocating and screw compressors and screw expanders.*

## Introduction

Screw machines are used today as both compressors and expanders. They operate with a variety of working fluids which may be gases, dry vapors, or multi-phase mixtures with phase changes taking place within the machine. Their mode of operation may be without internal lubrication, oil flooded, or with other fluids injected during the compression or expansion process. The rotor configuration and profile, as well as operating conditions required for optimum performance, are highly dependent on the machine application. Hence, there is no universal rotor profile and configuration or set of working parameters, which will produce an optimum design in all cases, even for a restricted class of machine. It follows that a set of well-defined criteria governed by an optimization procedure is a prerequisite for achieving the best performance for each application. Such guidelines are also essential for further improvement of existing screw machine designs, and broadening the range of their use.

Modern twin screw machines evolved almost exclusively from the patents of Alf Lysholm, which were commercialized by the Swedish company Svenska Rotor Maskiner (SRM) and virtually all the original manufacturers of these machines relied on the licensors to supply details of the rotor design. SRM did not publicize their design techniques and, as a result, there were very few west European and U.S. publications on rotor profiling until comparatively recently. Most of these were limited in scope since their authors were mainly employees of compressor manufacturing companies who were unwilling to reveal proprietary know how.

In contrast to this, three classical screw compressor textbooks were published in Russian where, presumably since there were no patent licensing agreements with western companies, there was a need to evolve design procedures from first principles. Sakun (1960) gives a full derivation of circular, elliptic, and cycloidal rotor lobe profile generation and, most importantly, a reproducible presentation of an asymmetric profile later named SKBK. The profile generation principle of this book is based on an envelope approach, which is also the basis of the procedure presented in this paper. Andreev (1961) effectively repeated Sakun's work on profiles to which he added his own contribution on rotor tool profile generation. 17 years later, Amosov et al. (1977) republished Sakun's profiles to which he added the first presentation in the open literature of a reproducible method for generating the classic SRM asymmetric and Lysholm profiles. Where available, these books have been translated privately into German or English.

Two textbooks were published in German: Rinder (1979) presented a profile generation method based on gear theory to reconstruct the SRM asymmetric profile 10 years after it was patented. Konka (1988) published some engineering aspects of screw compressors, but hardly described profiling procedures. Rinder's book has also been privately translated into English. There are two textbooks in English dealing partly with screw compressors: O'Neill (1993) on industrial compressors, and Arbon (1994) on rotary twin shaft compressors, but none makes sufficient mention of rotor profiling procedures, even for use as a general guide.

There are a few compressor manufacturers' handbooks on screw compressors and a number of brochures giving useful information on them, but they are either classified or available only for licencees.

There is an unusually large number of patents dealing with various aspects of screw compressors and especially their profiles. The SRM 1946 (symmetric), 1970 (unsymmetric), and 1982 ("D") profiles are classic examples, but rotor profiling patents by other companies were also highly successful. All profiles described in the patents were generated by a legitimate procedure, but insufficient information is given to make them readily reproducible.

Not surprisingly, there are few publications on screw machines in engineering journals apart from Lysholm's papers of

Contributed by the Fluids Engineering Division for publication in the JOURNAL OF FLUIDS ENGINEERING. Manuscript received by the Fluids Engineering Division January 4, 1996; revised manuscript received January 12, 1997. Associate Technical Editor: P. M. Sockol.

1942 and 1966, and even these do not refer to either the profiling method used or Lisholm's description of the profiling principles by which the blow-hole area may be reduced. An exception was Margolis (1978), who reproduced a symmetric circular profile three decades after it had been patented.

There are three regular conferences which deal exclusively or partly with screw compressors. These are the Purdue University Biennial Compressor Technology Conference in the USA, the IMechE Conference on Industrial Compressors in the U.K., and the "VDI Schraubenkompressoren Tagung" in Germany. Despite the abundance of screw machine papers to be found in their proceedings, few of them give much information on rotor profiling. Typical of these are the frequently cited publications of Singh and Onuschak (1984) and Singh and Schwartz (1990) also Peng and Xing (1990) Tang and Fleming (1992), and Stošić and Hanjalić (1994) from which a reader will gain little on profile generation. Zenan (1984), Xion and Dagang (1986), and Zhang and Hamilton (1992) indicate that they used an envelope theory to calculate some geometry features of their rotors. Only Rinder (1984), gives a clear exposition with a presentation of the rack generation procedure based on the theory used in his earlier book.

Textbooks on gear tooth generation, like that of Buckingham (1963), give useful background to screw rotor profiling, but all of them are limited to the gear conjugate action condition for specific gear form cases. Earlier and more fundamental analytical theory on gear tooth profiling based on an envelope approach was published in Russian as long ago as 1886 by Gohman, and recommended by Litvin (1956). Additional supplementary literature can be found in differential geometry textbooks which present an envelope of a family of curves, but it is still in a form requiring further elaboration for profiling purposes. An example of these is in Guggenheim (1963).

The restricted access to fundamental information was a major reason for the publication of the rotor profiling procedure given in this paper. It is based on Sakun's work, which the authors have significantly extended. In addition, the presented method offers several novelties in approach, making it simpler, more concise, and yet more general than most methods available in literature. The method has proved suitable for easy computer generation of a variety of screw profiles for engines with different duties and applications.

## Screw Rotor Profiling Methods

The conjugacy condition for gear tooth engagement is given in the majority of gear textbooks. It states that the common normal to the profiles at a point of contact contains a pitch point. If this condition is used in screw rotor profile generation, rotor profiles are generated in two stages: first, by choice of an appropriate curve on one of the rotors and second, by use of the conjugate condition requirement to produce a curve on the oposite rotor.

It is obvious that all circles with their centers on the pitch circles meet both these requirements unconditionally. This is also true for circles with their centers on the rotor axes. Circles with other centers and curves, like ellipses, parabolae, and hyperbolae require more elaborate curves as counterparts on the other rotor. Also, points located on one rotor will form epi- or hypocycloids on the other rotor.

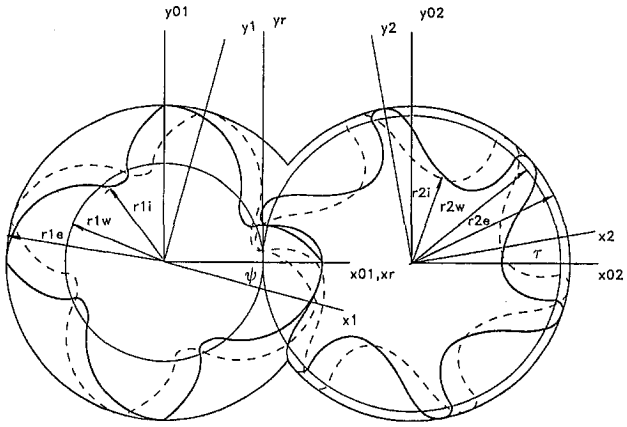


**Fig. 1 A screw rotor pair: definitions and symbols**

Symmetric circular profile rotors are comprised only of circular arcs with centers on pitch circles. Lysholm's first asymmetric profile was derived by the use of a set of cycloids on the high pressure side, apart from the pitch circle centered circles. Later, the SRM unsymmetric profile employed an offset circle on the low pressure side of the gate rotor. The SKBK profile introduced the same on the main rotor. In both cases, the evaluated curves were given analytically. The SRM "D" profile consists exclusively of circles, all of which are eccentrically positioned on the main or gate rotor. All patents which followed gave primary curves for one rotor and evaluated secondary curves for the other in analytical form, all presumably based on derivations of the basic conjugacy requirement or some other similar condition.

Complementary to the gearing practice, Sakun (1960), referring Gohman's theory, claims that an envelope of parametric curves of arcs on one rotor forms mating arcs on the other rotor which is consistent with the more general requirement of conjugacy: two surfaces are conjugate if each generates or envelopes the other under a specified relative motion. The theory itself is simple and it may be expressed for the planar case as follows:

The main and gate rotors, as indicated by numbers 1 and 2, respectively, in Fig. 1, roll on their pitch circles about their centers $O_1$ and $O_2$ by angles $\psi$ and $\tau = (z_1/z_2)\psi = \psi/i$. A primary arc is defined as an arbitrary function of an angular parameter $\phi$ as follows:

$$x_d = x_d(\phi) \tag{1}$$

$$y_d = y_d(\phi) \tag{2}$$

The secondary arc on another rotor is a function of $\phi$ and $\psi$

$$x = x(\phi, \psi) = -a \cos \frac{\psi}{i} + x_d \cos k\psi + y_d \sin k\psi \tag{3}$$

$$y = y(\phi, \psi) = a \sin \frac{\psi}{i} - x_d \sin k\psi + y_d \cos k\psi \tag{4}$$

## Nomenclature

$a$ = rotor center distance $a = r_{1w} + r_{2w}$
$i$ = lobe number ratio $i = z_2/z_1$
$k$ = ratio $k = 1 + 1/i$
$r$ = rotor radii
$x$ = coordinate
$y$ = coordinate
$z$ = number of lobes
$\psi$ = rotation angle of the main rotor
$\phi$ = angular parameter
$\tau$ = rotation angle of the gate rotor

**Subscripts**

$d$ = defined
$e$ = external
$i$ = internal
$r$ = rack
$w$ = rolling pitch
1 = main rotor
2 = gate rotor

where $\psi$ represents the value of the rotation angle of the main rotor at which the primary and secondary arcs have a contact point. This angle must satisfy the conjugacy condition:

$$\frac{\partial x_d}{\partial \phi}\frac{\partial y_d}{\partial \psi} - \frac{\partial x_d}{\partial \psi}\frac{\partial y_d}{\partial \phi} = 0 \tag{5}$$

which is a differential equation of an envelope of "d" curves. The expanded form is:

$$\frac{\partial y_d}{\partial x_d}\left(\frac{a}{i}\sin\psi - ky_d\right) - \left(-\frac{a}{i}\cos\psi + kx_d\right) = 0 \tag{6}$$

Sakun's practice was to insert convenient primary arcs such as circles, ellipses, or single points into Eq. (6) to obtain analytical functions $\psi = \psi(\phi)$ which, introduced into (3) and (4), give secondary arcs as analytical functions of only one independent parameter $\phi$. Amosov (1977) used the identical approach. As the basic requirement of gear conjugacy is retained in this procedure, it may be used as an effective means for the production of screw rotor and gear tooth profiles.

## Extensions of the Method

The method presented in the previous section additionally contains some advantages which were not previously recognized. It is possible to start with the explicit analytical or numerical solution for Eq. (6) and to introduce numerical values thus calculated into Eqs. (3) and (4) rather than an analytical function. It means that secondary arcs are generated automatically once the primary arcs are specified. By this means the design process is significantly simplified and the effort required to design the rotors is greatly reduced. Also, the range of primary arc curves which may be used is not restricted only to those which result in the analytical conjugacy condition. Since the primary arcs can be derived from numerical data, any analytical function or even a discrete point function can also be used to define them.

Finally, since all equations are independent of the coordinate system in which they are expressed, it is possible to define primary arcs as "d" curves using a coordinate system which is independent of both rotors. By this means, in many cases the defining equations may be simplified. Also, the use of one coordinate system to define all the curves further simplifies the design process. Typically, the template shown by a dashed line in Fig. 2 is specified in a rotor independent coordinate system. The same equations are valid for a rotor of infinite radius which is the rack described by "$r$" in Fig. 1. From the primary arc given on the rack, a secondary arc on some of the rotors is obtained by the same procedure. The rack is also shown in Fig. 2 by a dotted line.

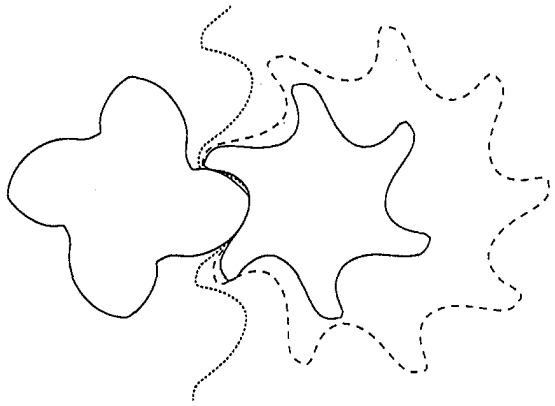

**Fig. 2 View of a pair of "N" rotors: solid—actual rotors, dashed—template rotor, dotted—rack**

In addition to the convenience of relating all curves to one coordinate system only, when compared with rotor profile generation, a rack formed rotor profile offers the following further advantages:

(i) A rack profile is the shortest profile. This means that all points taken from the rack will be transformed onto the rotors without overlaps or other loops.

(ii) Straight lines from the rack will be projected onto the rotors as involutes, ensuring the favorable rotor contact and appropriate rotor-to-rotor torque transfer.

(iii) Rack generated rotors are usually easier to manufacture.

(iv) A single rack generated main rotor can be matched with a range of sizes of gate rotor.

Unfortunately, rack rotor generation has a disadvantage when compared with rotor based profiling methods. In order to ensure tightness and to minimize the blow hole area, rotors should undercut each other on the high pressure side. This practice is widely accepted using either singular points on the main and gate rotors or circles, ellipses and parabolas as alternatives to single points. With rack profile generation there is no means of producing an appropriate undercut directly. With a rack, one analytical curve satisfies the conjugacy criterion for a such tight rotor contact. This is the cycloid developed on the rack which undercuts to form an epicycloid and a hypocycloid on the main and gate rotor, respectively, and which corresponds exactly to a singular point undercut on a rotor generated profile. If other curves are used on the rack, the tightness should be improved and the blow-hole area minimized by taking the outer diameter of the gate rotor significantly less than its pitch diameter. The penalty for this is that it also reduces the rotor throughput, as shown by Rinder (1984). This deficiency is here overcome by generating the high pressure side of a rack by means of a rotor conjugate action which undercuts a single appropriate curve on the rack. Such rack is then used for profiling both the main and gate rotors. The method and its extensions were used by authors to create a number of different rotor profiles, some of them used in Stošić et al. (1986) and Hanjalić and Stošić (1993). One application is described and patented by Stošić (1996).

## Generation of an "*N*" Profile

The following is a brief description of rotor profile, typical for a family of rotor profiles designed for the efficient compression of air, common refrigerants, and a number of process gases. Rotors are generated by the combined rack-rotor generation procedure. Its features are such that it may be readily modified further to optimize performance for any specific application.

The coordinates of all primary arcs on the rack are summarized here relative to the rack coordinate system. The lobe of the rack is divided into several arcs. The divisions between the profile arcs are denoted by capital letters and each arc is defined separately, as shown in Fig. 3 where the rack and rotors are shown. All curves are given as a "general arc" form of the type: $ax^p + by^q = 1$. Straight lines, circles, parabolae, elipses and hyperbolae are all easily described by selecting appropriate values for parameters $a$, $b$, $p$, and $q$.

**Segment E–F** is a circular arc, $p = q = 2$, $a = b$.

**Segment F–G** is a straight line for the upper involute, $p = q = 1$.

**Segment G–H** on the rack is an undercut by the arc $F_2 - H_2$ of type $ax_d^p + by_d^q = 1$, $p = 1$, $q = 0.25$ on the gate rotor.

**Segment H–A** on the rack is an undercut by the arc $A_1 - H_1$ of type $ax_d^p + by_d^q = 1$, $p = 1$, $q = 0.75$ on the main rotor. The rack coordinates $G - H - A$ are obtained through the procedure inverse to (3)–(6).

**Segment A–B** is an arc of the type $ax_d^p + by_d^q = 1$ on the rack with $p = 0.43$ and $q = 1$.

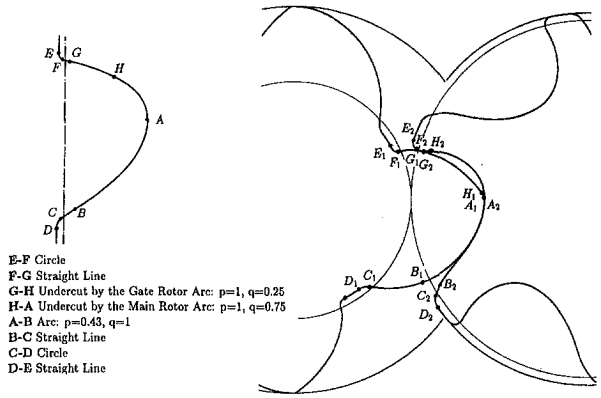


**Fig. 3 "N" rack and rotor profile points**

**Segment B–C** is a straight line on the rack required for the lower involute, $p = q = 1$.

**Segment C–D** is a circular arc on the rack, $p = q = 2$, $a = b$.

**Segment D–E** is a straight line on the rack which completes parts of the rotor inner/outer circles.

## Review of the "N" Profile Characteristics

A variety of modified profiles is possible. The "N" profile design is a compromise between full tightness, small blow-hole area, large displacement, short sealing lines, small confined volumes, involute rotor contact, and proper gate rotor torque distribution together with high rotor mechanical rigidity.

The number of lobes required varies according to the designated compressor duty and three configurations are shown in Fig. 4. The 3/5 arrangement is most suited for dry air compression, the 5/6 for oil flooded moderate pressure difference compression and the 6/7 for high pressure and large built-in volume ratio refrigeration applications.

Although the full evaluation of a rotor profile requires more than just a geometric assessment, some of the key features of the "N" profile may be readily appreciated by comparing it with three most popular screw rotor profiles which were defined (*a*) by Bammert (1979), (*b*) Astberg (1982), and (*c*) by Hough and Morris (1984). All rotors are shown in Fig. 5 where it can be seen that the "N" profiles have a greater throughput and a stiffer gate rotor for all cases where other characteristics such as blow-hole area, confined volume and high pressure sealing line lengths are identical in the designs compared. Also, the low pressure sealing lines are shorter, but this is less important because the corresponding clearance can be kept small.

The blow-hole area may be controlled by adjustment of the tip radii on both the main and gate rotors and also by making the gate outer diameter equal to or less than the pitch diameter. Also, sealing lines can be kept very short by constructing most of the rotor profile from circles whose centers are close to the pitch circle. But, any decrease in the blow-hole area will increase the length of the sealing line on the flat rotor side. A compromise between these trends is therefore required to obtain the best result. In Fig. 6 two rotors are presented, the first with a short sealing line but a large cusp blow-hole area and the other with the longer sealing line but a smaller blow-hole.

Rotor instability is often caused by the torque distribution in the gate rotor changing direction during a complete cycle. The profile generation procedure described in this paper makes it possible to control the torque on the gate rotor and thus avoid such effects. Furthermore, full involute contact between the "N" rotors enables any additional contact load to be absorbed more easily than with any other type of rotor. Two rotor pairs are shown in Fig. 7, the first exhibits what is described as "negative" gate rotor torque while the second shows the more usual "positive" torque.

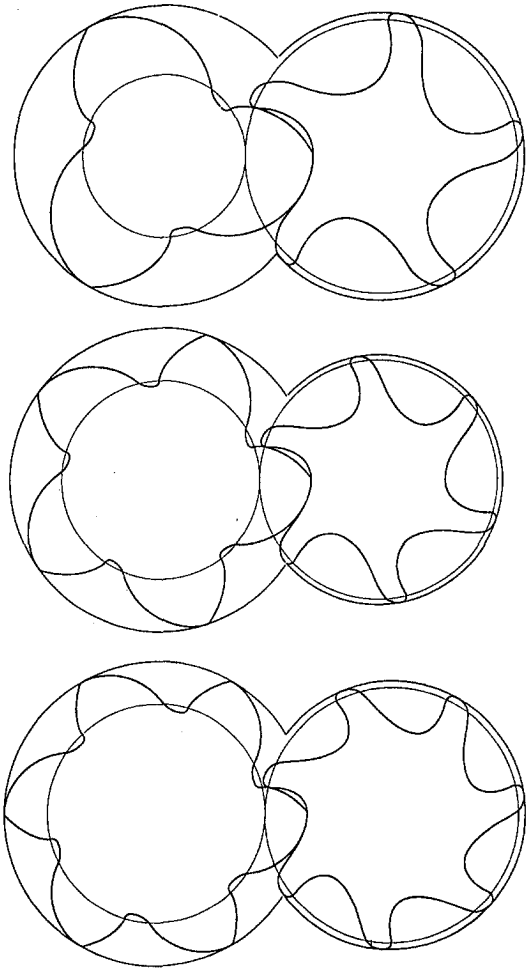

**Fig. 4 "N" profile: 3/5 for dry air compression, 5/6 for oil flooded air compression, and 6/7 for heavy duty refrigeration**

## Conclusions

A method for a screw rotor profile generation used by the authors for a long time to generate screw rotor profiles has been demonstrated. It is convenient both for the design of new rotors and the improvement of existing designs. Also, an extension to the rack based procedure has been used to generate a higher

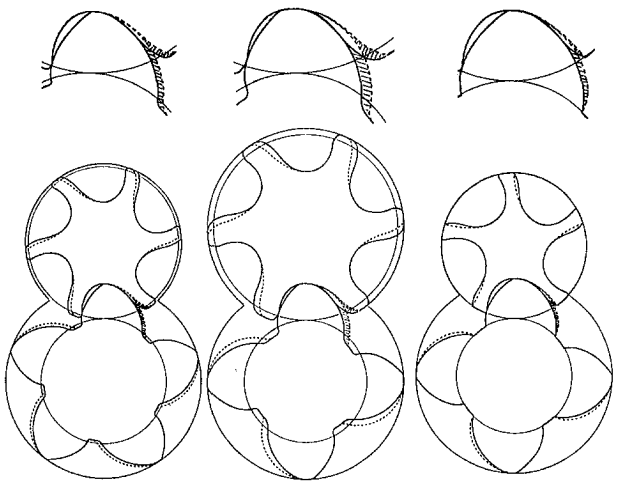

**Fig. 5 "N" profile (solid) compared with (*a*) Bammert (1979), (*b*) Astberg (1982), and (*c*) Hough and Morris (1984)**

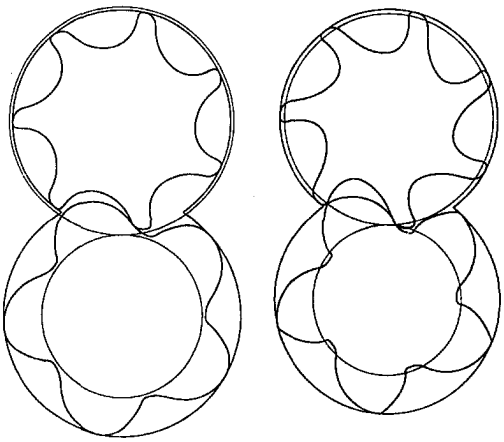

**Fig. 6 "N" rotors: (*a*) Shorter sealing line/large blow-hole, (*b*) longer sealing line/smaller blow-hole**

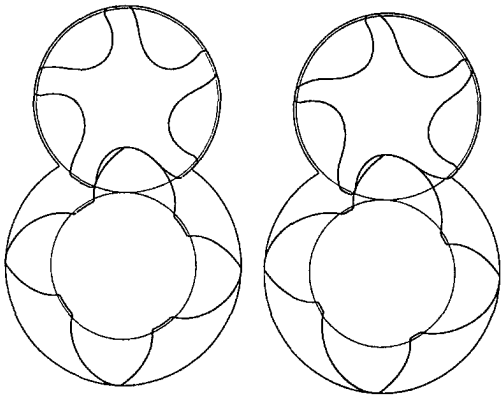

**Fig. 7 "N" Rotors: (*a*) negative torque on gate, (*b*) positive torque on gate**

efficiency profile. The matemathically rigorous method used has the additional advantage of simplicity which enables a variety of profiles to be created in a short time by almost all mechanical engineering designers, whereas at present, such skills are known to only a limited number of exclusive specialists.

## References


Amosov P. E., Bobrikov, N. I., Schwartz A. I., and Vernii A. L, 1977, *Vintovie kompresornie mashinii-Spravochnik* (*Screw Compression Machines–Handbook*), Mashinstroienie, Leningrad.

Andreev P. A., 1961, *Vintovie kompressornie mashinii (Screw Compression Machines*), SUDPROM Leninngrad.

Arbon, M., 1994, "The Design and Application of Rotary Twin-shfat Compressors in the Oil and Gas Process Industry," MEP London.

Astberg A., 1982: Patent GB 2092676B.

Bammert K., 1979, Patent Application FRG 2911415.

Buckingham E., 1963, *Analytical Mechanics of Gears*, Dover, New York.

Gohman H. I., 1886, *Teoria zaceplenia, obobschenaia i razvitaia putem analiza* (*Theory of Gearing, Generalized and Developed by Analysis*), Odessa, Russia.

Guggenheimer E. W., 1963, *Differential Geometry*, McGraw-Hill, New York.

Hanjalić K., and Stošić N., 1993, SCORPATH—Screw Compressors Rotor Profiling and Thermodynamics, User Manual.

Hough D., and Morris S. J., 1984, Patent Application GB 8413619

Konka K-H., 1988, *Schraubenkompressoren* (*Screw Compressors*) VDI-Verlag, Duesseldorf.

Litvin F. L., 1956, *Teoria zubchatiih zaceplenii* (*Theory of Gearing*), Nauka Moscow, also second edition 1968, also NASA Ref. Publ. 212 AVSCOM Techn. report 88-C-035 1990.

Lysholm A., 1942, "A New Rotary Compressor," *Proc. I. Mech. E.* Vol. 150, p. 11.

Lysholm A., 1966, "The Fundamentals of a New Screw Engine," ASME Paper No 66-GT-86.

Margolis D. L., 1978, "Analytical Modelling of Helical Screw Turbines for Performance Prediction," ASME *Journal of Engineering for Power*, Vol. 100(3) p. 482.

O'Neill P. A., 1993, *Industrial Compressors, Theory and Equipment*, Butterworth-Heinemann, Oxford.

Peng N., and Xing Z., 1990, "New Rotor Profile and its Performance Prediction of Screw Compressor," International Compressor Engineering Conference At Purdue, 18.

Rinder, L., 1979, *Schraubenverdichter* (*Screw Compressors*), Springer-Verlag, New York.

Rinder L., 1984, *Schraubenverdichterläufer mit Evolventenflanken* (*Screw Compressor Rotor with Involute Lobes*), *Proc. VDI Tagung "Schraubenmaschinen 84" VDI* Berichte Nr. 521 Düsseldorf.

Sakun I. A., 1960, *Vintovie kompresorii* (*Screw Compressors*), Mashinostroenie, Leningrad.

Singh P. J., and Onuschak A. D., 1984, "A Comprehensive Computerized Method For Twin Screw Rotor Profile Generation and Analysis," Purdue Compressor Technology Conference, p. 544.

Singh P. J., and Schwartz J. R., 1990, "Exact Analytical Representation of Screw Compressor Rotor Geometry," International Compressor Engineering Conference at Purdue, p. 925.

Stošić N., Hanjalić K., Koprivica J., Lovren N., and Ivanović M., 1986, "CAD of Screw Compressor Elements," *Strojarstvo Journal Zagreb*, Vol. 28, p. 181.

Stošić N., and Hanjalić K., 1994, "Development and Optimization of Screw Engine Rotor Pairs on the Basis of Computer Modeling," *Proc. XVII Conference on Compressor Engineering at Purdue*, p. 55.

Stošić N., 1996, Patent Application GB 9610289.2.

Tang Y., and Fleming J. S., 1992, "Obtaining the Optimum Geometrical Parameters of a Refrigeration Helical Screw Compressor," International Compressor Engineering Conference at Purdue, p. 213.

Xion Z., and Dagang X., 1986, "Study on Actual Profile Surface and Enganging Clearance of Screw Compressor Rotors," Purdue Compressor Technology Conference, p. 239.

Zenan X., 1984, "The Dynamic Measurment and Mating Design of a Screw Compressor Rotor Pair," Purdue Compressor Technology Conference, p. 314.

Zhang L., and Hamilton J. F., 1992, "Main Geometric Characteristics of the Twin Screw Compressor," International Compressor Engineering Conference at Purdue, p. 213.

# Development and Optimization of Screw Machines With a Simulation Model—Part II: Thermodynamic Performance Simulation and Design Optimization

**K. Hanjalić**
Professor,
Faculty of Applied Physics,
Delft University of Technology,
Lorentzweg 1, 2628 CJ Delft,
The Netherlands

**N. Stošić**
Professor,
Department of Mechanical
Engineering and Aeronautics,
City University,
London EC1V OHB, U.K.

*This paper presents a method for the design of twin screw compressors and expanders, which is based on a differential algorithm for defining the rotor profile and an analytical model of the fluid flow and thermodynamic processes within the machine. Part I of the paper presents a method for screw rotor profile generation which simplifies and improves design procedures. An example is given of its use in the development of a new "N" rotor profile, which is shown to be superior to other well-known types. Part II describes a numerical model of the thermodynamic and fluid flow processes within screw machines, which is valid for both the compressor and expander modes of operation. It includes the use of the equations of conservation of mass and energy applied to an instantaneous control volume of trapped fluid within the machine with allowance for fluid leakage, oil or other fluid injection, heat transfer, and the assumption of real fluid properties. By simultaneous solution of these equations, pressure-volume diagrams may be derived of the entire compression or expansion process within the machine. The procedure has been developed over a period of fifteen years and validated with experimental results obtained from both reciprocating and screw compressors and screw expanders, some of which are included. The rotor profile generation processor, thermofluid solver and optimizer, together with preprocessing facilities for the input data and graphical post-processing and CAD interface, have been incorporated into a design package which provided a suitable tool for analysis and optimization of twin screw machine design. An example of its use is given in the optimization of the gate tip radius of a selected compressor design.*

## Introduction

Screw compressors are rotary positive displacement machines of simple design capable of high speed operation over a wide range of operating pressures and flow rates with high efficiencies. They are both reliable and compact and consequently they comprise 80 percent of all positive displacement compressors sold nowadays and 50 percent of those currently in operation. However, their optimum design is very sensitive to the correct selection of a number of parameters which govern the thermodynamic and flow processes within them.

In textbooks such as those of Rinder (1979), Konka (1988), and Arbon (1994), as well as the earlier classical papers on compressors, the compression process is usually described by the assumption of a fixed mass of an ideal gas undergoing an adiabatic or polytropic compression in which the pressure-volume relationship is of the form $pV^n$ where $n$ is a constant or variable exponent. This is adequate only when leakage rates are very low; there is no fluid injection during the compression process and the working fluid is highly super-heated and far from the saturated vapor phase. In the case of screw compressors, internal leakage can be up to 40 percent of the bulk discharge flow, oil, and other fluids may be injected in large quantities, and wet vapors may be compressed, or even liquids expanded. Under these circumstances, a compression or expansion process is better described by means of an open system through which fluid may flow by admission, discharge, and leakage processes. These, in turn, are described by the equations of conservation of mass, momentum, and energy together with the transport equations which may be integrated numerically for a succession of rotor positions. This was recognized at an early stage in the development of techniques of analysis and Sakun (1960) made a good start to this approach. Soedel (1972) and Hamilton (1974) brought further understanding to positive displacement compressor processes in their compressor short courses at Purdue University using differential equations with temperature and pressure as the derived variables.

Mathematical modeling and computer simulation of compressor operation have now reached such a stage that much of the traditional trial-and-error experimental approach to design, still widely used in the compressor industry, is no longer necessary. Unfortunately, many computer models reported in the open literature differ in their assumptions and in the mathematical level at which various phenomena are modeled, while many have been inadequately verified by experiment. This has led to significant differences in the predictions made by the various models. Nonetheless, such models have evolved greatly during the past ten years. Their potential is so great that there is little doubt that as they become better validated, they are becoming an essential design tool and their use is likely to lead to further

Contributed by the Fluids Engineering Division for publication in the JOURNAL OF FLUIDS ENGINEERING. Manuscript received by the Fluids Engineering Division January 4, 1996; revised manuscript received January 12, 1997. Associate Technical Editor: P. M. Sockol.

improvements in machine performance. Confirmation of this is given by Fujiwara and Osada (1990), Jonsson (1990), and Sauls (1994).

Mathematical modeling started with the analysis of reciprocating compressors by Benson (e.g., Benson and Ucer, 1972; MacLaren et al., 1975; and Stošić and Hanjalić, 1977), but was extended to screw compressors by Fujiwara et al. (1984) and Sangfors (1984). The present authors modified the approach to use internal energy as the derived variable rather than temperature and pressure, as shown by Stošić et al. (1986). When this was used in conjunction with an effective equation of state for real fluids they were able to predict pressure changes accurately for various applications, as described by Stošić et al. (1988), (1989). Tang and Fleming (1992) and Fleming et al. (1994) used the same approach in their thorough studies of refrigeration screw compressors.

On the assumption that successful computer models should be readily accessible to designers and engineers, as well as specialists, the authors have developed a suite of subroutines for the purpose of screw machine design, Hanjalić and Stošić (1993). This provides facilities for generating new profiles and predicting thermodynamic processes in the machine and the results obtained from it have been verified by extensive comparison with laboratory measurements of the cyclic variation of all important local and bulk properties in screw compressors and expanders. The computational procedure used in it is divided into the following three phases.

(i) The preprocessor generates the lobe profiles and the complete screw-rotor pairs from the algebraically or otherwise prespecified profile curves following the general profiling theory presented in Part I, or by use of a set of user pregenerated points, to give a volume function incorporating all interlobe overlapping and blow hole areas, also sealing lines and leakage gap areas.

(ii) The main program simulates the machine processes by a set of differential equations for the conservation of mass, momentum, and energy which describe the thermodynamic and flow processes in an elementary volume within the screw machine at any angle of rotation or instant of time. The model incorporates relationships which account for most of the effects encountered in a real machine, such as the properties of a real gas-liquid mixture, heat transfer between the fluid and machine rotors and casing, leakages and oil, or other fluid, injection. The integration of the mass and energy equations yields the variation of the pressure and temperature of the gas as a function of the angle of rotation. A pressure-volume relationship is thereby produced, from which the integral compressor characteristics are evaluated. The computer code also contains a set of subroutines for calculating the thermodynamic and fluid properties of a number of different fluids, including most of the new refrigerants.

(iii) The post-processing program supplies all results in tabular and graphical form, together with plots of the rotor pair and machine suction and discharge ports exported in the required format for a CAD facility. All calculations necessary for mechanical design, like bearing forces, shaft and rotor stresses and deflections accompany the package.

The package, or some of its main elements, was used for the extensive calculation and design of positive displacement compressors, mainly of the screw type, and also of screw expanders. In all cases, the same screw rotor profiling technique and the same mathematical model of the thermodynamic and fluid flow process were employed, regardless of the machine duty, or fluid used.

## Modeling Rationale

**Thermodynamics of the Compression-Expansion Process.** A specific feature of the model is the use of the nonsteady flow energy equation with internal energy rather than enthalpy or pressure and temperature as the derived functions. This was found to be computationally more convenient. All the remaining thermodynamic and fluid properties within the machine cycle are calculated from it and the computation is carried out through several cycles until the solution converges.

The following forms of the conservation equations have been employed in the model:

The conservation of internal energy:

$$\omega \frac{dU}{d\psi} = (\dot{m}h)_{\text{in}} - (\dot{m}h)_{\text{out}} + \dot{Q} - \omega p \frac{dV}{d\psi} \tag{1}$$

The fluid total enthalpy inflow consists of the following components:

$$(\dot{m}h)_{\text{in}} = (\dot{m}_{\text{suc}}h_{\text{suc}}) + (\dot{m}_{l,g}h_{l,g}) + (\dot{m}_o h_{o,\text{in}}) \tag{2}$$

The fluid total enthalpy outflow consists of:

$$(\dot{m}h)_{\text{out}} = (\dot{m}_{\text{dis}}h_{\text{dis}}) + (\dot{m}_{l,l}h_{l,l}) \tag{3}$$

the terms of the energy equation may be better appreciated from the following:

$(\dot{m}h)_{\text{in}}$ represents the energy gain due to the gas inflow into the working volume by the mass inflow, and its average enthalpy $\dot{m}_{\text{suc}}h_{\text{suc}}$. As such, the energy inflow varies with the rotational angle. During the suction period gas enters the working volume bringing the gas enthalpy which dominates in the suction chamber. Also, during the process, a certain amount of the

## Nomenclature

$A$ = flow cross-sectional area
$D$ = characteristic length, diameter
$f$ = friction coefficient
$h$ = specific enthalpy, heat transfer coefficient
$M$ = Mach number
$\dot{m}$ = mass flow rate
$p$ = fluid pressure in the control volume (working chamber)
$\dot{Q}$ = heat transfer between the fluid and the compressor surrounding
$R$ = gas constant
Re = Reynolds number
$T$ = fluid temperature in the control volume (working chamber)
$u$ = specific internal energy
$U$ = internal energy
$v$ = specific volume
$V$ = local volume of the compressor working chamber
$w$ = fluid velocity
$x$ = vapor dryness, space variable
$\gamma$ = adiabatic exponent
$\mu$ = "discharge" coefficient
$\omega$ = the main rotor angular velocity
$\psi$ = angle of rotation of the main rotor
$\rho$ = fluid density
$\zeta$ = flow resistance

**Subscripts**

dis = discharge
$g$ = gas
in = inflow
$f$ = liquid
$l$ = leakage
$l, g$ = leakage gain
$l, l$ = leakage loss
$o$ = oil
out = outflow
suc = suction
1 = low pressure side
2 = high pressure side

compressed gas accounted for by $\dot{m}_{l,g}h_{l,g}$ leaks into the compressor working chamber through the clearances. The mass of this gas, as well as its enthalpy, are determined on the basis of gas leakage equations. The total enthalpy inflow is further corrected for the injected oil $\dot{m}_o h_{o,\text{in}}$.

The energy loss due to the gas outflow from the working volume is defined by the product of the mass outflow and its average gas enthalpy $(\dot{m}h)_{\text{out}}$. During the delivery this is $\dot{m}_{\text{dis}}h_{\text{dis}}$. The compressed gas entering the discharge plenum, together with $\dot{m}_{l,l}h_{l,l}$, leaks through the clearances from the working volume into the neighboring space at a lower pressure. In spite of the fact that the oil mass fraction in the mixture is significant, its volume fraction is usually small. The total fluid mass outflow includes the injected oil which remains mixed with the working fluid.

$\dot{Q}$ represents the heat exchange between the fluid and the compressor screw rotors and casing and, through them to the surroundings due to the difference in temperatures of the gas and the casing and rotor surfaces. It is accounted for by convection only. The surface over which the heat is exchanged, as well as the wall temperature and heat transfer coefficient, depend on the rotation angle $\psi$ of the main rotor.

The thermodynamic work supplied to the gas during the compression process is represented by the term $\omega p(dV/d\psi)$. This term is evaluated from the local values of pressure and $dV/d\psi$.

The mass continuity equation:

$$\omega \frac{dm}{d\psi} = \dot{m}_{\text{in}} - \dot{m}_{\text{out}} \tag{4}$$

The mass inflow rate consists of:

$$\dot{m}_{\text{in}} = \dot{m}_{\text{suc}} + \dot{m}_{l,g} + \dot{m}_o \tag{5}$$

The mass outflow rate consists of:

$$\dot{m}_{\text{out}} = \dot{m}_{\text{dis}} + \dot{m}_{l,l} \tag{6}$$

Each of the mass flow rates satisfies the continuity equation

$$\dot{m} = w\rho A \tag{7}$$

The instantaneous density $\rho$ is obtained from the instantaneous mass trapped in the control volume and the size of the corresponding instantaneous volume $V$, as $\rho = m/V$.

The equations of energy and continuity are solved to obtain $U(\psi)$ and $m(\psi)$. Together with $V(\psi)$, the specific internal energy $u = U/m$ and specific volume $v = V/m$ are now known. We can then calculate $T$ and $p$:

$(a)$ For an ideal gas:

$$T = (\gamma - 1)u/R \quad p = RT/v \tag{8}$$

$(b)$ For a real gas (i.e., refrigerant or other):

$$u = f_1(T, v) \quad p = f_2(T, v) \tag{9}$$

These equations are usually uncoupled, with $T$ obtained by numerical solution of the equation set, and $p$ explicitly from the equation of state.

$(c)$ For a wet vapor:

In the case of a phase change during the compression or expansion process, the specific internal energy and volume of the liquid-gas mixture are:

$$u = u_f + x(u_g - u_f), \quad v = v_f + x(v_g - v_f) \tag{10}$$

where the specific internal energy and volume of liquid and gas and a saturation pressure are functions of saturation temperature only. The equations require an implicit numerical procedure. As a result, $T$ and $x$ are obtained. The differential equation of internal energy is in the same form for any kind of fluid, and it is essentially simpler than any other in derived form.

Modeling of processes in a screw machine, based on differential rate equations for mass and energy, ensures, in principle, a reproduction of the the machine thermodynamics and fluid flow. However, its ability to mimic a real process depends strongly on how faithfully the model accounts for accompanying phenomena and effects, which have to be modeled in an approximate manner. Among the most important of these are the fluid and energy losses through the clearances between the rotors and casing, as well as between the main and gate rotors themselves, heat transfer between the fluid and its surroundings, fluid friction losses, real properties of the working fluid, phase changes and interphase transfer in the case of two-phase flows. As equations of conservation of mass and energy are in differential form, it is then possible to define most of the phenomena mentioned as derivative functions of the rotation angle. All these equations may then be integrated simultaneously over the entire compression or expansion cycle.

**Modeling Fluid Leakage.** The clearance flow leakage, $\dot{m}_l$, can be expressed in terms of local variables at a particular position in the machine,

$$\dot{m}_l = \mu_l w_l \rho_l A_l \tag{11}$$

The leakage gas velocity follows from the differential momentum equation, accounting for the fluid-wall friction

$$w_l dw_l + \frac{dp}{\rho} + f\,\frac{w_l^2}{2}\,\frac{dx}{D_e} = 0 \tag{12}$$

where the friction coefficient is dependent on local Reynolds and Mach numbers, as well as the shape of the clearance gap. All variables can be defined locally at any position in the machine as functions of the rotational angle. The model is sufficiently flexible to distinguish between different types of clearances such as the leading and trailing rotor tip-housing, interlobe and the rotor front-housing, and also a variable clearance gap due to discharge coefficients which must be assumed to allow for the variable shapes of each type of clearance.

If the leakage is assumed to correspond to a constant enthalpy throttling process, then the working fluid temperature will vary only slightly and hence its density may be treated as a pressure function only. In that case the continuity equation may be integrated between the high and low pressure sides of the gap to yield

$$\dot{m}_l = \mu_l A_l \sqrt{\frac{p_2^2 - p_1^2}{RT_2[\zeta + 2\ln(p_2/p_1)]}} \tag{13}$$

$\zeta$ can be evaluated for each clearance gap as a function of its dimensions and shape and flow Re and $M$. The full procedure requires the model to include the friction and drag coefficients in terms of Re and $M$ for each type of clearance. Likewise, the working fluid friction losses can also be defined in terms of the local friction factor and fluid velocity related to the tip speed, density, and elementary friction area.

**Oil Injection.** A similar approach was adopted for modeling the oil or other fluid injection and its effects on the gas cooling. Assuming that the oil injection nozzle has known characteristics so that the Sauter mean diameter of the oil droplets can be defined, the rate of change of droplet temperature may be derived from the local heat transfer equation between the oil droplets and gas as

$$\frac{dT_o}{d\psi} = \frac{h_o A_o (T_{\text{gas}} - T_o)}{m_o c_o \omega} \tag{14}$$

where $h_o$ is a heat transfer coefficient between the droplets and gas.

By using local fluid properties for a particular position in the machine at a given rotation angle $\psi$ supplied from separate

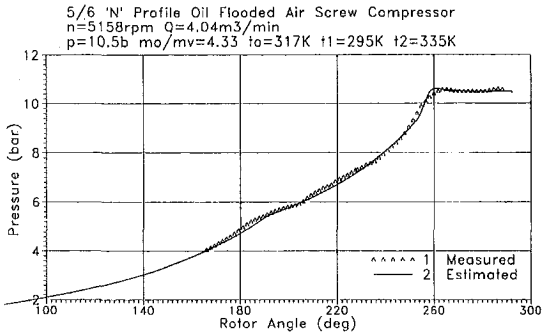


**Fig. 1 $p - \alpha$ Diagram for an oil flooded screw compressor**

subprograms, and incorporating the local values of leakage flows, friction losses and oil-gas interaction, the modeled equations can be integrated to yield the evolution of all thermodynamic and fluid properties as functions of the rotation angle. The derived data can then be further integrated over the cycle to estimate overall machine performance characteristics such as power input or output and volumetric and adiabatic efficiencies.

## Experimental Verification of the Model

Before a mathematical model may be used for performance prediction or design optimization, the assumed models of all flow effects within it must be verified either independently or within the computer program as a whole. In this case, predictions of all significant bulk and local changes within a screw machine were compared with extensive laboratory tests on a twin screw air compressor and two-phase expanders. These were carried out over several years in parallel with the development of the mathematical model until satisfactory agreement was obtained between the predicted and measured results.

There are two levels of data which are to be compared: overall process parameters, such as flow delivery, compressor power and efficiencies, and instantaneous ones and their variation over a cycle, such as fluid pressure, temperature and other thenmodynamic and kinematic properties. The pressure is particularly important since it is used to construct a p-V diagram. The instantaneous parameters are more significant, because if a calculated p-V and T-V diagrams agree with measured ones, the overall parameters are normally well predicted. Conversely, accurate prediction of overall values does not guarantee that the process itself was modeled adequately.

An example of a comparison between experimental and predicted p-V diagrams is given in Fig. 1 for an oil flooded compressor and in Fig. 2 for a two-phase expander. The first experiment was reported earlier (Stošić et al., 1992) and it will suffice here to recall that the instantaneous pressure was recorded by

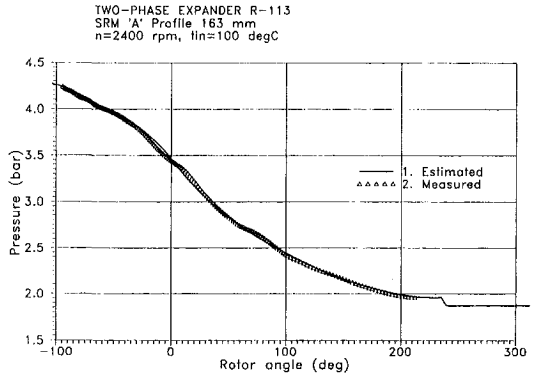


**Fig. 2 $p - \alpha$ Diagram for a two-phase screw expander**

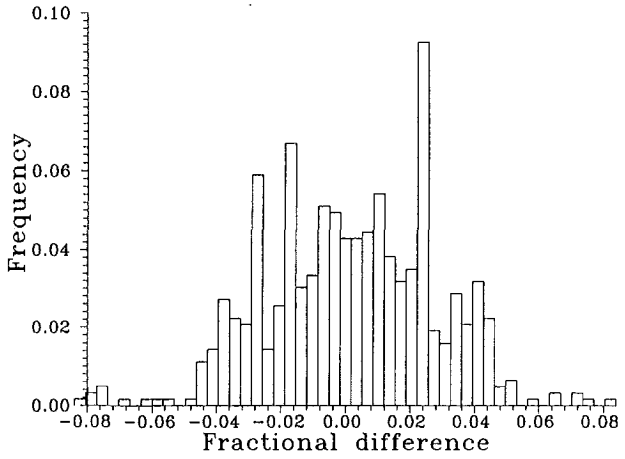


**Fig. 3(*a*)**

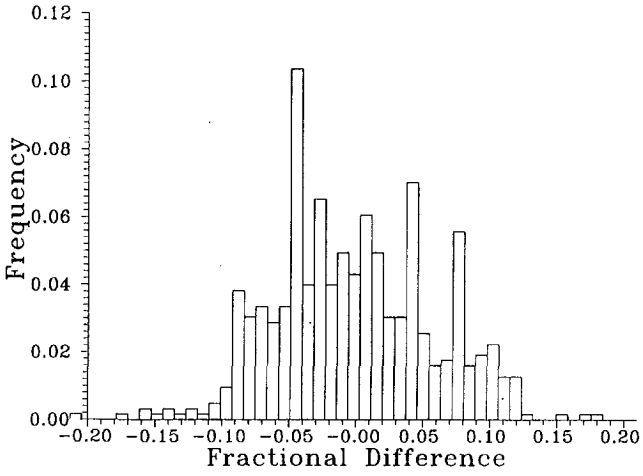


**Fig. 3(*b*)**

**Fig. 3 Fractional difference distribution: A comparison of experimental and calculated data (*a*) power output, (*b*) adiabatic efficiency**

precalibrated Kistler miniature piezoelectric pressure transducers, mounted in the compressor housing. The second experiment, recently reported by Smith et al. (1996), provided valuable information about the pressure variation in a two-phase expander, collected in over 600 tests. The fractional difference between experimental and calculated results is presented in Fig. 3, from which it may be observed that 96 percent have a scatter of less than 6 percent. These include tests on expanders with main rotor diameters of 81.6, 128, 163, 204, and 416 mm and $L/D$ ratios of 1.05, 1.1, 1.28 1.51, and 1.65, built-in volume ratios from 3 to 9.1 and water, R-12 and R-113 as the working fluids.

## The Effect of Rotor Profile on Performance

Screw compressor rotors with circular, SRM unsymmetric, SRM "D" and "N" rotor profiles are shown in Fig. 4. The main and gate rotors have a 4-6 combination and the study was applied to three types of machine; namely, dry air, oil-flooded air, and refrigeration compressors. For each compressor type, a different configuration of "N" profile is shown.

The same operating conditions were assumed for all cases. These are defined by the suction pressure and temperature, and the discharge pressure.

The SRM "D" and the new "N" profiles each produce a visible improvement on the symmetric circular and SRM unsymmetric design. These improvements are illustrated in Figs. 5, 6, and 7 where the estimated adiabatic efficiencies of the

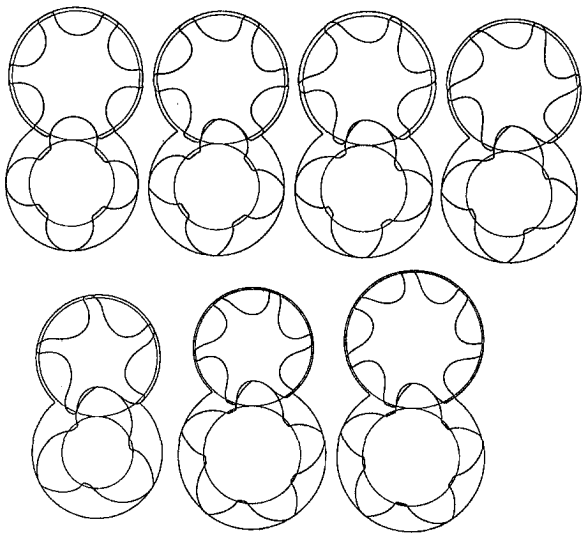

**Fig. 4 Symmetric circular profile, SRM unsymmetric profile, SRM "D" profile, "N" 4-6 profile, "N" 3-5 profile, "N" 5-6 profile, and "N" 5-7 profile**

three types of compressor considered are compared. As may be seen, the efficiency may be improved not only by changing the lobe shape but also by changing the number of lobes. For the particular cases considered here, as is well known, the optimum rotor configuration for the dry air compressor is the 3-5 but for the oil-flooded air compressor the optimum is 5-6, while for the refrigeration system compressor it is the 5-7. More details can be found in Stošić and Hanjalić (1994).

## Profile Optimization

There are several criteria for screw profile optimization which are valid irrespective of the machine type and duty. An efficient screw machine must admit the highest possible fluid flow rates for a given machine rotor size and speed. This implies that the fluid flow cross-sectional area must be as large as possible. In addition, the maximum delivery per unit size or weight of the machine must be accompanied by minimum power utilization for a compressor and maximum power output for an expander. This implies that the efficiency of the energy interchange between the fluid and the machine is a maximum. Accordingly, unavoidable fluid and energy losses must be kept to a minimum. Sometimes, the remedy seems straightforward, as in the case of fluid leakages, which are responsible for major fluid and energy losses. The effects of different parameters on the machine performance are intercoupled. All effects are present and often they exert an opposing influence. The geometry of screw machines is dependent on a number of parameters whose best values to meet specified criteria can, in principle, be determined by a general multi-variable optimization procedure. In practice, it is preferable to restrict the number of parameters to a few, which are known to be the most significant, and restrict the optimization to only them.

An example is given for a compressor since it is more sensitive to the design details than an expander. A dry air compressor

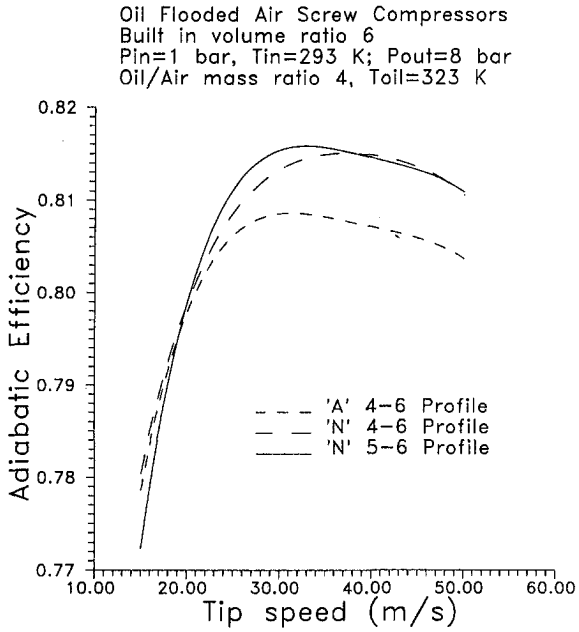


**Fig. 6 Oil flooded air compressor estimated adiabatic efficiency**

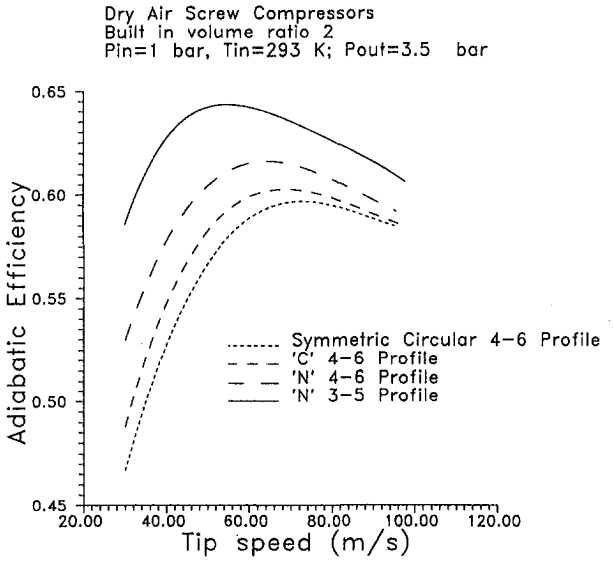


**Fig. 5 Dry air compressor etimated adiabatic efficiency**

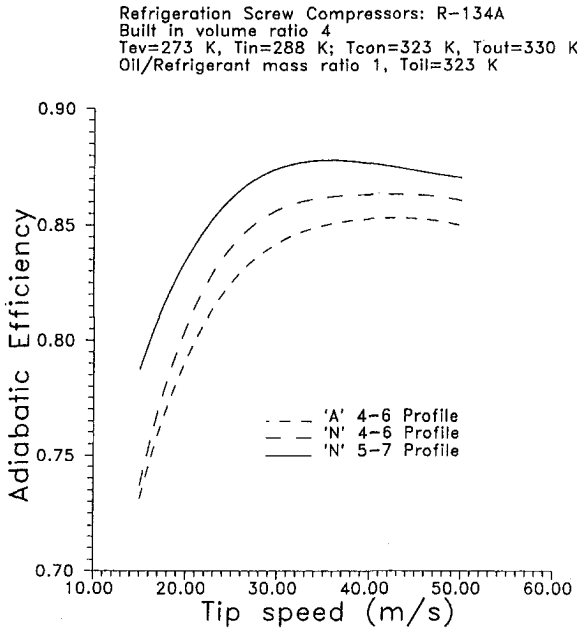


**Fig. 7 Refrigeration compressor estimated adiabatic efficiency**

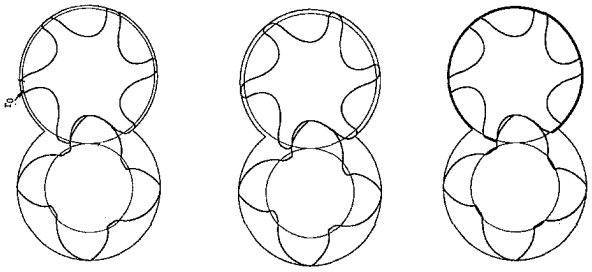

Fig. 8 Rotors of different gate lobe tip radii

was chosen since the process is nearly adiabatic with the relatively large value of the isentropic exponent $\gamma$ close to 1.4. A small, 102 mm diameter compressor with axes 80 mm apart operating at a tip speed of 50 m/s was selected to serve as a basis for the optimization. The inlet conditions selected were, $p_0 = 1.0$ bar and $T_0 = 300$ K to comply with normal compressor practice. A built in volume ratio of 2 was selected to correspond with a discharge pressure $p_d = 3.5$ bar.

As an example, the gate rotor tip radius $r_0$ was considered as the only variable and all other geometric and operating parameters kept constant. If a Lysholm system of cycloids is employed for the high pressure profile side, the size of the blow-hole area is almost directly proportional to the gate tip radius $r_0$ and in order to reduce the blow-hole, $r_0$ should be made as small as possible. Ideally, $r_0$ should be equal to zero or even be "negative" and thus theoretically the blow-hole area would be eliminated. However, reduction in $r_0$ decreases the fluid flow cross-sectional area and the flow rate. Also, rotors with very small values of $r_0$ are difficult to manufacture. Two rotor pairs with tip radii $r_0 = 0.5$ and 3 are shown in Fig. 8 and enlarged view of the rotor tips is shown in Fig. 9.

A series of discrete values of $r_0$ was selected and fed into the preprocessor, thereby generating a corresponding series of different profiles. For each of the profiles, the thermodynamic process was simulated to yield all relevant process parameters. All major parameters were plotted in terms of $r_0$. In the present study, we sought the minimum specific power while duly considering other performance characteristics. The figures which follow show the results of the computations. As shown in Figs. 10 and 11, the compressor power and delivery rate both increase monotonically by approximately 20 percent as $r_0$ is increased from 0.5 mm to 3 mm. Since neither of these parameters are directly proportional to $r_0$, it follows that their ratio should exhibit an extremum corresponding to the optimum solution and this is shown in Fig. 12, as the compressor power per unit delivery rate or "specific power." It should be noted that the computations yielded a smooth variation in a consistent manner

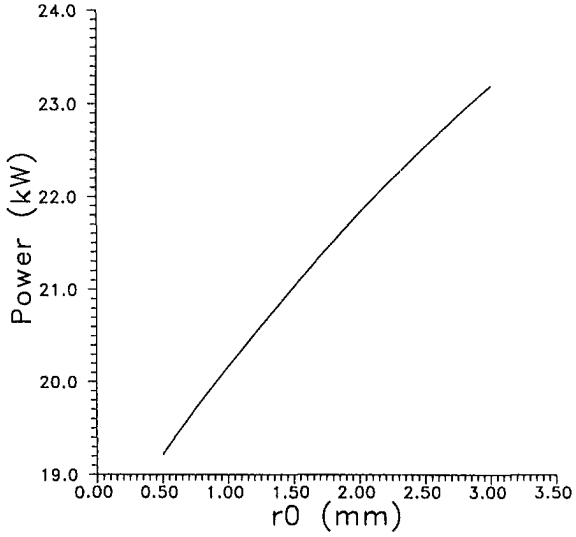


Fig. 10 Power variation with lobe tip radius

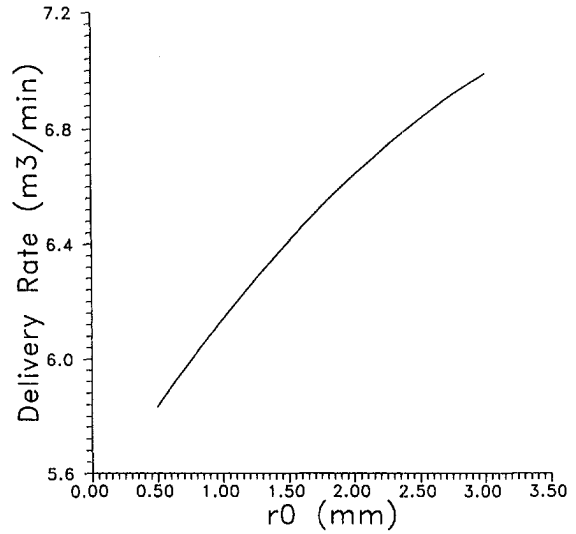


Fig. 11 Delivery variation with lobe tip radius

with a very pronounced minimum at $r_0 = 1.6$ mm, thus indicating the complex effect of the tip radius $r_0$ on the machine efficiency. More details can be found in Hanjalić and Stošić (1994).

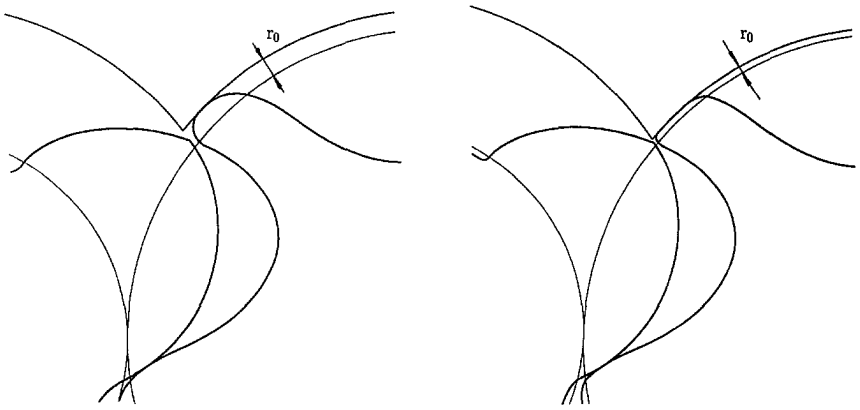


Fig. 9 Various gate lobe tip radii-enlarged

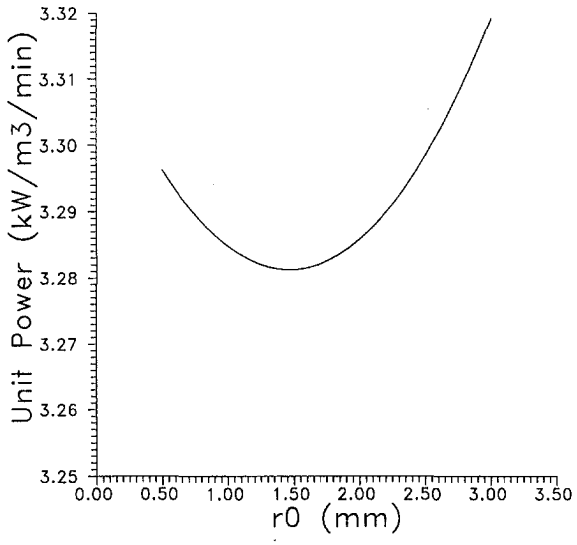


**Fig. 12 Specific power variation with lobe tip radius**

## Conclusions

A computer package, developed by the authors, provides the general specification of the lobe segments in terms of several key parameters, which can generate various lobe shapes, enabling the computation of instant cross-sectional area and working volume in terms of rotation angle. The package contains a mathematical model of the thermodynamic process, as well as models of associated processes encountered in real machines, such as variable fluid leakages, oil flooding or other fluid injection, heat losses to the surrounding, friction losses and other effects, all expressed in differential form in terms of an increment of the rotation angle. Although its use was limited in this case to consideration of the tip radius because of its complex effects upon the screw machine performance, the computer package could be applied to any multi-variable optimization of the machine geometry and its working parameters for defined optimization criteria. Moreover, it has been shown that for each application, a different configuration may be required to achieve optimum performance.

The new "N" profile in 4-6 configuration ensures a higher delivery and a better efficiency for the same tip speed, than other profiles in all applications considered. Still better performance may be achieved with other configurations, such as the 3-5, 5-6, and 5-7, but the effects vary from case to case and depend on the compressor type and duty. The final choice will depend on other factors and a comprehensive cost-effectiveness analysis.

## References


Amosov, P. E. et al., 1977, *Vintovie kompresornie mashinii-Spravochnik, Screw Compression Machines-Handbook,* Mashinstroienie, Leningrad.

Arbon, M, 1994, *The Design and Application of Rotary Twin-shaft Compressors in the Oil and Gas Process Industry,* MEP, London

Benson, R. S., and Ucer, A. S., 1972, "A Theoretical and Experimental Investigation of a Gasodynamic Model for a Single Stage Reciprocating Compressor," *Int. J. Mech. Sci.,* Vol. 14, p. 635.

Fleming, J. S., Tang, Y., Young, P., and Andersen, H. D., 1994, "Leakage Analysis of a Helical Screw Compressor," *Proceedings of Instn. Mech. Engrs.,* Vol. 1.

Fujiwara, M., Matsunaga, T., and Watanabe, M., 1984, "Computer Modeling for Performance Analysis of Rotary Screw Compressor," Purdue Compressor Technology Conference 536.

Fujiwara, M., and Osada, Y., 1990, "Performance Analysis of Oil-Injected Screw Compressors and its Applications," International Compressor Engineering Conference at Purdue 51.

Hamilton J. F., 1974, "Extensions of Mathematical Modeling of Positive Displacement Type Compressors," Purdue Compressor Technology Conference Short Course.

Hanjalić, K., and Stošić, N., 1990, "Development and Optimization of a New Family of Screw Compressors by Computer Modeling," *Mathematical Modeling and Computer Simulation of Processes in Energy Systems,* Hemisphere, New York, p. 329.

Hanjalić, K., and Stošić, N., 1993, "SCORPATH-*S*crew *C*ompressors *R*otor *P*rofiling *A*nd *TH*ermodynamics," *User Manual.*

Hanjalić, K., and Stošić, N., 1994, "Application of Mathematical Modeling of Screw Engines to the Optimization of Lobe Profiles," *Proc. VDI Tagung "Schraubenmaschinen 94",* VDI Berichte Nr. 1135 Dortmund.

Jonsson, S., 1990, "Performance Simulations of Twin-Screw Compressor with Economizer" *International Compressor Engineering Conference At Purdue,* p. 884.

Konka, K.-H., 1988, *Schraubenkompressoren (Screw Compressors),* VDI-Verlag, Duesseldorf.

MacLaren, J. F. T., Tramschek, A. B., Sanjines, A., and Pastrana, O. F., 1975, "A Comparison of Numerical Solutions of the Unsteady Flow Equations applied to reciprocating Compressor Systems," *J. Mech. Engng. Sci.,* Vol. 17, p. 5.

Rinder, L., 1979, *Scraubenverdichter (Screw Compressors),* Springer Verlag, New York.

Sakun, I. A., 1960, *Vintovie kompresorii (Screw Compressors),* Mashinostroenie-Leningrad.

Sangfors, B., 1984, "Computer Simulation of the Oil Injected Twin Screw Compressor," Purdue Compressor Technology Conference 528.

Sauls, J., 1994, "The Influence of Leakage on the Performance of Refrigerant Screw Compressors," *Proc. VDI Tagung "Schraubenmaschinen 94",* VDI Berichte Nr. 1135 Dortmund.

Soedel, W., 1972, "Introduction to Computer Simulation of Positive Displacement Compressors," Purdue Compressor Technology Conference Short Course.

Smith, I. K., Stošić, N., and Aldis, C. A., 1996, "Development of the Trilateral Flash Cycle System Part 3: The Design of High-Efficiency Two-Phase Screw Expanders," *Proc. Instn. Mech. Engrs.,* Vol. 210, p. 75.

Stošić, N., and Hanjalić, K., 1977, "Contribution towards Modelling of Two-Stage Reciprocating Compressors," *Int. J. Mech. Sci.,* Vol. 19, p. 439.

Stošić, N., Hanjalić, K., and Koprivica, J., 1986, "A Contribution Towards the Mathematical Modelling of Screw Compressor Working Process," *Strojarstvo Journal Zagreb,* Vol. 28, p. 95.

Stošić, N., Kovačević, A., Hanjalić, K., and Milutinović, Lj., 1988, "Mathematical Modelling of the Oil Influence upon the Working Cycle of Screw Compressors," *International Compressor Engineering Conference at Purdue,* p. 355.

Stošić, N., Hanjalic, K., Kovačević, a., Koprivica, J., and Marijanović, Z., 1989, "Mathematical Modelling and Experimental Investigation of Refrigeration Screw Compressor Working Process," *Strojarstvo Journal Zagreb,* Vol. 32, p. 17.

Stošić, N., Milutinović, Lj., Hanjalić, K., and Kovačević, A., 1992, "Investigation of the Influence of Oil Injection upon the Screw Compressor Working Process," *Int. J. Refrig.,* Vol. 15, 4, p. 206.

Stošić, N., and Hanjalić, K., 1994, "Development and Optimization of Screw Engine Rotor Pairs on the Basis of Computer Modeling," *Proc. XVII Conference on Compressor Engineering at Purdue,* p. 55.

Tang, Y., and Fleming, J. S., 1992, "Obtaining the Optimum Geometrical Parameters of a Refrigeration Helical Screw Compressor," International Compressor Engineering Conference at Purdue, p. 213.

**K. K. Botros**
Research Fellow,
NOVA Research & Technology Corporation,
Calgary, Alberta, Canada

**G. H. Dunn**
Condition Monitoring Specialist.

**J. A. Hrycyk**
Design Engineer.

NOVA Gas Transmission Ltd.,
Calgary, Alberta, Canada

# Riser-Relief Valve Dynamic Interactions

*The dynamic stability behavior of a typical pilot-operated relief valve has been investigated both numerically and experimentally. The valve piston equation of motion has been solved in connection with the conservation equations of the oscillating flow in the attached riser. The boundary condition at the riser tip is of a choked flow type and had to be given special attention in oscillatory flows. Pertinent quasi-steady flow equations have been formulated to describe the different phases of relief along the piston lift. A model describing the process of pressure relief is described briefly, followed by a parametric study of the effects of various factors on the oscillation levels and characters. Field measurements were taken on an NPS 8 pilot-operated dual-outlet relief valve mounted on a riser assembly of L/D = 15 in a natural gas compressor station.*

## Introduction

Flow-induced piston oscillations of high pressure pilot-operated relief valves have been discerned during the operation of several natural gas compressor stations. Subsequent overhaul and inspection of these valves showed symptoms of galling of the piston and the liner. Piston oscillations, combined with piston lateral forces (due to asymmetry in the flow field around the piston) are suspect and may lead to rubbing, sticking, or in extreme cases, galling. There seemed to be consistent areas of damage where the piston/liner had experienced this phenomenon. These areas were 180 degrees apart in a line perpendicular to the main valve outlets in cases of dual outlet valves, and opposite to the valve outlet in cases of single outlet valves (Dunn, 1991). Figure 1 shows a photo of the damage of the former type valve (Dunn, 1991). A complete metallurgical report (Semeniuk, 1995) indicated that this galling may limit the maximum piston stroke and hence compromises the overpressure protection provided by the relief valve.

The problem of safety relief valve stabilities has been investigated and reported in the literature. Two methods of dealing with this problem have usually been used. Both of the methods deal with the dynamic equations describing the mechanics of the safety valve in connection with the system under consideration. The resulting equations are generally unsolvable by analytical means, and therefore the following two methods have been suggested:

The first applies stability analysis to determine whether a safety valve is dynamically stable or unstable under any set of prevailing conditions. Examples of such analyses are given in (MacLeod, 1985; Krivosheev, 1988; D'Netto and Weaver, 1987; Thomann, 1976), where frictional forces are generally neglected and fluid inertial forces in the attached piping are considered to be insignificant. These assumptions are appropriate for simple gas-filled systems, such as a pressure vessel and a safety relief valve with a short riser.

The second considers the actual response of the valve piston determined from the solution of the dynamic equations in the time domain (Masuda, 1985; Watton, 1983; 1990; Nayfeh and Bouguerra, 1990). Almost all of these reports deal with spring loaded relief type valves. In these analyses, damping can be taken into account in a more rigorous way (Watton, 1983; 1990). Additionally, the effects of non-linearity and frequency response can be obtained from the time domain analysis (Nayfeh and Bouguerra, 1990).

Unfortunately, the above two methods are not readily adaptable to pilot-operated relief valve systems where the pilot supplies process gas to hold the main valve piston seated during normal operation (Foy, 1993). The first stability study of a pilot-operated relief valve connected to a pressure system through a riser was reported by Anderson/Greenwood & Co (Emerson, 1966; Powell, 1971). Here, valve instability was shown to be due to the proximity of the natural frequency of the piston-dome volume system to the acoustic resonance frequency of the riser length. Two riser resonance frequencies were referenced (Powell, 1971), one corresponding to a quarter-wave-length resonance when the valve is closed, and another corresponding to a half-wave-length resonance when the valve is open. Experience reported by Powell (1971) has also shown that an operationally unstable valve can be made stable if

$$0.5 > \omega/\omega_n > 2.5 \qquad (1)$$

In this paper, the dynamic stability behavior of an NPS 8 × 8 × 8 dual outlet pilot-operated relief valve has been studied both numerically and experimentally on a natural gas high pressure compressor station (pressure ~ 6000 kPa). Particular attention has been given to the interaction of acoustics and mechanics in the valves—an area that needs greater design capabilities for application to plant system.

## Relief Process of Pilot-Operated Relief Valves

A pilot-operated safety relief valve design consists of a main valve and a pilot as shown in Fig. 2. The pilot controls the pressure at the top (dome) side of the unbalanced piston, while the bottom side of the piston is exposed to the process gas pressure. At pressures below the set point, the pressures on opposite sides of the piston are equal but because of the larger area on the dome side, the net force is in the seat close direction. When the set pressure is reached, the pilot opens, depressurizes the dome and the unbalanced forces on the piston cause it to stroke upward. When the process pressure decreases below the set point, the pilot closes, the dome is repressurized and the valve piston moves downward to the closed position. For the NPS 8 dual outlet valve used in the present study, the area of the dome side of the piston is 1.4 times larger than the bottom seating area. Therefore, for the valve to open, the pilot must depressurize the dome to a pressure equal to 71 percent of the process pressure.

Four phases of piston stroking can be identified once the process pressure exceeds the set pressure. The corresponding

Contributed by the Fluids Engineering Division for publication in the JOURNAL OF FLUIDS ENGINEERING. Manuscript received by the Fluids Engineering Division March 16, 1996; revised manuscript received February 12, 1997. Associate Technical Editor: Jong H. Kim.

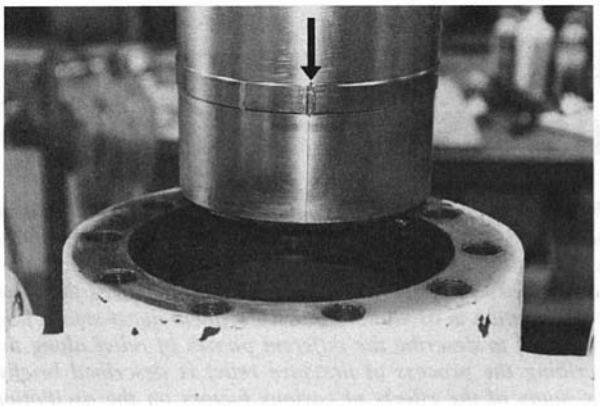

Fig. 1 Location of piston damage due to galling

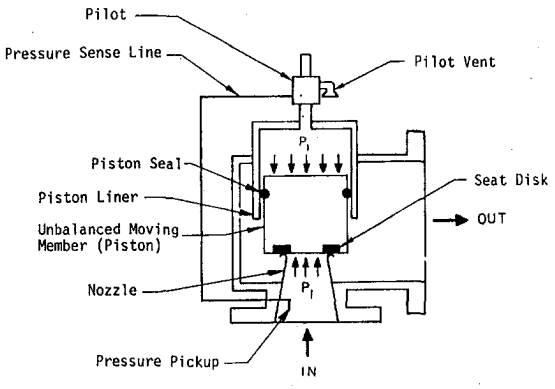


Fig. 2 Pilot-operated safety relief valve operational principle

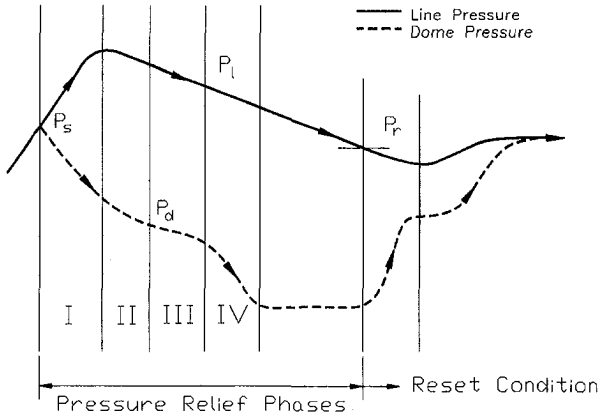


Fig. 3 Schematic showing the relationship between dome pressure and process gas pressure

process and dome pressures are represented schematically in Fig. 3 (and also in Fig. 4), and the various phases are described as follows:

*Phase I:* The pilot starts to vent the dome pressure to ambient through a minimum throat area ($A_o$) in the pilot. This process continues until the dome pressure drops to the threshold level of balanced forces on the piston.

*Phase II:* The valve piston starts to move upward, relieving process pressure, while the dome pressure continues to drop through dome gas evacuation via the pilot. The main process gas is released to ambient through the single or dual outlets. This causes the process gas to reach choked condition at the annulus area produced by the gap between the piston and the riser top (seat). This phase will terminate when the piston is lifted to a position where the process gas will start to choke at the riser nozzle rather than at the annulus gap. This will occur when the annulus' effective area becomes smaller than the nozzle flow area and is defined as "transitional piston height" ($h_t$). Follmer (1980), provided some Mach-Zender-Interferometer pictures of flow through a plane valve choked at the annulus gap.

*Phase III:* The piston continues to move upward from the transitional height to the top position. The dome gas continues to evacuate to ambient through the pilot, while the piston moves upward, giving rise to a moderate decline in the dome gas pressure. The process gas pressure continues to decline at a rate dictated by the choked flow through the riser nozzle.

*Phase IV:* Once the piston reaches its top position, the dome gas evacuates at a lower rate; however, its pressure depletes at a much faster rate than the previous phase due to the elimination of the compression action of the piston motion. The process gas pressure continues to relieve through a choked condition at the riser nozzle. This phase ends when the dome pressure reaches ambient pressure. Following this phase, the process gas pressure continues to decline until it reaches a reset pressure, at which time the pilot will reset to charge the dome with process gas to reverse the process.

## Numerical Simulation

In this section, a numerical model and governing equations for each of the above four phases will be described.

## Nomenclature

$A$ = cross-sectional area
$A_o$ = pilot's throat area
$c$ = speed of sound
$c^*$ = critical speed of sound
$C$ = damping parameter
$C_d$ = discharge coefficient for choked flow
$D$ = riser internal diameter
$D_d$ = piston diameter (dome diameter)
$h$ = piston position above nozzle seat
$h_t$ = piston position at transition between Phases II and III
$k$ = isentropic exponent
$K_s$ = spring constant
$L$ = riser length
$\dot{m}_p$ = pilot's vent mass flow rate
$M$ = effective mass of piston/spring (or Mach number)
$P$ = pressure
$t$ = time
$T$ = absolute gas temperature
$U$ = mean gas velocity
$V_d$ = dome volume
$V_{do}$ = maximum dome volume
$Z$ = acoustic impedance
$\omega$ = riser acoustic resonance frequency
$\omega_n$ = piston natural frequency
$\omega_p$ = piston actual oscillation frequency
$\rho$ = gas density
$\rho^*$ = critical gas density
$\xi$ = damping coefficient ($=C/2\omega_n M$)
$\delta$ = incremental value

**Subscripts**

0, 1, 2 = station locations
$d$ = dome
$p$ = pilot
$n$ = riser nozzle
min, max = minimum and maximum piston lift

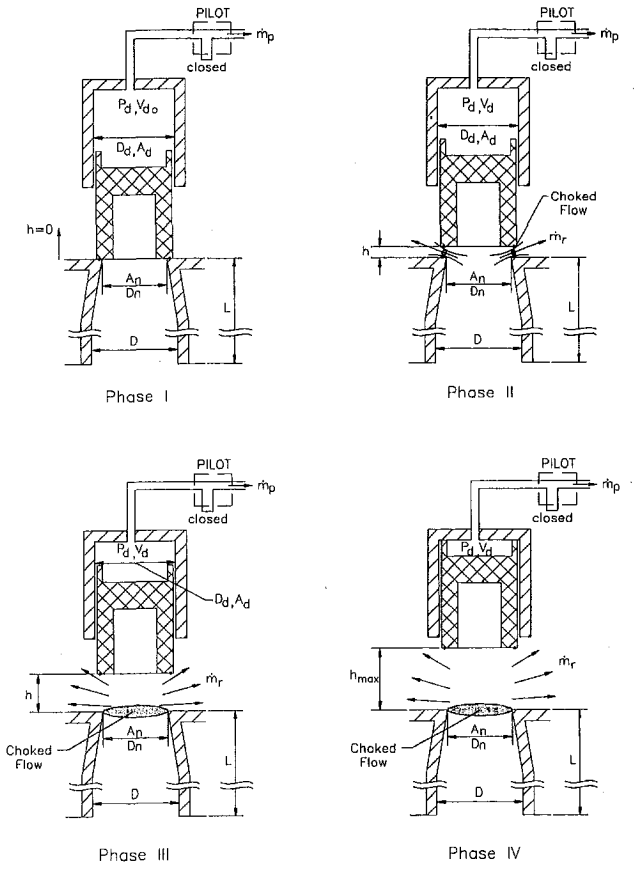


**Fig. 4 Model schematic of various valve stroke phases**

Phase I, shown in Fig. 4(I), represents the dome gas evacuation after the line pressure reaches the set pressure. The evacuation mass flow rate is given by:

$$\dot{m}_p = c_d^* \rho_d^* A_o C_d \tag{2}$$

Here, $C_d$ is a discharge coefficient for the sonic flow which is assumed to be 0.8 in the present work, according to Benedict (1971). Furthermore, the dome gas expansion caused by the pilot relief is assumed to be isentropic. Hence the associated change in the dome pressure can be determined from:

$$\dot{m}_p dt = -V_{do} \cdot d\rho_d = -V_{do}(dP_d/c_d^2) \tag{3}$$

The piston height ($h$) remains at $h = 0.0$ during this phase, and the process gas release rate is therefore equal to zero.

The Phase II model schematic is shown in Fig. 4(II). Here the pilot gas evacuation rate $\dot{m}_p$ is the same as described by Eq. (2) where $c_d^*$ and $\rho_d^*$ are gas properties at the critical condition of the dome gas at the instantaneous pressure and temperature. The change in the dome gas pressure is related to both gas evacuation and piston motion in the following manner:

$$\begin{aligned} \dot{m}_p dt &= -\rho_d \cdot dV_d - V_d \cdot d\rho_d \\ &= \rho_d A_d dh - (V_{do} - A_d \cdot h)(dP_d/c_d^2) \end{aligned} \tag{4}$$

The process gas release rate is choked at the annulus gap between the valve piston and riser nozzle and can be expressed as:

$$\dot{m}_n = c_n^* \rho_n^* (\pi D_n h) C_d \tag{5}$$

The term in brackets assumes that the flow area is the full circumferential gap which may not be true due to the effects of the valve casing. The piston lift ($h$) from the seating position is determined from the piston equation of motion:

$$M\ddot{h} + C\dot{h} + K_s h = P_n A_d - P_d A_d \tag{6}$$

Here the force acting on the bottom side of the piston is assumed to be uniform and equal to the static pressure at the riser nozzle. (A more realistic pressure distribution function would be needed, but is beyond the scope of the present work.) This pressure is determined from solving the full one-dimensional flow equations of the gas in the riser and associated process system using the method of characteristics (Botros and Petela, 1994). The instantaneous flow at the riser nozzle (Eq. (5)) is used as a boundary condition required for the solution of the hyperbolic P.D.E. representing the flow in the riser and associated process piping system. The upstream boundary conditions for these equations depend on the process piping system. In the present analysis, we assumed that the riser is connected to a large pressurized system (vessel). Hence, the boundary condition at the bottom of the riser is assumed to be an open end and is maintained at a pressure equal to the instantaneous process gas pressure.

Model equations for Phase III depicted schematically in Fig. 4(III) are similar to those for Phase II except that the process gas release mass flow rate is equal to:

$$\dot{m}_n = c_n^* \rho_n^* A_n C_d \tag{7}$$

This arose from the fact that the process gas flow is now choked at the riser nozzle rather than at the annulus gap between the piston and riser nozzle. The force distribution is still assumed to result from equal distribution of the riser static pressure at any instant in time.

The Phase IV model equations are the same as those for Phase III, the only difference lying in the thermodynamics of the dome gas. In this phase the piston has reached the top position (Fig. 4-IV), and hence the dome gas pressure changes according to the following relation:

$$\dot{m}_p dt = -(V_{d\min})(dP_d/c_d^2) \tag{8}$$

In all of the above phases, the piston equation of motion should be in effect at every time step of the solution procedure in order to allow for piston rebound at either top or bottom positions.

Additionally, the piston natural frequency can be evaluated from the dome gas thermodynamic relation. Assuming isentropic behavior of the dome gas during piston motion, and neglecting gas evacuation through the pilot, the following relation can be written:

$$d(P_d V_d^k) = 0 \tag{9}$$

Hence, the upward incremental force on the piston would be:

$$-A_d dP_d = \frac{kP_d A_d^2 dh}{V_d} \tag{10}$$

and from the piston equation of motion (6), the natural frequency of the piston would be:

$$\omega_n = \sqrt{\frac{kP_d A_d^2}{V_d M} + \frac{K_s}{M}} \tag{11}$$

Normally, the second term under the square root is negligible compared to the first term (by at least two orders of magnitude).

The model described above for all four phases utilizes the BWRS equation of state for natural gas to determine the gas density, the speed of sound and the isentropic exponent at the prevailing local pressure and temperature. Critical conditions are calculated from the stagnation conditions using ideal gas relations with real gas values of isentropic exponents at stagnation conditions. The error associated with this simplification

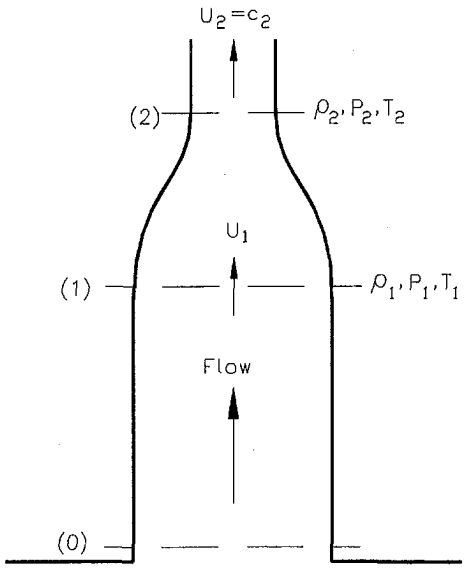


**Fig. 5 Choked flow acoustic resonance model**

was found to be less than 1 percent for critical pressure, 0.4 percent for critical temperature, 0.2 percent for critical density, and 0.6 percent for speed of sound.

**Solution Technique.** The above equations pertinent to the pilot's flow, dome volume thermodynamics, piston equation of motion and riser relief flow were solved simultaneously in a marching-in-time numerical scheme. At any step in time, the above equations form a set of mixed nonlinear algebraic and O.D.E. which form an initial value problem. A standard fourth order Runge-Kutta is used to advance the solution an incremental time step. The time step for the solution of these equations was selected to be $\frac{1}{50}$th of that required by the method of characteristics applied to the solution of the gas dynamics equations in the attached riser/process system. This was necessary for a stable solution of the O.D.E. system of equations and also for minimizing the resulting higher order truncation errors.

## Acoustic Boundary Condition for a Choked Flow

It was mentioned above that in Phases II, III, and IV, the piston has stroked up away from the nozzle allowing the process gas flow to the ambient. Depending on the phase, the gas flow is choked either at the gap between the nozzle and the bottom side of the piston (phase II) or at the nozzle throat (Phases III and IV). There is a need to determine the acoustic boundary condition in order to assess properly the acoustic interaction between the resonance condition in the riser and the piston oscillations, particularly in Phase II. In Phases III and IV, despite the fact that the piston oscillations cannot affect the riser flow condition due to the choke barrier, the opposite can occur in that the oscillating riser pressures affect the piston motion even when the flow is choked.

A one-dimensional treatment of the upstream acoustic boundary condition for choked flows has been given by Bloxsidge et al. (1988) in the context of acoustically coupled combustion instability. Study of downstream acoustic boundary conditions of near choked flows at the throat of a converging-diverging nozzle, analytically by Myers and Callegari (1977), and numerically by Nayfeh et al. (1980), alluded to high acoustic amplitude to incident wave ratios at the throat when $M$ approaches unity. This indicates that a choked flow resembles acoustically closed end boundary conditions for the upstream field.

To examine this further, consider the schematic of the choked flow boundary condition that is shown in Fig. 5; station (1) denotes an immediate upstream location on the riser where flow parameters are ($P_1$, $T_1$, $\rho_1$, $U_1$ and cross-sectional area = $A_1$), and station (2) denotes the choked location where flow parameters are ($P_2$, $T_2$, $\rho_2$, $U_2 = c_2$ and area = $A_2$). If an isentropic perturbation generated at the upstream station (1), is assumed, then

$$\frac{\delta P_1}{P_1} = k_1 \frac{\delta \rho_1}{\rho_1} \tag{12}$$

$$\frac{\delta P_1}{P_1} = \left(\frac{k_1}{k_1 - 1}\right) \frac{\delta T_1}{T_1} \tag{13}$$

Also, if an isentropic expansion of the gas from station (1) to station (2) where the flow is choked at (2) is assumed, then

$$T_1\left[1 + \frac{k_1 - 1}{2} M_1^2\right] = T_2\left[\frac{k_2 + 1}{2}\right]$$

and in a perturbation form:

$$\delta T_1\left[1 + \frac{k_1 - 1}{2} M_1^2\right] + T_1(k_1 - 1)M_1^2\left[\frac{\delta U_1}{U_1} - \frac{\delta T_1}{2T_1}\right] = \delta T_2\left[\frac{k_2 + 1}{2}\right] \tag{14}$$

Since perturbations are assumed to be isentropic at station (1) and that the flow between stations (1) and (2) is isentropic, it follows that perturbations at station (2) are also isentropic, and hence:

$$\frac{\delta P_2}{P_2} = k_2 \frac{\delta \rho_2}{\rho_2} \tag{15}$$

$$\frac{\delta P_2}{P_2} = \left(\frac{k_2}{k_2 - 1}\right) \frac{\delta T_2}{T_2} \tag{16}$$

As the condition at station (2) is choked, $U_2 = c_2$, and therefore;

$$\frac{\delta U_2}{U_2} = \frac{\delta c_2}{c_2} \quad \text{or, approximately} \quad \frac{\delta U_2}{U_2} = \frac{\delta T_2}{2T_2} \tag{17}$$

The continuity equation between stations (1) and (2) yields the following perturbation equation:

$$A_1 U_1 \delta \rho_1 + \rho_1 A_1 \delta U_1 = A_2 U_2 \delta \rho_2 + \rho_2 A_2 \delta U_2 \tag{18}$$

Equations (12) through (18) form a set of seven perturbation equations in eight perturbation quantities ($\delta P_1$, $\delta \rho_1$, $\delta T_1$, $\delta U_1$, $\delta P_2$, $\delta \rho_2$, $\delta T_2$, $\delta U_2$), which can be reduced to one equation in the form:

$$\delta P_1 = Z_1 \cdot \delta U_1 \cdot A_1$$

or

$$\delta P_2 = Z_2 \cdot \delta U_2 \cdot A_2$$

where,

$$Z_1 = \frac{P_1}{A_1 U_1}\left[\frac{2k_1(T_1 - T_2)}{T_1(k_1 - 1) - T_2(k_2 - 1)}\right] \tag{19}$$

and

$$Z_2 = \frac{P_2}{A_2 U_2}\left[\frac{2k_2}{(k_2 - 1)}\right] \tag{20}$$

$Z_1$ and $Z_2$ are known as the acoustic impedances at stations (1) and (2), respectively. A sample calculation was performed

on a 3.0 m riser containing natural gas at 6000 kPa, and 10°C, and a speed of sound equal to 396 m/s. The impedance at the bottom of the riser is related to $Z_1$ via the acoustic transfer matrix for the riser pipe between stations (0) and (1) of length = 3.0 m (Munjal, 1987). Consider a numerical case where $U_1$ = 60 m/s and $U_2 = c_2$ = 376 m/s and $k_1$ = 1.31. The fundamental acoustic resonance frequency can be determined from the spectrum of the acoustic impedance at station (0) where $Z_o$ is at the first minimum. This results in a value of 32 Hz. If, however, a closed boundary condition is assumed at station (2), the acoustic resonance condition would correspond to a quarter-wave resonance yielding a value of 33 Hz which is very close to that determined from the above treatment. Spectra of $Z_o$ calculated for frequencies up to 200 Hz based on either closed or choked flow boundary conditions were found to be almost the same. It is therefore confirmed that a choked flow can be treated as a closed end boundary condition from an acoustic point of view.

## Numerical Results of a Base Case

A numerical simulation of a base case considered a dual-outlet relief valve opening following a simulated increase in the line pressure beyond the set pressure. An NPS 8 × 8 × 8 valve was considered which is mounted on an NPS 8 riser as shown in Fig. 4. The line pressure was increased from 6000 kPa to 6010 kPa linearly in 100 ms. The pilot's set pressure was set at 6010 kPa. The following are pertinent parameters.

### Valve Characteristics

$D$ = 0.1937 m
$D_n$ = 0.160 m
$L$ = 3.0 m
$h_{max}$ = 0.065 m
$h_t$ = 0.04 m
$D_d$ = 0.189 m
$V_{do}$ = 0.002722 $m^3$
$V_{dmin}$ = 8.98E-04 $m^3$
$A_o$ = 5.47E-06 $m^3$
$M$ = 23.289 kg
$K_s$ = 7358 N/m
$C_d$ = 0.8

### Gas Composition:

C1 = 91.52%, C2 = 5.69%, C3 = 1.2%, iC4 = 0.16%, nC4 = 0.22%, iC5 = 0.08%, nC5 = 0.07%, $N_2$ = 0.65%, $CO_2$ = 0.50%

A laboratory flow test with air was conducted on the pilot to determine the effective flow area when it was forced fully open. The pilot was connected to an air cylinder and the upstream stagnation pressure was varied from 500 to 2500 kPa. Mass flow rate was measured by a calibrated Rockwell turbine meter. The effective throat area of the gas evacuation path through the pilot was found to vary from 4.94 $mm^2$ to 5.90 $mm^2$ when the stagnation pressure was varied from 500 kPa to 2500 kPa, respectively. Additionally, a simulated laboratory test was conducted on the piston/liner assembly to determine the range of the damping coefficient $C$. The lowest value of $C$ was found to be around 6000 N/(m/s).

Simulation results are shown in Figs. 6($a$) through ($h$), which are discussed below.

Piston oscillations (Fig. 6($a$)) started as a result of a step change in the net upward force (Fig. 6($g$)) due to the initial piston lift, thus exposing a larger piston area at its bottom to the riser gas pressure. Oscillations were then sustained at a slightly increasing net average upward force (Fig. 6($g$)). The net upward forces were much larger than the forces caused by the holding spring, or by the piston weight itself.

It took approximately 1.2 s for the valve to stroke to the full open position (Fig. 6($c$)) once it started to lift. A period of piston oscillation was observed for 200 ms following the initial lift, with amplitudes decaying in time. The piston oscillations occurred at piston lift ($h$) below the transitional height ($h_t$ = 0.04 m).

During the oscillation period, the riser nozzle static pressure (Fig. 6($c$)) was leading the riser flow (Fig. 6($e$)) by a 90 deg phase shift, consistent with an open end riser bottom from plane wave acoustic theory (Munjal, 1987). The phase angle between the net upward force on the piston (Fig. 6($g$)) and piston lift (Fig. 6($a$)) is 90° (the piston motion is lagging). This is consistent with the forced vibration theory.

The piston oscillation frequency ($\omega_p$) was approximately 56 Hz, while $\omega_n$ averaged around 60 Hz, and hence $\omega_d$ was around 56 HZ ($\xi$ = 0.37). This does not mean that, $\omega_p = \omega_d$ in general. The relationship between $\omega_p$, $\omega_n$, $\omega_d$ and $\omega$ will be discussed in more detail in the following section.

The dome pressure (Fig. 6($d$)) and pilot's flow (Fig. 6($f$)) went through the following phases: a steady decrease while piston was at zero height, an oscillatory phase due to piston oscillation, a constant level due to counter effects of piston moving upward and the pilot's gas evacuation, and finally, a steady decline at a much faster rate once the piston hits its maximum lift $h_{max}$.

The import of this simulation's result is that when an improper or low viscosity lubricant is used (hence lower damping coefficient $C$), the piston oscillations can occur during the opening stroke. This is why valve manufacturers always emphasize the use of specific types of lubricant with certain high shear stresses and viscosity. The $C$ value for such lubricants is at least an order of magnitude higher than the value used in the base case simulation. The reason for using the lower value in the base case simulation was to illustrate this message clearly. In order to substantiate this further, the same simulation was repeated with a higher value of $C$ [35,000 N/(m/s)], resulting in $\xi$ = 2.16. The result of the piston travel vs. time is shown in Fig. 7, indicating substantial suppression of piston oscillations.

## Effects of Geometrical and Operating Parameters

The influence of the inlet riser length in the above base case above was studied numerically. The lower value of $C$ [6000 N/(m/s)] was retained in order to manifest the effect of the riser's dimensionless length ($L/D$) on both the frequency and amplitude of piston oscillations. Figure 8($a$) shows the piston oscillation frequency for various values of $L/D$. In some cases, two distinct oscillation modes were observed along the piston stroke; the first mode (identified by the symbol ×) was observed first in time, followed by a second mode of different frequency (symbol ●). An example of the piston lift − time trace of such behavior is shown in Fig. 9, for $L/D$ = 90. The riser's acoustic resonance frequency curves corresponding to one quarter wave length ($L_1/D$) and to odd multiples ($L_{3,5,7,9}/D$) are also plotted in Fig. 8($a$), along with the piston damped and undamped natural frequencies ($\omega_d$, $\omega_n$). It is observed that the piston oscillation frequency follows the riser's one-quarter wave frequency for lower values of $L/D$. At $L/D$ = 20, the two mode oscillations described above started to emerge with two distinct frequencies. This is perhaps due to the fact that the three-quarter wave resonance in the riser started to approach the piston natural frequency. This two-mode oscillation phenomenon persisted for higher values of $L/D$ up to 140, the maximum considered in the present study, as shown in Fig. 8($a$).

The corresponding piston maximum amplitude ($pk$-to-$pk$) is shown in Fig. 8($b$). The various vertical lines correspond to $L/D$ values where the riser's acoustic resonance frequencies are equal to the piston damped natural frequency. Maximum oscillation amplitudes occur at $L_1/D$ corresponding to $\omega_d = \omega$ (one quarter wave). Amplitudes decreased at lower or higher values of $L/D$, particularly when $L/D$ approached zero. Interestingly, amplitudes appeared to increase when $L/D$ approached $L_5/D$ and $L_9/D$ but not $L_3/D$ and $L_7/D$.

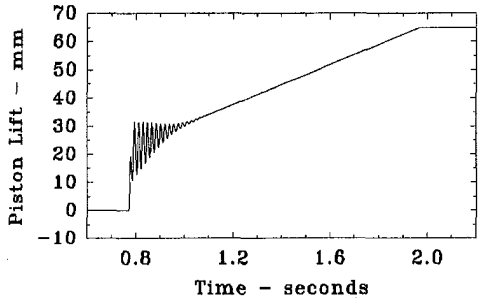


Fig. 6(*a*)

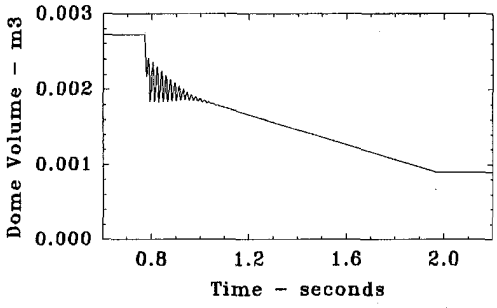


Fig. 6(*b*)

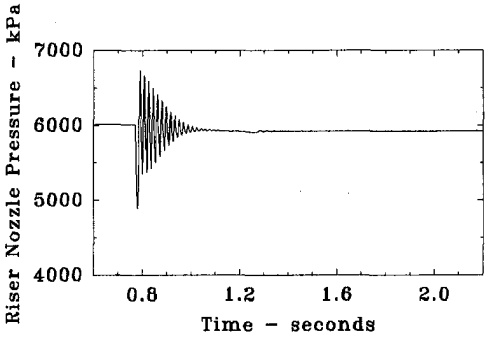


Fig. 6(*c*)

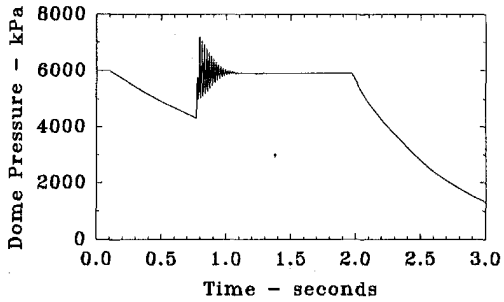


Fig. 6(*d*)

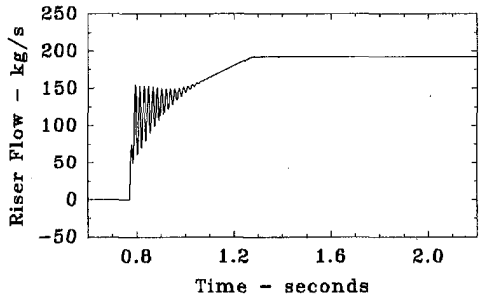


Fig. 6(*e*)

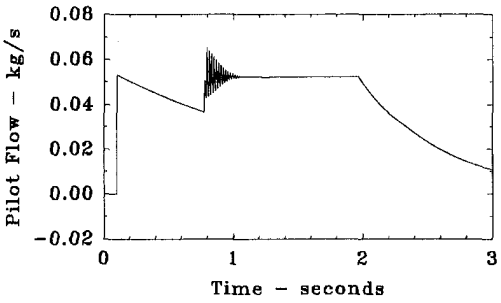


Fig. 6(*f*)

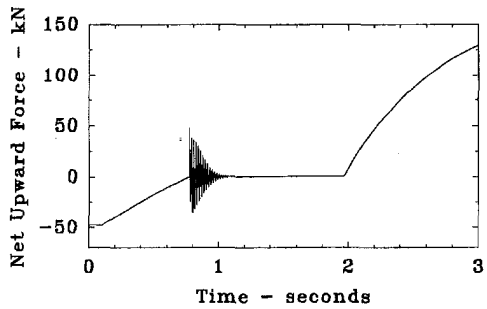


Fig. 6(*g*)

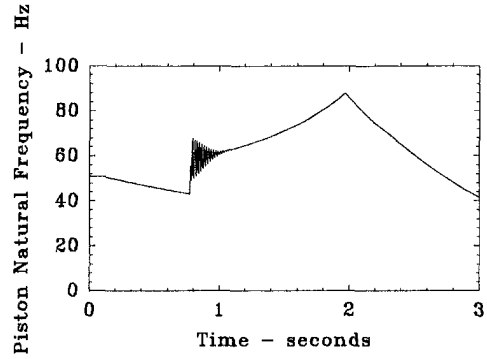


Fig. 6(*h*)

**Fig. 6 Numerical results of base case scenario (low damping ratio $\xi = 0.37$)**

The dome depressurization rate was evaluated to determine its effect on piston oscillations. Parametric results obtained by varying the pilot's throat area are shown in Fig. 10. Obviously, as the pilot's throat area was increased, the piston oscillations tended to vanish at the cost of higher impact velocity of the piston against the dome end. For example, an increase of the pilot's throat area of 20 times resulted in an increase in the impact velocity from 35 mm/s (Fig. 6(*a*)) to 700 mm/s (Fig. 10). Although valve manufacturers indicate that the current design of relief valves can cope with such an increase in the impact velocity, a careful optimization should be carried out before deciding on how large a pilot's throat area can be.

Reduction of the piston oscillations was also attempted by a valve manufacturer through a different design of the piston o-ring seals based on a wedge type mechanism. The main purpose of such a mechanism is to increase damping when the piston is moving upward. The device is called a 'pressure-loaded drag wedge seal' since it translates the dome pressure into a radial force via a split wedge ring. By utilizing a free body diagram of the wedge and balancing the axial and radial forces, it is

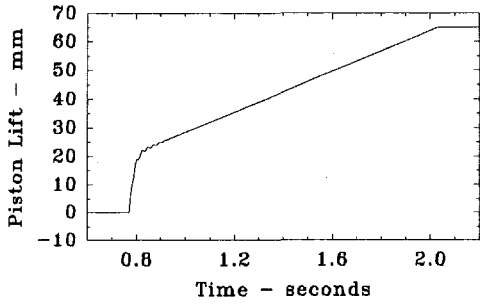


Fig. 7 Numerical results assuming higher damping ratio $\xi = 2.16$

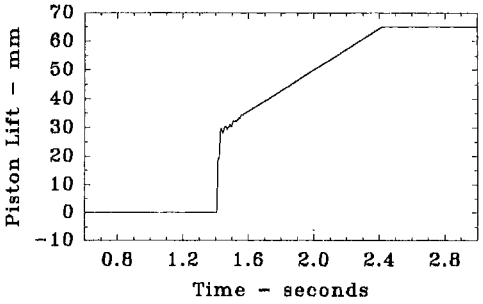


Fig. 11 Effects of wedge type ring seal on suppressing piston oscillations of the base case

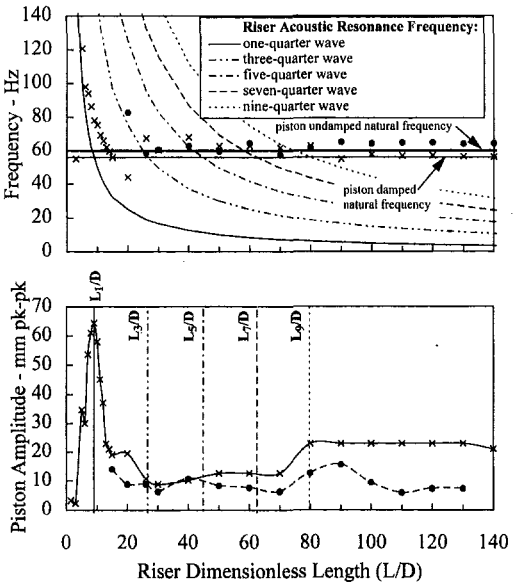


Fig. 8 Effects of riser length on piston oscillation frequency and amplitude

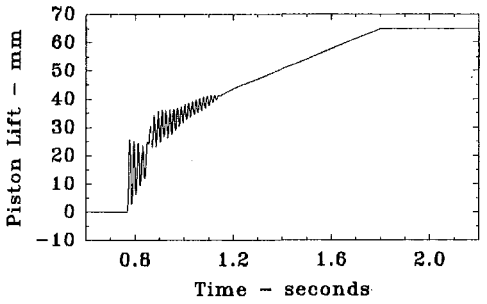


Fig. 9 Example of the two mode oscillations for $L/D > 20$

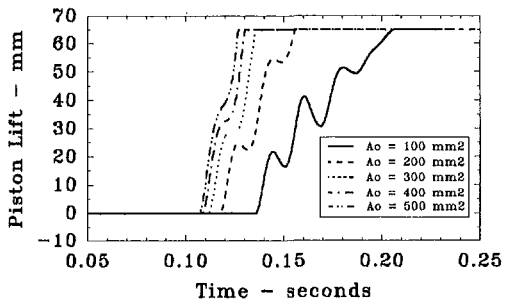


Fig. 10 Effects of pilot's exhaust throat area on piston oscillations during valve opening

possible to correlate the drag force to the dome pressure. This drag force is only effected during the upward motion of the piston. A wedge case study was simulated for a specific wedge mechanism with the following parameters: wedge angle (75 deg), radial area (3500 mm$^2$) and friction coefficient (0.2). Other parameters were exactly the same as in the base case in order to permit comparisons. The results are shown in Fig. 11, which show a substantial suppression of oscillations (compare to Fig. 6($a$)).

## Field Tests

Field measurements were taken at NOVA's Gas Dynamic Test Facility which is part of a compressor station on NOVA's gas Transmission System in Alberta. An NPS 8 × 8 × 8 dual-outlet relief valve was mounted on an NPS 8 riser branched off an NPS 30 yard pipe as shown in Fig. 12. This setup was supplied with high pressure natural gas from both the NPS 30 and an NPS 42 mainline, operating at 5800 kPa and 23°C. Testing was carried out under ambient temperatures ranging from −25°C to −15°C.

Relief actuation was controlled by a solenoid and manifold arrangement in place of the ordinary pilot. This allowed remote valve triggering and safe isolation. A changeable orifice assembly was used to vary the dome depressurization rate. Measurements were taken with high speed digital data acquisition equipment. The measured parameters included: line pressure immediately below the relief valve, dome pressure, and outlet piping pressure in the valve outlet piping (locations 1, 2, and 3 on Fig. 12, respectively). Data were also gathered from existing compressor station temperature, pressure, and flow elements.

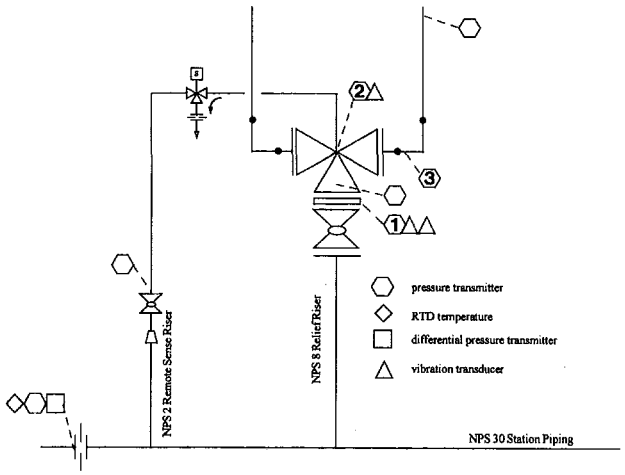


Fig. 12 Riser/relief valve assembly of the field test rig

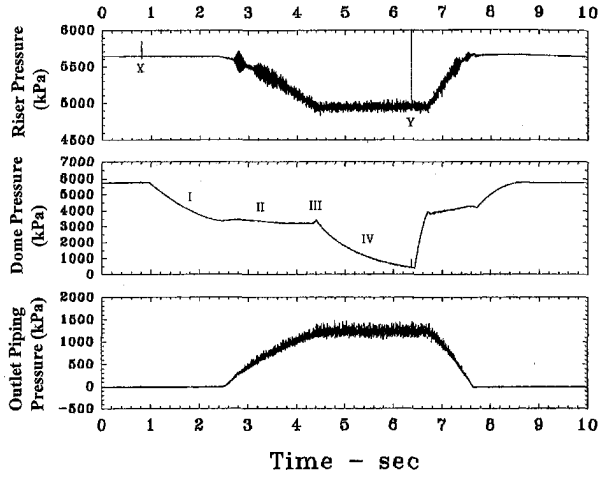


Fig. 13 Field measurements during relief valve opening and closing ($A_o \sim 5.48$ mm$^2$)

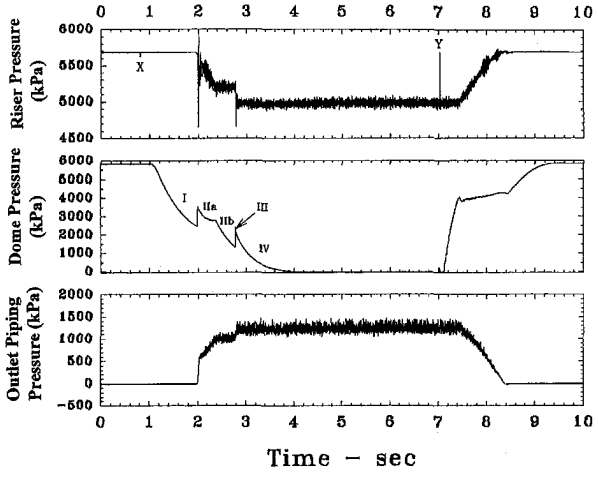


Fig. 14 Field measurements during relief valve opening and closing ($A_o \sim 9.0$ mm$^2$)

Figure 13 shows the dome pressure, the riser pressure, and the outlet piping pressure, measured for a pilot equivalent orifice size ~5.48 mm$^2$. Phase I began at the solenoid ($s$) trigger (point $X$)) and continued until the piston lifted off and the pressure began to rise in the outlet piping. The dome pressure at the end of Phase I was lower than that predicted from the physical area ratios of the valve. This difference was caused by the increased dampening effected by the wedge seal mechanism as will be in the simulation of this test later.

Phase II of dome depressurization is characterized by increasing outlet piping pressure and ends when the outlet piping pressure stabilizes. The dome pressure remained relatively constant throughout Phase II. Furthermore, there was no pressure increase at the beginning of this phase nor pressure oscillations, which are indicative of much higher damping likely caused by the extreme cold ambient condition.

The beginning of Phase III is characterized by the outlet piping pressure stabilization, indicating a maximum flow rate, and a transition from a choked piston annulus to a choked valve nozzle. From Fig. 13, it is unclear when this Phase ended and phase IV began. The numerical simulation (Fig. 6($e$)) clearly displays a transition prior to full piston travel. From this field measurement, however, it can be inferred that the transitional height is close to the maximum piston lift, indicating that the effective annulus flow area is lower than ($\pi D_n h$). Therefore, Phase III was seen to last for very a short time and was manifested by a small pressure overshoot as shown in Fig. 13. Phase IV (maximum piston lift) is indicated by a step change in dome depressurization rate similar to the numerical simulation.

Figure 14 shows the measurements for a case without an orifice (dome depressurization was limited by a $\frac{1}{2}''$ tubing and 9.0 mm$^2$ ball valve throat area). Phase I and Phase IV show results similar to the former case, and the higher depressurization rate exhibited in Fig. 14 is exactly matching the increase in the throat area.

The relatively constant dome pressure exhibited in Phase II by the former case (Fig. 13) is not demonstrated here due to the larger throat area of the dome gas evacuation path. However, the large step change in the outlet piping pressure (indicating a large change in valve flow and, therefore, piston lift) results in a large increase in dome pressure when the valve opens. The kink-shaped dome pressure during this phase can be attributed to the piston being jammed part-way along its upward stroke. This is evident from the constant outlet pressure during this piston jamming period (identified as IIb in Fig. 14). The exact cause for this piston jamming during this phase has not been clearly determined. Hence, simulation of this test case was not possible.

The step change in the outlet piping pressure terminating Phase IIb, followed by another pressure stabilization indicate a step change in piston position and an increase in valve flow rate. This reveals that Phase III is of very short duration followed by the normal Phase IV at maximum piston lift.

Additionally, Figs. 13 and 14 show the dome repressurization and reclosing of the valve following the reverse solenoid trigger (points Y). When the piston began to travel to a closed position (indicated by the peak in dome pressure and the drop in outlet piping pressure), the dome pressure required to begin closing the valve correlates very closely to the pressure calculated from the physical area ratios of the valve.

## Simulation of the First Field Test Case

Only the first field test case was simulated using the above numerical analysis method. (Simulation of the second case was not possible as the cause for the apparent piston jamming partway up was not clearly determined). The damping parameter $C$ had to be increased to a value equal to 90,000 N/(m/s) to correlate with the measurement results. This was not a surprisingly high value of $C$, considering that severe cold ambient temperature prevailed during the field test. Additionally, the wedge seal model with the specific parameters mentioned earlier was introduced since the relief valve tested was equipped with such a mechanism. The results of this simulation are shown in Fig. 15. Clearly, the good agreement between measurement and simulation results with regard to the dome pressure (compare Fig. 13 with Fig. 15) provides confidence in the modeling and solution techniques employed in the present study. Further effort will model the sticking (jamming) phenomenon which was apparent in the second field test.

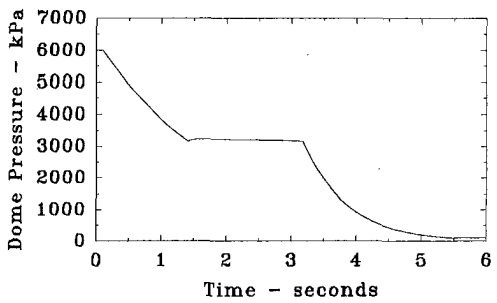


Fig. 15 Simulation results of the field measurement case of Fig. 13

## Conclusions

The following conclusions can be drawn from the above investigation:

1. Piston oscillations are possible during piston stroke. The overpressure protection of the relief valve may be compromised because oscillations may occur when the piston is at a position lower than the transitional height, possibly galling the piston and the liner. The amplitudes and duration of the oscillation depend on the geometrical and operational parameters of the relief valve, and particularly on the damping parameter and mechanism.
2. It is critical to use proper lubricants with high shear stresses and viscosity in order to prevent piston oscillations during the opening stroke. Additionally, piston oscillations can be suppressed by a larger pilot vent throat area. However, a larger pilot throat area has the adverse effect of increasing the piston impact velocity against the dome end. Although valve manufacturers indicate that the current design of relief valves can cope with such an increase in the impact velocity, a careful optimization should be carried out before deciding on how large a pilot's throat area can be.
3. Analysis of piston oscillation frequencies and amplitudes indicates that the piston oscillation frequency mirrors the riser's one-quarter-wave resonance frequency for lower values of $L/D$. At $L/D = 20$ and higher, two modes of oscillations started to emerge with two distinct frequencies. Maximum oscillation amplitudes occurred at $L/D$ corresponding to $\omega_d = \omega$ (one quarter wave). Amplitudes decreased at lower or higher values of $L/D$, particularly when $L/D$ approached zero.

## Acknowledgments

The work presented here is part of a research program sponsored by NOVA Gas Transmission Ltd., and permission to publish it is gratefully acknowledged. The authors also acknowledge the previous work of C. Foy, D. Kiel and G. Petela of NRTC. Thanks are also due to P. Tetreau for assistance in drawing the schematics and conducting some of the tests, and J. Geerligs for measuring the pilot's flow. Field measurements and data were collected by NGTL Performance Testing Group, hereby acknowledged.

## References

Benedict, R. P., 1971, "Generalized Contraction Coefficient of an Orifice for Subsonic and Supersonic Flows," ASME *Journal of Basic Engineering*, pp. 99–120.

Bloxsidge, G. J., Dowling A. P., and Langhorne, P. J., 1988, "Reheat buzz: An Acoustically Coupled Combustion Instability—Pert 2. Theory," *Journal of Fluid Mech.*, Vol. 193, pp. 445–473.

Botros, K. K., and Petela, G., 1994, "Use of Method of Characteristics & Quasi-Steady Approach in Transient Simulation of Compressor Stations," ASME Fluids Engineering Division Summer Meeting, *Advances in Computational Methods in Fluid Dynamics*, Lake Tahoe, Nevada, U.S.A., FED-Vol. 196, pp. 325–338.

D'Netto, W. and Weaver, D. S., 1987, "Divergence and Limit Cycle Oscillations in Valves Operating at Small Openings," *Journal of Fluids and Structures*, Vol. 1, pp. 3–18.

Dunn, G., 1991, "Safety Relief Valve Damage During Testing," NGTL Internal Report.

Emerson, G. B., 1966, "Safety Valve Operational Stability," Anderson/Greenwood & Co., Internal Report No 2-0089.

Follmer, B., 1980, "Oscillating Functioning of Safety Relief Valves Generated by Their Inlet Geometry," *Flow Visualization 2, Proceedings of the 2nd International Symposium*, Sept. 9–12, New York, pp. 203–208.

Foy, C. E., Kiel, D. E. Jungowski W. J., 1993, "The Effect of Pressure Pulsation and Pilot Setting on the Performance of Pressure Relief Valves," Society of Petroleum Engineers, Eastern Regional Meeting, SPE 26907, pp. 183–196.

Krivosheev, A. G., 1988, "Stability of Steady State Operation of Safety Relief Valves," UDC 621.646.4.001.5, pp. 81–84, Translated from Khimichskoe

Munjal, M. L., 1987, *Acoustics of Ducts and Mufflers*, John Wiley, New York.

MacLeod, G., 1985, "Safety Valve Dynamic Instability: An Analysis of Chatter," ASME *Journal of Pressure Vessel Technology*, Vol. 107, pp. 172–177.

Masuda, F., 1985, "Dynamic Response Analysis of a Safety Valve With Transients of a Fluid System," *Transactions of the 8th International Conference on Structural Mechanics in Reactor Technology*, Brussels, F1-(F2), pp. 53–58.

Myers, M. K., and Callegari, A. J., 1977, "On the Singular Behavior of Linear Acoustic Theory in Near-Sonic Flows," *Journal of Sound & Vibration*, Vol. 51(4), pp. 517–531.

Nayfeh, A. H., Shaker, B. S., and Kaiser, J. E., 1980, "Transmission of Sound Through Non Uniform Circular Ducts with Compressible Mean Flows," *AIAA Journal*, Vol. 18, No. 5, pp. 515–525.

Nayfeh, A. H., and Bouguerra H., 1990, "Non-Linear Response of a Fluid Valve," *International Journal of Non-Linear Mechanics*, Vol. 25, pp. 433–449.

Powell, W. W., 1971, "A Study of Resonant Phenomena in Pilot-Operated Safety Relief Valves," Anderson Greenwood & Co., Internal Report #2-0175-51.

Semeniuk, T., 1995, "Relief Valve Failure," NGTL Internal Metallurgical Report.

Thomann, H., 1976, "Oscillations of a Simple Valve Connected to a Pipe—Parts I, II and III," *Journal of Applied Mathematics and Physics (ZAMP)*, Vol. 27.

Watton, J., 1983, "Dynamic Characteristics of a Single Stage Pressure Rate Controlled Relief Valve With Directional Damping," ASME Winter Annual Meeting, Paper 83-WA/DSC-40, pp. 1–8.

Watton, J., 1990, "The Stability and Response of a Two Stage Pressure Rate Controllable Relief Valve," *Journal of Fluid Control*, pp. 50–66.

**R. Laborde**
Engineer.

**P. Chantrel**
Engineer.

GEC ALSTHOM ACB-CERG
(Centre d'études et de
recherche de Grenoble),
rue Lavoisier, 38800 Le Pont
de Claix, France

**M. Mory**
Researcher,
Laboratoire des Ecoulements
Géophysiques et Industriels
(Laboratoire mixte U.J.F-INPG-CNRS),
BP 53-38041, Grenoble Cédex 9, France

# Tip Clearance and Tip Vortex Cavitation in an Axial Flow Pump

*A combined study of tip clearance and tip vortex cavitations in a pump-type rotating machine is presented. Cavitation patterns are observed and cavitation inception is determined for various gap heights, clearance and blade geometries, and rotor operating conditions. An optimum clearance geometry is seen to eliminate clearance cavitation when the clearance edge is rounded on the blade pressure side. The gap height has a strong effect on clearance cavitation inception, but the trends vary considerably when other parameters are also modified. The gap height and clearance geometry have less influence on tip vortex cavitation but forward and backward blade skew is observed to reduce and increase tip vortex cavitation, respectively, as compared to a blade with no skew.*

## Introduction

Improvements in hydraulic machine design have led to much better control of cavitation effects. Consequently, other specific types of cavitation phenomena which were not much considered in the past are attracting more attention. Among these, tip clearance and tip vortex cavitation are becoming prominent research topics. Delaying or eliminating these two types of cavitation (entirely or partially) is a major goal in the design of axial pumps or turbines and shrouded propellers due to their undesirable consequences: noise, vibrations, mechanical damage, power loss.

Tip clearance cavitation and tip vortex cavitation are different, although related phenomena. Clearance cavitation (or gap cavitation) appears inside the gap between the rotating blade tip and the surrounding belt. It was analyzed a long time ago by Müller (1935) as being the cavitation that occurs when flow through the clearance generated by the intrados/extrados pressure difference is subjected to boundary layer separation. On the other hand, tip vortex cavitation (or leakage vortex cavitation) is that in the vortex attached to the blade tip, trailing in the channels between the blades. Actually, cavitation inside the vortex does not always extend up to the blade tip. Desinent cavitation in the vortex can be a chord length downstream from the trailing edge. The present study simultaneously focuses on tip clearance cavitation and tip vortex cavitation as it is of major importance to determine the relative values of inception numbers for these two types of cavitation. The results of a long-term experimental investigation are given here. An experimental facility was built at ACB-CERG and was used to investigate the effects of various parameters on tip clearance and tip vortex cavitation: clearance geometry, gap height, blade geometry, pressure difference between the blade pressure and suction sides.

A number of studies have been devoted to clearance flows but most of them were conducted in gas turbines or compressors and focused on the determination of losses through clearances, pressure distributions around the tip or secondary flows (see Murthy and Lakshminarayana, 1986, for a reference on the subject). Studies in linear cascades have also brought much insight into clearance flows (Heyes and Hodson, 1993, for instance). Few experimental studies have considered cavitation phenomena inside the gaps. To our knowledge, experimental studies on cavitation phenomena connected to tip clearance flows in a pump-type rotating machine were initiated by Rains (1956). Although they focused on tip vortex cavitation, the recent studies by Farrell and Billet (1994) and Zierke et al. (1995) are the main basis for comparison with our results.

## Experimental Facility

The experiments were conducted in water tunnel TH300 at ACB-CERG. A schematic outline of the facility is shown in Fig. 1. For the purpose of cavitation studies the absolute pressure in the test section could be continuously adjusted in the range 0–3 bars. The tunnel had a circular test section of internal diameter 394 mm in which an axial pump type machine rotated. The rotating wheel had 12 blades mounted on the 290 mm diameter hub. The blades could be removed and different sets of blades were tested. They differed in terms of blade geometry, clearance geometry and gap height. The chord length of the blades was 110 mm and the height 50 mm. The maximum blade thickness at the tip was 8 mm. For all experiments the rotation was fixed at 15 Hz. Two values of flow rate were used: $Q_1 = 0.288$ m$^3$s$^{-1}$ and $Q_2 = 0.262$ m$^3$s$^{-1}$, producing a head variation across the rotor of $\Delta H_1 = 200$ mb and $\Delta H_2 = 350$ mb, respectively. The operating condition ($Q_1$, $\Delta H_1$) was the design point condition.

Three rotors were successively investigated over a period of three years. They differed in terms of blade geometries, which are schematically compared in Fig. 2. Straight blades were mounted on the first rotor, i.e., the centers of the profile sections are located on the same radius from the bottom to the blade tip. Blades with a backward skew and blades with a forward skew were tested with the second and third rotor, respectively. A blade with a forward skew was twisted around the hub axis in the direction of rotation. The leading edge at the tip was at an angle of 45 deg with the radial direction. A blade with a backward skew was subjected to rotation in the opposite direction. For all rotors, the angle of incidence of the blade changed slightly from the bottom to the blade tip in order to obtain a constant load along the blade. The blade had an angle of 69 deg with the axial flow direction at the tip. The flow-rate $Q$ was slightly adjusted in order to operate all rotors with the same head variation across the rotor. Skew produces a different radial flow on the blade suction and pressure sides. For a forward skew, the radial flow is toward the tip on the suction side and directed from the tip to the hub on the pressure side. The oppo-

Contributed by the Fluids Engineering Division for publication in the JOURNAL OF FLUIDS ENGINEERING. Manuscript received by the Fluids Engineering Division July 10, 1996; revised manuscript received February 11, 1997. Associate Technical Editor: J. Katz.

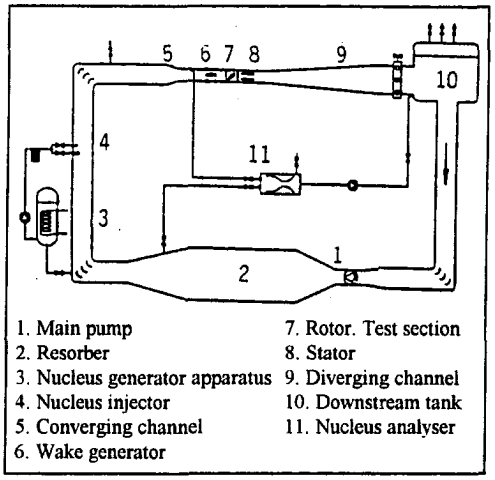


Fig. 1 Schematic diagram of TH 300 water tunnel

site flow direction is obtained for blades with a backward skew. The study of skew effects on cavitation was aimed at testing the conjecture that a forward skew decreases the flow through the clearance whereas a backward skew produces an increase. The inference is that clearance cavitation could be delayed for blades with a forward skew.

The twelve blades mounted on the first three rotors had different clearance geometries which are sketched in Fig. 3. The clearance geometry designs tested were chosen on the basis of the theoretical analysis by Novoderezhkin et al. (1983) and Papir and Golikov (1985). A first series involved clearances with sharp edges. The clearances of the second blade series had a rounded edge on the pressure side and a sharp edge on the suction side. For the third blade series the edge was rounded on the pressure side but the gap height diverged slightly toward the suction side. A rounded edge on the pressure side was aimed at eliminating boundary layer separation in the clearance. A diverging gap on the suction side was thought to reduce the intensity of the tip vortex and hence to delay tip vortex cavitation inception according to Gearhart (1966). A fourth clearance geometry was investigated on Rotors 2 and 3. Its edge was rounded on the pressure side but the clearance was prolonged on the suction side by a thin plate fixed to the blade and parallel to the wall. This geometry produced very intense cavitation in the wake of the plate and is therefore not mentioned later in the paper. For the different clearance geometries the blades were mounted on the hub with different gap heights. Table 1 summarizes the different cases tested.

Visualizations of the different cavitation patterns were carried out and served to determine cavitation inception. The circular annulus of the test section was made of plexiglass and the test

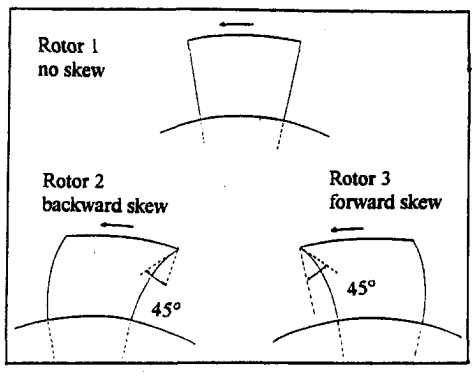


Fig. 2 Schematic drawing of the different blade geometries

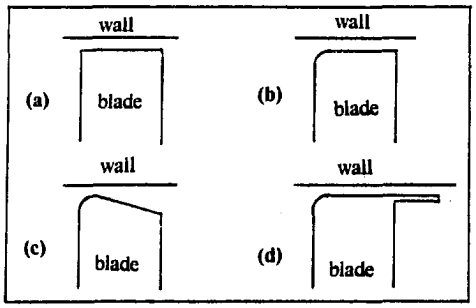


Fig. 3 Schematic drawing of clearance geometries. (*a*) clearance with sharp edges; (*b*) clearance with rounded edge on the pressure side; (*c*) clearance with rounded edge on the pressure side and diverging toward the suction side; (*d*) clearance with rounded edge on the pressure side and prolonged on the suction side by a thin plate.

section was equipped with two visualization water boxes in order to make observations free of optical distortion. The main window (dimensions 190 mm by 290 mm), located sideways to the test section, was used to view flow in the blade clearances and in the inter-blade channels using stroboscopic lighting. Wall pressure measurements were finally carried out to determine the wall pressure map in the region swept by the blades.

## Visual Observations

Visual observations showed that cavitation patterns change greatly depending on clearance geometry. Figure 4 shows the cavitation patterns for the three clearance geometries observed under the same experimental conditions. The cavitation number is low ($\sigma = 1.2$. Cavitation index is defined in the next section) and most of the different typical cavitating structures observed in the course of this work can be seen. Severe clearance cavitation is observed when the clearance has sharp edges (Fig. 4(*a*)) while no cavitation is observed in the clearance with a rounded edge on the pressure side (Fig. 4(*b*)). Tip vortex cavitation also occurs but the most intense vortex cavitation is observed for the clearance with sharp edges and for the diverging clearance. For these two clearance geometries (Figs. 4(*a*) and 4(*c*)) clearance cavitation rapidly becomes strongly linked to vortex cavitation when the pressure is lowered; the shear layer emerging from the clearance displays cavitation. For the diverging clearance (Fig. 4(*c*)), the cavitation of the shear layer extends inside the clearance and a specific cavitation pattern consisting of isolated bubbles is observed inside the clearance.

A striking effect of blade skew on clearance and tip vortex cavitation is shown in Fig. 5. Clearance cavitation and tip vortex cavitation are much less intense for blades with a forward skew than for blades with a backward skew. The cavitation patterns inside the clearance are located between the leading edge and about $\frac{2}{3}$ of the chord for a blade with a backward skew, whereas they are located between the middle of the chord and the trailing edge in the case of a forward skew.

Table 1 Blade geometries, clearance geometries and gap heights implemented on the three rotors tested

| blade | clearance (in mm) | | |
|---|---|---|---|
| | sharp edge | rounded on pressure side | rounded on pressure side & diverging |
| Rotor 1 no skew | 0.5, 1 & 2 | 0.5, 1 & 2 | 0.5, 1 & 2 |
| Rotor 2 backward skew | 0.5, 1 & 2 | 0.5, 1 & 2 | 0.5, 1 & 2 |
| Rotor 3 forward skew | 0.5, 1 & 2 | 0.5, 1 & 2 | 0.5, 1 & 2 |

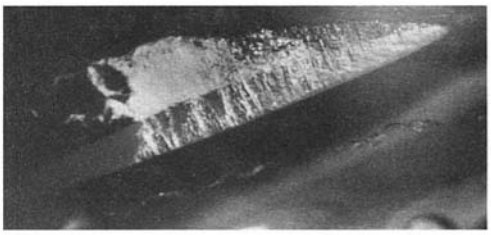

Fig. 4(*a*)

Fig. 4(*b*)

Fig. 4(*c*)

**Fig. 4 Clearance and tip vortex cavitation patterns for three clearance geometries ($\delta$ = 1 mm). Rotor 2 (backward skew). Experimental conditions: $\Delta H$ = 350 mb, $\sigma$ = 1.2. (*a*) Clearance with sharp edges; (*b*) clearance with rounded edge on pressure side; (*c*) clearance with rounded edge on pressure side and diverging toward the suction side.**

Inspection of cavitation in the clearances reveals several features of the flow, which highlight the close connection between clearance cavitation and tip vortex cavitation. This is more visible on blades with a backward skew since the clearance cavitation is mostly located near the leading edge where the vortex

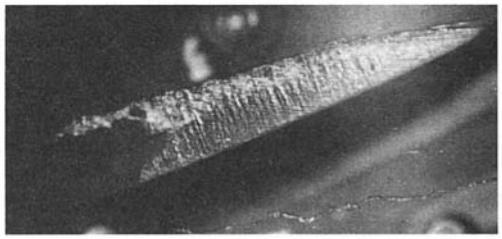

Fig. 5(*a*)

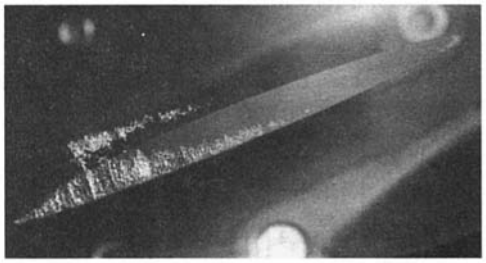

Fig. 5(*b*)

**Fig. 5 Clearance and tip vortex cavitation patterns for clearance with sharp edges ($\delta$ = 1 mm). Effects of backward and forward skew. (*a*) Rotor 2 (backward skew) $\Delta H$ = 200 mb, $\sigma$ = 1.50; (*b*) rotor 3 (forward skew) $\Delta H$ = 200 mb, $\sigma$ = 1.55.**

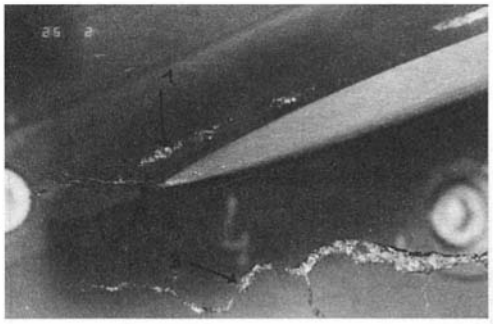

**Fig. 6 Interaction of vortices in the vicinity of the blade trailing edge**

is attached. Bubbles reveal the orientation of the streamlines inside the clearance and, in Figs. 4(*a*) and 5(*a*), streamlines oriented in the direction of rotation (horizontal direction in the picture) and streamlines oriented perpendicular to the blades are both seen. The streamlines oriented in the direction of rotation usually go through the clearance into the shear layer that emerges from it and are rolled up in the tip vortex.

An attached vortex produced inside the clearance was also observed when it was subjected to cavitation. This is shown in Fig. 6. Three vortices are seen interacting in this picture: the tip vortex of the blade (above the blade, label 1 in Fig. 6), the tip vortex generated by the preceding blade (below the blade, label 3) and the clearance vortex emerging at the blade trailing edge (label 2). A vortex similar to our so-called clearance vortex was identified by Farrell and Billet (1994) and subsequently investigated by Zierke et al. (1995). From surface flow visualizations on the blades the latter authors interpreted this vortex emission as resulting from the flow separation on the blade suction side. We did not carry out surface flow visualizations on the blades but the vortex (2) is seen in Fig. 6 to be prolonged inside the clearance by a cavitation streak. This indicates in our opinion that this vortex is emitted inside the clearance rather than on the blade suction side.

## Cavitation Inception

The inception cavitation indexes were determined from the visual observation of cavitation patterns. For each rotor the pressure was lowered (starting from a high pressure level) by steps of 10 to 50 mb and the possible existence of cavitation was examined on each blade using stroboscopic lighting. The thresholds were determined separately for the tip vortex cavitation and for cavitation inside the clearance. In order to reduce the uncertainty that follows from the subjectivity of the observer, two to four investigators took part simultaneously in the observations and in some cases independent investigators operated on different days. The thresholds for intermittent and permanent cavitation patterns were distinguished. As the uncertainty is greater for intermittent cavitation thresholds, this paper reports only on permanent cavitation structure inception.

The experiments were undertaken after degassing the water in the tunnel. The rate of dissolved oxygen was measured to be in the range 0.5–4 ppm. The cavitation inception numbers were determined for rotor 2 without and with moderate gas nucleus injection. No effect of gas nucleus injection was noticed as far as permanent cavitation structures were considered.

Figures 7 and 8 show cavitation inception conditions for clearance and tip vortex cavitation, respectively. The upstream pressure level $P_u$ of cavitation inception is plotted in dimensionless form using the cavitation parameter

$$\sigma = (P_u - P_v)/\Delta H,$$

where $P_v$ is the vapour pressure. Large variations in cavitation inception are noticed when the blade geometry, clearance geom-

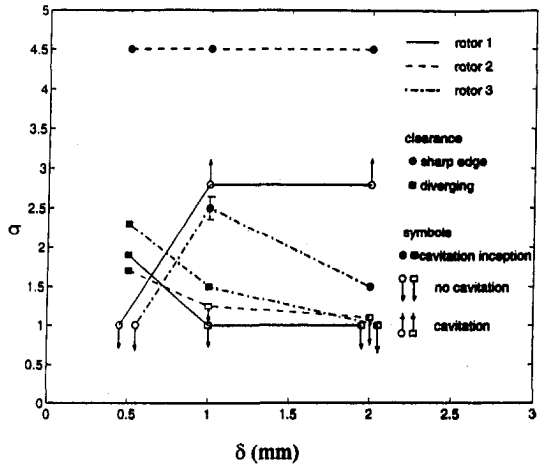


Fig. 7(*a*)

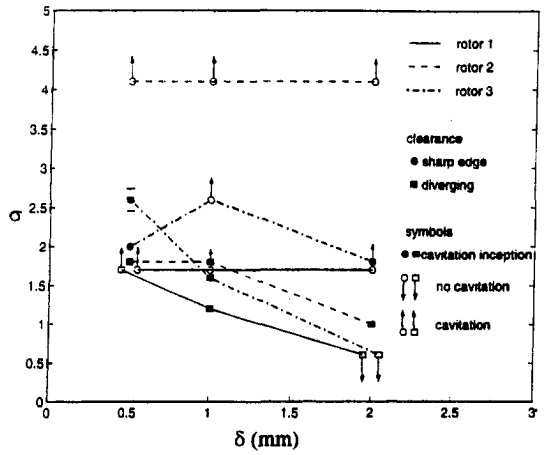


Fig. 7(*b*)

**Fig. 7 Inception conditions for clearance cavitation. (*a*) $\Delta H$ = 200 mb; (*b*) $\Delta H$ = 350 mb.**

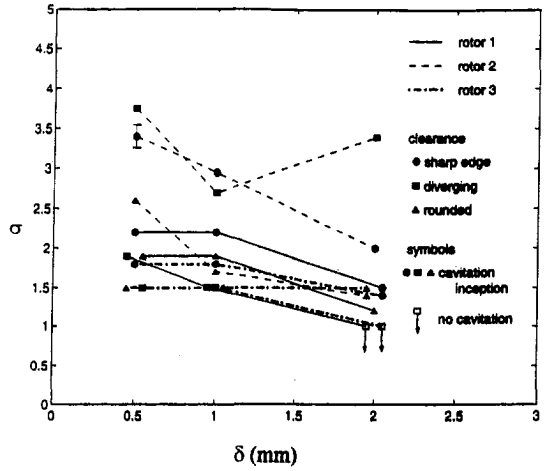


Fig. 8(*a*)

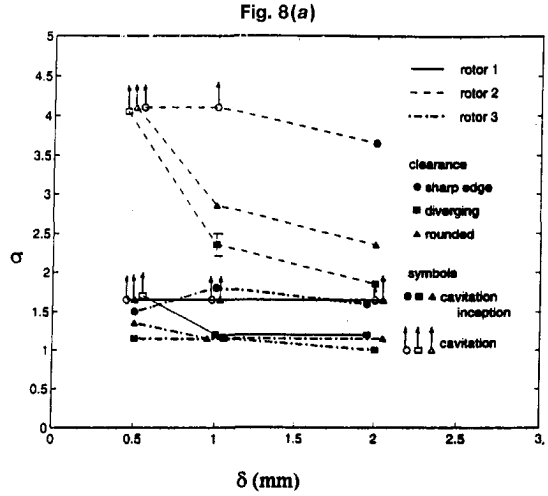


Fig. 8(*b*)

**Fig. 8 Inception conditions for tip vortex cavitation. (*a*) $\Delta H$ = 200 mb; (*b*) $\Delta H$ = 350 mb.**

etry, and gap height are varied but no general trend appears when the variations versus each parameter are considered separately. Figures 7 and 8 highlight the fact that clearance and tip vortex properties should be considered simultaneously for the practical design of rotor blades because some blade features that appear to be efficient for reducing clearance cavitation are less efficient for reducing tip vortex cavitation.

Clearance cavitation inception is observed to vary very much with the clearance geometry. Cavitation was never observed inside clearances having a rounded edge on the pressure side (geometry b in Fig. 4) and clearance cavitation inception is therefore not given in Fig. 7 for this clearance geometry. On the other hand, clearances with sharp edges were usually more rapidly subjected to clearance cavitation than other clearance geometries. Cavitation inception was determined only for a limited number of cases for clearances with sharp edges as it was often still observed at the highest pressure levels considered, in which case the plotted symbol is open and an arrow pointing upward indicates that cavitation inception occurs at a higher value of the cavitation parameter. A particular case was noticed for the gap height $\delta$ = 0.5 mm (Fig. 7($a$)) as no cavitation was observed for two cases inside clearances with sharp edges. Open symbols connected to an arrow pointing downward indicate that the inception condition is at a smaller value of the cavitation parameter. Inception could not be determined because at the lowest pressure levels considered, a large air pocket covered the blade suction side and the head variation across the rotor was drastically reduced. When the clearance diverges toward the suction side and the edge is rounded on the pressure side, clearance cavitation involves the production of small isolated bubbles (Fig. 4($c$)) for the smaller gap height ($\delta$ = 0.5 mm) but cavitation was often not observed inside the clearance for the largest gap height ($\delta$ = 2 mm). Variations in clearance cavitation inception with gap height are significant but the trends change with the clearance geometry. When $\delta$ is reduced to 0.5 mm, cavitation is eliminated inside a clearance with sharp edges whereas it is enhanced inside a rounded and diverging clearance. The only very significant effect of blade skew on clearance cavitation inception was observed for the clearances with sharp edges, in the form of a very strong enhancement of clearance cavitation when a backward skew is applied.

The clearance geometry has more limited effects on tip vortex cavitation (Fig. 8) than on clearance cavitation. Tip vortex cavitation inception does not vary much with gap height (in the range considered here). When variations are observed, tip vortex cavitation inception is usually delayed by increasing the gap height. It was not observed in our experiment that a diverging gap delays tip vortex cavitation, as initially suggested by Gearhart (1966). Figure 8 shows that blade skew may significantly modify cavitation inception. Backward skew strongly enhances tip vortex cavitation. When the clearance is rounded on the pressure side (diverging or non-diverging) tip vortex cavitation inception was delayed for several blades with a forward skew as compared to blades with no skew but an opposite observation was also made once ($\Delta H$ = 200 mb, $\delta$ = 2 mm).

The cavitation inception numbers obtained for $\Delta H = 200$ mb and $\Delta H = 350$ mb compare satisfactorily when clearance cavitation is considered, but more significant differences are noticed when tip vortex cavitation is considered. This leads to the conclusion that the magnitude of flow inside the clearance is basically scaled by the pressure variation across the rotor, while the vortex strength is not a simple function of $\Delta H$. It must be mentioned that Farrell and Billet (1994) introduced a cavitation index built on the tip speed that differs from ours. As a consequence the cavitation index in their experiment varies significantly in relation to the flow parameter, which basically represents the ratio of axial velocity to tip speed.

## Wall Pressure

**Measurement and Analysis Procedure.** Wall pressure was measured using 8 piezo-resistivity pressure gauges placed in the lower part of the test section in the region swept by the blades. The pressure gauges were spaced out in the axial direction with a distance between two successive gauges of 5 to 8 mm. The first gauge was located 6 mm upstream of the leading edges of the rotor blades while the last was located 6 mm downstream of the trailing edges. The other six gauges provided pressure measurements in the blade clearance when a blade passed over them. The gauges, manufactured by Kulite (type XTM 190 M 100 A), were placed in cavities connected by a 1 mm diameter tube to the inner wall of the test section. The uncertainty in pressure measurements was found to be ±4 mb. The pressure variations were digitized at a frequency of 30.72 kHz, which was included in the frequency band of the pressure gauge and its cavity. The pressure measurements were averaged over 31 rotation periods. The temporal variations in pressure were analysed as being the spatial distribution of pressure on the inner wall of the test section at 2048 points along the perimeters of 8 circles. Plotting of the pressure fields in the form of isobar maps makes the analysis easier (Figs. 9 and 10). A spline function is computed using the set of digitized data and the isobar map is plotted from this interpolated function. Error bars have not been included in the isobar maps because they are not determined uniformly over the whole area depending on the direction and pressure gradient. The lines in the azimuthal direction along which pressure was measured are indicated in Fig. 9($a$). The interval of digitization in the azimuthal direction (0.6 mm) is much smaller than that in the axial direction (5 to 8 mm).

**Results.** Wall pressure measurements were performed with the rotor operating both at low upstream pressure and high upstream pressure. Figure 9 shows the isobar maps for the blades photographed in Fig. 4. The plotted pressure $p*(x, y)$, which is the difference between the measured pressure and the upstream pressure, is between −400 mb and −500 mb over an area that covers a large fraction of the clearance. Since the upstream pressure is $P_u = 460$ mb, the pressure in those areas is close to the vapour pressure. Comparison of Figs. 4 and 9 shows that the areas surrounded by the isobar $p* = -400$ mb cover the observed cavitation zones very well. In particular, the wide cavitating zone that includes the clearance, shear layer and tip vortex is displayed in the isobar maps for the clearance with sharp edges (Fig. 9($a$)) and the cavitating tip vortex is clearly identified on all pressure maps.

The isobar maps measured for the same conditions of operation but at a much higher upstream pressure level ($P_u = 1.64$ bar) are shown in Fig. 10. The lowest pressure levels (−900 mb) are reached in the clearance with sharp edges (Fig. 10($a$)). The minimum pressure level is about −600 mb in the diverging clearance with a rounded edge on the pressure side (Fig. 10($c$)). The minimum values of $p*$ are approximately the same in Figs. 9($b$) and 10($b$), in agreement with the observation that no cavitation occurs in clearances with a rounded edge on

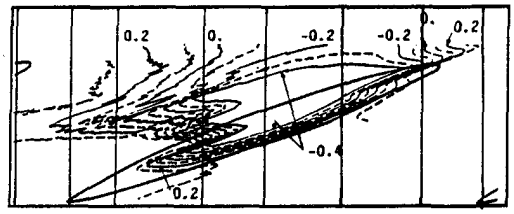


Fig. 9($a$)

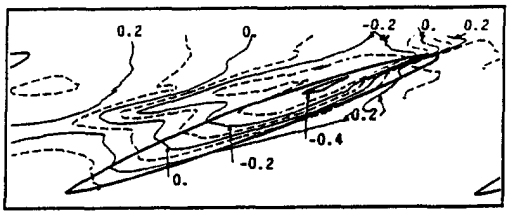


Fig. 9($b$)

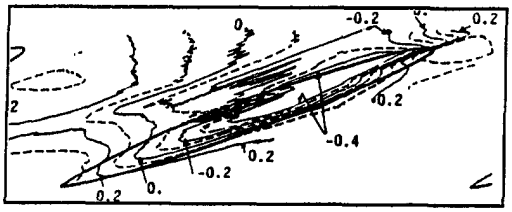


Fig. 9($c$)

**Fig. 9 Isobar maps measured on the annulus wall of the test section for three clearance geometries. Rotor 2 (backward skew). ($\delta$ = 1 mm) Exp. conditions: $\Delta H$ = 350 mb, $\sigma$ = 1.2, $P_u$ = 460 mb. Pressure step between two neighboring lines: 100 mb. ($a$) Clearance with sharp edges; ($b$) clearance with rounded edge on pressure side; ($c$) clearance with rounded edge on pressure side and diverging toward the suction side.**

the pressure side. For the blades considered in Figs. 10($a$) and 10($c$) there is almost no cavitation at this pressure level (except for some limited structures which could never be eliminated, as mentioned before). By comparing the minimum pressure values measured in the clearances it is possible to classify the efficiency of the various parameters considered in this study in terms of delaying or eliminating cavitation.

Isobar maps were plotted for the different rotors and blades. For the sake of space, the comparison between cases with no skew, forward skew and backward skew is not presented in this paper. It is confirmed by isobar maps that the pressure minima are displaced toward the trailing edge when the blades have a forward skew.

## Conclusions

The effects of various parameters on clearance and tip vortex cavitation in an axial flow pump were investigated simultaneously in a systematic way. Cavitation inception indexes were determined and the different cavitation patterns were described from visual observations and wall pressure measurements.

Whenever it was possible, the experimental procedures were chosen in order to make a reliable comparison of the effects of the different parameters. Cavitation inception was simultaneously determined for the different clearance geometries and gap heights that were implemented on each rotor with all other parameters being unchanged.

The most significant results can be summarized as follows:

- The clearance geometry has a very strong effect on clearance cavitation, which can be eliminated when the clearance edge is rounded on the pressure side. This is not a new observation, but it confirms that tip vortex cavitation is actually the most problematic cavitation arising. Modifying the clearance

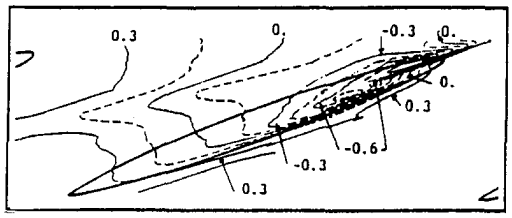


Fig. 10(*a*)

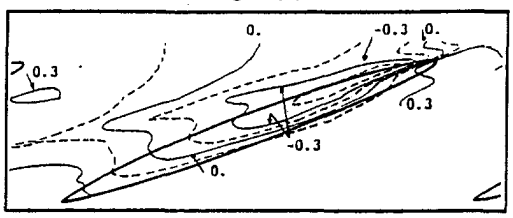


Fig. 10(*b*)

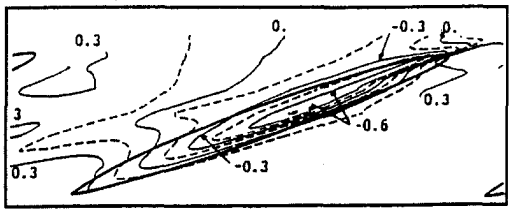


Fig. 10(*c*)

**Fig. 10 Isobar maps measured on the annulus wall of the test section for three clearance geometries. Rotor 2 (backward skew). ($\delta$ = 1 mm.) Exp. conditions: $\Delta H$ = 350 mb, $\sigma$ = 4.6, $P_u$ = 1640 mb. Pressure step between two neighboring lines: 150 mb. (*a*) clearance with sharp edges; (*b*) clearance with rounded edge on pressure side; (c) clearance with rounded edge on pressure side and diverging toward the suction side**

geometry with a gap diverging toward the suction side is not an efficient way of delaying tip vortex cavitation while small scale isolated bubbles are produced inside the gap in this case.

- The effects of gap height are hard to interpret from our experiments. Strong effects of gap height on clearance cavitation were observed in some cases but the trends depend on other parameters such as clearance and blade geometries. Farrell and Billet's (1994) model of leakage vortex inception shows a cavitation index minimum when the ratio $\lambda = \delta/e$ of the gap height to the gap length is about 0.2. The model predicts that the cavitation index will slowly increase for $\lambda > 0.2$ whereas it will increase very rapidly when $\lambda$ is below 0.1. The experimental inception conditions that were investigated by Farrell and Billet are, however, limited to a range of values of $\lambda$ ($0.1 < \lambda < 0.56$) where the tip vortex cavitation index does not vary much. The $\lambda$ parameter in our experiment was within the range $0.06 < \lambda < 0.38$. The effect of gap height on tip vortex cavitation appears to be less significant than it is on clearance cavitation in the range of variations of $\lambda$ considered in our experiment.
- Applying backward skew on rotor blades has a strong effect on clearance and tip cavitation, which are both increased. This is interpreted as being the result of modifying the pressure distribution along the blade chord. When the skew is backward, the clearance flow is concentrated in the vicinity of the leading edge where the tip vortex is initiated, leading to an increase of both clearance and tip vortex cavitation. On the other hand, when a forward skew is applied, a significant part of the clearance flow occurs in the vicinity of the trailing edge. The contribution of the clearance flow to tip vortex emission is more smoothly distributed along the blade chord, implying that tip vortex cavitation is delayed as compared with the case with no skew.

## Acknowledgments

This work was supported by the French Ministry of Defence (DRET contracts no. 89/403, 90/518 and 92/523).

## References

Farrell, K. J., 1989, "An Investigation of End-Wall Vortex Cavitation in a High Reynolds Number Axial Flow Pump," *Technical Report TR 89-004, Pennsylvania State University.*

Farrell, K. J., and Billet, M. L., 1994, "A correlation of leakage vortex cavitation in axial-flow pumps," ASME JOURNAL OF FLUIDS ENGINEERING, Vol. 116, pp. 551–557.

Gearhart, W. S., 1966, "Tip Clearance Cavitation in Shrouded Underwater Propulsors," AIAA, *Journal of Aircraft,* Vol. 3, No. 2, pp. 185–192.

Heyes, F. J. G., and Hodson, H. P., 1993, "Measurement and Prediction of Tip Clearance Flow in Linear Turbine Cascades," ASME *Journal of Turbomachinery,* Vol. 115, pp. 376–382.

Müller, H., 1935, "Cavitation dans l'entrefer des turbomachines rapides," *Z-VDI 79,* No. 39, pp. 1165–1169 (Neyrtec translation, 1978, R.20032).

Murthy, K. N. S., and Lakshminarayana, B., 1986, "Laser Doppler Velocimeter Measurement in the Tip Region of a Compressor Rotor," *AIAA Journal,* Vol. 24, No. 5, pp. 807–814.

Novoderezhkin, R. A., Karelin, V. Y., and Demidov, V. V., 1983, "Experimental Studies of Tip Clearance Cavitation," *Institute of Civil Engineering, Moscow.*

Papir, A. N., and Golikov, V. A., 1985, "The Evaluation of Slot Clearance Cavitation Formation in Hydraulic Machines," *Hydroturbo Conference,* Ostrava, Czechoslovakia, Vol. 2, D2, pp. 127–134.

Rains, A., 1956, "Tip Clearance Flows and Incipent Cavitation," Hydrodynamics Laboratory, California Institute of Technology, Report no. E.56–1.

Zierke, W. C., Farrell, K. J., and Straka, W. A., 1995, "Measurements of the Tip Clearance Flow for a High-Reynolds Number Axial-Flow Rotor," ASME *Journal of Turbomachinery,* Vol. 117, pp. 522–532.

**M. A. Dominguez-Cortazar**
Assistant,
Centro University,
Queretaro, Mexico

**J. P. Franc**
Research Assistant.

**J. M. Michel**
Research Director.

Laboratoire des Écoulements
Géophysiques et Industriels,
Institut de Mécanique de Grenoble,
BP 53, 38041 Grenoble Cédex 9, France

# The Erosive Axial Collapse of a Cavitating Vortex: An Experimental Study

*The erosive efficiency of cavitating vortices is well known, although its exact mechanism has not been clarified. In order to bring fundamental information to the subject, a new device called "Cavermod" was designed in which axial collapse of a cavitating vortex is produced. We consider in this paper the design principles of the apparatus, the measurement equipment necessary for observing the phenomenon (collapse time of the order of a few milliseconds, axial collapse velocity varying between 70 and 700 m/s), and the main features of the flow. We also study the damage produced on erosion targets in order to correlate the vortex collapse with the erosion indentation features.*

## 1 Introduction

The study of fundamental hydrodynamic mechanisms in cavitation erosion has been the subject of many research works and publications for about thirty years. In general, the research effort was directed to the situation in which a bubble collapses and rebounds, either producing high pressures and shock waves in its vicinity or giving a small re-entrant jet in the case of symmetry defect. It has been both theoretically and experimentally shown that if a cavitation bubble collapses near a rigid wall, it produces a very high-pressure over a small area of the solid surface. It has also been found that the impulsive pressure is strongly dependent on the distance of the bubble to the solid wall. Well-known papers are associated with those models, among them the studies of Hickling and Plesset (1963), Benjamin and Ellis (1966), Plesset and Chapman (1971), Lauterborn and Bolle (1975), Fujikawa and Akamatsu (1980), Blake et al. (1987), and Tomita and Shima (1986).

As well as bubble collapse, damage is also associated with the collapse of cavitating vortices. Selim and Hutton (1983) show that the wakes of partial cavities, in which a number of cavitating vortices are shed, seem to be intense sources of erosion. Soyama et al. (1992) also report that the cavitation erosion in hydraulic machinery is particularly severe when cavitation vortices are shed from the rear part of an attached cavity and collapse rapidly in the vicinity of a solid wall. This was at the origin of the development of the so-called Cavitation Vortex Generator devised by Lecoffre (1978) and realized by Lecoffre et al. (1981). In this device, a cavitating vortex is created then annihilated by successively closing and opening a valve on the input flow line of a conical chamber. It appears to be an efficient tool for carrying out metallurgical tests, see e.g., Karimi (1988). Very high speed visualizations of the vortex collapse by Avellan and Farhat (1989) have shown that it is mainly axial for most of its duration. However, the final stage is marked by the emission of spherical shock waves from several points which resemble collapsing bubbles. Thus, the situation is not simple and requires further examination.

In order to provide fundamental information about this subject, a special device called "Cavermod" (abbreviation of CAVitation ERosion MODel) was designed. Like the Vortex Generator, this device uses the axial collapse of a cavitating vortex, but here the vortex is created in a closed rotating chamber, filled with deaerated liquid. The volume of the chamber can be slightly increased in order to form a vapor core in the vicinity of the rotation axis; then it is suddenly decreased in such a way that an axial collapse of the vapour core is produced. Of course the basic motion of the liquid is a solid rotation and not a true vortex; it must be noted that a solid rotation is also found in the central region of the Vortex Generator.

In industrial situations, cavitating vortices appear either as continuous vapor cores or as chains of bubbles entrapped in the low pressure vorticity filaments. Their axial collapse can occur if they are properly directed relative to the ambient pressure gradient and/or the local directions of the strain rate tensor (example of such situations in case of a wake shear flow can be found in Belahadji et al., 1995). When these favorable conditions are fulfilled, a continuous core should disappear approximately as shown in the present paper whereas bubble chains would probably result in cascade mechanisms. In the present study, only the axial collapse of a vortex is studied, but the formation and collapse of a spinning bubble chain is possible and its study remains an interesting objective.

## 2 Basic Ideas

The first point to be examined concerns the transfer of mechanical energy from the liquid flow to the solid wall, by which erosion is brought about. Such a transfer needs two conditions be satisfied: a high level of stress, in order to exceed some limit of material resistance, for example the yield stress, and a loading time sufficient to make nonreversible transformation of the solid material. Concerning this last point, the shock wave coming from the bubble collapse and rebound, as calculated for example by Fujikawa and Akamatsu (1980), seems to give times of an order lower than one microsecond. If we consider microjets of diameter $d$, the time of the impulse they transmit to the wall is of the order $d/2C$, where $C$ is the sound velocity in water. With current values of $d$ (lower than 1 mm), we obtain 0.3 $\mu$s. It will be shown below that, due mainly to the larger size of the impact area, greater loading times are obtained with the present apparatus.

The second point is related to the physical model used in the design of the apparatus (Fig. 1). The solid rotation of a body of liquid with a central vapour core is created in a rotating chamber closed on one side by a piston. The piston plays the role of a wave-maker for that free surface flow in which gravity is replaced by the centrifugal forces. The required axial collapse can be obtained if the piston moves rapidly enough toward the chamber interior, creating a steeply fronted wave which progressively fills the vortex core. With a rigid cylindrical

Contributed by the Fluids Engineering Division for publication in the JOURNAL OF FLUIDS ENGINEERING. Manuscript received by the Fluids Engineering Division November 28, 1995; revised manuscript received February 11, 1997. Associate Technical Editor: O. C. Jones.

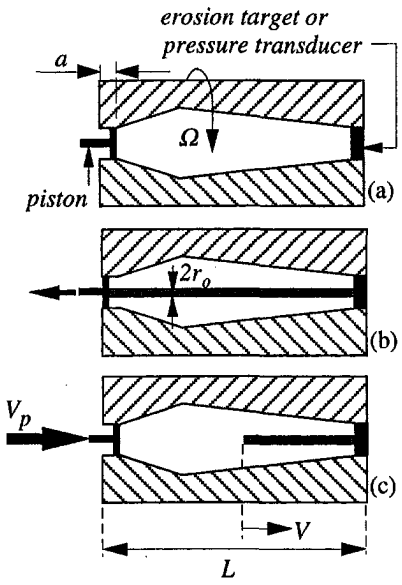


**Fig. 1 Principle of the apparatus**

chamber (radius $R$), calculations based on conservation of mass and momentum of an incompressible fluid are rather simple (Dominguez-Cortazar 1994). The main results are the following: ($a$) The minimum value of the piston speed required to obtain a wave to fill the vapor core is:

$$V_p \geq \frac{r_o^2 \Omega}{R\sqrt{2}}$$

In current circumstances, that limiting value is quite small and it can be easily obtained. For example we obtain about 0.2 m/s with $R$ = 20 mm, $r_0$ = 3.3 mm, $\Omega$ = 4000 rpm ($b$) Then the axial collapse velocity $V$ is related to $V_p$ by the following relation:

$$V = V_p \frac{L}{a} = V_p \frac{R^2}{r_o^2}$$

Very large collapse velocities can be thus obtained. In the case when $r_o$ becomes very small (which indeed needs a higher rotation speed, as mentioned in Section 3), these relations would give infinite values for $V$. In fact, two main mechanisms tend to limit the V-values: on one hand the compressibility effects and on the other, the volume expansion of the rotating chamber under centrifugal forces. These effects are not taken in acount in the last relations.

A rough estimate of the loading characteristics can be made if we suppose that the wave has a front perpendicular to the axis of the chamber. If that was the case, the value of the overpressure produced at the end of the collapse on the target or the pressure transducer would be expressed approximately by the water hammer formula:

$$P = \rho C V$$

which gives about 1500 bars with V = 100 m/s. The loading time can be estimated from the expression $r_o/C$, which gives 2.3 $\mu$s for $r_o$ = 3.3 mm. It must be understood that this model gives rather extreme values: actually, the core vortex closure does not take the shape of a wave with a steep front, but rather it resembles an ogive with length $l$ of 10 mm (see Fig. 4 for example). Then the end of the collapse takes a larger time of the order of $l/V$, ie about 0.1 or 0.01 ms, while the overpressure is smaller than the one given by the water hammer formula. Despite these differences, Cavermod proves to be very efficient in producing cavitation erosion.

## 3 The Experimental Apparatus

The main part of Cavermod is a closed rotating chamber filled with water. It is made of plexiglas in order to allow observation of the phenomena. At one end of the chamber, a pressure transducer or an erosion target is mounted to receive the collapse impact. At the other end, the chamber is closed by a piston and a rubber membrane. To make its complete filling with deaerated water easier, the internal geometry of the chamber is biconical.

The operating principle is shown in Fig. 1. The chamber filled with dearated water rotates at velocity $\Omega$ (Fig. 1($a$)); the control system allows the axial displacement of the piston, $a$, which results in the volume increase of the chamber and in the appearance of the vapor core (Fig. 1($b$)). Then, a sudden volume reduction, due to the shock of a projectile against the piston head, produces the expected cavity collapse (Fig. 1($c$)). In addition to the control of the three main parameters of the flow, $\Omega$, $r_o$ and $V$, some other less important advantages can also be expected from this configuration, for instance the concentration of the erosive impacts on a small area of the solid wall (some square millimeters) around the rotation axis and the use of liquids other than water.

The initial size of the vapor core is given by the conservation of the liquid volume. For a given size of the cavity, the axial collapse velocity is controlled by the driving pressure of the projectile $\Delta p$ (which controls the shock intensity between the projectile and the piston head). That driving pressure is ensured by a pneumatic system: thus, by adjusting $a$ and $\Delta p$, we can control two fundamental parameters of the flow: $r_o$ and $V$. This means that all kinds of vortex collapses (from the weakest to the most violent) can be realised. However, the minimum radius of the cavity is limited by the maximum rotation velocity of the chamber via the stability condition given by Rosenthal (1962): the vapor core radius has to be larger than a critical value expressed as

$$r_{oc} = (4S/\rho\Omega^2)^{1/3}$$

where $S$ is the surface tension. This equation gives 1.18 mm for the maximum rotation rate of 4000 rpm in the case of water. The sketch of the apparatus is shown in Fig. 2. The main design values are:

| | | |
|---|---|---|
| —Length of the test chamber | ($L$) | 156 mm |
| —Piston displacement range | ($a$) | 1 to 4 mm |
| —Chamber rotation range | ($\Omega$) | 0 to 4000 rpm |
| —Piston displacement velocity | ($V_p$) | 0 to 6 m/s |
| —Driving pressure of the projectile | ($\Delta p$) | 0 to 6 bars. |

## Nomenclature

$a$ = piston displacement (mm)
$C$ = sound velocity in water (m/s)
$L$ = chamber length (mm)
$r_o$ = initial radius of the vortex (mm)
$R$ = piston radius (mm)
$V$ = axial collapse velocity of the vortex (m/s)
$V_p$ = piston displacement velocity (m/s)
$P$ = impact pressure against the solid wall (Mpa)
$\Delta p$ = driving pressure of the projectile (bars)
$\rho$ = water density (kg/m3)
$\Omega$ = chamber rotation rate (rd/s)

Return now to the fundamental parameters of the flow. From the radius $R$ of the equivalent cylindrical chamber, the length $L$, the radius $r_o$, the collapse velocity $V$, and the rotation rate $\Omega$, it is possible to build three dimensionless numbers, the most important of them being the Rossby number $\Omega r_o/V$. As this number is very small in the normal running conditions, it might be inferred that Coriolis forces do not play an important role at first sight. Then, in order to model the flow numerically, it becomes possible to assume that in the rotating frame the flow is irrotational, which permits to use simplified techniques issued from the boundary integral method (Dominguez-Cortazar and Canot, 1995). Such methods result in the formation of a reentrant jet in the closure region of the vortex core. However, experimental tests do not show such a jet (see Section 5). Consequently, in spite of the small value of the Rossby number, it seems that Coriolis forces, by which the total axial moment of momentum of the liquid body remains constant during the vortex collapse, have to be taken in account for a correct representation of the Cavermod flow.

In addition to the previous discussion, dynamical parameters such as the liquid density $\rho$ and the vapor pressure $p_v$ should first be outlined. However, consideration of a cavitation parameter is not pertinent: on the one hand, no ambient pressure can be defined in the chamber before the formation of the vapor core, and on the other, when the vapor core appears, the pressure in the chamber is fixed by the vapor pressure near the axis. Then, as far as delays due to vaporization processes can be neglected and global flow behavior only is considered, comparison with real situations has to be made mainly on the basis of the Rossby number. If one is interested also in the final stage of the collapse and the splitting up phenomena (there is experimental evidence that the end of the first collapse is marked by a large number of local erosive events, the size of which is lower than the radius $r_o$ by one order of magnitude at least), one must also take into account the liquid surface tension and the Weber similarity. Of course, the overpressure produced on the erosion targets will be mainly correlated by the collapse velocity $V$, the speed of sound $C$ and the liquid density $\rho$, while the loading duration should be referred either to the time $r_o/C$ or to the time $l/V$, where $l$ is the length of the ogive in the collapsing zone, as previously discussed.

## 4 Specific Instrumentation and Uncertainties

The flow produced in the Cavermod is highly unsteady and the cavitation vortices are characterized by a total lifetime of about few milliseconds. In consequence various visualization techniques are needed for experimental study. The first one, a high speed camera, PHOTEC (up to 40,000 frames per second), has been used to record the main events of the phenomenon. However, the maximum rotation speed of its driving motor is not high enough (with a minimum interframe of 25 $\mu$s) so, only a few images of the first vortex collapse can be obtained. For the second visualization device, one takes advantage of the fact that the flow is fairly repeatable from one shot to the other when all control parameters are kept the same. The photographs can be taken under flash lighting which is triggered at increasing times from an initial instant given by a shock accelerometer.

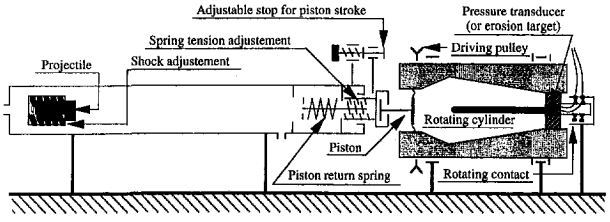


**Fig. 2 The main mechanical elements of Cavermod**

The light source is a Palflash 500 (from HADLAND Corp.) with light-pulse of about 250 ns. In this way it is possible to reconstitute the sequence of the first vortex collapse. The same device was used to measure the piston displacement as a function of time.

The vortex collapse velocity, just before its terminal phase, is measured by means of two parallel laser beams separated by 40 mm, which are received by two photoelectric cells in the absence of vortex and are occulted by the interface of the hollow vortex. Both signals are transfered to a digital oscilloscope, NICOLLET, with high acquisition rate (200 MHz), which enables measurements of the time interval between the two laser beams.

A piezo-electric pressure transducer (PCB 109A, diameter 6.3 mm, resonant frequency 500 kHz and rise time of about 1 $\mu$s) is flush-mounted at the end section of the chamber opposite to the piston (Fig. 1). Its signal is proportional to the total force it sustains, subject to the condition that its rise time is small enough (Vogel and Lauterborn, 1989). Even though its size is significantly larger than the size of the erosive events, we can at least deduce the mean pressure on the target as a function of time (Le et al., 1993).

The error on geometrical parameters (chamber length $L$, piston radius $R$) can be considered as negligible. For the fundamental quantities, the uncertainties are the following: 1 percent for $\Omega$, 0.05 mm for $a$, 0.1 bar for $\Delta p$. Despite of the geometrical relation between $r_o$, $R$, $L$, and $a$, the $r_o$-error is quite large due to the additional effect of centrifugal forces on the chamber volume (see Section 2): it can be estimated as 0.3 mm. The uncertainty on the collapse velocity is about 10 percent. In Fig. 6, the error on abscissae (time) is considered negligible, while the ordinates (tension) cannot be related precisely to a pressure value. The error on the vortex length is 3 mm. Finally in Fig. 8, the size of indentations is known within a range of about 5 percent. All those values are estimated as maximum values.

## 5 Main Features of the Flow

Figure 3 shows a schematic résumé of the main events recorded with the high speed camera. In general, four rebounds are observed, but only two are represented. Some interesting features of the flow can be observed on this diagram. First, the linear variation of the vortex length proves that the first collapse is mainly axial and the measured velocity $V$ is really typical of all the first collapse. Second, for the present experimental conditions, the duration of the axial stage of the collapse is about 0.3 ms. After the first collapse, subsequent formation and disappearance of the cavity are of radial type because the velocity of the secondary piston displacement becomes smaller than the critical value needed by the axial collapse.

Figure 4 shows a sequence of photographs of the first implosion reconstructed from separated shots. It confirms the axial nature of the vortex collapse. During the first instants, the free surface of the cavity appears to be unperturbed outside of the closure region. This one appears whitish and its details are not clear. Nevertheless, one can see some spots of interface instabilities on several images. The left end of the whitish region moves with a speed two or three times larger than the vortex closure and quickly invades all the cavity length.

The propagation of the whitish region produces, in the neighborhood of the target side, a kind of two-phase torus whose internal diameter is approximately equal to the initial diameter of the vapour core.

From the first instants of the collapse, on the right side of the closure region, we observe a narrow vapour core near the piston together with a more or less helicoidal vapour residue which follows the closure region of the cavity. The vapor residue is in good agreement with the conservation of local moment of momentum, which prevents the liquid elements from reaching the axis of rotation.

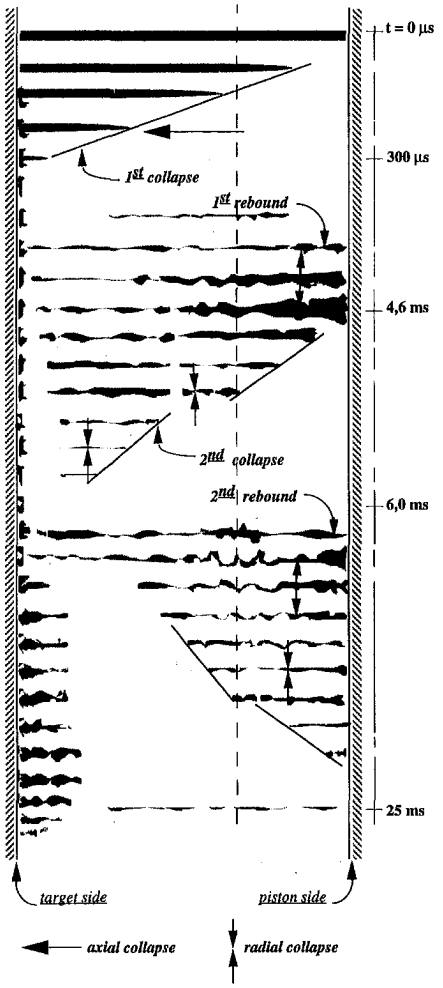


**Fig. 3 Schematic diagram of the main events during the total collapse time ($\Delta p$ = 3 bars, $r_o$ = 1.6 mm, $\Omega$ = 3500 rpm)**

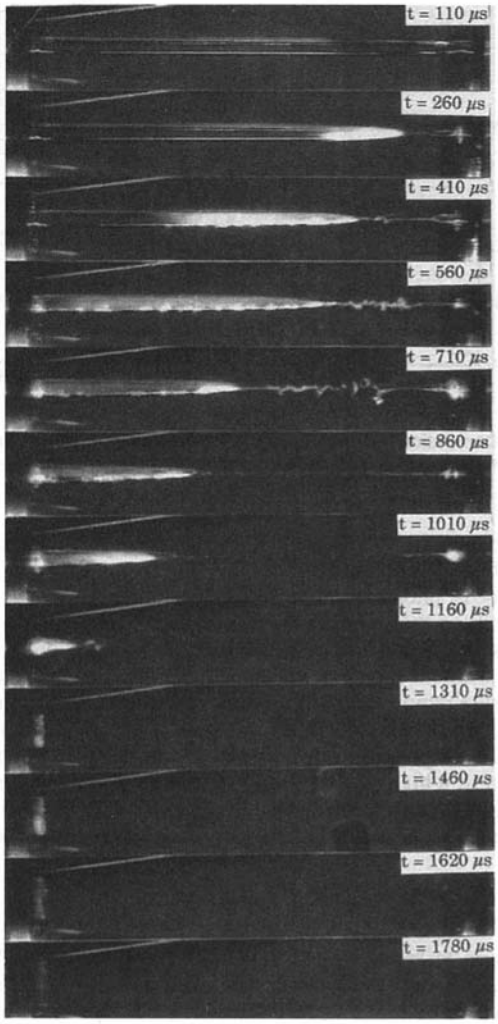


**Fig. 4 The first collapse of the cavity ($\Omega$ = 3500 rpm, $r_o$ = 2.9 mm, $\Delta p$ = 1.0 bar)**

The axial collapse velocity measured with the laser beam system is shown in Fig. 5 for several experimental conditions. These values are of the same order of magnitude as the velocity values estimated with the high speed camera. For a given value of the shock pressure $\Delta p$, the axial collapse velocity is as large as the initial size of the cavity is small. In the case of the smaller $\Delta p$-values, the dependence of the collapse velocity on the inverse of the vapor core area is almost linear, so that it can be inferred that the geometric effect is prominent. In the case of larger $\Delta p$-values, the results are less clear. In particular, the maximum collapse velocity seems to be not very dependent on the driving pressure (attention must be paid to the large uncertainties in Fig. 5). On the whole, for a first approach and if we assume that the high pressure during the vortex collapse is due to the rapid axial velocity of the interface which strikes the solid wall, the smaller cavities must be more aggressive than the larger one. For instance (at the same $\Delta p$ value of 1 bar), in the case of a cavity of $r_o$ = 2.9 mm, the axial velocity $V$ is about 100 m/s and the order of magnitude of the impact pressure, estimated from the water hammer formula $P = \rho CV$, is around 140 Mpa whereas it is equal to 540 Mpa if $r_o$ = 1.6 mm, because $V$ = 390 m/s. As already mentioned, that assertion has to be tempered by consideration of the loading time (which decreases with the vapor core radius) and also of the limiting effects of compressibility.

The direct pressure measurements give, at the final stage of the first collapse, about eight pressure peaks. The results obtained from the transducer were only qualitative because the amplitude signal is strongly dependent on the transducer area and on the frequency ratio between the transducer characteristics and those of the final stage collapse (Dominguez, 1994). However, the transducer allowed us a temporal characterisation of the main events of the phenomenon.

The pressure peaks seem to have the same duration as other classical cavitating structures (some microseconds). Figure 6 shows a temporal correlation between the evolution of the vortex length and the instant when the impulsive pressure appears.

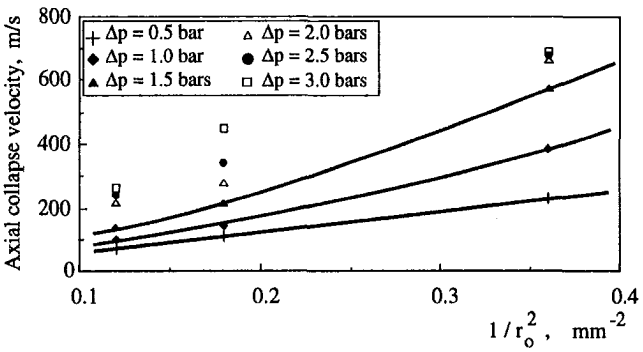


**Fig. 5 Variation of the axial velocity versus the initial size of the vapour core ($\Omega$ = 3500 rpm, relative uncertainties: $\delta\Delta p$ = 0.1 bar, $\delta V/V$ = 10%, $\delta(1/r_o^2)/1/r_o^2$ = 20%)**

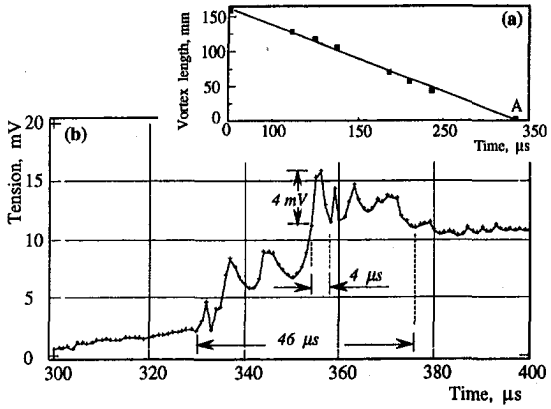


**Fig. 6 Correlation between the axial vortex collapse and the impulsive pressure peaks ($\Omega$ = 3500 rpm, $r_o$ = 1.6 mm, $\Delta p$ = 1.0 bar, $\delta l$ = 3 mm)**

At time $t = 330$ $\mu$s (cf. point A, Fig. 6($a$)), which corresponds to the final minimum length of the vortex (as deduced from a sequence of photographs of Fig. 4), we observe the first impulsive peak on the pressure signal (cf. Fig. 6($b$)).

Thus the first pressure peak in Fig. 6 is attributed to the impact from the interface vapour-liquid, when the ogive apex of the closure region reaches the pressure transducer. This interface impact probably results in the creation of tiny new bubbles due to the disintegration of the two-phase torus. These bubbles are exposed to a high-pressure field so that they may collapse rapidly. Consequently we note, in a very short time interval of about 50 $\mu$s, multiple pressure peaks like those shown in Fig. 6.

## 6 Erosion Tests

Erosion tests on various materials (stainless steel, bronze, copper, brass, and aluminium targets) are carried out with deareated distilled water (water is considered fully deaerated if no air bubbles appear after a shot). The erosive efficiency of the Cavermod has been successfully demonstrated. Indeed, with a single shot we obtain multiple erosion pits. After every shot, the pits have been observed with a differential interference microscope (Nikon Optiphot). The erosion damage at the surface of the test piece is analysed by the number, size and depth of the pits. The influence of the axial collapse velocity, initial size of the vortex and shot number on damage have been studied. We also studied the spatial distribution of the pits in order to correlate the vortex collapse and the erosion indentations features.

Figure 7 shows the damage patterns caused on pure aluminium targets (Vickers Hardness 50) and under increasing $\Delta p$ values. Each test corresponds to a single shot. As the driving pressure of the piston increases, the damage pattern increases. However, the average diameter of the damage pattern is conserved because the three tests are carried out with the same initial size of the vapour core. In some cases, as with $\Delta p = 6$ bars (cf. Fig. 7($c$)), the density of erosion pits is so high that they cannot be counted: in such a limiting case, the erosion pattern can be considered as due to the implosion of the vortex itself.

The numerous indentations illustrate the complexity of the final stage of collapse. However, by studying the damage pattern, some interesting observations can be drawn:

- Every vortex collapse is characterized by a nearly circular erosion spot. The size of this spot is approximately equal to the initial core diameter. It is formed by numerous indentations of very different sizes. In general, large indentations appear on the erosion spot periphery and the smaller in the central part.

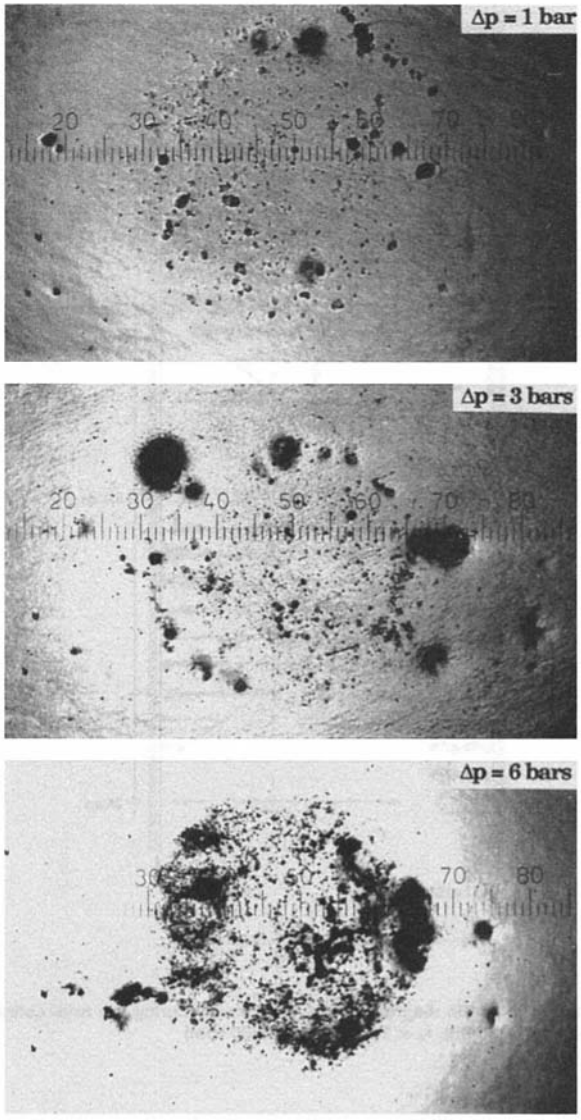


**Fig. 7 Erosion patterns on aluminium $\Omega$ = 3500 rpm, $r_o$ = 1.6 mm (10 div. = 0.62 mm)**

- After a single shot, the indentation distribution is often asymmetric: this means that the indentations appear on about $\frac{2}{3}$ of the total polar section. This observation seems to be related to photographic visualisation, which shows that the perturbations on the free surface of the vortex are not symmetrical with respect to the rotation axis.
- As regards the size of indentations (from some $\mu$m to 500 $\mu$m), the maximum number occurs for the sizes smaller than 10 $\mu$m in radius (cf. Fig. 8, for several experi-

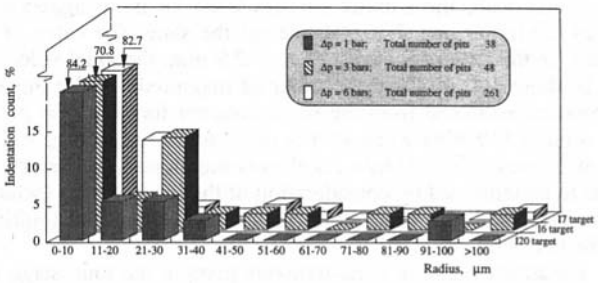


**Fig. 8 Distribution of indentation sizes on stainless steel specimens ($\Omega$ = 3500 rpm, $r_o$ = 1.6 mm, uncertainty of 5% on the indentation radii)**

mental conditions, with stainless steel 316 L, Vickers hardness 150). Nevertheless, the main contribution to the total volume eroded is provided by the largest indentations.

- For long-term exposure, shots produce indentations at a proportional rate. The number, the size, and the depth of indentations increase under larger $\Delta p$, that is under larger collapse velocity and also with the softer metal.
- For all the materials tested, the depth/diameter rate of the indentations is between 0.85 and 1.5 percent; those values are approximately the same as those reported in the literature (Belahadji et al., 1991).

Consequently, these observations lead us to think that in the final stage of the collapse, the erosion process, is dominated by the mechanisms which result from the implosion and rebounds of spherical bubbles. Those bubbles are isolated in space, but they are perhaps subject to reciprocal interactions. Now the problem is to know the way in which these events appear from the cavitating vortex flow. A possible scenario is that the large amount of bubbles are formed in the final torus described previously, which itself seems to result from instabilities of the vapour core free surface. But at the present time it is not possible to say if unstabilities are fundamental or if they result from the strong excitation of the mechanical system by the shock of the projectile on the piston head. However, the experimental work has allowed us to evaluate the moments when the critical events of the erosion take place.

## 7 Conclusion

A new device for the study of cavitation erosion due to the axial collapse of a cavitating vortex was presented. The three main parameters of the flow in this device can be controlled. The apparatus appears to be efficient as each shot produces a significant number of erosion indentations on metallic targets. Collapse velocities between 70 and 700 m/s are realized. Direct pressure measurements by a small transducer allowed us to identify the critical erosive instants. The visualization tests show the final stage of the axial vortex collapse at those critical instants when a two-phase torus is formed against the metal target or pressure transducer. A good correlation between the axial vortex evolution and the first appearance of the impulsive pressure has been observed. The pressure peaks and the presence of a number of pits over the impacted area seem to indicate that the targets are subject to a large number of local impulsive pressures. They probably result from the collapse and rebound of the spherical bubbles which are formed by the disintegration of the two-phase torus. Some reciprocal interactions are also possible. Finally, the duration of the high pressure final stage is of the order of 50 microseconds after the axial collapse, and the future work must be concentrated on this time interval.

## Acknowledgments

The present project was supported by the "Direction des Recherches, Etudes et Techniques" (contracts N° 89-072 and 91-115), Ministry of Defence, France.

## References

Avellan, F., and Farhat, M., 1989 "Shock Pressure Generated by Cavitation Vortex Collapse," ASME Fluids Engineering Conference, San Francisco, Proceedings pp. 119–125.

Belahadji, B., Franc, J. P., and Michel, J. M., 1991, "A Statistical Analysis of Cavitation Erosion Pits," ASME JOURNAL OF FLUIDS ENGINEERING, Vol. 113, No. 4, pp. 700–706.

Belahadji, B., Franc, J. P., and Michel, J. M., 1995 "Cavitation in the Rotational Structures of a Turbulent Wake," *Journal of Fluid Mechanics,* Vol. 287, pp. 383–403.

Benjamin, T., Ellis, A., 1966 "The Collapse of Cavitation Bubbles and the Pressure Thereby Produced Against Solid Boundaries," *Phil. Transactions,* Vol. A 260, pp. 221–240.

Blake, J., Taib, B., and Doherty, G., 1987 "Transient Cavities Near Boundaries. Part 2. Free Surface," *Journal of Fluid Mechanics,* Vol. 181, pp. 197–212.

Dominguez-Cortazar, M. A., Franc, J. P., and Michel, J. M., 1992 "Cavitating Vortex: Collapse Visualisation and Induced Damage," Third International I.Mech.E.Conference, Cambridge (U.K.), *Proceedings,* pp. 43–48.

Dominguez-Cortazar, M. A., 1994, "Le Cavermod, Modèle Physique de l'Erosion de Cavitation: Qualification Expérimentale et Numérique," Thesis, Joseph Fourier University, Grenoble (France), pp. 73–84.

Dominguez-Cortazar, M. A., and Canot, E., 1995 "Axial Collapse of a Cavitating Vortex: Numerical Simulation by an Integral Method," *International Symposium on Cavitation,* Deauville (France), *Proceedings,* pp. 459–464.

Fujikawa, S., and Akamatsu, T., 1980, "Effects of the Non-equilibrium Condensation of Vapour on the Pressure Wave Produced by the Collapse of a Bubble in a Liquid," *Journal of Fluid Mechanics,* Vol. 97, Part 3, 1980, pp. 481–512.

Hickling, R., and Plesset, M., 1963, "The Collapse of a Spherical Cavity in a Compressible Liquid," Div. of Eng. and Appl. Sciences, Report n° 85-24, California Institute of Technology.

Karimi, A., 1988, "Modèle Mathématique pour la Prediction de la Vitesse d'Erosion," *La Houille Blanche,* N° 7/8, pp. 571–576.

Lauterborn, W., and Bolle, H., 1975, "Experimental Investigation of Cavitation Bubble Collapse in the Neighbourhood of a Solid Boundary," *Journal of Fluid Mechanics,* Vol. 72, n° 2, 1975, pp. 391–399.

Le, Q., Franc, J. P., and Michel, J. M., 1993, "Partial cavities: Pressure Pulse Distribution Around Cavity Closure," ASME JOURNAL OF FLUIDS ENGINEERING, Vol. 115, No. 2, pp. 249–254.

Lecoffre, Y., 1978, "Cavitation Erosion by Shot Vortex," ASME, *Cavitation and Polyphase Flow Forum.*

Lecoffre, Y., Marcoz, J., and Valibouse, B., 1981, "Generator of Cavitation Vortex," ASME, Fluids Engineering Conference, Boulder.

Plesset, M., and Chapman, R., 1971, "Collapse of an Initially Spherical Vapour Cavity in the Neighbourhood of a Solid Boundary," *Journal of Fluid Mechanics,* Vol. 47, Part 2, 1971, pp. 283–290.

Rosenthal, D. K., 1962, "The Shape and Stability of a Bubble at the Axis of a Rotating Liquid," *Journal of Fluid Mechanics,* Vol. 12, 1962, pp. 358–386.

Selim, S., and Hutton, S., 1983, "Classification of Cavity Mechanics and Erosion," Second International I.Mech.E. Conference, *Proceedings,* pp. 41–49.

Soyama, H., Kato, H., and Oba, R., 1992, "Cavitation Observations of Severely Erosive Vortex Cavitation Arising in a Centrifugal Pump," *Third International I.Mech. E Conference,* Cambridge, Proceedings pp. 103–110.

Tomita, Y., and Shima, A., 1986, "Mechanisms of Impulsive Pressure Generation and Damage Pit Formation by Bubble Collapse," *Journal of Fluid Mechanics,* Vol. 169, pp. 535–564.

Vogel, O., Lauterborn, W., and Tiram, R., 1989, "Optical and Acoustic Investigations of the Dynamics of Laser-Produced Cavitation Bubbles Near a Solid Boundary," *Journal of Fluid Mechanics,* Vol. 206, 1989, pp. 299–338.

# Experimental Study of Deformation Mechanism of a Water Droplet Impinging on Hot Metallic Surfaces Above the Leidenfrost Temperature

**(Data Bank Contribution)***

**Natsuo Hatta**
Professor, Department of Energy Science and Technology, Graduate School of Energy Science, Kyoto University, Kyoto 606-01, Japan

**Hitoshi Fujimoto**
Instructor, Department of Energy Science and Technology, Graduate School of Energy Science, Kyoto University, Kyoto 606-01, Japan

**Kenji Kinoshita**
Graduate Student, Kyoto University; Presently, Engineer, Toray Industries Incorporated, Okazaki 444, Japan

**Hirohiko Takuda**
Associate Professor, Department of Energy Science and Technology, Graduate School of Energy Science, Kyoto University, Kyoto 606-01, Japan

*This paper is concerned with the collision dynamics of a water droplet impinging on three kinds of smooth surfaces (Inconel alloy 625, stainless-steel, and silicon) heated to above the Leidenfrost temperature (500°C). It has been found that the time histories of the droplet diameter, the height and the distance between the bottom of droplet and the hot surface after rebounding are almost unchangeable regardless of the kind of surface material, when the Weber number is kept so low that the droplet does not break up into some parts. However, the critical Weber number, whether or not the droplet is disintegrated into some pieces during deformation, has been confirmed to be changeable depending upon the kind of surface material. For relatively low Weber number cases, but above the critical one, the droplet breaks up into some parts after the droplet reaches a maximum diameter on the surface. As the Weber number is increased further, the droplet disintegration occurs during the spreading process. Also, the droplet disintegration mechanism has been discussed from an experimental point of view.*

## 1 Introduction

The mist/spray cooling technique is widely used in a number of industrial areas. For example, in the iron- and steelmaking industries, this is applied to the secondary cooling zone in the continuous casting process, because the shell surface just after solidification must be softly cooled by impingements of many water droplets. We analyzed numerically the flow field of gas-particle two-phase mixture jet impinging on a flat surface normal to the flow, corresponding to the mist/spray cooling situation (Hatta et al., 1993). In the numerical analysis, the assumption that all particles reflect elastically from a solid surface immediately after collision was introduced. However, as is well known, for lower Weber number cases corresponding to a low impact energy, a droplet impinging on a hot surface spreads in the form of the flattened disk, recoils and finally rebounds from it (Wachters and Westerling, 1966). On the other hand, for higher Weber number cases, the droplet breaks up into a number of small parts on the hot surface.

So far, the collision dynamics of a liquid droplet impinging on a hot surface have been investigated mainly from an experimental aspect. Some researchers presented a sequence of sharply observable photographs showing deformation process of liquid droplets impacting on a hot surface. Wachters and Westerling (1966) investigated the deformation process of a saturated water droplet of about 2 mm in diameter impacting on a polished gold surface heated to 400°C. Akao et al. (1980) inspected the deformation behavior of some kinds of liquid droplets with about 2 mm in diameter on a chromium-plated copper surface heated to 400°C. Xiong and Yuen (1991) measured the time history of a heptane droplet impinging on a stainless-steel surface in the temperature range from 63°C to 605°C. Chandra and Avedisian (1991) measured the time history of an n-heptane droplet impacting a stainless-steel surface in the temperature range from 24°C to 250°C keeping the Weber number constant (We = 43). Also, they examined the deformation process of the droplet on a porous ceramic surface (Chandra and Avedisian, 1992). Naber and Farrell (1993) examined the deformation process of three kinds of liquid droplets of 0.1 ~ 0.3 mm in diameter on a hot stainless-steel surface. Anders et al. (1993) investigated the rebounding phenomenon of ethanol droplets impacting obliquely on a smooth chromium-plated copper surface at 500°C.

Many of these studies treated the deformation behavior of the droplet impacting the hot surface in a relatively low Weber number range, so that the breaking up of droplet does not occur. Wachters and Westerling (1966), Akao et al. (1980) demonstrated a sequence of photographs showing the droplet disintegration process. Naber and Farrell (1993) measured the number of disintegrated droplets and the coefficient of restitution of disintegrated droplets in some Weber number cases. However, the details of droplet disintegration mechanism remain unknown.

Fujimoto and Hatta (1996) investigated numerically the deformation and rebounding processes of a water droplet on a hot surface above the Leidenfrost temperature in a low Weber number range. We found that the recoiling and rebounding of droplet occur owing to the surface tension effect. Also, the numerical results were found to be in fairly good agreement with the experimental data. However, it is impossible to analyze numerically the droplet deformation process for higher Weber number cases, because the droplet breaks up into small parts

* Data have been deposited to the JFE Data Bank. To access the file for this paper, see instructions on p. 738 of this issue.

Contributed by the Fluids Engineering Division for publication in the JOURNAL OF FLUIDS ENGINEERING. Manuscript received by the Fluids Engineering Division April 17, 1996; revised manuscript received March 19, 1997. Associate Technical Editor: J. Katz.

on the surface during the deformation. Therefore, in the present paper, the droplet disintegration mechanism has been discussed from an experimental point of view.

When the droplet impacts on a hot surface above the Leidenfrost temperature, the droplet is in direct contact with the solid surface first, at least, for a short time just after collision; then a thin vapor film is formed on liquid/solid interface (Nishio and Hirata, 1977). This fact suggests that the droplet deformation process on the hot surface is strongly influenced by the surface conditions such as the surface temperature, the surface roughness, the surface material, etc. In fact, the critical Weber number, whether or not the droplet breaks up into many small parts on the hot surface, is scattering in the range of 50 ~ 90 according to the experimental conditions (Wachters and Westerling, 1966; Ueda et al., 1979; Shoji et al., 1984; and Hatta et al., 1995a).

The purpose of the present study is to clarify the disintegration process of droplet impacting the hot surface heated to above the Leidenfrost temperature. The experiments have been performed on condition that the water droplet with 0.3 ~ 0.6 mm in diameter impacts perpendicularly the three kinds of smooth metallic surfaces (Inconel alloy 625, stainless-steel, and silicon) heated to 500°C. To visually understand the collision dynamics of a water droplet, the progressive stages of the droplet deformation have been photographed in the Weber number range from We = 10 to 65. It has been found from a set of the experimental results that the droplet disintegration process is divided into two types according to the Weber number. For the case of low Weber number, but above the critical one, the droplet breaks up into small parts in the recoiling process and, subsequently, these disintegrated droplets coalesce with each other. On the other hand, for a higher Weber number case, the droplet disintegration occurs in the spreading process and disintegrated droplets move far away outerwards. Furthermore, we have found that there is almost no effect of the kind of surface material on the droplet deformation process in a Weber number range less than the critical one. However, it has been confirmed that the critical Weber number is changeable depending upon the kind of surface material, that is, the thermal conductivity of surface material.

## 2 Experimental Apparatus

Figure 1 shows a schematic diagram of the experimental apparatus by which the deformation process of a droplet impinging on a rigid surface heated to above the Leidenfrost temperature can be measured. The water is pressurized statically by high pressure air to ensure a jet running out of the needle tip. The needle is flat tipped and set vertically. A needle oscillator using speaker coil, which vibrates at a particular frequency, is attached to the needle tip. Thereby, a uniformly spaced stream of droplets is generated with an almost equal diameter and velocity. A disk of 200 mm in diameter rotates horizontally between the needle exit and the heated surface. Only one droplet per revolution can pass through the slit hole of the rotating disk and reach the heated surface. The droplet size, as well as the impinging velocity, is easily changeable by the water pressure, the vibration frequency of the needle oscillator, and the inner diameter of the needle. But, it is impossible to change only the droplet diameter with keeping the impinging velocity constant, and the inverse is also impossible.

The droplet falls vertically onto a test surface. Inconel alloy 625, stainless-steel and silicon are used as a test plate in order to inspect the effect of surface material on the droplet deformation process. The test surface temperature is measured by the chromel-alumel thermocouples and adjusted by the thermocontroller unit (Omron, E5A2). Throughout the present paper, the surface temperature is fixed at 500°C. But, it should be added that the temperature change during the experiments is confirmed to be within ±20°C.

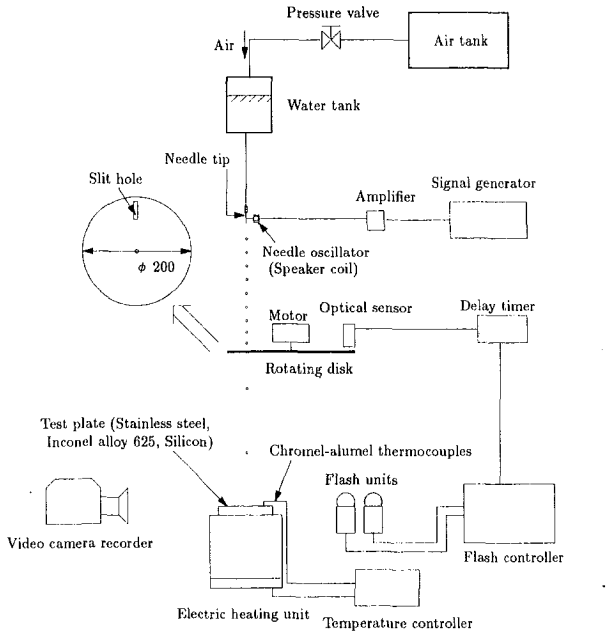


**Fig. 1 A schematic diagram of experimental apparatus**

The deformation process of a droplet is recorded by using a video camera equipped with a macrolens. The droplet images are exposed by the back light method using two microflash units (Sugawara, MS230), which can be operated at a constant time interval. The first flash is adjusted to catch the droplet just before the collision with the surface. The flash timing is met by using both an optical sensor perceiving the slit position on the rotating disk and a delay timer. In the present experiment, the droplet is photographed in the range of the time interval from 100 $\mu$s to 2000 $\mu$s. The time interval of the two flash units can be set by a flash controller. The lightning period of the flash units is kept below 2 $\mu$s. The droplet image can be exposed only during flashing. The time variation of the droplet height and diameter during the deformation on the hot surface is recorded by many double exposure video images on the basis of the statistical procedure. The droplet diameter before reaching the heated surface can be directly measured from the video image. Also, the impinging velocity can easily be estimated from both the moving distance of the droplet and the time interval of the two flashes.

The residence time of the droplet during the deformation on the hot surface just after making contact with it can be easily evaluated from the distance between the droplet and the surface in the first exposed image, the impinging velocity and the time interval of two flashes. Thereby, the height and the diameter of the droplet on the surface can be measured directly from the second exposed image. The droplet deformation process is pursued by a number of droplet images. Again, the measurement accuracy determined by the resolution of the video image is within ±0.006 mm in the present measurement unit.

## 3 Results and Discussions

As a first approach, the deformation process of a water droplet impinging on a solid surface at room temperature has been inspected for the cases where the solid surface material is Inconel alloy 625 and silicon. The static contact angle between liquid and surface was measured to be 57 degrees for the water/Inconel alloy combination case and 25 degrees for the water/silicon case, respectively. Therefore, it follows that the final water film diameter can be larger on the silicon surface than that on the Inconel alloy one, and that the final liquid film height on the silicon surface is kept small compared with that on the

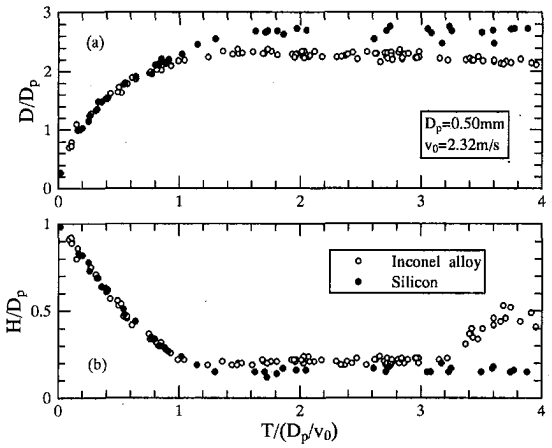


**Fig. 2 Time variations of droplet diameter $D$ (*a*) and height $H$ (*b*) impinging on cold Inconel as well as silicon surfaces for We = 37.4. It is noted that the measurement accuracy is within ±0.006 mm.**

Inconel alloy surface on the same water volume condition. Then we have investigated whether or not the droplet behavior during the deformation is influenced by the kind of surface material. This experiment has been carried out on condition that the initial droplet diameter $D_p = 0.5$ mm and the impinging velocity $v_0 = 2.32$ m/s. The Weber number We ($=\rho D_p v_0^2/\sigma$) is evaluated to be 37.4 in this case, where $\rho$ and $\sigma$ denote the liquid density and surface tension, respectively. The Weber number can be estimated by $\rho$ and $\sigma$ at room temperature (say, 20°C). Figure 2 shows the comparison of time histories of the droplet diameter $D$ and the height $H$ (see Fig. 3) on two kinds of surfaces. Here, it is noted that the time $T$ is nondimensionalized by $(D_p/v_0)$. $D$ and $H$ are done by the initial droplet diameter $D_p$. Also, $T = 0$ denotes the moment of the collision of droplet with surfaces. It can be seen from Fig. 2 that the time evolutions of $D$ and $H$ on two kinds of solid surfaces are very similar in the initial stage. It suggests that the evolution of wetted area and the spreading rate of a droplet are independent of the kind of surface material during the early period of impact. However, it is found that in the time range of $T/(D_p/v_0) > 1$, $D$ becomes larger and $H$ becomes smaller on the silicon surface compared with the case of water-Inconel alloy system.

Next, we consider the case where the material surface is heated to 500°C. Figure 4 shows the time histories of droplet diameter $D$, height $H$, and distance $C$ between the hot surface and the bottom of droplet after rebounding from the hot surface (see Fig. 3(*e*)) on condition that $D_p = 0.42$ mm and $v_0 = 2.05$ m/s (We = 24.5). The experimental results for both the water/Inconel alloy and the water/silicon cases reveal the almost same deformation process in the whole time range. It follows that the effect of surface material on the droplet deformation process is negligibly small. It can be judged that this is owing to the fact that the vapor film is formed at the liquid/solid interface and the droplet is isolated from the solid surface through it.

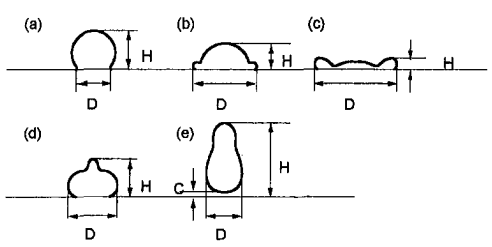


**Fig. 3 Definitions of droplet diameter $D$, height $H$ and distance between droplet bottom and surface $C$ after rebounding from it**

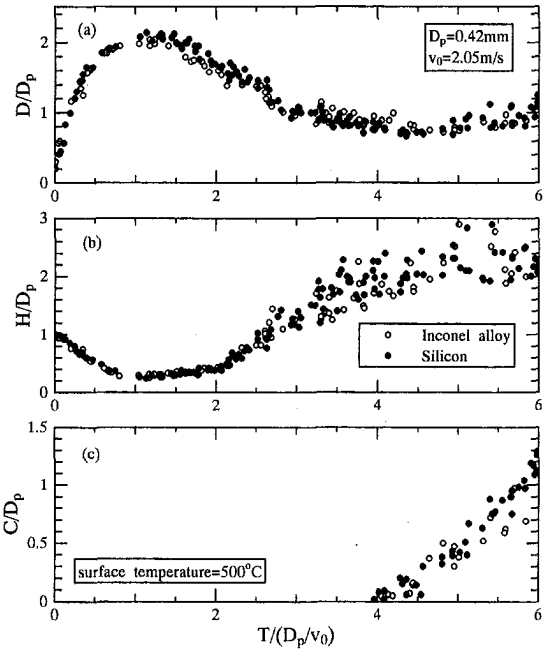


**Fig. 4 Time histories of droplet diameter $D$ (*a*), droplet height $H$ (*b*) and distance $C$ (*c*) impinging on Inconel alloy 625 as well as silicon surfaces heated to 500°C for We = 24.5. It is noted that the measurement accuracy is within ±0.006 mm.**

Incidentally, Nishio and Hirata (1977) confirmed experimentally that a droplet at room temperature contacts directly with a stainless-steel surface heated at 607°C in a very short time after collision. The surface temperature in the present study is lower than that of their experiment. Therefore, it is reasonable to consider that in the present situation, the droplet is in direct contact with the solid surface first in a short time just after impact and then a thin vapor film is formed on liquid/solid interface.

It is well known that the collision behavior of liquid droplet impinging on a hot surface is roughly divided into two types. For a lower Weber number case corresponding to a low impact energy, a droplet spreads in the form of the flattened disk, recoils owing to the surface tension effect, and finally rebounds from the hot surface (Wachters and Westerling, 1966). On the other hand, for a higher Weber number case, the droplet breaks up into many small parts on hot surfaces. The best method to understand the collision dynamics of a water droplet on a hot solid surface is to photograph the progressive stages of deformation of the droplet on the various experimental conditions. Table 1 shows six kinds of experimental conditions. A sequence of

**Table 1 Experimental conditions of water droplet impinging on a hot silicon surface shown in Figs. 5 and 6. It is noted that measurement accuracy is within ±0.006 mm.**

| case | $D_p$(mm) | $v_0$(m/s) | $We$ |
|---|---|---|---|
| (i) | 0.34 | 1.48 | 10.3 |
| (ii) | 0.34 | 1.75 | 14.5 |
| (iii) | 0.42 | 2.05 | 24.5 |
| (iv) | 0.40 | 2.83 | 44.5 |
| (v) | 0.38 | 3.35 | 59.2 |
| (vi) | 0.40 | 3.42 | 65.0 |

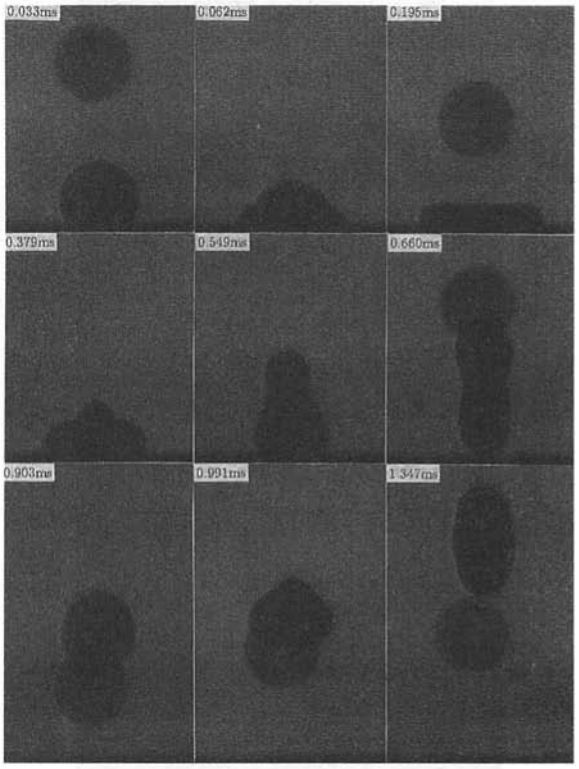


Fig. 5(*a*)

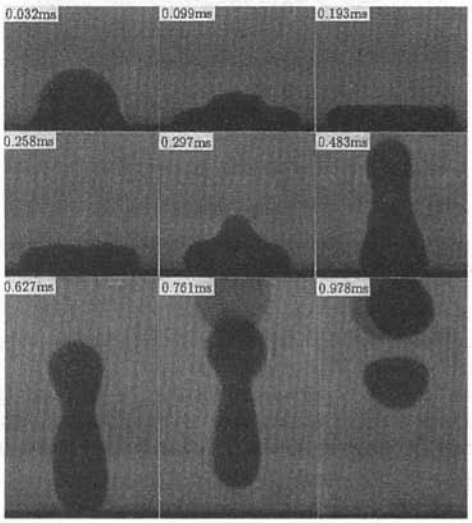


Fig. 5(*b*)

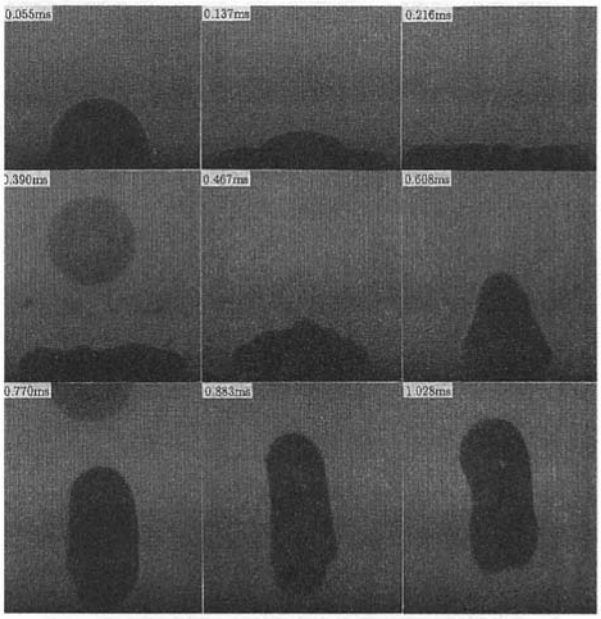


Fig. 5(*c*)

**Fig. 5 A sequence of photographs showing the water droplet impinging on the hot silicon surface with low Weber numbers**

photographs showing the progressive stages of deformation of the droplet impinging on the silicon surface heated to 500°C have been taken on the above condition.

First, Figs. 5(*a*) to (*c*) demonstrate a sequence of photographs showing the deformation process of the droplet for the relatively low Weber number cases corresponding to the experimental conditions (i), (ii), and (iii) in Table 1, respectively. The liquid spreads monotonously in the radial direction and reaches a maximum diameter after making contact with the hot surface. Subsequently, the water film begins to recoil backwards toward the center and the recoiling continues to occur owing to the surface tension effect at the periphery. Finally, the droplet is observed to rebound from the surface as a somewhat long and narrow mass. The shape of the droplet flying in space is observed to be changeable owing to the velocity difference between the top and bottom parts. The detailed deformation process of the liquid droplet for the low Weber number case was described in our previous work (Fujimoto and Hatta, 1996).

Next, Figs. 6(*a*) to (*c*) are a sequence of photographs showing the deformation process of a droplet for the relatively high Weber number cases corresponding to the experimental conditions (iv), (v), and (vi) in Table 1, respectively. At any case, it can be recognized that the droplet breaks up into small parts on the hot surface, and that the number of disintegrated droplets on the hot surface has a significant tendency to increase with the Weber number.

What should be noticed first is that with the high Weber numbers (say, We $\geq$ 44.5), a larger scale deformation occurs in a shorter time in comparison with the low Weber number cases (say, We $\leq$ 24.5), although the deformation process seems to be very similar regardless of the Weber number, until the droplet begins to break up. The question which we must consider is when and how the droplet breaks up. It can be understood that the droplet is broken into some parts on the recoiling process after reaching a maximum diameter for the cases where We = 44.5 and 59.2 (corresponding to Figs. 6(*a*) and (*b*)). In fact, the disintegrated droplets are seen to move towards the central zone and to coalesce with each other. On the other hand, the case is also seen where the droplet is broken on the spreading process. This can be understood from the fact that the disintegrated droplets move far away outwards from the central zone, as shown in Fig. 6(*c*).

The liquid film before and after reaching a maximum diameter is composed of two regions (Hatta et al., 1995b, Fujimoto and Hatta, 1996), one of which is the part of the thin water film in the central region. The other is the part of the doughnut-like shape in the peripheral region which corresponds to the ring structure. However, it is natural to consider that the sectional area of the ring structure is not uniform in the circumferential direction, at least, just before the droplet begins to break up. For example, it is self-evident that such a case occurs, if we see the photographs at $t$ = 0.380 ms in Fig. 6(*a*), at $t$ = 0.320 ms in Fig. 6(*b*) and at $t$ = 0.255 ms in Fig. 6(*c*), respectively. Here, the difference in the rotational velocity of the ring structure occurs locally in the circumferential direction regardless of whether it is on the spreading or recoiling process. As a result, it is not unnatural to suppose that the ring structure

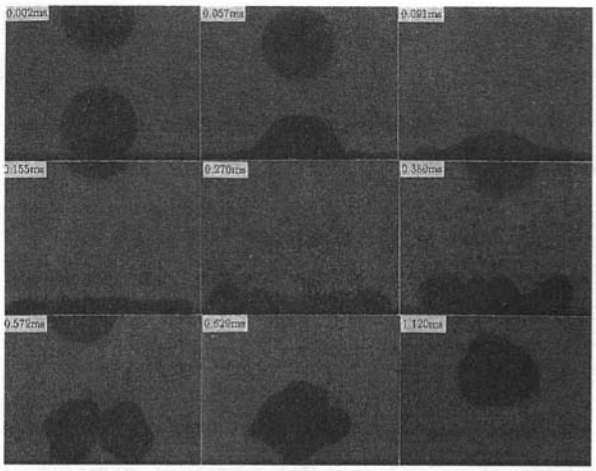


Fig. 6(*a*)

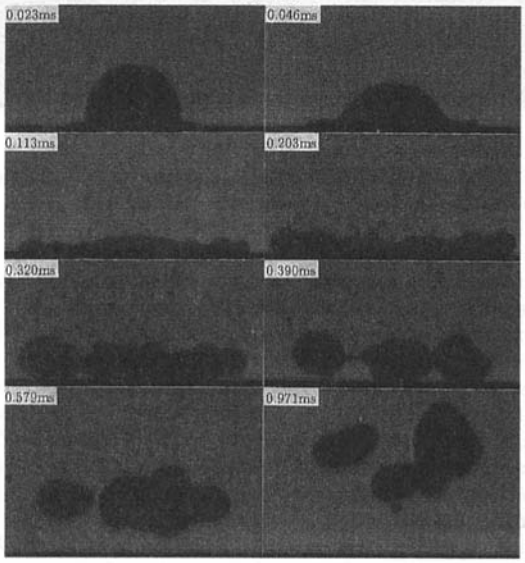


Fig. 6(*b*)

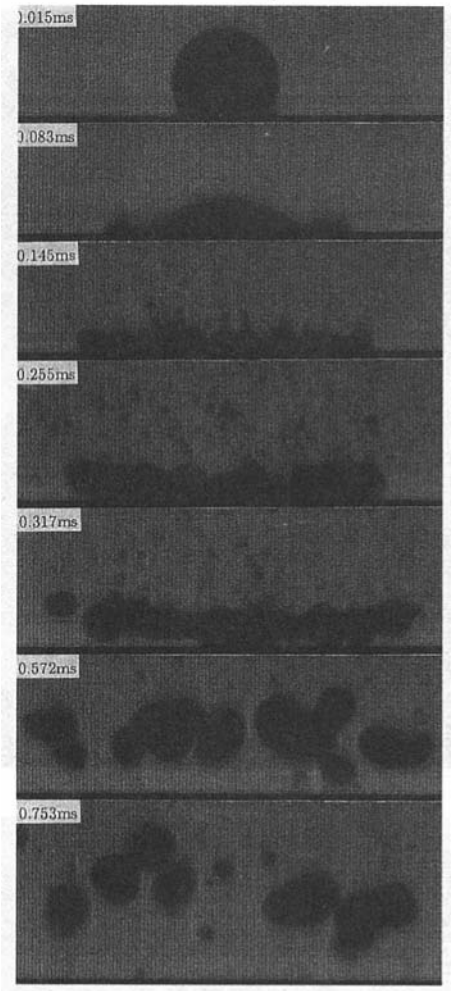


Fig. 6(*c*)

**Fig. 6 A sequence of photographs showing the water droplet impinging on the hot silicon surface with relatively high Weber numbers**

breaks up by twisting or shearing, and that this phenomenon occurs locally in the circumferential direction of the ring structure.

Next, it can be recognized that the disintegrated droplets become small in size and therefore small parts increase in the number with the Weber number. This is due to the fact that the deformation scale of the water droplet on the hot surface is enlarged with increasing the Weber number corresponding to the initial impact energy. Naber and Farrell (1993) counted the number of disintegrated water drops after collision with the hot stainless-steel surface heated at 400°C and found that the droplet is separated into an average of 8.8 droplets for We = 74, and 16.8 for We = 115 during the collision. Also, a similar tendency has been obtained in the present experiment.

Figure 7 gives the time history of deformation process of the droplet impacting the silicon surface heated to 500°C for We = 10.3(*a*), 20.1(*b*) and 32.0(*c*), respectively. The comparison among three kinds of Weber numbers shows that the water film diameter is larger and the water film thickness is smaller as the Weber number is increased. Also, the time at which $D/D_p$ reaches the maximum value, as well as the time at which the droplet rebounds just from the surface, becomes longer with the Weber number. Incidentally, it is noted that in a later stage after collision with the surface, the measured values tend to scatter with the increase in the Weber number. We believe that this is due to the fact that droplets cannot keep the shape axially symmetric with the Weber number.

In our previous paper (Hatta et al., 1995a), we proposed the experimental formula capable of predicting the maximum diameter of the droplet on the hot surface as a function of the Weber number We alone,

$$D_{max}/D_p = 0.093\ \mathrm{We}^{0.74} + 1 \qquad (1)$$

This gave best-fit to the case where a water droplet impinges on the Inconel alloy surface heated to 500°C on condition of We < 50. Figure 8 gives the variation of the maximum diameter on three kinds of metallic surfaces heated to 500°C against the Weber number. The solid curve in this figure denotes the value estimated by Eq. (1). It can be seen from this figure that the predicted maximum droplet diameters are in fairly good agreement with the experimental data and that the effect of surface material on the maximum diameter is negligibly small. Also, the data obtained by other researchers (Ueda et al., 1979, Akao et al., 1980) are additionally plotted in this figure. These data were measured on condition that the droplet impacts perpendicularly the polished surface heated to above the Leidenfrost temperature with low Weber numbers. It is seen that the numerical results estimated by Eq. (1) give good fit to the experimental data obtained by other researchers.

Chandra and Avedisian (1991) proposed the expression for the maximum droplet diameter obtained from a simple energy balance as follows:

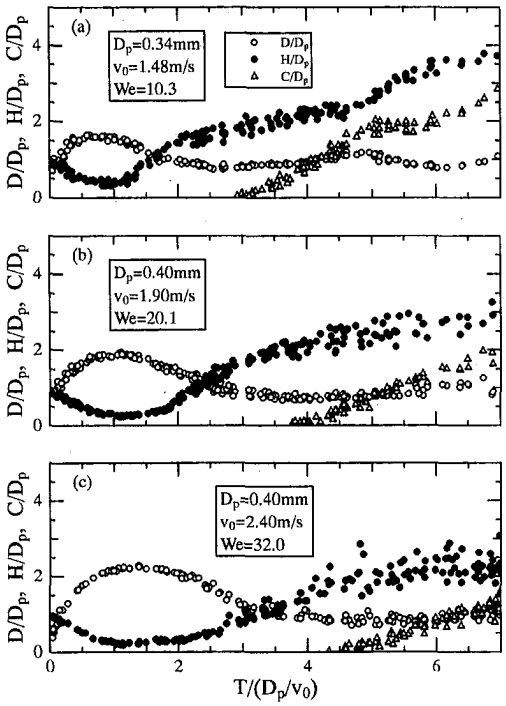


**Fig. 7 Time histories of deformation process of a droplet impacting a hot silicon surface with We = 10.3(*a*), 20.1(*b*) and 32.0(c), respectively. *It is noted that measurement accuracy is within ±0.006 mm.***

$$\frac{3}{2}\frac{\mathrm{We}}{\mathrm{Re}}\left(\frac{D_{\max}}{D_p}\right)^4 + (1-\cos\theta)\left(\frac{D_{\max}}{D_p}\right)^2 - \left(\frac{1}{3}\mathrm{We}+4\right) \simeq 0 \quad (2)$$

where Re and $\theta$ denote the Reynolds number and the contact angle between the liquid and the solid surface, which is fixed at 180 deg on condition that the surface temperature is above the Leidenfrost point. They predicted that the effect of the Reynolds number on $D_{\max}/D_p$ is significant if the droplet is small or the liquid viscosity is high. Then, we have checked the relation between $D_{\max}/D_p$ and Re, but almost no significant effect could be found, at least, for our experimental data. We add to note that Re ranges between 450 and 1400, and that We/Re ranges between 0.018 and 0.042 in the present experimental condition. At any rate, it can be regarded from Fig. 8 that $D_{\max}/D_p$ can be predicted sufficiently well by the Weber number alone. In addition, we have confirmed that $D_{\max}/D_p$ evaluated by Eq. (2) are much larger than the experimental data in all cases.

Next, the time $T_{\max}$ required for the circular water film to reach the maximum spreading diameter from the moment of collision with surfaces has been investigated for three kinds of surface materials. Figure 9 indicates the variation of $T_{\max}/(D_p/v_0)$ against the Weber number We. Here, it is noted that the time $T_{\max}$ is nondimensionalized by $(D_p/v_0)$. It has been found that there is the strong correlation between the Weber number and $T_{\max}/(D_p/v_0)$, while almost no effect of the kind of surface material on $T_{\max}/(D_p/v_0)$ has been recognized. Here, we propose the empirical formula capable of giving the relation between $T_{\max}/(D_p/v_0)$ and We as

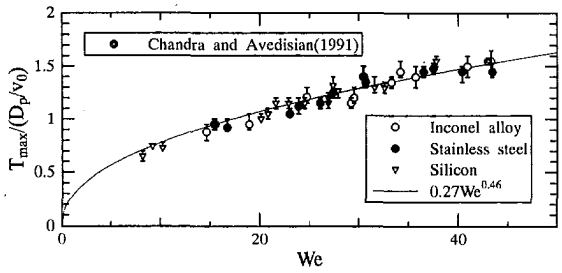


**Fig. 9 Time needed for a spreading droplet to reach a maximum diameter on hot surfaces heated to 500°C against the Weber number**

$$T_{\max}/(D_p/v_0) = 0.27\ \mathrm{We}^{0.46} \quad (3)$$

By the way, the solid line in this figure denotes the value estimated by Eq. (3) and the experimental data measured by Chandra and Avedisian (1991) is additionally plotted there. The result of Eq. (3) has also been found to be in good agreement with their experimental data.

Next, the time from the moment of collision to the moment of departure from the surface has been inspected for the lower Weber number cases. According to some researchers (Wachters and Westerling, 1966; Ueda et al., 1979; and Shoji et al., 1984), it has been commonly accepted that the droplet residence time $T_R$ on a hot surface is approximately equal to the first-order vibration period of a freely oscillating droplet as follows:

$$T_R/(D_p/v_0) = \frac{\pi}{4}\sqrt{\frac{\rho D_p^3}{\sigma}}\Big/(D_p/v_0) = \frac{\pi}{4}\sqrt{\mathrm{We}} \quad (4)$$

Figure 10 gives the relation between the nondimensional droplet residence time and the Weber number, for three kinds of hot surfaces. The dotted line shows the result calculated by Eq. (4). The calculated results are not necessarily matchable with the experimental data, in particular, in a lower Weber number range. Then, we propose the following empirical formula as

$$T_R/(D_p/v_0) = 1.25\ \mathrm{We}^{0.37} \quad (5)$$

The solid line in Fig. 10 denotes the result calculated by Eq. (5). It is seen that this numerical result is in better agreement with the experimental data even in the lower Weber number range than that calculated by Eq. (4).

The critical Weber number, whether or not the droplet is disintegrated on the surface during the deformation, was pro-

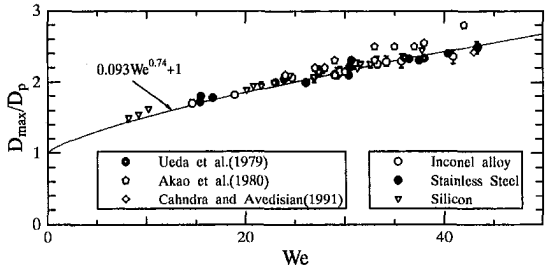


**Fig. 8 Relation between the droplet maximum diameter on three kinds of hot surfaces heated to 500°C and the Weber number**

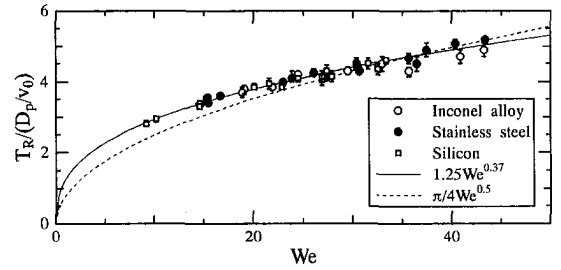


**Fig. 10 Relation between droplet residence time on three kinds of surface materials heated to 500°C and the Weber number**

posed by some researchers (Wachters and Westerling, 1966; Ueda et al., 1979; Akao et al., 1980; and Shoji et al., 1984). It is reasonable to consider that the critical Weber number is subject to the various factors such as the kinds of surface material/liquid, the surface temperature and so on. In fact, Ueda et al. (1979) proposed that the critical Weber number is 65 for water droplets and 75 for Freon 113 droplets impinging on the copper surface heated to 300°C. In the present investigation, the effect of the kind of surface material on the critical Weber number has been experimentally examined on condition that the water droplet impinges on three kinds of surfaces heated to 500°C. As a result, the critical Weber number is approximately 50 for the Inconel alloy 625 (Hatta et al., 1995a), approximately 45 for the stainless-steel, and approximately 40 for the silicon surfaces, respectively. The effect of the kind of surface material on the critical Weber number has clearly been recognized.

When the droplet impacts the hot surface, the surface temperature falls once a little owing to direct contact on the solid/liquid interface and then rises again owing to the thermal conduction from the inner side of the solid material to the surface. At the same time, the temperature at the bottom of liquid droplet reaches the boiling point and a vapor film is formed on the solid/liquid interface. It may be natural to consider that the recovering rate of the initial surface temperature after the impact depends upon the thermal conductivity of the surface material. The larger value of the thermal conductivity operates upon promoting the vapor film generation. This leads to isolating the liquid droplet from the solid surface through the vapor film faster. The liquid droplet floating on the vapor film cannot uniformly spread/recoil in the radial direction. As a result, the ring structure of liquid droplet is cut off by twisting/shearing at or above a certain value of the Weber number. That is to say, the larger thermal conductivity of the surface material results in lowering the critical Weber number. We believe that if heat transmission from the hot surface to the droplet bottom is more remarkable, the droplet tends to be unstable on the vapor film and break up. Therefore, the critical Weber number lowers. Incidentally, the conductivity of these materials is 17 W/(m·K) for Inconel alloy 625 (Aerospace Structural Metals Handbook, 1994), 23 W/(m·K) for stainless-steel and 42 W/(m·K) for silicon (JSME Data Book, 1986), respectively, at 500°C.

## 4 Conclusion

The collision dynamics of a water droplet impinging on hot solid surfaces have been investigated from an experimental point of view. Emphasis has been placed upon understanding the spreading, recoiling, and rebounding/breaking-up processes of a water droplet after collision with surfaces. Three kinds of solid surfaces (Inconel alloy 625, stainless-steel, and silicon) have been used as the test surface and heated to 500°C. The impact Weber number has been taken in the range between We = 10 and 65. As a result, we have found that the time evolutions of the droplet diameter, the height and the distance between the hot surface and the droplet bottom after rebounding are almost unchangeable regardless of the kind of surface material, if the surface temperature is above the Leidenfrost temperature and the Weber number is kept so small that the liquid droplet does not break up into some parts. However, the critical Weber number, whether or not the droplet is disintegrated into some parts, has been experimentally confirmed to be changeable depending upon the kind of surface material.

Furthermore, the droplet disintegration mechanism has been discussed from an experimental point of view. The droplet disintegration occurs in the Weber number range above the critical one in the spreading/recoiling process. With increasing the Weber number, the deformation scale of the droplet is enlarged and the sectional area of the ring structure in the peripheral region tends to be small and ununiform, before/after the droplet reaches a maximum diameter. Hence, the difference in the rotational velocity of the ring structure occurs locally in the circumferential direction and consequently the ring structure is disintegrated into a lot of parts by twisting or shearing. Also, the number of disintegrated parts has been found to increase with the Weber number. The results obtained in the present investigation are summarized as follows:

(1) As a first approach, the deformation process of a water droplet impinging on different kinds of solid surfaces at room temperature has been tried on the same experimental condition. It has been found that the time evolution of the droplet diameter $D$ and height $H$ are very similar during the early period of impact regardless of the kind of surface material, but changeable in the later stage. It suggests that the effect of the contact angle on the deformation process becomes significant in the later stage on the wetting condition.

(2) However, the time variations of $D$, $H$, and $C$ denoting the distance between the surface and the bottom of droplet after rebounding have been found to be very similar regardless of the kind of surface material, if the surface is kept to above the Leidenfrost temperature. This leads to the fact that the effect of the kind of surface material on the droplet deformation process is negligibly small, when the surface temperature is so high that the vapor film is formed on the solid/liquid interface.

(3) It has been found from the photographic observation of the impact process of droplet on hot surfaces that the droplet disintegration process can be divided into two types according to the Weber number. For the case of low Weber number, but above the critical one, the droplet breaks up into small parts in the recoiling process and then these disintegrated droplets coalesce with each other. On the other hand, as the Weber number is increased further, the droplet disintegration occurs in the spreading process and disintegrated droplets move far away outerwards.

(4) It has been suggested that the critical Weber number whether or not the droplet is broken on hot surfaces changes depending upon the kind of surface material, concretely upon the thermal conductivity of the surface material. The small thermal conductivity leads to enlarging the critical Weber number. The converse is also true.

(5) The empirical formulae capable of predicting the time needed for the spreading droplet to reach a maximum diameter and the time at which the droplet rebounds from the surface have been built up as a function of the Weber number alone.

## Acknowledgment

The authors would like to note that the present study was supported through a Grant in Aid for Scientific Research (07455287) of the Ministry of Education, Science, Sports and Culture in Japan.

Also, the data presented in this paper have been saved in the JFE Data Bank for the use of other researchers. The data included nondimensional time $T/(D_p/v_0)$, nondimensional diameter $D/D_p$, nondimensional height $H/D_p$, and nondimensional distance $C/D_p$ between the bottom of rebounding droplet and the surface.

## References

*Aerospace Structural Metals Handbook,* CINDAS/USAF CRDA Handbooks Operation Purdue University, 1994.

Akao, F., Araki, K., Mori, S., and Moriyama, A., 1980, "Deformation Behaviors of a Liquid Droplet Impinging onto Hot Metal Surface," *Transaction of ISIJ,* Vol. 20, pp. 737–743.

Anders, K., Roth, N., and Frohn, A., 1993, "The Velocity Change of Ethanol Droplets During Collision with a Wall Analysed by Image Processing," *Experiments in Fluids,* Vol. 15, pp. 91–96.

Chandra, S., and Avedisian, C. T., 1991, "On the Collision of a Droplet with a Solid Surface," *Proceedings of the Royal Society,* London, Series A, 432, pp. 13–41.

Chandra, S., and Avedisian, C. T., 1992, "Observations of Droplet Impingement on a Ceramic Porous Surface," *International Journal of Heat and Mass Transfer,* Vol. 35–10, pp. 2377–2388.

Fujimoto, H., and Hatta, N., 1996, "Deformation and Rebounding Processes of a Water Droplet Impinging on a Flat Surface Above the Leidenfrost Temperature," ASME JOURNAL OF FLUIDS ENGINEERING, Vol. 118, pp. 142–149.

Hatta, N., Fujimoto, H., and Takuda, H., 1993, "Numerical Analysis of Flow Pattern of Impinging Liquid Sprays in a Cold Model for Cooling a Hot Plate," *Applied Scientific Research,* Vol. 50, pp. 129–147.

Hatta, N., Fujimoto, H., Takuda, H., Kinoshita, K., and Takahashi, O., 1995, "Collision Dynamics of a Water Droplet Impinging on a Rigid Surface above the Leidenfrost Temperature," *ISIJ International,* Vol. 35-1, pp. 50–55.

Hatta, N., Fujimoto, H., and Takuda, H., 1995, "Deformation Process of a Water Droplet Impinging on a Solid Surface," ASME JOURNAL OF FLUIDS ENGINEERING, Vol. 117, pp. 394–401.

*JSME Data Book:* Heat Transfer 4th Edition, 1986, Maruzen.

Naber, J. D., and Farrell, P. V., 1993, "Hydrodynamics of Droplet Impingement on a Heated Surface," SAE technical paper, 930919.

Nishio, S., and Hirata, M., 1977, "Experimental study concerning the Leidenfrost temperature (in Japanese)," Transaction of Japan Society of Mechanical Engineers, Part 2, 43–374, pp. 3856–3867.

Shoji, M., Wakunaga, T., and Kodama, K., 1984, "Heat transfer between a heated surface and impinging droplet (in Japanese)," *Transaction of the Japan Society of Mechanical Engineers,* Series B, 50, pp. 716–723.

Ueda, T., Enomoto, T., and Kanetsuki, M., 1979, "Heat Transfer Characteristics and Dynamic Behavior of Saturated Droplets Impinging on a Heated Vertical Surface," *Bulletin of the JSME,* Vol. 22, pp. 724–732.

Wachters, L. H. J., and Westerling, N. A., 1966, "The Heat Transfer from a Hot Wall to Impinging Water Drops in the Spheroidal State," Chemical Engineering Science, Vol. 21, pp. 1047–1056.

Xiong, T. Y., and Yuen, M. C., 1991, "Evaporation of a Liquid Droplet on a Hot Plate," *International Journal of Heat and Mass Transfer,* Vol. 34, pp. 1881–1894.

# Two Types of Nonlinear Pressure-Drop Versus Flow-Rate Relation Observed for Saturated Porous Media

## (Data Bank Contribution)*

**J. L. Lage**
J. L. Embrey
Associate Professor,
Mechanical Engineering Department,
Southern Methodist University,
Dallas, TX 75275-0337. Mem. ASME

**B. V. Antohe**
Technology Development Staff Member,
MicroFab Technologies Inc.,
Plano, TX 75074. Assoc. Mem. ASME

**D. A. Nield**
Associate Professor,
Department of Engineering Science,
University of Auckland,
Private Bag 92019, Auckland, NZ

*Previous reports of experiments performed with water (Fand et al., 1987 and Kececioglu and Jiang, 1994) indicated that beyond the Forchheimer regime the rate of change of the hydrostatic pressure gradient along a porous medium suddenly decreases. This abnormal behavior has been termed "transition to turbulence in a porous medium." We investigate the relationship between the hydrostatic pressure gradient of a fluid (air) through a porous medium and the average seepage fluid velocity. Our experimental results, reported here, indicate an increase in the hydrostatic pressure rate beyond a certain transition speed, not a decrease. Physical arguments based on a consideration of internal versus external incompressible viscous flow are used to justify this distinct behavior, a consequence of the competition between a form dominated transition and a viscous dominated transition. We establish a criterion for the viscous dominated transition from consideration of the results of three porous media with distinct hydraulic characteristics. A theoretical analysis based on the semivariance model validation principle indicates that the pressure gradient versus fluid speed relation indeed departs from the quadratic Forchheimer-extended Darcy flow model, and can be correlated by a cubic function of fluid speed for the velocity range of our experiments.*

## Introduction

We consider here the incompressible flow of a Newtonian fluid through a regular channel filled with a fixed and rigid porous matrix. For low fluid speed the Darcy law is valid. As the fluid speed increases the form drag effect becomes increasingly important. To accommodate this phenomenon the Darcy law is extended with a quadratic velocity term as suggested by Dupuit (1863) and Forchheimer (1901).

Fand et al. (1987) and Kececioglu and Jiang (1994) performed experiments using water flowing through a pipe filled with solid spheres playing the role of a porous medium. Fand et al. (1987) presented their experimental results plotting graphs of $(\Delta p/L)d/\mu v$, where $\Delta p$ is the static pressure drop along the pipe, $L$ is the distance between the two pressure taps, $d$ is the diameter of the spheres, $\mu$ is the fluid dynamic viscosity, and $v$ is the average (seepage) fluid velocity, versus the Reynolds number $\rho v d/\mu$, where $\rho$ is the fluid density. Here we denote $(\Delta p/L)d/\mu v$ by $P$ and $\rho v d/\mu$ by $\mathrm{Re}_d$ for simplicity. The pressure drop was measured outside the porous medium.

Kececioglu and Jiang (1994) had the pressure drop measured inside the region occupied by the porous medium. They presented their experimental results in a similar form, the only difference being the multiplication of the pressure $P$ term (ordinate) by $d$. In both cases a series of three main flow regimes was identified, namely a Darcy regime shown as a horizontal line in the $Pd$ versus $\mathrm{Re}_d$ graph ($Pd$ constant), a Forchheimer regime shown as an inclined (positive slope) straight line ($Pd \sim f(\mathrm{Re}_d)$), and a third regime called by the authors the "*turbulence regime*" where another straight line, with smaller slope than the inclination of the Forchheimer regime, was identified. Their main conclusion was that the turbulence regime is characterized by a quadratic relationship between pressure drop and fluid velocity, as the Forchheimer regime, but having distinct permeability and inertia coefficient. Therefore, a two-equation model would be needed to represent the entire flow range, one for the Darcy and Forchheimer regimes and one for the third regime.

We present our own experimental tests of fluid flowing through a porous medium to show that indeed a third regime sets in at a high fluid speed and that this regime is characterized by an increase in the velocity rate of change of pressure drop (when $P$ is plotted versus Re). We also demonstrate that this flow regime can be fitted well with a cubic velocity term, an extension to the Forchheimer-Darcy model. This one-equation model is valid for the entire flow regime of our experiments. We then use physical arguments and published results to support our hypothesis that in incompressible viscous flow through a porous medium the friction (drag) coefficient can either increase or decrease during transition from the Forchheimer regime to the third regime.

## Turbulence Regime

A fundamental detail, not discussed at length by Fand et al. (1987) or Kececioglu and Jiang (1994) when analyzing their experimental data, is the decrease in the inclination of the line relating $P$ and $\mathrm{Re}_d$ as the flow proceeds from the Forchheimer regime to the third regime. This reduced inclination indicates that the rate of increase of pressure drop with velocity becomes smaller when regime three sets in. In other words, if the Forchheimer-Darcy regime could be extended to higher fluid speeds,

* Data have been deposited to the JFE Data Bank. To access the file for this paper, see instructions on p. 738 of this issue.

Contributed by the Fluids Engineering Division for publication in the JOURNAL OF FLUIDS ENGINEERING. Manuscript received by the Fluids Engineering Division April 17, 1996; revised manuscript received March 31, 1997. Associate Technical Editor: F. Giralt.

into the third regime zone, the total pressure drop would be higher than the pressure drop of the third flow regime. This phenomenon is abnormal for internal flows because it implies a decrease of flow resistance at high fluid speed.

The labeling of the third regime as a turbulence regime associated with a drag reduction is somewhat misleading. In many situations a transition from laminar to turbulent flow leads to a restriction of the flow, rather than the opposite. For instance, the fundamental Moody diagram (White, 1994, p. 318) for pipe flow indicates that if one is capable of extending the laminar regime into the turbulence flow range then the pressure drop of laminar flow, for the same fluid speed, will be always smaller than the pressure drop of turbulent flow. It is true that for flow around a bluff body the transition to turbulence is associated with a reduction in drag, resulting from a delayed boundary layer separation and hence a narrower wake. However, one needs to be careful in extrapolating from a single bluff body to a porous medium composed of several such bodies. The wake behind one body will be dispersed by the presence of the other bodies. If the bodies are very close together along the main flow direction, the form drag dominated transition to turbulence of bluff bodies might be masked by the viscous dominated transition characteristic of internal flows. A dual transition behavior, dependent on the morphology of the porous medium, is then conceivable from a theoretical point-of-view.

It is noteworthy that though the curves of drag coefficient (plotted versus Re) for bundles of long cylinders exhibit variations in slope similar to that of bluff bodies, they do not exhibit the dramatic drop found in similar curves for a single sphere or a single cylinder. Compare, for example, Figs. 6.19 and 6.20 with Fig. 6.5 in Zukauskas (1987). The case of staggered tubes (Fig. 6.20) shows transition beyond the laminar form drag (flat) regime. However, in the case of aligned tubes the transition occurs before the prevailing of form drag, more in line with a viscous dominated flow transition (internal flow—Moody diagram).

Recent experimental evidence (Short, 1994, p. 44, Fig. 2.12) indicated that for flow across bundles of in-line short cylinders the drag coefficient can decrease or increase during transition depending on the ratio of length to diameter of the cylinders. For instance, with a ratio equal to 1.75 (short cylinders—closely spaced channel surfaces) the drag decreased during transition (because the horseshoe vortex effect dominates along most of the cylinder's length) and with a ratio of 7.25 the drag increased during transition because now the horseshoe vortex influences a proportionally smaller area along the length of the cylinder and as a consequence the transition is viscous (not form) dominated.

Another important point is that results obtained from consideration of turbulence at the microscopic level (pore level) may not carry over to turbulence at the macroscopic level. For example, Fand et al. (1987) refer to the results of Dybbs and Edwards (1975). These results, obtained using laser anemometry, indicated local turbulence (at the pore level) beyond a certain fluid speed. But it does not follow that there was any turbulence at the macroscopic level.

## Experimental Equipment and Procedure

We performed experimental tests using three aluminum blocks with a porous aluminum layer inserted in it, Fig. 1. The experimental setup is designed to obtain accurate determination of the fluid flow (seepage velocity) and pressure drop across each test block.

All aluminum blocks have inlet and outlet plena connected by a 76.2 mm long ($L$), 50.8 mm wide ($W$), and 1.0 mm thick ($H$) test channel (Fig. 1). A porous layer is bonded with a very thin coating of Sheldahl T1401 spray adhesive to the internal surface of the test channel and to the lateral surfaces with 1177/cab-o-sil filling.

Each porous layer is obtained by compressing a 1570 pores per meter aluminum 6101-O alloy matrix, shown in Fig. 1 lower left, in the direction perpendicular to the flow direction (along $H$, Figure 1). The compression ratio, $r = H_0/H$ (where $H_0$ is the initial matrix thickness and $H$ is the final matrix thickness), of each layer is indicated in Table 1 next to its initial (uncompressed) density, $\rho_s = 1 - \phi_0$ (where $\phi_0$ is the initial volumetric porosity of the matrix), and its measured porosity $\phi$ after compression. The advantage of using these aluminum porous layers as test material instead of spheres is the flexibility of having different hydraulic characteristics (porosity, permeability, inertia coefficient, etc.) but employing the same material.

A flow setup is built for performing measurements using air (Figure 1, upper left) including a pressure regulator to adjust the maximum inlet air pressure. The air flow rate range is from $1.7 \times 10^{-6}$ to $10^{-3}$ m$^3$/s corresponding to an air velocity range of 0.033 to 19.26 m/s. The rotameters (OMEGA FL111, FL112, and FL114) are calibrated to two percent of the reading value. Their repeatability is within one-half percent of reading value.

The differential pressure is measured between the inlet and outlet ports of the block. A 300 Pa gauge micromanometer manufactured by Combustion Instruments Ltd. (0.1 Pa accurate) is utilized to measure small pressure drops. For the moderate pressure drop regime a 0.5 kPa gauge inclined portable manometer, manufactured by Dwyer Inc., is used. The uncertainty of the instrument is 2.5 Pa. A 46.5 kPa, accurate to 30 Pa, and a 78.5 kPa accurate to 10 Pa, $U$-shaped manometer are used to measure the pressure drop at higher range. Pressures above 68.9 kPa were measured with a 690 kPa Marsh pressure gage, accurate to 6.9 kPa. The Mach number at maximum air speed is approximately 0.06 allowing one to neglect compressibility effects.

The inlet air temperature is recorded in order to correct the air density and viscosity. A type J thermocouple wire is inserted in the air stream with the temperature displayed by a 450 AJT OMEGA thermocouple thermometer. The air properties are obtained by linear interpolation as a function of temperature (Air Properties Table, Bejan, 1993). The outlet air temperature is also measured with a portable thermocouple thermometer. The air temperature difference between inlet and outlet is negligible (within thermocouple uncertainty of 0.5°C) for all experiments.

Air test results represent the arithmetic average of at least five experimental runs for each block. For each test block the

## Nomenclature

$c$ = cubic coefficient
$c_F$ = inertia coefficient
$d$ = sphere diameter
$H$ = thickness
$i$ = summation index
$K$ = permeability
$L$ = length, distance between pressure taps
$n$ = number of data points
$N$ = number of data pairs
$p$ = static pressure
$P$ = modified pressure, $(\Delta p/L)d/\mu v$
$r$ = compression ratio
$\mathrm{Re}_d$ = Reynolds number, $\rho v d/\mu$
$\mathrm{Re}_K$ = Reynolds number, $\rho v K^{0.5}/\mu$
$v$ = seepage velocity
$W$ = width
$\delta$ = residual, Eq. (4)
$\phi$ = porosity
$\kappa$ = average deviation, Eq. (2)
$\mu$ = dynamic viscosity
$\rho$ = density
$\sigma$ = semivariance, Eq. (5)

**Subscripts**

exp = experimental
0 = initial
$s$ = solid
theo = theoretical

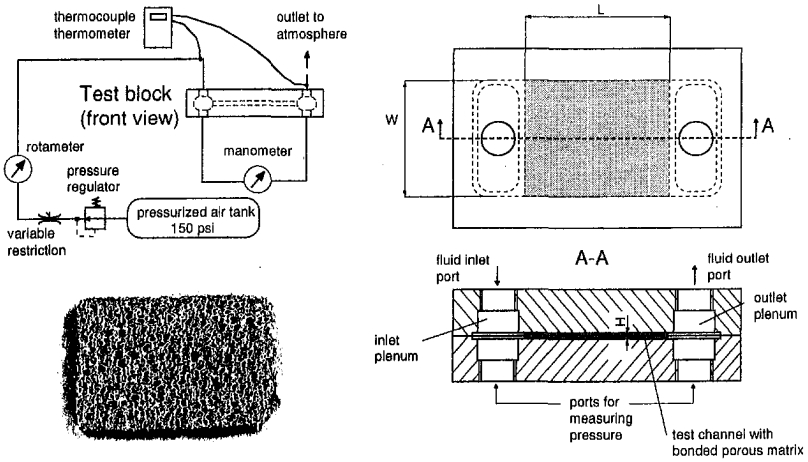


**Fig. 1 Experimental apparatus: hydraulic setup (upper left); aluminum porous medium layer (lower left); test block with porous medium insert (right).**

data acquisition starts at low flow rate, increasing in finite steps. No hysteresis is observed when acquiring data reducing the flow rate.

## Results and Analysis

We now present the flow test results for all three blocks. We refer to a low flow range with maximum velocity around 1.5 m/s. Full range includes all experimental points up to the maximum measured velocity value.

Experimental results from hydraulic tests performed within the low flow range limit were presented by Antohe et al. (1996). They also described in detail a procedure for estimating the uncertainties of the experimental data (not repeated here). Once the pressure gradient $\Delta p/L$ and the seepage fluid speed $v$ were obtained, they curve-fitted the experimental data using least-square fitting and the Forchheimer-extended Darcy model written as

$$\frac{\Delta p}{L} = \frac{\mu}{K} v + \frac{\rho c_F}{K^{1/2}} v^2 \tag{1}$$

The permeability and inertia coefficient values for each layer, and their uncertainties, are included in Table 1. In all cases the permeability based Reynolds number, $\mathrm{Re}_K = \rho v K^{1/2}/\mu$ was larger than 1.0 and so the flow was within the Forchheimer range.

We have here extended the experimental results of each layer to a high fluid speed range, and compared the results with the pressure gradient predicted, within this flow range, by the Forchheimer-extended Darcy equation obtained by Antohe et al. (1996). The comparison is presented in Fig. 2 in which the experimental results are presented next to the results of the Forchheimer-extended Darcy equation shown with straight lines. All graphs exhibit a deviation of the experimental points from the theoretical curves, for fluid velocity beyond a critical velocity value. There is indeed a departure from the Forchheimer-extended Darcy regime. We computed the average deviation $\kappa$,

$$\kappa = \frac{1}{n} \sum_{i=1}^{n} |\Delta p_{\mathrm{exp}} - \Delta p_{\mathrm{theo}}| \tag{2}$$

where $n$ is the total number of experimental points, for each layer. The results are: 337.4 kPa/m for layer 1, 676.6 kPa/m for layer 2, and 459.2 kPa/m for layer 3.

We investigated further the possibility of having the quadratic velocity equation fitting the full regime. In Fig. 3 we show the results of interpolating the experimental results with the Forchheimer-extended Darcy equation, but this time determining the inertia coefficient $c_F$ by fitting the full range of data and not only the low range as done by Antohe et al. (1996). The permeability coefficient $K$ obtained using the low range is kept fixed (recall that permeability is a parameter related with the Darcy—low speed—regime). The new inertia coefficient values for layers 1, 2, and 3 are, respectively, 0.468, 0.661, and 0.570. The average deviations in this case are: 66.2 kPa/m for layer 1, 80.9 kPa/m for layer 2, and 65.5 kPa/m for layer 3.

Although a much better agreement between experimental and theoretical results is obtained when the inertia coefficient is computed using the entire velocity range, the inertia coefficient becomes "range dependent" varying in the present case by 26, 60, and 36 percent for layer 1, 2, and 3, respectively. This might indicate a departure from the quadratic model proposed by Forchheimer (1901).

Figure 4 presents the experimental results in a form similar to the form used by Fand et al. (1987) and Kececioglu and Jiang (1994), in terms of $(\Delta p/L)/v$ versus $v$. Two distinct straight lines fit the data very well. The difference in the inclination is obvious for all three test blocks. Moreover, the inclination increases past a critical point indicating an increase in the pressure drop as compared with the pressure drop that would have been obtained if the preceding flow regime were extended to the same fluid speed. It is clear at this stage that a third flow regime, beyond the Forchheimer-extended Darcy regime, indeed exists. The corresponding $\mathrm{Re}_K$ of transition are: 19.3, 3, and 7.4 for layers 1, 2, and 3, respectively.

**Table 1 Hydraulic parameters obtained by Antohe et al. (1996); $\rho_s$ is the initial density of the aluminum layer, $r$ is the compression ratio, $\phi$ is the measured porosity, $U_K$ and $U_{c_F}$ are estimated uncertainties of computed permeability $K$ and inertia coefficient $c_F$ values**

| Layer | $\rho_s$ [%] | $r$ | $\phi$ | $K$ [$10^{-10}$m$^2$] | $U_K$ [%] | $c_F$ | $U_{c_F}$ [%] |
|---|---|---|---|---|---|---|---|
| 1 | 4 | 7 | 0.64 | 11.36 | 5.4 | 0.371 | 8 |
| 2 | 4 | 14 | 0.46 | 1.75 | 3.6 | 0.413 | 11.5 |
| 3 | 8 | 7 | 0.32 | 5.36 | 4.7 | 0.418 | 8.8 |

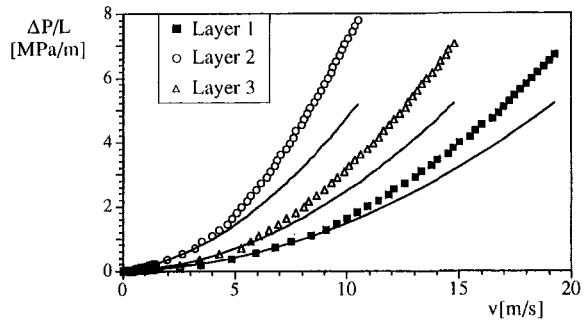


**Fig. 2 Experimental and theoretical pressure gradient (continuous lines) versus fluid speed; theoretical results follow the Forchheimer-extended Darcy model with $K$ and $c_F$ determined from the low range velocity results. Uncertainties: 2.1 percent for fluid velocity and 5.6 percent for pressure gradient.**

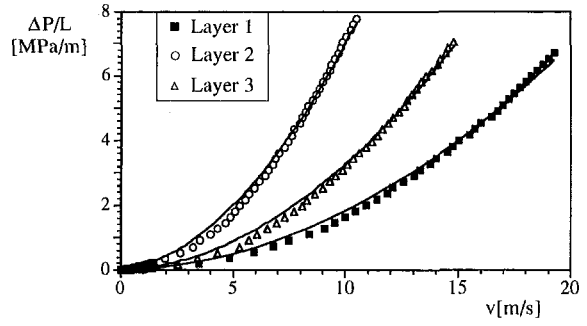


**Fig. 3 Experimental and theoretical pressure gradient (continuous lines) versus fluid speed; theoretical results follow the Forchheimer-extended Darcy model with $K$ determined from the low velocity range results and $c_F$ determined considering the entire velocity range. Uncertainties: 2.1 percent for fluid velocity and 5.6 percent for pressure gradient.**

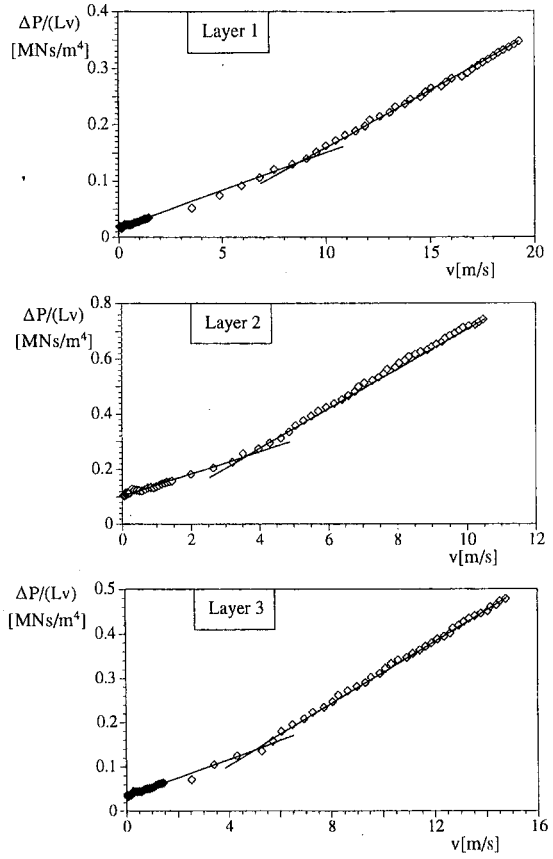


**Fig. 4 Experimental modified pressure gradient versus fluid speed. Two distinct straight lines, with different inclinations, fit well the experimental data. Uncertainties: 2.1 percent for fluid velocity and 6.2 percent for modified pressure gradient.**

We then tried fitting the experimental results with a cubic law of the form

$$\frac{\Delta p}{L} = \frac{\mu}{K} v + \frac{\rho c_F}{K^{1/2}} v^2 + c v^3 \tag{3}$$

where the cubic coefficient $c$ has units Pa $s^3/m^4$. The results are presented in Fig. 5. The continuous lines are the least square cubic curves fitting the experimental results. In this case, the permeability and the inertia coefficients are the same as the ones obtained interpolating the low velocity range (Table 1). Therefore, the fitting of the high velocity range is affected only by the cubic term. The values of the cubic coefficient $c$ are listed in the figure. The corresponding average deviations are: 21.1 kPa/m for layer 1, 48.8 kPa/m for layer 2, and 29.5 kPa/m for layer 3. Comparing them with the deviations of the quadratic fitting, the cubic curve fitting leads to a much better agreement, corresponding to 32, 60, and 45 percent of the deviations obtained with the Forchheimer-extended Darcy model when $c_F$ is determined from the full range. Moreover, it provides a unique model for the entire velocity range of our experiments.

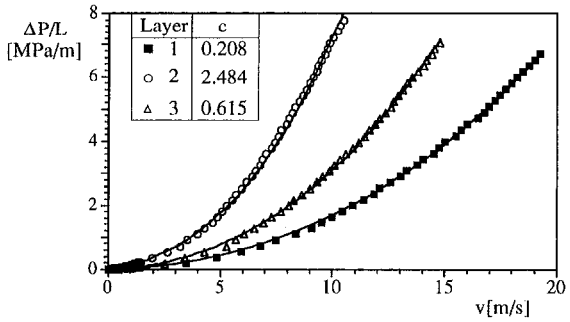


**Fig. 5 Experimental and theoretical pressure gradient (continuous lines) versus fluid speed; theoretical results follow the cubic-Forchheimer-extended Darcy model with $K$ and $c_F$ determined from the low range velocity results; the cubic coefficient is obtained from curve fitting. Uncertainties: 2.1 percent for fluid velocity and 5.6 percent for pressure gradient.**

## Model Verification

We note in passing that Joseph, Nield and Papanicolaou (1982) wrote "The suggestion that the one-dimensional form of (1) be modified by the addition to the right-hand side of a term proportional to $\rho v^2$ dates back to Dupuit (1863), but the modified equation is usually associated with the name of Forchheimer (1901). Forchheimer and others have also included a term proportional to $v^3$, but this does not seem to be consistent with experiment . . . The available experimental data correlates well with a quadratic drag law (see, for example, MacDonald et al., 1979)." Muskat (1937) remarks that the cubic term was added by Forchheimer, not in his (1901) paper (which just had a $v^2$ term) but later, in Forchheimer (1930).

The discussion in the previous section indicates that a cubic model yields better agreement (substantially smaller deviation) with the experimental results. To substantiate this result we consider the strategy for model validation suggested by Davis et al. (1992). The suggested method tests if there is any correlation between the residuals, defined as

$$\delta(v_i) = \Delta p_{\exp}(v_i) - \Delta p_{\text{theo}}(v_i) \tag{4}$$

The semivariance used to estimate the "correlation" is pre-

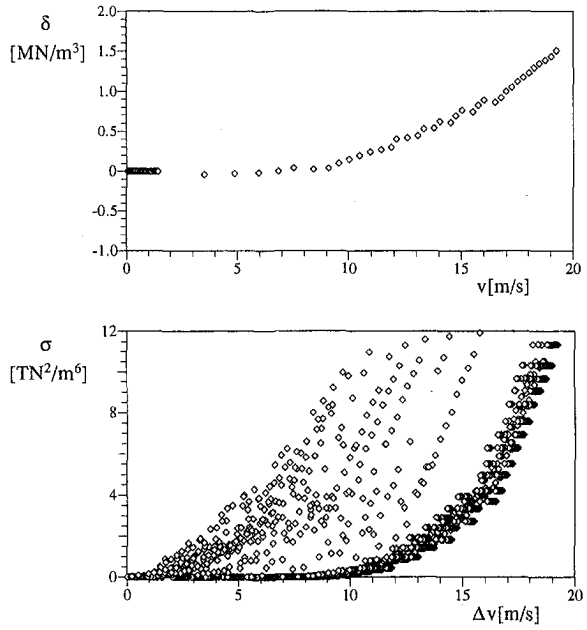


**Fig. 6 Residuals (top) and variogram (bottom) of the Forchheimer-extended Darcy model (with $c_F$ and $K$ determined from the low velocity range) for porous layer 1**

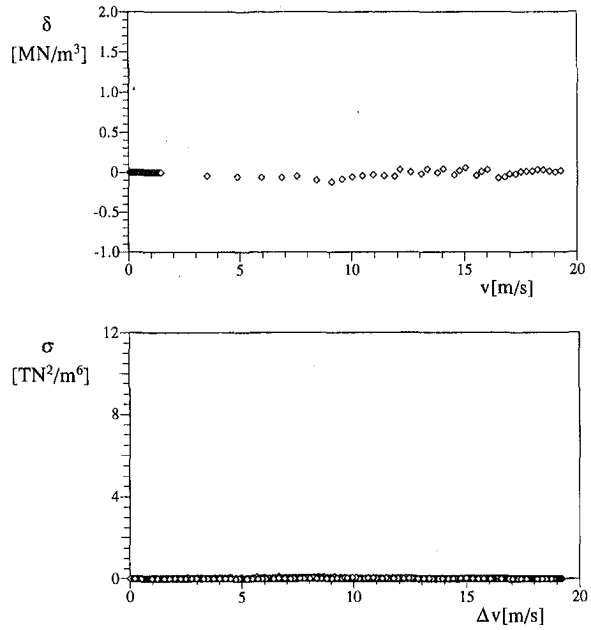


**Fig. 7 Residuals (top) and variogram (bottom) for the cubic-Forchheimer-extended Darcy model for porous layer 1**

sented in more detail by Delhomme (1978). Briefly, the semivariance is a function of the "lag distance" (distance between two experimental points) and defined as

$$\sigma(\Delta v) = \frac{1}{2N(\Delta v)} \sum_{i=1}^{N(\Delta v)} [\delta(v_i + \Delta v) - \delta(v_i)]^2 \qquad (5)$$

where in the present case $v_i$ is a fluid speed, $\Delta v$ is the "distance" between two experimental fluid speeds, and $N(\Delta v)$ is the number of pairs of experimental points $\Delta v$ units apart. If the semivariance tends to a finite value as the "lag distance" $\Delta v$ increases then the residuals do not correlate and the theoretical model is valid. Otherwise, the residuals correlate and the theoretical model is invalid.

We then tested three hypotheses: (1) a Forchheimer-extended Darcy model (results shown in Figure 2) with the permeability and the inertia coefficient obtained from the low speed range, (2) a cubic-Forchheimer-extended Darcy model with $K$ and $c_F$ obtained from low speed range and the cubic coefficient $c$ determined by the best fitting of the full range, and (3) a Forchheimer-extended Darcy model with the inertia coefficient obtained from the full speed range.

The results of the two layers with lowest and highest cubic coefficient value, namely layers 1 and 2, are presented next. The residuals and the corresponding variance of layer 1 following from the hypothesis (1) are shown in Fig. 6. Observe the increase on the residual with the fluid speed. The variogram (lower graph) clearly shows in a parabolic shape the increase in semivariance with the "lag distance" $\Delta v$. This shows that the theoretical Forchheimer-extended Darcy model is inappropriate for correlating the experimental data. Now, observe in Fig. 7 the residuals (top) and the variogram (bottom) when hypothesis (2) is tested. The reduction in the residual values, when compared with Fig. 6, is noteworthy. The variogram is flat, indicating that the cubic-Forchheimer-extended Darcy model is an appropriated model for representing the experimental data.

The observations and conclusions of the previous paragraph could be media dependent. That is, there is no guarantee at this point that a porous medium with distinctly different hydraulic parameters would behave similarly. We now present the results of layer 2. Notice from Table 1 and Fig. 5 the differences in hydraulic parameters between layers 1 and 2: porosity $\phi_1/\phi_2 = 1.39$, permeability $K_1/K_2 = 6.49$, inertia coefficient $c_{F1}/c_{F2} = 0.90$, and cubic coefficient $c_1/c_2 = 0.08$. It is clear that layer 2 is very different from layer 1.

Figure 8 presents the residuals (top) and semivariances (bottom) for hypothesis (1). Again, the Forchheimer-extended Darcy model is not appropriate. In Fig. 9, hypothesis (2) leads to much lower residuals and flat variance throughout the velocity range. The results support the validity of the cubic-Forchheimer-extended Darcy model. Notice that the residuals graphs of Figures 6 and 8 indicate the validity range of the Forchheimer-extended Darcy model in agreement with the previous estimates of Figure 4.

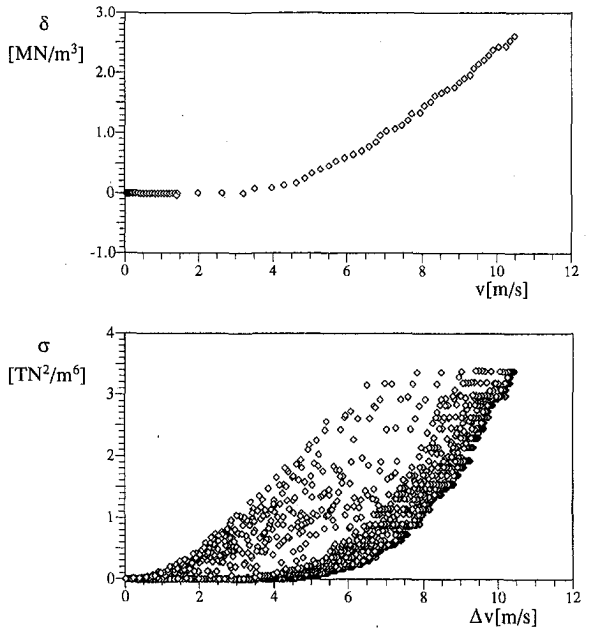


**Fig. 8 Residuals (top) and variogram (bottom) of the Forchheimer-extended Darcy model (with $c_F$ and $K$ determined from low velocity range) for porous layer 2**

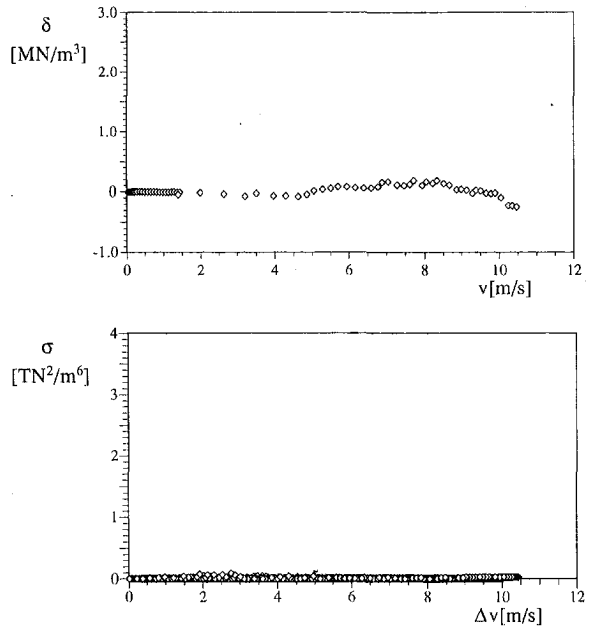


**Fig. 9 Residuals (top) and variogram (bottom) of the cubic-Forchheimer-extended Darcy model for porous layer 2**

In Fig. 10 we present two variograms. The results are for layer 1 considering hypothesis (3). The top graph refers to the Forchheimer-extended Darcy (quadratic) model but with $c_F$ determined from the full range data. The bottom graph refers to the cubic case (the same as the bottom graph in Fig. 7 but with a different scale). The purpose of the inclusion of Figure 10 is to investigate how the quadratic model, with $c_F$ determined from full velocity range, compares with the cubic model. The results show that the cubic model is more appropriate (there is a uniform semivariance close to zero), while the quadratic (full) model indicates a lot of scattering in the data and a tendency of $\sigma$ to increase sharply as $\Delta v$ increases past 15 m/s.

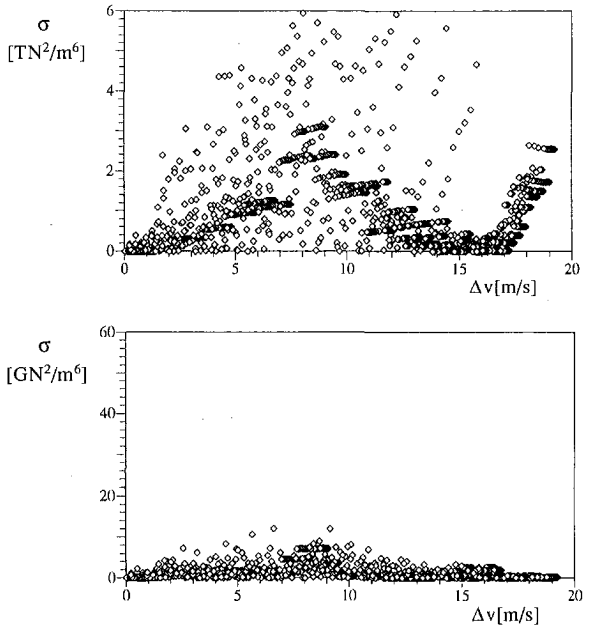


**Fig. 10 Variogram for the Forchheimer-extended Darcy model (with $K$ determined from the low velocity range and $c_F$ determined from the full velocity range) (top) and variogram for the cubic-Forchheimer-extended Darcy model (bottom) for porous layer 1**

We do not attach any special significance to the cubic term. We concur with Fand et al. (1987) and Kececioglu and Jiang (1994) that the transition under discussion is essentially one from one velocity range for which there is $v^2$-dependent drag to another, with the same velocity dependence but with an altered drag coefficient. The simplest assumption is that, in the transition region, the drag coefficient varies linearly with $v$, and so the drag itself is a cubic function of $v$. The $v^3$ term is simply a correction term and never becomes dominant; it is applicable for a limited velocity range. If one is concerned only with very large values of $v$ (beyond the transition region) then a quadratic drag law is appropriate. This is in accordance with the argument by Joseph et al. (1982) that at large velocities the drag is essentially form drag, and hence on dimensional grounds must depend on $v^2$.

## Conclusions

Initial tests at relatively low flow speed were performed for determining the permeability and the inertia coefficient of three distinct porous layers. The experimental tests were then extended to a high flow regime, beyond the Forchheimer regime. Our experimental results indicate a subtle transition to a third regime at $\mathrm{Re}_K \sim O(10)$. This regime, also quadratic in $v$, is unequivocally observed when plotting the experimental data as $\Delta P/(Lv)$ versus $v$.

The rate of change of static pressure gradient along the porous medium in our experiments is increased when compared with the gradient at the same speed yielded by the Forchheimer regime. This observation, contrary to what was reported previously from experiments with water flowing through solid spheres, is in line with what one would expect of transition in confined geometries in which form drag is not predominant. Indeed, the internal morphology of the porous media used in our experiments is more like that of a capillary reticulate in which form drag should be relatively small as compared with the form drag effect induced by the bluff-body like morphology of a porous medium made of spheres.

Although lacking data to substantiate the published claim of transition to turbulence, we can anticipate the existence of two distinct types of transition of incompressible viscous flow through a porous medium depending on the morphology of the solid matrix. This would explain the anomalous pressure rate behavior described previously.

The experimental results were then analyzed theoretically considering two hypotheses: (1) Forchheimer-extended Darcy model, or (2) cubic-Forchheimer-extended Darcy model. Using the residual parameter we show that the cubic model of hypothesis (2) correlates the experimental data much more accurately than the best curve fit using the Forchheimer-extended Darcy model. Calculating the semivariances at various "lag distances" we demonstrate that the cubic velocity model is more appropriate for high speed (beyond $\mathrm{Re}_K \sim O(10)$) flow through a porous medium.

## Acknowledgments

Professor Lage is thankful for the support provided by the J. L. Embrey Professorship in Mechanical Engineering. This work was partially supported by the Defense Systems and Electronics Group of Texas Instruments.

## References

Antohe, B. V., Lage, J. L., Price, D. C., and Weber, R. M., 1997, "Experimental Determination of Permeability and Inertia Coefficients of Mechanically Compressed Aluminum Layers," ASME JOURNAL OF FLUIDS ENGINEERING, to appear.

Bejan, A., 1993, *Heat Transfer,* Wiley, New York, p. 646.

Davis, P. A., Olague, N. E., and Goodrich, M. T., 1992, "Application of a Validation Strategy to Darcy's Experiment," *Advances in Water Resources,* Vol 15, pp 175–180.

Delhomme, J. P., 1978, "Kriging in the Hydrosciences," *Advances in Water Resources,* Vol 1, No. 5, pp. 251–266.

Dupuit, J., 1863, *Etudes Theoriques et Pratiques sur le Mouvement des Eaux,* Dunod, Paris.

Dybbs, A., and Edwards, R. V., 1975, Department of Fluid, Thermal and Aerospace Sciences report, FTAS/TR (Case Western Reserve University) No. 75-117, Workshop on Heat and Mass Transfer in Porous Media (PB-252 387) (NTIS: Springfield, VA), 228 pp..

Fand, R. M., Kim, B. Y. K., Lam, A. C. C., and Phan, R. T., 1987, "Resistance to the Flow of Fluids through Simple and Complex Porous Media whose Matrices are Composed of Randomly Packed Spheres," ASME JOURNAL OF FLUIDS ENGINEERING, Vol. 109, pp. 268–274.

Forchheimer, P., 1901, "Wasserbewegung durch Boden," *VDI Zeitschrift,* Vol. 45, pp. 1782–1788.

Forchheimer, P., 1930, *Hydraulik,* 3rd edition, B. G. Teubner, Leipzig.

Joseph, D. D., Nield, D. A., and Papanicolaou, G. 1982 "Nonlinear equation governing flow in a saturated porous medium," *Water Resources Research,* Vol. 18, pp. 1049–1052 and Vol. 19, p. 591.

Kececioglu, I., and Jiang, Y., 1994, "Flow through Porous Media of Packed Spheres Saturated with Water," ASME JOURNAL OF FLUIDS ENGINEERING, Vol. 116, pp. 164–170.

Macdonald, I. F., El-Sayed, M. S., Mow, K. and Dullien, F. A. L., 1979, "Flow through Porous Media: The Ergun Equation Revisited," *Industrial Chemistry Fundamentals,* Vol. 18, pp. 199–208.

Muskat, M., 1937, *The Flow of Homogeneous Fluids through Porous Media,* McGraw-Hill, New York.

Short, B. E., 1994, "Pressure Drop and Heat Transfer in Cast Pin Fin Cold Walls," Ph.D. dissertation, Southern Methodist University, Dallas, TX.

White, F. M., 1994, *Fluid Mechanics,* 3rd ed., McGraw-Hill, New York.

Zukauskas, A., 1987, "Convective Heat Transfer in Cross Flow," *Handbook of Single Phase Convective Heat Transfer,* S. Kacac et al., eds., Wiley, New York, Chapter 6.

**T. R. Oakley**
Former M. S. student; Currently,
Senior Engineer-Flight Test,
McDonnell Douglas Aerospace,
22098 James Road, Hangar 2133,
Naval Air Warfare Center-Aircraft Division,
Patuxent River, MD 20670

**E. Loth**
Associate Professor,
Department of Aeronautical and
Astronautical Engineering.

**R. J. Adrian**
Professor,
Department of Theoretical and
Applied Mechanics.

University of Illinois,
Urbana, IL 61801-2935

# A Two-Phase Cinematic PIV Method for Bubbly Flows

*A cinematic particle image velocimeter (PIV) for measurement of time varying fields in two-phase flow is described. This system has the capability to track detailed characteristics of individual bubbles moving through a turbulent flow field, e.g., size, shape, velocity, and acceleration, and simultaneously to measure the instantaneous fluid velocity field on a two-dimensional plane. The system employs an argon-ion laser, a rotating polygonal mirror and a single 35 mm movie camera. Two features of this technique are the ability to capture bubble trajectories for long periods of time and the use of bubble images which appear as two fine point images for each instant, from which centroid and diameter can be deduced. The instrument is evaluated in an experiment on the dispersion of nominally 3.5 mm diameter bubbles from a point source in a two stream, turbulent, planar free-shear layer. Characteristics of the fluid field and the bubble motion are described.*

## Introduction

The dispersion of bubbles in a turbulent flow is a complex, not fully understood phenomenon. Its description requires an understanding of the spatially complex, temporally evolving random fluid flowfield, and observations of the motion of the bubbles in response to that flow. In simple liquid velocity fields such as quiescent fields or laminar fields with simple temporal behavior, it has been possible for decades to measure several interesting properties of bubble motion, such as terminal velocities, shapes, trajectories and the wake behind the bubble. In turbulent flow fields, the phase-Doppler velocimeter offers a powerful ability to distinguish between liquid and bubble phase making it possible to measure point-wise statistics of both the liquid phase and the bubbles. The present experimental technique provides the ability to track the bubble motion through a two-dimensional temporally evolving flowfield and to quantitatively establish the kinematics of both phases simultaneously. This information is attained on a two-dimensional plane in the fluid as a function of time. While complete three-dimensional information is an obvious goal, the step from point-wise measurements to two-dimensional measurements is a large increment which may offer several new insights into the phenomena.

**Particle Image Velocimetry.** The particle image velocimetry (PIV) technique directly determines instantaneous velocity vectors for an entire plane of a flowfield. For unsteady flows, PIV provides significant advantages over point-wise measurement techniques such as pitot probes, hot wires and laser Doppler anemometry, because of the ability to record flow structure. Adrian (1991) reviews the theory and advances in PIV, as well as other particle imaging techniques. Hinsch (1994) also reviews advances in PIV and with particular regard to full three-dimensional, time-dependent velocity fields. The basic principle of PIV involves photographically recording double-exposures or multiple-exposures of tracer particle images illuminated by successive pulses of a laser sheet. With the photographic magnification and the light sheet pulse separation time known, and the local average particle displacement measured by correlations of subsets of the digitized image, the velocity is simply given by displacement divided by time. The low image density limit of PIV involves looking at individual tracer particles rather than groups of particles, and is commonly referred to as particle tracking velocimetry (PTV).

Studies of two-phase flow usually employ the low image density particle tracking method to observe motion of suspended matter. The resulting measurements of the particle or bubble velocities are sparse and irregularly spaced. In contrast, if the fluid is seeded in fine particles and the correlation method is used to measure displacements in small local areas, the fluid velocity field is obtained on a uniform grid of typically higher spatial resolution and thus does not suffer from large interpolation uncertainties. The ideal for a two-phase flow is to combine both of these techniques into a single measurement process which is able to discriminate between the light scattered by fine seed particles that mark the fluid motion and the large suspended matter of interest in the two-phase flow. Further, since the Lagrangian trajectories of the suspended matter are of fundamental interest, it is desirable to obtain these data with resolution in time and over long periods of time.

Previous research on two-phase flow measurements has included the work of Vogel and Lauterborn (1988) in which liquid velocity vectors for the collapse of a cavitation bubble were recorded for a limited number of frames at very high rates. Hassan and Canaan (1991) used PIV to determine bubble velocities and pathlines in a steady flow around a circular cylinder, tracking only the bubble motion. Recent work which achieved simultaneous measurement of the liquid velocity and micro bubble velocity with a single-frame, single instant measurement has been done by Sridhar et al. (1991), Hassan et al. (1992), Liu and Adrian (1993). Two-phase flow of solid particles in air has also been studied by McCluskey et al. (1993), using PTV to measure particle velocities in a gas jet. The challenge in such work was to distinguish between images of the suspended phase and images of the seed phase.

In principle, extension of the PIV or PTV method to unsteady flow fields is a straightforward process, accomplished by recording sequences of images. In practice the method is limited by the filming rates of film or video cameras. Measurements of high filming rates are possible (Vogel and Lauterborn, 1988, Stolz et al. 1992), but such drum film cameras typically have a limited number of frames per sequence and have been used in the non-uniform PTV regime to date. Lin and Rockwell

Contributed by the Fluids Engineering Division for publication in the JOURNAL OF FLUIDS ENGINEERS. Manuscript received by the Fluids Engineering Division October 2, 1995; revised manuscript received April 29, 1997. Associate Technical Editor: O. C. Jones.

(1994) demonstrated measurements of single-phase flow behind the cylinder using a photographic filming camera with a single-frame cross-correlation PIV technique. Recently, Sridhar and Katz (1995) combined cinematic PIV with long-time exposure photography to simultaneously obtain velocities of liquid and microbubbles in simple laminar vortices. Their work involved the combined use of cinematic camera and a single-frame photographic camera which observed multiple images of the particle tracks. Other sequences may also be recorded by video cameras, often called digital PIV (Willert and Gharib, 1991, Huang et al. 1993, Hassan et al. 1992). The digital camera framing rates are already approaching those of cinematic film cameras and with the advent of high resolution video cameras (e.g., $2K \times 2K$), there is close parity to the spatial resolution of a 24 mm $\times$ 35 mm film camera. Hence either may be used where of course the digital recording format removes the analog to digital transfer.

The system described here uses cinematic recording which offered the best resolution at the time the system was developed. It seeks to provide simultaneous measurements of the fluid and bubble velocities as functions of time over relatively long spans of time so that the Lagrangian characteristics of the bubbles can be observed over the time scale of the turbulent flow. The approach taken is similar to that of the work of Sridhar and Katz (1995). It differs by considering the more complex case of turbulent flow, and by using a single movie camera instead of a combination of a cinematic camera and a long-time exposure single-frame camera. The present work also treats much larger bubbles which are capable of deforming and seeks to measure their instantaneous diameter. As such, a novel method for tracking and determining bubble diameter is described.

## Experimental Equipment and Techniques

**Free Shear Layer Apparatus.** This experimental study was conducted in a closed-loop water tunnel with a vertical test section. The tunnel has a total recirculation length of about 20 meters and a 9:1 contraction ratio just upstream of the test section and just downstream of a set of rectangular grid flow conditioners. The test section is approximately 1 meter long with interior cross-section dimensions of 30 cm $\times$ 30 cm. Optical access is available on all sides through four removable Plexiglas windows with a thickness of 2.86 cm. The tunnel volume is approximately 4500 liters, with a passive bubble trap located at the top of the water tunnel to eliminate bubble recirculation. The tap water in the tunnel was filtered (prior to seeding with PIV tracers) through filter papers with a 2.5 micron pore size. This filtration was necessary to eliminate any particulates with diameter on the order of the seeding particle size of 8 microns.

The unforced free shear layer is created by a splitter plate with pressure-correcting screens, similar to the one used by Dimotakis and Brown (1976). It produced a high speed velocity of 42.5 cm/s and a velocity ratio of 0.23, yielding an average liquid velocity ($U_{ave}$) of 0.26 m/s. Further details of the water tunnel and splitter plate design can be found in Loth and Cebrzynski (1995).

**Bubble Injection System.** For this study, it was desired to have a low bubble injection rate (<5 Hz) so that individual bubbles could be easily distinguished and tracked through the liquid flowfield. Compressed air was delivered through a succession of tubings to a slender stainless steel injector tip. The injector tip inner diameter of 0.5 mm was the size determined by Cebrzynski (1994) to provide nominally 3.5 mm bubbles. To minimize the integrated effects of turbulent dispersion which can cause a large majority of the bubbles to wander out of the light sheet, the bubble injector was located just below the camera field of view, which coincided with the vertical light sheet located in the spanwise center of the test section (see Fig. 1). This configuration of relatively thin tubing primarily aligned with the streamwise direction had little effect on the downstream shear layer development and structure. Air bubbles in water achieve their terminal velocity in less than a centimeter, such that these bubbles were essentially at terminal velocity as they passed through the field of view.

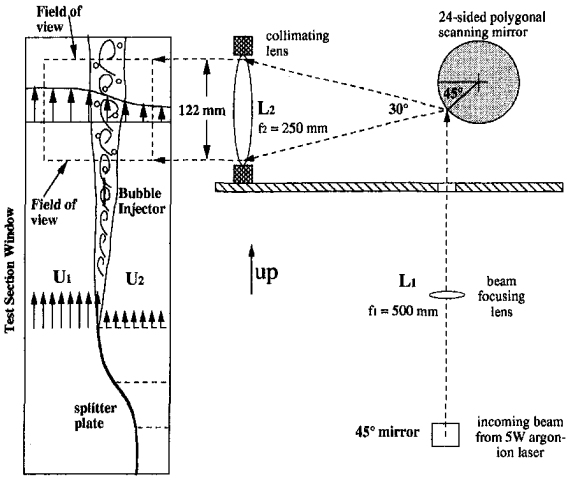


**Fig. 1 Experimental schematic and optics arrangement with respect to the field of view (where *x* is upwards and *y* is to the right).**

**Cinematic PIV System.** The cinematic PIV system design and optimization were carried out according to principles set forth in Adrian (1991), Keane and Adrian (1990, 1991, 1992), and Prasad et al. (1992). The primary components of the system are a Mitchell 35 mm framing movie camera with double-pin register for high film stability, a 5W argon-ion laser (principal lines at 488 and 514 nm), a 24-sided rotating polygonal mirror, and a 145 mm diameter collimating lens (see Fig. 1). Various other lenses and mirrors are included for beam steering and focusing. The 8 micron hollow glass sphere tracer particles (specific gravity = 1.1) are illuminated by the scanning laser beam and the images recorded on 35 mm black and white Kodak Wide Latitude Surveillance film (125 lines per mm). The available film area per frame is 19 mm $\times$ 25 mm. For a magnification of 0.1654 and the given resolution and mean flow speed (0.26 m/s), the optimal pulse separation time, $\Delta t'$, was 5.21 ms. At a framing rate of 30 fps, this allows a triple sweep to occur during the shutter opening (170° rotating angular shutter). Use of a triple pulse (instead of just a double) eliminates the need for precise synchronization between the shutter and the scanning mirror and increases the signal-to-noise ratio of the PIV correlation (Keane & Adrian, 1991). Further details of this design, as well as results of both the single-phase shear layer and bubbly flows, can be found in Oakley (1995) and Oakley et al. (1996).

A single-frame cross-correlation technique was applied to 0.87 mm square interrogation spots on film, which corresponds to a physical vector spacing of 2.6 mm, using 50 percent overlap. A matrix of 43 (transverse) by 47 (streamwise) vectors was obtained for each frame. The vector spacing is 3.3 percent of the shear layer thickness, $b$, which is based on the 5–95 percent points in the mean velocity profile. The temporal resolution of the velocity field evolution is given by $(U_{ave}\Delta t'')/b = 0.11$ (where $\Delta t''$ is the time between frames), so that the structures can easily be tracked between frames and the distortion of eddies is seen as a gradual process. Taking into account finite film and CCD resolution, uncertainty of the scanning mirror speed, and the small variation of $\Delta t'$ for a given particle (which is a function of its velocity for a scanning beam system) revealed a maximum instantaneous liquid velocity uncertainty ($\delta u_L$) of 2.1 percent (Oakley et al., 1996).

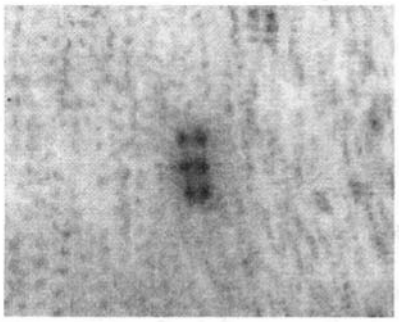

**Fig. 2 Close up of raw image showing bubble images and tracer particles. One example set showing six dark points (as sketched in Fig. 3*a*) is located in the center of the Figure. These are a result of three pairs of reflections caused by a triple exposure of a single bubble of nominal 3.5 mm diameter moving upward. Note the 8 $\mu$m seed particles are not as reflective and can only be clearly observed with an extreme close-up, as was used for the liquid velocity vector interrogation.**

The vorticity is spatially averaged from the instantaneous velocity field by evaluating the circulation, $\Gamma$, around the square of the eight neighboring grid points and dividing by the enclosed area, $4\Delta x^2$ ($\Delta x$ is the grid spacing). Thus, the uncertainty in vorticity combines the uncertainties of eight independent velocity vectors, i.e., $\delta\omega = \sqrt{8}\,\delta u_L/4\Delta x$, where $\delta u_L \approx 0.016\Delta U$ is the maximum uncertainty in a given velocity vector and where $\Delta U$ is the liquid velocity difference across the shear layer. This results in a relative uncertainty of the local vorticity (scaled by the mean vorticity, $\Delta U/b$) of 30 percent.

However, an additional error is introduced because the bubble centroid may be out of the 1 mm thick two-dimensional plane that illuminates the seed particles. This occurs because the reflections from the bubbles are much stronger than that of the particles (e.g., Fig. 2) and as such the thickness of the plane containing possible bubble images was observed to be approximately 2 mm in thickness. Therefore, centroid uncertainties of $\pm 1$ mm relative to the measured liquid velocity position are possible. Based on a peak of 10 Hz for the velocity spatial gradients at the bubble location (Oakley et al., 1996), this yields a maximum liquid velocity uncertainty caused by spatial interpolation of 10 mm/s. Combining this with the uncertainty before interpolation yields a total maximum uncertainty in liquid velocity at the bubble centroid of 4.0 percent of $U_{\text{ave}}$. The total liquid acceleration uncertainty due to spatial interpolation at the bubble location is estimated by assuming it is equal to the combined total uncertainty of two velocities divided by the temporal resolution (0.033 s), yielding a value of 0.47 m/s$^2$.

**Bubble Position and Diameter Determination.** Once the velocity vector maps were obtained from the PIV interrogations, the locations of the bubbles were individually determined for each frame. Individual bubbles were selected by examining sequences of the movie film and finding bubbles with distinct images which could be tracked across a significant portion of the light sheet (i.e., several successive frames). Bubbles which were more isolated from their nearest neighboring bubbles were preferred due to the desire to eliminate significant bubble-bubble hydrodynamic interaction. Typically, those selected were at least four bubble diameters from their nearest neighbors. In general, several bubbles may be in the field of view at any time, so great care was necessary to properly track a given bubble. Figure 2 shows an expanded portion of a raw image of triple exposed bubbles and particles.

It was observed by examining the prints that the instantaneous image of a bubble illuminated by a scanning laser beam (for the sizes studied herein) is two points of light. This is consistent with the more general scattering optics of bubbles described by Langley and Marston (1984). The bubbles in the PIV pictures then appear as six points, which are really three pairs of points from the triple-exposure (see Fig. 3($a$)). The circumference of the bubble is typically not seen. These points of light come from a first point on the bubble surface where the surface normal is at a 45° angle to the lens optical axis and a second point which results from an internal bubble reflection as shown in Fig. 3($b$). Since the bubble is approximately circular in the horizontal plane, we may calculate the angle ($\alpha$ = 25.8 deg) and thus compute the ratio of the bubble width to the image pair spacing (=1.75). This ratio was used to compute the average bubble width ($w$) for each bubble along its trajectory (which typically included five to six frames). To verify this ratio when the bubble is no longer spherical, photographs of the bubbles in both the shear layer and in quiescent flow were analyzed to obtain bubble width. The deviation of the measured width to theoretical width was found to be less than 6 percent. From the bubble height ($h$), the aspect ratio of the bubble ($E = h/w$) was also measured from the photographs and compared to the expected values for ellipsoidal bubbles in a contaminated liquid, e.g., ordinary tap water, as given by eq. 7–22 of Clift et al. (1978). Again, the photographs of the bubbles were analyzed to obtain aspect ratio and the largest deviation of the measured to theoretical $E$ was found to be less than 3 percent.

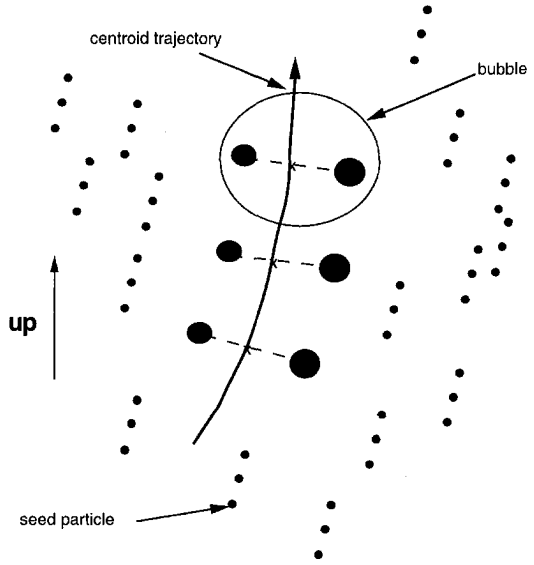


**Fig. 3($a$) Schematic of bubble image on film showing two-spot reflection and the local trajectory (small spots represent tracer particles).**

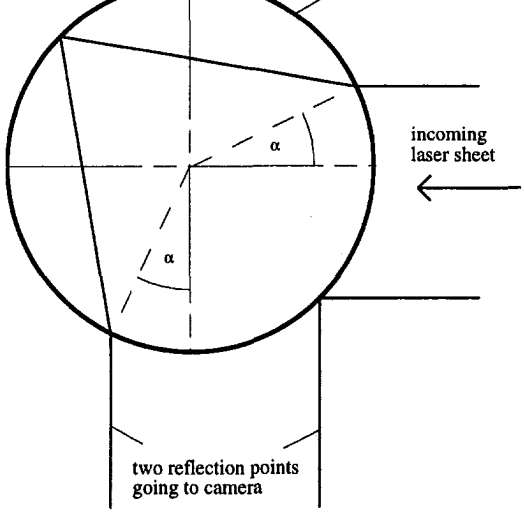


**Fig. 3($b$) Schematic of two-point reflection mechanism looking down on a bubble which is assumed circular in the horizontal plane.**

Therefore, the total uncertainty of equivalent bubble diameter, $d_B = w(E)^{1/3}$, is expected to be less than 7 percent.

With regard to bubble position accuracy, the positions of the bubble image pair of points are obtained by using the same CCD camera and monitor used in the PIV interrogations. Using the joystick controller, the film is moved with respect to the camera to find the location of the bubble points. The micron movement mode of a Unidex motion controller and use of cross-hairs on the monitor allows for precise location of these points. Therefore, the centroid of each reflection spot can be located to within a pixel, which corresponds to 0.04 mm physical dimension. The error in the bubble centroid location is $\sqrt{2}$ times the error in locating one of the points, or 0.058 mm. This error is approximately 2 percent of both the liquid vector grid spacing and the bubble diameter, so it is negligible.

**Bubble Velocity and Acceleration Uncertainty.** We now turn our attention to uncertainties which directly influence bubble velocity and acceleration. The first uncertainty we will consider is that of applying curvefits to the trajectories. The coordinates of the 6 points of reflected light per frame (triple-exposure) were processed to find the centroid of each pair. The coordinates of the trios of centroids from several successive frames were plotted vs. time and fitted with ninth-order least mean square polynomials. The curve through these centroids is assumed to define the local trajectory (see Fig. 3($a$)). Analytical derivatives of these curvefits give the velocity and acceleration components. The curve fits for $x$ and $y$ vs. time were found to have an rms deviation from the original centroid coordinates of 0.15 mm. Although the curvefits are intended to correct some of the error in centroid location due to the unknown instantaneous deformation, in a worst-case scenario, this error could increase the uncertainty level to 0.161 mm.

In order to make a simple estimate of errors in bubble velocity, we consider a finite difference approximation, even though use of curvefits should provide a lower level uncertainty in velocity by providing a higher order trajectory definition. Note that the three positions of the bubbles in the preceding frame and the following frame provide the strongest influence on determining the curve fitted trajectory. Thus an appropriate estimate of the velocity uncertainty is given by using the interframe time interval, $\Delta t'' = 33.3$ ms. The velocity error due to the 0.161 mm uncertainty in centroid locations can be approximated as that from a centered difference calculation from data of three consecutive frames, i.e.,

$$\delta U_{B1} = \frac{\sqrt{2}\delta x}{2(\Delta t'')}, \tag{1}$$

where $\Delta t''$ is the time between frames (33.3 ms), so $\delta U_{B1} = 0.34$ cm/s. If, on the other hand, we assume that the centroid locations are perfect, the central finite difference formula from the Taylor series expansion of position will have a leading second order error of

$$\delta U_{B2} = \frac{(\Delta t'')^2}{6}\frac{\partial^3 x}{\partial t^3}, \tag{2}$$

which can be approximated as $(\Delta t'')^2 a_{B\text{rms}} f_B/6$, where the rms acceleration, $a_{\text{rms}}$, of bubbles in the shear layer was found to be 4.77 m/s$^2$ and the average bubble oscillation frequency, $f_B$, was 7.63 Hz, so $\delta U_{B2} = 0.67$ cm/s. Thus the total estimated uncertainty in bubble velocity ($\delta U_B$) is 0.76 cm/s. This value is approximately 1.5% of the mean streamwise bubble velocity component and 8 percent of the rms transverse bubble velocity.

Finally, errors in bubble acceleration are similarly considered. The contribution due to the maximum uncertainty in centroid location yields

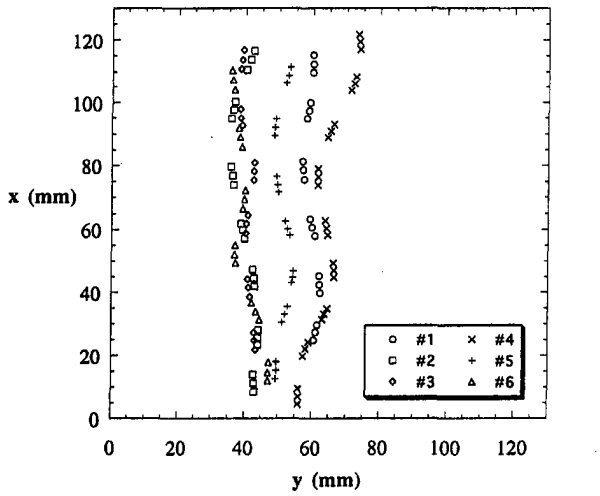


**Fig. 4 Combined trajectories for the six bubbles analyzed in the shear layer.**

$$\delta a_{B1} = \frac{\sqrt{6}\delta x}{(\Delta t'')^2}, \tag{3}$$

which is estimated as 0.35 m/s$^2$. The leading order error from a three point finite difference formulation is given by

$$\delta a_{B2} = (\Delta t'')^2 a_{B\text{rms}} f_B^2/24 \tag{4}$$

$\delta a_{B2} = 0.013$ m/s$^2$, which is nearly negligible in comparison with $\delta a_{B1}$. Thus the total uncertainty in bubble acceleration is 0.36 m/s, which is 7 percent of the bubble rms acceleration.

## Example Flowfield Results

Presently, only nominally 3.5 mm diameter bubbles have been studied in the shear layer. The same injector tip was used for the bubbles in the shear layer as for a previous rising bubble study, but the mean liquid flow past the injector tip and/or the turbulence in the shear layer caused the bubbles to detach sooner, resulting in smaller diameters than in quiescent water.

**Trajectories.** The basic oscillating character of the bubble trajectories is unchanged whether the bubbles are rising in quiescent water or through a shear layer. The quasi-sinusoidal motion for six different bubbles in the shear layer is apparent in Fig. 4. We shall examine in more detail the motion of an example bubble rising through the turbulent flowfield of the shear layer, which is typical of the motions of other interrogated bubbles. Figure 5 shows this particular bubble at its instantaneous location within the liquid velocity field and the corresponding vorticity maps for three typical sequential frames. The complex flowfield with detailed small-scale structure is much different than the classic large-eddy/braid structure of low Reynolds number shear layers and in several regions, the computed two-dimensional vector field is not divergence free indicating significant three-dimensionality (Oakley et al., 1996). The vorticity map shows a spectrum of structure sizes. However, it should be noted that the vorticity field is not resolved to the Kolmogorov scale nor to the scale of the vortices shed in the bubble wake (which can be sub-millimetric) and that the spatially-averaged vorticity uncertainty was estimated at 30 percent. This suggests that one should be careful in interpreting the instantaneous vorticity at the bubble location.

Figure 6 shows the transverse coordinate of the bubble centroid as a function of time. The counterpart streamwise location as a function of time is approximately linear, but with variations large enough to significantly affect the velocity and acceleration. The trajectory curve fits were used to obtain bubble

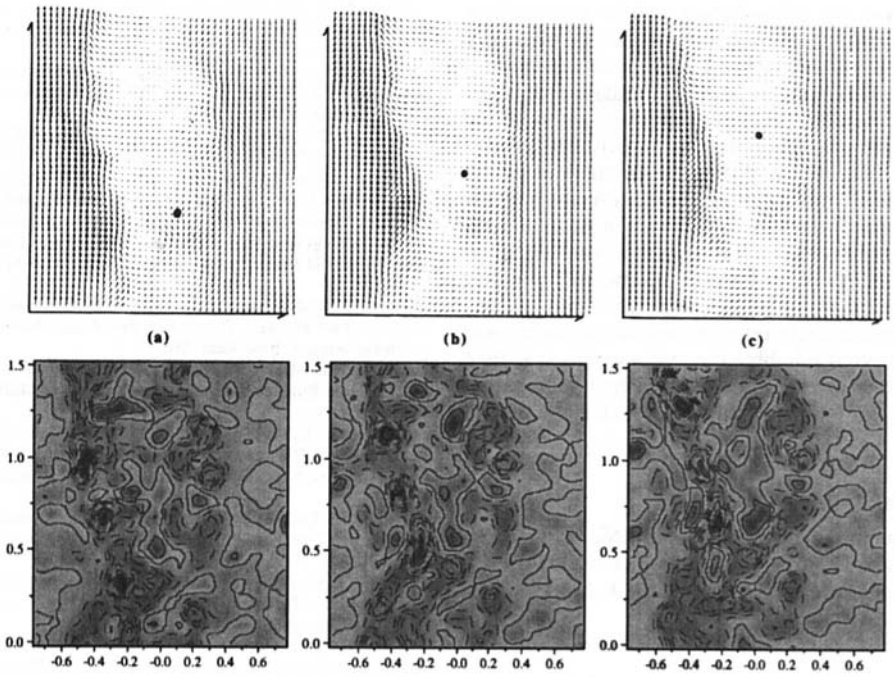


*Fig. 5* **Sequence of velocity vectors and the corresponding total vorticity maps for a bubble in a turbulent free shear layer. The dashed lines correspond to negative vorticity, and the approximate range of values present is from $-30\ s^{-1}$ to $+10\ s^{-1}$.**

velocity and acceleration, and derivatives were evaluated at discrete times when necessary. The unique aspect of two-phase cinematic PIV is the ability to simultaneously obtain the time history of the two-dimensional bubble velocity ($u_B$, $v_B$) and the liquid velocity ($u_L$, $v_L$) which can be interpolated to the bubble location, as shown in Fig. 7. The transverse components of the liquid and bubble velocity appear to be centered around zero, as expected. The mean streamwise liquid velocity component is less than the mean shear layer convection velocity, which is due to the appearance of this particular bubble toward the lower speed portion of the shear layer (see bubble 1 in Fig. 4).

**Hydrodynamic Variables.** To examine the bubble dynamics, the liquid quantities at the bubble locations (including velocity, acceleration and vorticity) were obtained for several such bubbles. From the independently measured liquid and bubble velocities, the relative velocity was calculated. It was seen that large variations of relative velocity exist (~20 to 45 cm/s), even for a single bubble. However, the average of these scattered values is approximately equal to the expected terminal velocity, based on previous rising bubble studies (Oakley, 1995). The two-dimensional Reynolds number is not simply a direct multiplicative factor times each value of relative velocity, because the diameter of each individual bubble is somewhat different. A large spread of values was seen again, ranging from approximately 700 to 1700, with a mean of around 1200.

Instantaneous vorticity of both signs was seen by the bubbles, which was expected based on the single-phase results (Oakley et al., 1996). The mean of these vorticity values was negative, which is also consistent with the shear layer negative mean velocity gradient. The measured rms magnitudes of vorticity will always be underestimates, due to limited measuring resolution of the PIV. However, the vorticity resolution is of the order of the bubble size such that increased resolution is not necessarily beneficial in determining an average vorticity surrounding the bubble. In general, we have shown that bubble and liquid characteristics can be simultaneously obtained with relatively high accuracy and temporal resolution.

## Conclusions

A two-phase cinematic PIV technique was developed, which allowed simultaneous measurement of the time-resolved liquid velocity field and the time histories of bubble position, velocity,

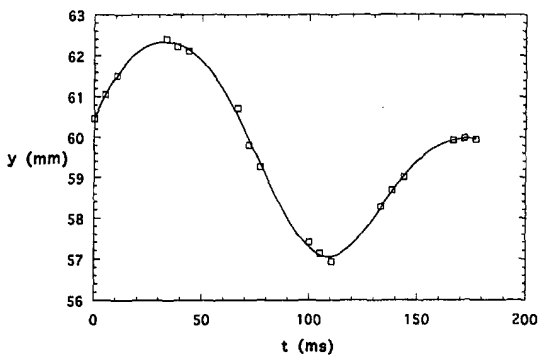


*Fig. 6* **Transverse bubble position as a function of time.**

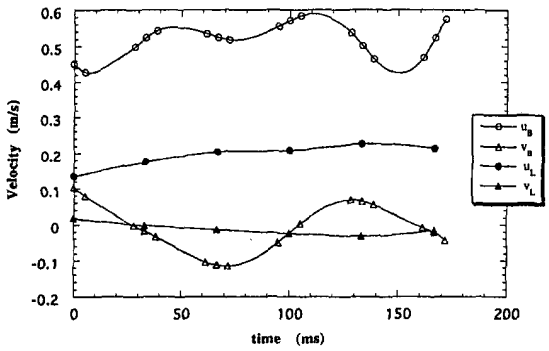


**Fig. 7 Combined plot of the streamwise and transverse velocity components of the bubble and the liquid at the bubble location as a function of time.**

and acceleration. From the triple-pulsed bubble images in a sequence of PIV pictures, the bubble size and bubble trajectory can be accurately determined. The technique was applied to a dilute flow of bubbles moving through a turbulent free shear layer as they rose due to buoyancy and the convection of the liquid flow. The images of the bubbles were easily distinguishable from the tracer particles, and direct measurement of the bubble size was possible from the images. Direct measurements of the bubble two-dimensional velocity and acceleration as well as the coincident liquid velocity and vorticity were obtained along the trajectories of several bubbles in a turbulent free shear flow. This technique can thus provide enough details of the bubble and liquid kinematics to estimate instantaneous lift and drag forces. Application of a bubble dynamics equation is then possible to allow further investigation of interphase momentum transport for modeling of multi-phase flows, which is the subject of future work.

## Acknowledgments

This work was supported by the Office of Naval Research (ONR) under contracts N00014-95-1-0313 and N00014-96-1-0312. We wish to acknowledge C. Meinhart, B. Ford, and G. Lundstrum for their assistance.

## References

Adrian, R. J., 1991, "Particle-Imaging Techniques for Experimental Fluid Mechanics," *Annual Review of Fluid Mechanics,* Vol. 23, pp. 261–304.

Clift, R., Grace, J. R., and Weber, M. E., 1978, *Bubbles, Drops, and Particles,* Academic Press, New York, NY.

Hassan, Y. A. and Canaan, R. E., 1991, "Full-Field Bubble Flow Velocity Measurements Using a Multiframe Particle Tracking Technique," *Experiments in Fluids,* Vol. 12, pp. 49–60.

Hassan, Y. A., Blanchat, T. K., Seeley, C. H. and Canaan, R. E., 1992, "Simultaneous Velocity Measurements of Both Components of a Two-Phase Flow Using Particle Image Velocimetry," *Int. J. Multiphase Flow,* Vol. 18, no. 3, pp. 371–395.

Hinsch, K. D., 1994, "The Many Dimensions of Optical Flow Diagnostics," Carl von Ossietzky Universität Oldenburg, Oldenburg, Germany.

Huang, H. T., Fiedler, H. E., and Wang, J. J., 1993, "Limitation and Improvement of PIV, Part II: Particle Image Distortion, a Novel Technique," *Experiments in Fluids,* Vol. 15, pp. 263–273.

Keane, R. D. and Adrian, R. J., 1990, "Optimization of Particle Image Velocimeters. Part I: Double Pulsed Systems," *Measurement Science Technology,* Vol. 1, pp. 1202–1215.

Keane, R. D. and Adrian, R. J., 1991, "Optimization of Particle Image Velocimeters: Part II. Multiple Pulsed Systems," *Measurement Science Technology,* Vol. 2, pp. 963–974.

Keane, R. D. and Adrian, R. J., 1992, "Theory of Cross-correlation Analysis of PIV Images," *Applied Scientific Research,* Vol. 49, pp. 191–215.

Langley, D. and Marston, P., 1984, "Critical-angle Scattering of Laser Light from Bubbles in Water: Measurements, Models, and Application to Sizing of Bubbles," *Applied Optics* Vol. 23, (7), April, pp. 1044–1054.

Lin, J. C. and Rockwell, D., 1994, "Cinematographic System for High-Image-Density Particle Image Velocimetry," *Experiments in Fluids,* Vol. 17, pp. 110–114.

Liu, Z. C. and Adrian, R. J., 1993, "Simultaneous Imaging of the Velocity Fields of Two Phases," *Particulate Two-Phase Flow,* M. C. Roco, ed., Butterworth-Heinemann, Stoneham, MA.

Loth, E. and M. S. Cebrzynski, 1995, "Modulation of Shear Layer Thickness Due to Large Bubbles," *International Journal of Multiphase Flow,* Vol. 21, pp. 919–927.

McCluskey, D. R., Elgaard, C., Easson, W. J. and Greated, C. A., 1993, "The Application of PIV to Turbulent Two-phase Flows," *Flow Visualization and Image Analysis,* Nieuwstadt, F. T. M., ed., Kluwer Academic Publishers, pp. 207–226.

Oakley, T., Loth, E. and Adrian, R. J., 1996, "Cinematic PIV of a High Reynolds Number Turbulent Free Shear Layer," *AIAA Journal,* Vol. 34 (2), Feb., pp. 299–308.

Oakley, T. R., 1995, "A Cinematic Particle Image Velocimetry Study of Bubble Dispersion in a Turbulent Free Shear Layer" M.S. thesis, University of Illinois at Urbana-Champaign.

Oguz, H. N. and Prosperetti, A., 1993, "Dynamics of Bubble Growth and Detachment from a Needle," *Journal of Fluid Mechanics,* Vol. 257, pp. 111–145.

Prasad, A. K., Adrian, R. J., Landreth, C. C., and Offutt, P. W., 1992, "Effect of Resolution on the Speed and Accuracy of Particle Image Velocimetry Interrogation," *Experiments in Fluids,* Vol. 13, pp. 105–116.

Sridhar, G., Ran, B. and Katz, J., 1991, "Implementation of Particle Image Velocimetry to Multi-Phase Flow," FED-Vol. 109, *Cavitation and Multiphase Flow Forum,* ASME, pp. 205–210.

Sridhar, G. & Katz, J., 1995, "Drag and Lift Forces on a Bubble Entrained by a Vortex," *Physics of Fluids,* Vol. 7, No. 2, pp. 389.

Stolz, W., Köhler, J., Lawrenz, W., Meier, F., Bloss, W. H., Maly, R. R., Herweg, R., and Zahn, M., 1992, "Cycle Resolved Flow Field Measurements Using a PIV Movie Technique in a SI Engine," SAE Paper 922354, pp. 1–10.

Vogel, A. and Lauterborn, W., 1988, "Time-Resolved Particle Image Velocimetry used in the Investigation of Cavitation Bubble Dynamics," *Applied Optics,* Vol. 27, No. 9, pp. 1869–1876.

Willert, C. E. and Gharib, M., 1991, "Digital Particle Image Velocimetry," *Experiments in Fluids,* Vol. 10, pp. 181–193.

Journal of Fluids Engineering

Technical Briefs

# The Production of Shear Flow Profiles in a Wind Tunnel by a Shaped Honeycomb Technique

F. Ahmed[1] and B. E. Lee[2]

## Introduction

There are many methods in use to produce shear velocity profiles in the wind tunnel. The most well known and commonly used among these are the use of grid of rods proposed by Owen and Zienkiewicz (1957) and that of curved mesh screens by Elder (1959). Two generalized theories of flow through nonuniform gauzes were presented by Elder (1959) and McCarthey (1964). Both of them are complex in the mathematical treatments and Cockrell and Lee (1966) have extended the work of Elder (1959) to practical use. However, Castro (1976) and Turner (1969) have discussed some of the discrepancies of the Elder's theory. As far as McCarthy's analysis is concerned, it is suitable only for three-dimensional shear flows and it is not applicable to an arbitrary shape gauze and to a nonuniform upstream flow distribution. A very serious disadvantage of using curved wire gauzes to produce linear shear profiles is that the method of fixing the gauzes precisely in the wind tunnel is very difficult. A slight slackness or deviation from the desired shape causes serious distortion of the resulting shear profile downstream from the gauze. Cowdrey (1967) presented a theory of spacing grids of rods for use in simulating the atmospheric velocity profile. This method is simple and popular, but its main disadvantage is that, immediately behind the grid, the velocity profile is not smooth and the displacement of a single rod can produce a serious velocity excess or defect in the required profile.

Regarding shear flow production techniques, there are a number of interesting practical problems for which the generation of a linear shear profile is required. They include the behavior of shear flow in the presence of turbulence in the free stream. Perhaps the most important application is the experimental simulation for various shear flow gradients on the study of wind effects on structures, but equally important is the study of diffuser and duct behavior when they are to be tested with a variety of known and convenient velocity profiles.

[1] Associate Professor, Department of Mathematics, University of Bahrain, P O Box 32038, Bahrain.

[2] Balfour Beatty Professor, Department of Civil Engineering, Portsmouth University, Portsmouth, U.K.

Contributed by the Fluids Engineering Division of THE AMERICAN SOCIETY OF MECHANICAL ENGINEERS. Manuscript received by the Fluids Engineering Division October 20, 1994; revised manuscript received May 31, 1997. Associate Technical Editor: H. Hashimoto.

## Theoretical Analysis

To calculate the desired velocity profile, the following assumptions are made.

(1) The flow in the honeycomb cell is fully developed, therefore the friction factor "$f$" can be considered as reasonably constant for the range of Reynolds number considered.

(2) The desired shear velocity profile is formed by streamline deviation immediately upstream of the honeycomb. The flow regime upstream of the honeycomb, excluding wall boundary layers, can be regarded as a potential flow regime in which Laplace's equation for a two dimensional stream function is applied.

(3) There is no flow normal to the boundary walls of the tunnel. A complete set of boundary conditions are shown in Fig. 1.

## Calculation Procedure

The calculation of the honeycomb profile to produce the required shear velocity profile is based on the experimental value of the cell friction factor $f$ defined by,

$$f = \frac{\Delta P \cdot D}{(4L \cdot \frac{1}{2}\rho U)} \tag{1}$$

where $\Delta P$ is the pressure drop across the cell length "$L$" and diameter "$D$." $U$ is the undisturbed upstream velocity and $\rho$ is the density. In the present experiments two types of honeycomb were used. Evaluation of $f$ for both of paper and aluminium foil honeycombs showed it in the range $.0073 < f < .0082$, for the Reynolds numbers in the rang of 3500–8000, depending on the cell size of the honeycomb, at the mean free steam velocity of ~9–10 m/s. The values of friction coefficient were also obtained by using the relations suggested by Bradshaw and Gee (1960), Sigalla (1958), and Hammon (1982). The values obtained showed only a difference of less than six percent.

In the potential flow region upstream of the honeycomb, Laplaces equation is satisfied as follows,

$$\nabla^2 \psi = 0 \tag{2}$$

where $\psi$ is two-dimensional stream function, and the velocity components $u$ and $v$ are given by

$$u = \frac{\partial \psi}{\partial y}, \quad v = -\frac{\partial \psi}{\partial x}$$

The pressure drop across the honeycomb cell can be written, as a function of height "$y$" above the floor,

$$P(o, y) - P_{+\infty} = \Delta P(y) = \left[\frac{4fL(y)}{D}\right] \frac{1}{2} \rho U^2(y) \tag{3}$$

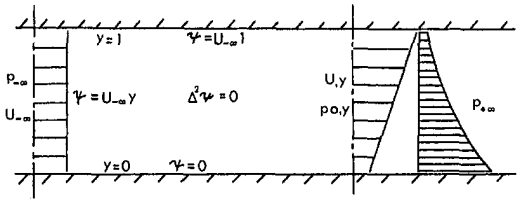


**Fig. 1 Identification of terms and boundary conditions**

From Bernoulli's equation for the potential flow region.

$$P_{-\infty} + \tfrac{1}{2}\rho U^2_{-\infty} = P(o, y) + \tfrac{1}{2}\rho U^2(o, y) \qquad (4)$$

where "$v$" is the lateral velocity component of the flow at entry to the honeycomb. From Eqs. (3) and (4) we have

$$\left[\frac{4fL(y)}{D}\right]\cdot\frac{1}{2}\rho U^2(y) + \frac{1}{2}\rho U^2(y) + \frac{1}{2}\rho v^2(o, y)$$

$$= P_{-\infty} + \frac{1}{2}\rho U^2_{-\infty} \qquad (5)$$

If the right-side of Eq. (5) is equal to a constant $K$, the length of the honeycomb cell $L(y)$ at a particular height $y$ is determined as

$$L(y) = \frac{D}{4f}\left[\frac{K}{\frac{1}{2}\rho U^2(y)} - \frac{v^2(o, y)}{U^2(y)}\right] \qquad (6)$$

If "$K$" is known from the wind tunnel calibration and the operating conditions and $D$ and $f$ are known from the specification of the honeycomb, the cell length $L(Y)$ can be calculated by Eq. (6) with the velocity profile $U(y)$, once $v(O, y)$ is known.

## The Calculation of Lateral Velocity Component, $v(O, y)$

The lateral velocity component $v(O, y)$ may be calculated by applying Laplaces equation to the potential flow region upstream of the honeycomb. If required velocity profile is specified as

$$u(Y) = CU_{-\infty} + \frac{mU_{-\infty}}{l}y \qquad (7)$$

where $\lambda = mU_{-\infty}/l$ is the degree of velocity shear and $CU_{-\infty}$ is the velocity on the wind tunnel floor, the general solution of the Laplaces equation in the potential flow region which satisfy the boundary conditions at the walls i.e., $y = 0$, $l$ and $x = -\infty$ can be written as

$$\psi(x, y) = U_{-\infty}y + \sum_{n=1}^{\infty} a_n \sin\frac{n\pi y}{l}\, e\,\frac{n\pi x}{l} \qquad (8)$$

At the entrance of the honeycomb ($x = 0$),

$$U(y) = \frac{\partial\psi}{dy} = U_{-\infty} + \sum_{n=1}^{\infty} a_n \frac{n\pi}{l}\cos\frac{n\pi y}{l} \qquad (9)$$

By using Eqs. (7) and (9), together with the Fourier series method, $a_n$ can be obtained as,

$$a_n = \frac{2}{n\pi}\int_0^l \cos\frac{n\pi y}{l}\left[CU_{-\infty} + \left(\frac{U_{-\infty}m}{l}\right)y - U_{-\infty}\right]dy \qquad (10)$$

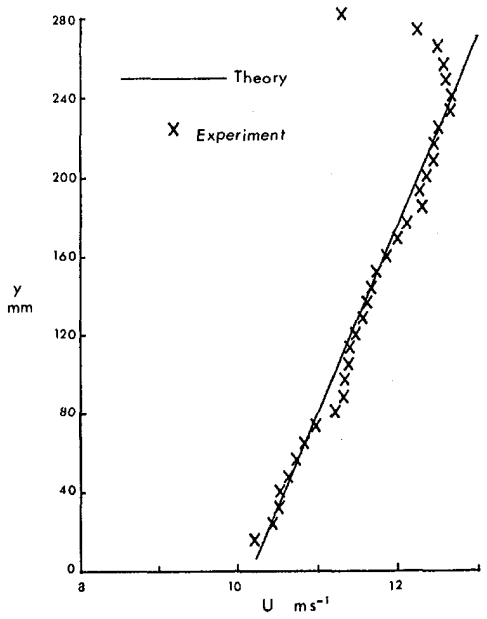


**Fig. 2 Typical velocity profile with paper honeycomb at $d$ = 880 mm ($d$ is distance downstream of honeycomb trailing edge)**

The lateral velocity is given by

$$\frac{\partial\psi}{\partial x} = v(o\cdot y) = \sum_{n=1}^{\infty} a_n \frac{n\pi}{l}\sin\frac{n\pi y}{l} \qquad (11)$$

Equation (10) can be further written as

$$a_n\cdot\frac{n\pi}{l} = \frac{2}{l}\int_0^l \cos\frac{n\pi y}{l}\left[CU_{-\infty} + \left(\frac{U_{-\infty}m}{l}\right)y - U_{-\infty}\right]dy$$

Hence the integration and simplification of this equation together with use of Eq. (11) yields

$$V(o, y) = \frac{4U_{-\infty}m}{\pi^2}\left[\sin\frac{\pi y}{l} + \frac{1}{3^2}\sin\frac{3\pi y}{l} + \frac{1}{5^2}\sin\frac{5\pi y}{l} + \cdots\right] \qquad (12)$$

Substitution of Eqs. (7) and (12) into Eq. (6) then enables $L(y)$ to be evaluated and the shape of the honeycomb to be determined.

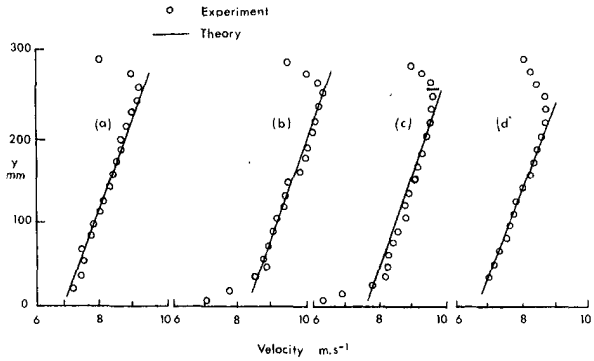


**Fig. 3 Shear profiles produced by metal honeycomb. (*a*) $d$ = 40 mm; (*b*) 200 mm; (*c*) $d$ = 690 mm; (*d*) $d$ = 1190 mm**

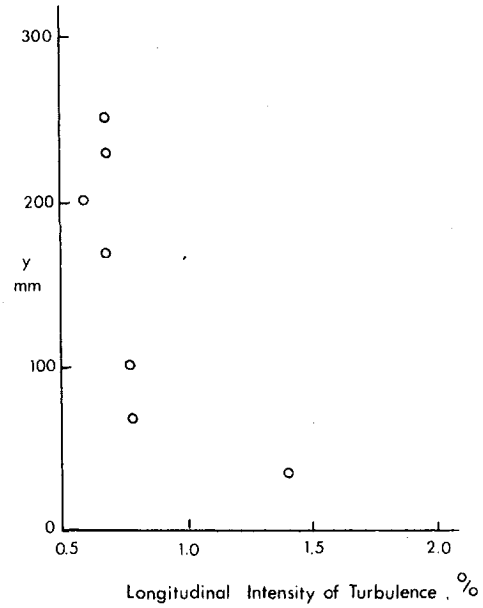


**Fig. 4 Longitudinal turbulence intensity behind honeycomb at $d$ = 440 mm**

## Experimental Results

The experiment was carried out in a wind tunnel with a working section of 0.6 m × 0.6 m × 2.5 m, in the Department of Building Science at Sheffield University, U.K. The experimental arrangements are shown in Fig. 1. To measure the velocity profiles downstream of the honeycomb, a standard NPL type pitot static tube connected to Beltz manometer was used. The turbulence level along the centre line behind the honeycomb was less than one percent.

As mentioned above two types of honeycomb were used. Preliminary results were obtained with a paper honeycomb having a hexagonal cell type measuring 14.3 mm across flats. A typical velocity profile is shown in Fig. 2, having a shear gradient ($H/2U \cdot dU/dy$) of 0.26, where $H$ is the total height of the working section and $U$ is the average mean velocity of the shear flow. This velocity profile was measured at 0.88 m downstream of the trailing edge of honeycomb. The experimental data in Fig. 2, show good agreement with the specified values of velocity gradient adopted in the theoretical calculation to determine the honeycomb shape. The typical velocity profiles at four different downstream positions were obtain with the metal honeycomb (cell size 6.5 mm), and are shown in Fig. 3. Again the agreement between the theoretical value and experimental profiles were good.

It is clear from these results that this method produces accurate specified linear shear profiles with very low downstream turbulence level. The distribution of turbulence level behind the honeycomb was less than one percent and is shown in Fig. 4.

It is of interest to estimate the incidence angle of the streamlines at the entrance of the honeycomb. If the same velocity profile as Eq. (7) is assumed

$$U(y) = CU_{-\infty} + \frac{mU_{-\infty}}{l} y$$

then using Eqs. (7) and (12), the value of $v/u$ was found to be equal to 0.1 with corresponding value of $\{\arctan(v/u)\}$ = 6 degrees. The incidence effect are dependent on the particular flow geometry selected. However, if the cut surface of the honeycomb is not clean then nonuniformities resulting from the poor surface could outweigh these incidence effects. The inclusion of $v^2(O, y)$ term in (6) is only one percent correction. However, the main effect of $v(O, y)$ would be to change the pressure drop coefficient of the honeycomb because of the oblique flow into the cell.

The serious problem in using the honeycomb was the shaping of the blocks supplied by the manufacturer. However, it was found that if the honeycomb was held firmly in a jig whose shape conformed to that of the required finished product, it could be cut on a fine toothed band saw with little trouble, particularly without crumbling the ends of the honeycomb cells.

Kotansky (1966) did not discuss if there is any effect of partial blockage of the cells on the resulting shear profiles. He also did not elaborate if there is any critical length for the cell to get the fully developed flow. During the present experiment it was found that the cell length was not critically important as the flow seemed to behave exactly the same way as the flow behaved in the turbulent pipe flow. In the turbulent pipe flow the fully developed pressure drop is reached quite near the entrance, so it is justifiable to assume that the flow in the honeycomb cell to be fully developed regardless of its length. It was also found that the partial blockage of some of the cells did produce velocity excess and defect regions in the resulting shear profiles. However, the profiles with unclean honeycomb cut also distort the resulting shear profile in the immediate neighbourhood of the honeycomb downstream. Therefore, it is suggested that a good quality honeycomb with clean cut is necessary if one wants to get the full advantage from this technique.

## Conclusion

The present method of shaped honeycomb technique to produce linear shear flows is useful to obtain the most reasonable and accurate results. The most important and significant implication of this method is that linear shear flows with very low turbulence levels downstream of the honeycomb can be produced. The production of low turbulence linear shear flows are important if studies are to be made of the interaction between free stream turbulence and the shear flow originating from a point of separation on a bluff body. Such studies are considered to be necessary for a full understanding of aerodynamic loading mechanisms.

## Acknowledgment

The authors of this paper are very grateful to Professor Peter Bradshaw of Stanford University and the referees for reviewing this paper and the useful comments made.

## References

Bradshaw, P. and Gee, M. T., 1960, Aeronautical Research Council, Reports and Memoranda 3252.

Castro, I. P., 1976, "Some Problems Concerning the Production of a Linear Shear Flow Using Curved Wire Gauze Screen," *Journal of Fluid Mechanics,* Vol. 76, p. 689.

Cockrell, D. J., and Lee, B. E., 1966, "Production of Shear Profiles in a Wind Tunnel," *Journal of Royal Aeronautics Society,* Vol. 70, p. 724.

Cowdray, C. F., 1967, "A Simple Method for the Design of Wind Tunnel Velocity Profile Grids," National Physical Laboratory Aero Notes 1055.

Elder, J. W., 1959, "Steady Flow Through Non-Uniform Gauze of Arbitrary Shape," *Journal of Fluid Mechanics,* Vol. 5, p. 355.

Hammond, G. P., 1982, ASME JOURNAL OF FLUIDS ENGINEERING, Vol. 104, pp. 59–66.

Kotansky, D. R., 1996, "The Use of Honeycomb for Shear Flow Generation," *American Institute of Aeronautics and Astronautics Journal,* Vol. 4, p. 1490.

McCarthy, J. H., 1964, "Steady Flow Past Non-Uniform Grids," *Journal of Fluid Mechanics,* Vol. 19.

Owen, P. R., and Zienkiewiez, H. K., 1957, "The Production of Uniform Shear Flow in a Wind Tunnel," *Journal of Fluid Mechanics,* Vol. 2, p. 521.

Sigalla, A., 1958, *The Aeronautical Journal,* Royal Aeronautical Society, Vol. 62.

Turner, J. R., 1969, "A Computational Method for the Flow Through Non-Uniform Gauzes," *Journal of Fluid Mechanics,* Vol. 36, p. 367.

# Analytical Solutions for the Developing Jet From a Fully-Developed Laminar Tube Flow

**D. S. Lee,[1] K. D. Kihm,[2] and S. H. Chung[3]**

## Introduction

The very classical problem of the developing jet exiting from a tube flow (Fig. 1) is of particular interest to those involved with gaseous or particulate fuel injection as an initial condition for the successive combustion analysis. The fully developed flow field farther away from the tube exit is generally well described by the Schlichting's similarity solution (Schlichting, 1968). However, the similarity assumption fails to hold in the developing region of the jet close to the exit. Conventional analysis of the developing region numerically solves the Prandtl's nonlinear boundary layer equations for detailed velocity profiles (Pai and Hsieh, 1972; du Plessis et al., 1973; Dmitriev and Kulesova, 1974; Arulraja, 1982). Though most of the numerical solutions agree reasonably well with the existing experimental data (Okabe, 1948; Abramovich and Solan, 1973; Rankin et al., 1983) achieving an analytical solution will be of an important value based on its closed-form comprehensiveness and physically intuitive nature.

Arulraja et al. (1983) derived an analytical solution only for the maximum center velocity decay along the jet axis. The results show that the maximum velocity decays linearly in the developing region. Matching of the maximum velocity at the boundary between the developing and fully developed similarity regions determined the length of the developing region.

For the simpler case of uniform nozzle exit velocity profile, Rankin and Sridhar (1978) developed an analytical solution for the velocity profiles in the developing region assuming a potential core of uniform velocity. In their analysis, the surrounding region was assumed as annular free shear flow holding the Schlichting's similarity velocity profile.

The current work proposes two approximate methods to analytically calculate the developing jet velocity field from a fully-developed laminar (parabolic) axisymmetric tube flow.

## Method I: Linearization of the Boundary Layer Equations

The Prandtl's boundary layer equation, a nonlinear second-order parabolic partial differential type (Schlichting, 1968), describes the axisymmetric laminar jet flow field (Fig. 1).

$$u\frac{\partial u}{\partial x}+v\frac{\partial u}{\partial r}=\frac{\mu}{\rho}\frac{1}{r}\frac{\partial}{\partial r}\left[r\frac{\partial u}{\partial r}\right] \tag{1}$$

in which the total momentum remains unchanged along the jet, the total mass flow rate gradually increases because of the entrainment from the ambiance.

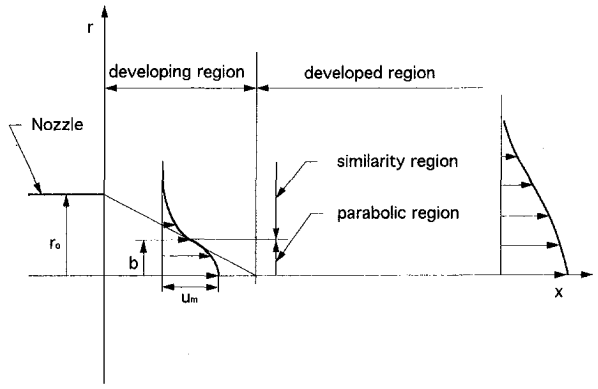


**Fig. 1 An axisymmetric laminar jet developing from the parabolic exit velocity profile**

Three assumptions are made particularly for the jet developing region near the tube exit: (1) the relatively short jet evolving distance negates the entrainment effect, (2) the linear radial diffusion dominates over the nonlinear axial convection, and (3) the Lagrangian particle motion along the centerline describes the axial convection. With these assumptions the nonlinear boundary layer equation, Eq. (1), can be decoupled into two linear differential equations, i.e., one is a diffusion type equation that describes the radial diffusion in the absence of entrainment,

$$\frac{\partial u(t,r)}{\partial t}=\frac{\mu}{\rho}\frac{1}{r}\frac{\partial}{\partial r}\left[r\frac{\partial u(t,r)}{\partial r}\right] \tag{2}$$

and the other is a Lagrangian description of fluid particle motion along the centerline, which substitutes the nonlinear convection,

$$\frac{dx}{dt}=u_m(x) \tag{3}$$

where the subscript $m$ denotes the maximum or centerline velocity.

The boundary and initial conditions are

$$\frac{\partial u}{\partial r}=0 \quad \text{at} \quad r=0 \quad \text{and} \quad u\to 0 \quad \text{as} \quad r\to\infty \tag{4a,b}$$

$$u(r,t=0)=u_{m,o}[1-(r/r_o)^2] \quad \text{for} \quad 0\le r\le r_o \tag{4c}$$

where $u_{m,o}=u_m\,(x=0)$, the maximum centerline velocity at the tube exit, and $r_o$ is the nozzle radius. Solving Eq. (2) together with Eqs. (4$a$, $b$, $c$) gives

$$\frac{u(t^*,R)}{u_{m,o}}=2t^*e^{-R^2t^*}\int_0^1\eta(1-\eta^2)e^{-\eta^2t^*}I_0(2\eta Rt^*)d\eta \tag{5}$$

where $t^*$ is a dimensionless Lagrangian time defined as $r_o^2/4\nu t$, $R\equiv r/r_o$, and $I_0$ is the zeroth-order modified Bessel function of the first kind.

Integration of Eq. (3) using the initial condition of Eq. (4$c$) provides a relationship between the Eulerian axial coordinate $X$ and the Lagrangian time coordinate $t^*$ as

$$X\equiv\frac{x}{d_o}\cdot\frac{\nu}{u_{m,o}d_o}=\frac{1}{16}\int_0^{1/t^*}[1-\eta(1-e^{-1/\eta})]d\eta \tag{6}$$

where $d_o$ denotes the nozzle diameter.

Substituting Eq. (6) into Eq. (5) determines the jet velocity profiles $u(X,R)$, or $u(x,r)$, for the developing region—this solution is called near-field solution where the flow similarity is not established. The well-known Schlichting's similarity solu-

[1] Graduate Research Assistant, Department of Mechanical Engineering, Seoul National University, Seoul 151-742, Korea.

[2] Associate Professor, Department of Mechanical Engineering, Texas A&M University, College Station, TX 77843-3123, Mem. ASME.

[3] Professor, Department of Mechanical Engineering, Seoul National University, Seoul 151-742, Korea. Mem. ASME.

Contributed by the Fluids Engineering Division of THE AMERICAN SOCIETY OF MECHANICAL ENGINEERS. Manuscript received by the Fluids Engineering Division February 9, 1996; revised manuscript received March 11, 1997. Associate Technical Editor: F. Hussain.

tion (1968) constitutes far-field solution for the developed region, where the flow similarity prevails.

## Method II: Velocity Profile Matching

The experimental data of Rankin et al. (1983) indicate that the jet core of a certain radial distance in the developing region maintains approximately the initial parabolic profile, and this "parabolic core" region diminishes as the similarity velocity profile prevails in the annular outer region (Fig. 1). The radius of the parabolic core decreases to zero as the developing region ends at $X = X_l$ where $X_l$ denotes the developing regional length.

Method II assumes that a parabolic inner core represents the developing region and the similarity solution recovers in the annular outer region. Thus, for the developing inner core

$$U_{\text{inner}}(X, R) = \left(\frac{u(X, R)}{u_{m,o}}\right)_{\text{inner}} = \frac{u_m(X)}{u_{m,o}}[1 - R^2] \quad \text{for} \quad 0 \le R \le B \quad (7a)$$

and for the outer region (Schlichting, 1968)

$$U_{\text{outer}}(X, R) = \left(\frac{u(X, R)}{u_{m,o}}\right)_{\text{outer}} = \frac{2(\gamma/\text{Re}_{d_o})^2}{(X + X_v)} \times \left[1 + \left(\frac{1}{4}\frac{\gamma}{\text{Re}_{d_o}}\frac{R}{(X + X_V)}\right)^2\right]^{-2} \quad \text{for} \quad B \le R \le \infty \quad (7b)$$

where $B(X)$ denotes the core radius normalized by the nozzle radius, i.e., $b(x)/r_o$, $X_V$ is the location of virtual origin measured from the nozzle exit, and the dimensionless radius $R \equiv r/r_o$.

An interpolation of the maximum center velocity calculated from Method I gives

$$\frac{u_m(X)}{u_{m,o}} = 1 - 17.72X \quad \text{for} \quad 0 \le X \le X_l \quad (8)$$

with a confidence of multiple determination $R^2 = 0.99$.

The jet velocity profiles, Eqs. (7$a$) and (7$b$), must be continuous and smooth at the regional boundary $R = B$;

$$U_{\text{inner}} = U_{\text{outer}} \quad \text{and} \quad \left[\frac{\partial U}{\partial R}\right]_{\text{inner}} = \left[\frac{\partial U}{\partial R}\right]_{\text{outer}} \quad \text{at} \quad R = B \quad (9a, b)$$

In addition, the axial momentum of the free shear axisymmetric incompressible jet must be conserved:

$$\frac{d}{dx}\int_0^\infty RU^2 dR = 0 \quad (10)$$

where $U = U_{\text{inner}}$ (Eq. 7$a$) for $0 \le R \le B$, $U = U_{\text{outer}}$ (Eq. 7$b$) for $B \le R \le \infty$, and $U = 1 - R^2$ at $X = 0$.

Solving Eqs. (9$a$, $b$) and (10) determines the inner core radius $B$,

$$B = \sqrt{1 - \left\{\frac{1}{(1 - 17.72X)^2} - 1\right\}^{1/3}}, \quad (11)$$

the location of the virtual origin,

$$X_v = -X + \frac{1 - 17.72X}{16} \cdot \frac{(1 - B^2)^3}{1 - 1.5B^2} \quad (12)$$

and the jet spread parameter

$$\frac{\gamma}{\text{Re}_{d_o}} = \frac{1 - 17.72X}{2^{2.5}}\left(\frac{1 - B^2}{\sqrt{1 - 1.5B^2}}\right)^3 \quad (13)$$

Substitution of Eqs. (11) through (13) back into Eqs. (7$a$) and (7$b$) determines the jet velocity distribution $U(X, R)$ for the whole developing region. The length of the inner core, $X_l = 0.0165$, is readily calculated by setting the core radius $B$ equal to zero in Eq. (11).

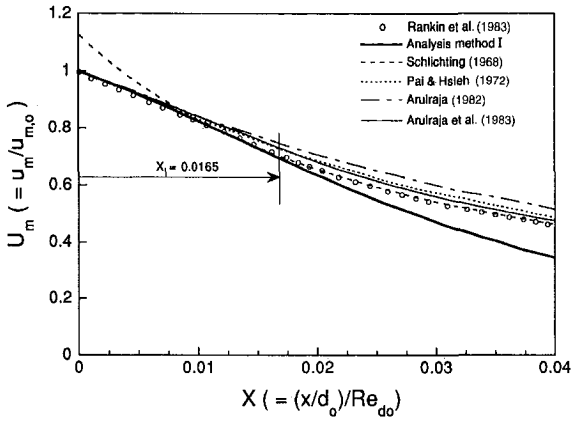


**Fig. 2 Comparison of maximum velocity variations along the jet axial distance**

## Comparison With Experimental Results

Figure 2 presents the axial decay of the centerline velocity normalized by $u_{m,o}$ at the tube exit. For the developing region, $X < X_l$, the linearized analysis of Method I shows better agreement with the experimental data (Rankin et al., 1983) than the other numerical (Pai and Hsieh, 1972) and analytical results (Arulraja, 1982, Arulraja et al., 1983). The Schlichting's similarity solution deviates from the experiment in the developing region which lacks the flow similarity.

In the developed region, $X > X_l$, the center line velocity calculations from Method I underpredict compared with the experimental data. This deficiency comes primarily from the fact that Method I does not account for the flow entrainment. The effect of entrainment remains small in the developing region due to the shorter jet travel distance. When $X$ is large, however, the gradual addition of the entrained flow enhances the total flow rate, and in turn, the centerline velocity is greater than the Method I prediction given under no entrainment. The similarity solution, which accounts for the entrainment, well predicts the centerline velocity variation when $X > X_l$.

Figure 3 presents the jet velocity profiles calculated from both Method I and Method II along $X$ inside the developing region, compared with experiment (Rankin et al., 1983) and the similarity solutions (Schlichting, 1968). Near the nozzle exit ($X = 0.001$), both Method I and Method II predict fairly well while the Schlichting's similarity solution gives large discrepancies from the experimental data particularly at the center and near the jet boundary. The linearized approximation of Method I is fairly well justified in this region close to the nozzle exit where the jet develops with negligibly small entrainment.

As $X$ increases ($X = 0.005$ and 0.01), the entrainment effect is no longer negligible and Method I underpredicts since its result does not account for the entrainment. In practice, the entrainment effect will gradually increase the jet flow rate and expand the jet radius as the jet develops. This can explain the underprediction of Method I and the deficiency increases with increasing axial distance.

Method II analysis is exclusively based on the velocity matching between the near (parabolic) and far (similar) fields. Therefore, Method II retains the entrainment effect by its nature and the calculated velocity profiles show excellent agreement with the experimental data for all the tested $X$ locations inside the developing region. Although not shown, the maximum centerline velocities calculated from Method II also show excellent agreement with experiment.

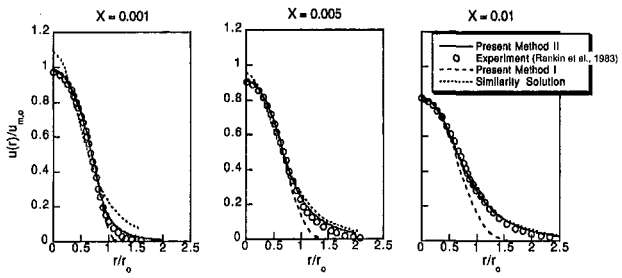


**Fig. 3 Comparison of the axial jet velocity profiles calculated from Method I and Method II with experimental data [8] and the Schlichting's similarity solution [1]**

In summary, both Methods I and II accurately calculate the maximum centerline velocity decay for the jet developing region, but Method II more accurately predicts the jet velocity fields in detail. Outside the developing region, the Schlichting's similarity solution is well accepted.


## Acknowledgment

The research was partially supported by the Turbo and Power Machinery Research Center, Seoul National University, Seoul, Korea.


## References


Abramovich, S., and Solan, A., 1973, "The Initial Development of a Submerged Laminar Round Jet," *Journal of Fluid Mechanics,* Vol. 59, pp. 791–801.

Arulraja, M., 1982, "Analysis of Developing Region of a Submerged Laminar Free Jet," M.A.Sc. Thesis, University of Windsor.

Arulraja, M., Rankin, G. W., and Sridhar, K., 1983, "Maximum Velocity Decay in a Submerged Laminar Jet Issuing from a Long Tube," *Transaction of Canadian Society of Mechanical Engineering,* Vol. 7, No. 1, pp. 41–43.

Dmitriev, V. N., and Kulesova, N. A., 1974, "The Calculation of a Laminar Jet in the Surrounding of the Supply Nozzle," *Proceedings of the 5th Jablonna Fluidics Conference,* Budapest, Hungary, Nov. pp. 83–91.

Okabe, J., 1948, "Approximate Calculations of Laminar Jets," *Research Institute of Fluid Engineering,* Kyushu Univ., Vol. 5, pp. 1–13 and pp. 15–22.

Pai, S. I., and Hsieh, T., 1972, "Numerical Solution of Laminar Jet Mixing With and Without Free Stream," *Applied Scientific Research,* Vol. 27, pp. 39–62.

du Plessis, M. P., Wang, R. L., and Tsang, S., 1973, "Development of a Submerged Round Laminar Jet From an Initially Parabolic Profile," ASME *Journal of Dynamic System, Measurement and Control,* pp. 148–154.

Rankin, G. W., and Sridhar, K., 1978, "Developing Region of Laminar Jets with Uniform Exit Velocity Profiles," ASME JOURNAL OF FLUIDS ENGINEERING, Vol. 100, Mar., pp. 55–59.

Rankin, G. W., Sridhar, K., Arulraja, M., and Kumar, K. R., 1983, "An Experimental Investigation of Laminar Axisymmetric Submerged Jets," *Journal of Fluid Mechanics,* Vol. 133, pp. 217–231.

Schlichting, H., 1968, *Boundary Layer Theory,* 6th ed., McGraw-Hill, New York.


# The Effect of Negative Spanwise Rotation on Dean Vortices


## Liqiu Wang[1]



*A finite-volume numerical analysis is performed to examine effect of spanwise rotation on Dean vortices. The specific problem considered is fully developed flow in a square channel with streamwise curvature and spanwise rotation in a negative sense, i.e., the Coriolis force counteracts the centrifugal force. The rotation of the channel is found to have a significant effect on the flow structure in general, and the Dean vortices in particular. The nonlinear interaction of the Coriolis instability and the centrifugal instability results in several new flow structures, including one with coexistence of Ekman, Dean, and corner vortices, one with coexistence of Ekman and corner vortices, one with one-pair vortices and an agostrophic, virtually inviscid core, and one with Coriolis vortices on the inner convex wall. These are in agreement with the experimental findings.*


## 1 Introduction

The curvature and rotation of a channel introduce centrifugal and Coriolis forces in the momentum equations describing the relative motion of fluids with respect to the channel. Such body forces usually cause an instability in forms of streamwise-oriented vortices. The knowledge of formation and development of such vortices is essential to have the ability to predict and control the performance for technical applications of the flow in blade passages of radial flow pump, compressor impellers, centrifuges, cooling channels of rotating machinery, and particle separation devices among others.

In a streamwise pressure-driven flow in a curved channel, streamwise vortices may develop near the outer concave wall above a critical Dean number due to the centrifugal instability, an imbalance between the pressure gradient and the centrifugal force. Here the Dean number De is a combination of the Reynolds number Re and the curvature ratio of channel $\sigma$ ($De = Re\sqrt{\sigma}$, $Re = W_m d_h/\nu$ with $W_m$ as the streamwise mean velocity, $d_h$ the hydrodynamic diameter of the channel, and $\nu$ the kinematic viscosity; $\sigma = d_h/R_c$ with $R_c$ as the curvature radius). These vortices are usually called Dean vortices, as Dean first examined viscous flow in the curved channels (Dean, 1928). Coriolis force, due to the spanwise rotation of a straight channel, has a role similar to that of the centrifugal force in the curved channels, resulting in the appearance of the Coriolis vortices near the pressure (leading) wall (Hart, 1971).

The combined effects of both curvature and rotation appear in a curved channel with spanwise rotation. Depending on the direction of rotation, destabilizing effects due to the curvature and the rotation may either enhance or counteract each other. Nonlinear interaction of these two destabilizing mechanisms will result in a complicated flow structure. We examine this structure in the present study using a finite-volume method.

The effect of the spanwise rotation on the curved channel flows has been examined recently by Selmi et al. (1994), Matsson and Alfredsson (1994), and Wang and Cheng (1995, 1996). When the rotation is positive, the flow was found to remain similar to those observed in stationary curved channels, in straight channels with a spanwise rotation, and in heated horizontal channels, i.e., with two or four vortex secondary flows (for a circular or square cross section) in addition to the pressure-driven main flow. There are, however, quantitative changes due to the rotation. When the rotation is negative, however, the nonlinear competition of the Coriolis force and the centrifugal force leads to a more complicated flow situation. In particular, three major features have been identified experimentally: (1) the centrifugal instability in forms of Dean vortices could be cancelled by a negative rotation, (2) the inward Coriolis force due to a negative rotation could give rise to vortices on the inner convex wall, and (3) the secondary flow appears to be of multiple pairs of vortices for some negative rotation rates. Note that the questions regarding the detailed flow structure have been left unanswered. Also a numerical analysis is desirable to predict and confirm these experimental findings and to reveal the mechanism behind these phenomena.


[1] Assistant Professor, Department of Mechanical Engineering, University of Hong Kong, Hong Kong. Mem. ASME.



Contributed by the Fluids Engineering Division of THE AMERICAN SOCIETY OF MECHANICAL ENGINEERS. Manuscript received by the Fluids Engineering Division July 11, 1996; revised manuscript received March 27, 1997. Associate Technical Editor: J. A. C. Humphrey.

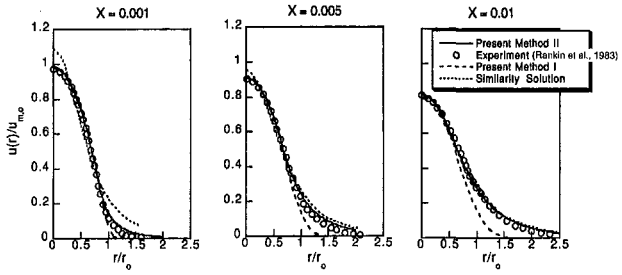


**Fig. 3 Comparison of the axial jet velocity profiles calculated from Method I and Method II with experimental data [8] and the Schlichting's similarity solution [1]**

In summary, both Methods I and II accurately calculate the maximum centerline velocity decay for the jet developing region, but Method II more accurately predicts the jet velocity fields in detail. Outside the developing region, the Schlichting's similarity solution is well accepted.


## Acknowledgment

The research was partially supported by the Turbo and Power Machinery Research Center, Seoul National University, Seoul, Korea.


## References


Abramovich, S., and Solan, A., 1973, "The Initial Development of a Submerged Laminar Round Jet," *Journal of Fluid Mechanics,* Vol. 59, pp. 791–801.

Arulraja, M., 1982, "Analysis of Developing Region of a Submerged Laminar Free Jet," M.A.Sc. Thesis, University of Windsor.

Arulraja, M., Rankin, G. W., and Sridhar, K., 1983, "Maximum Velocity Decay in a Submerged Laminar Jet Issuing from a Long Tube," *Transaction of Canadian Society of Mechanical Engineering,* Vol. 7, No. 1, pp. 41–43.

Dmitriev, V. N., and Kulesova, N. A., 1974, "The Calculation of a Laminar Jet in the Surrounding of the Supply Nozzle," *Proceedings of the 5th Jablonna Fluidics Conference,* Budapest, Hungary, Nov. pp. 83–91.

Okabe, J., 1948, "Approximate Calculations of Laminar Jets," *Research Institute of Fluid Engineering,* Kyushu Univ., Vol. 5, pp. 1–13 and pp. 15–22.

Pai, S. I., and Hsieh, T., 1972, "Numerical Solution of Laminar Jet Mixing With and Without Free Stream," *Applied Scientific Research,* Vol. 27, pp. 39–62.

du Plessis, M. P., Wang, R. L., and Tsang, S., 1973, "Development of a Submerged Round Laminar Jet From an Initially Parabolic Profile," ASME *Journal of Dynamic System, Measurement and Control,* pp. 148–154.

Rankin, G. W., and Sridhar, K., 1978, "Developing Region of Laminar Jets with Uniform Exit Velocity Profiles," ASME JOURNAL OF FLUIDS ENGINEERING, Vol. 100, Mar., pp. 55–59.

Rankin, G. W., Sridhar, K., Arulraja, M., and Kumar, K. R., 1983, "An Experimental Investigation of Laminar Axisymmetric Submerged Jets," *Journal of Fluid Mechanics,* Vol. 133, pp. 217–231.

Schlichting, H., 1968, *Boundary Layer Theory,* 6th ed., McGraw-Hill, New York.


# The Effect of Negative Spanwise Rotation on Dean Vortices


## Liqiu Wang[1]



*A finite-volume numerical analysis is performed to examine effect of spanwise rotation on Dean vortices. The specific problem considered is fully developed flow in a square channel with streamwise curvature and spanwise rotation in a negative sense, i.e., the Coriolis force counteracts the centrifugal force. The rotation of the channel is found to have a significant effect on the flow structure in general, and the Dean vortices in particular. The nonlinear interaction of the Coriolis instability and the centrifugal instability results in several new flow structures, including one with coexistence of Ekman, Dean, and corner vortices, one with coexistence of Ekman and corner vortices, one with one-pair vortices and an agostrophic, virtually inviscid core, and one with Coriolis vortices on the inner convex wall. These are in agreement with the experimental findings.*


## 1 Introduction

The curvature and rotation of a channel introduce centrifugal and Coriolis forces in the momentum equations describing the relative motion of fluids with respect to the channel. Such body forces usually cause an instability in forms of streamwise-oriented vortices. The knowledge of formation and development of such vortices is essential to have the ability to predict and control the performance for technical applications of the flow in blade passages of radial flow pump, compressor impellers, centrifuges, cooling channels of rotating machinery, and particle separation devices among others.

In a streamwise pressure-driven flow in a curved channel, streamwise vortices may develop near the outer concave wall above a critical Dean number due to the centrifugal instability, an imbalance between the pressure gradient and the centrifugal force. Here the Dean number De is a combination of the Reynolds number Re and the curvature ratio of channel $\sigma$ ($De = Re\sqrt{\sigma}$, $Re = W_m d_h/\nu$ with $W_m$ as the streamwise mean velocity, $d_h$ the hydrodynamic diameter of the channel, and $\nu$ the kinematic viscosity; $\sigma = d_h/R_c$ with $R_c$ as the curvature radius). These vortices are usually called Dean vortices, as Dean first examined viscous flow in the curved channels (Dean, 1928). Coriolis force, due to the spanwise rotation of a straight channel, has a role similar to that of the centrifugal force in the curved channels, resulting in the appearance of the Coriolis vortices near the pressure (leading) wall (Hart, 1971).

The combined effects of both curvature and rotation appear in a curved channel with spanwise rotation. Depending on the direction of rotation, destabilizing effects due to the curvature and the rotation may either enhance or counteract each other. Nonlinear interaction of these two destabilizing mechanisms will result in a complicated flow structure. We examine this structure in the present study using a finite-volume method.

The effect of the spanwise rotation on the curved channel flows has been examined recently by Selmi et al. (1994), Matsson and Alfredsson (1994), and Wang and Cheng (1995, 1996). When the rotation is positive, the flow was found to remain similar to those observed in stationary curved channels, in straight channels with a spanwise rotation, and in heated horizontal channels, i.e., with two or four vortex secondary flows (for a circular or square cross section) in addition to the pressure-driven main flow. There are, however, quantitative changes due to the rotation. When the rotation is negative, however, the nonlinear competition of the Coriolis force and the centrifugal force leads to a more complicated flow situation. In particular, three major features have been identified experimentally: (1) the centrifugal instability in forms of Dean vortices could be cancelled by a negative rotation, (2) the inward Coriolis force due to a negative rotation could give rise to vortices on the inner convex wall, and (3) the secondary flow appears to be of multiple pairs of vortices for some negative rotation rates. Note that the questions regarding the detailed flow structure have been left unanswered. Also a numerical analysis is desirable to predict and confirm these experimental findings and to reveal the mechanism behind these phenomena.


[1] Assistant Professor, Department of Mechanical Engineering, University of Hong Kong, Hong Kong. Mem. ASME.



Contributed by the Fluids Engineering Division of THE AMERICAN SOCIETY OF MECHANICAL ENGINEERS. Manuscript received by the Fluids Engineering Division July 11, 1996; revised manuscript received March 27, 1997. Associate Technical Editor: J. A. C. Humphrey.

In the present work, the effect of the negative spanwise rotation on Dean vortices is examined numerically by a finite-volume method at low to relatively rapid rotation rates where both convective and diffusive terms play an important role, and consequently, the full nonlinear equations must be solved. The specific problem considered here is the steady, hydrodynamically fully developed flow in a square channel with streamwise curvature and spanwise rotation in a negative sense (Fig. 1). Attention is focused on the Coriolis-force-driven transitions in both secondary and streamwise main flow structures. The emphasis is also placed on the interactions of the centrifugal instability due to the curvature and the Coriolis instability from the negative spanwise rotation, and not their secondary instabilities or the transition to turbulence, although the vortices studied ultimately have an important influence on the transition.

## 2 Governing Parameters and Numerical Method

Using the finite-volume method, we obtain fully developed solutions of the continuity and Navier-Stokes equations governing the laminar flow in a rotating curved channel. No-slip boundary conditions are used on the channel walls. The governing equations contain three dimensionless parameters (curvature ratio $\sigma$, pseudo Dean number $D_k$, and modified rotation number $L_1$) defined as:

$$\sigma = \frac{a}{R_c}; \quad D_k = \frac{\sigma a^3 c}{4\nu\mu}; \quad L_1 = \frac{3\ \mathrm{Re}_\Omega}{2Dk}$$

in which

$$\mathrm{Re}_\Omega = \frac{a^2\Omega}{\nu}$$

with $a$, $R_c$ as the channel width and curvature radius (Fig. 1), $\mu$, $\nu$ as the viscosity and kinematic viscosity, and $c$, $\Omega$ as the streamwise pressure gradient and angular rotating speed. The main features of the numerical method include a staggered mesh system, a power-law formulation for the combined effect of convection and diffusion terms, an equation-solving scheme consisting of an alternating direction line-by-line iterative procedure (ADI) with block correction technique, and a well-known SIMPLE scheme for velocity-pressure coupling.

The initial calculation for the Dean problem was performed by setting angular velocity $\Omega = 0$ to verify the code. Both mean friction factor and detailed flow structure obtained by the present study are in excellent agreement with the published theoretical, numerical, and experimental results. The computational grid covers whole cross section of the channel to allow the possible asymmetric solution with respect to the $x$-axis. The grid density is $51 \times 51$ in both $X$- and $Y$-directions ($X = x/a$, $Y = y/a$). The grid spacing is uniform in both the $X$- and $Y$-directions. The accuracy of the $51 \times 51$ grid computation was confirmed by repeating calculations with finer and coarser grids ($35 \times 35$, $43 \times 43$, $51 \times 51$, $59 \times 59$) for six typical flow structures. The solution was assumed to be convergent in a numerical sense if the maximum relative error in each of the primitive variables (i.e., velocity components and the pressure) over the whole grids is less than $10^{-6}$ between successive iterations.

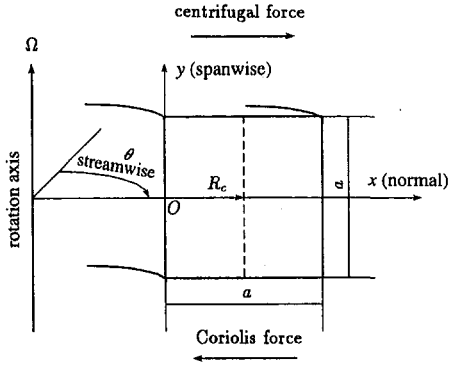


**Fig. 1 Pressure-driven flow in a square channel with streamwise curvature and spanwise rotation (pressure-driven main flow is along positive $\theta$-direction)**

## 3 Results and Discussion

The typical secondary flow patterns and streamwise velocity isopleths and profiles are shown in Figs. 2 and 3 for several representative values of $L_1$ at $\sigma = 0.02$ and $Dk = 500$. In each contour figure, the left and right frames are the upper half of inner (convex) and outer (concave) walls, respectively. Also the upper and bottom frames are the upper wall and the horizontal centerline, respectively. The stream function and streamwise velocity are normalized by their corresponding maximum absolute values $|\psi|_{\max}$ and $w_{\max}$, respectively. A cross is drawn to denote the position at which they reach these maximum values. A vortex with a positive (negative) value of the stream function indicates a counter-clockwise (clockwise) circulation.

For the case with vanishing value of $L_1$, the Coriolis force disappears and the problem becomes the classical Dean problem which has been well examined by many investigators. The secondary flow consists of two-pair of counter-rotating vortices, as shown in Fig. 2($a$), when the Dean number is beyond its critical value for the appearance of the Dean vortices. The larger vortices are called Ekman vortices which are always present for any no-zero value of Dean number. The smaller vortices are called Dean vortices which come from the centrifugal instability and appear only when the Dean number is above the critical value. A strong inward secondary flow exists between two Dean vortices, while a strong outerward secondary flow appears between the Ekman vortices and the Dean vortices.

As the channel rotates in the negative direction, the corner vortices appear first at the upper-inner corner [Fig. 2($b$)], then at the upper-outer corner [Fig. 2($c$)]. The circulation direction of these corner vortices is clockwise which is opposite to that of the Ekman vortices. This forms a structure with coexistence of Ekman, Dean, and corner vortices. The formation and development of the corner vortices squeeze the Ekman and Dean vortices [Fig. 2($b$)–($d$)], reduce the maximum absolute value of the secondary stream function, and increase the maximum value of streamwise velocity.

Shown in Fig. 3($b$)–($d$) are the streamwise velocity corresponding to the secondary flow patterns in Fig. 2($b$)–($d$). They are qualitatively similar to that in Fig. 3($a$). However, the formation and development of the corner vortices have two effects on the streamwise main flow: (1) moving the streamwise velocity peak upward to the boundary between the Ekman and Dean vortices, and (2) reducing the value of the streamwise velocity in the region with the corner vortices.

When the negative rotation becomes more rapid, the growth of the corner vortices pushes the Ekman and Dean vortices further toward the center part of the outer wall. Essentially, the Dean vortices presented in Fig. 2($a$)–($d$) disappear and the secondary flow restabilizes to a structure with the Ekman vortices and the corner vortices [Fig. 2($e$)]. The maximum absolute value of the stream function and the maximum value of the streamwise velocity are all seen to increase. Furthermore, the streamwise velocity distribution experiences a dramatic change. In particular, the isovels [Fig. 3($e$)] become more densely spaced near the inner wall while they become more sparsely spaced near the outer wall as compared with the previous case [Fig. 3($d$)]. This will lead a change in the distributions of the local friction factor ratio. The flow in the channel core is neither ageostrophic nor geostrophic. The viscous shear is not confined in a thin layer along the walls, but exists in the whole cross

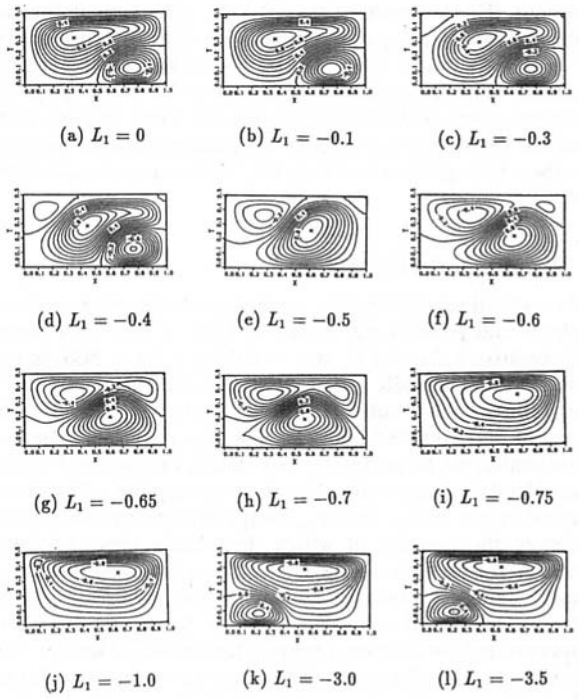


**Fig. 2 Coriolis-force-driven transitions in secondary flow structure at $\sigma$ = 0.02 and $D_k$ = 500 ($X = x/a$, $Y = y/a$)**

section of the channel. The boundary layer theory is, apparently, not valid for the analysis in this flow region.

Increasing rotation speed further in the negative direction, the corner vortices with a clockwise direction of circulation grow, merge together and push the original Ekman vortices toward the horizontal centerline. The maximum absolute value of the stream function decreases while the maximum value of the streamwise velocity increases. Figures 2(*f*)–(*h*) illustrate this process. In this region, the streamwise velocity [Fig. 3(*f*)–(*h*)] remains similar to that shown in Fig. 3(*e*). It is noted that such a multiple pair vortex structure does not exist in the Dean problem and in the Coriolis problem. However, similar results are also found for case of circular cross section (Wang and Cheng, 1996). Also, secondary flow patterns in Fig. 2(*e*)–(*h*) are very similar to those observed through flow visualization experiments (Wang and Cheng, 1995).

Further growth of corner vortices finally causes the original Ekman vortices to disappear and secondary flow becomes one-pair vortex configuration with a clockwise direction of circulation, as shown in Fig. 2(*i*), (*j*). This confirms that flow reversal can result from an inward Coriolis force. And the reverse direction of secondary flow indicates domination of the Coriolis force over the centrifugal force. Isovels are observed to be more sparsely spaced near the outer wall than near the inner wall [Fig. 3(*i*)(*j*)]. The densely distributed isovels near the center part of the inner wall result in a high pressure region since centrifugal force and Coriolis force are proportional to $w^2$ and $w$, respectively. Flow in the channel core appears ageostrophic, i.e., pressure gradients are balanced by both Coriolis force and convective inertial force. Two streamwise velocity peaks are observed near the inner wall rather than the outer wall with one on the upper half of the cross section and the other on the lower half. The regions with higher velocity are moved toward the upper and lower walls while they are shifted toward the inner wall by the rotation in the negative direction. A depression in the streamwise velocity profile near the inner wall shown in Fig. 3(*i*), (*j*) foreshadows onset of a Coriolis instability to be described later. A striking feature of this ageostrophic one-pair vortex structure can be inferred from profiles of the streamwise velocity along the horizontal and vertical centerlines which are not shown here. The streamwise velocity $w$ changes linearly across the core and a little from the lower wall to the upper wall. The vorticity is, then, nearly constant. Slow-moving fluid from the outer wall is accelerated across the core mainly at a constant rate until the inner wall is approached. The Coriolis and convective inertial forces dominate the ageostrophic core. Streamwise velocity falls to zero in viscous layers on outer and inner walls. This constant-vorticity, inviscid core flow structure suggests a possible analysis by the asymptotic method. It appears that no such attempt was made so far in the literature.

When the negative rotation becomes more rapid, the ageostrophic one-pair vortex breaks down into a configuration of two-pair of counter-rotating vortices that is asymmetric with respect to the vertical centerline [Fig. 2(*k*), (*l*)]. The additional pair of counter-rotating vortices near the center of the inner wall is called Coriolis vortices. They result from the Coriolis instability and are similar to the Dean vortices due to the centrifugal instability. Secondary flow and the streamwise velocity [Figs. 2, 3(*k*)(*l*)] are qualitatively similar to those shown in Figs. 2, 3(*a*) by interchanging inner wall and outer wall. However, the inward Coriolis force gives rise to them in the inner convex wall. This differs from the centrifugal instability. Also, their size is smaller than the Dean vortices shown in Fig. 2(*a*).

The onset of the Coriolis vortices on the inner convex wall is consistent with the instability explanation given by Cheng et al. (1976) for the centrifugal instability. In the region near the central inner wall, the pressure gradient across the channel in $x$-direction is negative but the Coriolis force increases from zero at the inner wall to a maximum value at the position with

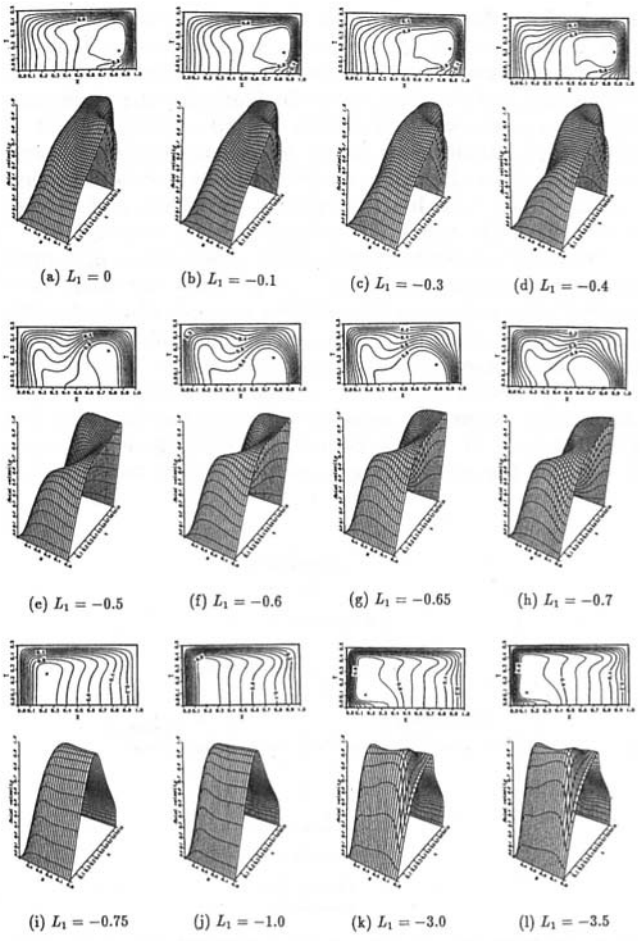


**Fig. 3 Coriolis-force-driven transitions in streamwise main flow structure at $\sigma$ = 0.02 and $D_k$ = 500 ($X = x/a$, $Y = y/a$)**

maximum streamwise velocity. The instability due to the imbalance between pressure gradient and Coriolis force results in an unstable region near the inner convex wall. If the rotation speed is large enough, viscous effects can no longer hold the one-pair vortex structure in place, thus additional vortices may appear.

It is interesting to note that upon increasing rotating speed further, we cannot obtain a convergent solution. Two possible sources can cause this divergence: numerical instability and physical instability. By numerical instability we mean the instability due to improper numerical scheme. By physical instability we mean the instability caused by physical problem itself, which means that there exists no steady, two-dimensional solution if the rotation speed is increased further. At this stage, it is not clear which factor causes the divergence. However, we reasonably suspect that it may be the physical instability based on two facts: (1) we fail to obtain the convergent solution by trying smaller grid sizes and initial guesses for the velocity and pressure fields for several cases; (2) we can easily detect the Coriolis vortices shown in Fig. 2(*l*). This suggests possible further analysis using unsteady three-dimensional model and bifurcation analysis in the region of the parameter space with a higher rotation rate.

## 4 Concluding Remarks

The centrifugal instability in forms of Dean vortices can be completely cancelled by a negative rotation of channel. This cancelling process is characterized with the secondary flow reversal through formation and development of clockwise circulating corner vortices. This leads to new flow structures with the coexistence of Ekman, Dean, and corner vortices, with the coexistence of Ekman and corner vortices, and with one-pair vortices and an agostrophic, virtually inviscid core. Also a higher rotation rate leads to a Coriolis instability in forms of Coriolis vortices on the inner convex channel wall. These are in agreement with the experimental findings by Matsson and Alfredsson (1994) and Wang and Cheng (1995).


## Acknowledgment

The author is indebted to Professors K. C. Cheng, K. Nandakumar, W. H. Finlay, D. J. Steigmann, and J. H. Masliyah at the University of Alberta for their valuable suggestions and discussion during author's five years at the University of Alberta.


## References


Cheng, K. C., Lin, R. C., and Ou, J. W., 1976, "Fully Developed Laminar Flow in Curved Rectangular Channels," ASME JOURNAL OF FLUIDS ENGINEERING, Vol. 98, pp. 41–48.

Dean, W. R., 1928, "The Stream-line Motion of A Fluid in A Curved Pipe," *Philosophical Magazine,* Vol. 5, pp. 673–695.

Hart, J. E., 1971, "Instability and Secondary Motion in A Rotating Channel Flow," *Journal of Fluid Mechanics,* Vol. 45, pp. 341–353.

Matsson, O. J. E., and Alfredsson, P. H., 1994, "The Effect of Spanwise System Rotation on Dean Vortices," *Journal of Fluid Mechanics,* Vol. 274, pp. 243–265.

Selmi, M., Nandakumar, K., and Finlay, W. H., 1994, "A Bifurcation Study of Viscous Flow through A Rotating Curved Duct," *Journal of Fluid Mechanics,* Vol. 262, pp. 353–375.

Wang, L., and Cheng, K. C., 1995, "Flows in Curved Channels with A Low Negative Rotation Speed," *Physical Review E,* Vol. 51, pp. 1155–1161.

Wang, L., and Cheng, K. C., 1996, "Flow Transitions and Combined Free and Forced Convective Heat Transfer in A Rotating Curved Circular Tube," *International Journal of Heat and Mass Transfer,* Vol. 39, pp. 3381–3400.


# New Parameters Describing Extra Straining Effects in Turbulence Models


**Hyon Kook Myong**[1]


## 1 Introduction

The standard k – ϵ turbulence model is currently incorporated into general purpose CFD (Computational Fluid Dynamics) codes and widely used as a practical and cost-effective design tool to analyze complex shear flows commonly encountered in many engineering problems. This is mainly attributed to the fact that this model, with its simplicity and reasonable accuracy, satisfies a tensor invariant condition representing the coordinate independence and thus can be generalized for arbitrary flows. However, it is also evident from many of the calculations presented previously that, although most of the standard turbulence models such as the two-equation models are successful in predicting simple flows, they are invalid or inadequate for complex shear flows subjected to extra rates of strain by three-dimensionality, curvature, rotation, flow separation, and other effects (see Lakshminarayana, 1986).

Several investigators (cf. Launder et al., 1977; Leschziner and Rodi, 1981) have modified the standard turbulence model in order to include the extra straining effects arising in practical complex flows. In these modified models the parameters such as the dimensionless Richardson numbers or the stability parameters are commonly adopted in the model constants as functional forms to accounts for the extra straining effects. These parameters depend on streamline curvature coordinates. In general, however, it is difficult to use them in the Cartesian coordinates and also to generalize them for arbitrary three-dimensional complex shear flows. These deficiencies are not shown in the standard models which are expressed in the Cartesian tensor notation satisfying the tensor invariant condition. One way to remedy the deficiency of the existing modified models is to replace the existing parameters adopted to account for the extra straining effects with new suitable parameters satisfying the tensor invariant condition. In order to solve the problem, I propose new parameters and emphasize their importance in this paper.

## 2 Brief Review of Existing Parameters Accounting for Extra Straining Effects

Among many existing parameters dealing with the extra straining effects, the stability parameters and several forms of the Richardson number are commonly adopted in turbulence models, although they are originally used in both theoretical and experimental research to describe the stability mechanism. The stability parameters are dimensionless, characterizing the ratio of the extra rate of strain produced by curvature and rotation, respectively, to the inherent shear strain. The extra rate of strain produced by curvature in the stability parameters is, however, in general expressed in terms of streamline curvature coordinates.

Among several Richardson numbers, the turbulent gradient Richardson number $R_{it}$ proposed by Launder et al. (1977) is adopted in most of modified $k - \epsilon$ models, which is generally expressed as follows:

$$R_{it} = \left(\frac{k}{\epsilon}\right)^2 \omega_{BV}^2 \tag{1}$$

where $\omega_{BV}$ denotes the Brunt-Väisälä frequency. Bradshaw


[1] Assistant Professor, School of Mechanical and Automotive Engineering, Kookmin University, 861-1, Chongnung-dong, Songbuk-ku, Seoul 136-702, Korea.



Contributed by the Fluids Engineering Division of THE AMERICAN SOCIETY OF MECHANICAL ENGINEERS. Manuscript received by the Fluids Engineering Division August 21, 1996; revised manuscript received March 27, 1997. Associate Technical Editor: J. A. C. Humphrey.

maximum streamwise velocity. The instability due to the imbalance between pressure gradient and Coriolis force results in an unstable region near the inner convex wall. If the rotation speed is large enough, viscous effects can no longer hold the one-pair vortex structure in place, thus additional vortices may appear.

It is interesting to note that upon increasing rotating speed further, we cannot obtain a convergent solution. Two possible sources can cause this divergence: numerical instability and physical instability. By numerical instability we mean the instability due to improper numerical scheme. By physical instability we mean the instability caused by physical problem itself, which means that there exists no steady, two-dimensional solution if the rotation speed is increased further. At this stage, it is not clear which factor causes the divergence. However, we reasonably suspect that it may be the physical instability based on two facts: (1) we fail to obtain the convergent solution by trying smaller grid sizes and initial guesses for the velocity and pressure fields for several cases; (2) we can easily detect the Coriolis vortices shown in Fig. 2(*l*). This suggests possible further analysis using unsteady three-dimensional model and bifurcation analysis in the region of the parameter space with a higher rotation rate.

## 4 Concluding Remarks

The centrifugal instability in forms of Dean vortices can be completely cancelled by a negative rotation of channel. This cancelling process is characterized with the secondary flow reversal through formation and development of clockwise circulating corner vortices. This leads to new flow structures with the coexistence of Ekman, Dean, and corner vortices, with the coexistence of Ekman and corner vortices, and with one-pair vortices and an agostrophic, virtually inviscid core. Also a higher rotation rate leads to a Coriolis instability in forms of Coriolis vortices on the inner convex channel wall. These are in agreement with the experimental findings by Matsson and Alfredsson (1994) and Wang and Cheng (1995).


## Acknowledgment

The author is indebted to Professors K. C. Cheng, K. Nandakumar, W. H. Finlay, D. J. Steigmann, and J. H. Masliyah at the University of Alberta for their valuable suggestions and discussion during author's five years at the University of Alberta.


## References


Cheng, K. C., Lin, R. C., and Ou, J. W., 1976, "Fully Developed Laminar Flow in Curved Rectangular Channels," ASME JOURNAL OF FLUIDS ENGINEERING, Vol. 98, pp. 41–48.

Dean, W. R., 1928, "The Stream-line Motion of A Fluid in A Curved Pipe," *Philosophical Magazine,* Vol. 5, pp. 673–695.

Hart, J. E., 1971, "Instability and Secondary Motion in A Rotating Channel Flow," *Journal of Fluid Mechanics,* Vol. 45, pp. 341–353.

Matsson, O. J. E., and Alfredsson, P. H., 1994, "The Effect of Spanwise System Rotation on Dean Vortices," *Journal of Fluid Mechanics,* Vol. 274, pp. 243–265.

Selmi, M., Nandakumar, K., and Finlay, W. H., 1994, "A Bifurcation Study of Viscous Flow through A Rotating Curved Duct," *Journal of Fluid Mechanics,* Vol. 262, pp. 353–375.

Wang, L., and Cheng, K. C., 1995, "Flows in Curved Channels with A Low Negative Rotation Speed," *Physical Review E,* Vol. 51, pp. 1155–1161.

Wang, L., and Cheng, K. C., 1996, "Flow Transitions and Combined Free and Forced Convective Heat Transfer in A Rotating Curved Circular Tube," *International Journal of Heat and Mass Transfer,* Vol. 39, pp. 3381–3400.


# New Parameters Describing Extra Straining Effects in Turbulence Models


**Hyon Kook Myong**[1]


## 1 Introduction

The standard k – ϵ turbulence model is currently incorporated into general purpose CFD (Computational Fluid Dynamics) codes and widely used as a practical and cost-effective design tool to analyze complex shear flows commonly encountered in many engineering problems. This is mainly attributed to the fact that this model, with its simplicity and reasonable accuracy, satisfies a tensor invariant condition representing the coordinate independence and thus can be generalized for arbitrary flows. However, it is also evident from many of the calculations presented previously that, although most of the standard turbulence models such as the two-equation models are successful in predicting simple flows, they are invalid or inadequate for complex shear flows subjected to extra rates of strain by three-dimensionality, curvature, rotation, flow separation, and other effects (see Lakshminarayana, 1986).

Several investigators (cf. Launder et al., 1977; Leschziner and Rodi, 1981) have modified the standard turbulence model in order to include the extra straining effects arising in practical complex flows. In these modified models the parameters such as the dimensionless Richardson numbers or the stability parameters are commonly adopted in the model constants as functional forms to accounts for the extra straining effects. These parameters depend on streamline curvature coordinates. In general, however, it is difficult to use them in the Cartesian coordinates and also to generalize them for arbitrary three-dimensional complex shear flows. These deficiencies are not shown in the standard models which are expressed in the Cartesian tensor notation satisfying the tensor invariant condition. One way to remedy the deficiency of the existing modified models is to replace the existing parameters adopted to account for the extra straining effects with new suitable parameters satisfying the tensor invariant condition. In order to solve the problem, I propose new parameters and emphasize their importance in this paper.

## 2 Brief Review of Existing Parameters Accounting for Extra Straining Effects

Among many existing parameters dealing with the extra straining effects, the stability parameters and several forms of the Richardson number are commonly adopted in turbulence models, although they are originally used in both theoretical and experimental research to describe the stability mechanism. The stability parameters are dimensionless, characterizing the ratio of the extra rate of strain produced by curvature and rotation, respectively, to the inherent shear strain. The extra rate of strain produced by curvature in the stability parameters is, however, in general expressed in terms of streamline curvature coordinates.

Among several Richardson numbers, the turbulent gradient Richardson number $R_{it}$ proposed by Launder et al. (1977) is adopted in most of modified $k - \epsilon$ models, which is generally expressed as follows:

$$R_{it} = \left(\frac{k}{\epsilon}\right)^2 \omega_{BV}^2 \tag{1}$$

where $\omega_{BV}$ denotes the Brunt-Väisälä frequency. Bradshaw


[1] Assistant Professor, School of Mechanical and Automotive Engineering, Kookmin University, 861-1, Chongnung-dong, Songbuk-ku, Seoul 136-702, Korea.



Contributed by the Fluids Engineering Division of THE AMERICAN SOCIETY OF MECHANICAL ENGINEERS. Manuscript received by the Fluids Engineering Division August 21, 1996; revised manuscript received March 27, 1997. Associate Technical Editor: J. A. C. Humphrey.

(1969, 1973) has suggested proper forms of the Brunt-Väisälä frequency for a simple flow system with rotation and for a simple curved flow. For a simple rotating channel flow with angular rotation $\Omega$, the turbulent gradient Richardson number is given as follows according to Bradshaw:

$$R_{it} = \left(\frac{k}{\epsilon}\right)^2 \omega_{BV}^2 = -2\Omega\left(\frac{k}{\epsilon}\right)^2\left(\frac{dU}{dy} - 2\Omega\right) \tag{2}$$

For general two-dimensional curved or separating flows, this number is expressed approximately as

$$R_{it} = R_{sn} = \left(\frac{k}{\epsilon}\right)^2 \omega_{BV}^2 = 2\left(\frac{k}{\epsilon}\right)^2 \frac{U_s}{R}\left(\frac{\partial U_s}{\partial n} + \frac{U_s}{R}\right) \tag{3}$$

in the streamline curvature coordinates ($s - n$ coordinates). Here $s$ is the streamline direction, $n$ the direction normal to the streamline, $R$ the local radius of curvature, and $R_{sn}$ a turbulent gradient Richardson number expressed in the streamline curvature coordinates, respectively. Note here that this parameter is a modified version of the gradient Richardson number first proposed by Bradshaw (1969, 1973); the latter is defined as the square of the ratio of the Brunt-Väisälä frequency to a typical frequency scale of the shear flow, while the former is formed by replacing the mean flow time scale in the denominator of the latter with a turbulence time scale $(k/\epsilon)$ (see Launder et al., 1977). Thus, the turbulent gradient Richardson number still relies on the Brunt-Väisälä frequency. However, since the Brunt-Väisälä frequency is expressed in the streamline curvature coordinates, it is difficult in general to use the turbulent gradient Richardson number in Cartesian coordinates and also to extend them to three-dimensional complex flows. Consequently, all of the existing modified turbulence models adopting this parameter have problems to generalize for arbitrary flows.

## 3 New Parameters Describing Extra Straining Effects

As discussed above, the deficiency of the existing parameters to account for the extra straining effects is traced to the fact that they still maintain the Brunt-Väisälä frequency $\omega_{BV}$ proposed by Bradshaw, which depends in nature on the streamline curvature coordinate. The simplest possible way to remedy the problem of existing parameters is to introduce a new frequency scale satisfying the invariant condition with the Cartesian tensor notation, by which the Brunt-Väisälä frequency may be replaced.

In general, both the mean strain rate tensor $S_{ij}$ and the mean vorticity tensor $\Omega_{ij}$ defined by

$$S_{ij} = \frac{1}{2}\left(\frac{\partial U_i}{\partial x_j} + \frac{\partial U_j}{\partial x_i}\right), \quad \Omega_{ij} = \frac{1}{2}\left(\frac{\partial U_i}{\partial x_j} - \frac{\partial U_j}{\partial x_i}\right) \tag{4}$$

are widely used to describe the flow phenomena in the field of fluid mechanics. They have the same frequency (or time scale) in simple shear flows where the significant strain rate component is one. In complex shear flows, however, they have in general distinct different frequencies due to extra rates of strain by additional velocity gradients, curvature, buoyancy and Coriolis forces. Based on this consideration, it is assumed that the characteristic frequency accounting for the extra strain effects is determined simply by the relative difference between these two tensors. Consequently, as a characteristics frequency, we propose a new frequency $\omega_M$ defined as follows:

$$\omega_M^2 = (\Omega_{ij}\Omega_{ij} - S_{ij}S_{ij}) \tag{5}$$

Note here that $\partial U_i/\partial x_j$ is replaced with $\partial U_i/\partial x_j + \epsilon_{ijk}\Omega_k$ in the rotating coordinate and $\epsilon_{ijk}$ denotes the permutation tensor. This new frequency satisfies the tensor invariant condition and works significantly only in the complex shear complex shear flow where several types of the extra rate of strain exist. It is meaningful to recognize here that, although the present frequency is derived from a simple consideration, its physical meaning can be obtained from the Poisson equation for the mean pressure $P$ in an incompressible turbulent flow expressed as follows:

$$\frac{1}{\rho}\frac{\partial^2 P}{\partial x_k \partial x_k} = -\left(\frac{\partial U_i}{\partial x_j}\frac{\partial U_j}{\partial x_i} + \overline{\frac{\partial u_i}{\partial x_j}\frac{\partial u_j}{\partial x_i}}\right)$$
$$= (\Omega_{ij}\Omega_{ij} - S_{ij}S_{ij}) - \overline{\frac{\partial u_i}{\partial x_j}\frac{\partial u_j}{\partial x_i}} \tag{6}$$

The second term on the right-hand side of Eq. (6) represents the turbulent nonlinear interaction and vanishes in the case of homogeneous turbulence. In contrast, the first term on the right-hand side represents direct influence of both mean deformation and mean rotation, and is in the same form as the present characteristic frequency accounting for the extra straining effects of Eq. (5). This is consistent with the fact that the mean pressure field physically varies significantly due to the extra straining effects.

Nondimensionalizing the square of this frequency by the square of the typical frequency scale of the shear flow having generality, i.e., the mean strain rate tensor, we obtain a new parameter $M_f$ representing the extra strain effects as follows:

$$M_f = \frac{\omega_M^2}{2S_{ij}S_{ij}} = \frac{(\Omega_{ij}\Omega_{ij} - S_{ij}S_{ij})}{2S_{mn}S_{mn}} \tag{7}$$

In addition, following the practice of Launder et al. (1977), another new (turbulent) parameter $M_{ft}$ is formed by replacing the mean flow time scale in the denominator of Eq. (7) $2S_{ij}S_{ij}$ with a turbulence time scale $(k/\epsilon)^2$ as follows:

$$M_{ft} = \left(\frac{k}{\epsilon}\right)^2 \omega_M^2 = \left(\frac{k}{\epsilon}\right)^2 (\Omega_{ij}\Omega_{ij} - S_{ij}S_{ij}) \tag{8}$$

These new parameters, satisfying the tensor invariant condition, are expressed in the Cartesian tensor notation with simple functional forms. Thus, the parameters can be easily extended up to three-dimensional complex shear flows, which is a contrast to the existing parameters such as the gradient Richardson numbers. More details on the new parameters are given in Myong (1994).

## 4 Discussion

As a typical rotating flow, the fully-developed rotating channel flow with counterclockwise rotation $\Omega$ about a spanwise axis (i.e., an axis perpendicular to the $(x - y)$ plane of the mean rate of strain) has been investigated both theoretically and experimentally by several researchers (see e.g., Johnston et al., 1972; Howard et al., 1980). It has been discovered that the standard $k - \epsilon$ turbulence model does not reproduce the trends of the available experimental data, while several modified models adopting several parameters to account for extra straining effects show correct trends. The new parameter $M_{ft}$, the turbulent gradient Richardson number $R_{it}$, and the "turbulent" stability parameter $S_{rott}$ (or the "turbulent flux" Richardson number $R_{ft}$) can be expressed in the rotating coordinate as follows:

$$M_{ft} = \left(\frac{k}{\epsilon}\right)^2 \omega_M^2 = -2\Omega\left(\frac{k}{\epsilon}\right)^2\left(\frac{dU}{dy} - \Omega\right) \tag{9}$$

$$R_{it} = \left(\frac{k}{\epsilon}\right)^2 \omega_{BV}^2 = -2\Omega\left(\frac{k}{\epsilon}\right)^2\left(\frac{\partial U}{\partial y} - 2\Omega\right) \tag{10}$$

$$S_{rott} = R_{ft} = -2\Omega\left(\frac{k}{\epsilon}\right)^2\left(\frac{\partial U}{\partial y} - 0\right) \tag{11}$$

Note that the parameters of Eqs. (10) and (11) have been actually used in the modified models to calculate the above flow by Howard et al. (1980). The new parameter lies as an average between these two parameters, suggesting a good possibility that, instead of the existing parameters, the present parameter

can be used to account for extra straining effects, at least, due to rotation. This fact has been confirmed by Myong (1995).

Note also here that the existing form of Eq. (10) can be derived in a straightforward fashion, following the analysis of Rodi (1976), from an algebraic Reynolds stress model which adds simply the generation term associated with rotation to the production rate terms due to the shear strain rate. Thus, it is generally recognized that this is the correct form describing the relative characteristics of rotational effect to main strain term, and currently adopted as a parameter to account for rotational effects in existing modified $k - \epsilon$ models. However, Launder et al. (1987) have recently pointed out that the substantial derivative $\overline{Du_iu_j}/Dt$ is not, as it stands, materially invariant, and suggested that a frame-indifferent convective derivative is obtained by assigning half the rotation "generation" term to the convective term; i.e., the effective generation associated with rotation is only half as great relative to shear generation. The author (in preparation) has recently found from the systematic analysis that, in the case of rotating flows the correct form describing the relative characteristics of rotational effect to main strain term is not that of Eq. (10) but the present one ofEq. (9).

In case of separating flows such as backward-facing step flows, the turbulent gradient Richardson number expressed in the streamline curvature coordinates ($s - n$ coordinates) is widely used in turbulence models. However, it is difficult to use this parameter in Cartesian coordinates as mentioned above. On the contrary, the new parameter is convenient to use for complex separating flows and also possible to extend to three-dimensional flows, because it is expressed in Cartesian tensor notation which satisfies the tensor invariant condition. In order to demonstrate this fact clearly, let us consider the new parameter applied to a two-dimensional flow as

$$M_{ft} = -\left(\frac{k}{\epsilon}\right)^2\left[2\frac{\partial U}{\partial y}\frac{\partial V}{\partial x} + \left(\frac{\partial U}{\partial x}\right)^2 + \left(\frac{\partial V}{\partial y}\right)^2\right] \quad (12)$$

in the Cartesian coordinates. Equation (12) is also expressed correctly by coordinate transformation in the streamline curvature coordinates ($s - n$) as follows (Myong, 1994):

$$M_{ft} = -\left(\frac{k}{\epsilon}\right)^2\left[-2\frac{U_s}{R}\frac{\partial U_s}{\partial n} + \left(\frac{\partial U_s}{\partial s} + \frac{U_n}{R}\right)^2 + \left(\frac{\partial U_n}{\partial n}\right)^2\right] \quad (13)$$

Equation (13) is a general form of the new parameter satisfying the tensor invariant condition in two-dimensional flow. Apparently, it is significantly different from that of Leschziner and Rodi (1981). However, with the fact that $\partial U_n/\partial s = 0$ by the definition in the streamline curvature coordinate, introducing the following simplifications used by Leschziner and Rodi,

$$\frac{U_n}{R} = \frac{\partial U_s}{\partial s} = \frac{\partial U_n}{\partial n} = 0 \quad (14)$$

we can obtain the following expression from Eq. (13):

$$M_{ft} = \left(\frac{k}{\epsilon}\right)^2 \omega_M^2 = 2\left(\frac{k}{\epsilon}\right)^2 \frac{\partial U_s}{\partial n}\frac{U_s}{R} \quad (15)$$

It can be seen from Eqs. (3), (9), (10), (12), and (15) that the parameter $M_{ft}$ has very strong similarity to the existing parameters such as the turbulent gradient Richardson number and that for small curvature or rotational effects they are identical, i.e., $M_{ft} = R_{it}$. And, the frequency $\omega_M$ has very similar characteristics to the Brunt-Väisälä frequency $\omega_{BV}$. It is valuable to note here that Myong (1995) has demonstrated the usefulness of the parameter $M_{ft}$ through its application to the backward-facing step flow.

It is recognized that extra strain rates produce in general the extra production rate of Reynolds stresses which may be directly related to the parameters representing the extra straining effects. In this respect, the form of Eq. (3) is currently widely adopted as a parameter to account for the curvature effects in existing modified $k - \epsilon$ models and also is known to be the correct form describing the relative characteristics of curvature effect to main strain rate term, since Leschziner and Rodi (1981) have derived this form straightly from an algebraic Reynolds stress model. However, Lee et al. (1988) have recently pointed out that Leschziner and Rodi included incorrectly production-like terms in the production terms of Reynolds stresses under deriving procedure in the streamline coordinate system. These incorrect terms were found to be occurred by the coordinate transformation from convection terms of Reynolds stresses. And, they have suggested that the correct form is of Eq. (15). In addition, the form of the present parameter has been also obtained by Kim and Chung (1987), in the course of derivation of the new eddy diffusivity model capable of predicting a weak-swirl flow from an algebraic Reynolds stress model.

Finally, since swirling flows are in general three-dimensional complex shear flows having extra straining effects due to both the curvature and swirl at the same time, these effects should be compositely considered in the parameter accounting for the extra straining effects. However, it is difficult to represent these effects compositely in the existing parameter. Even if possible, they lose generality because they do not satisfy the tensor invariant condition. For example, Rodi (1978) has reported that these

$$R_f = \frac{2W\frac{\partial}{\partial r}\left(\frac{W}{r}\right)}{2\left[\left(\frac{\partial U}{\partial x}\right)^2 + \left(\frac{\partial U}{\partial r}\right)^2 + \left(\frac{V}{r}\right)^2\right] + \left(\frac{\partial U}{\partial r} + \frac{\partial V}{\partial x}\right)^2 + \left(\frac{\partial W}{\partial x}\right)^2 + \left[r\frac{\partial}{\partial r}\left(\frac{W}{r}\right)\right]^2}. \quad (16)$$

On the contrary, the new parameter satisfying the tensor invariant condition is expressed in the cylindrical coordinates as follows:

$$M_f = \frac{2\frac{W}{r}\frac{\partial W}{\partial r} - 2\frac{\partial U}{\partial r}\frac{\partial V}{\partial x} - \left[\left(\frac{\partial U}{\partial r}\right)^2 + \left(\frac{\partial V}{\partial r}\right)^2 + \left(\frac{V}{r}\right)^2\right]}{2\left[\left(\frac{\partial U}{\partial x}\right)^2 + \left(\frac{\partial V}{\partial r}\right)^2 + \left(\frac{V}{r}\right)^2\right] + \left(\frac{\partial U}{\partial r} + \frac{\partial V}{\partial x}\right)^2 + \left(\frac{\partial W}{\partial x}\right)^2 + \left[r\frac{\partial}{\partial r}\left(\frac{W}{r}\right)\right]^2} \quad (17)$$

effects are compositely considered in the following parameter expressed in the cylindrical coordinates ($x - r - \theta$ coordinates). From the above results, it can be clearly seen that the parameter proposed by Rodi represents only the extra straining effect mainly due to the swirl, while the new parameter represents compositely the extra straining effects due to both the curvature and swirl at the same time.

## 5 Concluding Remarks

The turbulent Richardson numbers and stability parameters are widely used in turbulence models to account for the extra straining effects due to three-dimensionality, curvature, rotation, swirl, and others arising in practical complex flows. Although not impossible, it has some difficulties to describe these parameters with Cartesian coordinates and thus to generalize them for arbitrary flows. In the present paper, we have introduced a new frequency scale satisfying the tensor invariant condition in a simple form, considering the characteristics of both the mean strain rate and the mean vorticity tensors. With this new frequency scale, two new parameters are proposed to describe the extra straining effect on complex shear flows. The new parameters are convenient to use for complex shear flows such as separating flows or rotating flows with relatively simple forms and also possible to extend to three-dimensional flows, since they are expressed in the Cartesian tensor notation with satisfying the tensor invariant condition. And, through a semi-quantitative analysis between the new and existing parameters for several typical complex flows, the newly proposed parameters are found to be general and more adequate than the existing parameters in representing the extra straining effects on complex shear flows in turbulence models. Thus, it is recommended that the existing parameters adopted to account for the extra straining effects in the modified models be replaced with the present ones satisfying the tensor invariant condition and the resultant modified models be applied to the complex shear flows. Finally, it is anticipated that the newly proposed parameters are also helpful to describe the stability mechanism experimentally.


## Acknowledgments

This work was supported by the Korea Science and Engineering Foundation (KOSEF) through AFERC at POSTECH under Contract No. AF9611-13 and Korea Ministry of Education through Mechanical Engineering Research Fund (No. ME95-B-01).


## References


Bradshaw, P., 1969, "The Analogy between Streamwise Curvature and Buoyancy in Turbulent Shear Flow," *Journal of Fluid Mechanics,* Vol. 36, Part 1, pp. 177–191.

Bradshaw, P., 1973, "Effects of Streamline Curvature on Turbulent Flows," AGARDograph, No. 169.

Howard, J. H. G., Patankar, S. V. and Bordynuik, R. M., 1980, "Flow Prediction in Rotating Ducts using Coriolis-Modified Turbulence Models," ASME JOURNAL OF FLUIDS ENGINEERING, Vol. 102, pp. 456–461.

Johnston, J. P., Hallen, R. M., and Lezius, D. K., 1972, "Effects of Spanwise Rotation on the Structure of Two-Dimensional Fully Developed Turbulent Channel Flow," *Journal of Fluid Mechanics,* Vol. 56, pp. 533–557.

Kim, K. Y., and Chung, M. K., 1987, "New Eddy Viscosity Model for Computation of Swirling Turbulent Flows," *AIAA Journal,* Vol. 25, pp. 1020–1022.

Lakshminarayana, B., 1986, "Turbulence Modeling for Complex Shear Flows," *AIAA Journal,* Vol. 24, No. 12, pp. 1900–1917.

Launder, B. E., Priddin, C. H., and Sharma, B. L., 1977, "The Calculation of Turbulent Boundary Layers on Spinning and Curved Surfaces," ASME JOURNAL OF FLUIDS ENGINEERING, Vol. 99, pp. 231–239.

Launder, B. E., Tselepidakis, D. P., and Younis, B. A., 1987, "A Second-moment Closure Study of Rotating Channel Flow," *Journal of Fluid Mechanics,* Vol. 183, pp. 63–75.

Lee, B. K., Cho, N. H., and Choi, Y. D., 1988, "Analysis of Periodically Fully Developed Turbulent Flow and Heat Transfer by $k - \epsilon$ Equation Model in Artificially Roughened Annulus," *International Journal of Heat and Mass Transfer,* Vol. 31, pp. 1797–1806.

Leschziner, M. A., and Rodi, W., 1981, "Calculation of Annular and Twin Parallel Jets Using Various Discretization Schemes and Turbulence Model Variations," ASME JOURNAL OF FLUIDS ENGINEERING, Vol. 103, pp. 352–360.

Myong, H. K., 1994, "Proposal of a New Parameter for Extra Straining Effects," (in Korean) *Transactions of the Korea Society of Mechanical Engineers,* Vol. 18, No. 1, pp. 184–192.

Myong, H. K., 1995, "Turbulence Model Having Generality for the Prediction of Complex Shear Flows," *Advances in Turbulence Research-1995,* Postech, Pohang, Korea, Mar. 27–29, pp. 241–258.

Park, S. W., and Chung, M. K., 1989, "Curvature-Dependent Two-Equation Model for Prediction of Turbulent Recirculating Flows," *AIAA Journal,* Vol. 27, No. 3, pp. 340–344.

Rodi, W., 1976, "A New Algebraic Relation for Calculating Reynolds Stresses," *Zeit. Angew. Math. Mech.,* Vol. 56, pp. T219–T221.


# Developing Laminar Flow in Eccentric Annuli


**Maged A. I. El-Shaarawi,[1] Habib I. Abualhamayel,[1] and Esmail M. A. Mokheimer[1,2]**


## Introduction

A thorough search of the literature has revealed that only two papers by Feldman et al. (1982a and 1982b) have dealt with developing flow in the entry-region of eccentric annuli. In these two papers, the two transverse momentum equations were dropped; the hydrodynamic model comprised only two equations, namely, a reduced axial momentum equation and the continuity equation. Consequently, this two-equation model does not form a complete mathematical model and additional assumptions regarding the transverse flows were used to facilitate a solution.

The first objective of this note is to present a mathematically well-posed model for the problem under consideration, i.e., a model capable of describing the forced flow in the entry-region of eccentric annuli without need of assumptions dependent on prior knowledge of the mechanism of transverse flows. The second objective is to develop a numerical algorithm to solve the obtained model. Finally, numerical results not available in the literature are presented for the developing velocity profiles and pressure drop.

## Governing Equations and Method of Solution

A two-dimensional cross-section of the geometry under consideration is shown in Fig. 1($a$). This eccentric geometry can easily be described by the bipolar coordinate system ($\eta$, $\xi$ and $z$) shown in Fig. 1($b$). The transformed geometry in the complex $\eta - \xi$ plane is a slab of length ($\eta_i - \eta_o$), where $\eta_i$ and $\eta_o$ are the values of the bipolar coordinate $\eta$ that coinside with the inner and outer cylinder surfaces, respectively, and width equal to the limits of $\xi$, that is $2\pi$.

The fluid is assumed to be Newtonian with constant physical properties. The flow is steady, laminar and enters the annular passage with a uniform velocity, $u_o$. Body forces are absent.


[1] Professor, Associate Professor, and Assistant Professor, respectively, Mechanical Engineering Department, King Fahd University of Petroleum and Minerals, Dhahran 31261, Saudi Arabia.

[2] On leave from Ain Shams University, Cairo, Egypt.



Contributed by the Fluids Engineering Division of THE AMERICAN SOCIETY OF MECHANICAL ENGINEERS. Manuscript received by the Fluids Engineering Division April 29, 1996; revised manuscript received March 25, 1997. Associate Technical Editor: S. P. Vanka.

effects are compositely considered in the following parameter expressed in the cylindrical coordinates ($x - r - \theta$ coordinates). From the above results, it can be clearly seen that the parameter proposed by Rodi represents only the extra straining effect mainly due to the swirl, while the new parameter represents compositely the extra straining effects due to both the curvature and swirl at the same time.

## 5 Concluding Remarks

The turbulent Richardson numbers and stability parameters are widely used in turbulence models to account for the extra straining effects due to three-dimensionality, curvature, rotation, swirl, and others arising in practical complex flows. Although not impossible, it has some difficulties to describe these parameters with Cartesian coordinates and thus to generalize them for arbitrary flows. In the present paper, we have introduced a new frequency scale satisfying the tensor invariant condition in a simple form, considering the characteristics of both the mean strain rate and the mean vorticity tensors. With this new frequency scale, two new parameters are proposed to describe the extra straining effect on complex shear flows. The new parameters are convenient to use for complex shear flows such as separating flows or rotating flows with relatively simple forms and also possible to extend to three-dimensional flows, since they are expressed in the Cartesian tensor notation with satisfying the tensor invariant condition. And, through a semi-quantitative analysis between the new and existing parameters for several typical complex flows, the newly proposed parameters are found to be general and more adequate than the existing parameters in representing the extra straining effects on complex shear flows in turbulence models. Thus, it is recommended that the existing parameters adopted to account for the extra straining effects in the modified models be replaced with the present ones satisfying the tensor invariant condition and the resultant modified models be applied to the complex shear flows. Finally, it is anticipated that the newly proposed parameters are also helpful to describe the stability mechanism experimentally.


## Acknowledgments

This work was supported by the Korea Science and Engineering Foundation (KOSEF) through AFERC at POSTECH under Contract No. AF9611-13 and Korea Ministry of Education through Mechanical Engineering Research Fund (No. ME95-B-01).


## References


Bradshaw, P., 1969, "The Analogy between Streamwise Curvature and Buoyancy in Turbulent Shear Flow," *Journal of Fluid Mechanics,* Vol. 36, Part 1, pp. 177–191.

Bradshaw, P., 1973, "Effects of Streamline Curvature on Turbulent Flows," AGARDograph, No. 169.

Howard, J. H. G., Patankar, S. V. and Bordynuik, R. M., 1980, "Flow Prediction in Rotating Ducts using Coriolis-Modified Turbulence Models," ASME JOURNAL OF FLUIDS ENGINEERING, Vol. 102, pp. 456–461.

Johnston, J. P., Hallen, R. M., and Lezius, D. K., 1972, "Effects of Spanwise Rotation on the Structure of Two-Dimensional Fully Developed Turbulent Channel Flow," *Journal of Fluid Mechanics,* Vol. 56, pp. 533–557.

Kim, K. Y., and Chung, M. K., 1987, "New Eddy Viscosity Model for Computation of Swirling Turbulent Flows," *AIAA Journal,* Vol. 25, pp. 1020–1022.

Lakshminarayana, B., 1986, "Turbulence Modeling for Complex Shear Flows," *AIAA Journal,* Vol. 24, No. 12, pp. 1900–1917.

Launder, B. E., Priddin, C. H., and Sharma, B. L., 1977, "The Calculation of Turbulent Boundary Layers on Spinning and Curved Surfaces," ASME JOURNAL OF FLUIDS ENGINEERING, Vol. 99, pp. 231–239.

Launder, B. E., Tselepidakis, D. P., and Younis, B. A., 1987, "A Second-moment Closure Study of Rotating Channel Flow," *Journal of Fluid Mechanics,* Vol. 183, pp. 63–75.

Lee, B. K., Cho, N. H., and Choi, Y. D., 1988, "Analysis of Periodically Fully Developed Turbulent Flow and Heat Transfer by $k - \epsilon$ Equation Model in Artificially Roughened Annulus," *International Journal of Heat and Mass Transfer,* Vol. 31, pp. 1797–1806.

Leschziner, M. A., and Rodi, W., 1981, "Calculation of Annular and Twin Parallel Jets Using Various Discretization Schemes and Turbulence Model Variations," ASME JOURNAL OF FLUIDS ENGINEERING, Vol. 103, pp. 352–360.

Myong, H. K., 1994, "Proposal of a New Parameter for Extra Straining Effects," (in Korean) *Transactions of the Korea Society of Mechanical Engineers,* Vol. 18, No. 1, pp. 184–192.

Myong, H. K., 1995, "Turbulence Model Having Generality for the Prediction of Complex Shear Flows," *Advances in Turbulence Research-1995,* Postech, Pohang, Korea, Mar. 27–29, pp. 241–258.

Park, S. W., and Chung, M. K., 1989, "Curvature-Dependent Two-Equation Model for Prediction of Turbulent Recirculating Flows," *AIAA Journal,* Vol. 27, No. 3, pp. 340–344.

Rodi, W., 1976, "A New Algebraic Relation for Calculating Reynolds Stresses," *Zeit. Angew. Math. Mech.,* Vol. 56, pp. T219–T221.


# Developing Laminar Flow in Eccentric Annuli


**Maged A. I. El-Shaarawi,[1] Habib I. Abualhamayel,[1] and Esmail M. A. Mokheimer[1,2]**


## Introduction

A thorough search of the literature has revealed that only two papers by Feldman et al. (1982a and 1982b) have dealt with developing flow in the entry-region of eccentric annuli. In these two papers, the two transverse momentum equations were dropped; the hydrodynamic model comprised only two equations, namely, a reduced axial momentum equation and the continuity equation. Consequently, this two-equation model does not form a complete mathematical model and additional assumptions regarding the transverse flows were used to facilitate a solution.

The first objective of this note is to present a mathematically well-posed model for the problem under consideration, i.e., a model capable of describing the forced flow in the entry-region of eccentric annuli without need of assumptions dependent on prior knowledge of the mechanism of transverse flows. The second objective is to develop a numerical algorithm to solve the obtained model. Finally, numerical results not available in the literature are presented for the developing velocity profiles and pressure drop.

## Governing Equations and Method of Solution

A two-dimensional cross-section of the geometry under consideration is shown in Fig. 1($a$). This eccentric geometry can easily be described by the bipolar coordinate system ($\eta$, $\xi$ and $z$) shown in Fig. 1($b$). The transformed geometry in the complex $\eta - \xi$ plane is a slab of length ($\eta_i - \eta_o$), where $\eta_i$ and $\eta_o$ are the values of the bipolar coordinate $\eta$ that coinside with the inner and outer cylinder surfaces, respectively, and width equal to the limits of $\xi$, that is $2\pi$.

The fluid is assumed to be Newtonian with constant physical properties. The flow is steady, laminar and enters the annular passage with a uniform velocity, $u_o$. Body forces are absent.


[1] Professor, Associate Professor, and Assistant Professor, respectively, Mechanical Engineering Department, King Fahd University of Petroleum and Minerals, Dhahran 31261, Saudi Arabia.

[2] On leave from Ain Shams University, Cairo, Egypt.



Contributed by the Fluids Engineering Division of THE AMERICAN SOCIETY OF MECHANICAL ENGINEERS. Manuscript received by the Fluids Engineering Division April 29, 1996; revised manuscript received March 25, 1997. Associate Technical Editor: S. P. Vanka.

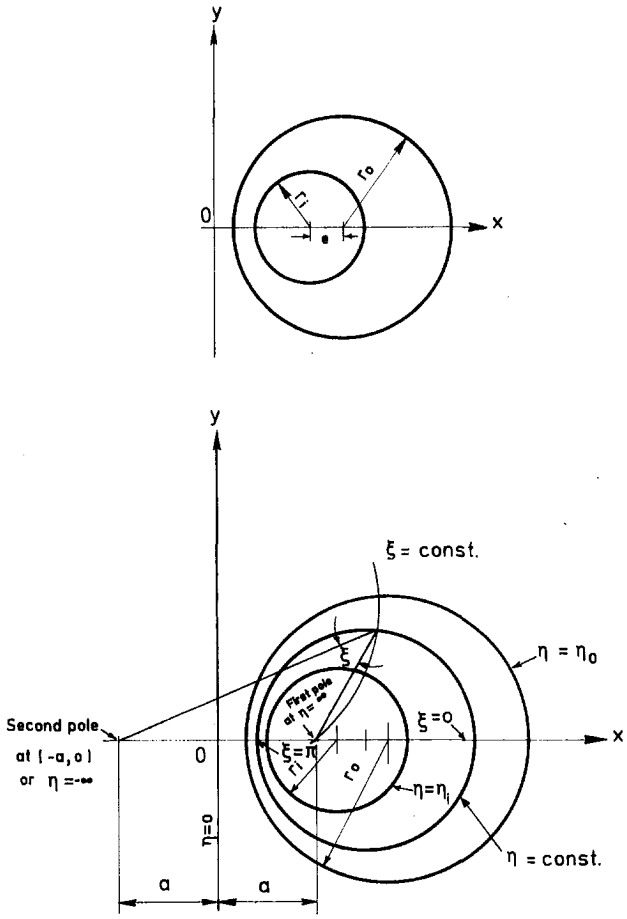


**Fig. 1 (*a*) Two-dimensional cross-section of the geometry under consideration; (*b*) bipolar coordinate system**

Using the appropriate coordinate scale factors (Hughes and Gaylord, 1964), assuming the pressure to be a function of the axial coordinate only ($\partial p/\partial\eta = \partial p/\partial\xi = 0$), neglecting the axial diffusions of momentum and energy ($\partial^2/\partial z^2 = 0$), dropping the $\eta$-momentum equation since the $\eta$-velocity component ($v$) is much smaller than the $\xi$- and $z$-velocity components ($w$ and $u$) and introducing the proper dimensionless parameters, the governing four equations can be replaced by the following three dimensionless boundary-layer equations.

$$\frac{\partial(HW)}{\partial\xi} + \frac{\partial(HV)}{\partial\eta} + \frac{\partial(H^2U)}{\partial Z} = 0 \tag{1}$$

$$\frac{W}{H}\frac{\partial W}{\partial\xi} + \frac{V}{H^2}\frac{\partial HW}{\partial\eta} + U\frac{\partial W}{\partial Z} - \frac{V^2}{H^2}\frac{\partial H}{\partial\xi} = \frac{1}{H^3}\left(\frac{\partial^2 HW}{\partial\eta^2} + \frac{\partial^2 HW}{\partial\xi^2}\right) - \frac{2}{H^4}\left(\frac{\partial HW}{\partial\eta} - \frac{\partial HV}{\partial\xi}\right)\frac{\partial H}{\partial\eta} + \frac{2}{H^2}\frac{\partial H}{\partial\xi}\frac{\partial U}{\partial Z} \tag{2}$$

$$\frac{W}{H}\frac{\partial U}{\partial\xi} + \frac{V}{H}\frac{\partial U}{\partial\eta} + U\frac{\partial U}{\partial Z} = -\frac{dP}{dZ} + \frac{1}{H^2}\left[\frac{\partial^2 U}{\partial\xi^2} + \frac{\partial^2 U}{\partial\eta^2}\right] \tag{3}$$

$U$, $V$, and $W$ are the dimensionless velocity components in $Z$, $\eta$, and $\xi$ directions, $P$ is the dimensionless pressure, $Z$ is the dimensionless axial direction, and $H$ is the dimensionless coordinate scale factor (Mokheimer, 1995).

The differential continuity Eq. (1) subject to the no-slip conditions on the two boundaries can be written in the following integral form.

$$\frac{8(1-N)}{\pi(1+N)}\int_0^{\pi}\int_{\eta_o}^{\eta_i} UH^2 d\eta d\xi = 1 \tag{4}$$

$N$ is the annulus radius ratio ($N = r_i/r_o$), see Fig. 1($a$).

Equations (1) through (3) are subject to the following boundary conditions

$$\left.\begin{aligned}
&\text{for}\quad Z=0 \quad\text{and}\quad \eta_o<\eta<\eta_i, \\
&\qquad\qquad V=W=P=\theta=0 \quad\text{and}\quad U=1 \\
&\text{for}\quad Z\geq 0 \quad\text{and}\quad \eta=\eta_i, U=V=W=0 \\
&\text{for}\quad Z\geq 0 \quad\text{and}\quad \eta=\eta_o, U=V=W=0 \\
&\text{for}\quad Z>0 \quad\text{and}\quad \xi=0 \quad\text{and} \\
&\qquad\qquad \pi \quad\text{(the line of symmetry):} \\
&\frac{\partial V}{\partial\xi}=\frac{\partial W}{\partial\xi}=\frac{\partial U}{\partial\xi}=0
\end{aligned}\right\} \tag{5}$$

Equations (1) through (4) were numerically handled using a linearized finite-difference algorithm (Mokheimer, 1995). Due to symmetry, the above equations need to be solved in only half of the slab, i.e., for $0 \leq \xi \leq \pi$. The hydrodynamically fully developed flow, which occurs if the channel is sufficiently long, provides an analytical check on the numerical solution to be obtained. For hydrodynamic full development, $V = W = 0$, $\partial U/\partial Z = 0$, $dP/dZ$ = constant, the $\xi$-momentum Eq. (2) and the inertia terms on the left-hand side of Eq. (3) vanish and the resulting axial momentum equation reduces to

$$\frac{\partial^2 U_{fd}}{\partial\xi^2} + \frac{\partial^2 U_{fd}}{\partial\eta^2} = H^2\left(\frac{dP}{dZ}\right)_{fd} \tag{6}$$

In the above equation, the subscript *fd* stands for fully developed conditions. This equation is identical to the equation of steady-state heat conduction with internal heat generation which was solved by El-Saden (1961). The solution of Eq. (6) is

$$U_{fd} = A^*\eta + B - \frac{C^*}{2}\coth\eta + \sum_{n=1}^{\infty}\cos n\xi[C_e^{n\eta} + (D - C^*\coth\eta)e^{-n\eta}] \tag{7}$$

Applying the boundary conditions (5) the constants of integration $A^*$, $B$, $C$, and $D$ can be determined (Mokheimer, 1995).

## Results and Discussion

Computations were carried out for annuli of $N = 0.5$ and 0.9. The radius ratio 0.5 was chosen since it represents a typical annular geometry and some of the results presented by Feldman et al. (1982a) are for this particular radius ratio. These results provide a means of verification of the present work and can also be used to compare the present model with the two-equation model of Feldman et al. (1982a).

Due to space limitations, only a representative sample of the results will be shown here. Figure 2 shows examples of the developing axial velocity profiles in the widest and narrowest sides of the gap of an annulus of $N = 0.5$ and $E = 0.5$ ($E$ is the dimensionless eccentricity, $E = e/(r_o - r_i)$, see Fig. 1($a$)). The profiles shown in Fig. 2 show that at early stages of the axial velocity development (small values of $Z$) fluid adjacent to the annulus two walls (e.g., $\phi = 0.05$ and 0.95, where $\phi = (\eta - \eta_o)/(\eta_i - \eta_o)$) decelerates due to the formation of the two hydrodynamic boundary-layers on these boundaries. Consequently, as a result of continuity principle, fluid outside these

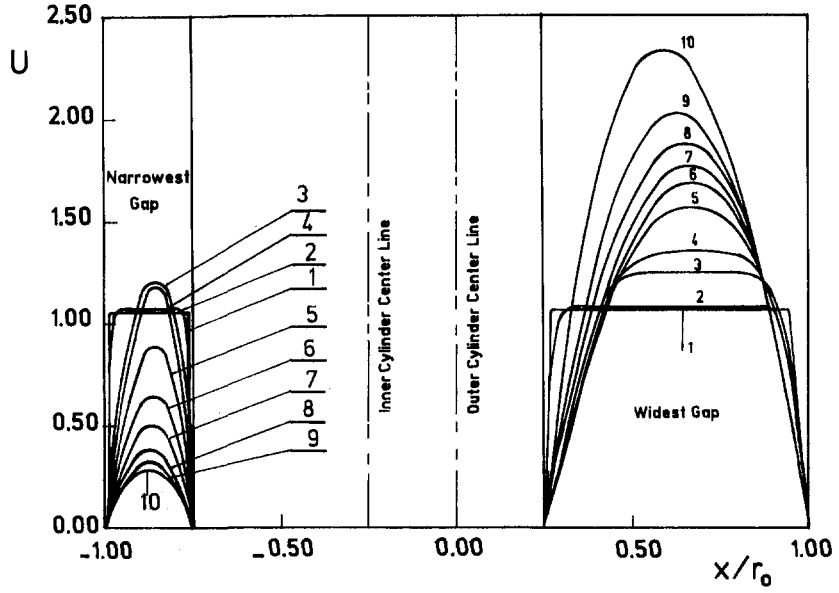


**Fig. 2 Development of the axial velocity profiles, $N = E = 0.5$. The numbers on the profiles indicate the following values of $Z \times 10^4$: (1) $10^{-3}$, (2) 0.6, (3) 12, (4) 17, (5) 67, (6) 117, (7) 167, (8) 267, (9) 467, (10) 2167 (fully developed).**

two boundary-layers (e.g., $\phi = 0.4$ or 0.3) accelerates. However, due to the increased resistance to flow in the narrow side of the annulus (as a result of eccentricity) the fluid on this narrow gap side moves in a tangentially-like direction (in $\xi$-direction with a velocity component $W$) to the wide gap side of the annulus. Such a tangentially-like fluid transportation from the narrow gap side to the wide gap side increases as the flow moves away from the entrance ($Z$ increases) and thus causes a reduction in the values of the axial velocity profile on the narrow gap side and vice versa on the wide gap side. However, far enough from the entrance such a tangential-like transportation decays as the flow approaches hydrodynamic full-development with $V = W = 0$.

The acceleration of fluid outside the developing boundary layers on the widest gap side of the annulus is created by (1) transportation of fluid from inside these two boundary layers by means of the $V$-component of velocity and (2) transportation of fluid from the narrowest gap side of the annulus by means of the $W$-component of velocity. On the other hand, the fluid outside the two developing hydrodynamic boundary layers on the narrowest gap side of the annulus undergoes two counteracting actions, namely, acceleration due to fluid transportation from inside these two boundary layers by means of the $V$-component of velocity and deceleration engendered by transportation of fluid from the narrowest gap side to the widest gap side by means of $W$-component of velocity. The latter action overcomes the first as the flow moves downstream the entrance cross-section and hence the resultant effect creates decreasing values of the axial velocity component on the narrowest gap side of the annulus. However, both actions gradually decay with further increases in the axial distance $Z$ and finally vanish when the flow becomes hydrodynamically fully developed.

Other unpresented results indicate also how the eccentricity makes the profile asymmetric. Differences in the velocity at different angular locations ($\psi = \xi/\pi$), and over the cross section at any angular location, become more pronounced with increasing eccentricity. Such asymmetry will be reflected on the other two velocity components ($V$ and $W$). Examples of the developing tangential-like velocity component ($W$) near the widest-gap side of the annulus ($\psi = 0.05$) are presented in Fig. 3 for $N = E = 0.5$. To the authors' knowledge, this is the first time that the development of such a velocity component has been considered for the case of entrance-region flows in eccentric annuli. An appreciation of this development leads to a better understanding of the mechanism of development in the entry region. At the lines of symmetry (i.e., $\psi = 0.0$ and $\pi$), the $W$-component of velocity has a zero value. On the other hand, at $\psi = 0.05$, Fig. 3 shows how the tangential-like velocity component develops as the flow moves away from the annulus entrance. As can be seen from this figure, such a tangential-like flow is mainly from the narrowest-side of the annulus toward its widest side (i.e., in the opposite direction of $\xi$ with negative values of $W$). In all cases, the $W$-velocity component starts from zero at the annulus entrance and ends again at zero at the position where the flow reaches the fully developed state.

Engineers are not frequently concerned with the details of the fluid velocities but only with pressure drop. When the flow becomes hydrodynamically fully developed, the pressure drop is due to only the viscous shear action. In this case the pressure drop as obtained by means of Eq. (6) is a linear function of $Z$. Under the assumption of whole channel fully developed flow

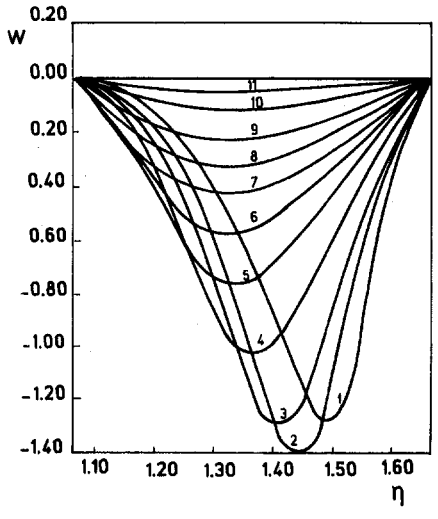


**Fig. 3 Development of the tangential-like velocity profiles near the widest gap ($\psi = 0.05$), $N = E = 0.5$. The numbers on the profiles indicate the following values of $Z \times 10^4$: (1) 4, (2) 12, (3) 17, (4) 67, (5) 167, (6) 317, (7) 517, (8) 717, (9) 917, (10) 1417, (11) 2017.**

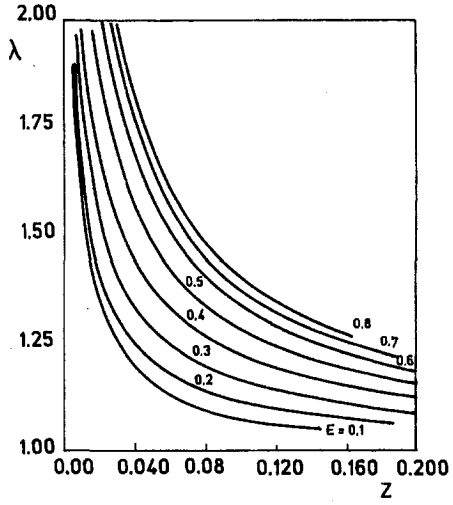


**Fig. 4(*a*) Development of the friction coefficient with *Z*, for different eccentricities, *N* = 0.5**

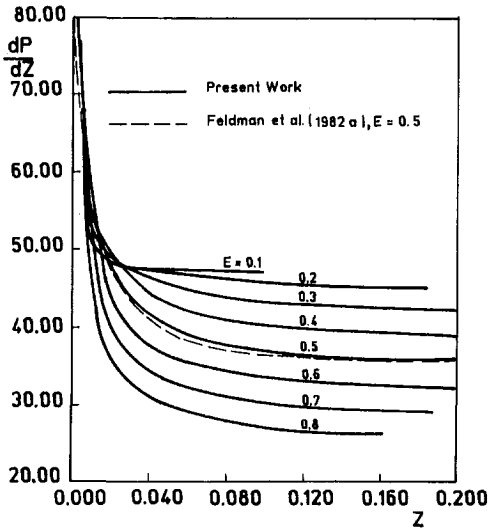


**Fig. 4(*b*) Development of the pressure gradient with *Z*, for different eccentricities, *N* = 0.5**

(i.e., if the flow were fully developed right from the annulus entrance) Eqs. (6) and (7) can be used to find the dimensionless pressure gradient $(dP/dZ)_{fd}$ and hence the linear variation of the dimensionless pressure $P_{fd}$ with $Z$. For a developing flow, the pressure drop is due to both inertia and viscous actions. Consequently the dimensionless pressure $P$ in the entry region is a non-linear function of $Z$. However, if the annulus is sufficiently long, the developing local dimensionless pressure ($P$) should finally (at large values of $Z$) follow a linear relationship with $Z$ having the slope as that given by Eq. (6), $(dP/dZ)_{fd}$. The difference between $P$ and $P_{fd}$, for a given $Z$, will be referred to as the pressure drop increment ($\nabla$). This pressure drop increment is due to the inertia forces in the developing region. For an annulus of given radius ratio $N$ and eccentricity $E$, the pressure drop increment must asymptotically approach a constant value which will be referred to as the fully-developed pressure drop increment ($\nabla_{fd}$).

Unpresented results show that the variation of $P$ with $Z$ follows the above-mentioned trends and that the pressure drop, for a given $Z$ in a given annulus ($N$), decreases with increasing $E$. Therefore, for a given pressure drop along an annulus, increasing the eccentricity causes an increase in the flow rate through the annular channel. The variation of the ratio between the local friction coefficient (at any value of $Z$) to the fully developed friction coefficient, $\lambda$, is plotted against $Z$ in Fig. 4($a$) for different eccentricities in an annulus of radius ratio $N = 0.5$.

Table 1 gives the computed values of the fully-developed pressure drop increment ($\nabla_{fd}$) in the two annuli under investigation ($N = 0.5$ and 0.9) for various values of the eccentricity $E$. Figure 4($a$), together with Table 1, indicate that the assumption of whole channel fully-developed flow would lead to considerable underestimated values for the pressure drop in the entry region. It is worth mentioning that in all the computer runs the obtained numerical results for the developing axial velocity profiles $U$ approached asymptotically (at large values of $Z$) the fully developed velocity profile given by Eq. (7). Moreover, validation of the present computer code and its numerical results have also been checked by the trend of other results at large values of $Z$; the dimensionless pressure ($P$), the pressure drop increment ($\nabla$), and the pressure gradient $\partial P/\partial Z$ for given $N$ and $E$, were found to follow the aforesaid linear relationship, has a constant value ($\nabla_{fd}$) and approaches the fully developed analytical value $(dP/dZ)_{fd}$, respectively.

In both the present work and that of Feldman et al. (1982a), the hydrodynamic development length ($Z_{fd}$) is arbitrarily defined as the distance required for the maximum of the axial velocity profile ($U_{\max,fd}$) to approach within 1 percent of its fully developed value. This length is given in Table 1 for various values of $E$. It is worth mentioning that Feldman (1974) used ten series-terms in Eq. (7) when computing the fully developed axial velocity profile (and hence the value of $U_{\max,fd}$). In the present work ten, fifteen, and twenty series-terms have been used for $E = 0.1$, $0.2 \le E \le 0.4$ and $E \ge 0.5$, respectively. The corresponding values of $U_{\max,fd}$, as obtained from Eq. (7), are given in Table 1.

The pressure gradient at full development $(dP/dZ)_{fd}$ is given also in Table 1 for all the annuli investigated. For each value

**Table 1 Values of $\nabla_{fd}$, $Z_{fd}$, $U_{\max,fd}$, and $(-dP/dZ)_{fd}$ for different annular geometries**

| | | | | | | | $-(dP/dZ)_{fd}$ | | | | | |
|---|---|---|---|---|---|---|---|---|---|---|---|---|
| | $\nabla_{fd}$ | | $Z_{fd}$ | | $U_{\max,fd}$ | | $N = 0.5$ | | | $N = 0.9$ | | |
| $E$ | $N = 0.5$ | $N = 0.9$ | $N = 0.5$ | $N = 0.9$ | $N = 0.5$ | $N = 0.9$ | Analytical | Numerical | Tiedt* | Analytical | Numerical | Tiedt* |
| 0.1 | 0.37525 | 0.57572 | 0.146 | 0.102 | 1.78713 | 1.76178 | 47.1381 | 47.2193 | 46.962 | 45.2964 | 47.5808 | 47.284 |
| 0.2 | 0.54370 | 0.94046 | 0.185 | 0.188 | 2.01820 | 2.02849 | 45.2434 | 45.3949 | 45.082 | 44.8168 | 45.5380 | 45.278 |
| 0.3 | 0.75370 | 0.84310 | 0.204 | 0.265 | 2.19275 | 2.23086 | 42.4360 | 42.6407 | 42.278 | 42.1640 | 42.5180 | 42.290 |
| 0.4 | 0.94820 | 1.01910 | 0.216 | 0.340 | 2.31356 | 2.37268 | 39.0702 | 39.2628 | 38.916 | 38.7796 | 38.9100 | 38.716 |
| 0.5 | 1.08601 | 1.17190 | 0.217 | 0.401 | 2.38109 | 2.45643 | 35.4916 | 35.7084 | 35.342 | 35.0092 | 35.0876 | 34.920 |
| | 1.0715** | | 0.254** | | 2.372** | | 35.33** | | | | | |
| 0.6 | 1.24395 | 1.20680 | 0.208 | 0.455 | 2.40494 | 2.49495 | 31.9629 | 32.2533 | 31.818 | 31.2728 | 31.3396 | 31.186 |
| 0.7 | 1.14876 | 1.28770 | 0.189 | 0.501 | 2.39610 | 2.49876 | 28.6525 | 29.0170 | 28.512 | 27.7584 | 27.8068 | 27.686 |
| 0.8 | 1.01915 | 1.25340 | 0.163 | 0.532 | 2.36449 | 2.47875 | 25.6476 | 26.0630 | 25.510 | 24.5780 | 24.6156 | 24.516 |

* Results of Tiedt (1971) as presented by Shah and London (1978).
** Results of Feldman et al. (1982a).

of $E$, both the analytical value, which has been obtained by Eqs. (6) and (7), and the computed numerical value are given. The agreement between these two sets of results provided another means of validation of the present model and computer code. On the other hand, Table 1 compares also all the present results for $(dP/dZ)_{fd}$ with those of Tiedt (1971) and some of the present results for $\nabla_{fd}$, $Z_{fd}$, $U_{\max,fd}$ and $(dP/dZ)_{fd}$ with the corresponding results of Feldman et al. (1982a) for the case of $N = 0.5$ and $E = 0.5$. As can be seen from this table, there is good agreement between the present results for $(dP/dZ)_{fd}$ and those of Tiedt (1971). Moreover, the agreement between the present results and those of Feldman et al. (1982a) for $\nabla_{fd}$, $U_{\max,fd}$, and $(dP/dZ)_{fd}$ is excellent (the difference between the two sets of results is less than 1 percent for any of $\nabla_{fd}$, $U_{\max,fd}$ and $(dP/dZ)_{fd}$). However, the present hydrodynamic development length is 14.6 percent shorter than that obtained by Feldman et al. (1982a). This difference might be due to Feldman's use of only ten series-terms in calculating $U_{\max,fd}$ (upon which is based the criterion for determining $Z_{fd}$) while twenty terms were used in the present work. However, another comparison for the variation of $\partial P/\partial Z$ with $Z$, presented in Fig. 4($b$), has shown an excellent agreement with the corresponding results of Feldman et al. (1982a).

## References


El-Saden, M. R., 1961, "Heat Conduction in an Eccentrically Hollow, Infinitely Long Cylinder with Internal Heat Generation," ASME *Journal of Heat Transfer,* Vol. 83, No. 4, pp. 510–511.

Feldman, E. E., 1974, "The Numerical Solution of the Combined Thermal and Hydrodynamic Entrance Region of an Eccentric Annulus," Ph.D. dissertation, Carnegie-Mellon University, Pittsburgh, PA.

Feldman, E. E., Hornbeck, R. W., and Osterle, J. F., 1982a, "A Numerical Solution of Laminar Developing Flow in Eccentric Annular Ducts." *International Journal of Heat and Mass Transfer,* Vol. 25, No. 2, pp. 231–241.

Feldman, E. E., Hornbeck, R. W., and Osterle, J. F., 1982b, "A Numerical Solution of Developing Temperature for Laminar Developing Flow in Eccentric Annular Ducts," *International Journal of Heat and Mass Transfer,* Vol. 25, No. 2, pp. 243–253.

Hughes, W. F., and Gaylord, E. W., 1964, *Basic Equations of Engineering Science,* Schaum's outline series, McGraw-Hill, New York, pp. 1–11, 151.

Mokheimer, E. M. A., 1995, "Heat Transfer in Eccentric Annuli," Ph.D. dissertation, Mechanical Engineering Department, KFUPM, Dhahran 31261, Saudi Arabia.

Shah, R. K. and London, A. L., 1978, *Laminar Flow Forced Convection in Ducts,* Academic Press, New York, pp. 326–330.

Tiedt, W., 1971, English translation-Transl. Bur. No. 0151, P. 248, Transp. Dev. Agency Libr., Montereal.

Journal of Fluids Engineering

# Discussion

## Experimental Measurements in a Centrifugal Pump Impeller[1]

**Y. N. Chen.**[2] The authors presented very interesting and comprehensive experimental results on a centrifugal pump impeller with air as working medium. Their experimental results are compiled in Fig. 23 in order to obtain a better overview.

The authors explain the reduction of the axial relative velocity on the shroud surface at $y/y_o = 0.3$ of Station 2 (Fig. 9) to be caused by the secondary flows induced by the shroud curvature and the blade to blade Coriolis force. A secondary vortex in this zone as revealed by Fig. 8 is not considered. At Station 3, the low relative velocity travels along the shroud to the suction-side corner. The authors attribute this phenomenon to the thickening of the boundary layer in the pressure-side corner, and exclude the effect of the shroud curvature. No vortex behaviour of this low velocity flow is considered either.

The writer would like to point out the discovery of the vortex in the field of the relative velocities induced by the curvature of the blade channel due to bending from the axial to the radial direction. This vortex is indicated by an arrow L. It is a vortex low because of its rotation in the same sense as the impeller rotation.

The relative velocities over Station 2 show the pattern of a huge passage vortex, which has a property of vortex high H because of its rotational sense being against that of the impeller rotation. This passage vortex is induced by the rotating impeller due to suction of the fluid from the absolute frame of zero vorticity.

At Station 3 a vortex low L appears in the suction side shroud corner, developing from the Dean's type vortex pair of the curvature mentioned. The vortex high H of this pair cannot be distinguished from the prevailing passage vortex high H. This vortex low L also shrinks to a small size under the influence of the passage vortex high H. It extends to Stations 4, 5, and 6. The vortex low L is driven by the pressure field of the blade channel to this corner.

Station 2 already penetrates through the curvature of the blade channel. Therefore, the vortex low L of the Dean's type vortex pair can be formed there. However, this vortex low L is stabilized in the middle field of the cross section, because there is scarcely a pressure field generated by the inlet edge of the impeller.

The tangential relative flow at Station 1 is then the prerotation caused by the passage vortex of the impeller. No vortex low L is found there because this station lies in the straight part of the channel.

The core of the vortex low L is always formed in the field of both the lowest throughflow and the lowest pressure (Figs. 7, 10, 13, 16, and 20). Thus, the wake is a longitudinal vortex low L rotating in the same sense as the impeller (Chen et al., 1996). Very regular vorticities of the same sense are embedded in the vortex, so that a circulation can be assigned to it.

At Station 6 a second field of the lowest throughflow arises in the middle region of the hub side. This appears to be caused by the unsteadiness of the curvature of the blade at the outlet (Fig. 2).

### Reference

Chen, Y. N., Seidel, U., Haupt, U. and Rautenberg, M., 1996, "Jet Wake and Intrinsic Motion in Impellers of Centrifugal Compressors," ASME Paper 96-GT-261.

## Authors' Closure

The authors thank Dr. Chen for his discussion. The vortex pair (low L and high H) described by Dr. Chen is the classic secondary flow pattern generated through either passage curvature or rotation superimposed on a passage vortex which enhances the vortex H. The passage vortex, as Dr. Chen states, is a result of the change from a stationary coordinate system to a rotating one. The strength of the secondary flows is directly dependent on the boundary layer development and it is interesting that there is little evidence in the current results (for a pump) of secondary flow up the SS and PS of the blades whereas secondary flow is apparent here in a compressor impeller (Johnson and Moore, 1983a, b). This is believed to be because the blade boundary layers are only formed beyond the leading edge of the blade. For the pump, the blade leading edge is close to Station 2 at which point the flow has already been turned through about 45 deg in the axial to radial direction. Thus the effects of the axial to radial bend on secondary flow are greatly diminished. This leads to the wake (and vortex L) moving onto the suction surface earlier in the pump than in the compressor.

[1] By A. C. Bwalya and M. W. Johnson published in the December 1996 issue of the JOURNAL OF FLUIDS ENGINEERING, Vol. 118, No. 4, pp. 692–697.

[2] Sulzer Innotec Ltd., P.O. Box, CH-8401 Winterthur, Switzerland.